

Nano Mechanics and Materials

Nano Mechanics and Materials

Theory, Multiscale Methods and Applications

Wing Kam Liu

Northwestern University, Illinois, USA

Eduard G. Karpov

Northwestern University, Illinois, USA

Harold S. Park

Vanderbilt University, Tennessee, USA



John Wiley & Sons, Ltd

Copyright © 2006

John Wiley & Sons Ltd, The Atrium, Southern Gate, Chichester,
West Sussex PO19 8SQ, England

Telephone (+44) 1243 779777

Email (for orders and customer service enquiries): cs-books@wiley.co.uk
Visit our Home Page on www.wiley.com

All Rights Reserved. No part of this publication may be reproduced, stored in a retrieval system or transmitted in any form or by any means, electronic, mechanical, photocopying, recording, scanning or otherwise, except under the terms of the Copyright, Designs and Patents Act 1988 or under the terms of a licence issued by the Copyright Licensing Agency Ltd, 90 Tottenham Court Road, London W1T 4LP, UK, without the permission in writing of the Publisher. Requests to the Publisher should be addressed to the Permissions Department, John Wiley & Sons Ltd, The Atrium, Southern Gate, Chichester, West Sussex PO19 8SQ, England, or emailed to permreq@wiley.co.uk, or faxed to (+44) 1243 770620.

This publication is designed to provide accurate and authoritative information in regard to the subject matter covered. It is sold on the understanding that the Publisher is not engaged in rendering professional services. If professional advice or other expert assistance is required, the services of a competent professional should be sought.

Other Wiley Editorial Offices

John Wiley & Sons Inc., 111 River Street, Hoboken, NJ 07030, USA

Jossey-Bass, 989 Market Street, San Francisco, CA 94103-1741, USA

Wiley-VCH Verlag GmbH, Boschstr. 12, D-69469 Weinheim, Germany

John Wiley & Sons Australia Ltd, 42 McDougall Street, Milton, Queensland 4064, Australia

John Wiley & Sons (Asia) Pte Ltd, 2 Clementi Loop #02-01, Jin Xing Distripark, Singapore 129809

John Wiley & Sons Canada Ltd, 22 Worcester Road, Etobicoke, Ontario, Canada M9W 1L1

Wiley also publishes its books in a variety of electronic formats. Some content that appears in print may not be available in electronic books.

British Library Cataloguing in Publication Data

A catalogue record for this book is available from the British Library

ISBN-13: 978-0-470-01851-4

ISBN-10: 0-470-01851-8

Typeset in 10/12pt Times by Laserwords Private Limited, Chennai, India

Printed and bound in Great Britain by Antony Rowe Ltd, Chippenham, Wiltshire

This book is printed on acid-free paper responsibly manufactured from sustainable forestry
in which at least two trees are planted for each one used for paper production.

To Our Families

Contents

Preface	xi
1 Introduction	1
1.1 Potential of Nanoscale Engineering	1
1.2 Motivation for Multiple Scale Modeling	2
1.3 Educational Approach	5
2 Classical Molecular Dynamics	7
2.1 Mechanics of a System of Particles	7
2.1.1 Generalized Coordinates	8
2.1.2 Mechanical Forces and Potential Energy	8
2.1.3 Lagrange Equations of Motion	10
2.1.4 Integrals of Motion and Symmetric Fields	12
2.1.5 Newtonian Equations	13
2.1.6 Examples	14
2.2 Molecular Forces	17
2.2.1 External Fields	18
2.2.2 Pair-Wise Interaction	20
2.2.3 Multibody Interaction	24
2.2.4 Exercises	26
2.3 Molecular Dynamics Applications	28
3 Lattice Mechanics	37
3.1 Elements of Lattice Symmetries	37
3.1.1 Bravais Lattices	38
3.1.2 Basic Symmetry Principles	40
3.1.3 Crystallographic Directions and Planes	42
3.2 Equation of Motion of a Regular Lattice	42
3.2.1 Unit Cell and the Associate Substructure	43
3.2.2 Lattice Lagrangian and Equations of Motion	45
3.2.3 Examples	47
3.3 Transforms	49
3.3.1 Fourier Transform	50
3.3.2 Laplace Transform	51
3.3.3 Discrete Fourier Transform	53

3.4	Standing Waves in Lattices	54
3.4.1	Normal Modes and Dispersion Branches	55
3.4.2	Examples	57
3.5	Green's Function Methods	58
3.5.1	Solution for a Unit Pulse	59
3.5.2	Free Lattice with Initial Perturbations	61
3.5.3	Solution for Arbitrary Dynamic Loads	61
3.5.4	General Inhomogeneous Solution	62
3.5.5	Boundary Value Problems and the Time History Kernel	62
3.5.6	Examples	65
3.6	Quasi-Static Approximation	66
3.6.1	Equilibrium State Equation	66
3.6.2	Quasi-Static Green's Function	67
3.6.3	Multiscale Boundary Conditions	67
4	Methods of Thermodynamics and Statistical Mechanics	79
4.1	Basic Results of the Thermodynamic Method	80
4.1.1	State Equations	81
4.1.2	Energy Conservation Principle	84
4.1.3	Entropy and the Second Law of Thermodynamics	86
4.1.4	Nernst's Postulate	88
4.1.5	Thermodynamic Potentials	89
4.2	Statistics of Multiparticle Systems in Thermodynamic Equilibrium	91
4.2.1	Hamiltonian Formulation	92
4.2.2	Statistical Description of Multiparticle Systems	93
4.2.3	Microcanonical Ensemble	97
4.2.4	Canonical Ensemble	101
4.2.5	Maxwell–Boltzmann Distribution	104
4.2.6	Thermal Properties of Periodic Lattices	107
4.3	Numerical Heat Bath Techniques	111
4.3.1	Berendsen Thermostat	112
4.3.2	Nosé–Hoover Heat Bath	118
4.3.3	Phonon Method for Solid–Solid Interfaces	119
5	Introduction to Multiple Scale Modeling	123
5.1	MAAD	124
5.2	Coarse-Grained Molecular Dynamics	126
5.3	Quasi-Continuum Method	126
5.4	CADD	128
5.5	Bridging Domain	129
6	Introduction to Bridging Scale	131
6.1	Bridging Scale Fundamentals	131
6.1.1	Multiscale Equations of Motion	133
6.2	Removing Fine Scale Degrees of Freedom in Coarse Scale Region	136
6.2.1	Relationship of Lattice Mechanics to Finite Elements	137
6.2.2	Linearized MD Equation of Motion	139

6.2.3	Elimination of Fine Scale Degrees of Freedom	141
6.2.4	Commentary on Reduced Multiscale Formulation	143
6.2.5	Elimination of Fine Scale Degrees of Freedom: 3D Generalization	143
6.2.6	Numerical Implementation of Impedance Force	150
6.2.7	Numerical Implementation of Coupling Force	151
6.3	Discussion on the Damping Kernel Technique	152
6.3.1	Programming Algorithm for Time History Kernel	157
6.4	Cauchy–Born Rule	158
6.5	Virtual Atom Cluster Method	159
6.5.1	Motivations and General Formulation	159
6.5.2	General Idea of the VAC Model	163
6.5.3	Three-Way Concurrent Coupling with QM Method	164
6.5.4	Tight-Binding Method for Carbon Systems	167
6.5.5	Coupling with the VAC Model	169
6.6	Staggered Time Integration Algorithm	170
6.6.1	MD Update	170
6.6.2	FE Update	172
6.7	Summary of Bridging Scale Equations	172
6.8	Discussion on the Bridging Scale Method	173
7	Bridging Scale Numerical Examples	175
7.1	Comments on Time History Kernel	175
7.2	1D Bridging Scale Numerical Examples	176
7.2.1	Lennard-Jones Numerical Examples	176
7.2.2	Comparison of VAC Method and Cauchy–Born Rule	178
7.2.3	Truncation of Time History Kernel	179
7.3	2D/3D Bridging Scale Numerical Examples	182
7.4	Two-Dimensional Wave Propagation	184
7.5	Dynamic Crack Propagation in Two Dimensions	187
7.6	Dynamic Crack Propagation in Three Dimensions	195
7.7	Virtual Atom Cluster Numerical Examples	200
7.7.1	Bending of Carbon Nanotubes	200
7.7.2	VAC Coupling with Tight Binding	200
8	Non-Nearest Neighbor MD Boundary Condition	203
8.1	Introduction	203
8.2	Theoretical Formulation in 3D	203
8.2.1	Force Boundary Condition: 1D Illustration	207
8.2.2	Displacement Boundary Condition: 1D Illustration	210
8.2.3	Comparison to Nearest Neighbors Formulation	211
8.2.4	Advantages of Displacement Formulation	212
8.3	Numerical Examples: 1D Wave Propagation	212
8.4	Time-History Kernels for FCC Gold	213
8.5	Conclusion for the Bridging Scale Method	215
8.5.1	Bridging Scale Perspectives	220

9 Multiscale Methods for Material Design	223
9.1 Multiresolution Continuum Analysis	225
9.1.1 Generalized Stress and Deformation Measures	227
9.1.2 Interaction between Scales	231
9.1.3 Multiscale Materials Modeling	232
9.2 Multiscale Constitutive Modeling of Steels	234
9.2.1 Methodology and Approach	235
9.2.2 First-Principles Calculation	235
9.2.3 Hierarchical Unit Cell and Constitutive Model	237
9.2.4 Laboratory Specimen Scale: Simulation and Results	239
9.3 Bio-Inspired Materials	244
9.3.1 Mechanisms of Self-Healing in Materials	244
9.3.2 Shape-Memory Composites	246
9.3.3 Multiscale Continuum Modeling of SMA Composites	250
9.3.4 Issues of Modeling and Simulation	256
9.4 Summary and Future Research Directions	260
10 Bio–Nano Interface	263
10.1 Introduction	263
10.2 Immersed Finite Element Method	265
10.2.1 Formulation	265
10.2.2 Computational Algorithm of IFEM	268
10.3 Vascular Flow and Blood Rheology	269
10.3.1 Heart Model	269
10.3.2 Flexible Valve–Viscous Fluid Interaction	270
10.3.3 Angioplasty Stent	270
10.3.4 Monocyte Deposition	272
10.3.5 Platelet Adhesion and Blood Clotting	272
10.3.6 RBC Aggregation and Interaction	274
10.4 Electrohydrodynamic Coupling	280
10.4.1 Maxwell Equations	281
10.4.2 Electro-manipulation	283
10.4.3 Rotation of CNTs Induced by Electroosmotic Flow	285
10.5 CNT/DNA Assembly Simulation	287
10.6 Cell Migration and Cell–Substrate Adhesion	290
10.7 Conclusions	295
Appendix A Kernel Matrices for EAM Potential	297
Bibliography	301
Index	315

Preface

Within the past decade, the emphasis of scientific research worldwide has shifted to the study of the behavior of materials at the atomic scale of matter. The proliferation of scientists and engineers studying matter at this length scale has led to the coining of the phrase *nanotechnology*. This term can generally be taken to imply the investigation and technological utilization of the properties of matter at length scales of one thousand nanometers or smaller. Generally, a few thousand atoms will exist in the space of thousand nanometers.

As engineers typically study the mechanical properties of materials, the corresponding emphasis of research in the engineering community has been on *nano mechanics*. The term “nano mechanics” is typically associated with the study and characterization of the mechanical behavior of individual atoms, atomic-scale systems and structures in response to various types of forces and loading conditions. The specific nature of nano mechanics research generally varies depending on the discipline of the engineer; the topic of interest can involve the atomic-scale effect of fracture and wear on material performance, mechanical properties of nanocomposites, atomic-scale flow and locomotion of individual biological cells.

Regardless of the interest of the particular scientist or engineer, what is universally agreed upon is the overall potential that nanotechnology, and particularly nano mechanics, has for the betterment of our society, including the sectors of private industry, national defense and homeland security. An emphasis on nanoscale entities will make our manufacturing technologies and infrastructure more sustainable in terms of reduced energy usage and environmental pollution. Recent advances made by the research community in this topic have stimulated ever-broader research activities in science and engineering that are devoted to their development and applications.

Many areas of research are rapidly advancing owing to the combined efforts of science and engineering. In mechanics and materials, we are particularly excited with the progress in research and education that can be achieved by combining engineering and basic sciences through modeling and simulation together with experimentation. Owing to the combination of constantly increasing computational power and the increased knowledge and understanding of material behavior, *multiple scale modeling methods* have recently emerged as the tool of choice to link the mechanical behavior of materials from the smallest scale of atoms to the largest scale of structures. Multiple scale methods offer the best hope for bridging the traditional gap that exists between experimental approach, the theoretical approach and computational modeling for studying and understanding the behavior of materials.

Owing to the central role that multiple scale methodology appears poised to play in the computational mechanics and materials science in the foreseeable future, this book aims to summarize the past and the current developments in multiple scale modeling to

provide a coherent starting point from which interested scientists and engineers can begin their journey into this vast and rapidly expanding subject. We hope that this book is one of the first systematic works aimed at providing knowledge about fundamental concepts behind nanoscale mechanics and materials and the relevant applications. The book contains both published and previously unpublished material and is aimed at nanoscale engineers, designers, materials scientists and interested students and researchers.

A salient feature of this book is that it is also intended to be used as an educational tool. The major reason is to synthesize the state of the art in multiple scale modeling techniques into the classroom such that the crucial tools being made available today are passed onto the next generation of scientists and engineers. Thus, the materials in this book which were previously used for courses at Northwestern University and the National Science Foundation (NSF) Summer Institute on Nano Mechanics and Materials have been coherently combined with Powerpoint lecture notes and selected computer codes (available online at www.wiley.com/go/nanomechanics) to make the material presented readily accessible for those researchers who are interested in joining and contributing to the field of multiple scale modeling and analysis. Along with the review of basic theoretical concepts, they present the solutions and dynamic visualization of numerous practical problems, ranging from simple one-dimensional systems to state-of-the-art applications. The solutions of the simple illustrative problems are augmented by Matlab and Mathematica codes which serve to highlight the numerical implementation of the theoretical approaches presented in this book.

There are many other novel and unique aspects to this book. As mentioned above, the integration of teaching and research is one of the key features. The material contains detailed expositions on all the topics that are necessary to fully comprehend multiple scale analysis. As such, the book is logically divided into three parts. The first part consists of Chapters 2–4, which cover the theoretical basis needed to understand the behavior of multiparticle atomistic systems. The second part consists of Chapters 5–8, and introduces multiple scale methods. In particular, the bridging scale concurrent approach, which is based on the theoretical considerations provided in the first part of the book, is given special attention here. The third part comprising Chapters 9–10 is devoted to contemporary applications in the area of nanostructured and bioinspired materials, biofluidics and cell mechanics.

Chapter 1 contains an introduction, and emphasizes the need for multiple scale simulations by presenting case studies from different scientific disciplines, including materials design and biofluidics. Chapter 2 introduces the notion of Lagrangian dynamics description of systems of interacting particles, including nonconservative equations of motion, multi-body interatomic potentials and arbitrary molecular shapes. Chapter 3 details the extension of the Lagrangian method to spatially periodic lattice structures; it reviews the relevant symmetry concepts, and derives the basic response solutions for a general three-dimensional lattice in semianalytical forms that are important in nanoscale engineering applications. Chapter 4 gives a systematic, though condensed, exposition on contemporary approaches that allow an averaged macroscopic characterization of multiparticle systems in thermodynamic equilibrium; these include the methods of thermodynamic potentials, statistical averaging, microcanonical and canonical ensemble theories.

Chapter 5 provides an overview of multiple scale modeling. As such, previously developed multiple scale methods are reviewed and analyzed, and capabilities that are needed in

multiple scale modeling are discussed and provided as a basis for the remaining chapters. Chapter 6 introduces the bridging scale concurrent method, which couples atomistic and continuum scale models; here, connections are made between the bridging scale, particle dynamics and lattice mechanics concepts introduced in Chapters 2–3.

Numerical validation of the bridging scale approach is given in Chapter 7. The numerical examples in one, two and three dimensions highlight the applicability of the bridging scale to highly nonlinear physical phenomena, including the fracture and subsequent failure of materials. The recent extension of the bridging scale to incorporate quantum mechanical information into the coupling of length scales framework is also described in this chapter. Chapter 8 provides an extension of the MD impedance force such that it can be utilized with long-ranged interatomic potentials; this extension is crucial as most realistic interatomic potentials incorporate non-nearest neighbor bonding. This chapter concludes the section on multiple scale modeling with comments on future research directions.

Chapter 9 highlights applications of multiple scale methods in crucial areas of physical interest. In the realm of solids, the topics covered are the hierarchical and concurrent design of realistic materials, including novel steel and metallic alloys, shape memory composites and self-healing materials. Lastly, Chapter 10 emphasizes new research in the area of computational biofluidics, electrohydrodynamics, bioengineering and nano-bio interfacial problems. The topics include electrophoresis multiscale and multiphysics modeling of red blood cell (RBC) aggregation and the effect on blood rheology, capillary flow, cell migration, nanomanipulation and assembly of macromolecules.

We would like to thank our colleagues and graduate students for their contributions to this book, in particular, Ted Belytschko, Antonio Bouze, Dmitry Dorofeev, David Farrell, Mark Horstemeyer, Sukky Jun, Hiroshi Kadowaki, Adrian Kopacz, Yaling Liu, Cahal McVeigh, Sergey Medyanik, Dong Qian, Leonid Shilkrot, Shaoqiang Tang, Franck Vernerey and Sulin Zhang. Finally, we would like to thank and acknowledge the following sponsors for their support: the National Science Foundation (NSF), the NSF Summer Institute on Nano Mechanics and Materials, the NSF Integrative Graduate Education and Research Traineeship (IGERT) program, the Army Research Office (ARO), the Office of Naval Research (ONR) CyberSteel 2020 project and the ONR Nanofilament-Based Combined Chemical/Biological Detectors Project.

Evanston, Illinois
Nashville, Tennessee

*Wing Kam Liu
Eduard G. Karpov
Harold S. Park*

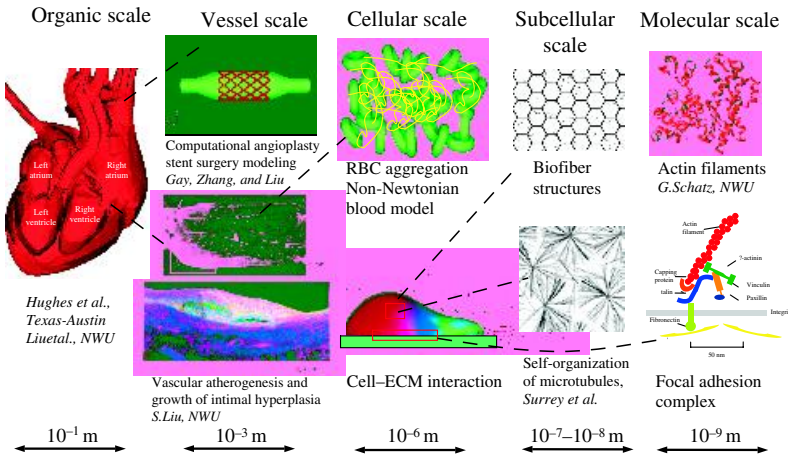


Plate 1 Modeling of biological processes using multiscale techniques. Middle image in the second column is reproduced from Liu (1998) with permission from Elsevier. Reprinted from Atherosclerosis, 140(2), Liu S. Q., Prevention of focal intimal hyperplasia in rat vein grafts by using a tissue engineering approach, 365–377, 1998, with permission from Elsevier.

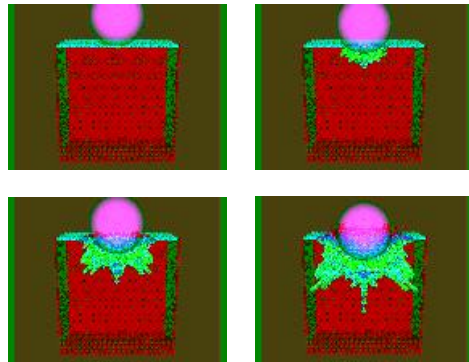


Plate 2 Deposition of an amorphous carbon film (green atoms) on top of a diamond substrate (red atoms).

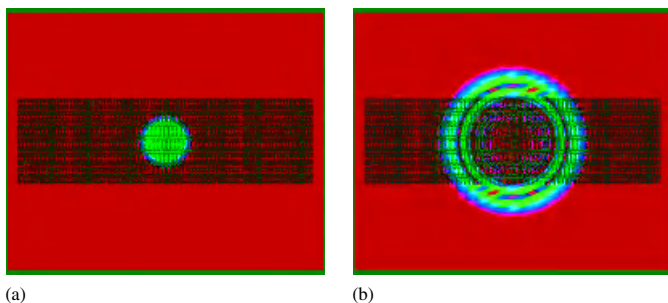


Plate 3 Initial conditions for two-dimensional wave propagation example. Contours of displacement magnitude shown. A later snapshot of wave propagation from the MD region into the continuum region. Contours of displacement magnitude shown. Reproduced from Park et al. (2005c) with permission from Taylor & Francis.

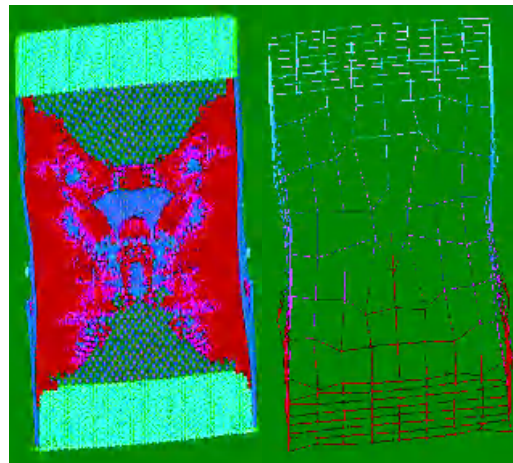


Plate 4 Snapshots of FEM deformation as a response to MD crack propagation. Reprinted from Journal of Computational Physics, 207(2), Park et al., Three-dimensional bridging scale analysis of dynamic fracture, 588–609, 2005, with permission from Elsevier.

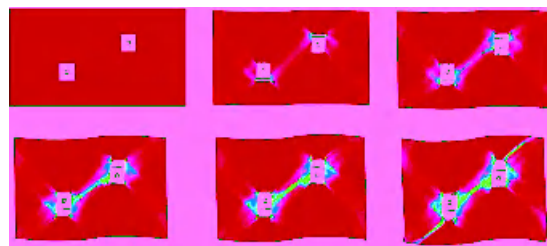


Plate 5 Submicro scale mechanism of failure between two microscale voids. High stress between the voids leads to debonding of submicro scale particles, and eventual void linkage.

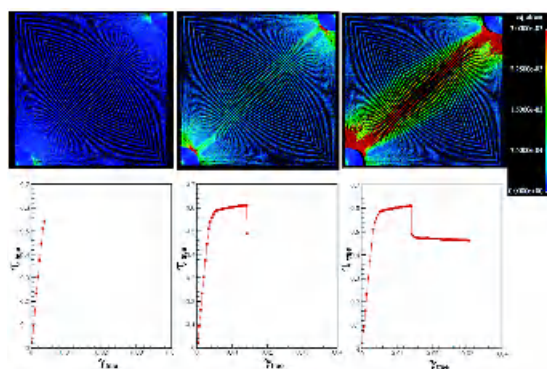


Plate 6 Snap-shots of the localization-induced debonding process. Reprinted from Computer Methods in Applied Mechanics and Engineering, 193, Hao et al., Multi-scale constitutive model and computational framework for the design of ultra-high strength, high toughness steels, 1865–1908, 2004, with permission from Elsevier.

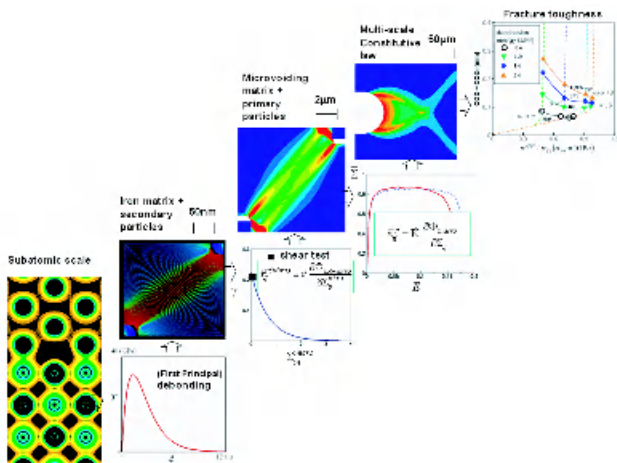


Plate 7 Ductile fracture simulator. Reprinted from Computer Methods in Applied Mechanics and Engineering, 193, Hao et al., Multi-scale constitutive model and computational framework for the design of ultra-high strength, high toughness steels, 1865–1908, 2004, with permission from Elsevier.

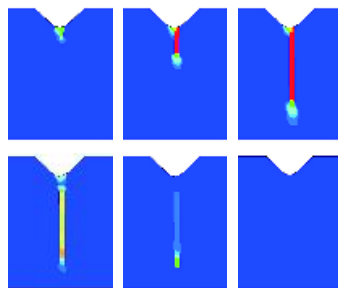


Plate 8 Homogenized continuum modeling of crack propagation and healing in the BSS SMA composite.

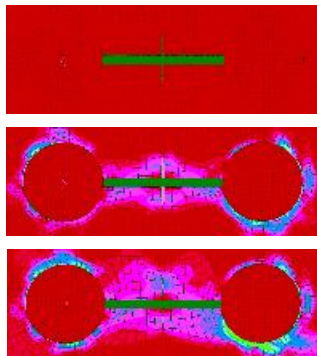
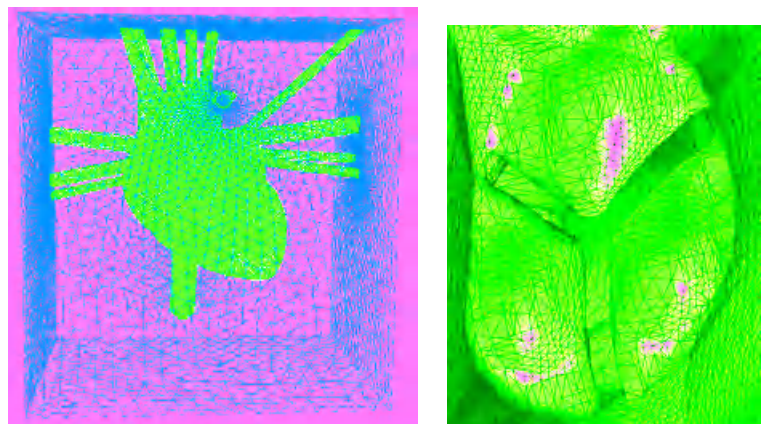


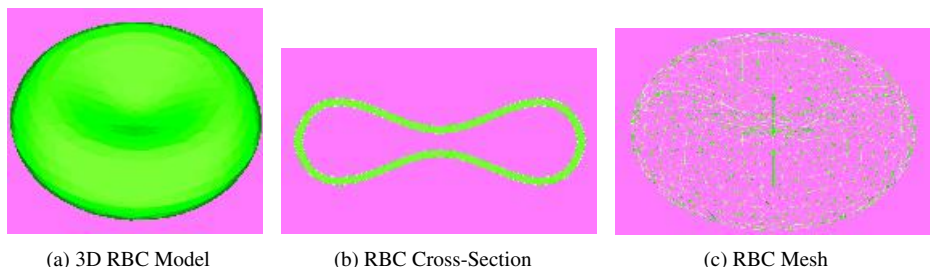
Plate 9 Fiber–matrix debonding in the SMA composite on the course of a fracture–healing cycle. Seen on the middle and bottom snapshots of this simulation, voids are formed in between the spherical parts of the reinforcing inclusion and the matrix material.



(a) Heart model immersed in fluid mesh

(b) Aortic valve

Plate 10 The Heart model (Liu et al. 2004b).



(a) 3D RBC Model

(b) RBC Cross-Section

(c) RBC Mesh

Plate 11 Three-dimensional finite element mesh of a single RBC model. Reproduced with permission from Liu Y et al., International Journal for Numerical Methods in Fluids, published by John Wiley and Sons Ltd, 2004.

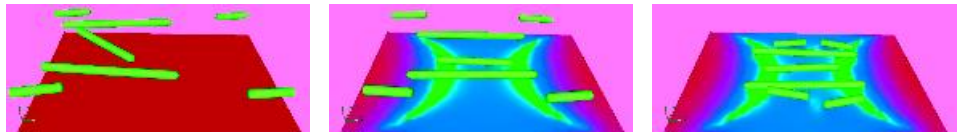


Plate 12 Simulation of the assembly of CNTs between semicircular electrodes by the application of an AC field. Three processes of assembly, namely, the transport, attraction and alignment of the nanotubes are shown.

1

Introduction

Over the past three decades, we have acquired new tools and techniques to synthesize nanoscale objects and learn their many incredible properties. The high-resolution electron microscopes that are available today enable the visualization of single atoms; furthermore, the manipulation of these individual atoms is possible using scanning probe techniques. Synthesis of advanced materials provides the technology to tailor-design systems from as small as molecules to as large as the fuselage of a plane. We now have the technology to detect single molecules, bacteria or virus particles. We can make protective coatings more wear-resistant than diamond and fabricate alloys and composites such that they are stronger than ever before. Advances in the synthesis of nanoscale materials have stimulated ever-broader research activities in science and engineering devoted entirely to these materials and their applications. This is due in large part to the combination of their expected structural perfection, small size, low density, high stiffness, high strength and excellent electronic properties. As a result, nanoscale materials may find use in a wide range of applications in material reinforcement, field emission panel display, chemical sensing, drug delivery, nanoelectronics and tailor-designed materials. Nanoscale devices have a great potential as sensors and medical diagnostic and delivery systems.

With the confluence of interest in nanotechnology, the availability of experimental tools to synthesize and characterize systems at the nanometer scale, and computational tools widely accessible to model microscale systems by coupled continuum/molecular/quantum mechanics, we are poised to unravel the traditional gap between the atomic and the macroscopic world of mechanics and materials. This in turn opens up new opportunities in education and research.

1.1 Potential of Nanoscale Engineering

Nanotechnology is making, and will continue to make, an impact in key areas for societal improvement. In particular, it has been found that basic mechanics principles have found many applications in nanoscience and nanoengineering. For example, current research

efforts deal with the application of cell mechanics to neurobiology and cancer research. Currently, a key limitation is in understanding the behavior of the myriad of different cellular structures, interactions and adhesive forces. Once this is established, these mechanisms can be used to develop treatment strategies for cancer, for example, in the prevention of metastasis.

The design and production of materials from the atomic scale up is a goal that is becoming increasingly realizable by the application of DNA to nanotechnology and biotechnology. Owing to the predictable manner in which DNA strands interact, research is now being performed to design solid materials by manipulating individual DNA strands as the basic building blocks. Use of DNA will lead to new materials with novel mechanical, chemical and optical properties, controllable at the unit of the basic building block.

Nanotechnology also has the potential to greatly improve our resistance to terrorism and improve our national security by improving the technologies available to our armed forces. Nanoscale sensors are being developed for the purpose of detecting illegal and harmful airborne chemicals. Our soldiers will benefit from new, energy-absorbing polymer-based nanomaterials that will provide ballistic protection while being light enough to allow maximum mobility. Research along these crucial lines is being done, for example, at the MIT Institute for Soldier Nanotechnologies.

Protective coatings is another area that has greatly benefited from nanotechnology. These coatings have a wide range of applicability, examples being gears and bearings in the automotive industry, and naval vessels for the military. In all these applications, the goal has been to replace or augment previously known super hard materials such as diamond in designing tribological parts that use nanoceramic-type coatings to reduce friction and wear. Extending the lifetime of these parts is crucial, and will lead to a massive reduction in maintenance costs for these components.

Another key area in nanotechnology is in electronics, microelectromechanical systems (MEMS) and nanoelectromechanical systems (NEMS). For example, the storage capacity of computer hard drives has been increased by orders of magnitude, thanks to magnetic materials whose thickness is on the order of nanometers. Medicine is another key area in which NEMS and MEMS devices have made, and will make, large contributions. Here, nanotechnology can be used to dynamically image living biological systems, such that the real-time study of bacteria and diseases can be performed.

1.2 Motivation for Multiple Scale Modeling

Current research in engineering is just beginning to impact molecular scale mechanics and materials and would benefit from interaction with the basic sciences. For solids, research in the area of plasticity and damage has experienced some success in advancing microscale component design. The development of carbon nanotubes is also an area in which nanoscale research has clearly played a major role. For fluids, coupling physics phenomena at the nanoscale is crucial in designing components at the microscale. Electrophoresis and electroosmotic flows coupled with particulate motion in a liquid have been important research areas that have had great impact in the homeland security area. Microfluidic devices often comprise components that couple chemistry, and even electrochemistry, with fluid motion. Once the physics-based models are determined for the solids and fluids,

computational approaches will need to be employed or developed to capture the coupled physics phenomena.

While microscale and nanoscale systems and processes are becoming more viable for engineering applications, our knowledge of their behavior and our ability to model their performance remains limited. Continuum-based computational capabilities are obviously not applicable over the full range of operational conditions of these devices. Noncontinuum behavior is observed in large deformation behavior of nanotubes, ion deposition processes, gas dynamic transport, and material mechanics as characteristic scales drop toward the micron scale. At the scales of nanodevices, interactions between thermal effects and mechanical response can become increasingly important.

Furthermore, nanoscale components will be used in conjunction with components that are larger and respond at different timescales. In such hybrid systems, the interaction of different time and length scales may play a crucial role in the performance of the complete system. Single scale methods such as ab initio methods or molecular dynamics (MD) would have difficulty in analyzing such hybrid structures owing to the large range of timescales and length scales. For the design and study of nanoscale materials and devices in microscale systems, models must span length scales from nanometers to hundreds of microns.

Computational power has doubled approximately every 18 months, in accordance with Moore's law. Despite this fact and the fact that desktop computers can now routinely simulate million atom systems, simulations of realistic atomic system require at least tens of billions of atoms. In short, such systems cannot be modeled by continuum methods, because they are too small, nor can they be modeled by molecular methods because they are too large. Hence, coupled multiscale methods are urgently needed for this class of problems.

Multiple scale methods generally imply the utilization of information at one length scale to subsequently model the response of the material at larger length scales. These methods can be divided into two categories: hierarchical and concurrent. Hierarchical multiple scale methods directly utilize the information at a small length scale as an input into a larger model via some type of averaging process. The Young's modulus is a good example of this; the structural material stiffness is found as a single quantity, through homogenization of all defects and microstructure at the micro- and nanoscales. Concurrent multiple scale methods are those that run simultaneously; in these methods, the information at the smaller length scale is calculated and inputted into the larger scale model on the fly. In this book, we shall concentrate on the development of concurrent multiple scale methods, much of which has occurred within the past decade. We note in particular the work of Li and Liu (2004), as well as two excellent review papers that comprehensively cover the field, namely, those of Liu et al. (2004c) and Curtin and Miller (2003).

Multiscale simulation methods will be a valuable tool in design; just as computer-aided engineering (CAE) on the microscale was facilitated by finite element methods. We envision that the availability of tools for multiscale analysis will provide a powerful impetus to the development of new nanodevices. More specifically, we believe that the next generation of CAE software will integrate nano and microstructures into the fundamental CAE capabilities for design and manufacturing. To move toward this goal, the development and validation of predictive multiscale simulation models that integrate materials design into virtual manufacturing processes is imperative. These multiscale models must incorporate

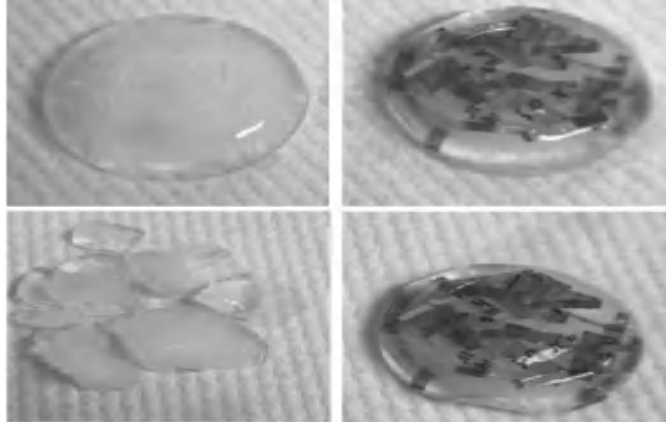


Figure 1.1 Left: brittle fracture of non-reinforced ice after drop test. Right: unbroken reinforced ice after drop test. Images are courtesy of Prof. Yip-Wah Chung, Northwestern University.

the statistical nature of defects and uncertainty analysis in processing and modeling in order to be considered complete.

A simple example of the necessity to account for microstructure in material modeling is shown in Figure 1.1. In the first case, a simple block of ice is dropped from a certain height onto the ground; as can be seen, the ice fractures into multiple pieces, reflecting its brittle nature. In the second case, the ice has been reinforced by strips of newspaper. Upon being dropped from the same height, the block of ice stays intact, and does not break. Clearly, the added microstructural effects in the form of the newspaper dramatically enhanced the strength of the ice.

A real-life example of the strengthening properties of material microstructure is given in Figure 1.2. There, the various complicated deformation mechanisms that exist at different material length scales in a typical high-strength steel is illustrated in a schematic. As can be seen, the overall structural response of the steel is governed by the interactions between the inclusions, second phase particles and defects that occur in the steel at different length scales. The TiN primary inclusions are typically micron sized, and govern fracture toughness due to decohesion and debonding. The secondary TiC inclusions are typically nanometer sized, and provide strengthening after yield by controlling the interfacial separation. Thus, the resultant mechanical properties of the steel are a competition between strength and toughness, with the inclusions at different scales dominating at each end of the spectrum.

We emphasize that while the mechanical response of the steel can be modeled hierarchically, that is, by using average properties from smaller length scales to control the macroscopic response, it is currently impossible to concurrently model all the way from atomistics to continuum without leaving out the crucial intermediate, mesoscopic length scales. Modeling from atoms to continuum represents a grand challenge in material design

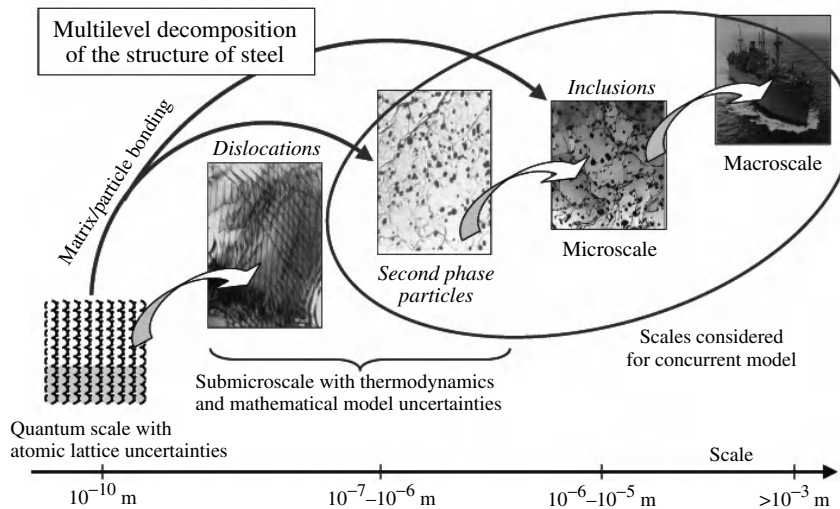


Figure 1.2 Multiple scale properties of steel.

and solid mechanics; a focus of this book is on the development of efficient computational techniques and algorithms to assist in the modeling process.

In nano-bio systems, the multiple scale mechanics of the human heart is seen in Plate 1. The heart and its associated arteries, veins, valves and blood represent the smallest scale at which continuum solid and fluids mechanics can be utilized to model the heart as an elastic body. The second scale is the vessel scale, where the properties of the vessel wall and thrombus deposition on the wall are the interactions of interest. The third scale is the cellular scale, where blood components such as red blood cells, white cells, platelets, as well as their interactions are considered. At these small scales, the blood needs to be simulated using a non-Newtonian model. The smallest scale under consideration is the subcellular scale, where the biofibers, focal adhesion complexes, and other macromolecules and substructures are studied utilizing MD or some hybrid method. The goal of the multiple scale modeling is to better understand the nature of cellular forces and adhesion; as the blood flows in the vessel, cells and proteins in the blood may deposit onto the vessel wall and may finally block the blood flow, leading to heart attacks. The understanding of cellular interactions will result in the development of computational models that can assist in the accuracy of treatments to retard metastasis.

1.3 Educational Approach

The material presented in this book provides information to researchers and educators about specific fundamental concepts and tools in nanomechanics and materials, including solids and fluids, and their modeling via multiple scale methods and techniques. In recognition of

the importance of engineering education, a key component of this book is in the synthesis of the literature with Powerpoint instructional slides, which were used as the basis for two newly developed courses at Northwestern entitled Multiscale Simulations and Molecular Modeling and the Interface to Micromechanics. Furthermore, these lecture notes were utilized as the basis for the interdisciplinary NSF-sponsored Summer Institute on Nano Mechanics and Materials (www.tam.northwestern.edu/summerinstitute/Home.htm), which has been held at Northwestern for the past three summers. These lecture notes, in combination with instructional computer programs that cover all fundamental concepts introduced in the book, will serve as a starting point from which interested researchers may jump into and contribute to the emerging field of computational nanotechnology.

We would like to emphasize that this book is specifically oriented towards the study of nanomechanics. The emphasis on nanomechanics is a crucial point, as nanomechanics serves as a theoretical foundation of nanotechnology in the area of nanoscale materials as well as biomechanical systems. Our goal in this book is to demonstrate methods for modeling the mechanical behavior of materials at the nanoscale, while interpreting that behavior in a larger context. These models will then be tested on modern applications to validate the approaches presented.

Traditional educators and researchers in mechanics and materials are well versed in continuum mechanics including topics such as elasticity, plasticity, dislocations and fracture. As we evolve toward smaller and smaller components and systems, there is no doubt that we must move beyond continuum treatments into characterizations of mechanics and materials at the nanoscale. Therefore, the material presented in this book is invaluable for introducing engineers to the fundamental methods of modeling and characterization of nano and multiscale systems, that is, molecular dynamics, statistical physics and quantum mechanics. These tools, when combined with continuum mechanics and multiple scale modeling, will allow engineers to continue the fruitful collaborations with scientists who have been responsible for the surge in interest in nanoscale engineering.

One important impact of engineering education is the multiplying effect. Participants may launch their own initiatives in nanotechnology, such as curriculum development or enhancement, initiation of new research ideas or products, and so on. Since engineers are not trained in the fields that bridge the nanosciences with engineering, their training is of great importance in providing society useful applications of these technologies. Training for those in the basic sciences is also needed to bring products of practical use from these technologies to the marketplace. This book will serve these needs by providing education and resource for both engineers and scientists in the technologies that bridge the nanosciences with engineering.

2

Classical Molecular Dynamics

This chapter is devoted to the methods of classical mechanics that allow the study of the motion of gas, liquid and solid particles as a system of interactive, dimensionless mass points. The classical dynamic equations of motion are valid for slow and heavy particles, with typical velocities $v \ll c$, c being the speed of light, and masses $m \gg m_e$, m_e being the electron mass. Therefore, only slow motion (slower than thermal vibrations) of atoms, ions and molecules can be considered, and the internal electronic structure is ignored. The atoms and molecules exert internal forces on each other that are determined by instantaneous values of the total potential energy of the system. The potential energy is typically considered only as a function of the system spatial configuration and is described by means of *interatomic potentials*. These potentials are considered as known input information; they are either found experimentally or are computed by averaging over the motion of the valence electrons in the ion's Coulomb field by means of quantum ab initio methods. During the course of the system's dynamics, the interatomic potentials are not perturbed by possible changes in the internal electronic states of the simulated particles.

Analytical solutions of the equations of particle dynamics are possible only for a limited set of interesting problems and only for systems with a small number of degrees of freedom. Numerical methods of solving the classical equations of motion for multiparticle systems with known interatomic potentials are collectively referred to as *molecular dynamics (MD)*. MD is regarded as a major practical application of the classical particle dynamics. The subsequent computer postprocessing and visualization of the results accomplished in a dynamic manner are called the *molecular dynamics simulation*.

2.1 Mechanics of a System of Particles

Classical dynamics studies the motion of mass points (ideal dimensionless particles) due to known *forces* exerted on them. These forces serve as qualitative characteristics of the interaction of particles with each other (internal forces) and with exterior bodies (external forces). The general task of dynamics consists in solving for the positions (trajectories) of all particles in a given mechanical system over the course of time. In principle, such a solution

is uniquely determined by a set of initial conditions, that is, positions and velocities of all particles at time $t = 0$ and the interaction forces. If there are no external forces applied to the system, then this system is *isolated* or *closed*; otherwise it is called *nonisolated*.

2.1.1 Generalized Coordinates

The spatial configuration of N dimensionless particles can be determined by N radius vectors $\mathbf{r}_1, \mathbf{r}_2, \dots, \mathbf{r}_N$, or by $3N$ coordinates (Cartesian x_i, y_i, z_i , spherical r_i, θ_i, ϕ_i , etc.). In some cases, the motion of these particles is constrained in a specific manner, that is, under given provisos it cannot be absolutely arbitrary. Then, we say that such a system has *mechanical constraints*, and the system itself is called *constrained*; otherwise, the system is called *nonconstrained*. If some mechanical constraint can be expressed as a function of the coordinates of the particles,

$$f(\mathbf{r}_1, \mathbf{r}_2, \dots, \mathbf{r}_N) = 0, \quad (2.1)$$

we call them *holonomic*; otherwise they are called *nonholonomic*. Examples of systems with holonomic constraints are a pendulum in the field of gravity and gas diatomic molecules with rigid interatomic bonding.

In the presence of k holonomic constraints of the type (2.1), there exist only $s = 3N - k$ independent coordinates. Any s independent variables q_1, q_2, \dots, q_s (lengths, angles, etc.) that fully determine the spatial configuration of the system are referred to as the *generalized coordinates*, and their time derivatives $\dot{q}_1, \dot{q}_2, \dots, \dot{q}_s$ are referred to as the *generalized velocities*. The relationship between the radius vectors and the generalized coordinates can be expressed by the *transformation equations*

$$\mathbf{r}_i = \mathbf{r}_i(q_1, q_2, \dots, q_s), \quad i = 1, 2, \dots, N \quad (2.2)$$

which provide parametric representations of the old coordinates \mathbf{r}_i in terms of the new coordinates q_i . The corresponding velocities are given by

$$\mathbf{v}_i = \dot{\mathbf{r}}_i = \frac{\partial \mathbf{r}_i}{\partial t} + \sum_{j=1}^s \frac{\partial \mathbf{r}_i}{\partial q_j} \dot{q}_j, \quad i = 1, 2, \dots, N \quad (2.3)$$

The transformations are assumed to be invertible, that is, the equations (2.2) combined with the constraint rules (2.1) can be inverted to obtain the generalized coordinates as functions of the radius vectors.

2.1.2 Mechanical Forces and Potential Energy

Besides being classified as internal or external, all mechanical forces in a system of particles can be classified as *conservative* or *nonconservative*. Conservative forces are those whose work depends *only* on positions of the particles, without regard to their instantaneous velocities and trajectories of passage between these positions. For any loop of the trajectory, the work of conservative forces is zero (Figure 2.1):

$$A_{12} + A_{21} = 0 \quad (2.4)$$

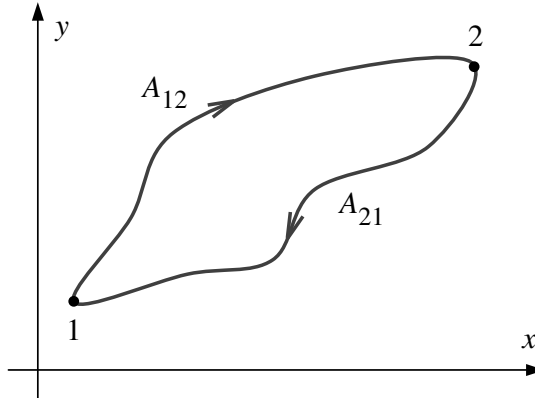


Figure 2.1 Looped trajectory of a particle moving in the xy -plane. Mechanical work of conservative forces is zero (equation (2.4)).

Example: The electrostatic force between a pair of monoatomic ions is conservative, because at the current time t it depends only on the instantaneous separation distance $r(t) = |\mathbf{r}_2(t) - \mathbf{r}_1(t)|$. This force is independent of the atomic velocities at all times, as well as the atomic positions at all *earlier* times $\tau < t$. Conservative forces are said to be independent of the *time history*, $r(\tau)$, of the atomic motion.

All forces not qualifying as conservative are called *nonconservative*. They comprise two major types: dissipative and gyroscopic. Forces of mechanical friction and viscous friction in gases and liquids are dissipative. Current magnitudes and directions of dissipative forces may depend on instantaneous velocities and/or a time history of the atomic motion in the system. The work of these forces in a closed system is always negative, including the case of looped trajectories,

$$A_{12} + A_{21} < 0 \quad (2.5)$$

Gyroscopic forces depend on instantaneous velocities of particles and act in directions that are orthogonal to these velocities. The work of these forces is always trivial over the course of motion of the particles. Examples of gyroscopic forces are the Coriolis forces, felt by mass particles moving in a rotating coordinate system inward or outward from the axis of rotation as well as the Lorentz forces felt by charged particles moving in a magnetic field.

For a system characterized by only conservative forces, there exists a specific function of coordinates of the particles,

$$U = U(\mathbf{r}_1, \mathbf{r}_2, \dots, \mathbf{r}_N) \quad (2.6)$$

called the *potential energy*, or simply the *potential*, of the system. At the same time, partial derivatives of U with respect to the coordinates of a particle i yield the corresponding components of the resultant force felt by this particle because of the potential U , that is,

$$\mathbf{F}_i = -\frac{dU}{d\mathbf{r}_i} = -\left(\frac{\partial}{\partial x_i} + \frac{\partial}{\partial y_i} + \frac{\partial}{\partial z_i}\right)U \equiv -\nabla_i U, \quad i = 1, 2, \dots, N \quad (2.7)$$

2.1.3 Lagrange Equations of Motion

An arbitrary system of N particles with k holonomic constraints is described by the *Lagrange equations of motion* (Goldstein 1980)

$$\frac{d}{dt} \left(\frac{\partial T}{\partial \dot{q}_j} \right) - \frac{\partial T}{\partial q_j} = Q_j, \quad j = 1, 2, \dots, s \quad (2.8)$$

where $s = 3N - k$ is the total number of independent degrees of freedom and Q_j are the *generalized forces*,

$$Q_j = \sum_{i=1}^N \Phi_i \frac{\partial \mathbf{r}_i}{\partial q_j} \quad (2.9)$$

Here, Φ_i is the resultant of *all* forces felt by the i th particle and T is the full *kinetic energy* of the system. The form of the kinetic energy function can be elucidated on the basis of the classical frame invariance principle that requires invariance of the equations of motion with regard to the choice of inertial coordinate systems. These arguments provide (Landau and Lifshitz 1976)

$$T = \sum_{i=1}^N \frac{m_i \dot{r}_i^2}{2}, \quad \dot{r}_i^2 = \dot{x}_i^2 + \dot{y}_i^2 + \dot{z}_i^2 \quad (2.10)$$

where m_i are the masses of the particles.

For a system with only conservative forces related to the system's potential according to (2.7), the Lagrange equations (2.8) are simplified by employing (2.7) in (2.9), and accounting for the velocity-independent form of the potential energy (2.6). This gives

$$\frac{d}{dt} \frac{\partial L}{\partial \dot{q}_j} - \frac{\partial L}{\partial q_j} = 0, \quad j = 1, 2, \dots, s \quad (2.11)$$

and, in particular, for the case of $k = 0$ (a nonconstrained system),

$$\frac{d}{dt} \frac{\partial L}{\partial \dot{\mathbf{r}}_i} - \frac{\partial L}{\partial \mathbf{r}_i} = \mathbf{0}, \quad i = 1, 2, \dots, N \quad (2.12)$$

Here,

$$L = T - U \quad (2.13)$$

is the *Lagrange function* or *Lagrangian* of a system of interacting particles. The specific form of the Lagrange function is determined by the intrinsic mechanical properties of the system. The potential energy term in L can be added with an arbitrary constant U_0 ; this will not alter the equations of motion.

In the presence of nonconservative forces in the system, the Lagrange equations take the form

$$\frac{d}{dt} \frac{\partial L}{\partial \dot{q}_j} - \frac{\partial L}{\partial q_j} = \sum_{i=1}^N \mathbf{F}_i \frac{\partial \mathbf{r}_i}{\partial q_j}, \quad j = 1, 2, \dots, s \quad (2.14)$$

or

$$\frac{d}{dt} \frac{\partial L}{\partial \dot{\mathbf{r}}_i} - \frac{\partial L}{\partial \mathbf{r}_i} = \mathbf{F}_i, \quad i = 1, 2, \dots, N \quad (2.15)$$

for constrained and nonconstrained systems, respectively. Here, \mathbf{F}_i is the resultant of all nonconservative forces felt by the i th particle. Nonconservative forces, in general, may explicitly depend on time.

According to the general theory of ordinary differential equations, the unique solution of the Lagrangian equations requires $2s$ *initial conditions*. These are initial positions and velocities for all degrees of freedom in the system, viewed as a $2s$ -component vector

$$\mathbf{A} = [q_1(0) \dots q_s(0) \dot{q}_1(0) \dots \dot{q}_s(0)] \quad (2.16)$$

Provided that the Lagrangian (2.13) and nonconservative forces are known for a given system, the Lagrange equations of motion have unique solutions (trajectories) for all the generalized coordinates. These solutions are considered functions of time and the initial conditions, and they comprise a time-dependent vector \mathbf{Q} that completely describes the mechanical state of the system at any given time t .

$$\mathbf{Q}(t) = [q_1(t, \mathbf{A}) \dots q_s(t, \mathbf{A}) \dot{q}_1(t, \mathbf{A}) \dots \dot{q}_s(t, \mathbf{A})] \quad (2.17)$$

By substituting the generalized coordinates from (2.17) into (2.2), one obtains the time-dependent radius vectors,

$$\mathbf{r}_1(t, \mathbf{A}), \mathbf{r}_2(t, \mathbf{A}), \dots, \mathbf{r}_N(t, \mathbf{A}) \quad (2.18)$$

that is, trajectories, of all particles in the system. The dependence of the solutions (2.17) and (2.18) on the vector of initial conditions \mathbf{A} is often omitted.

Combining (2.10) and (2.6), we get the general form of the Lagrange function for a system of N nonconstrained mass points in Cartesian coordinates,

$$L = \sum_{i=1}^N \frac{m_i \dot{r}_i^2}{2} - U(\mathbf{r}_1, \mathbf{r}_2, \dots, \mathbf{r}_N) \quad (2.19)$$

which satisfies the equations of motion (2.12) or (2.14). The system described by this Lagrangian can be multiphase, for example, a mixture of several different gases or liquids; the general form of the equations of motion will not change. The multiphase character of the system can be represented by distinct masses in the kinetic energy term and a relevant structure of the potential function that should also include the interaction between particles of different types.

Taking into account the coordinate transformation equations (2.2), we can also write L for a system with k holonomic constraints (2.1) in terms of the generalized coordinates,

$$L = \frac{1}{2} \sum_{j,l} a_{jl}(q_1, q_2, \dots, q_s) \dot{q}_j \dot{q}_l - U(q_1, q_2, \dots, q_s) \quad (2.20)$$

to satisfy (2.11) or (2.14). Specific forms of the potential energy functions are distinct in (2.19) and (2.20); however, we have used the uniform notation U to represent them. The functional dependence of the coordinates a_{jl} in (2.20) are determined by the particular forms of the parametric representations (2.2).

The fact that the potential energy term depends only on the spatial configuration of the particles implies that any change in this configuration results in an immediate effect on

the motion of all particles in the system. Indeed, if such an effect propagated with a finite speed, the former would depend on the choice of an inertial system of coordinates. In this case, the laws of motion would be dissimilar in various systems, and would contradict the classical frame invariance principle.

2.1.4 Integrals of Motion and Symmetric Fields

During the time evolution of a system of particles, there exist some functions of the $2s$ generalized coordinates and velocities, $q_1(t), q_2(t), \dots, q_s(t)$, $\dot{q}_1(t), \dot{q}_2(t), \dots, \dot{q}_s(t)$, that depend only on the initial conditions (2.16) and stay constant in time. These functions are known as *integrals of motion*. In total, there are $2s - 1$ independent integrals of motion for a system with s degrees of freedom (Landau and Lifshitz 1976). Some of these integrals play important roles, such as providing information about valuable physical quantities of the system without solving for the equations of motion. Such quantities are the system's total energy, momentum and angular momentum.

If a system of particles is characterized by only conservative forces, its *total energy* is constant and is defined as

$$E = \sum_{j=1}^s \dot{q}_j \frac{\partial L}{\partial \dot{q}_j} - L \quad (2.21)$$

Mathematically, this gives

$$\frac{dE}{dt} = 0 \quad (2.22)$$

Mechanical systems whose total energy is conserved over the course of time are called *conservative systems*. A conservative system, in principle, can be isolated, or nonisolated. It is only required that all internal and external forces satisfy the condition (2.4). This condition cannot be achieved for a general time-dependent external field; therefore, the potential (2.6) includes no explicit dependence on time. One example of a nonisolated conservative system is a group of frictionless particles submerged into a (static) field of gravity. In later sections, we repeatedly refer to another case of such systems—motion in potential wells, or boxes, constraining the physical space occupied by particles.

Closed conservative systems also conserve the vector of *total momentum*

$$\mathbf{p} = \sum_{i=1}^N \frac{\partial L}{\partial \mathbf{v}_i}, \quad \frac{d\mathbf{p}}{dt} = \mathbf{0} \quad (2.23)$$

and the vector of *total angular momentum*

$$\mathbf{M} = \sum_{i=1}^N (\mathbf{r}_i \times \mathbf{p}_i), \quad \frac{d\mathbf{M}}{dt} = \mathbf{0} \quad (2.24)$$

Though all three components of the total momentum vectors, p_x, p_y, p_z , can be conserved only in the absence of any external fields, some of these components may also conserve for a class of symmetric static fields, where the potential energy does not depend on one or two of the Cartesian coordinates. In particular, if such a field has a zero gradient along the z -axis, the p_z projection of the total momentum \mathbf{p} will be conservative. Besides,

we can have a time-invariant projection of the total angular momentum vector onto the axis of an axisymmetric field. For a spherically symmetric (central) field, the projection of the vector \mathbf{M} onto *any* fixed axis passing through the center of the field is an integral of motion.

2.1.5 Newtonian Equations

For a system of N interacting monoatomic molecules, treated as individual mass points, there are no holonomic constraints, and the generalized coordinates can be chosen to be equivalent to the Cartesian coordinates. The Lagrangian of a conservative monoatomic system is given by (2.19), and the equations of motion (2.12) reduce to the *Newtonian form*

$$m_i \ddot{\mathbf{r}}_i = -\nabla_i U + \mathbf{F}_i, \quad i = 1, 2, \dots, N \quad (2.25)$$

where the nabla operator is such as in equation (2.7), and \mathbf{F}_i is a nonconservative or external force on the i th particle. The Newtonian equations are also applicable to a system of polyatomic molecules, provided that these molecules can be approximated as structureless mass points.

Dissipative equations

For a nonconservative system, the right-hand side of the equations (2.25) will also include all the available nonconservative forces. One typical example is the dissipative system, where the damping force exerted on a particle is proportional to its instantaneous velocity with the opposite sign,

$$m_i \ddot{\mathbf{r}}_i = -\nabla_i U - m_i \gamma_i \dot{\mathbf{r}}_i, \quad i = 1, 2, \dots, N \quad (2.26)$$

and γ is the damping constant. The damping force

$$\mathbf{F}_i^S = -m_i \gamma_i \dot{\mathbf{r}}_i \quad (2.27)$$

is also called the *viscous*, or *Stokes' friction*, because it is similar to decelerating forces exerted on a solid particle moving in a liquid solvent. This model can be updated with a stochastic external force \mathbf{R}_i that represents thermal collisions of the system particle i with the hypothetical solvent molecules,

$$m_i \ddot{\mathbf{r}}_i = -\nabla_i U - m_i \gamma_i \dot{\mathbf{r}}_i + \mathbf{R}_i(t), \quad i = 1, 2, \dots, N \quad (2.28)$$

Assuming that interactions/collisions between the particle i and the solvent molecules are frequent and fast, that is, the magnitude of the random force \mathbf{R} varies over much shorter timescales than the timescale over which the particle's position and velocity change, equation (2.28) is said to represent *Brownian motion* of the particle i . Furthermore, if the stochastic force satisfies the following relationships

$$\lim_{t \rightarrow \infty} \frac{1}{t} \int_0^t \mathbf{R}(\tau) d\tau = 0 \quad (2.29)$$

$$\lim_{t \rightarrow \infty} \frac{1}{t} \int_0^t \mathbf{R}_i(\tau) \cdot \mathbf{R}_{i'}(t_0 + \tau) d\tau = a \delta(t_0) \delta_{ii'} \quad (2.30)$$

where a is a constant and $\delta(t_0)$ and $\delta_{ii'}$ are the Dirac (3.32) and Kronecker(3.35) deltas, respectively, then equation (2.28) is often called the *Langevin equation*, and the particle i is referred to as a Langevin particle.

Generalized Langevin equations

The relationship (2.29) implies that there is no directional preference for the stochastic force in the Langevin model. An integral of the type (2.30) is called the *autocorrelation function* of a continuous function \mathbf{R} . The Dirac delta autocorrelation (2.30) implies that the function \mathbf{R} does not represent any time history, so that the current value of \mathbf{R} is not affected by behavior of this function at preceding times. The Kronecker delta in (2.30) means that the force exerted on the particle i is uncorrelated with the force exerted on another particle i' .

A more general form of the equation (2.28), which is used in application to solids, gas/solid and solid/solid interfaces, is given by

$$m_i \ddot{\mathbf{r}}_i(t) = -\nabla_i U - \sum_{i'} \int_0^t \boldsymbol{\beta}_{ii'}(t-\tau) \dot{\mathbf{r}}_{i'}(\tau) + \mathbf{R}_i(t), \quad i = 1, 2, \dots, N \quad (2.31)$$

Here, the second term on the right-hand side represents a dissipative damping force that depends on the entire *time history* of velocities of the current atom i and a group of neighboring atoms i' . The matrix $\boldsymbol{\beta}$ is called the *time-history damping kernel*. This damping force can be alternatively defined in terms of the history of atomic positions, rather than velocities,

$$m_i \ddot{\mathbf{r}}_i(t) = -\nabla_i U - \sum_{i'} \int_0^t \boldsymbol{\theta}_{ii'}(t-\tau) \mathbf{r}_{i'}(\tau) + \mathbf{R}_i(t), \quad i = 1, 2, \dots, N \quad (2.32)$$

where $\boldsymbol{\theta}$ is a new damping kernel. Newtonian equations of the type (2.31), or (2.32), are often called the *generalized Langevin equations*, for example, Adelman and Doll (1976). Adelman and Garrison (1976) and Karpov et al. (2005b). One application of these equations is related to the motion of individual atoms in a large crystal lattice subjected to external pulse excitations. We will consider this application in greater detail in Chapter 3.

2.1.6 Examples

In this section, we demonstrate the Lagrangian formalism on two example systems: diatomic molecules, and coupled harmonic oscillators—two atoms connected by three springs to each other and with fixed boundaries.

Diatomc molecules

A typical configuration for a system of diatomic molecules is depicted in Figure 2.2(a). Each of these molecules has in general six degrees of freedom: three translational, two rotational and one vibrational. The corresponding generalized coordinates (distances and angles) can be introduced to provide the positions of the centers of mass, rotational states and the current separation distances between atoms of the coupled pairs. The simplest way to define any

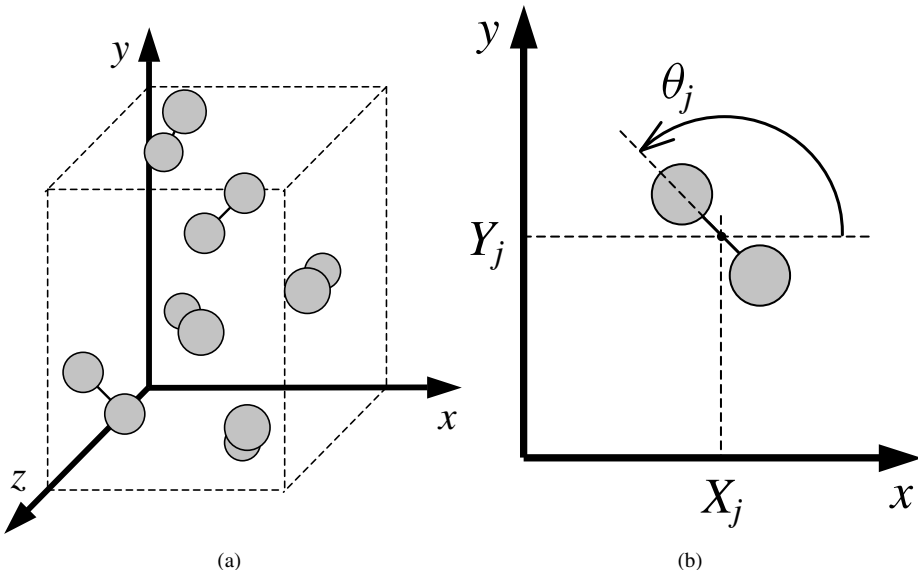


Figure 2.2 (a) Diatomic gas; (b) generalized coordinates in the xy -plane.

arbitrary configuration of this system consists in introducing $2N$ radius vectors for all atoms in the system, where N is the total number of molecules. Provided that the potential energy function U is available to characterize the intermolecular as well the interatomic interaction in terms of the radius vectors, the $2N$ standard Newtonian equations (2.25) can be utilized for studying the dynamics of this system.

For the purpose of effective numerical modeling, one can ignore the vibrational degrees of freedom, provided that its contribution to interesting dynamic properties of the system under investigation is negligible. Characteristic times of molecular vibrations are typically much shorter than times associated with translational and rotational motion of the same molecules. Therefore, accounting for the molecular vibrations requires a significant reduction of the time step of numerical simulations, and leads to a corresponding increase in the computational cost. This issue can be resolved by assuming a constant separation distance $2l$ between two atoms of each molecule, that is, by setting

$$(x_{i+1} - x_i)^2 + (y_{i+1} - y_i)^2 + (z_{i+1} - z_i)^2 = 4l^2, \quad i = 1, 3, \dots, 2N - 1 \quad (2.33)$$

This equality provides one holonomic constraint for each of the N molecules in the system. For compactness, we can also assume that the molecules are confined to move only in the xy -plane, that is,

$$z_i = 0, \quad i = 1, 2, \dots, 2N \quad (2.34)$$

Then, there are in total three holonomic constraints per each molecule, whose configuration can be now described by only three generalized coordinates: X and Y Cartesian coordinates of the center of mass and the rotation angle θ , as depicted in Figure 2.2(b). The relationship between the generalized coordinates and radius vectors of the individual atoms gives the

transformation equations,

$$\begin{aligned} x_i &= X_i + l \cos \theta_i, & y_i &= Y_i + l \sin \theta_i \\ x_{i+1} &= X_i - l \cos \theta_i, & y_{i+1} &= Y_i - l \sin \theta_i, \quad i = 1, 3, \dots, 2N-1 \end{aligned} \quad (2.35)$$

The Lagrangian in terms of the generalized coordinates X, Y and θ is obtained by substituting (2.35) into (2.19). We first write the kinetic energy of a single molecule,

$$\begin{aligned} \frac{m}{2}(\dot{x}_i^2 + \dot{y}_i^2) + \frac{m}{2}(\dot{x}_{i+1}^2 + \dot{y}_{i+1}^2) \\ = m(\dot{X}_i^2 + l^2\dot{\theta}_i^2 \sin^2 \theta_i) + m(\dot{Y}_i^2 + l^2\dot{\theta}_i^2 \cos^2 \theta_i) \\ = m(\dot{X}_i^2 + \dot{Y}_i^2 + l^2\dot{\theta}_i^2) \end{aligned} \quad (2.36)$$

for which the Lagrangian reads

$$L = m \sum_{j=1}^N (\dot{X}_j^2 + \dot{Y}_j^2 + l^2\dot{\theta}_j^2) - U(X, Y, \theta) \quad (2.37)$$

where the index j indicates a summation over all the molecules.

Finally, the equations of motion are derived by substituting (2.37) into (2.11),

$$2m\ddot{X}_j = -\frac{\partial U}{\partial X_j}, \quad 2m\ddot{Y}_j = -\frac{\partial U}{\partial Y_j}, \quad 2ml^2\ddot{\theta}_j = -\frac{\partial U}{\partial \theta_j}, \quad j = 1, 2, \dots, N \quad (2.38)$$

Note that the Newtonian equations (2.25) cannot be written for the diatomic molecules constrained according to (2.33). Essentially, they are applicable only to the structureless mass points or effectively spherical molecules, while the general Lagrangian formalism illustrated in this example is applicable to arbitrary molecular shapes, constrained or non-constrained.

Coupled harmonic oscillators; normal coordinates

Consider a system of two identical atoms of masses m that are bonded with each other and with the fixed boundaries, as depicted in Figure 2.3. Each atom has one (longitudinal) degree of freedom. For small displacements, the interactions of the atoms with each other and with the boundaries are characterized by the linear atomic force constant k , the bond stiffness, which is similar to the spring stiffness in macroscopic systems. One obvious choice of the generalized coordinates is the use of two Cartesian coordinates x_1 and x_2 for the left and right particles, respectively. The corresponding Lagrangian is

$$L = \frac{m}{2}(\dot{x}_1^2 + \dot{x}_2^2) - k(x_1^2 + x_2^2 - x_1x_2) \quad (2.39)$$

where the last three terms represent the potential energy of the system. Utilizing this function in the Lagrange equation (2.11), we get two *coupled* equations of motion in the form,

$$m\ddot{x}_1 = -2kx_1 + kx_2, \quad m\ddot{x}_2 = -2kx_2 + kx_1 \quad (2.40)$$

where each of the equations involves both the coordinates, x_1 and x_2 .

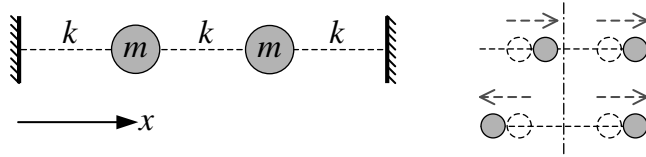


Figure 2.3 Coupled harmonic oscillators and the corresponding normal modes.

Another method of characterizing the configuration of this system is to specify the position of the center of mass and the relative displacement of the two atoms,

$$q_1 = \frac{x_1 + x_2}{2}, \quad q_2 = -\frac{x_1 - x_2}{2} \quad (2.41)$$

Then, the configuration vector can be represented by

$$\begin{pmatrix} x_1 \\ x_2 \end{pmatrix} = q_1 \begin{pmatrix} -1 \\ 1 \end{pmatrix} + q_2 \begin{pmatrix} 1 \\ 1 \end{pmatrix} \quad (2.42)$$

Using the coordinates in (2.41), we write the Lagrangian,

$$L = m(\dot{q}_1^2 + \dot{q}_2^2) - k(q_1^2 + 3q_2^2) \quad (2.43)$$

and the equations of motion,

$$m\ddot{q}_1 = -kq_1, \quad m\ddot{q}_2 = -3kq_2 \quad (2.44)$$

These equations possess two important features: (1) the potential energy in (2.43) is uncoupled, that is, it has no cross-terms similar to x_1x_2 in (2.39); (2) the equations of motion (2.44) are independent, and they can be written in the uniform format, $\ddot{q}_i = -\omega_i^2 q_i$, where ω_i are the characteristic vibration frequencies of the system.

Generalized coordinates that decouple the potential energy and equations of motion of a vibrational system are called *normal coordinates*, the relevant ω_i are the normal frequencies, and the basis vectors in the right-hand side of the equation (2.42) are called the *normal modes* of vibration (see Figure 2.3). The solution to (2.44) is given by,

$$q_i = a_i \cos(\omega_i t + \phi_i), \quad i = 1, 2 \quad (2.45)$$

where ϕ_i are arbitrary initial phases, and the constants a_i are called the *normal amplitudes*. We will recall the basic concepts associated with the normal mode analysis in the next chapter for the study of large repetitive atomic lattices.

2.2 Molecular Forces

As discussed in the previous sections, the general forms of the governing equation of particle dynamics are given by straightforward second-order ordinary differential equations that allow a variety of numerical solution techniques. Meanwhile, the potential function U for (2.11) or (2.25) can be an extremely complicated object, when an accurate representation

of the atomic interactions within the system under consideration is required. The nature of these interactions is due to complicated quantum effects taking place at the subatomic level that are responsible for chemical properties such as valence and bond energy. The effects also are responsible for the spatial arrangement (topology) of the interatomic bonds, their formation and breakage. In order to obtain reliable results in MD computer simulations, the classical interatomic potentials should accurately account for the quantum effects, even in an averaged sense. Typically, the function U is obtained from experimental observations, as well as from the quantum scale modeling and simulation, for example, La Paglia (1971), Mueller (2001) and Ratner and Schatz (2001).

The issues related to the form of the potential function for particular types of atomic systems have been extensively discussed in the literature. The general structure of this function can be presented by the following:

$$U(\mathbf{r}_1, \mathbf{r}_2, \dots, \mathbf{r}_N) = \sum_i V_1(\mathbf{r}_i) + \sum_{i,j>i} V_2(\mathbf{r}_i, \mathbf{r}_j) + \sum_{i,j>i, k>j} V_3(\mathbf{r}_i, \mathbf{r}_j, \mathbf{r}_k) + \dots \quad (2.46)$$

where \mathbf{r} are radius vectors of the particles, and the function V_m is called the m -body potential. The first term represents the energy due to an external force field, such as gravity or electrostatic, which the system is immersed in, or bounding fields, such as potential barriers and wells. The second term shows potential energy of pair-wise interaction of the particles; the third gives the three-body components, and so on. Accordingly, the function V_1 is also called the *external potential*, V_2 the interatomic (pair-wise), and V_m at $m > 2$ a multibody potential. In order to reduce the computational expense of numerical simulations, it is practical to truncate the sum (2.46) after the second term and incorporate all the multibody effects into V_2 with some appropriate degree of accuracy; more specific details on this issue are provided in the subsections that follow.

2.2.1 External Fields

The effect of external fields for a particle i can be generally described as

$$V_1 = V_1(\mathbf{r}_i) \quad (2.47)$$

where V_1 is a function of the radius vectors of this particle. Thus, the instantaneous force exerted on this particle due to V_1 depends only on the spatial location of this particular particle, and it is independent of the positions of any other particle in the system. Simple examples include the uniform field of gravity,

$$V_G(\mathbf{r}) = V_G(y) = mgx \quad (2.48)$$

where x is the component of the radius vector, orthogonal to the Earth's surface; the field of a one-dimensional harmonic oscillator,

$$V_h(x) = kx^2 \quad (2.49)$$

and a spherical oscillator,

$$V_h(r) = kr^2, \quad r^2 = x^2 + y^2 + z^2 \quad (2.50)$$

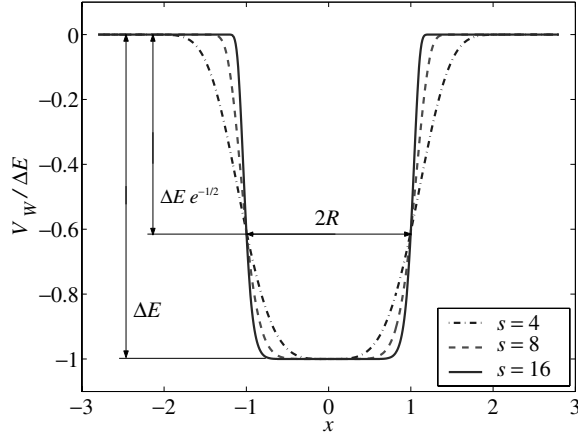


Figure 2.4 One-dimensional potential well (2.51) at $x_0 = 0$, $R = 1$ and various s .

External bounding fields and potential barriers give further examples of the one-body interaction: a one-dimensional potential well

$$V_W(x) = -\Delta E e^{-\frac{(x-x_0)^s}{2R^s}} \quad (2.51)$$

and a two-sided potential barrier,

$$V_B(x) = -V_W(x) \quad (2.52)$$

where x_0 , $2R$, s and ΔE are the coordinates of the center, width, steepness and total depth/height of the well/barrier, respectively. The steepness s is an even integer, and the width $2R$ corresponds to $V_W = \Delta E e^{-1/2}$ (see Figure 2.4).

Three-dimensional extensions for (2.51) are the 3D (parallelepiped) box,

$$V_W(\mathbf{r}) = V_W(x, y, z) = -\Delta E e^{-\frac{(x-x_0)^s}{2R_x^s} - \frac{(y-y_0)^s}{2R_y^s} - \frac{(z-z_0)^s}{2R_z^s}} \quad (2.53)$$

with $2R_x$, $2R_y$ and $2R_z$ —linear dimensions of the box, as well as the spherical chamber with the center at $x_0 = y_0 = z_0 = 0$ and radius R ,

$$V_W(r) = -\Delta E e^{-\frac{r^s}{2R^s}}, \quad r = \sqrt{x^2 + y^2 + z^2} \quad (2.54)$$

By manipulating these functions, one can also obtain cylindrical and ellipsoid chamber shapes. In the case that ΔE is increasingly large compared with an average kinetic energy of particles, a function similar to V_W is also called a “wall function” that models a system of particles inside a vessel with impenetrable walls.

In general, potential wells and barriers are introduced in order to confine the spatial domain occupied by a finite system of atoms and molecules in gaseous or liquid phase.

2.2.2 Pair-Wise Interaction

The pair-wise function V_2 describes the dependence of the total potential energy U on the interparticle distances. By taking \mathbf{r}_i and \mathbf{r}_j as the radius vectors of two arbitrary particles in the system, we can generally write

$$V_2(\mathbf{r}_i, \mathbf{r}_j) = V_2(r), \quad r = |\mathbf{r}_{ij}| = |\mathbf{r}_i - \mathbf{r}_j| \quad (2.55)$$

Such a function serves as an addition to V_1 , formula (2.47), which provides the dependence of U only on the radius vectors \mathbf{r}_i and \mathbf{r}_j . Pair-wise coordination of particles is depicted in Figure 2.5.

There are two major types of pair-wise interactions: long-range electrostatic interactions and short-range interactions between electrically neutral particles.

Long-range Coulomb interaction

One basic physical characteristic of atoms, molecules and their elementary components is the electric charge, e . Electric charge is related to the property of particles to exert forces on each other by means of electric fields. The standard SI unit of electric charge is 1 coulomb, $[e] = 1 \text{ C}$. The electric charge of a particle is always quantized, occurring as a multiple of the elementary charge $e_0 = 1.602177 \times 10^{-19} \text{ C}$. An electron, proton and neutron, the atomic components, have the charges $-e_0$, e_0 and 0, respectively. The charge of an atomic nucleus, composed of protons and neutrons, is Ze_0 , where Z is the number of protons. An atomic ion can have a charge $(Z - N_e)e_0$, where N_e is the number of available electrons. As a result, classical particle dynamics deals with positively and negatively charged atomic and molecular ions, as well as with electrically neutral particles ($e = 0$).

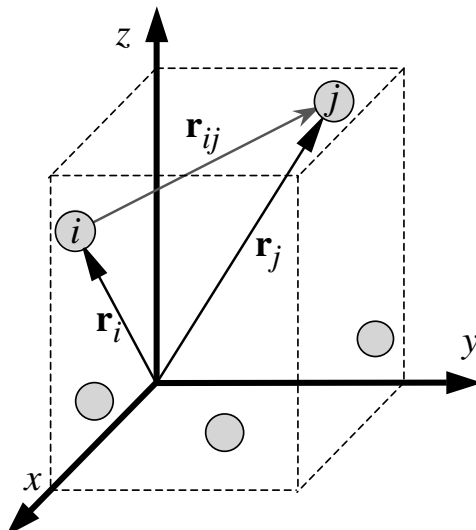


Figure 2.5 Pair-wise coordination of particles.

A pair of particles bearing electric charges e_1 and e_2 exert repulsive (at $e_1/e_2 > 0$), or attractive (at $e_1/e_2 < 0$) forces on each other, described by

$$\mathbf{F}_1 = -\mathbf{F}_2 = -\nabla_i V_C(\mathbf{r}_1, \mathbf{r}_2), \quad i = 1, 2 \quad (2.56)$$

where \mathbf{r}_1 and \mathbf{r}_2 are radius vectors of the particles, and

$$V_C(\mathbf{r}_1, \mathbf{r}_2) = V_C(r) = \frac{1}{4\pi\epsilon_0} \frac{e_1 e_2}{r}, \quad r = |\mathbf{r}_{12}| = |\mathbf{r}_2 - \mathbf{r}_1| \quad (2.57)$$

is the electrostatic *Coulomb potential*; $\epsilon_0 = 8.854188 \times 10^{-12} \text{ C(Vm)}^{-1}$ is the permittivity constant in a vacuum. Equations (2.56) and (2.57) account for the convention where attractive forces are defined as negative and repulsive forces as positive.

The absolute value of the interaction force (2.56) can be expressed as a function of the separation distance,

$$F_C(r) = -\frac{\partial V(r)}{\partial r} = \frac{1}{4\pi\epsilon_0} \frac{e_1 e_2}{r^2} \quad (2.58)$$

For a system of N charged particles, the pair-wise interaction energy is written as

$$U_C = \sum_{i,j>i} V_C(r_{ij}), \quad r_{ij} = |\mathbf{r}_{ij}| = |\mathbf{r}_j - \mathbf{r}_i| \quad (2.59)$$

where V_C is the Coulomb potential (2.57) and r_{ij} is the separation distance for a pair of particles i and j (see Figure 2.5). The relevant interaction forces can be computed according to the general formula (2.7).

The Coulomb interaction is noticeable even at large separation distances, because the potential (2.57) decays slowly with the growth of r . For this reason, it is called a *long-range* interaction.

Short-range interaction

For a pair of electrically neutral atoms or molecules, the electrostatic field of the positively charged atomic nuclei or ion is neutralized by the negatively charged electron clouds surrounding the nuclei. Quantum mechanical descriptions of the electron motion involve a probabilistic framework to evaluate the probability densities at which the electrons can occupy particular spatial locations; in other words, quantum mechanics provides probability densities in the configuration space of electrons, for example, La Paglia (1971) and Ratner and Schatz (2001). The term “electron cloud” is typically used in relation to the spatial distributions of these densities. The negatively charged electron clouds, however, experience cross-atomic attraction, which grows as the distance between the nuclei decreases. On reaching some particular distance, which is referred to as the equilibrium (bond) length, this attraction is equilibrated by the repulsive force due to the positively charged atomic nuclei or ions. A further decrease in the interparticle distance results in a quick growth of the resultant repulsive force. The potential energy of such a system will be a continuous function of the separation distance, provided that internal quantum states of the electron cloud are not excited. Alternatively, these quantum states are excited and, consequently, relaxed at timescales that are significantly faster than the characteristic time of the ion’s thermal motion. Then the “heavy” and “slow” (in the quantum sense) nuclei or ions can

be considered as a classical system of particles, interacting through a time-independent potential, averaged over the electronic degrees of freedom.

There exist a number of mathematical models to adequately describe the dual attractive/repulsive character of interactions between a pair of neutral atoms or molecules. In 1924, Jones (1924a,b) proposed the following potential:

$$V_{\text{LJ}}(r) = 4\varepsilon \left(\frac{\sigma^{12}}{r^{12}} - \frac{\sigma^6}{r^6} \right) \quad (2.60)$$

This model is currently known as the *Lennard-Jones (LJ) potential*, and it is used in computer simulations of a great variety of nanoscale systems and processes. Here, σ is the collision diameter, the distance at which $V_{\text{LJ}} = 0$, and ε is the dislocation energy. In a typical atomistic system, the collision diameter is equal to several angstroms (\AA), $1\text{\AA} = 10^{-10} \text{ m}$. The value ε corresponds to the minimum of function (2.60), which occurs at the equilibrium bond length $\rho = 2^{1/6}\sigma$; $V_{\text{LJ}}(\rho) = -\varepsilon$. Physically, ε represents the amount of work that needs to be done in order to move the interacting particles apart from the equilibrium distance ρ to infinity. The availability of a minimum in the LJ potential represents the possibility of bonding for two colliding particles, provided that their relative kinetic energy is less than ε .

The first term of the LJ potential represents atomic repulsion, dominating at small separation distances while the second term shows attraction (bonding) between two atoms or molecules. Since the quantity in brackets is dimensionless, the choice of units for V depends on the definition of ε . Typically, $\varepsilon \sim 10^{-19} \dots 10^{-18} \text{ J}$; therefore, it is more convenient to use a smaller energy unit, such as the electron-volt (eV),

$$1 \text{ eV} = 1.602 \times 10^{-19} \text{ J} \quad (2.61)$$

rather than joules. One electron-volt represents the work done if an elementary charge is accelerated by an electrostatic field of unit voltage. This is a typical atomic-scale unit, and therefore it is often used in computational nanomechanics and materials.

The absolute value of the LJ interaction force, as a function of the interparticle distance, gives

$$F_{\text{LJ}}(r) = 24\varepsilon \left(\frac{2\sigma^{12}}{r^{13}} - \frac{\sigma^6}{r^7} \right) \quad (2.62)$$

The potential (2.60) and force (2.62) functions are plotted in Figure 2.6(a) in terms of dimensionless quantities. Note that $F_{\text{LJ}}(\rho) = 0$.

Another popular model for pair-wise interactions is the Morse potential shown in Figure 2.6(b):

$$V_{\text{M}}(r) = \varepsilon \left(e^{2\beta(\rho-r)} - 2e^{\beta(\rho-r)} \right) \quad (2.63)$$

and

$$F_{\text{M}}(r) = 2\varepsilon\beta \left(e^{2\beta(\rho-r)} - e^{\beta(\rho-r)} \right) \quad (2.64)$$

This potential is commonly used for systems found in solid state at normal conditions. These include elemental metallic systems and alloys, for example, Harrison (1988). For the solid state, the typical kinetic energy of particles is less than the dislocation energy, and the particles are restrained to move in the vicinity of some equilibrium positions that form

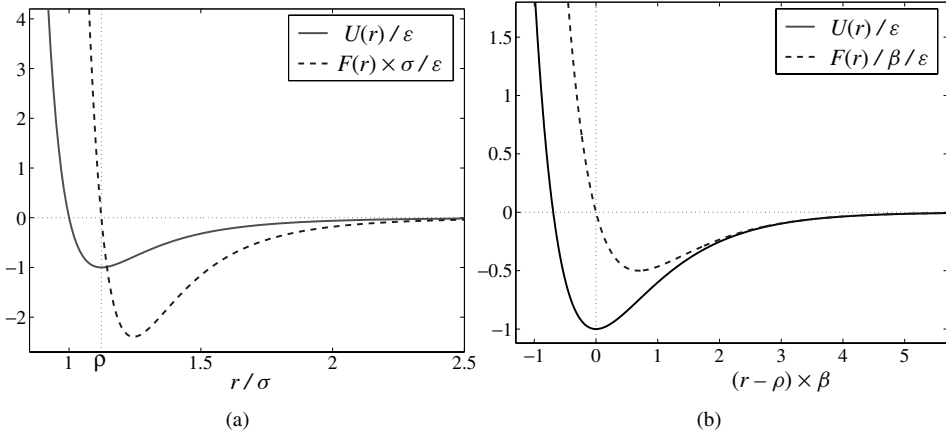


Figure 2.6 Short-range potentials: (a) Lennard–Jones and (b) Morse.

a regular spatial pattern, the crystal lattice. The dynamics of particles forming a crystal lattice is considered in greater detail in the next chapter.

In the case of multiple particles, the total potential energy due to the LJ or Morse interaction is computed as in (2.59), and the required internal forces are found by utilizing (2.7).

The interaction between neutral particles described by an LJ or a Morse potential is said to be short ranged, as contrasted with the long-range Coulomb interactions. As seen from Figure 2.6, short-range potentials are effectively zero if the separation r is larger than several equilibrium distances.

The LJ and Morse potentials are the most common models for short-range pair-wise interactions. They have found numerous applications in computational chemistry, physics and nanoengineering.

Cutoff radius

One important issue arising from MD computer simulations relates to the truncation of the potential functions, such as (2.60) and (2.63). Note that computing the internal forces (2.7) for the equations of motion due to only the pair-wise interaction in (2.46) results in $(N^2 - N)/2$ terms, where N is the total number of particles. This value corresponds to the case when one takes into account the interaction of each current atom i with all other atoms in the system $j \neq i$; this can be computationally expensive even for considerably small systems. For short-range potentials, we can assume that the current atom only interacts with its nearest neighbors that are found not further than some critical distance R . Typically, the value R is equal to several equilibrium distances ρ , and is called the *cutoff radius* of the potential. Limiting the cutoff radius to a sphere of several neighboring atoms can reduce the computational effort significantly. A truncated pair-wise potential can then be written as the following:

$$V^{(\text{tr})}(r) = \begin{cases} V(r), & r \leq R \\ 0, & r > R \end{cases} \quad (2.65)$$

If each atom interacts with only n atoms in its R -vicinity, the evaluation of the internal pairwise forces will result in only $nN/2$ terms, which is considerably less than the $(N^2 - N)/2$ terms for a nontruncated potential.

In order to assure continuity (differentiability) of V^{tr} , a “skin” factor can be alternatively introduced for the truncated potential by means of a smooth steplike function f_c , which is referred to as the *cutoff function*,

The function f_c provides a smooth and quick transition from 1 to 0, when the value of r approaches R , and it is usually chosen as a simple analytical function of the separation distance r . One example of a trigonometric cutoff function is given by equation (2.70) in the next section.

2.2.3 Multibody Interaction

The higher-order terms of the potential function (2.46) ($m > 2$) can be of importance in modeling solids and complex molecular structures to account for chemical bond formation, their topology and spatial arrangement, as well as the chemical valence of atoms. However, the practical implementation of multibody interactions can be extremely complex. As a result, all the multibody effects of the order higher than three are usually ignored.

Meanwhile, the three-body potential V_3 is intended to provide contributions to the total potential energy U that depend on the value of the angle θ_{ijk} between a pair of interparticle vectors \mathbf{r}_{ij} and \mathbf{r}_{ik} , forming a triplet of particles i , j and k (see Figure 2.7)

$$V_3(\mathbf{r}_i, \mathbf{r}_j, \mathbf{r}_k) = V_3(\cos \theta_{ijk}), \quad \cos \theta_{ijk} = \frac{\mathbf{r}_{ij} \cdot \mathbf{r}_{ik}}{r_{ij} r_{ik}} \quad (2.66)$$

Such a function is viewed as an addition to the two-body term (2.55), which accounts only for the absolute values of r_{ij} and r_{ik} . Three-body potentials are dedicated to reflect changes

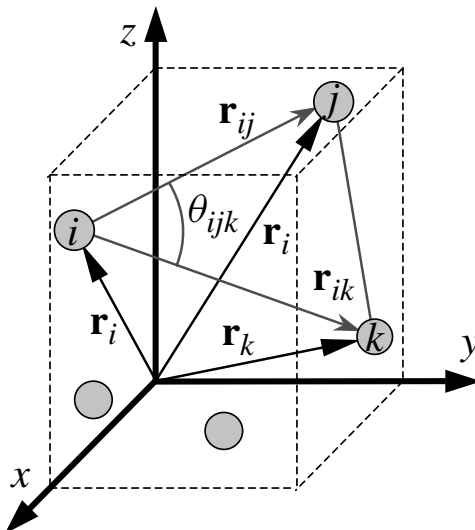


Figure 2.7 Three-body coordination of particles.

in molecular shapes and bonding geometries in atomistic structures, for example, Stillinger and Weber (1985) and Takai et al. (1985).

Local environment potentials

As a matter of fact, explicit three-body potentials, such as (2.66), are impractical in terms of computer modeling. Furthermore, there has been a criticism that these potentials are not useful for describing the energetics of all possible bonding geometries; see Biswas and Hamann (1985, 1987) and Tersoff (1988b). At the same time, four- and five-body potentials appear computationally intractable, and generally contain too many free parameters. As a result, a number of advanced two-body potentials have been proposed to efficiently account for the specifics of a local atomistic environment by incorporating some specific multibody dependencies inside the function V_2 , known as *bond-order functions*, rather than introducing the multibody functions $V_{m>2}$. Such potentials are called *local environment potentials*. The bond order function is intended to implicitly describe the angular dependence of interatomic forces, while the overall pair-wise formulation is preserved. Local environment potentials are usually short-ranged, and therefore cutoff functions can be utilized. Some of the most common models of this type are the Tersoff potential for a class of covalent systems, such as carbon, silicon and germanium, the Tersoff (1986, 1988a,b), Brenner (1990), Los and Fasolino (2002), Rosenblum et al. (1999), and REBO Brenner et al. (2002) potentials for carbon and hydrocarbon molecules, and the Finnis-Sinclair potential for BCC metals, Finnis and Sinclair (1984) and Konishi et al. (1999).

Most of the existing local environment potentials feature the following common structure:

$$V_{\text{LE}}(\mathbf{r}_i, \mathbf{r}_j) = (V_R(r_{ij}) - B_{ij} V_A(r_{ij})), \quad r_{ij} = |\mathbf{r}_{ij}| \quad (2.67)$$

where V_R and V_A are pair-wise repulsive and attractive interactions, respectively and B is the bond-order function, which is intended to represent multibody effects by accounting for spatial arrangements of the bonds in a current atom's vicinity.

The silicon potential model by Tersoff (1988b) gives an example of the local environment approach:

$$V_T(r_{ij}) = f_c(r_{ij}) (A e^{-\lambda_1 r_{ij}} - B_{ij} e^{-\lambda_2 r_{ij}}) \quad (2.68)$$

where A is a constant, and

$$\begin{aligned} B_{ij} &= \left(1 + \beta^n \zeta_{ij}^n\right)^{-1/2n}, \\ \zeta_{ij} &= \sum_{k \neq i, j} f_c(r_{ik}) g(\theta_{ijk}) e^{\lambda_2^3 (r_{ij} - r_{ik})^3}, \\ g(\theta) &= 1 + c^2/d^2 - c^2/[d^2 + (h - \cos \theta)^2] \end{aligned} \quad (2.69)$$

The cutoff function is chosen as

$$f_c(r) = \frac{1}{2} \begin{cases} 2, & r < R - D \\ 1 - \sin(\pi(r - R)/2D), & R - D < r < R + D \\ 0, & r > R + D \end{cases} \quad (2.70)$$

where the middle interval function is known as the “skin” of the potential. Note that if the local bond order is ignored, so that $B = 2A = \text{const}$, and $\lambda_1 = 2\lambda_2$, the Tersoff potential

reduces to the Morse model (2.63). In other words, all deviations from a simple pair potential are ascribed to the dependence of the function B on the local atomic environment. The value of this function is determined by the number of competing bonds, the strength α of the bonds and the angles θ between them; for example, θ_{ijk} shows the angle between the bonds $i-j$ and $i-k$. The function ζ in (2.69) is a weighted measure of the number of bonds competing with the bond $i-j$, and the parameter n shows how much the closer neighbors are favored over more distant ones in the competition to form bonds.

The potentials proposed by Brenner and coworkers, for example, Brenner (1990), Brenner et al. (2002), Los and Fasolino (2002) and Rosenblum et al. (1999), are considered to be more accurate, though more involved, extensions of the Tersoff (1986, 1988a,b) models. The Brenner potentials include more detailed functions V_A , V_R and B_{ij} to account for different types of chemical bonds that occur in the diamond and graphite phases of the carbon, as well as in hydrocarbon molecules.

Embedded atom potential

Another special form of a multibody potential is provided by the *embedded atom method* (EAM) for metallic systems, for example, Daw (1989), Daw et al. (1993) and Johnson (1988). One appealing aspect of the EAM potential is its physical picture of metallic bonding, where each atom is embedded in a host electron gas created by all neighboring atoms. The atom–host interaction is inherently more complicated than the simple pairwise model. This interaction is described in a cumulative way, in terms of an empirical *embedding energy function*. The embedding function incorporates some important many-atom effects by providing the amount of energy (work) required to insert one atom into the electron gas of a given density. The total potential energy U includes the embedding energies G of all the atoms in the system, and an electrostatic Coulomb interaction V_C :

$$U = \sum_i G_i \left(\sum_{j \neq i} \rho_j^a(r_{ij}) \right) + \sum_{i,j > i} V_C(r_{ij}) \quad (2.71)$$

Here, ρ_j^a is the averaged electron density for a host atom j , viewed as a function of the distance between this atom and the embedded atom i . Thus, the host electron density is employed as a linear superposition of contributions from individual atoms, which in turn are assumed to be spherically symmetric. Information on the specific shapes of the functions G , ρ and V_C for various metals and alloys can be gathered from the two references, Clementi and Roetti (1974) and Foiles et al. (1986). The embedded atom method has been applied successfully to study defects and fractures, grain boundaries, interdiffusion in alloys, liquid metals and other metallic systems and processes; a comprehensive review of the embedded atom methodology and applications is provided in Daw et al. (1993).

2.2.4 Exercises

Derive the Lagrangians and equations of motion for the systems depicted in Figure 2.8, (a) “bouncing ball”; (b) pendulum; (c) double pendulum; (d) particle in a smooth circular cavity (the xy -plane motion); and (e) particle in a circular cavity formed by 18 discrete immovable particles, using the generalized coordinates q_i shown. The pendulum and bouncing particle

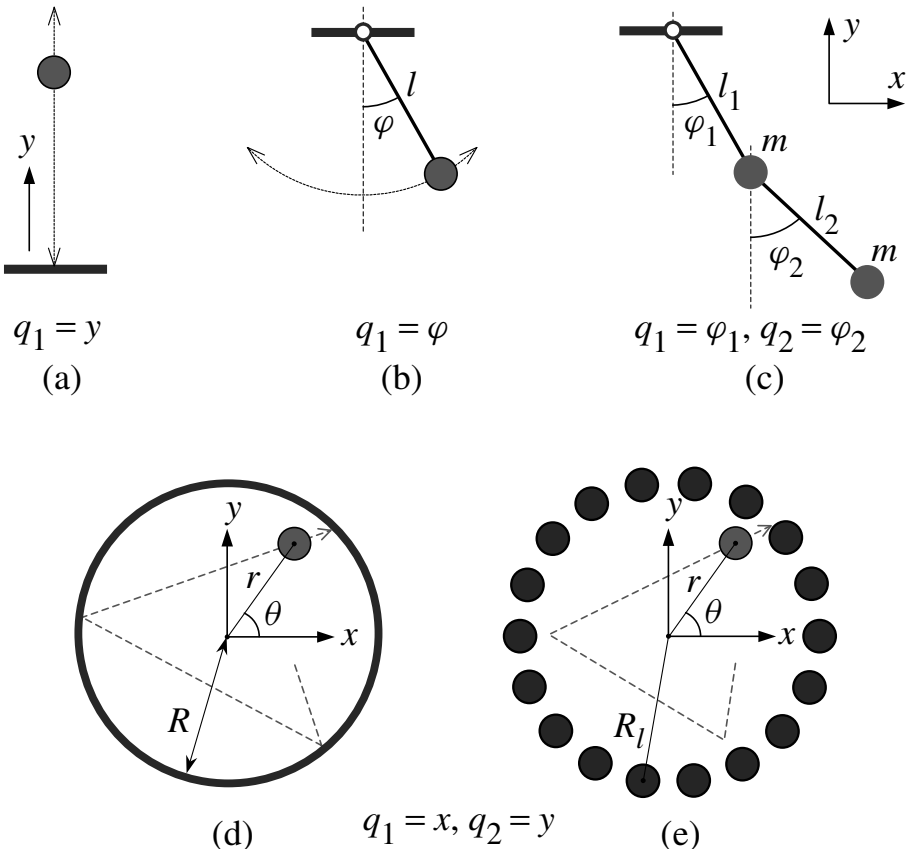


Figure 2.8 Example systems.

are in the field of gravity (2.50). The repulsive interaction of the bouncing particle with the horizontal surface is described by the one-body potential $V_R = \alpha e^{-\beta y}$, where α and β are free parameters. The repulsion between the particle and the cavity wall in example (d) is given by the “wall function” $V_R = \alpha e^{-\beta(R-r)}$, where $r = \sqrt{x^2 + y^2}$ and R is the cavity radius. In the last example, the repulsion between the particle and the wall is represented by the potential $V_R = \alpha \sum_{l=1}^{18} e^{-\beta(R_l-r)}$, where R_l are radius vectors of the wall particles. In all the examples, m is the particle mass.

Answers:

$$\text{Bouncing ball: } L = \frac{m}{2} \dot{y}^2 - mgy - \alpha e^{-\beta y}, \quad \ddot{y}(t) + g - \frac{\alpha\beta}{m} e^{-\beta y(t)} = 0$$

$$\text{Pendulum: } L = \frac{m}{2} l^2 \dot{\varphi}^2 + mgl \cos(\varphi), \quad \ddot{\varphi}(t) + \frac{g}{l} \sin(\varphi(t)) = 0$$

$$\begin{aligned} \text{Double pendulum: } L = & ml_1^2 \dot{\varphi}_1^2 + \frac{m}{2} l_2^2 \dot{\varphi}_2^2 + ml_1 l_2 \dot{\varphi}_1 \dot{\varphi}_2 \cos(\varphi_1 - \varphi_2) \\ & + 2mgl_1 \cos \varphi_1 + mgl_2 \cos \varphi_2 \end{aligned}$$

$$\text{Circular cavity: } L = \frac{m}{2}(\dot{x}^2 + \dot{y}^2) - \alpha e^{-\beta(R-r)}, \quad r = \sqrt{x^2 + y^2}$$

$$mr\ddot{x}(t) + \alpha\beta e^{-\beta(R-r)}x(t) = 0, \quad mr\ddot{y}(t) + \alpha\beta e^{-\beta(R-r)}y(t) = 0$$

$$\text{Discrete cavity: } L = \frac{m}{2}(\dot{x}^2 + \dot{y}^2) - \alpha \sum_{l=1}^{18} e^{-\beta(R_l-r)}$$

Note that in the example with a circular cavity, one can alternatively use the polar coordinates r and θ , such that

$$x = r \cos \theta, \quad y = r \sin \theta \quad (2.72)$$

The corresponding equations of motion give

$$m\ddot{r} + \alpha\beta e^{-\beta(R-r)} - mr\dot{\theta}^2 = 0, \quad \frac{d}{dt}(mr^2\dot{\theta}^2) = 0 \quad (2.73)$$

where the second equation represents the angular momentum conservation principle (2.24). Here, the absolute value of angular momentum, $M = mr^2\dot{\theta}$, is an integral of motion due to the circular symmetry of potential energy. This quantity can also be viewed as a projection of the angular momentum vector onto the z -axis, orthogonal to the plane of motion, that is, $M \equiv M_z = \text{constant}$.

2.3 Molecular Dynamics Applications

Molecular dynamics, or MD is used for the numerical solution of Lagrange (2.14) or Newtonian (2.25) equations for classical multiparticle systems, as well as for postprocessing and computer visualization of the time-dependent solution data.

In this section, we review applications of the Newtonian formalism to some typical MD simulations in the field of nanomechanics and materials.

Modeling inelasticity and failure in gold nanowires

A current research emphasis in nanostructured materials is the behavior of metallic nanowires. Nanowires are envisioned to have great potential as structural reinforcements, as biological sensors, as elements in electronic circuitry, and in many other applications. Interested readers can find reviews on this comprehensive subject by Lieber (2003) and Yang (2005).

The examples shown here are MD simulations of the tensile failure of gold nanowires as shown in Park and Zimmerman (2005). The wire size was initially 16 nm in length with a square cross section of length 2.588 nm. The wire was first quasi-statically relaxed to a minimum energy configuration with free boundaries everywhere, and then thermally equilibrated at a fixed length to 300 K using a Nosé–Hoover thermostat, which will be described in Section 4.3.3. Finally, a ramp velocity was applied to the nanowire ranging from zero at one end to a maximum value at the loading end; thus, one end of the nanowire was fixed, while the other was elongated at a constant velocity at each time step corresponding to an applied strain rate of $\dot{\epsilon} = 3.82 \times 10^9 \text{ s}^{-1}$.

As can be seen in Figure 2.9, the gold nanowire shows many of the same failure characteristics as macroscopic tension specimens, such as necking and yield. However, one

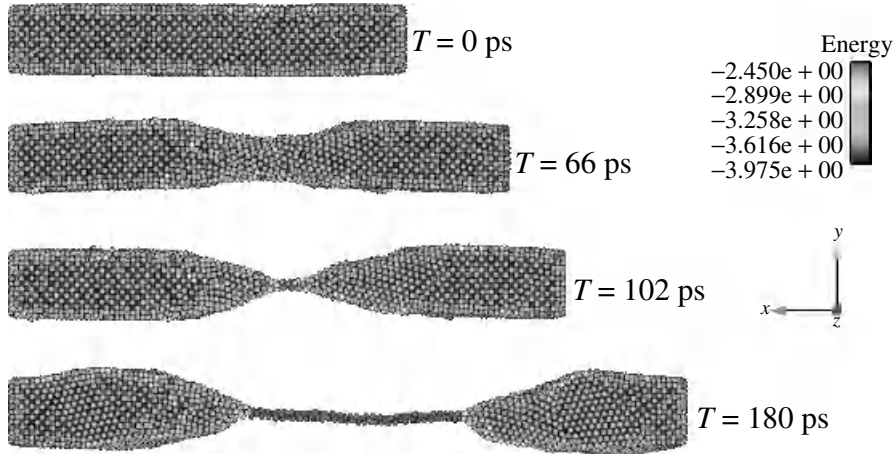


Figure 2.9 MD simulation of the tensile failure of a gold nanowire using an EAM potential.

very interesting quality of gold nanowires is their incredible ductility, which is manifested in the elongation of extremely thin nanobridges, as seen in the later snapshots in Figure 2.9. These nanobridges are extremely low coordinated chains of atoms that in first principle simulations are shown to form single atom chains. For MD simulations to capture these phenomena, it is very important to utilize an interatomic potential that can accurately model the material stacking fault energy; this point is elucidated clearly in Zimmerman et al. (2000).

As quantum mechanical calculations cannot yet model entire nanowires, MD simulations will continue to be a necessary tool in modeling nanostructured materials and atomic-scale plasticity.

Interaction of nanostructures with gas/liquid molecules

There has been significant effort aimed at the modeling and simulation of interactions between nanostructures and the flow of liquids and gases at the atomic scale. Particular interest arose from the interaction of carbon nanotubes (CNT), for example, Qian et al. (2002) and Saether et al. (2003), with a surrounding liquid or gas, including the resultant deformation and vibration of the CNT, drag forces, slip boundary effects, hydrophobic/hydrophilic behavior of the nanotubes, and nanosensors applications. Example references on these topics are the following: Bolton and Gustavsson (2003), Bolton and Rosen (2002), Li et al. (2003) and Walther et al. (2001, 2004).

Snapshots of a typical gas-structure atomic-scale simulation are shown in Figure 2.10. Here, a CNT is immersed in helium at a given temperature and concentration. The carbon atoms are initially at rest; however, collisions with the fast moving helium atoms induce vibration and deflection of the nanostructure. The mathematical modeling of these types of systems, considered a system of N spherical particles, utilizes the Newtonian equations of motion,

$$m_i \ddot{\mathbf{r}}_i = -\nabla_i U, \quad i = 1, 2, \dots, N \quad (2.74)$$

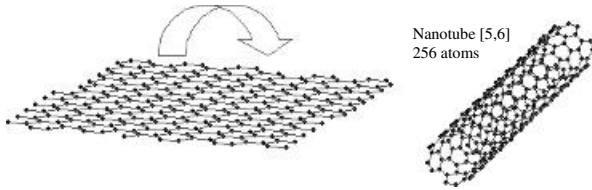


Figure 2.10 Molecular dynamics simulation of a carbon nanotube immersed in monoatomic helium gas at a given temperature and concentration.

where the potential function describes three types of atomic interactions present in the system,

$$U = U_{\text{C-C}} + U_{\text{He-He}} + U_{\text{C-He}} \quad (2.75)$$

The first term describes the interaction between carbon atoms, the second is the interaction of helium molecules (note that helium molecules are monoatomic), and the third is the potential of interaction between carbon atoms and helium molecules. For the specific example shown in Figure 2.10, the C–C interaction is modeled by the Tersoff potential (2.68), while the He–C and He–He interactions occur via two LJ potentials (2.60) with different sets of the parameters σ and ϵ . In general, if the system under analysis is composed of n_f distinct phases, the total number of different components in the potential U is equal to $n_f(n_f + 1)/2$.

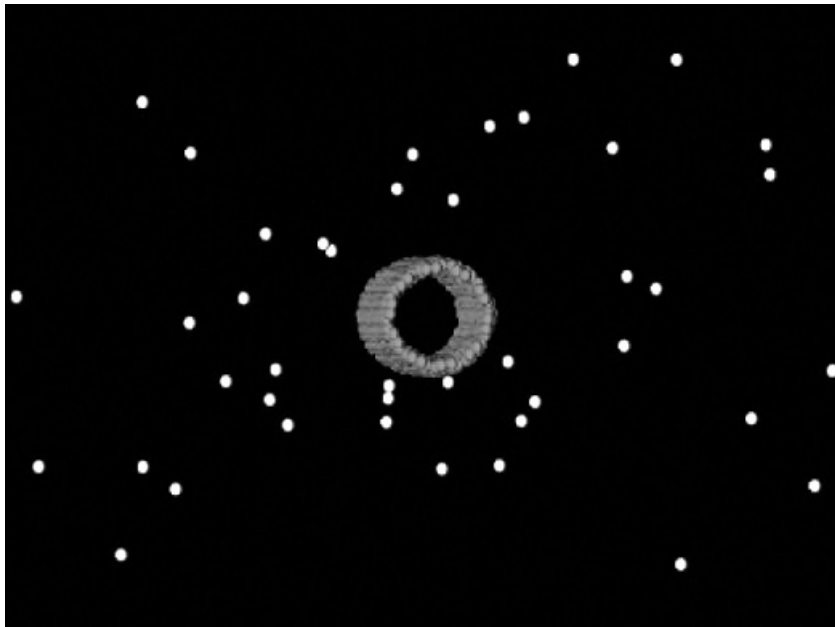


Figure 2.11 Approach to modeling three-dimensional nanotube structures.

One convenient approach to modeling cylindrical macromolecules, such as the CNT, is depicted in Figure 2.11; the modeling procedure consists in first producing a flat sheet of carbon rings, on the basis of given chirality and tubule translation vectors (Qian et al. 2002), followed by wrapping of the flat sheet into a three-dimensional structure.

Initial radius vectors for the equations of motion (2.74) are determined by geometry of the system, as well as physical properties of the gas, such as concentration and volume occupied. Initial velocities of the carbon and helium particles are determined by the initial temperature of the CNT and the gas, and are evaluated on the basis of the Maxwell–Boltzmann distribution discussed in Section (4.2.5).

Nanoindentation

Atomic-scale indentation of thin films and nanostructured materials is an effective experimental technique for the analysis of material properties. This technique consists of pushing a sharp tip made of a hard material, usually diamond, into a matrix/substrate material under investigation (see Figure 2.12) and measuring the loading force as a function of indentation depth. Material properties of the matrix are then evaluated from the analysis of a resultant load-indentation curve and properties of the tip, as well as plastic behavior of the substrate material.

Numerical modeling and simulation of the nanoindentation process for a tip-substrate system composed of N spherical atoms or molecules requires utilization of the Newtonian equations (2.74), where the gradient of function U determines the internal potential forces of atomic interaction. The function U describes the interaction between the substrate atoms and may also include components describing interactions between matrix and indenter and between indenter atoms. In the simplest case, displacement boundary conditions are applied throughout the domain including atoms subject to the indenter load, so that a sole substrate potential is required for (2.74). Note that for solid domains this potential is such that the substrate atoms, in the absence of external forcing, cannot move freely in the domain; they are constrained to vibrate in the vicinity of some equilibrium configuration determined by the local minima of function U . Initial coordinates of the atoms utilized for solving (2.74) usually correspond to one of these equilibrium configurations. As in most atomic-scale

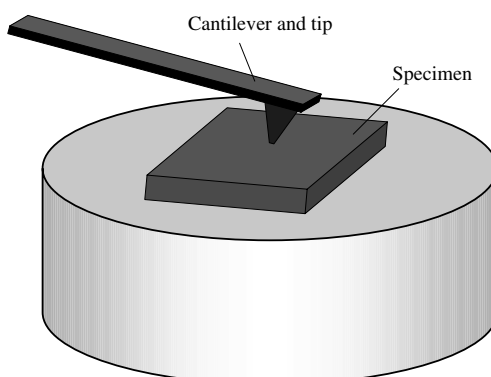


Figure 2.12 Nanoindentation, experimental scheme.

simulations, initial velocities are evaluated on the basis of Maxwell–Boltzmann distribution (see Section (4.2.5)).

The results of a typical two-dimensional simulation are depicted in Figure 2.12. One interesting feature of nanoindentation simulations, which is emphasized in this example, is the initiation and propagation of lattice dislocations that determine the plastic behavior of the substrate. Here, the substrate material is modeled as an initially perfect hexagonal lattice structure (see Figure 3.3) governed by the LJ potential (2.60) with a cutoff between the second and third nearest neighbors. The boundary conditions are the following: fixed y -components on the lower edge of the block and under the rectangular indenter. The speed of sound in this material is 1 km s^{-1} . The loading rate is 15 m s^{-1} .

Figure 2.13 shows a sequence of averaged contour plots of potential energy of the atoms. As seen from this figure, in the vicinity of a dislocation, core atoms are miscoordinated and have a higher potential energy than other atoms in the material. Dislocations move away

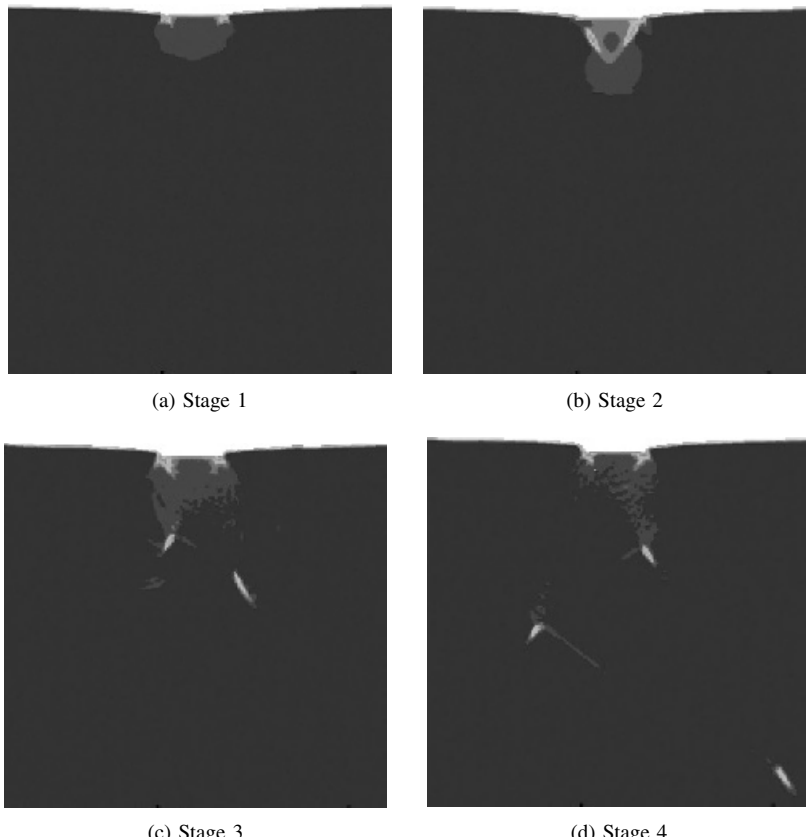


Figure 2.13 Dislocation dynamics in a two-dimensional nanoindentation simulation: averaged contour plots of potential energy of the atomic system; individual atoms are not shown.

from the nucleation site with the velocity of about 0.2 of the speed of sound, or 13 times the indenter speed.

Plate 2 shows a cross section through a relatively small, though typical, three-dimensional nanoindentation problem. Here, the domain is a 25 nm face-centered cube with roughly 376,000 atoms that interact through a $\sigma = \epsilon = 1$ LJ potential (2.60); for details of the face-centered lattice symmetry, see Section 3.1.1 and Figure 3.5(c). The interactions are nearest neighbor, and the indenter, shown as a sphere, is modeled as a repulsive pair-wise potential,

$$V_2 = V_2(|\mathbf{r}_i - \mathbf{r}_I|) \quad (2.76)$$

Here, \mathbf{r}_i are radius vectors of the substrate atoms, and \mathbf{r}_I is the radius vector of the center of the indenter.

The coloring is given in Plate 2 by coordination number, that is, the total number of neighboring atoms within the cut off radius of the potential for a given atom: blue is lowest, red is highest, and all atoms with coordination number equal to 12 (perfect face-centered lattice) have not been visualized to show lattice defects more clearly. Thus, the colored atoms shown represent the region of plastic deformation in the vicinity of the indenter. In contrast to the previous example, far-reaching localized dislocations are not formed here because of the large relative size and smoothness of the indenter.

Nanodeposition

The modeling and simulation of deposition of individual vapor (gas) molecules on the surface of a solid body (substrate) are important problems in the area of surface engineering, mechanics of thin films, and physical chemistry. The computational modeling of this process, which is often called *nanodeposition*, is composed typically of a solid structure and a gaseous domain governed by a three-component potential, similar to (2.75).

A directional deposition process viewed as a sequence of depositions of individual atomic or molecular ions with known orientation and modulus of the incident velocity vector is sometimes called *ion-beam deposition*; more generally, they are referred to as a physical or chemical *vapor deposition* process. Atomic ions can be controlled by means of electromagnetic fields to provide the required intensity, kinetic energy and orientation of the ion beam with respect to the surface of a substrate.

The ion-beam deposition process is illustrated in the MD simulation frame depicted in Figure 2.14. Individual carbon atoms of known mean kinetic energy and angle of incidence are deposited on the surface of a monocrystal diamond substrate to form a thin amorphous film. The situation shown corresponds to energetic ions with mean kinetic energy several times higher than the bonding energy of carbon atoms in the diamond substrate. Then, the bombarding ions destroy the crystalline structure of the substrate surface, and the growing amorphous film is composed of cross-diffused deposited and substrate atoms. The carbon–carbon interaction can be modeled via the Tersoff (1988a) or Brenner (1990) potentials.

Crack propagation simulations

MD simulations have been successful in their application to atomic-scale dynamic fracture processes, for example, Abraham et al. (1997, 2002). Two snapshots of a typical MD

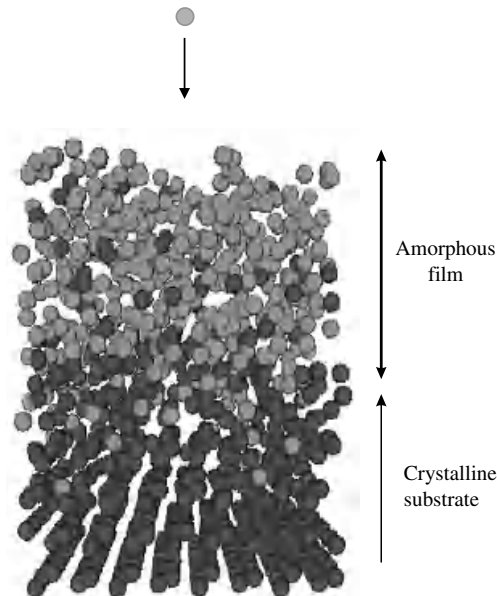


Figure 2.14 Deposition of an amorphous carbon film (light gray atoms) on top of a diamond substrate (dark gray atoms).

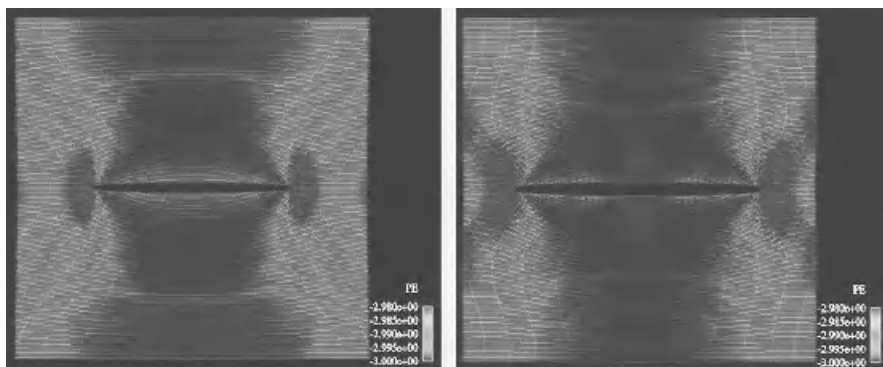


Figure 2.15 Averaged potential energy profiles for an MD fracture simulation at two different time steps. Reprinted from Computer Methods in Applied Mechanics and Engineering, 193(17–20), Liu et al., An introduction to computational nano mechanics and materials, 1529–1578, 2004, with permission from Elsevier.

simulation of fracture in a two-dimensional structure under tensile load are depicted in Figure 2.15. Note that the wave created because of opening the fracture surfaces heads out toward the MD boundary, reflects from it, and propagates back toward the crack.

Fracture under shear loading is presented in Figure 2.16. It shows a reproduction of the numerical experiments performed by Abraham and Gao (2000) and Gao et al. (2001) to



Figure 2.16 MD simulation of a shear-dominant crack propagation process; the middle snapshot shows the formation of a “daughter” crack ahead of the main crack tip.

analyze the mechanism by which a mode II (shear) dominated crack is able to accelerate past the Rayleigh wave speed, the lower theoretical max limit, over the “forbidden” velocity zone to the longitudinal speed of sound, the absolute theoretical maximum. The mechanism was seen to be the formation of a “daughter” crack ahead of the main crack tip; see the second snapshot in Figure 2.16. The system shown is a 2D hexagonal lattice with an LJ $\sigma = \epsilon = 1$ strip through which the crack propagates. The loading is mixed shear/tension, but the shear is dominant (5:1 shear:tensile strain rate ratio). The system is 1424 atoms long and 712 atoms high and the precrack is 200 atoms long in the center of the left vertical

face. The model shows several interesting phenomena, namely, the presence of a distinct displacement wavefront, and corresponding boundary reflections, as well as the formation of a Mach cone upon accelerating to the speed of sound in the material. Additionally, an expanding halo can be seen behind the Mach cone as a result of the passing shock wave. The main crack tip propagates at nearly the speed of sound and produces shock waves that form the Mach cone. The third snapshot indicates that the resultant crack propagation speed is higher than the speed of sound, since the Mach cone is still approaching the right vertical boundary after complete separation of the structure.

In conclusion, we note that material applications of classical particle dynamics, such as nanoindentation, deposition, atomic-scale failure, and others, often require the MD simulation to be very large, in order to diminish boundary effects. Otherwise, the waves that have been emitted by the indenter, atoms deposited, or crack tip reflect from the boundaries and continue to incorrectly participate in the phenomena under investigation. Though the increase in computational power has made million atom MD calculations fairly commonplace, it appears to be computationally and physically unnecessary to have full atomistic resolution far from the crack, or indenter tip. The waves emitted are usually elastic in nature, and do not cause atomic lattice imperfections, that is, plasticity, far from the localized domains of plastic deformation. Then, for example, the crack propagation can be correctly modeled using full atomistic resolution, while the propagation of the elastic waves away from the cracktip can be accurately modeled and captured using a continuum formulation. The usage of finite elements at a sufficient distance from the crack tip would reduce the computational expense of having full atomistic resolution, while still accurately capturing the necessary physics. These issues are discussed in greater detail in Chapters 5–7, which are devoted to hybrid, or multiscale, modeling methods that allow concurrent coupling of MD and finite element method (FEM) simulations.

3

Lattice Mechanics

Crystalline solid states are of particular interest to the nanoscale researcher. Amorphous systems that display nonrepetitive, irregular patterns of spatial atomic arrangements are in many respects closer to liquids. The computer modeling and characterization of amorphous materials requires the standard particle dynamics formulation of Chapter 2, as in the case of liquids and gaseous domains. When referring to solid states, one usually implies those having regular crystal structures. Crystalline bodies are usually represented by an individual monocrystal or by a polycrystal formed by a large number of smaller monocrystals. Crystalline materials provide further opportunities in terms of computer simulations, analysis and characterization. Another type of spatially regular system is polymer molecules/chains, formed by a large number of repetitive atomic cells. Chemical bonds between atoms of a given cell as well as cross-cell bonding provide stability for the entire polymer chain. Classical particle mechanics can be made to utilize the intrinsic symmetries and translational invariance of *regular lattices*, such as crystals and polymer chains. These applications of particle mechanics comprise the classical theory of lattice mechanics reviewed in this chapter.

The issues discussed in this chapter relate to the possibility of predicting acoustic and dispersion properties of a regular lattice, finding dynamic and quasi-static solutions for lattices with a vast number of degrees of freedom in closed form, evaluating response solutions for a small group of atoms without solving for the entire domain, eliminating unnecessary degrees of freedom in numerical simulations, and others.

3.1 Elements of Lattice Symmetries

In the general theoretical consideration of regular polymer and crystal lattices, one usually implies an infinite structure in order to eliminate the effects of free surfaces. Mechanical properties of a regular lattice are normally associated with two types of lattice symmetries: (1) *translational symmetry*, which is a spatially periodic pattern of identical groups of atoms, ions or molecules and (2) *point symmetry*, that is, a geometrical order of the individual periodic cells.

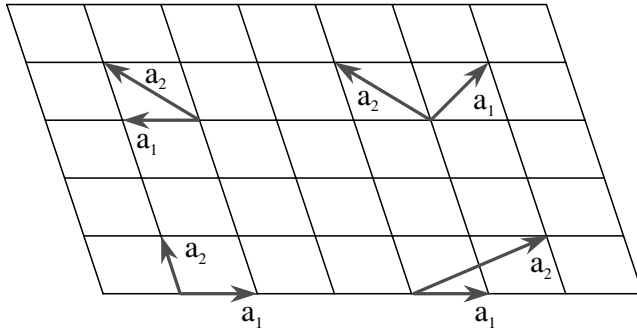


Figure 3.1 Ambiguity of the translational vector basis.

The smallest part of the lattice whose spatial repetition forms the entire lattice under analysis is called the *elementary cell*. Such a cell may include one or several particles (atoms, ions or molecules). Owing to translational symmetry, each particle from one elementary cell can be associated with an identical particle from another elementary cell. The spatial locations of such identical particles are determined by *lattice vectors*, or *lattice site vectors*,

$$\mathbf{n} = \rho + \sum_{i=1}^I n_i \mathbf{a}_i, \quad n_i = 0, \pm 1, \pm 2, \dots \quad (3.1)$$

where I is the dimensionality of the lattice; at $I = 1, 2$ and 3 , the lattice is called one-dimensional (beamlike), two-dimensional (platelike), and three-dimensional, respectively. The triplets of lattice site parameters (n_1, n_2, n_3) uniquely define the elementary cells. The noncoplanar vectors \mathbf{a}_i are the lattice *translation vectors* and ρ is the lattice origin vector that shows positions of particles in the cell $(0, 0, 0)$ with respect to the origin of the Cartesian axes. The components of the vectors ρ and \mathbf{a}_i are given in groups of three elements for each particle in the elementary cell; for example, vector $\mathbf{a}_i = (x, y, 0, x, y, 0)$ describes a translation of diatomic cells in the x - y Cartesian plane.

The entire set of lattice site vectors (3.1) defines the equilibrium positions of all particles that comprise the given lattice structure. The choice of translation vectors in (3.1) is not unique; Figure 3.1 illustrates multiple possibilities for \mathbf{a}_i in a two-dimensional lattice. Typically, the translation vectors are chosen to have the smallest possible absolute values. The lattice translational symmetry manifests itself in the fact the translation vectors do not depend on the lattice site parameters n_i .

3.1.1 Bravais Lattices

Besides translational symmetry, the lattice structure may also feature point symmetries, that is, invariance with respect to reflection in a point (inversion), rotation about an axis at a specific angle, and reflection in a plane. Then, the symmetric structure is said to have a center, axis or plane of symmetry, respectively. The term “point” symmetry is due to the fact that the relevant symmetry transformation leaves at least one point of a symmetric

object unaltered. A complete set of all possible point transformations, including the identity transformation, forms the symmetry group of a *Bravais lattice*.

There exist 6 two-dimensional and 14 three-dimensional standard Bravais lattices. However, there is no standard convention regarding one-dimensional lattices, whose point symmetry is usually trivial. They may have one transversal and sometimes one longitudinal plane or axis of symmetry; see examples depicted in Figure 3.2. In many cases, beamlike lattices have no particular point symmetries, for example, the second example in Figure 3.2.

The standard two-dimensional Bravais lattices are depicted in Figure 3.3. Their point symmetry is determined by the symmetry of a parallelogram with the angle α between the sides a and b . Trigonal and orthorhombic lattices are alternatively called the *rhombohedral (rhombic)* and *rectangular lattices*; they have the point symmetry of a rhombus and a rectangle, respectively.

The three-dimensional Bravais lattices are subdivided conventionally into seven systems: cubic, tetragonal, trigonal, hexagonal, orthorhombic, monoclinic and triclinic (see Table 3.1). The point symmetry of lattices from each of these systems is determined by the symmetry of a parallelepiped with the edges a , b and c that form the angles α , β and γ , as depicted in Figure 3.4. Each system includes one or several lattice types: primitive (P), base-centered (C), body-centered (I) and face-centered (F). For example, there exist simple cubic, body-centered cubic (bcc) and face-centered cubic (fcc) lattices. The cubic lattices have the highest symmetry; they are typical for metallic monocrystals, simple metallic compounds and frozen monoatomic gases. The simple cubic lattice is observed in diatomic crystals, such as CuZn, CsCl and NaCl. The bcc lattice structure is typical for the alkali elements, such as Li, Na, K and Rb, as well as for Fe, Cr, V and other metals. The fcc structures occurs in Ca, Ni, Sr, Cu, Pb, the noble metals (Ag, Au, Pd, Ir, Pt), and the frozen noble gases (Ne, Ar, Kr, Xe, Rn). The complete set of the 14 standard lattices is shown in Figure 3.5.

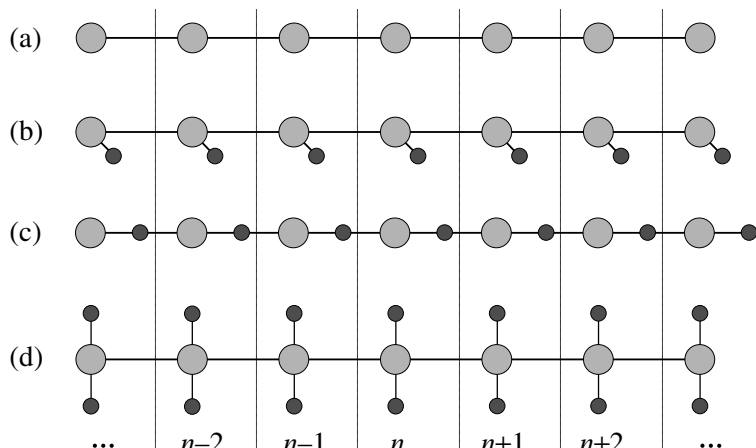


Figure 3.2 Examples of periodic one-dimensional lattices; index n numbers the elementary cells.

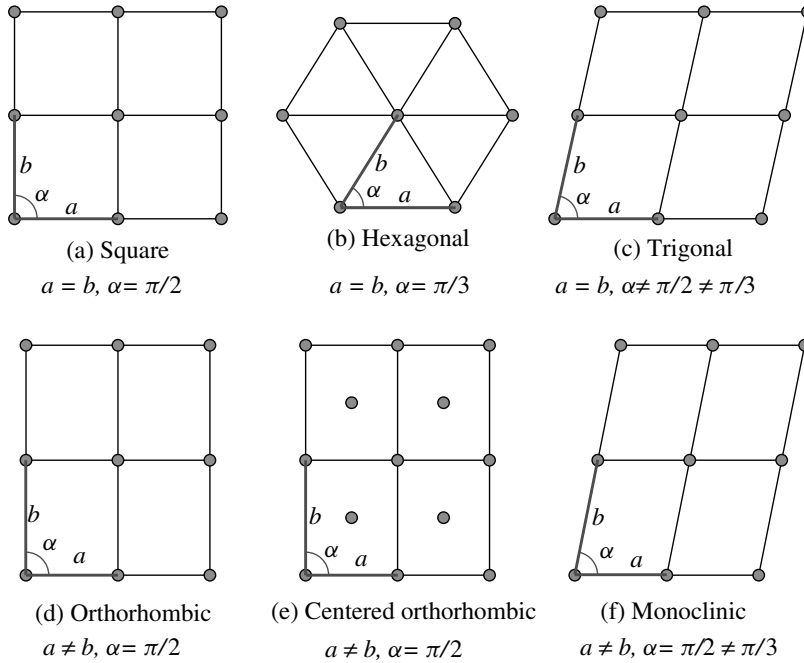


Figure 3.3 Two-dimensional Bravais lattices.

Table 3.1 Classification of the three-dimensional Bravais lattices

System	Restrictions	Lattice types
Cubic	$a = b = c, \alpha = \beta = \gamma = \pi/2$	P, I, F
Tetragonal	$a = b \neq c, \alpha = \beta = \gamma = \pi/2$	P, I
Trigonal	$a = b = c, \alpha = \beta = \gamma \neq \pi/2$	P
Hexagonal	$a = b \neq c, \alpha = 2\pi/3, \beta = \gamma = \pi/2$	P
Orthorhombic	$a \neq b \neq c, \alpha = \beta = \gamma = \pi/2$	P, C, I, F
Monoclinic	$a \neq b \neq c, \alpha = \beta = \pi/2 \neq \gamma$	P, C
Triclinic	$a \neq b \neq c, \alpha \neq \beta \neq \gamma$	P

3.1.2 Basic Symmetry Principles

A better understanding of the mechanical properties of lattice structures can be obtained by taking their symmetry into account. The symmetry arguments often provide intuitive tests for the adequacy of the mathematical description and the accuracy of numerical calculations. The relevant symmetry-based arguments are based upon the following basic principles:

Principle 1. Geometric symmetry of a mechanical system implies the corresponding invariance of the mathematical models. Mathematical objects, such as functions, matrices and operators that are associated with inherent physical properties of the system (the physical observables of the system) are invariant with respect to the same symmetry

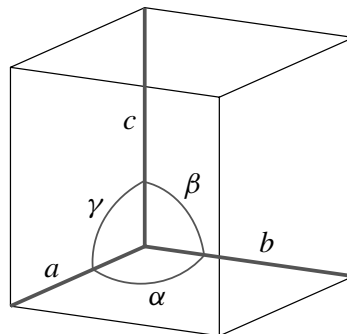


Figure 3.4 Relative orientation of parallelogram edges.

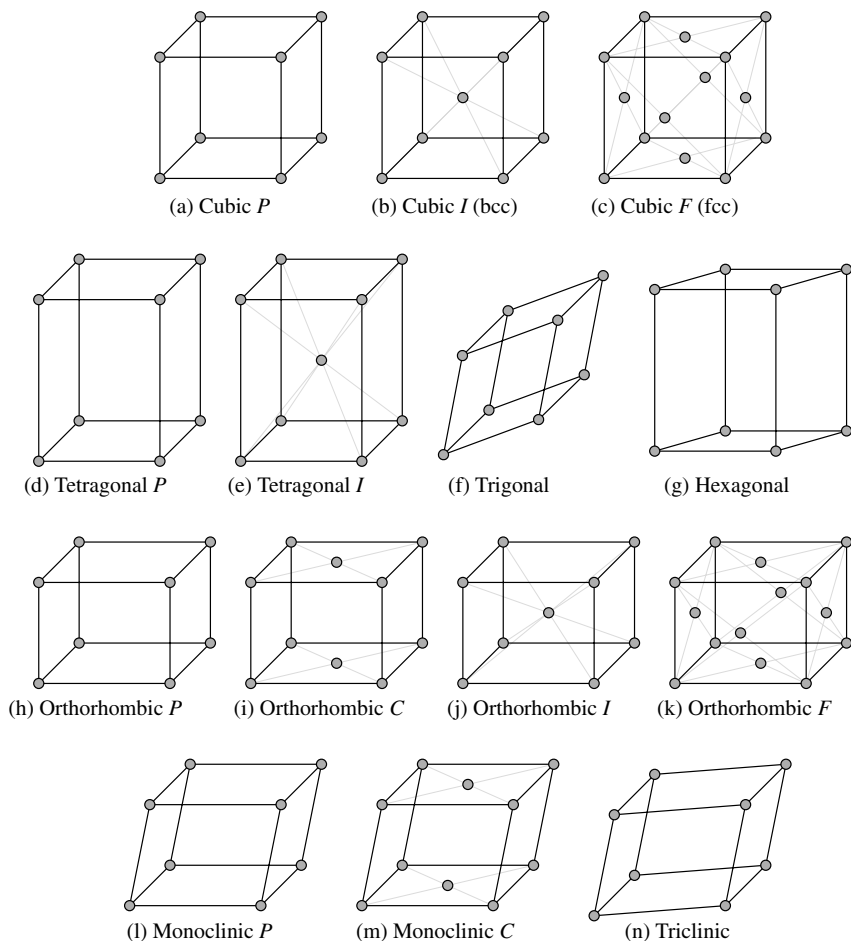


Figure 3.5 Three-dimensional Bravais lattices.

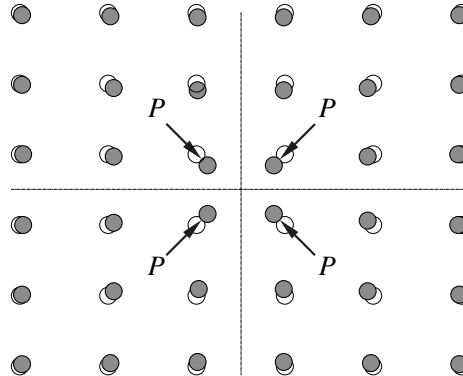


Figure 3.6 Rectangular lattice under symmetric loading. Empty circles indicate the preload configuration.

transformations that are typical of this system. For example, the potential energy function of a rotationally symmetric lattice must be invariant with respect to the same set of rotations of a global coordinate system. Correspondingly, the elastic tensor of an equivalent continuum media should have the same symmetries as the original lattice structure.

Principle 2. Symmetric causes, when acting on symmetric entities, result in symmetric effects with the same type of symmetry. One illustration of this principle is depicted in Figure 3.6. Here, a rectangularly symmetric load applied to a rectangular platelike lattice results in a deformation pattern that has the same symmetry as the original nondeformed Bravais lattice, namely, one horizontal and one vertical plane of symmetry, and one center of symmetry.

3.1.3 Crystallographic Directions and Planes

Translation vectors \mathbf{a}_i , $i = 1, 2, 3$, in the equation (3.1) define the major crystallographic directions/axes of a three-dimensional periodic lattice. In case of a multiatomic unit cell, such a direction is determined with respect to Cartesian axes by three repetitive components of \mathbf{a}_i . The vectors determining the major crystallographic directions provide a basis in a three-dimensional vector space, and the relevant basis vectors are denoted by [100], [010] and [001]. This basis is used to span an arbitrary vector of three integer components $[nml]$ that defines a specific *crystallographic axis* in the lattice structure.

Any plane orthogonal to the vector $[nml]$ and passing through nonempty lattice sites, is called the *crystal plane* (nml). Curly brackets around indices, $\{hkl\}$, are used in relation to a set of coplanar crystal planes equivalent by translation symmetry. For example, a set of cube faces shown in Figure 3.7 is {100}.

3.2 Equation of Motion of a Regular Lattice

Dynamic solutions for the system of particles that comprise a stable lattice structure can be sought according to the Lagrangian formalism presented in the previous chapter. Similarly,

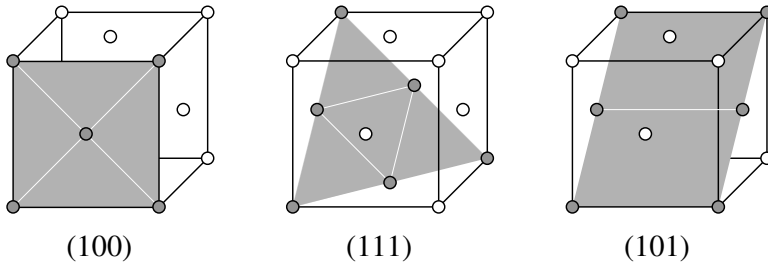


Figure 3.7 Some important crystal planes in the face-centered cubic lattice.

the lattice atoms, ions or molecules are exerting internal forces, the values of which are determined by the instantaneous values of the lattice potential energy. This energy is considered to be a known function of the spatial configuration of lattice particles only. Over the course of the system's dynamics, the structure of the interatomic potentials (2.46) is not perturbed by any possible changes in the internal quantum states of the vibrating lattice particles, as well as by any possible electronic excitations. This assumption is known as the *adiabatic approximation*, a major approximation of classical lattice dynamics and mechanics.

3.2.1 Unit Cell and the Associate Substructure

In studying the mechanical properties of lattice structures, it is convenient to choose a formal mathematical *unit cell* in the lattice. The unit cell is an *arbitrary* part of the lattice, whose spatial translations in arbitrarily fixed directions and distances form the whole lattice under analysis. The unit cell is a more general concept than the elementary cell (see Section 3.1); it can be larger/smaller than the elementary cell, or identical to it.

In accordance with translational symmetry, each particle from one unit cell can be associated with an identical particle from another unit cell, just as in the case of elementary cells. The spatial locations of the repetitive unit cells are determined by the lattice site vectors, \mathbf{n} such as (3.1). For a given unit cell, we introduce the time-dependent configuration vector $\mathbf{r}_n(t)$, which is composed of the radius vectors of all particles in the unit cell that correspond to the lattice site vector, as well as the vector of displacements of particles from their equilibrium positions,

$$\mathbf{u}_n(t) = \mathbf{r}_n(t) - \mathbf{n} \quad (3.2)$$

The discussion below concerns the displacement vectors only, and therefore we will refer to the subscript lattice site vector simply as a triplet of integer numbers, $\mathbf{n} \equiv (n_1, n_2, n_3)$, where $n_i = 0, 1, \dots, N_i$ is the *lattice site index*. In other words, $\mathbf{u}_n(t) \equiv \mathbf{u}_{n_1, n_2, n_3}(t)$. In some cases, we will use the following equivalent notations: $\mathbf{n} \equiv (n, m, l)$, where $n = 0, 1, \dots, N$, $m = 0, 1, \dots, M$, $l = 0, 1, \dots, L$, and $\mathbf{u}_n(t) \equiv \mathbf{u}_{n, m, l}(t)$. For one- and two-dimensional lattices, we have $\mathbf{n} \equiv n$ and $\mathbf{n} \equiv (n_1, n_2) \equiv (n, m)$, respectively. Since the vector \mathbf{n} uniquely defines the unit cells, the indices n_i can be used for their successive numbering.

The use of a unit cell, nonidentical with the elementary cell, can be dictated by the provisos of a given problem. These include the interatomic potential range, domain shape,

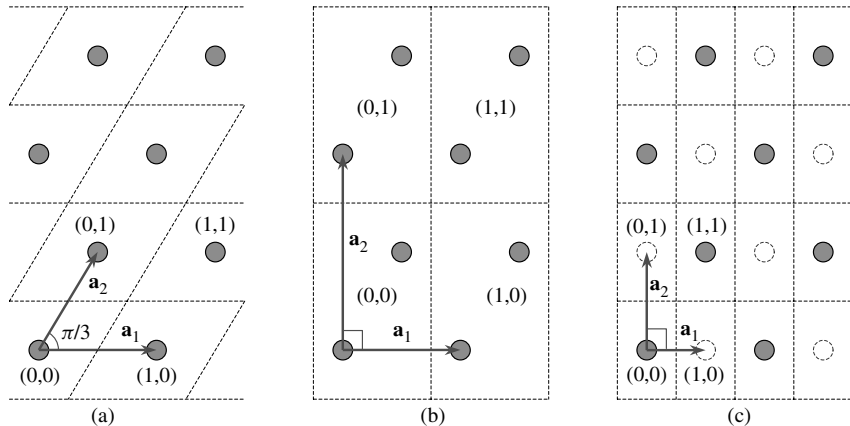


Figure 3.8 Three possible choices of the unit cell in a 2D hexagonal lattice. The unit cells are bounded by the dashed lines.

symmetry of the equations of motion, and convenience in applying boundary and interfacial conditions. For example, consider a hexagonal two-dimensional lattice with a natural choice of the elementary cell, composed of a single lattice atom, as shown in Figure 3.8(a). Next, assume that some special circumstances require numbering of the repetitive lattice cells to be applied in two orthogonal directions. One possibility is then to choose a diatomic unit cell, and apply the numbering as depicted in Figure 3.8(b).

According to the unit cell definition, it is not required that any translation of the type (3.1) should give a physical unit cell. Some of these translations may result in the so-called virtual (empty) lattice sites. It is required, though, that the actual unit cells are generated by applying a specific restriction on the values of lattice site indices. For example, for the hexagonal two-dimensional lattice shown in Figure 3.8(c), the actual lattice sites correspond to even $n_1 + n_2$, and the virtual lattice sites are those with odd $n_1 + n_2$.

One current unit cell plus all the neighboring unit cells, whose particles interact directly with the current cell particles, form the *associate substructure*, or *associate cell*. The size and shape of the associate cell are determined by the cutoff radius of an interatomic potential (see equation (2.65)). Figure 3.9 shows an example of an associate cell for the hexagonal lattice, where the atomic interaction is truncated after the second-nearest neighbor; here, the numbering of unit cells is chosen as in Figure 3.8(c). In the case that the interaction is truncated after the first-nearest neighbor, the associate cell is shaped similar to the hexagon depicted in Figure 3.3(b).

The associate cell is the smallest part of the lattice that fully represents its mechanical properties. In deriving the lattice governing equations, it is sufficient to consider only one associate cell, which is sufficient in deriving the lattice potential energy in a repeating manner, as in the equations (3.7) and (3.8). However, the associate cell does not necessarily generate the complete lattice by translations. If the associate cell is constructed

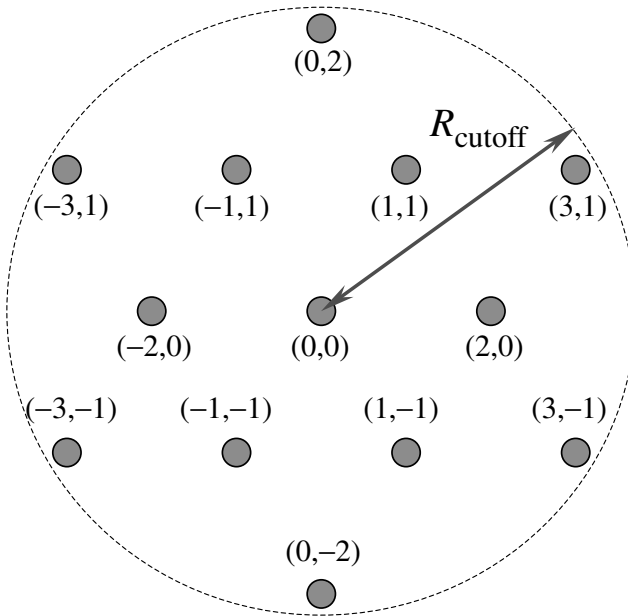


Figure 3.9 Associate cell for the hexagonal lattice. Atomic interaction is truncated after the second nearest neighbor.

from the smallest possible unit cells, it usually has the same point symmetry as the corresponding Bravais lattice; see the structures depicted in Figure (3.3), and also Figures 3.8(c) and 3.9.

3.2.2 Lattice Lagrangian and Equations of Motion

In order to write the lattice equation of motion, we require the lattice Lagrangian in terms of the particle displacement vectors \mathbf{u}_n . The kinetic energy of lattice particles can be written in the matrix form,

$$T = \frac{1}{2} \sum_n \dot{\mathbf{u}}_n^T \mathbf{M} \dot{\mathbf{u}}_n \quad (3.3)$$

where \mathbf{M} is a diagonal matrix of particle masses written for one unit cell. This gives the lattice Lagrangian in the general form

$$L = \frac{1}{2} \sum_n \dot{\mathbf{u}}_n^T \mathbf{M} \dot{\mathbf{u}}_n - U(\mathbf{u}) \quad (3.4)$$

Here, U is the lattice potential energy, and \mathbf{u} is a formal notation for all the displacement vectors \mathbf{u}_n in a given lattice.

Substituting (3.4) into the Lagrange equation of motion, written for one unit cell with S degrees of freedom,

$$\frac{d}{dt} \frac{\partial L}{\partial \dot{u}_{\mathbf{n},s}} - \frac{\partial L}{\partial u_{\mathbf{n},s}} = f_{\mathbf{n},s}^{\text{ext}}, \quad s = 1, 2, \dots, S \quad (3.5)$$

we obtain the lattice equations of motion,

$$\mathbf{M} \ddot{\mathbf{u}}_{\mathbf{n}} + \frac{\partial U}{\partial \mathbf{u}_{\mathbf{n}}} = \mathbf{f}_{\mathbf{n}}^{\text{ext}}, \quad \mathbf{n} = (n_1, n_2, n_3) \quad (3.6)$$

where $\mathbf{f}_{\mathbf{n}}^{\text{ext}}$ is the vector of external forces exerted on the current unit cell \mathbf{n} . In equation (3.6), $u_{\mathbf{n},s}$ and $f_{\mathbf{n},s}^{\text{ext}}$ are individual components of the vectors $\mathbf{u}_{\mathbf{n}}$ and $\mathbf{f}_{\mathbf{n}}^{\text{ext}}$, respectively. Utilizing all the lattice site vectors in (3.6) we get a coupled system of generally nonlinear ordinary differential equations.

One special form of the lattice equation of motion can be obtained within the *harmonic approximation*, which consists of expanding the potential energy in a Taylor series about the equilibrium lattice configuration,

$$U(\mathbf{u}) = U(\mathbf{0}) + \sum_{\mathbf{n},s} \frac{\partial U}{\partial u_{\mathbf{n},s}} \Big|_0 u_{\mathbf{n},s} + \frac{1}{2} \sum_{\mathbf{n},\mathbf{n}',s,s'} \frac{\partial^2 U}{\partial u_{\mathbf{n},s} \partial u_{\mathbf{n}',s'}} \Big|_0 u_{\mathbf{n},s} u_{\mathbf{n}',s'} + \dots \quad (3.7)$$

and truncating the series after the second-order terms. Meanwhile, the first-order terms in (3.7) are trivial, as soon as expanded about the equilibrium configuration, that is, about the global minimum of the lattice potential. The zero-order term can be ignored in (3.7), because a constant shift of the Lagrangian does not alter the equations of motion. Finally, the harmonic approximation gives the lattice Lagrangian,

$$L = \frac{1}{2} \sum_{\mathbf{n}} \dot{\mathbf{u}}_{\mathbf{n}}^T \mathbf{M} \dot{\mathbf{u}}_{\mathbf{n}} + \frac{1}{2} \sum_{\mathbf{n},\mathbf{n}'} \mathbf{u}_{\mathbf{n}}^T \mathbf{K}_{\mathbf{n}-\mathbf{n}'} \mathbf{u}_{\mathbf{n}'} \quad (3.8)$$

where the superscript symbol T indicates a transposed vector, and the equation of motion reads as the finite difference matrix form:

$$\mathbf{M} \ddot{\mathbf{u}}_{\mathbf{n}}(t) - \sum_{\mathbf{n}'} \mathbf{K}_{\mathbf{n}-\mathbf{n}'} \mathbf{u}_{\mathbf{n}'}(t) = \mathbf{f}_{\mathbf{n}}^{\text{ext}}(t) \quad (3.9)$$

Here, \mathbf{K} are the lattice stiffness matrices, or “ K -matrices”, which represent linear elastic properties of the lattice structure. These matrices are composed of the atomic force constants, according to

$$\mathbf{K}_{\mathbf{n}-\mathbf{n}'} = - \frac{\partial^2 U(\mathbf{u})}{\partial \mathbf{u}_{\mathbf{n}} \partial \mathbf{u}_{\mathbf{n}'}} \Big|_{\mathbf{u}=0} \quad (3.10)$$

For a one-, two- or three-dimensional lattice with nearest unit cell interactions, there are up to 3, 9 or 27 nontrivial K -matrices, respectively. Owing to symmetry of the second-order derivative in (3.10), they have the following general property:

$$\mathbf{K}_{\mathbf{n}} = \mathbf{K}_{-\mathbf{n}}^T \quad (3.11)$$

One important feature of the equations (3.9) is their invariance with respect to the value of a current lattice site vector \mathbf{n} . This invariance is due to the fact that the K -matrices do not

depend on the individual values of \mathbf{n} and \mathbf{n}' , but depend only on the difference $\mathbf{n} - \mathbf{n}'$, that is, on the distance between the current unit cell, specified by \mathbf{n} , and a neighboring cell \mathbf{n}' that interacts with the current cell. Sometimes, a single subscript \mathbf{n} is used for brevity, as in equation (3.11). In such a case, it still implies the difference $\mathbf{n} - \mathbf{n}'$, that is, $\mathbf{n} \equiv \mathbf{n} - \mathbf{n}'$.

According to the first symmetry principle discussed in Section 3.1.2, the spatial invariance of the K -matrices serves as a consequence of the lattice translational symmetry. In the derivations of K -matrices, it is sufficient to consider the potential energy for one associate cell only.

The lattice equation of motion (3.9) is an ordinary differential equation with a finite difference with respect to the spatial lattice site indices. This finite difference is given by a discrete convolution sum with a spatially invariant matrix kernel. The effective solution of this equation involves transform methods that convert the operation of convolution into ordinary matrix multiplication in the transform domain. The relevant solution techniques are discussed in Sections 3.3–3.5.

3.2.3 Examples

In this section, we construct the harmonic equations of motion for several specific examples of repetitive lattice structures governed by a pair-wise potential ((2.60) or (2.63)).

Monoatomic chain lattice

The monoatomic chain lattice (Figure 3.2 (a)) is the simplest example where all mathematical derivations of the present chapter can be accomplished in closed form.

Assuming a single longitudinal degree of freedom for each atom, the displacement vector becomes a scalar quantity, $\mathbf{u}_n = u_n$. Next, we assume that interactions exist only between the nearest lattice atoms; this can be viewed so that the cutoff radius of the potential function is close to 1.5ρ , where ρ is the equilibrium distance for the potential. The corresponding associate cell is shown in Figure 3.10.

In deriving the K -matrices (3.10), the potential energy of the atomic interactions needs to be written for one associate cell only; this gives

$$U = V(u_n - u_{n-1} + \rho) + V(u_{n+1} - u_n + \rho) \quad (3.12)$$

where V is a pair-wise potential with the previously defined equilibrium distance ρ . According to (3.10) and (3.12), the K -matrices yield

$$\mathbf{K}_{-1} = \frac{-\partial^2 U}{\partial u_n \partial u_{n+1}} = k, \quad \mathbf{K}_0 = \frac{-\partial^2 U}{\partial u_n^2} = -2k, \quad \mathbf{K}_1 = \frac{-\partial^2 U}{\partial u_n \partial u_{n-1}} = k \quad (3.13)$$

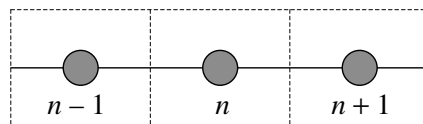


Figure 3.10 Associate cell for a monoatomic chain lattice interacting via nearest-neighbor interactions.

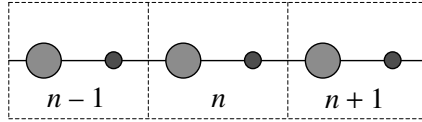


Figure 3.11 Associate cell for a diatomic polymer chain.

Here, the linear force constant k depends on the parameters of the potential,

$$k = 36 \cdot 2^{2/3} \varepsilon / \sigma^2 \text{ (Lennard - Jones), } k = 2\varepsilon\beta^2 \text{ (Morse)} \quad (3.14)$$

Note that all other matrices \mathbf{K}_n , $|n| > 1$, are trivial owing to the nearest-neighbor assumption.

Substitution of the K -matrices (3.13) into the general equation of motion (3.9) yields (M is the atomic mass)

$$M \ddot{\mathbf{u}}_n - k(u_{n-1} - 2u_n + u_{n+1}) = f_n^{\text{ext}} \quad (3.15)$$

Diatom polymer molecule

A unit cell for the diatomic polymer molecule (Figure 3.2 (third from top)), is given by a pair of nearby atoms. The lattice associate cell is depicted in Figure 3.11; it consists of a current unit cell, numbered as n , and two adjacent cells, $n - 1$ and $n + 1$, interacting directly with the current cell.

As in the previous example, we assume a single longitudinal degree of freedom per each atom with nearest-neighbor interactions. Then, the displacement vector consists of two components, $\mathbf{u}_n = (v_n, w_n)^T$, where v and w are the displacements of the left and right atoms in the unit cell, respectively. The potential energy of the associate cell is given by

$$\begin{aligned} U = & V(w_{n-1} - v_{n-1} + \rho) + V(v_n - w_{n-1} + \rho) + V(w_n - v_n + \rho) \\ & + V(v_{n+1} - w_n + \rho) + V(w_{n+1} - v_{n+1} + \rho) \end{aligned} \quad (3.16)$$

where V is a potential of interaction of two adjacent atoms and ρ is the equilibrium distance of this potential. The corresponding lattice stiffness matrices are found by utilizing (3.10):

$$\mathbf{K}_0 = \begin{pmatrix} -2k & k \\ k & -2k \end{pmatrix}, \quad \mathbf{K}_1 = \mathbf{K}_{-1}^T = \begin{pmatrix} 0 & k \\ 0 & 0 \end{pmatrix} \quad (3.17)$$

where k is the force constant (3.14). Substitution of these matrices into

$$\mathbf{M} \ddot{\mathbf{u}}_n - (\mathbf{K}_1 \mathbf{u}_{n-1} + \mathbf{K}_0 \mathbf{u}_n + \mathbf{K}_{-1} \mathbf{u}_{n+1}) = \mathbf{f}_n^{\text{ext}} \quad (3.18)$$

gives the equation of motion in matrix form.

Hexagonal lattice

The hexagonal lattice pattern (Figure 3.12) is observed for the (111) crystallographic plane of a face-centered cubic lattice(see Figure 3.7). As a result, this geometry is often used in two-dimensional modeling of fcc metals.

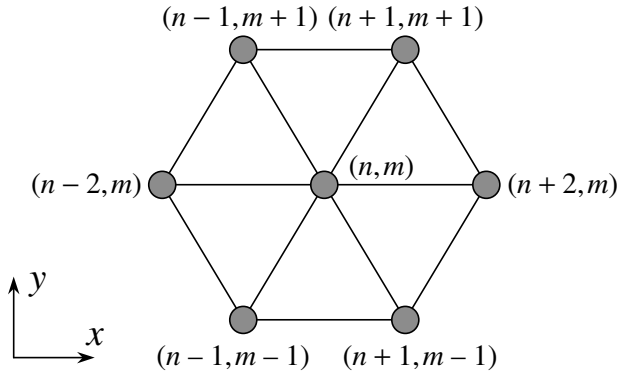


Figure 3.12 Associate cell for a two-dimensional hexagonal lattice interacting via nearest-neighbor interactions.

Consider an orthogonal numbering of unit cells in the hexagonal lattice, such as that displayed in Figure 3.8(c). Then the unit cell is represented by a single lattice atom, and the vector \mathbf{u}_n shows in-plane displacements of this atom with the reference to x and y Cartesian axes: $\mathbf{u}_n \equiv \mathbf{u}_{n,m} = (x_{n,m}, y_{n,m})^T$. Within the nearest-neighbor assumption, the associate cell is formed by a symmetric group of seven lattice atoms as depicted in Figure (3.12).

Similar to (3.12) and (3.16), the potential energy of the associate cell in the hexagonal lattice can be expressed through $x_{n,m}$, $y_{n,m}$ and ρ . Further, use of the definition (3.10) provides seven nonzero matrices:

$$\begin{aligned}\mathbf{K}_{0,0} &= -3k \begin{pmatrix} 1 & 0 \\ 0 & 1 \end{pmatrix}, & \mathbf{K}_{1,1} = \mathbf{K}_{-1,-1} &= \frac{k}{4} \begin{pmatrix} 1 & \sqrt{3} \\ \sqrt{3} & 3 \end{pmatrix} \\ \mathbf{K}_{1,-1} = \mathbf{K}_{-1,1} &= \frac{k}{4} \begin{pmatrix} 1 & -\sqrt{3} \\ -\sqrt{3} & 3 \end{pmatrix}, & \mathbf{K}_{2,0} = \mathbf{K}_{-2,0} &= k \begin{pmatrix} 1 & 0 \\ 0 & 0 \end{pmatrix}\end{aligned}\quad (3.19)$$

Finally, the lattice equation of motion is given by

$$\mathbf{M} \ddot{\mathbf{u}}_{n,m} - \sum_{n'=n-2}^{n+2} \sum_{m'=m-1}^{m+1} \mathbf{K}_{n-n',m-m'} \mathbf{u}_{n',m'} = \mathbf{f}_{n,m}^{\text{ext}} \quad (3.20)$$

In equation (3.126) of Section 3.6.3, we also show the lattice stiffness matrices for a three-dimensional fcc crystal.

3.3 Transforms

The concept of a functional transform can be explained in analogy with the definition of a function. While the function f assigns to every element x from set Ω_x a unique element $y = f(x)$ from set Ω_y , where x and y are numbers, the functional transform A is a similar operation, but with x and y being functions themselves, $y = A\{x\}$. Thus, the functional transform assigns a new (transform) function X for each original function x suitable

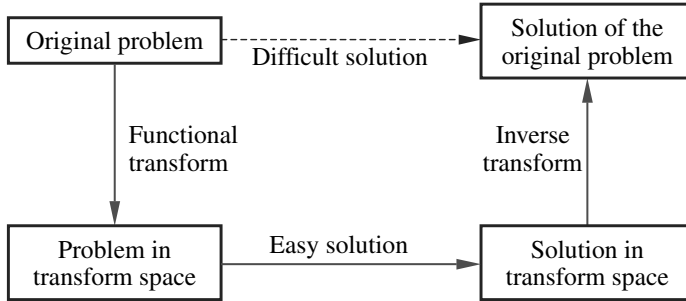


Figure 3.13 General idea of the transform solution methods, Arfken and Weber (2001).

for the given transformation. Examples include $X(t) = \frac{d}{dt}x(t)$, $X(\beta) = \int_a^b x(t)Q(\beta, t) dt$, and so on. The second of these examples is known as the integral transform with the kernel function Q ; a suitable candidate x for the integral transform has to be a function integrable on the interval $[a,b]$.

Integral transforms take on physical significance in the time-frequency relations established by the *Fourier transform*, as well as the *Laplace transform*, which are reviewed in this section. Another type of functional transform used in the following sections is the *discrete Fourier transform* (DFT) accomplished over discontinuous sequences, such as the displacement vectors \mathbf{u}_n and the matrices \mathbf{K}_n ; these sequences are viewed as discrete functions of the lattice site indices n_i . The discrete Fourier transform establishes relations between the quantities in the real-space quantities and the space of wave numbers. The common idea behind the transform solution methods is explained in Figure 3.13. The transform methods are effective in applications to ordinary differential equations with a finite difference of the type (3.9).

The Laplace, Fourier and discrete Fourier transforms outlined in this section are *linear*, that is, they satisfy the following general property,

$$A\{C_1x + C_2y\} = C_1A\{x\} + C_2A\{y\} = C_1X + C_2Y \quad (3.21)$$

where x and y are functions, and C_1 , C_2 are constant numbers.

The inverse transform, A^{-1} , is defined as the following:

$$A^{-1}\{A\{x\}\} = A^{-1}\{X\} = x \quad (3.22)$$

The inverse of a linear transform is also a linear transform,

$$A^{-1}\{C_1X + C_2Y\} = C_1x + C_2y \quad (3.23)$$

3.3.1 Fourier Transform

The Fourier transform is used to transform a time-dependent function into the frequency space,

$$X(\omega) = \mathcal{F}_{t \rightarrow \omega}\{x(t)\} = \int_{-\infty}^{\infty} x(t) e^{-i\omega t} dt \quad (3.24)$$

Fourier transforms obey the time-derivative theorem,

$$\mathcal{F}_{t \rightarrow \omega} \left\{ \left(\frac{\partial}{\partial t} \right)^n f(t) \right\} = (i\omega)^n F(\omega) \quad (3.25)$$

The inverse Fourier transform is defined as

$$x(t) = \mathcal{F}_{\omega \rightarrow t}^{-1} \{ X(\omega) \} = \frac{1}{2\pi} \int_{-\infty}^{\infty} X(\omega) e^{i\omega t} d\omega \quad (3.26)$$

3.3.2 Laplace Transform

The Laplace transform of a continuous function in time gives

$$X(s) = \mathcal{L}_{t \rightarrow s} \{ x(t) \} = \int_0^{\infty} e^{-st} x(t) dt \quad (3.27)$$

where s is known as the complex frequency. The Laplace transform has the following valuable properties: the convolution theorem,

$$\mathcal{L}_{t \rightarrow s} \left\{ \int_0^t x(t - \tau) y(\tau) d\tau \right\} = X(s) Y(s) \quad (3.28)$$

and the time-derivative rules,

$$\mathcal{L}_{t \rightarrow s} \{ \dot{x}(t) \} = sX(s) - x(0-) \quad (3.29)$$

$$\mathcal{L}_{t \rightarrow s} \{ \ddot{x}(t) \} = s^2 X(s) - sx(0-) - \dot{x}(0-) \quad (3.30)$$

Here, the notation “ $0-$ ” stands for a value of the argument t “right before” the zero point. Mathematically, $x(0-)$ and $\dot{x}(0-)$ are limits of the functions $x(t)$ and $\dot{x}(t)$, as t approaches zero from negative values.

The convolution theorem implies that the transform of a convolution integral of two functions is equal to the product of the transforms of the individual functions. The time-derivative rules imply that the transform of a time derivative is equivalent to multiplication of a function by s . This property allows reducing differential equations to simple algebraic equations in the transform domain, and therefore it is useful in finding analytical solutions to the classical equations of motion; see the example below in this section.

The inverse Laplace transform is defined as

$$x(t) = \mathcal{L}_{s \rightarrow t}^{-1} \{ X(s) \} = \lim_{b \rightarrow \infty} \frac{1}{2\pi i} \int_{a-i b}^{a+i b} e^{st} X(s) ds, \quad a, b \in \mathbf{R} \quad (3.31)$$

However, this general mathematical definition is rarely used in practical applications. In some cases, the inverse Laplace transform for $X(s)$, that is, the function $x(t)$, can be found in the standard tables, such as Oberhettinger and Badii (1973). In Table 3.2, we provide a short listing of some standard Laplace transforms. This table includes power, exponential and trigonometric functions, as well as two special functions: the Dirac delta,

$$\delta(t) = \begin{cases} \infty, & t = 0, \\ 0, & t \neq 0; \end{cases} \quad \int_{-\infty}^{\infty} \delta(t) dt = 1, \quad \int_{-\infty}^{\infty} \delta(t - t_0) x(t) dt = x(t_0) \quad (3.32)$$

Table 3.2 Standard Laplace transforms

	$x(t)$	$X(s)$
1.	$x(at)$	$\frac{1}{a} X\left(\frac{s}{a}\right)$
2.	$e^{-at}x(t)$	$X(s + a)$
3.	$t^n x(t) \quad (n = 0, 1, \dots)$	$(-1)^n X^{(n)}(s)$
4.	$\int_0^t x(\tau) d\tau$	$\frac{1}{s} X(s)$
5.	$x(t - t_0) \quad (t > t_0)$	$e^{-st_0} X(s)$
6.	$\delta(t)$	1
7.	$\delta(t - t_0)$	e^{-st_0}
8.	$t^n \quad (n = 0, 1, \dots)$	$\frac{n!}{s^{n+1}}$
9.	\sqrt{t}	$\frac{1}{2s} \sqrt{\frac{\pi}{s}}$
10.	$\frac{1}{\sqrt{t}}$	$\sqrt{\frac{\pi}{s}}$
11.	e^{-at}	$\frac{1}{s + a}$
12.	$\ln t$	$-\frac{\gamma + \ln s}{s} \quad (\gamma = 0.57722\dots)$
13.	$\sin at$	$\frac{a}{s^2 + a^2}$
14.	$\cos at$	$\frac{s}{s^2 + a^2}$
15.	$\sinh at$	$\frac{a}{s^2 - a^2}$
16.	$\cosh at$	$\frac{s}{s^2 - a^2}$
17.	$J_n(at) \quad (n = 0, 1, \dots)$	$\frac{(\sqrt{s^2 + a^2} - s)^n}{a^n \sqrt{s^2 + a^2}}$
18.	$\frac{1}{t} J_n(at) \quad (n = 1, 2, \dots)$	$\frac{(\sqrt{s^2 + a^2} - s)^n}{na^n}$

and the Bessel function,

$$J_n(t) = \frac{1}{\pi} \int_0^\pi \cos(t \sin \phi - n\phi) d\phi \quad (3.33)$$

For a more comprehensive list of Laplace transforms, we refer the reader to mathematics literature.

More generally, the inverse Laplace transform can be computed numerically. One effective numerical algorithm applicable to a wide range of functions was proposed by Weeks

(1966). This algorithm can be summarized as follows:

$$\begin{aligned} x(t) &= e^{ct - \frac{t}{2T}} \sum_{\gamma=0}^A b_\gamma L_\gamma(t/T) \\ b_\gamma &= \frac{2 - \delta_{\gamma,0}}{2T(A+1)} \sum_{\alpha=0}^A \left(\operatorname{Re}X(s_\alpha) - \cot \frac{z_\alpha}{2} \operatorname{Im}X(s_\alpha) \right) \cos(\gamma z_\alpha) \\ z_\alpha &= \frac{\pi(2\alpha+1)}{2(A+1)}, \quad s_\alpha = c + \frac{i}{2T} \cot \frac{z_\alpha}{2}, \\ T &= \frac{t_{\max}}{A}, \quad c = \frac{1}{t_{\max}} \end{aligned} \quad (3.34)$$

Here, L_γ are Laguerre polynomials, X is the Laplace transform of x , t_{\max} is the maximum required value of the argument for the function x , and δ is the Kronecker delta,

$$\delta_{i,j} = \begin{cases} 1, & i = j \\ 0, & i \neq j \end{cases} \quad (3.35)$$

The value A controls the accuracy of the result, and its choice depends on t_{\max} and the behavior of $f(t)$ at $t \in [0, t_{\max}]$. For the kernel functions considered in this section and in the subsequent sections of this book, a sufficient value for A is of the order 100. Weeks's method has been found by Davies and Martin (1979) to give excellent accuracy for the inversion of a wide range of functions. Other numerical inversion algorithms are discussed in Davies and Martin (1979) and Duffy (1993).

Example: harmonic oscillator

Consider the solution to the equation of motion of a harmonic oscillator subject to the initial conditions:

$$\ddot{y}(t) + \omega^2 y(t) = 0, \quad y(0) = B, \quad \dot{y}(0) = 0 \quad (3.36)$$

Applying the Laplace transform and taking into account (3.21) and (3.30), one obtains a simple algebraic equation for the transform solution $Y(s)$,

$$s^2 Y(s) + \omega^2 Y(s) = sB \quad (3.37)$$

This gives

$$Y(s) = B \frac{s}{s^2 + \omega^2} \quad (3.38)$$

The original for this function can be found in Table 3.2; application of the inverse Laplace transform to (3.38) yields

$$y(t) = B \cos \omega t \quad (3.39)$$

3.3.3 Discrete Fourier Transform

In lattice mechanics, the DFT is used to transform functional sequences, such as the displacement vector \mathbf{u}_n or matrix \mathbf{K}_n from real space to wave number space.

A key issue in solving the lattice equation of motion (3.9) is the deconvolution of the internal force term. This is accomplished naturally with the discrete Fourier transform,

$$\hat{x}(p) = \mathcal{F}_{n \rightarrow p} \{x_n\} = \sum_n x_n e^{-ipn}, \quad p \in [-\pi, \pi] \quad (3.40)$$

$$x_n = \mathcal{F}_{p \rightarrow n}^{-1} \{\hat{x}(p)\} = \frac{1}{2\pi} \int_{-\pi}^{\pi} \hat{x}(p) e^{ipn} dp \quad (3.41)$$

which obeys the convolution theorem,

$$\mathcal{F}_{n \rightarrow p} \left\{ \sum_{n'} x_{n-n'} y_{n'} \right\} = \hat{x}(p) \hat{y}(p) \quad (3.42)$$

Here, the calligraphic symbol \mathcal{F} denotes the Fourier transform operator, and the hatted notation is used for the Fourier domain function.

The inverse transform can be computed numerically by applying a trapezoidal or midpoint scheme to the integral (3.41). The trapezoidal scheme yields

$$x_n = \mathcal{F}_{p \rightarrow n}^{-1} \{\hat{x}(p)\} = \frac{1}{N} \sum_{\tilde{p}=(1-N)/2-1}^{(N-1)/2} \hat{x}(2\pi \tilde{p}/N) e^{i2\pi \tilde{p}n/N} \quad (3.43)$$

Here, N is the total number of integration steps, which gives an effective size of the real-space domain, and the value \tilde{p} is an integer wave number, varying from $-N/2$ to $N/2 - 1$. The midpoint scheme gives an alternative symmetric form,

$$x_n = \mathcal{F}_{p \rightarrow n}^{-1} \{\hat{x}(p)\} = \frac{1}{N} \sum_{\tilde{p}=(1-N)/2}^{(N-1)/2} \hat{x}(2\pi \tilde{p}/N) e^{i2\pi \tilde{p}n/N} \quad (3.44)$$

where the half-integer wave number \tilde{p} varies from $(1 - N)/2$ to $(N - 1)/2$ with a unit step.

Provided the function \hat{x} is simple enough, the integral (3.44) can be used for analytical inversion of the DFT. Meanwhile, solutions involving a standard summation (3.43) or (3.44) are called semianalytical.

A final valuable property of the DFT is the shift theorem,

$$\mathcal{F}\{x_{n+h}\} = \hat{x}(p)e^{ihp}, \quad h \in \mathbf{Z} \quad (3.45)$$

3.4 Standing Waves in Lattices

In this section, we consider the solution of the equation of motion of a free lattice,

$$\mathbf{M} \ddot{\mathbf{u}}_n(t) - \sum_{n'} \mathbf{K}_{n-n'} \mathbf{u}_{n'}(t) = \mathbf{0} \quad (3.46)$$

that is, with all trivial external loadings, $\mathbf{f}_n^{\text{ext}} = \mathbf{0}$, as compared to (3.9). A general solution to this equation can be found as a superposition of standing waves in the polymer or crystal lattice. Each of these waves represents one normal mode of the free lattice vibration, for example, thermal vibrations. For a given normal mode, the lattice atoms oscillate with a unique frequency around their equilibrium positions. We demonstrate below the structure of such a solution by utilizing Fourier transform methods.

3.4.1 Normal Modes and Dispersion Branches

In deriving the free lattice solution, we first utilize the DFT in space over both sides of equation (3.46) for all components of the vector \mathbf{n} . Further use of the convolution theorem (3.42) gives an equation in the space of wave numbers,

$$\mathbf{M} \hat{\mathbf{u}}(t, \mathbf{p}) - \hat{\mathbf{K}}(\mathbf{p}) \hat{\mathbf{u}}(t, \mathbf{p}) = \mathbf{0} \quad (3.47)$$

Here, each wavevector \mathbf{p} gives a triplet of wave numbers, $\mathbf{p} = (p_1, p_2, p_3)$.

We next apply the continuous Fourier transform in time (3.24), and employ the time-derivative theorem (3.25). This gives the equation of motion in the frequency/wave number Fourier domain,

$$(\omega^2 \mathbf{M} + \hat{\mathbf{K}}(\mathbf{p})) \hat{\mathbf{U}}(\mathbf{p}, \omega) = \mathbf{0} \quad (3.48)$$

As compared to the original time/space equation (3.46), this equation is simply an algebraic equation with small parametric matrices \mathbf{M} and $\hat{\mathbf{K}}(\mathbf{p})$ of the size $S \times S$, where S is the number of degrees of freedom per unit cell. The solution of this equation is straightforward.

At first, note that equation (3.48) has nontrivial solutions only if

$$\det(\omega^2 \mathbf{M} + \hat{\mathbf{K}}(\mathbf{p})) = 0 \quad (3.49)$$

This characteristic equation imposes a functional dependence of the normal frequency upon the wave vector, $\omega(\mathbf{p})$, known as the *dispersion law*. For an S -component vector $\hat{\mathbf{U}}$, there exist S linearly independent functions $\omega_s(\mathbf{p})$, $s = 1, 2, \dots, S$, called the *dispersion branches*.

The dispersion branches are divided into two classes: acoustic branches with $\omega(0) = 0$ and optical branches with $\omega(0) \neq 0$. They refer respectively to a particular value of the function $\omega_s(\mathbf{p})$ as an acoustic or optical frequency. Normally, the total number of acoustic branches is equal to I , the dimensionality of the lattice; then, the total number of optical branches is $S - I$. Dispersion properties of periodic lattices are discussed in greater detail in solid-state physics literature, for example, Kittel (1976). Some simple examples are also considered in Section 3.4.2.

For a finite lattice, there exists a discrete set of characteristic normal frequencies $\omega_{\mathbf{p},s}$ corresponding to each of the dispersion branches. Thus, a solution of equation (3.48) can be nontrivial only for $\omega = \pm\omega_{\mathbf{p},s}$:

$$\hat{\mathbf{U}}(\mathbf{p}, \omega) = \sum_s a_{\mathbf{p},s} \mathbf{d}_{\mathbf{p},s} (\delta(\omega - \omega_{\mathbf{p},s}) + \delta(\omega + \omega_{\mathbf{p},s})) \quad (3.50)$$

where $a_{\mathbf{p},s}$ is a participation coefficient, δ is the Dirac's delta function (3.32), and $\mathbf{d}_{\mathbf{p},s}$ is a complex parametric eigenvector that satisfies

$$-\mathbf{M}^{-1} \hat{\mathbf{K}}(\mathbf{p}) \mathbf{d}_{\mathbf{p},s} = \omega_{\mathbf{p},s}^2 \mathbf{d}_{\mathbf{p},s} \quad (3.51)$$

We next apply the inverse Fourier transform (3.26) for ω , and the inverse DFT (3.43) for the components of \mathbf{p} , onto the equation (3.50) to get

$$\mathbf{u}_n(t) = \frac{1}{2\pi N} \sum_{\mathbf{p},s} a_{\mathbf{p},s} \cos(\omega_{\mathbf{p},s} t) \mathbf{d}_{\mathbf{p},s} e^{i \bar{\mathbf{p}} \cdot \mathbf{n}} \quad (3.52)$$

where $\tilde{\mathbf{p}} = 2\pi(p_1/N_1, p_2/N_2, p_3/N_3)$ and $N = N_1N_2N_3$. Obviously, the temporal parts of the normal modes in (3.52) may also contain some arbitrary initial phases ϕ . Furthermore, the constant $(2\pi N)^{-1}$ can be viewed as the scaling factor for the participation coefficients. Thus, we rewrite the solution (3.52) in the form

$$\mathbf{u}_n(t) = \sum_{\mathbf{p}, s} a_{\mathbf{p}, s} \cos(\omega_{\mathbf{p}, s} t + \phi_{\mathbf{p}, s}) \mathbf{d}_{\mathbf{p}, s} e^{i \tilde{\mathbf{p}} \cdot \mathbf{n}} \quad (3.53)$$

Here, each term of the summation represents a normal mode of the lattice. For each value of the wave vector \mathbf{p} , there exist s linearly independent normal modes. The oscillatory quantities $a_{\mathbf{p}, s} \cos(\omega_{\mathbf{p}, s} t + \phi_{\mathbf{p}, s})$ are normal coordinates and the values $a_{\mathbf{p}, s}$ and $\omega_{\mathbf{p}, s}$ are normal amplitudes and normal frequencies of the lattice vibration. The structure of solution (3.53) implies that the vector $\mathbf{d}_{\mathbf{p}, s}$ determines the direction of polarization of a normal mode vibration. Also, the form of this solution indicates that the normal modes represent standing waves in the lattice.

Note that because of (3.11) the Fourier transform matrix $\hat{\mathbf{K}}(\mathbf{p})$ is Hermitian, that is, it has the property

$$\hat{\mathbf{K}}^*(\mathbf{p}) = \hat{\mathbf{K}}^T(\mathbf{p}) \quad (3.54)$$

where the asterisk stands for complex conjugation, and also

$$\hat{\mathbf{K}}^*(\mathbf{p}) = \hat{\mathbf{K}}(-\mathbf{p}) \quad (3.55)$$

Indeed,

$$\hat{\mathbf{K}}^*(\mathbf{p}) = \sum_{\mathbf{n}} \mathbf{K}_{\mathbf{n}} e^{i \tilde{\mathbf{p}} \cdot \mathbf{n}} = \hat{\mathbf{K}}(-\mathbf{p}) = \sum_{\mathbf{n}} \mathbf{K}_{-\mathbf{n}} e^{-i \tilde{\mathbf{p}} \cdot \mathbf{n}} = \sum_{\mathbf{n}} \mathbf{K}_{\mathbf{n}}^T e^{-i \tilde{\mathbf{p}} \cdot \mathbf{n}} = \hat{\mathbf{K}}^T(\mathbf{p}) \quad (3.56)$$

As a result of (3.55), the eigenvectors in (3.51) obey

$$\mathbf{d}_{-\mathbf{p}, s} = \mathbf{d}_{\mathbf{p}, s}^* \quad (3.57)$$

Taking into account this symmetry, we can construct two real-valued solutions to the lattice equation of motion (3.46):

$$\mathbf{u}_n^+(t) = \sum_{\mathbf{p}, s} a_{\mathbf{p}, s}^+ \cos(\omega_{\mathbf{p}, s} t + \phi_{\mathbf{p}, s}^+) (\cos(\tilde{\mathbf{p}} \cdot \mathbf{n}) \operatorname{Re} \mathbf{d}_{\mathbf{p}, s} - \sin(\tilde{\mathbf{p}} \cdot \mathbf{n}) \operatorname{Im} \mathbf{d}_{\mathbf{p}, s}) \quad (3.58)$$

and

$$\mathbf{u}_n^-(t) = \sum_{\mathbf{p}, s} a_{\mathbf{p}, s}^- \cos(\omega_{\mathbf{p}, s} t + \phi_{\mathbf{p}, s}^-) (\sin(\tilde{\mathbf{p}} \cdot \mathbf{n}) \operatorname{Re} \mathbf{d}_{\mathbf{p}, s} + \cos(\tilde{\mathbf{p}} \cdot \mathbf{n}) \operatorname{Im} \mathbf{d}_{\mathbf{p}, s}) \quad (3.58')$$

Here, the operators Re and Im give the real and imaginary parts of the polarization vectors. The normal amplitudes and phases can be different in (3.58) and (3.58') for the same pair \mathbf{p} and s ; however, they should satisfy

$$a_{-\mathbf{p}, s}^+ = a_{\mathbf{p}, s}^+, \quad a_{-\mathbf{p}, s}^- = -a_{\mathbf{p}, s}^-, \quad \phi_{-\mathbf{p}, s}^\pm = \phi_{\mathbf{p}, s}^\pm \quad (3.59)$$

Owing to the symmetries (3.57) and (3.59), any pair of terms in (3.58) corresponding to $-\mathbf{p}$ and \mathbf{p} are identical. Thus, the solutions (3.58) are in total composed of SN linearly

independent real-valued normal modes of the lattice structure that correspond to a complete set of vibrational and translational degrees of freedom. Obviously, any linear combination of (3.58) and (3.58') will also satisfy the governing equation (3.46).

Note that only two parameters of the standing wave solution, the normal frequency and polarization vector, depend on the intrinsic lattice properties. The remaining parameters, the normal amplitudes and phases, are only determined by initial conditions, or general provisos, such as the lattice system temperature (see Section 4.2.6). Thus, the knowledge of only normal frequencies and polarization vectors provides the homogeneous lattice solutions in a general form (3.58). In this section, we consider the dispersion functions $\omega(\mathbf{p})$ and vectors $\mathbf{d}_{p,s}$ for the three lattice structures discussed earlier in Section 3.2.3.

3.4.2 Examples

In this section, we review dispersion properties, that is, frequency spectra and polarization vectors of three common types of lattice structures: the beamlike monoatomic and diatomic lattices, and the planer monoatomic hexagonal lattice. These structures are depicted in Figures 3.2(a), 3.2(b) and 3.3(b), respectively.

Monoatomic chain lattice

Evaluation of the normal frequencies as functions of the wave number is accomplished in accordance with the characteristic equation (3.49), which contains the discrete Fourier transform of the lattice stiffness matrices. Applying the DFT (3.40) to the monoatomic lattice matrices (3.13) gives

$$\hat{\mathbf{K}}(p) = \mathbf{K}_{-1}e^{ip} + \mathbf{K}_0 + \mathbf{K}_1e^{-ip} = 2k(\cos p - 1) = -4k \sin^2 p/2 \quad (3.60)$$

Then, the lattice characteristic equation gives a single acoustic branch:

$$\omega^2 M - 4k \sin^2 \frac{p}{2} = 0 \Rightarrow \omega_p^2 = \frac{4k}{M} \sin^2 \frac{p}{2} \quad (3.61)$$

The corresponding polarization vectors (3.51) are equal to unity for all p .

Diatom polymer molecule

DFT applied to the K -matrices of a diatomic polymer chain, equation (3.17), yields

$$\hat{\mathbf{K}}(p) = k \begin{pmatrix} -2 & 1 + e^{-ip} \\ 1 + e^{ip} & -2 \end{pmatrix} \quad (3.62)$$

This gives one acoustic ($s = 1$) and one optical ($s = 2$) branch,

$$\det \left[\omega^2 \begin{pmatrix} M_1 & 0 \\ 0 & M_2 \end{pmatrix} + k \begin{pmatrix} -2 & 1 + e^{-ip} \\ 1 + e^{ip} & -2 \end{pmatrix} \right] = 0 \Rightarrow \omega_{p,s}^2 = \frac{k}{\mu} + (-1)^s \sqrt{\frac{k^2}{\mu^2} - \frac{4k^2}{M_1 M_2} \sin^2 \frac{p}{2}}, \quad \mu = \frac{M_1 M_2}{M_1 + M_2} \quad (3.63)$$

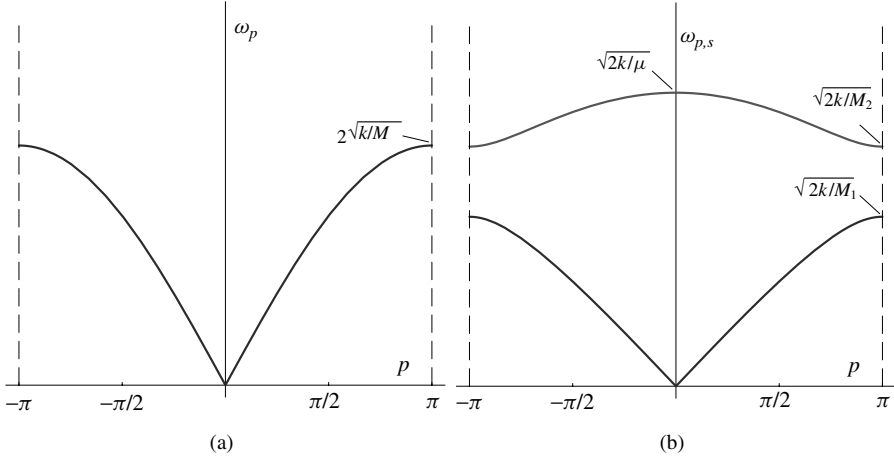


Figure 3.14 Dispersion branches of one-dimensional lattices: (a) monatomic and (b) diatomic. The reduced mass μ is defined in equation (3.63).

The relevant polarization vectors are found from (3.51),

$$\mathbf{d}_{p,s} = \begin{pmatrix} 2k - M_2 \omega_{p,s}^2 \\ k(1 + e^{ip}) \end{pmatrix}, \quad s = 1, 2 \quad (3.64)$$

Components of these vectors become dimensionless after normalization.

General shapes of the dispersion curves (3.61) and (3.63) are displayed in Figure 3.14.

Hexagonal lattice

The normal frequencies of a two-dimensional hexagonal lattice are derived similarly by utilizing the general equation (3.49) and the lattice stiffness matrices (3.19). There are in total two acoustic branches ($s = 1, 2$) and there are no optical branches; the normal frequencies are determined by two wave numbers, p and q :

$$\frac{M}{k} \omega_{p,q,s}^2 = 3 - \cos 2p - 2 \cos p \cos q + (-1)^s \sqrt{(\cos 2p - \cos p \cos q)^2 + 3 \sin^2 p \sin^2 q} \quad (3.65)$$

Here, M is the atomic mass. Polarization vectors of this lattice are given by

$$\mathbf{d}_{p,q,s} = \begin{pmatrix} 3k(\cos p \cos q - 1) + M\omega_{p,q,s}^2 \\ \sqrt{3}k \sin p \sin q \end{pmatrix}, \quad s = 1, 2 \quad (3.66)$$

3.5 Green's Function Methods

A direct solution of the original equation of motion (3.9) with a general external load $\mathbf{f}_n^{\text{ext}}(t)$ is difficult, and in most cases it requires numerical time integration, similar to classical

particle dynamics. In this section, we discuss one special technique, known as the Green's function method, which allows a semianalytical solution of the general inhomogeneous equation of motion (3.9). The term semianalytical, or near-analytical, is used because this method usually involves numerical methods in obtaining some special preliminary solutions, the Green's functions, while the final solution to the problem of interest is written in closed form in terms of the Green's functions.

The Green's function method has important advantages over direct numerical solutions. The first is universality; the Green's function is a unique structural characteristic. Once obtained for a given lattice structure, it can be used in solving many specific problems involving this lattice. The second is computational effectiveness; as a semianalytical approach, the Green's function method can provide up to several orders of magnitude reduction in processing time and computer memory requirement. Finally, Green's function techniques are important in developing the modern numerical methods that couple classical particle dynamics and continuum simulations, Karpov et al. (2005b), Liu et al. (2004c) and Park et al. (2005c).

3.5.1 Solution for a Unit Pulse

Before we proceed to the solution of a general inhomogeneous equation (3.46), at first consider the following subsidiary equation:

$$\mathbf{M} \ddot{\mathbf{g}}_{\mathbf{n}, \mathbf{n}''}(t) - \sum_{\mathbf{n}'} \mathbf{K}_{\mathbf{n}-\mathbf{n}'} \mathbf{g}_{\mathbf{n}', \mathbf{n}''}(t) = \mathbf{I} \delta_{\mathbf{n}, \mathbf{n}''} \delta(t) \quad (3.67)$$

where \mathbf{I} gives an $S \times S$ identity matrix, $\delta_{\mathbf{n}, \mathbf{n}''} = \delta_{n_1, n_1''} \delta_{n_2, n_2''} \delta_{n_3, n_3''}$, $\delta_{i,j}$ is the Kronecker delta (3.35), and $\delta(t)$ is the Dirac's delta function (3.32). This equation describes the response of the lattice structure due to localized pulses of a unit momentum given to each of the S degrees of freedom of an arbitrary unit cell \mathbf{n}'' . This response is represented by the $S \times S$ matrix function $\mathbf{g}_{\mathbf{n}, \mathbf{n}''}(t)$, which is called the *lattice dynamics Green's function*, and its physical meaning is explained in Figure 3.15.

We can simplify the equation (3.67) by utilizing the second symmetry principle of Section 3.1.2. Particularly, owing to the spatial invariance of the K -matrices that follows

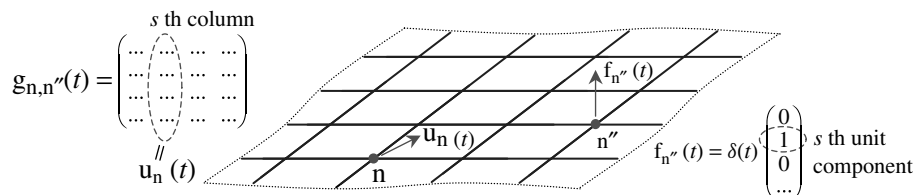


Figure 3.15 The s -th column of the Green's function matrix shows the vector of displacements for the current cell \mathbf{n} , due to the s -th unit component of load vector applied to a source cell \mathbf{n}'' .

from the definition (3.10), as well as the formal invariance of the load function,

$$\mathbf{I} \delta_{\mathbf{n}+\mathbf{a}, \mathbf{n}''+\mathbf{a}} \delta(t) = \mathbf{I} \delta_{\mathbf{n}-\mathbf{n}'', 0} \delta(t) = \mathbf{I} \delta_{\mathbf{n}, \mathbf{n}''} \delta(t) \quad (3.68)$$

where $\mathbf{a} = (a_1, a_2, a_3)$ is an arbitrary triplet of integer numbers, the lattice Green's function must feature the same translation symmetry,

$$\mathbf{g}_{\mathbf{n}+\mathbf{a}, \mathbf{n}''+\mathbf{a}} = \mathbf{g}_{\mathbf{n}, \mathbf{n}''} = \mathbf{g}_{\mathbf{n}-\mathbf{n}''} \quad (3.69)$$

Thus, the Green's function depends only on the distance between the loaded cell \mathbf{n}'' and the current cell \mathbf{n} . This implies independence of the solutions of equation (3.67) with respect to positioning of the load. Therefore, we can assume an arbitrary vector \mathbf{n}'' , for example, corresponding to the origin cell $(0, 0, 0) = \mathbf{0}$, and simplify the equation (3.67) to give

$$\mathbf{M} \ddot{\mathbf{g}}_{\mathbf{n}}(t) - \sum_{\mathbf{n}'} \mathbf{K}_{\mathbf{n}-\mathbf{n}'} \mathbf{g}_{\mathbf{n}'}(t) = \mathbf{I} \delta_{\mathbf{n}, \mathbf{0}} \delta(t) \quad (3.70)$$

Similar to the case of K -matrices, a single subscript \mathbf{n} at \mathbf{g} is used for brevity only; such a notation implies $\mathbf{n} \equiv \mathbf{n} - \mathbf{n}''$, or a similar difference.

We assume all trivial initial conditions for the equation (3.70),

$$\mathbf{g}_{\mathbf{n}}(0-) = \dot{\mathbf{g}}_{\mathbf{n}}(0-) = \mathbf{0} \quad (3.71)$$

where $\mathbf{0}$ is a zero matrix, that is, all lattice particles are at rest right before the unit pulse is applied.

The solution of equation (3.70) is straightforward with the application of functional transforms (see Figure (3.13)). We first apply the discrete Fourier transform (3.40) over the equation (3.70) for all components of the lattice site vector \mathbf{n} , and utilize the convolution theorem (3.42) to obtain

$$\mathbf{M} \hat{\mathbf{g}}(t, \mathbf{p}) - \hat{\mathbf{K}}(\mathbf{p}) \hat{\mathbf{g}}(t, \mathbf{p}) = \mathbf{I} \delta(t) \quad (3.72)$$

We next apply the Laplace transform to (3.72) and check Table 3.2 for the transform of a Dirac's delta; this gives

$$(s^2 \mathbf{M} - \hat{\mathbf{K}}(\mathbf{p})) \hat{\mathbf{G}}(s, \mathbf{p}) = \mathbf{I} \quad (3.73)$$

Thus, the Green's function solution in the transform domain reads

$$\hat{\mathbf{G}}(s, \mathbf{p}) = (s^2 \mathbf{M} - \hat{\mathbf{K}}(\mathbf{p}))^{-1} \quad (3.74)$$

Application of the inverse transforms gives the real-space function sought:

$$\mathbf{g}_{\mathbf{n}}(t) = \mathcal{L}_{s \rightarrow t}^{-1} \mathcal{F}_{\mathbf{p} \rightarrow \mathbf{n}}^{-1} \{ \hat{\mathbf{G}}(s, \mathbf{p}) \} \quad (3.75)$$

Here, the inverse Laplace transform can be accomplished numerically, for example, according to the Weeks algorithm (3.34).

3.5.2 Free Lattice with Initial Perturbations

A result identical to (3.75) can be obtained by considering the equation of a free lattice (3.46) with unit initial velocities of particles in one cell,

$$\mathbf{u}_n(0-) = \mathbf{0}, \quad \dot{\mathbf{u}}_n(0-) = \mathbf{I} \delta_{n,0} \quad (3.76)$$

Application of the inverse Laplace and discrete Fourier transforms, along with the second time-derivative rule (3.30) to equation (3.46) with the initial conditions (3.76) yields

$$\hat{\mathbf{U}}(s, \mathbf{p}) = (s^2 \mathbf{M} - \hat{\mathbf{K}}(\mathbf{p}))^{-1} = \hat{\mathbf{G}}(s, \mathbf{p}) \quad (3.77)$$

Thus, we can write

$$\mathbf{u}_n(t) = \mathbf{g}_n(t), \quad t > 0 \quad (3.78)$$

Another possibility is a free lattice with unit initial displacements,

$$\mathbf{u}_n(0-) = \mathbf{I} \delta_{n,0}, \quad \dot{\mathbf{u}}_n(0-) = \mathbf{0} \quad (3.79)$$

The transform solution to (3.46) and (3.79) is given by

$$\hat{\mathbf{U}}(s, \mathbf{p}) = s \hat{\mathbf{G}}(s, \mathbf{p}) \quad (3.80)$$

Employing the first time-derivative rule (3.30) and the fact that $\mathbf{g}_n(0-) = \mathbf{0}$, we obtain

$$\mathbf{u}_n(t) = \dot{\mathbf{g}}_n(t), \quad t > 0 \quad (3.81)$$

Thus, the Green's function also solves a free lattice with localized initial perturbations. This observation is important in understanding initial conditions for atomic thermal vibrations in lattices, which is discussed in the next chapter.

3.5.3 Solution for Arbitrary Dynamic Loads

As a subsequent complication, consider the solution to the lattice equation (3.9) with a general distributed dynamic loading $\mathbf{f}_n^{\text{ext}}(t)$ and with the trivial initial conditions (3.71). Application of the discrete Fourier and Laplace transform then yields

$$(s^2 \mathbf{M} - \hat{\mathbf{K}}(\mathbf{p})) \hat{\mathbf{U}}(s, \mathbf{p}) = \hat{\mathbf{F}}^{\text{ext}}(s, \mathbf{p}) \quad (3.82)$$

where \mathbf{U} and \mathbf{F}^{ext} are the displacement and force vectors in the transform domain. According to (3.74) and (3.82), the transform solution is simply

$$\hat{\mathbf{U}}(s, \mathbf{p}) = \hat{\mathbf{G}}(s, \mathbf{p}) \hat{\mathbf{F}}^{\text{ext}}(s, \mathbf{p}) \quad (3.83)$$

The real-space solution is obtained by applying the inverse discrete Fourier and inverse Laplace transforms and taking into account the convolution theorems (3.28) and (3.42),

$$\mathbf{u}_n(t) = \sum_{\mathbf{n}'} \int_0^t \mathbf{g}_{\mathbf{n}-\mathbf{n}'}(t-\tau) \mathbf{f}_{\mathbf{n}'}^{\text{ext}}(\tau) d\tau \quad (3.84)$$

3.5.4 General Inhomogeneous Solution

The most general situation with the lattice equation of motion involves arbitrary dynamic loading and arbitrary initial conditions. We write the general *initial-value problem* concisely as

$$\mathbf{M} \ddot{\mathbf{u}}_{\mathbf{n}}(t) - \sum_{\mathbf{n}'} \mathbf{K}_{\mathbf{n}-\mathbf{n}'} \mathbf{u}_{\mathbf{n}'}(t) = \mathbf{f}_{\mathbf{n}}^{\text{ext}}(t) \quad (3.85)$$

$\mathbf{u}_{\mathbf{n}}(0-), \dot{\mathbf{u}}_{\mathbf{n}}(0-)$

The solution of this problem is straightforward in the Fourier/Laplace domain,

$$\hat{\mathbf{U}}(s, \mathbf{p}) = \hat{\mathbf{G}}(s, \mathbf{p}) (\hat{\mathbf{F}}(s, \mathbf{p}) + s \mathbf{M} \hat{\mathbf{u}}(0, \mathbf{p}) + \mathbf{M} \hat{\mathbf{u}}(0, \mathbf{p})) \quad (3.86)$$

Thus, in the original domain, we obtain the following solution:

$$\begin{aligned} \mathbf{u}_{\mathbf{n}}(t) &= \sum_{\mathbf{n}'} \int_0^t \mathbf{g}_{\mathbf{n}-\mathbf{n}'}(t-\tau) \mathbf{f}_{\mathbf{n}'}^{\text{ext}}(\tau) d\tau \\ &\quad + \mathbf{M} \sum_{\mathbf{n}'} \dot{\mathbf{g}}_{\mathbf{n}-\mathbf{n}'}(t) \mathbf{u}_{\mathbf{n}'}(0-) + \mathbf{M} \sum_{\mathbf{n}'} \mathbf{g}_{\mathbf{n}-\mathbf{n}'}(t) \dot{\mathbf{u}}_{\mathbf{n}'}(0-) \end{aligned} \quad (3.87)$$

In some special cases, particularly for external loadings \mathbf{f}^{ext} acting during a short period of time, the following alternative approach to solving the problem (3.85) can be more effective computationally. According to the general theory of ordinary differential equations, a general solution of the inhomogeneous equation (3.9) can be given by a particular solution to (3.9), augmented with a general solution of the homogeneous equation (3.46). In other words, the solution (3.88) can be replaced by

$$\mathbf{u}_{\mathbf{n}}(t) = \sum_{\mathbf{n}'} \int_0^t \mathbf{g}_{\mathbf{n}-\mathbf{n}'}(t-\tau) \mathbf{f}_{\mathbf{n}'}^{\text{ext}}(\tau) d\tau + \mathbf{u}_{\mathbf{n}}^+(t) + \mathbf{u}_{\mathbf{n}}^-(t) \quad (3.88)$$

where the displacement vectors $\mathbf{u}_{\mathbf{n}}^\pm(t)$ are given by (3.58). The normal amplitudes a and phases ϕ can be found in (3.58) by employing initial conditions for the problem (3.85), or by using other arguments.

3.5.5 Boundary Value Problems and the Time History Kernel

In the previous sections, we considered solutions of the initial value problem over periodic lattices, including several special cases. Another class of problems in lattice mechanics is the dynamic boundary value problem, where the solution to the lattice equation of motion is determined by known dynamic displacements of lattice edges.

A straightforward solution to this problem can be obtained with the assumption that the lattice boundary is given by a straight line/strip or plane/slab for the two- and three-dimensional lattices respectively. Meanwhile, the domain of interest on one side of this boundary is large enough so that the effects of any peripheral boundaries are negligible. These assumptions are justified in most cases when we are looking for the solution only in the direct vicinity of the boundary for a considerably short period of time.

This problem statement is particularly important in modern multiscale methods that couple molecular dynamics and continuum simulations of solids. Since the continuum description can only provide an approximate description of the atomic displacements through the

interpolation by finite element shape functions, it is important to know accurate displacements of lattice particles in the finite element domain in close vicinity of the interface. A projection of the accurate atomic displacements onto the finite element displacement field can provide necessary updates to the coupled model; this comprises a key idea of the bridging multiscale method, for example, Karpov et al. (2005b), Park et al. (2005c), Wagner and Liu (2003) and Wagner et al. (2004). We discuss this application in greater detail in the later chapters of this book.

A straight line or planelike boundary can be defined by fixing one of the lattice site indices n_1 in the triplet $\mathbf{n} = (n_1, n_2, n_3)$. Owing to translational symmetry, we can employ any specific value of this index; the final results will be identical. For example, let $n_1 = 0$; then we write the boundary value problem of interest as follows:

$$\begin{aligned} \mathbf{M} \ddot{\mathbf{u}}_{\mathbf{n}}(t) - \sum_{\mathbf{n}'} \mathbf{K}_{\mathbf{n}-\mathbf{n}'} \mathbf{u}_{\mathbf{n}'}(t) &= \mathbf{0} \\ \mathbf{n} = (n_1 > 0, n_2, n_3), \quad \mathbf{u}_{\mathbf{n}}(0-) &= \dot{\mathbf{u}}_{\mathbf{n}}(0-) = \mathbf{0}, \quad \mathbf{u}_{0,n_2,n_3}(t) \end{aligned} \quad (3.89)$$

where the displacements \mathbf{u}_{0,n_2,n_3} are enforced and the value n_1 is small.

An important detail regarding the solution of the problem (3.89) consists in realizing that the motion of the boundary atoms can be caused either by the displacements of the atoms to be kept or by an external force acting upon the boundary atoms in a hypothetical large lattice that extends also for $n_1 < 0$. Therefore, we assume that the motion of the boundary atoms is due to unknown external forces that act only at $n_1 = 0$,

$$\mathbf{M} \ddot{\mathbf{u}}_{\mathbf{n}}(t) - \sum_{\mathbf{n}'} \mathbf{K}_{\mathbf{n}-\mathbf{n}'} \mathbf{u}_{\mathbf{n}'}(t) = \delta_{n_1,0} \mathbf{f}_{0,n_2,n_3} \quad (3.90)$$

Applying the DFT (3.40) and Laplace transform (3.27) to the equation of motion (3.90), we get

$$\hat{\mathbf{U}}(\mathbf{p}, s) = \hat{\mathbf{G}}(\mathbf{p}, s) \hat{\mathbf{F}}^{\text{ext}}(\mathbf{p}, s) + \hat{\mathbf{R}}(\mathbf{p}, s) \quad (3.91)$$

$$\hat{\mathbf{R}}(\mathbf{p}, s) = \mathbf{M} \hat{\mathbf{G}}(\mathbf{p}, s) (s \hat{\mathbf{u}}(\mathbf{p}, 0-) + \hat{\mathbf{u}}(\mathbf{p}, 0-)) \quad (3.92)$$

where the transform domain force is $\hat{\mathbf{F}}^{\text{ext}} = \hat{\mathbf{F}}_0(p_2, p_3)$. Substitution of this force into (3.91) and further application of the inverse DFT over p_1 lead to

$$\tilde{\mathbf{U}}_{n_1} - \tilde{\mathbf{R}}_{n_1} = \tilde{\mathbf{G}}_{n_1} \hat{\mathbf{F}}_0 \quad (3.93)$$

Here, the tilde notation stands for the mixed (transform/real space) quantities that depend on n_1 and also p_2, p_3, s . The force vector $\hat{\mathbf{F}}_0$ can be eliminated by writing two equations (3.93) for a general n_1 and for $n_1 = 0$ and substituting $\hat{\mathbf{F}}_0$ from the second of these equations into the first; this gives

$$\tilde{\mathbf{U}}_{n_1} - \tilde{\mathbf{R}}_{n_1} = \tilde{\Theta}_{n_1} (\tilde{\mathbf{U}}_0 - \tilde{\mathbf{R}}_0) \quad (3.94)$$

$$\tilde{\Theta}_{n_1} = \tilde{\mathbf{G}}_{n_1} \tilde{\mathbf{G}}_0^{-1} \quad (3.95)$$

Finally, application of the inverse DFT transform over p_1 and p_2 as well the inverse Laplace transform onto (3.94) results in a solution of the form

$$\mathbf{u}_{\mathbf{n}}(t) = \sum_{\mathbf{n}'} \delta_{n'_1,0} \int_0^t \boldsymbol{\theta}_{\mathbf{n}-\mathbf{n}'}(t-\tau) (\mathbf{u}_{\mathbf{n}'}(\tau) - \mathbf{R}_{\mathbf{n}'}(\tau)) d\tau + \mathbf{R}_{\mathbf{n}}(t) \quad (3.96)$$

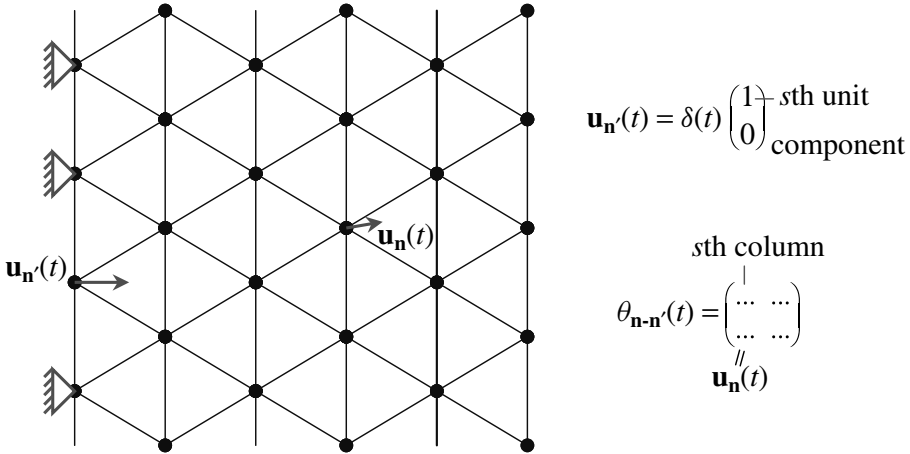


Figure 3.16 The s th column of kernel matrix θ shows the vector of displacements for the current cell \mathbf{n} , due to the s th unit component of a boundary displacement vector at \mathbf{n}' , with the rest of boundary being fixed.

where

$$\theta_{\mathbf{n}}(t) = \mathcal{L}_{s \rightarrow t}^{-1} \mathcal{F}_{p_2 \rightarrow n_2}^{-1} \mathcal{F}_{p_3 \rightarrow n_3}^{-1} \{\tilde{\mathbf{G}}_{n_1} \tilde{\mathbf{G}}_0^{-1}\} \quad (3.97)$$

and the vector \mathbf{R} depends on the initial conditions (the capital letter \mathbf{R} is used for both Laplace and time domain functions),

$$\mathbf{R}_{\mathbf{n}}(t) = \mathbf{M} \sum_{\mathbf{n}'} (\mathbf{g}_{\mathbf{n}-\mathbf{n}'}(t) \dot{\mathbf{u}}_{\mathbf{n}'}(0-) + \dot{\mathbf{g}}_{\mathbf{n}-\mathbf{n}'}(t) \mathbf{u}_{\mathbf{n}'}(0-)) \quad (3.98)$$

The time history kernel matrix θ in equation (3.96) represents another class of lattice dynamics Green's functions. While the function (3.75) relates displacements of the lattice particles with the localized external forcing, the kernel (3.97) relates the displacement solution with the localized boundary perturbations. The physical meaning of the kernel θ is explained in Figure 3.16.

Let the external force in (3.90) formally represent all nonrandom, nonequilibrium effects at the lattice boundary. Then, the initial conditions in (3.89) and (3.92) can be associated with the chaotic thermal motion only. Therefore, the random thermal part of the displacement solution, vector \mathbf{R} , can be replaced by the general homogeneous solution (3.58),

$$\mathbf{R}_{\mathbf{n}}(t) = \mathbf{u}_{\mathbf{n}}^+(t) + \mathbf{u}_{\mathbf{n}}^-(t) \quad (3.99)$$

Here, the normal amplitudes and phases for $\mathbf{u}_{\mathbf{n}}^\pm$ can be found by employing the methods of statistical mechanics in application to periodic lattices in thermal equilibrium. This technique is discussed later in this book. As compared to (3.98), utilizing the random term of the form (3.99) is more effective computationally. For lattices initially at rest, we have $\mathbf{R}_{\mathbf{n}} = 0$.

For one-dimensional lattices, such as the polymer chains depicted in Figure 3.2, the solution (3.96) reduces to

$$\mathbf{u}_n(t) = \int_0^t \theta_n(t-\tau)(\mathbf{u}_0(\tau) - \mathbf{R}_0(\tau)) d\tau + \mathbf{R}_n(t) \quad (3.100)$$

3.5.6 Examples

In this section, we derive the Green's function solution for the monoatomic chain lattice discussed earlier in sections 3.2.3 and 3.4.2. The simplest monoatomic lattice, Figure 3.10, with a single longitudinal degree of freedom per unit cell and the lattice stiffness matrices (3.13) is unique, which allows all the Green's function solutions to be found in closed form. Considering a more general lattice structure, numerical inversion of the Fourier or/and Laplace transforms is typically required.

Dynamic Green's function

The lattice dynamics Green's function in the transform domain is derived by substituting the Fourier transform of K -matrices (3.60) into equation (3.74),

$$\hat{\mathbf{G}}(s, p) = \frac{1}{s^2 M - 2k(\cos p - 1)} \quad (3.101)$$

The inverse Fourier integral (3.41) of this function gives

$$\mathbf{G}_n(s) = \frac{1}{s} \frac{(\sqrt{s^2 + \omega^2} - s)^{2n}}{M\omega^{2n}\sqrt{s^2 + \omega^2}}, \quad \omega = 2\sqrt{\frac{k}{M}} \quad (3.102)$$

where the characteristic frequency ω is equal to the maximum normal frequency of the monoatomic lattice (see Figure 3.14).

The inverse Laplace transform of the above function can be accomplished by utilizing entries 4 and 17 of Table 3.2,

$$\mathbf{g}_n(t) = \frac{1}{M} \int_0^t J_{2n}(\omega\tau) d\tau, \quad \dot{\mathbf{g}}_n(t) = \frac{1}{M} J_{2n}(\omega t) \quad (3.103)$$

where J is the Bessel function (3.33). In Figure 3.17, we plot this function for various spatial order parameters n .

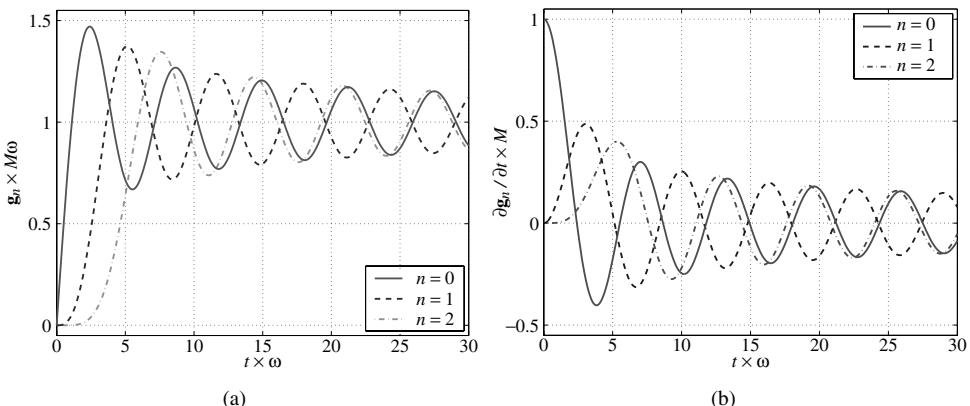


Figure 3.17 Dynamic Green's function of a monoatomic chain. Dispersion branches of one-dimensional lattices: (a) displacement and (b) velocity.

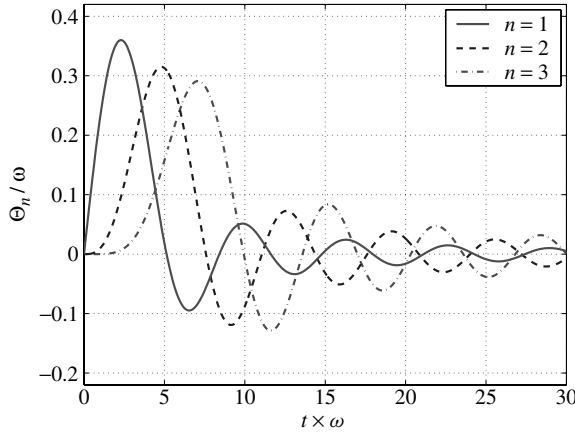


Figure 3.18 Time-history kernel of a monoatomic chain lattice.

Time history kernel

The derivation of the lattice time history kernel, a solution to the boundary value problem (3.89), starts from substitution of the transform function into equation (3.95):

$$\Theta_n = \mathbf{G}_n \mathbf{G}_0^{-1} = \frac{(\sqrt{s^2 + \omega^2} - s)^{2n}}{\omega^{2n}} \quad (3.104)$$

Note that the DFT is not relevant for the one-dimensional version of (3.95). The time domain function is found by employing the last entry of Table 3.2:

$$\theta_n = \frac{2n}{t} J_{2n}(\omega t), \quad n = 1, 2, \dots \quad (3.105)$$

A plot of this function is provided in Figure 3.18.

Qualitatively, the behavior of the functions (3.103) and (3.105) is typical for most monoatomic lattices, including two- and three-dimensional systems.

3.6 Quasi-Static Approximation

The quasi-static (time-independent) approximation is used in various applications of the lattice model, where any noticeable change of the external forcing in (3.9) occurs during a period of time that is much longer than the characteristic time of atomic vibrations, $\omega_{p,s}^{-1}$. Typical examples include mechanical failure, indentation and scratching of crystal lattices, where the peripheral elastic region can be considered within the harmonic approximation (3.7).

3.6.1 Equilibrium State Equation

The mathematical formulation for the quasi-static model is obtained by assuming that the external loading is equilibrated by the elastic response of the lattice structure *at all times*,

that is, by ignoring the inertial force term in equation (3.9). This leads to

$$-\sum_{\mathbf{n}'} \mathbf{K}_{\mathbf{n}-\mathbf{n}'} \mathbf{u}_{\mathbf{n}'} = \mathbf{f}_{\mathbf{n}}^{\text{ext}}, \quad \mathbf{n} = (n_1, n_2, n_3) \quad (3.106)$$

Thus, the static lattice deformation is described with the displacement vectors $\mathbf{u}_{\mathbf{n}} = \mathbf{r}_{\mathbf{n}} - \mathbf{n}$, where the vectors \mathbf{n} and $\mathbf{r}_{\mathbf{n}}$ determine equilibrium positions of the lattice particles before and after application of the external forcing. The nonloaded configuration represents a periodic lattice structure. As before, the subscript vector \mathbf{n} gives a triplet of lattice site indices (n_1, n_2, n_3) .

3.6.2 Quasi-Static Green's Function

The solution of the static equation is straightforward with the use of DFTs (Section 3.3.3). In the Fourier domain, we obtain

$$-\hat{\mathbf{K}}(\mathbf{p}) \hat{\mathbf{u}}(\mathbf{p}) = \hat{\mathbf{f}}^{\text{ext}}(\mathbf{p}) \quad (3.107)$$

This leads to the transform solution

$$\hat{\mathbf{u}}(\mathbf{p}) = \hat{\mathbf{g}}(\mathbf{p}) \hat{\mathbf{f}}^{\text{ext}}(\mathbf{p}), \quad \mathbf{p} = (p_1, p_2, p_3) \quad (3.108)$$

where

$$\hat{\mathbf{g}}(\mathbf{p}) = -\hat{\mathbf{K}}^{-1}(\mathbf{p}) \quad (3.109)$$

The real-space solution is obtained by applying the inverse DFT over (3.107) and accounting for the convolution theorem (3.42),

$$\mathbf{u}_{\mathbf{n}} = \sum_{\mathbf{n}'} \mathbf{g}_{\mathbf{n}-\mathbf{n}'} \mathbf{f}_{\mathbf{n}'}^{\text{ext}} \quad (3.110)$$

Here, the matrix \mathbf{g} is the lattice static Green's function,

$$\mathbf{g}_{\mathbf{n}} = \mathcal{F}_{\mathbf{p} \rightarrow \mathbf{n}}^{-1}\{-\hat{\mathbf{K}}^{-1}(\mathbf{p})\} \quad (3.111)$$

In order to avoid possible singularity of the matrix $\hat{\mathbf{K}}(\mathbf{p})$ at $\mathbf{p} = \mathbf{0}$ in numerical calculations, the DFT procedures over the quasi-static equations should utilize the half-integer wave number p_i , as in equation (3.44). This singularity is due to the fact that the solution (3.110) can be augmented with an arbitrary constant vector to describe a rigid-body displacement of the lattice structure. If required, a rigid-body indeterminacy of the quasi-static solution can be eliminated by applying displacement boundary conditions as in engineering structural analysis.

3.6.3 Multiscale Boundary Conditions

Over the past decade, there has been considerable effort in finding fundamental descriptions of strength and failure properties of nanoscale materials, taking into account their atomic structures. Numerous experimental observations of material behavior cannot be readily explained within the framework of continuum mechanics: dislocation patterns in fatigue and creep, surface roughening and crack nucleation in fatigue, the statistical nature

of brittle failure, plastic flow localization in shear bands, and so on. The use of classical atomistic simulations has provided useful information of chemical interactions at the nanoscale. However, typical atomistic simulations are still restricted to very small systems consisting of several million atoms or less and timescales on the order of picoseconds. Thus, even for nanoscale structures and materials, atomistic modeling would be computationally prohibitive. The limitations of atomistic simulations and continuum mechanics, along with practical needs arising from the heterogeneous nature of engineering materials, have motivated the research on *multiscale simulations* that bridge atomistic simulations and continuum modeling; this topic is discussed in greater detail in Chapter 5.

In order to make the computations tractable, multiscale models generally make use of a coarse–fine grain decomposition for the physical domain under analysis. An atomistic simulation method is used in a small subregion, the fine grain, where it is crucial to capture the individual atomistic behavior accurately. A continuum simulation is used in a larger peripheral region, the coarse grain, where the deformation is considered to be homogeneous and smooth; the macroscopic material behavior and properties are mainly determined by the collective atomic motion. Since the continuum region is usually chosen to be much larger than the atomistic region, the overall domain of interest can be considerably large. A purely atomistic solution is normally not affordable on this domain, though the multiscale solution is expected to provide the detailed atomistic information only where it is necessary.

The key issue is then the coupling between the coarse and fine scales. Typically, concurrent coupling involves the idea of a “handshake” or “pad” region, where pseudoatoms are available on the continuum part of the interface and share the physical space with finite elements, as shown in Figure 3.19. The purpose of the handshake region is to assure

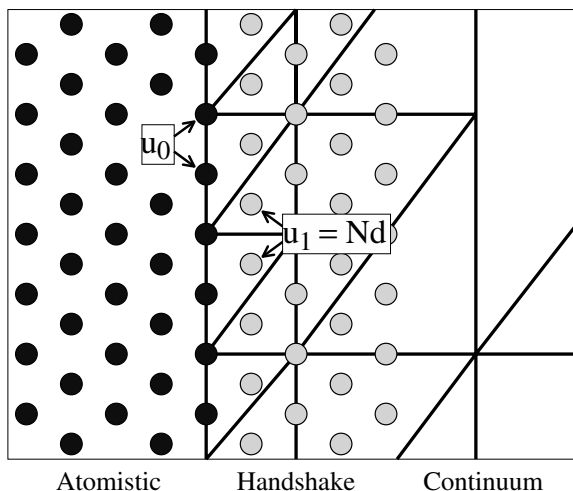


Figure 3.19 Structure of the transition region in coupled atomistic/continuum simulations. Positions of pseudoatoms in the handshake area are interpolated with finite element shape functions. Reprinted from International Journal of Solids and Structures, E. G. Karpov, H. Yu, H. S. Park et al., Multiscale boundary conditions in crystalline solids: Theory and application to nanoindentation, 2005, with permission from Elsevier.

a smoother coupling between the atomistic and continuum regimes. The group of pseudoatoms serves to eliminate nonphysical surfaces in the atomistic lattice structure, so that the real atoms along the interface have a full set of interactive neighbors in the continuum domain. However, introduction of a nonphysical handshake region leads to several concerns. The *first* is double counting of the strain energy in the handshake region by the atomistic and continuum models. The *second* is ill-conditioning of the finite element stiffness matrices, due to the need for atomic length scale refinement of the finite element mesh for the handshake region. Indeed, an extremely fine mesh is required in order to provide accurate positions of the pseudoatoms, since they are found by interpolating the finite element nodal positions. The *third* concern is related to the need, in a nonlocal continuum model, for the small length scales that are typical for the handshake region.

The FE interpolation procedure for the handshake atoms can be written symbolically as

$$\mathbf{u}_1 = \mathbf{N}\mathbf{d} \quad (3.112)$$

where \mathbf{u}_1 are displacements of the pseudoatoms interacting with the interface atoms, \mathbf{d} are finite element nodal displacements, and the columns of the rectangular matrix \mathbf{N} give a set of interpolation basis vectors, computed by utilizing the FE shape functions.

The handshake and continuum domains serve to absorb the fine grain excitations and to transfer effects of the peripheral (coarse grain) boundary into the central atomistic region of interest. In principle, this requires evaluation of the displacement vector \mathbf{u}_1 , which depends on the interface displacements \mathbf{u}_0 and the peripheral boundary displacements \mathbf{u}_a (a is a coarse grain size parameter) at each step of the solution procedure. This dependence can be written in the symbolic form,

$$\mathbf{u}_1 = \Theta\{\mathbf{u}_0\} + \Xi\{\mathbf{u}_a\} \quad (3.113)$$

which represents the *multiscale boundary conditions (MSBCs)* for the atomistic model on the fine grain Karpov et al. (2005). The concept behind this relationship is illustrated in Figure 3.20. In equation (3.113), Θ and Ξ are unknown mathematical operators. In principle, if both of these operators were known from alternative arguments, for example, by employing the methods of lattice mechanics, the explicit continuum model as well as the handshake domain would become redundant. Meanwhile, all the atomistic degrees of freedom between u_1 and u_a (Figure 3.20) could be *eliminated* from the numerical solution. In this section, we discuss a semianalytical quasi-static method to derive the multiscale boundary conditions for periodic lattice interfaces, expressed by the equation (3.113). This approach involves only lattice mechanics tools; it is based on the intrinsic atomic structure model without involving a continuum homogenization procedure. The method is applied to nanoindentation of a crystalline gold substrate.

Boundary condition operators

Similar to the dynamic boundary value problems (Section 3.5.5), we consider a planelike interface determined by fixing one of the lattice site indices; in this section, we use the (n, m, l) notation for the components of lattice vector \mathbf{n} , instead of (n_1, n_2, n_3) . The corresponding components of the vector \mathbf{p} will be referred to as (p, q, r) . The task of deriving the 3D multiscale boundary conditions reduces to expressing, for example, the atomic

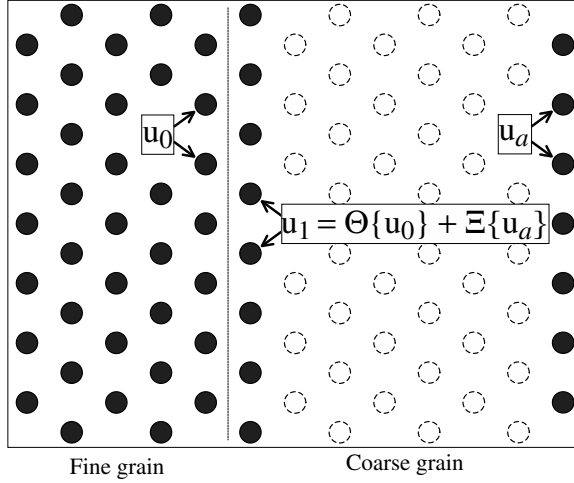


Figure 3.20 Multiscale boundary conditions: atomic positions within the coarse grain are evaluated through the displacements of atoms at the interface and the outer boundary of the coarse grain. Continuum modeling is not used. Reprinted from International Journal of Solids and Structures, E. G. Karpov, H. Yu, H. S. Park et al., Multiscale boundary conditions in crystalline solids: Theory and application to nanoindentation, 2005, with permission from Elsevier.

displacements $\mathbf{u}_{n,m,1}$ in terms of $\mathbf{u}_{n,m,0}$ and $\mathbf{u}_{n,m,a}$,

$$\mathbf{u}_{n,m,1} = \Theta\{\mathbf{u}_{n,m,0}\} + \Xi\{\mathbf{u}_{n,m,a}\} \quad (3.114)$$

where the slab $l = 0$ represents the fine/coarse grain interface, and $l = a$ assigns the coarse grain boundary. A more general (polyhedron) shape of the fine grain can be obtained by combining several planelike interfaces, where each of them is treated independently using an equation similar to (3.114).

The deformation of the coarse grain domain can be viewed as occurring owing to the external boundary forces applied to the atoms $(n, m, 0)$ and (n, m, a) :

$$\mathbf{f}_n^{\text{ext}} \equiv \mathbf{f}_{n,m,l} = \delta_{l,0}\mathbf{f}_{n,m,0} + \delta_{l,a}\mathbf{f}_{n,m,a} \quad (3.115)$$

We then apply the DFT to the static equation (3.106) for all three spatial indices, utilizing the external force vector (3.115) and the convolution theorem (3.42) to obtain the Fourier domain solution

$$\hat{\mathbf{u}}(p, q, r) = \hat{\mathbf{g}}(p, q, r) (\hat{\mathbf{f}}_0(p, q) + e^{-ira} \hat{\mathbf{f}}_a(p, q)) \quad (3.116)$$

$$\hat{\mathbf{g}}(p, q, r) = -\hat{\mathbf{K}}^{-1}(p, q, r) \quad (3.117)$$

Further use of the shift theorem (3.45) with the inverse ($r \rightarrow l$) DFT of equation (3.116) yields

$$\tilde{\mathbf{u}}_l(p, q) = \tilde{\mathbf{g}}_l(p, q) \hat{\mathbf{f}}_0(p, q) + \tilde{\mathbf{g}}_{l-a}(p, q) \hat{\mathbf{f}}_a(p, q) \quad (3.118)$$

$$\tilde{\mathbf{g}}_l(p, q) = \mathcal{F}_{r \rightarrow l}^{-1} \{ \hat{\mathbf{g}}(p, q, r) \} \quad (3.119)$$

We then write three equations (3.118) by substituting $l = 0$, $l = 1$ and $l = a$, and rearrange them to express the vector $\tilde{\mathbf{u}}_1$ through $\tilde{\mathbf{u}}_0$, $\tilde{\mathbf{u}}_a$, and to eliminate the vectors $\hat{\mathbf{f}}_0$, $\hat{\mathbf{f}}_a$:

$$\tilde{\mathbf{u}}_1(p, q) = \hat{\Theta}(p, q) \tilde{\mathbf{u}}_0(p, q) + \hat{\Xi}(p, q) \tilde{\mathbf{u}}_a(p, q) \quad (3.120)$$

where

$$\begin{pmatrix} \hat{\Theta}(p, q) & \hat{\Xi}(p, q) \end{pmatrix} = \begin{pmatrix} \tilde{\mathbf{g}}_1(p, q) & \tilde{\mathbf{g}}_{1-a}(p, q) \end{pmatrix} \begin{pmatrix} \tilde{\mathbf{g}}_0(p, q) & \tilde{\mathbf{g}}_{-a}(p, q) \\ \tilde{\mathbf{g}}_a(p, q) & \tilde{\mathbf{g}}_0(p, q) \end{pmatrix}^{-1} \quad (3.121)$$

By applying the inverse DFT for p and q to equation (3.120), and taking into account the convolution theorem (3.42), we obtain the final form of the 3D multiscale boundary conditions:

$$\mathbf{u}_{n,m,1} = \sum_{n',m'} \Theta_{n-n',m-m'} \mathbf{u}_{n',m',0} + \sum_{n',m'} \Xi_{n-n',m-m'} \mathbf{u}_{n',m',a} \quad (3.122)$$

$$\Theta_{n,m} = \mathcal{F}_{p \rightarrow n}^{-1} \mathcal{F}_{q \rightarrow m}^{-1} \{ \hat{\Theta}(p, q) \}, \quad \Xi_{n,m} = \mathcal{F}_{p \rightarrow n}^{-1} \mathcal{F}_{q \rightarrow m}^{-1} \{ \hat{\Xi}(p, q) \} \quad (3.123)$$

Thus, the operators of MSBCs act as discrete convolution sums over the interface and coarse grain boundary displacements. These operators are represented by compact matrix kernels Θ and Ξ , depending on the lattice geometry and structure of the interatomic potential.

In some applications, including the nanoindentation simulations to be discussed later in this section, the coarse scale boundary can be assumed to be rigidly fixed, so that $\mathbf{u}_{n,m,a} = \mathbf{0}$ for all n and m . This assumption simplifies equation (3.122) to the form

$$\mathbf{u}_{n,m,1} = \sum_{n',m'} \Theta_{n-n',m-m'} \mathbf{u}_{n',m',0} \quad (3.124)$$

Note that the kernel matrices Θ and Ξ are *dimensionless* quantities, because they relate “displacements with displacements” (see equations (3.122) and (3.124)). This indicates that, for a given interatomic potential, their values should depend on the geometry of the crystal lattice and the choice of the elementary cell, rather than on scaling parameters of the potential. This feature is attractive because it implies the existence of unique kernel matrices for various materials with identical or similar crystalline structures.

Application: nanoindentation of crystalline gold

We verify correctness of the MSBCs on a benchmark nanoindentation problem with a crystalline metallic substrate. Consider a parallelepipedic fine grain with periodic boundary conditions on the side faces and the multiscale boundary conditions on the bottom face (Figure 3.21). The top face of the fine grain domain is originally traction free and is then subjected to a solid nondeformable indenter.

A substantial part of the substrate is considered as a bulk coarse scale domain, whose atomistic degrees of freedom will be eliminated from the multiscale model. The resultant multiscale solution will be compared with the benchmark data, obtained by molecular mechanics simulations on the original full domain, that is, by preserving the complete atomistic resolution and all the relevant degrees of freedom at both fine grains and coarse

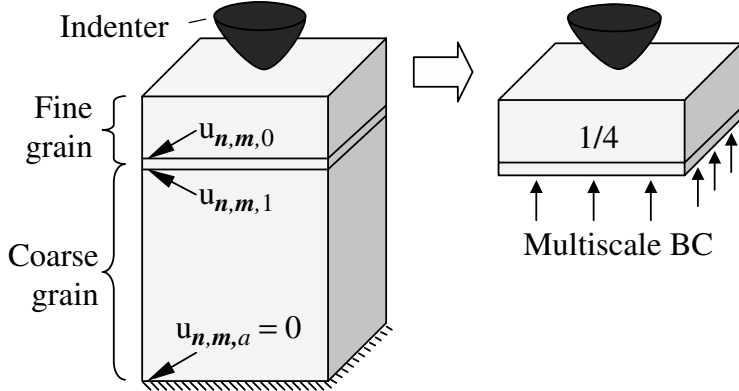


Figure 3.21 Nanoindentation problem with the multiscale boundary conditions applied to the bottom face of the fine grain; periodic boundary conditions are applied to the lateral faces. Reprinted from International Journal of Solids and Structures, E. G. Karpov, H. Yu, H. S. Park et al., Multiscale boundary conditions in crystalline solids: Theory and application to nanoindentation, 2005, with permission from Elsevier.

grains. The coarse scale boundary displacements in both problems are set to be zero; therefore, equation (3.124) will be utilized.

We introduce the three-dimensional numbering of the atomic locations in the fcc lattice, so that the atoms occupy the even staggered locations (n, m, l) as illustrated in Figure 3.22. For this lattice, we utilize the pair-wise Morse potential (2.63) with parameters of crystalline

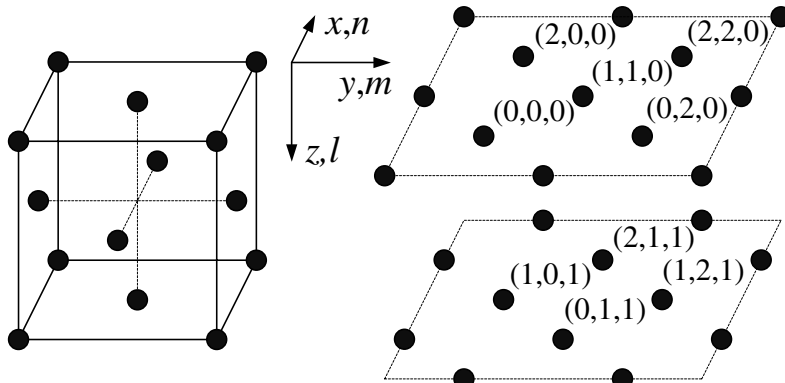


Figure 3.22 Face-centered cubic crystal: Bravais lattice (left); numbering of equilibrium atomic positions (n, m, l) in two adjacent (001) planes, corresponding to $l = 0$ and $l = 1$ (right). The interplanar distance is exaggerated. Reprinted from International Journal of Solids and Structures, E. G. Karpov, H. Yu, H. S. Park et al., Multiscale boundary conditions in crystalline solids: Theory and application to nanoindentation, 2005, with permission from Elsevier.

gold, for example, Harrison (1988),

$$\varepsilon = 0.560 \text{eV}, \beta = 1.637 \text{\AA}^{-1}, \rho = 2.922 \text{\AA} \quad (3.125)$$

Accounting only for nearest-neighbor interactions in equations (2.46) and (3.10), we obtain the following set of K -matrices in the Cartesian coordinate system shown in Figure 3.22:

$$\begin{aligned} \mathbf{K}_{1,1,0} &= k \begin{pmatrix} 1 & 1 & 0 \\ 1 & 1 & 0 \\ 0 & 0 & 0 \end{pmatrix}, \quad \mathbf{K}_{1,-1,0} = k \begin{pmatrix} 1 & -1 & 0 \\ -1 & 1 & 0 \\ 0 & 0 & 0 \end{pmatrix}, \quad \mathbf{K}_{1,0,1} = k \begin{pmatrix} 1 & 0 & 1 \\ 0 & 0 & 0 \\ 1 & 0 & 1 \end{pmatrix}, \\ \mathbf{K}_{1,0,-1} &= k \begin{pmatrix} 1 & 0 & -1 \\ 0 & 0 & 0 \\ -1 & 0 & 1 \end{pmatrix}, \quad \mathbf{K}_{0,1,1} = k \begin{pmatrix} 0 & 0 & 0 \\ 0 & 1 & 1 \\ 0 & 1 & 1 \end{pmatrix}, \quad \mathbf{K}_{0,1,-1} = k \begin{pmatrix} 0 & 0 & 0 \\ 0 & 1 & -1 \\ 0 & -1 & 1 \end{pmatrix}, \\ \mathbf{K}_{0,0,0} &= -8k \begin{pmatrix} 1 & 0 & 0 \\ 0 & 1 & 0 \\ 0 & 0 & 1 \end{pmatrix}, \quad k = \varepsilon\beta^2 \end{aligned} \quad (3.126)$$

Six additional matrices are obtained from (3.126) by employing $\mathbf{K}_{-n,-m,-l} = \mathbf{K}_{n,m,l}$, while any other subscript triplet (n, m, l) yields a zero matrix. The Fourier transform (3.40) of these matrices can be shown in closed form:

$$\hat{\mathbf{K}}(p, q, r) = -8k\mathbf{I} + 4k \begin{pmatrix} (\cos q + \cos r)\cos p & -\sin p \sin q & -\sin p \sin r \\ -\sin p \sin q & (\cos p + \cos r)\cos q & -\sin q \sin r \\ -\sin p \sin r & -\sin q \sin r & (\cos p + \cos q)\cos r \end{pmatrix} \quad (3.127)$$

where p, q and r are real-valued Fourier parameters on the interval $[-\pi, \pi]$ and \mathbf{I} is the identity matrix.

Further steps in computing the kernel matrix Θ are accomplished numerically, according to the procedures (3.117), (3.119), (3.121), (3.123) and the DFT inversion formula (3.44). The coarse scale parameter a is chosen to be 31.

Elements of the matrix Θ decay quickly with increasing absolute values of the spatial order parameters n and m . We illustrate this property in Figure 3.23 by plotting element (1,1) of this matrix as a function of n at various m . The overall trends shown are typical for all other elements of Θ . In accordance with the staggered atomic arrangements in the fcc crystal, the matrices Θ for even $n+m$ appear trivial, and they are ignored in Figure 3.23. The value of the element (1,1) is seen to decay by a factor of 100 with the growth of $|n|$ or $|m|$ from 0 to 4. This decay is a valuable property of the kernel matrix. Taking this into account, we can truncate the summation in equation (3.124) at some critical differences $n-n'$ and $m-m'$ without a considerable loss of the accuracy. By denoting these critical values n_c and m_c , we can update equation (3.124) to give the final form,

$$\mathbf{u}_{n,m,1} = \sum_{n'=n-n_c}^{n+n_c} \sum_{m'=m-m_c}^{m+m_c} \Theta_{n-n',m-m'} \mathbf{u}_{n',m',0} \quad (3.128)$$

which is used in the computer simulation. In most applications of the fcc lattice model, it is proper to truncate this convolution sum at $n_c, m_c = 4 \sim 6$. This truncation can dramatically reduce the computational cost of the MSBCs.

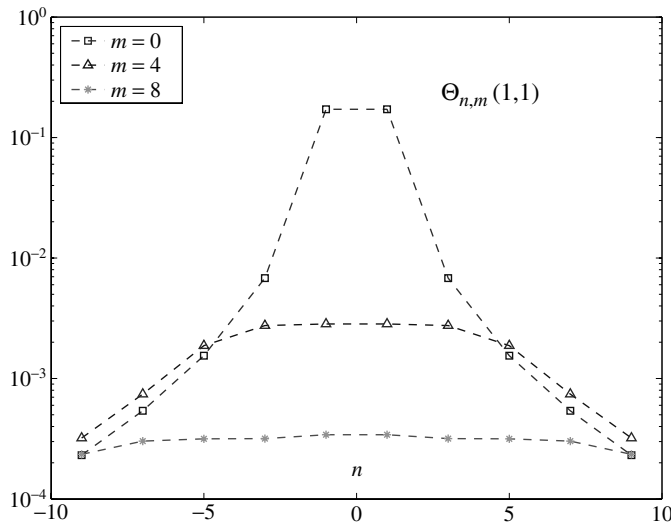


Figure 3.23 Typical dependence of the components in the kernel matrix on the values of spatial order parameters. Reprinted from International Journal of Solids and Structures, E. G. Karpov, H. Yu, H. S. Park et al., Multiscale boundary conditions in crystalline solids: Theory and application to nanoindentation, 2005, with permission from Elsevier.

Another important feature of this kernel matrix is that it is *invariant* with respect to the value of the interaction coefficient k in matrices (3.126), and therefore with respect to parameters of pair-wise potentials. Thus, the present kernel matrix Θ for a given value a is a general characteristic of all monoatomic fcc crystals with nearest neighbor interactions.

In the course of the simulation, the atomic displacements along the deformable boundary layer $l = 1$ in the reduced domain (see Figure 3.21) are related to the displacements of atoms in the adjacent layer $l = 0$ through the discrete convolution operator, according to equation (3.128). The original size of the full domain is $17 \times 17 \times 40$ atomic layers, and the fine grain domain (the reduced domain) comprises 1/4 of the total volume, that is, $17 \times 17 \times 10$ layers. This reduction corresponds to the value $a = 31$. According to (3.125), the interlayer distance along the coordinate axes is 2.066\AA , and the total height of the fine grain is 18.6\AA . The curvature radius of the indenter is 10\AA .

The indentation process is simulated in a series of iteration steps, where the maximum indentation depth of 10\AA is achieved at the 100th step. The result of this simulation, the load/indentation depth curve, is plotted in Figure 3.24 in comparison with the benchmark simulation that preserves the complete atomistic resolution for both the fine grain and the coarse grain. The plot shows a good agreement between the benchmark and multiscale simulations at all three indentation regimes: elastic load, plasticity (the top part of the indentation curve) and unload. Meanwhile, the multiscale approach reduces the computational effort by a factor of 10. More details on the MSBCs in solids can be found in Karpov et al. (2005) and Medyanik et al. (2005).

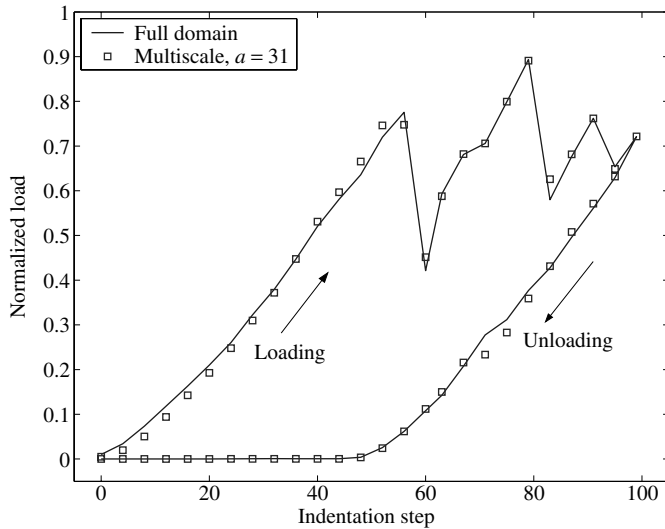


Figure 3.24 Load versus indentation depth: comparison of full domain atomistic and multiscale solutions for nanoindentation problem described in Figure 3.21.

Application: deformation of graphene monolayers

Application of the MSBC method to the mechanics of carbon nanostructures was demonstrated by Medyanik et al. (2005). In this work, a spherical indenter of radius R is applied in a displacement controlled manner to the center of a graphene sheet of hexagonal shape in a direction perpendicular to the plane of the sheet (see Figure 3.25). During each step, the indenter is lowered by 0.5 \AA followed by energy minimization using the conjugate gradient method. The indenter is modeled using a repulsive potential so that a repulsive force acts on every atom located in the vicinity of the center of the indenter closer than the indenter radius:

$$F_i = \alpha(R - r_i)^2 \quad (3.129)$$

where α is a parameter governing indenter stiffness and r_i is a distance between the centers of the indenter and current atom. In the numerical simulations, the value of A is taken as 100 eV/\AA corresponding to a very stiff (nearly rigid) indenter compared to transverse stiffness of the graphene structure; the radius of the indenter is $R = 10 \text{ \AA}$.

The outer boundary of the full domain, represented by a solid line in Figure 3.25, is fixed; the first term in equation (3.113) is then trivial. MSBCs are applied at the boundary of the reduced domain, which is shown with a dashed line. The size of the reduced domain is determined by the domain reduction parameter a , which represents the number of unit cell layers between the boundaries of the reduced domain and the full domain. The characteristic dimension of the coarse scale region being eliminated from the simulations, L_a , is equal to the domain reduction parameter times the size of the representative unit cell. The MSBCs are applied to each of the six zigzag sides of the reduced domain.

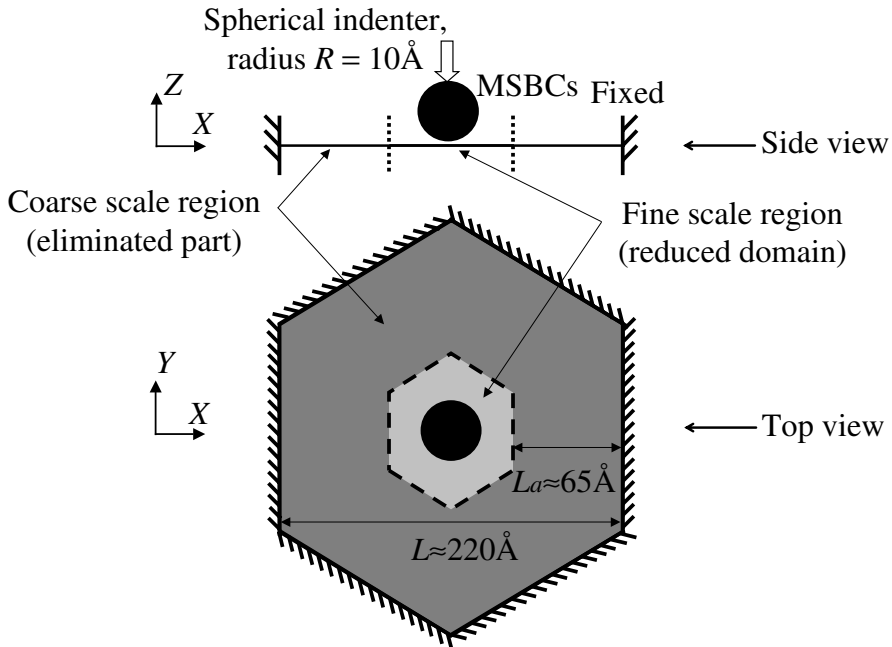


Figure 3.25 Application of multiscale boundary conditions to nanoindentation of a single graphene sheet: schematic problem statement. The dark gray domain of width L_a has been eliminated from the molecular mechanics simulation.

Molecular mechanics simulations were carried out for reduced domains of different sizes, using the MSBCs of the type

$$\mathbf{u}_{m,1} = \sum_{m'=m-m_c}^{m+m_c} \Theta_{m-m'} \mathbf{u}_{m',0} \quad (3.130)$$

Note that this equation is a reduced form of (3.128) that is valid for planar structures. The following domain reduction and cutoff parameters were utilized: $a = 30$ and $m_c = 4$. The full domain and the reduced domain were composed of 2646 and 15,000 atoms, respectively.

The results were compared with the corresponding full domain (benchmark) solutions. Figure 3.26 shows the reduced domain along with the fixed boundary of the full domain at four stages of the indentation process starting from the initial configuration, when all the atoms were in the same plane, and then after the indenter penetrates to the depths of 10, 20, and 30 Å. The pictures in Fig 3.26 represent the true aspect ratio, that is, they use the same scale in all dimensions.

The deformed configuration of the reduced domain at the final stage (after indenting to the depth of 30 Å) can be seen in more detail in Figure 3.27. This figure shows a comparison of the vertical displacements of the reduced domain to the full domain solution for the atoms at the cross section of the sheet along the vertical plane $y = 0$. Initially, the graphene sheet

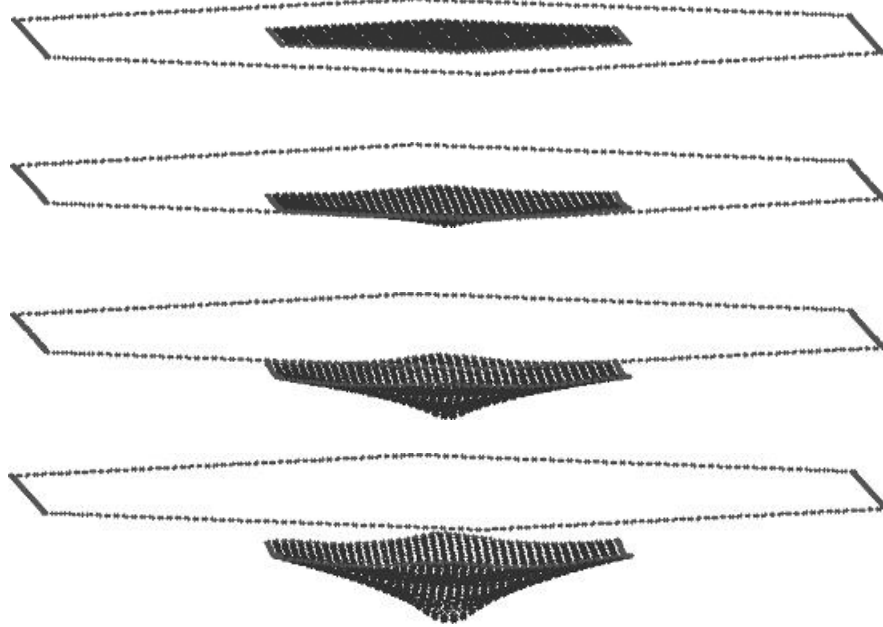


Figure 3.26 Multiscale simulations of the indentation of a graphene layer; only the reduced domain and the fixed boundary of the full domain are shown. The snapshots correspond to four different indentation depths: 0, 10, 20 and 30 Å.

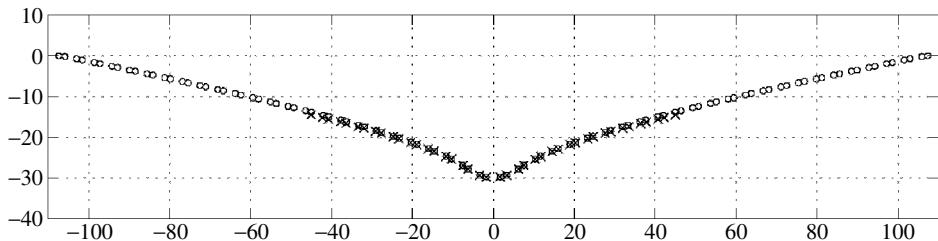


Figure 3.27 Vertical (z -axis) displacements of the atoms lying on the middle line cross section: reduced domain multiscale simulations (crosses) versus full domain solution (circles). Domain reduction parameter, $a = 30$.

was positioned at $z = 0$. It can be seen that owing to the applied multiscale boundary conditions (MSBC) the whole boundary of the reduced domain has moved from its initial position downward in the direction of indentation, representing a deformable boundary. The comparison of the benchmark and multiscale displacements shown in Figure 3.27 shows the high degree of accuracy of the MSBC method. Note that Figures 3.26 and 3.27 show the actual scale of deformation, proving that the method works well even for moderate deformations. Figure 3.28 shows very good agreement between multiscale and full domain

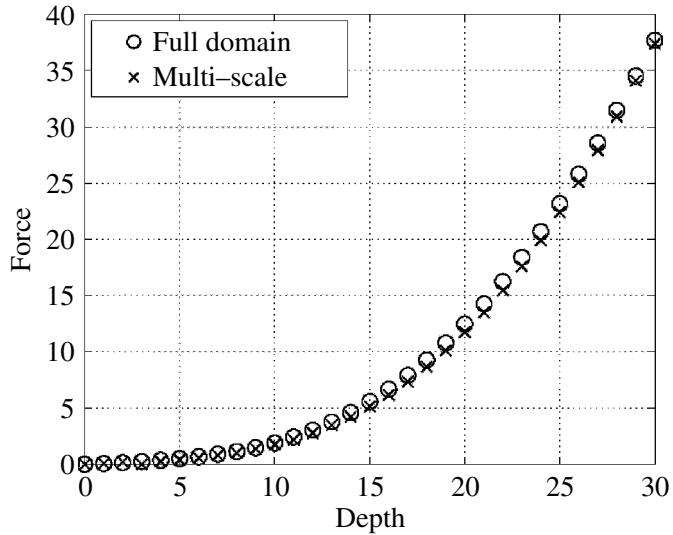


Figure 3.28 Force (eV/Å) versus indentation depth (Å).

results for the force versus depth of indentation curve. The force is given here in units of eV/Å.

Copyright

Material of pages 67–74, including Figures 3.19–3.23, is reproduced from Karpov et al. (2005), Copyright 2005, with permission from Elsevier.

4

Methods of Thermodynamics and Statistical Mechanics

Classical molecular dynamics and lattice dynamics, considered in previous chapters, are adequate in terms of the *microscopic* characterization of atomic-scale systems and processes. The derivation of the relevant *macroscopic* properties, and the elucidation of the long-term behavior are separate issues that require the tools of thermodynamics and statistical mechanics.

Thermodynamics is the study of averaged macroscopic properties of physical substances associated with the kinetic thermal motion of atoms and molecules. Thermodynamics is a phenomenological theory governed by a small group of general experimental principles and the laws of thermodynamics, which establish relationships between various macroscopic properties. These properties are characterized in an averaged sense through a small number of thermodynamic parameters, such as internal energy, temperature, specific heat capacity, thermal expansion coefficient, compressibility, and so on. Evaluation of these parameters is *the essence of macroscopic characterization of atomistic systems*. The thermodynamic method, reviewed in this chapter, is aimed at deriving various unknown thermodynamic parameters by utilizing a small number of known (measurable) parameters.

Statistical mechanics is the study of the relationships between the macroscopic properties of a system under investigation, and the microscopic properties and character of motion of particles that constitute this system. Here, one objective is to determine the macroscopic properties, based on the microscopic information, and the second objective is the opposite, that is, to obtain the microscopic properties of particles by utilizing the known thermodynamic parameters. Realistic physical bodies are composed of a huge number of atoms; for instance, 1 mm^3 of bulk metal contains about 10^{19} atoms. This points out the need for unique approaches to the atomic scale characterization of macroscopic systems, where a deterministic molecular dynamics approach is no longer feasible. Systems of vast numbers of degrees of freedom are controlled by governing principles that can be utilized to give a *probabilistic* description of properties of the individual atoms and molecules. Thus, statistical mechanics is a theory of multiparticle systems that utilizes statistical methods.

4.1 Basic Results of the Thermodynamic Method

The thermodynamic description of multiparticle systems, as distinct from classical particle dynamics, involves only a small number of macroscopic parameters. These are divided into two major groups: state parameters and system parameters. *State parameters* are assigned to characterize any current physical state of the system; examples include volume V , temperature T , pressure P , internal energy U , entropy S and enthalpy I . Meanwhile, *system parameters* represent, at given state conditions, intrinsic properties of the system, for example, the mass m , number of particles N , heat capacity C , thermal expansion coefficient α , thermal pressure coefficient β and compressibility κ . In some cases, the number of particles N serves as a state parameter.

Generally, system parameters depend on the current physical state of the system; for example, the heat capacity of solids is different at various temperatures. Therefore, system parameters are usually considered by fixing one or several state parameters, and imposing a limited range for the remaining state parameters. For example, heat capacity is evaluated at constant volume or pressure and within a narrow temperature range.

Evaluation of various macroscopic parameters by utilizing a smaller number of known, measurable or computable parameters, can be done using (1) thermodynamic state equations, Section 4.1.1 and (2) thermodynamic potentials (state functions), Section 4.1.5. The practical role of the general thermodynamic laws, reviewed in Sections 4.1.2–4.1.4, consists of the following: (1) they allow the derivation of the necessary state equation and state functions for a selected system and (2) they provide valuable insight into overall physical behavior of the system and general trends of the relevant thermodynamic parameters.

The application of the thermodynamic method to a given system implies that this system resides in a state of *thermodynamic equilibrium*, that is, in a state X defined by time-invariant state parameters, such as volume, temperature and pressure,

$$X = (V, T, P) \quad (4.1)$$

These parameters are called *measurable*, because they can be determined from direct experimental observations. Alternatively, one or two components of the vector (4.1) can be replaced by nonmeasurable parameters, such as internal energy or entropy, which can be found by analytical means or numerical calculations. The total number of parameters required for a complete description depends on the type of system under analysis. For example, the state of an ideal gas in equilibrium with a heat bath at a constant temperature (isothermal system) is determined by only two parameters: volume and pressure.

Since classical thermodynamics is a theory of equilibrium states, it would be more appropriate to call it thermostatics. However, the original title has historical roots, and therefore it is adopted by most authors. Meanwhile, the theory of nonequilibrium systems and processes activated by the kinetic motion of constitutive atoms and molecules (examples include mass and heat transport) is called *physical kinetics*, for example, Lifshitz and Pitaevskii (1981).

The concept of thermodynamic equilibrium is an idealization. In relation to time, the values of macroscopic state parameters make small spontaneous *fluctuations* about their mean values. In thermodynamic equilibrium, these mean values are time invariant (see Figure 4.1), and the vector (4.1) is understood in terms of the time-invariant *mean values* of volume, pressure and temperature. A typical fluctuation amplitude decays with an increase in the number of particles. For microscopically sized systems, fluctuations are negligible

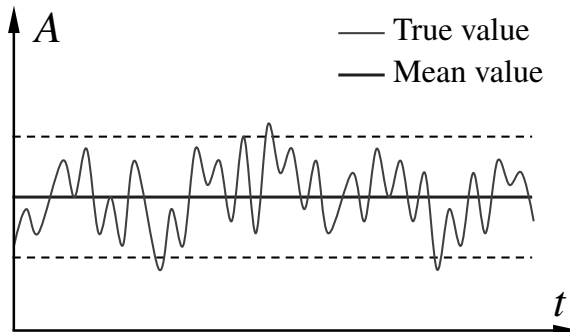


Figure 4.1 Fluctuation of a macroscopic state parameter A in thermodynamic equilibrium; the mean value of A is constant in time.

in most instances. However, in engineering micro- and nanoscale applications, fluctuations can be quite considerable.

The thermodynamic method is also applicable to slow processes, called *quasi-static processes*, which can be regarded as a continuous sequence of near-equilibrium states. Clearly, there is a difference in using the term “quasi static” in thermodynamics and Lagrangian mechanics (Section 3.6). The application of thermodynamic analytical tools to small-scale engineering systems and processes requires that they can be considered as quasi static in the thermodynamic sense.

A large system of particles (mass points), continuum bodies and fields that can exchange energy with each other and with external objects is called a *thermodynamic system*. If the system is not exchanging energy with external media, it is called an *isolated system*, whereas, if it does, it is called a *nonisolated system*. A special case of a nonisolated system is the adiabatic system, which can exchange energy with external bodies only through mechanical work.

One general principle associated with these definitions is that an isolated system, if given sufficient time, always achieves a state of thermodynamic equilibrium, regardless of the choice of an initial state. The spontaneous (self-induced) process of transition of the system from a nonequilibrium state to an equilibrium state, without external incentives, is called *relaxation*. The period of time required to complete this transition is called *relaxation time*.

Another general principle is the postulate of the *existence of temperature* as a parameter defining thermodynamic equilibrium between two thermodynamic systems in thermal contact. This postulate claims that the equilibrium states of two systems brought into thermal contact are not altered and the resultant system is in equilibrium only if the original systems have the same temperature. On the basis of this postulate, the special role of temperature, as a thermodynamic parameter, is elucidated. Most applications of the thermodynamic method require a priori consideration of temperature trends.

4.1.1 State Equations

Any state of a thermodynamic system, which can be described by a vector X (4.1), is called a *macroscopic state* (macrostate), while the corresponding vector X is called the

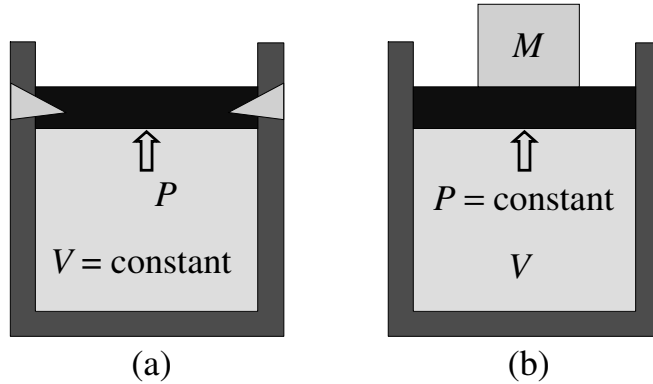


Figure 4.2 Illustration: the same parameter may appear as external and internal in various systems. Isochoric system (a): V – external parameter, P – internal parameter; isobaric system (b): V – internal parameter, P – external parameter.

state vector. Such a concise and averaged description of a multiparticle system compares to the detailed microscopic description by means of a large state vector (2.17), which includes exact coordinates and velocities of all particles in the system. An equation that relates all the state parameters for a given system, by means of one or several system parameters, is referred to as the governing *equation of state*:

$$f(V, T, P, \xi) = 0 \quad (4.2)$$

Here, ξ is a vector of system parameters.

All the state parameters are divided into external and internal parameters. Parameters that can be prescribed through external influence on the system by fixing external bodies and fields are called external. Meanwhile, internal parameters are determined by the state of the system itself for given values of external parameters. The same thermodynamic parameters may appear as external in one system and as internal in another; one example of such a situation is shown in Figure 4.2. One standard situation arising from atomic-scale modeling is related to a smaller system in contact with a large heat reservoir that is at a constant temperature. Here, the temperature serves as an external parameter for the smaller system.

As follows from empirical observations, each internal parameter in thermodynamic equilibrium is uniquely defined by external parameters and temperature. Thus, the actual values of internal parameters can be obtained from a relevant state equation (4.2), provided that all external parameters and temperature are either fixed, measured or computed a priori. Once all the state parameters are determined, the knowledge of a state equation allows the computation of the following system parameters:

(i) isothermal compressibility coefficient

$$\kappa_T^{-1} = -V \left(\frac{\partial P}{\partial V} \right)_T \quad (4.3)$$

(ii) isobaric volume expansion coefficient

$$\alpha_P = \frac{1}{V} \left(\frac{\partial V}{\partial T} \right)_P \quad (4.4)$$

(iii) isochoric pressure coefficient

$$\beta_V = \frac{1}{P} \left(\frac{\partial P}{\partial T} \right)_V \quad (4.5)$$

Below, we provide specific forms of the state equation for some standard types of thermodynamic systems. They can be regarded as experimental facts found in compliance with the general laws of thermodynamics. A more universal approach to computing the state and system parameters is the method of thermodynamic potentials, reviewed in Section 4.1.5.

Ideal gas

An ideal gas is a system of weakly interacting molecules, where the potential energy of interaction is negligible compared to the kinetic energy of thermal motion of the particles. The state equation of an ideal gas reads

$$PV = Nk_B T \quad (4.6)$$

where N is the total number of gas molecules, and $k_B = 1.38066 \times 10^{-23} \text{ J K}^{-1}$ is the Boltzmann constant.

The internal energy of the ideal gas is given by

$$U = \frac{i}{2} N k_B T \quad (4.7)$$

Here, $i = 3$ and 5 for monoatomic and diatomic gases respectively. For tri- and polyatomic molecules, in general $i = 6$. The ideal gas systems are discussed in more detail, in Section 4.2.3.

Real gas

Real gas models account for the intermolecular forces and finite size of gas particles by means of a pair-wise potential $V(r)$, typically the Lennard-Jones potential (2.60). The real gas state equation, known also as the *van der Waals equation*, is given by

$$\left(P + n^2 \frac{a}{V^2} \right) (V - nb) = Nk_B T, \quad n = \frac{N}{N_a} \quad (4.8)$$

In this equation, n is the amount of substance measured in moles, and $N_a = 6.02214 \times 10^{23} \text{ mol}^{-1}$ is Avogadro's number, the number of molecules comprising one mole of gas.

Parameters a and b are the van der Waals gas constants determined by

$$a = -2\pi N_a^2 \int_d^\infty V(r) r^2 dr, \quad b = \frac{2}{3} N_a \pi d^3 \quad (4.9)$$

where d is the effective diameter of gas molecules. Meanwhile, laboratory experiments indicate that these parameters depend on temperature also. More accurate constants a and b can be obtained experimentally, or from numerical simulations, by manipulating the system parameters (P, V, T, N) and using (4.8).

Liquids and solids

One universal form of the state equation that is applicable to liquids and solids is derived within the assumption that any change of volume is linearly related to the change of temperature and pressure:

$$V = V_0 (1 + \alpha(T - T_0) - \kappa(P - P_0)) \quad (4.10)$$

This linear equation gives a good description of homogeneous liquids and homogeneous isotropic solids over a wide range of state parameters. The volume $V_0 = V(T_0, P_0)$ corresponds to an arbitrary initial state. The thermal expansion coefficient α and the compressibility κ are defined according to

$$\alpha = \frac{1}{V_0} \left(\frac{\partial V}{\partial T} \right)_{P=P_0}, \quad \kappa = -\frac{1}{V_0} \left(\frac{\partial V}{\partial P} \right)_{T=T_0} \quad (4.11)$$

Results of numerical calculations of the system parameters, such as the expansion and compressibility coefficients (4.11), van der Waals constants (4.9), and others, can be compared to standard values available for a large variety of substances in the literature, for example, Lide (2004).

4.1.2 Energy Conservation Principle

Energy conservation in a closed thermodynamic system is expressed by the first law of thermodynamics. This law provides a relationship between the quantity of heat given to the system and the successive change of internal energy and mechanical work done by the same system.

The *quantity of heat* Q is the energy given to the thermodynamic system by external media via physical contact and radiation. The process of heat transfer is associated with the work done by atoms and molecules in the course of their chaotic thermal motion. Standard units for Q are the same as for energy, that is, joules (J) in SI, as well as electron volts (2.61).

An infinitesimally small quantity of heat δQ given to the thermodynamic system leads to a rise of its temperature from T to $T + dT$; that is to say

$$\delta Q = C dT \quad (4.12)$$

The coefficient C is called the *heat capacity*. The specific heat capacity is computed as $c = C/m$, where m is the system mass, at a constant volume (c_V) or pressure (c_P) and in a given temperature range. The heat capacity of one mole of substance is called *molar heat capacity*, and is denoted by C_V or C_P , accordingly. These coefficients represent intrinsic thermal properties of a given thermodynamic system. Note that $c_P/c_V = C_P/C_V$.

The amount of *work* A done by the thermodynamic system during a small quasi-static expansion between the volumes V and $V + dV$ is expressed by

$$\delta A = P dV \quad (4.13)$$

For a quasi-static process, the internal pressure P is always equal to external pressure P' , $P = P'$. Therefore, $\delta A' = -\delta A$, where $\delta A' = -P'dV$ is work of external forces. The total

work for a finite process between two states 1 and 2 is given by the integral,

$$A_{12} = \int_{(1)}^{(2)} P dV \quad (4.14)$$

The variation sign δ is used instead of the differential notation d in equations (4.12) and (4.13), in order to emphasize that the quantities Q and A cannot serve as state functions (see Section 4.1.5).

The *first law of thermodynamics* states that the amount of heat δQ given to a system is equal to the change in its internal energy dU augmented by the amount of work δA done by this system over external bodies and fields:

$$\delta Q = dU + \delta A \quad (4.15)$$

For a finite quasi-static process, this gives

$$Q = \Delta U + A_{12} \quad (4.16)$$

According to (4.14) and (4.16), we have

$$Q = \Delta U \quad (V = \text{constant}), \quad Q = \Delta I \quad (P = \text{constant}) \quad (4.17)$$

Here, ΔI is the change of *enthalpy* during the transition of the system between two equilibrium states. The enthalpy,

$$I = U + PV \quad (4.18)$$

is a function of state whose variance determines the quantity of heat obtained by the system in isobaric processes ($P = \text{constant}$).

Thermodynamic processes in an ideal gas

The first law of thermodynamics provides simple forms of the state functions, internal energy and enthalpy, for adiabatic ($\delta Q = 0$), isothermal ($dT = 0$), isobaric ($dP = 0$) and isochoric ($dV = 0$) processes in an ideal gas that take place at a constant heat capacity (the so-called polytropic process). The corresponding equations are summarized without derivation in Table 4.1. Note that for monoatomic ideal gases, the adiabatic index, $c_P/c_V = 5/3$.

Let us consider the adiabatic and isothermal volume expansions of the ideal gas in more detail. In the course of an adiabatic process, any volume expansion leads to a faster pressure decrease, as compared to the isothermal process (see Figure 4.3). For the isothermal process,

Table 4.1 Characteristics of polytropic processes in ideal gas

	State equation	Internal energy	Enthalpy
Adiabatic:	$PV^{c_P/c_V} = \text{constant}$	$dU = C_V dT = -\delta A$	$dI = C_P dT = \frac{c_P}{c_V} \delta A$
Isothermal:	$PV = \text{constant}$	$dU = 0$	$dI = 0$
Isobaric:	$V/T = \text{constant}$	$dU = C_V dT$	$dI = dU + PdV = C_P dT$
Isochoric:	$P/T = \text{constant}$	$dU = C_V dT = \delta Q$	$dI = dU + VdP = C_P dT$

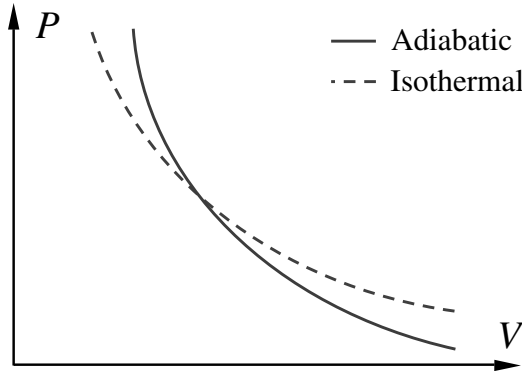


Figure 4.3 Adiabatic and isothermal expansion of the ideal gas.

mechanical work done during such an expansion is higher. The adiabatic and isothermal expansions can be viewed as two limiting cases of the same expansion process in a system that is interacting weakly with an external heat bath. They correspond to very fast and very slow expansion rates, respectively. In the first case, the expansion time is not sufficient for the system to absorb thermal energy from the heat bath, and the system cannot replenish the loss of its internal energy due to expansion. In the second case, the system is given sufficient time to completely replenish its internal energy at each specific iteration step of the process.

4.1.3 Entropy and the Second Law of Thermodynamics

The second law of thermodynamics imposes limitations on allowed directions of thermodynamic processes in isolated systems. In particular, it provides insight about the direction and possible outcomes of quasi-static and spontaneous relaxation processes, and establishes exact quantitative relationships between various thermodynamic parameters in equilibrium.

The *second law of thermodynamics* states that heat cannot flow spontaneously from a colder system to a hotter system. Thus, it is impossible to devise an engine that, working in cycle, produces no other effect than the transformation of heat, provided by external media, into mechanical work.

The most important result of this law is the existence of a special thermodynamic parameter, the *entropy* S , which is defined as

$$dS = \frac{\delta Q}{T} \quad (4.19)$$

Similar to internal energy and enthalpy, entropy can serve as a state function of a thermodynamic system. Entropy cannot be measured experimentally. However, it can be determined numerically in molecular dynamics simulations. In some simple cases, entropy can be found in a closed form.

By comparing the definition (4.19) with the first law (4.15), we obtain the fundamental differential equation of thermodynamics,

$$dU = T dS - P dV \quad (4.20)$$

It can be shown quite generally that variance of entropy in the course of a finite thermodynamic process is given by

$$\Delta S = S_2 - S_1 \geq \int_{(1)}^{(2)} \frac{\delta Q}{T} \quad (4.21)$$

where the inequality sign corresponds to irreversible changes. This provides an *alternative form* of the second law: all spontaneous processes in isolated and adiabatic systems ($\delta Q = 0$) occur at a constant or growing entropy,

$$\Delta S \geq 0 \quad (4.22)$$

Thus, any decrease of entropy in thermodynamic systems requires the input of energy from the surrounding media.

Probabilistic interpretation of entropy

The second law of thermodynamics implies that entropy grows in the course of a nonreversible process and achieves a maximum value in a state of thermodynamic equilibrium. Transition to an equilibrium state is said to be more probable, compared to any other transition. In other words, spontaneous evolution of a closed system is characterized by the passage of the system from less probable states to more probable states. There exists a relationship between the entropy of a given macrostate and the probability W of this state, expressed by the *Boltzmann equation*,

$$S = k_B \ln W \quad (4.23)$$

Any macroscopic state, such as (4.1), is determined by one or several equivalent microstates described by the Lagrangian state vector (2.17). In statistical mechanics (see Section 4.2), it is shown that all the microstates have an equal probability in thermodynamic equilibrium. Then, the probability of a given macrostate is given by

$$W = \frac{\Omega}{\Omega_m} \quad (4.24)$$

Here, Ω is the number of equiprobable microstates leading to a given macrostate, and Ω_m is the total number of possible microstates for a given system. The value Ω is also called the *statistical weight* or thermodynamic probability of the macrostate. These arguments indicate that, up to a constant value, the entropy can be written in the form

$$S = k_B \ln \Omega \quad (4.25)$$

Example: evaluation of entropy using probabilistic arguments

Consider a gaseous or liquid system of N identical, though distinguishable, molecules in a spherical or cylindrical chamber, whose cross section is shown in Figure 4.4(a). The chamber is divided by penetrable walls into three equal cells, where each of the cells contain N_i molecules. Assume that a given distribution of particles between the cells, N_1 , N_2 and N_3 , defines a macrostate, while the microstate is altered by any permutation of the particles. The binomial coefficient,

$$C_{N_1}^N = \frac{N!}{N_1!(N - N_1)!} \quad (4.26)$$

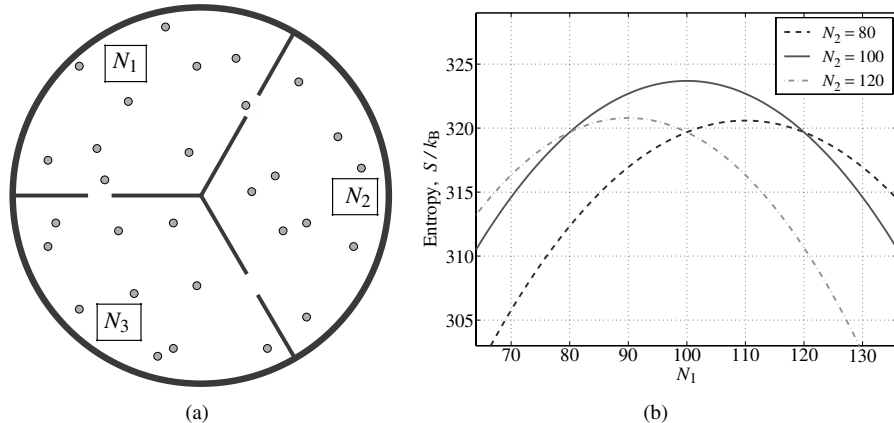


Figure 4.4 (a) Gas or liquid particles in a cylindrical chamber divided into three cells by penetrable walls. (b) Entropy of the system at various distributions of particles between the cells. Total number of particles, $N = N_1 + N_2 + N_3 = 300$.

shows the total number of configurations with N_1 molecules in the first cell. Further, the number

$$C_{N_2}^{N-N_1} = \frac{(N-N_1)!}{N_2!(N-N_1-N_2)!} = \frac{(N-N_1)!}{N_2!N_3!} \quad (4.27)$$

gives the number of microstates, where N_2 of the remaining particles are found in the second cell. The product of these two coefficients gives the total number of microstates, corresponding to the macrostate (N_1, N_2, N_3) , that is, the statistical weight/probability of this macrostate:

$$\Omega = C_{N_1}^N C_{N_2}^{N-N_1} = \frac{N!}{N_1!N_2!N_3!}, \quad (4.28)$$

The entropy of the system, evaluated according to (4.25) and (4.28), is plotted for various macrostate distributions of particles in Figure 4.4(b). It is seen that the highest (equilibrium) entropy corresponds to the state where all the molecules are equally distributed between the cells. Besides, for a fixed number of particles in one cell, a maximum value of entropy is achieved by equally distributing the molecules between two remaining cells.

The formula (4.28) can be generalized for an arbitrary number of cells, n ,

$$\Omega = \frac{N!}{N_1!N_2 \dots N_n!}, \quad N = N_1 + N_2 + \dots + N_n \quad (4.29)$$

We note that for large numbers of particles, computational effort can be saved by utilizing Stirling's formula,

$$N! \simeq \sqrt{2\pi} N^{N+1/2} e^{-N} \quad (4.30)$$

4.1.4 Nernst's Postulate

The original definition of entropy (4.19) is accurate up to a constant value only. An absolute value of entropy is determined from the *Nernst's postulate*, which states that the entropy

of a thermodynamic system at zero temperature serves as a universal constant, S_0 , which is invariant with respect to other state parameters, such as volume, pressure, and so on. Equivalently, this postulate can be rephrased as follows: at zero temperature, all quasi-static processes occur without entropy change. Conventionally, the constant value S_0 is set to zero, that is,

$$T = 0 : S = 0 \quad (4.31)$$

This empirical principle cannot be derived by utilizing other basic principles; therefore it is called the *third law of thermodynamics*. This law serves as a macroscopic manifestation of quantum properties of thermodynamic systems at the atomistic level, and it cannot be interpreted by only considering classical particle dynamics.

There are several important consequences of Nernst's postulate related to the behavior of thermodynamic parameters at (nearly) zero temperature. These consequences have been proven experimentally, and therefore should be referenced as benchmarks in atomic-scale modeling and simulation:

(i) At zero temperature, the heat capacity of all bodies approaches zero,

$$T \rightarrow 0 : C \rightarrow 0 \quad (4.32)$$

(ii) At zero temperature, the coefficient of isobaric thermal expansion and the isochoric pressure coefficient approach zero,

$$\begin{aligned} T \rightarrow 0 : \alpha_P &= \frac{1}{V} \left(\frac{\partial V}{\partial T} \right)_P = -\frac{1}{V} \left(\frac{\partial S}{\partial P} \right)_T \rightarrow 0 \\ T \rightarrow 0 : \beta_V &= \frac{1}{P} \left(\frac{\partial P}{\partial T} \right)_V = \frac{1}{P} \left(\frac{\partial S}{\partial V} \right)_T \rightarrow 0 \end{aligned} \quad (4.33)$$

Meanwhile, this behavior is determined by *quantum* properties of the matter, therefore, it cannot be reproduced within the classical molecular dynamics simulations. Experimental observations indicate that, as a result of the quantum effects, the ideal gas state equation (4.6) does not hold for very low temperatures. This fact can be interpreted formally as a consequence of the third law of thermodynamics.

4.1.5 Thermodynamic Potentials

A *Thermodynamic potential*, or *state function*, is a function of the parameters for a given system, which completely describes the equilibrium state of this system.

In principle, if the state equation (4.2) can provide an explicit dependence of one state parameter on all others, such a state parameter, according to the definition, can be considered as a thermodynamic potential. Meanwhile, the following abstract potentials are of particular importance in thermodynamics:

Internal energy	$U(S, V),$	$dU = T dS - P dV$
Enthalpy	$I(S, P) = U + PV,$	$dI = T dS + V dP$
Free energy	$F(T, V) = U - ST,$	$dF = -S dT - P dV$
Gibbs potential	$G(T, P) = F + PV,$	$dG = -S dT + V dP$

(4.34)

These state functions have two distinctive features: (1) knowledge of at least one of these functions allows the derivation of the state equation (4.2) for a selected system; (2) all

thermodynamic parameters of the system can be expressed in terms of partial derivatives of these functions (see below). The choice of a state function depends on the choice of state parameters utilized. A full set of state parameters is given by the state function itself and all its arguments. For example, free energy is used in combination with temperature and volume, and the corresponding state vector reads $X = (F, T, V)$.

The method of thermodynamic potentials is the most powerful analytical tool of thermodynamics. Indeed, the state parameters can be found simply as partial derivatives of the potentials (4.34),

$$\begin{aligned} T &= \left(\frac{\partial U}{\partial S} \right)_V = \left(\frac{\partial I}{\partial S} \right)_P, & P &= - \left(\frac{\partial U}{\partial V} \right)_S = - \left(\frac{\partial F}{\partial V} \right)_T \\ V &= \left(\frac{\partial I}{\partial P} \right)_S = \left(\frac{\partial G}{\partial P} \right)_T, & S &= - \left(\frac{\partial F}{\partial T} \right)_V = - \left(\frac{\partial G}{\partial T} \right)_P \end{aligned} \quad (4.35)$$

and numerous system parameters can be obtained according to the following:

(i) heat capacities

$$\begin{aligned} C_V &= \left(\frac{\partial U}{\partial T} \right)_V = T \left(\frac{\partial S}{\partial T} \right)_V = -T \left(\frac{\partial^2 F}{\partial T^2} \right)_V \\ C_P &= \left(\frac{\partial I}{\partial T} \right)_P = T \left(\frac{\partial S}{\partial T} \right)_P = -T \left(\frac{\partial^2 G}{\partial T^2} \right)_P \end{aligned} \quad (4.36)$$

(ii) adiabatic compressibility κ_S and isothermal compressibility κ_T

$$\begin{aligned} \kappa_S^{-1} &= -V \left(\frac{\partial P}{\partial V} \right)_S = V \left(\frac{\partial^2 U}{\partial V^2} \right)_S \\ \kappa_T^{-1} &= -V \left(\frac{\partial P}{\partial V} \right)_T = V \left(\frac{\partial^2 F}{\partial V^2} \right)_T \end{aligned} \quad (4.37)$$

(iii) adiabatic pressure coefficient β_S and isochoric pressure coefficient β_V

$$\begin{aligned} \beta_S &= \frac{1}{P} \left(\frac{\partial P}{\partial T} \right)_S = -\frac{1}{P} \left(\frac{\partial^2 U}{\partial V \partial T} \right)_S \\ \beta_V &= \frac{1}{P} \left(\frac{\partial P}{\partial T} \right)_V = -\frac{1}{P} \left(\frac{\partial^2 F}{\partial V \partial T} \right)_{T,V} \end{aligned} \quad (4.38)$$

These formulas, written in terms of partial derivatives of the state functions, are extremely convenient in practice. They indicate that the evaluation of the thermodynamic parameters does not require knowledge of the state functions over a wide range of system parameters. For example, in order to compute the heat capacity C_V at temperature T in molecular dynamics simulations, it is sufficient to fix the volume of the system and compute only two values of internal energy, U and $U + \Delta U$, corresponding to closed system temperatures, T and $T + \Delta T$. Then the sought heat capacity is simply $\Delta U / \Delta T$.

The equations (4.34) imply that the knowledge of internal energy U and free energy F (or entropy S), as the functions of state, provides the remaining thermodynamic potentials. Therefore, a pair of functions U, F , or U, S completely describes the macroscopic properties of a thermodynamic system in equilibrium, and provides all the relevant state and

system parameters. Meanwhile, the state parameters are determined by a single thermodynamic potential (4.34). In Section 4.2, we review the methods of statistical mechanics that allow evaluation of various state parameters and state functions, including U , F and S , by utilizing the function of the microscopic total energy of the thermodynamic system, the system Hamiltonian.

Minimization of thermodynamic potentials

In accordance with the first and second laws of thermodynamics, the free energy F and Gibbs potential G display decreasing behavior during the course of irreversible relaxation processes at constant temperature and volume,

$$\begin{aligned} T = \text{constant}, V = \text{constant} : \quad dF < 0 \\ T = \text{constant}, P = \text{constant} : \quad dG < 0 \end{aligned} \quad (4.39)$$

On achieving thermodynamic equilibrium, we obtain

$$\begin{aligned} T = \text{constant}, V = \text{constant} : \quad dF = 0 \\ T = \text{constant}, P = \text{constant} : \quad dG = 0 \end{aligned} \quad (4.40)$$

Hence, the free energy and the Gibbs potential of a given system are minimized in thermodynamic equilibrium: $F = F_{\min}$, $G = G_{\min}$. Minimization of the free energy and Gibbs potential, being equivalent to maximization of entropy, is a fundamental property of relaxation processes at constant temperature.

Free energy: mechanical interpretation

The thermodynamic meaning of free energy is elucidated in isothermal systems, where the free energy change dF determines the mechanical work accomplished by, or over, the system. Indeed,

$$T = \text{constant} : \quad dF = -S \, dT - P \, dV = -P \, dV = -\delta A \quad (4.41)$$

4.2 Statistics of Multiparticle Systems in Thermodynamic Equilibrium

The thermodynamic method reviewed in Section 4.1 provides insight into the relationships between various macroscopic properties of a selected system. Such an analysis implies preknowledge of a small number of thermodynamic parameters, and consequently provides further parameters by utilizing the system's state equation and/or the thermodynamic potentials. Meanwhile, all the state and system parameters, from the microscopic perspective, are determined by trajectories of atoms and molecules comprising the selected system, that is, by the components of a Lagrangian state vector (2.17). The methods of statistical mechanics allow the averaging of these trajectories and provide a minimal set of macroscopic parameters required for a comprehensive thermodynamic analysis.

For example, to use state equation (4.2) in order to compute pressure, one requires knowledge of the volume and temperature of the system. One of these parameters, for

instance, volume, can be set up as an external parameter, and therefore is known in advance. Meanwhile, the system temperature can be computed by statistically averaging (postprocessing) the velocities of all the system particles obtained from simulations of molecular dynamics of the system.

Classical statistical mechanics also provides a powerful analytical tool, the method of the partition function, which is based on the fundamental statistics of adiabatic and isothermal systems. The partition function is a fundamental characteristic of a given multiparticle system that allows the evaluation of various state parameters, including entropy and free energy, and therefore an arbitrary thermodynamic potential (4.34).

Derivations of the thermodynamic potentials, as well as other macroscopic parameters of interest, can be accomplished by utilizing the methods of statistical mechanics in the most systematic manner. In general, the role of statistical mechanics in the analysis of multiparticle systems in thermodynamic equilibrium consists of the following: (1) evaluation of thermodynamic state parameters by statistical averaging of the detailed atomistic information obtained from molecular dynamics computer simulations; (2) derivation of thermodynamic potentials, and subsequent evaluation of the numerous thermodynamic parameters for a system of interest; (3) probabilistic description of atomic scale behavior of multiparticle systems by utilizing information about their averaged macroscopic properties.

4.2.1 Hamiltonian Formulation

The Lagrangian description of multiparticle systems, Section 2.1, which involves the generalized coordinates q_1, q_2, \dots, q_s and velocities $\dot{q}_1, \dot{q}_2, \dots, \dot{q}_s$ of the particles is not unique. The dynamics of a multiparticle system can also be described by means of the generalized coordinates and *generalized momenta* p_1, p_2, \dots, p_s , defined as

$$p_j = \frac{\partial L}{\partial \dot{q}_j}, \quad j = 1, 2, \dots, s \quad (4.42)$$

where $2s$ gives the total number of independent degrees of freedom in the system. Then the Lagrange equation (2.11) can be rearranged to give two first-order differential equations:

$$\dot{q}_j = \frac{\partial H}{\partial \dot{p}_j}, \quad \dot{p}_j = -\frac{\partial H}{\partial \dot{q}_j} \quad (4.43)$$

where H is the *Hamilton function* or *Hamiltonian* of the system,

$$H = \sum_{j=1}^s \dot{q}_j p_j - L \quad (4.44)$$

The equations (4.43) are called *Hamilton's equations of motion*.

For conservative systems, the Hamiltonian represents the time-independent total energy of the system,

$$\frac{dH}{dt} = \frac{\partial H}{\partial t} = 0, \quad H = E_k + U \quad (4.45)$$

where, E_k and U are the kinetic (2.10) and potential (2.46) energies.

The generalized coordinates and momenta of all particles in the system, found by solving (4.43), form a time-dependent state vector \mathbf{Q} , which completely describes the mechanical state of the system at the time t ,

$$\mathbf{Q}(t) = [q_1(t, \mathbf{A}) \dots q_s(t, \mathbf{A}) \ p_1(t, \mathbf{A}) \dots p_s(t, \mathbf{A})] \quad (4.46)$$

Here, \mathbf{A} is a vector of initial conditions

$$\mathbf{A} = [q_1(0) \dots q_s(0) \ p_1(0) \dots p_s(0)] \quad (4.47)$$

These vectors are similar to those written for the Lagrangian formalism, the equations (2.16) and (2.17).

Example: system of monoatomic molecules

The Hamilton function for a system of N monoatomic molecules, characterized by a potential energy function U in Cartesian coordinates gives

$$H(p, r) = \sum_{i=1}^N \frac{\mathbf{p}_i^2}{2m_i} + U(\mathbf{r}_1, \mathbf{r}_2, \dots, \mathbf{r}_N), \quad \mathbf{p}_i^2 = m_i^2(\dot{x}_i^2 + \dot{y}_i^2 + \dot{z}_i^2) \quad (4.48)$$

where m_i is the mass of the i th molecule.

4.2.2 Statistical Description of Multiparticle Systems

The dynamics of multiparticle systems can be interpreted geometrically by introducing the concept of *phase space*. Phase space is an abstract $2s$ -dimensional vector space, spanned by all the possible state vectors (4.46) for a selected multiparticle system. In this regard, the microscopic state vector (4.46) is referred to as the *phase vector* that determines a specific phase point in the $2s$ -dimensional phase space. In course of time, this point moves along an abstract $2s$ -dimensional curve, which is called the *phase trajectory* of the system, see Figure 4.5. The infinitesimally small volume

$$d\Gamma = dq_1 \dots dq_s \ dp_1 \dots dp_s \quad (4.49)$$

is called the *elementary volume of the phase space*.

Within statistical mechanics, for example, Landau and Lifshitz (1980), Mayer and Mayer (1977), Pathria (1996) and Terletskii (1971), laws of motion of the individual components of the multiparticle systems are not sought, and the microscopic state vector (4.46) is not determined as a specific function of time. Instead, the motion of a whole set of phase points representing a collection of possible states of the given system is considered. Such a set of phase points is called the *phase space ensemble*. If each point of the phase space is considered as a random quantity with a particular probability density (statistical weight) $w(\mathbf{Q})$ ascribed to each possible state (4.46), the relevant phase space ensemble is called a *statistical ensemble*. Below, the functional dependence on the complete set of microscopic variables q_j and p_j , the components of the phase space vector \mathbf{Q} , will be denoted symbolically, as $w(p, q)$, $H(p, q)$, and so on.

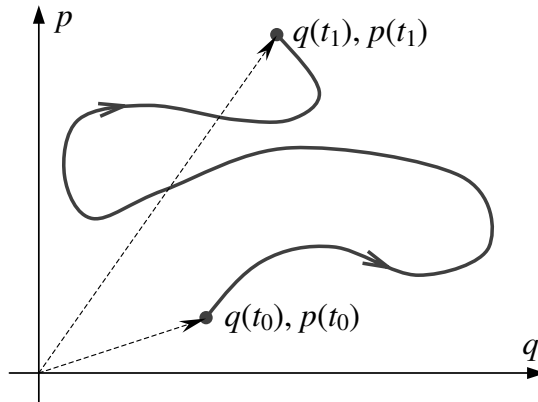


Figure 4.5 Phase space trajectory for a system with one independent degree of freedom ($s = 1$). Dashed arrows represent phase space vectors at various times.

The motion of a statistical ensemble can be thought of as the motion of a phase space fluid in analogy to the motion of an ordinary fluid in a 3D space. One basic result of statistical mechanics theory is the Liouville theorem: in the course of time evolution of the system, the phase volume Γ occupied by the statistical ensemble that represents this system in the phase space is invariant (see Figure 4.6). This can be written as

$$\Gamma_0 = \Gamma_1 = \Gamma_2 = \dots, \quad \Gamma = \int d\Gamma \quad (4.50)$$

Assume that F is a physical parameter of a multiparticle system, which is determined, in principle, by the configuration and microscopic motion of atoms and molecules comprising this system. Then, the *ensemble average* of this parameter is given, generally, by the phase space integral

$$\langle F \rangle = \int w(p, q) F(p, q) d\Gamma \quad (4.51)$$

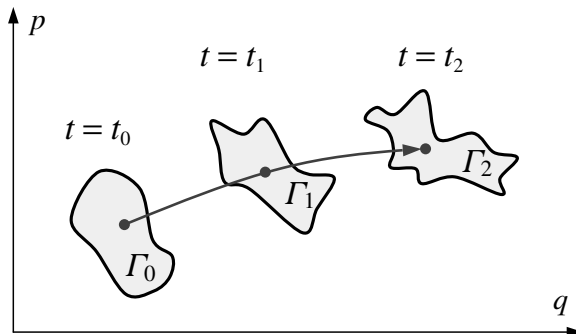


Figure 4.6 Illustration of the Liouville theorem.

This expression is valid for all micro- and macroscopic parameters. For a system composed of a large number N of identical particles (such systems are common in practice), ensemble average of parameters associated with the kinetic motion or interaction of the particles can be approximated by a finite sum over the systems' degrees of freedom:

$$\langle F \rangle \simeq \frac{1}{3N} \sum_{j=1}^{3N} F(p_j, q_j), \quad N \rightarrow \infty \quad (4.52)$$

As an example, the average square velocity of particles in such a system can be estimated according to

$$\langle v^2 \rangle \simeq \frac{1}{3N} \sum_{j=1}^{3N} v_j^2 = \frac{1}{3N} \sum_{j=1}^{3N} \frac{p_j^2}{m} \quad (4.53)$$

Other examples, where (4.52) is applicable, include the mean kinetic energy per particle, mean magnitude of interaction, mean drift of particles, and so on. We note that in the cases in which the value N is not large enough, the mean value (4.52) may show noticeable fluctuations in the course of time.

The *time average* value of the parameter F is evaluated as

$$\bar{F} = \frac{1}{t} \int_0^t F(p(\tau), q(\tau)) d\tau \quad (4.54)$$

According to basic principles of statistical mechanics, there exist mechanical systems for which the Hamiltonian plays a decisive role for their statistical behavior, and completely determines the form of the statistical distribution. In other words,

$$w(p, q) = w(H(p, q)) \quad (4.55)$$

Such systems are called *ergodic*. The relationship (4.55) is associated with the so-called *ergodic hypothesis*, which assumes that all realistic physical systems are ergodic, and claims that the probability density in phase space is a function of only the total energy of the system and does not depend on other integrals of motion.

There are two important statistical properties of ergodic systems in thermal equilibrium: (1) the probability distribution w representing the phase space statistics of an ergodic system is time invariant,

$$\frac{\partial w}{\partial t} = 0 \quad (4.56)$$

and (2) ensemble and time averaged values of physical quantities are equivalent,

$$\langle F \rangle = \bar{F} \quad (4.57)$$

The latter relationship is regarded as an alternative mathematical form of the ergodic hypothesis.

The relationship (4.57) implies that for a system in thermal equilibrium, the average value of the parameter F can often be provided by molecular dynamics simulations, rather than the involved phase space integral (4.51). This property is particularly valuable in the modeling and simulation of such multiparticle systems that do not assume knowledge of the exact statistical distribution w .

Practical usage of formulas (4.52) and (4.54) still requires knowledge of a “microscopic definition,” $F = F(p, q)$, an expression for the current value of parameter F in terms of the components of the phase space vector (4.46), or (2.17). Such a definition utilizes the physical content of the parameter F ; various examples can be found throughout the existing literature. Several examples are provided below:

Internal energy, where H is the Hamiltonian,

$$U = \overline{H(p, q)} \quad (4.58)$$

Temperature, as a measure of mean kinetic energy E_k per translational degree of freedom in the system (see (4.100)),

$$T = \frac{2}{k_B} \langle E_k \rangle \simeq \frac{1}{3Nk_B} \sum_{j=1}^{3N} m_j v_j^2 \quad (4.59)$$

Pressure created by N ideal gas particles of mass m confined in volume V ,

$$P = \frac{Nm}{V} \langle v_x^2 \rangle \quad (4.60)$$

where v_x is the x -axis projection of velocity of a particle. In equations (4.59) and (4.60), averaging over a group of particles may also be utilized.

Change of entropy (at constant volume),

$$\Delta S = \int_{U_1}^{U_2} \frac{dU}{T} = \int_{T_1}^{T_2} \frac{C_V}{T} dT \quad (4.61)$$

where U is the internal energy (4.58) and C_V is the heat capacity (4.36). Calculation of entropy-related parameters, including free energy and chemical potential from molecular dynamics simulations, has been discussed extensively in the literature, for example, Frenkel (1986), Jacucci and Quirke (1982) and Mezei and Beveridge (1986). On the basis of (4.58–4.61), one may also calculate a wide range of equilibrium thermodynamic parameters, by utilizing the definitions (4.34–4.38).

Transport properties of gases, including the diffusion constant D , viscosity η , and heat conductivity λ are related to the mean velocity \bar{v} and mean free path l of gas molecules:

$$D = \frac{1}{3} \bar{v} l, \quad \eta = \frac{N}{V} D, \quad \lambda = \frac{3}{2} k_B \eta \quad (4.62)$$

where l is the mean distance between two successive collisions of a molecule with other molecules in the system. For spherical gas molecules of an effective diameter d , the following estimate is valid:

$$l = \frac{V}{\sqrt{2} \pi N d^2} \quad (4.63)$$

Calculation of nonequilibrium/kinetic properties of gases and liquids are often associated with the *mean square force* exerted on the particle i , and *mean square drift* of this particle,

$$\overline{F_{x,i}^2} = \overline{\left(\frac{\partial U}{\partial x_i} \right)^2}, \quad \overline{D_{x,i}^2} = \overline{(x_i(t) - x_i(0))^2} \quad (4.64)$$

Assessments for solid mechanics parameters may also be obtained; for example, the mean stress per area A of a crystal plane orthogonal to the x -axis occupied by N atoms can be computed as

$$\overline{\sigma_x} = \frac{1}{A} \sum_{i=1}^N \overline{F_{x,i}} \quad (4.65)$$

This assessment is valid within the assumption that atoms of the given plane interact only with the atoms of two nearest coplanar planes.

The Liouville theorem (4.50), and the relationships (4.55) and (4.56) associated with the ergodic hypothesis, allow evaluation of the statistical distributions for some standard types of equilibrium systems. If the statistical distribution is known for a system of interest, all the equilibrium macroscopic parameters, including the thermodynamic potentials, can be computed by utilizing only the overall structure of the system Hamiltonian by means of some specific phase space integration techniques. In Sections 4.2.3 and 4.2.4 below, we illustrate these techniques on two standard types of ergodic systems for which the phase space statistical distributions are well known. These are the closed equilibrium systems represented by the so-called *microcanonical* distribution, and the closed isothermal system (system in thermal equilibrium with an external heat bath of a given temperature) represented by the *canonical* distribution.

4.2.3 Microcanonical Ensemble

The microcanonical statistical ensemble is associated with isolated systems, maintained at constant external parameters, which do not exchange energy or matter with the surrounding media. One example of a system of this type is shown in Figure 4.7, where the gas or liquid substance is maintained at a constant volume in a thermally insulated vessel. Obviously, the total energy of such a system is constant,

$$E = H(p, q, a) = \text{constant} \quad (4.66)$$

Here, H is the system Hamiltonian, and a represents a set of values of the fixed external parameters.

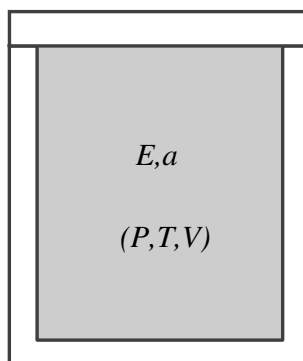


Figure 4.7 Isolated thermodynamic system represented by the microcanonical distribution in the phase space.

On the basis of the ergodic hypothesis (Section 4.2.2), it can be shown that the phase space statistical distribution for this system gives

$$w(p, q) = \frac{1}{g(E, a)} \delta(E - H(p, q, a)) \quad (4.67)$$

where δ is the Dirac's delta function (3.32), and g is the normalization factor

$$g(E, a) = \left(\frac{\partial \Gamma(E, a)}{\partial E} \right)_a, \quad \Gamma(E, a) = \int_{H(p, q, a) \leq E} d\Gamma \quad (4.68)$$

Here, $\Gamma(E, a)$ is the phase space volume enclosed within the hypersurface $H(p, q, a) = E$; see Figure 4.8 for an illustration.

The physical interpretation of the statistical distribution (4.67) consists of the following: within a microcanonical ensemble, all energetically allowed microstates are equally likely to occur. Meanwhile, phase space vectors corresponding to $H(p, q, a) \neq E$ are not allowed, and the system total energy does not fluctuate.

The major qualitative characteristic of the microcanonical ensemble is the phase space integral Γ ((4.68)). By utilizing Γ as a function of external parameters and total energy, one can compute the necessary thermodynamic parameters of the system:

$$U = E, \quad S = k_B \ln \Gamma, \quad T = \left(\frac{\partial S}{\partial E} \right)_V^{-1}, \quad P = \frac{1}{g(E, V)} \left(\frac{\partial \Gamma}{\partial V} \right)_E \quad (4.69)$$

These equations assume that $a \equiv V$, that is, the volume (along with the total energy) is a control parameter of the system, while any other external parameter is a fixed constant. According to the discussion of Sections 4.1.1 and 4.1.5, the set of parameters given by (4.69) provides a complete macroscopic description of a microcanonical ensemble in thermodynamic equilibrium. The remaining state and system parameters, such as free energy, concentration, heat capacity, pressure coefficient, and so on, can be computed by employing this basic set.

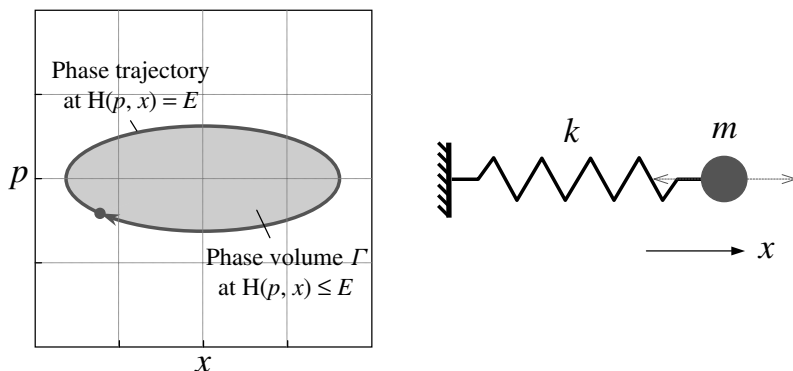


Figure 4.8 Harmonic oscillator: the phase space trajectory and volume Γ confined by the hypersurface $H(p, x) = E$, (4.68).

The above theory implies that the macroscopic thermodynamic parameters of an isolated equilibrium system depend only on the Hamiltonian of this system. In other words, these parameters can be obtained by solving the phase space integral (4.68) with a known Hamiltonian, rather than by running a molecular dynamics simulation.

Numerical techniques

Numerical evaluation of the phase space integral (4.68) is simplified by rewriting it in the following equivalent form

$$\Gamma(E, V) = \int \theta(E - H(p, q, V)) d\Gamma \quad (4.70)$$

Here, the integration is performed over a $2s$ -dimensional box in the phase space that fully accommodates the phase space trajectory, and θ is the Heaviside step function,

$$\theta(x) = \begin{cases} 0, & x < 0 \\ 1, & x \geq 0 \end{cases} \quad (4.71)$$

By utilizing this function, one automatically accounts for the shape of a phase space volume enclosed within the hypersurface $H(p, q, V) = E$. The system entropy is then computed by utilizing $S = k_B \ln \Gamma$.

During the next stage, two additional values of the phase space integral, Γ_E and Γ_V , are computed. The first of these is obtained by perturbing the system total energy by a small ΔE at constant volume and any other external parameters, and the second by perturbing the volume by ΔV at constant total energy. Then the numerical values of temperature and pressure are

$$T = \frac{\Delta E}{\Delta S} = \frac{\Delta E}{k_B \ln \Gamma_E / \Gamma}, \quad P = \frac{\Delta E}{\Gamma_E - \Gamma} \frac{\Gamma_V - \Gamma}{\Delta V} \quad (4.72)$$

Analytical example: ideal gas at constant (E, V)

Most generally, an *ideal gas* is a multiparticle system, whose Hamiltonian is additive, that is, can be represented as a sum of Hamiltonians, corresponding to the individual generalized degrees of freedom,

$$H = \sum_{j=1}^s h_j \quad (4.73)$$

The potential energy of such a system may only have one-body contributions (2.47) arising because of imposition of external fields and constraints. Alternatively, the potential energy has to be constant, or so small that it can be ignored, when compared to the mean kinetic energy of the system.

Consider the evaluation of the phase space integral, entropy and temperature for a closed system of N identical monoatomic molecules (Figure 4.9), using the microcanonical ensemble theory. The system is maintained at a constant physical volume V and a constant total energy E . It is assumed that the system is ideal, where the mean kinetic energy thermal motion is much higher than the mean potential energy of interaction of the molecules with

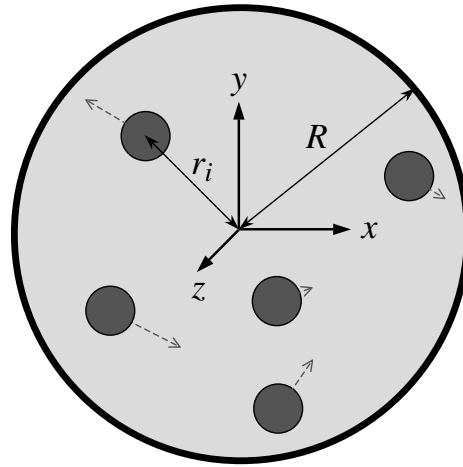


Figure 4.9 Monoatomic gas in a closed chamber.

other and with the chamber's wall. In practice, this assumption is valid only for rarefied gases. In accordance with (4.48), the Hamiltonian of this system gives

$$H = \sum_{i=1}^N h(\mathbf{p}_i), \quad h(\mathbf{p}_i) = \frac{\mathbf{p}_i^2}{2m} = \frac{1}{2m}(p_{x,i}^2 + p_{y,i}^2 + p_{z,i}^2) \quad (4.74)$$

where N is the total number of gas particles, m is the mass of individual particles. The phase space integral (4.68) corresponding to this Hamiltonian can be computed analytically; for more complicated Hamiltonians, the formula (4.70) can be utilized within a numerical integration scheme. Invariance of the ideal gas Hamiltonian with respect to the coordinates allows separation of the momentum variables:

$$\Gamma(E, V) = \int_V (dx dy dz)^N \int_{H(p) \leq E} d\mathbf{p}_1 d\mathbf{p}_2 \dots d\mathbf{p}_N = V^N \Gamma_p \quad (4.75)$$

Here, Γ_p is a projection of the $6N$ -dimensional phase space volume (4.75) onto the $3N$ -dimensional momentum subspace. The Hamiltonian (4.74) suggests that the projection Γ_p takes the shape of a $3N$ -dimensional hypersphere $H(p) = E$ of the radius $\sqrt{2mE}$. The hypersphere volume is given by

$$v_n = b(n) r^n \quad (4.76)$$

where n and r are the dimensionality and the radius of the hypersphere, and b is a constant that depends on n .

According to (4.75) and (4.76),

$$\Gamma(E, V) = V^N (2mE)^{3N/2} b(3N) \quad (4.77)$$

Substitution of this result into (4.69) gives the entropy, temperature and pressure of the ideal gas, as functions of the known parameters (E, V):

$$S = Nk_B \ln V + \frac{3}{2} Nk_B \ln E + S_0, \quad T = \frac{2}{3Nk_B} E, \quad P = \frac{Nk_B T}{V} \quad (4.78)$$

Here, S_0 is a constant depending on N and m . Obviously, the entropy and pressure are invariant with respect to a specific shape of the gas system, and only depend on the overall physical volume V occupied by gas particles. Note that the above equation for pressure is equivalent to the ideal gas state equation (4.6).

In concluding this section, we note that the microcanonical ensemble can be viewed as an idealization, where atoms and molecules comprising the thermodynamic system have no physical contact with surrounding bodies. In fact, this situation is more adequate for systems confined by idealized potential wells, rather than by realistic physical boundaries. Referring to the example of the system depicted in Figure 4.9, we would expect small-scale fluctuations of the total energy, even in the state of thermal equilibrium, provided that the chamber wall represents a realistic material with an intrinsic atomic structure. Collisions between the gas molecules and the atoms of the chamber wall material will stipulate for a microscopic energy exchange along the gas–solid interface and, therefore, fluctuations of the total energy of the gas system.

These fluctuations will take place even in the state of macroscopic thermal equilibrium between the gas and the chamber wall. If the physical boundaries represent a massive peripheral domain, the latter can be regarded as a *heat bath*, or *thermostat*, for the bounded (localized) system under analysis. The notion of a heat bath/thermostat arises from the assumption that any macroscopic perturbation of internal energy of the local system can be smothered by the heat bath on achieving a global thermal equilibrium, without a noticeable change of the heat bath temperature. This requires that the absolute heat capacity (4.36) of the thermostat is infinitely large.

The small-scale energy fluctuations in a local system equilibrated with the peripheral heat bath imply inapplicability of the microcanonical ensemble theory. Nonetheless, properties of such a system can be evaluated on the basis of the canonical ensemble theory reviewed in the next section.

4.2.4 Canonical Ensemble

The canonical statistical ensemble is associated with closed isothermal systems, maintained at constant temperature, which can exchange energy with the surrounding media but cannot exchange mass. Normally, these systems are understood as being in thermal equilibrium with a massive external heat bath, Figure 4.10. Due to the energy exchange, the instantaneous value of the system Hamiltonian fluctuates about some mean value of the system total energy, $E = \bar{H}$, so that

$$H(p(t), q(t), a) \neq \text{constant} \quad (4.79)$$

Here, a represents a vector of fixed external parameters. In most instances, this vector is composed of two components, $a = (T, V)$, where T and V are the temperature and physical volume of the system.

By utilizing the ergodic hypothesis in the form (4.55), it can be shown that the phase space statistical distribution for the canonical ensemble takes the following form

$$w(p, q) = \frac{1}{Z} \exp\left(-\frac{H(p, q, a)}{k_B T}\right) \quad (4.80)$$

This expression is known as the *Gibbs canonical distribution*, one of the most important results of the classical statistical mechanics. The normalization factor Z , called the *partition*

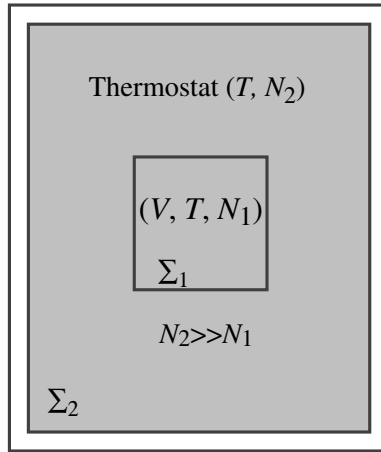


Figure 4.10 System Σ_1 is in thermal equilibrium with a massive thermostat Σ_1 at temperature T . In the phase space, the system Σ_1 can be represented by the canonical ensemble.

function, is found according to

$$Z(T, a) = \int \exp\left(-\frac{H(p, q, a)}{k_B T}\right) dp dq \quad (4.81)$$

where the integration is accomplished formally over the entire phase space. The partition function is the major qualitative characteristic of the canonical ensemble. The knowledge of Z as a function of temperature and other external parameters represented by a allows evaluation of all the system and state parameters, including the thermodynamic potentials (4.34).

For a canonical ensemble maintained at constant temperature and volume, $a = (T, V)$, the basic set of thermodynamic characteristics gives

Free energy	$F(T, V) = -k_B T \ln Z$
Entropy	$S = -\left(\frac{\partial F}{\partial T}\right)_V = k_B \ln Z + k_B T \frac{\partial}{\partial T} \ln Z$
Pressure	$P = -\left(\frac{\partial F}{\partial V}\right)_T = k_B T \frac{\partial}{\partial V} \ln Z$
Internal energy	$U = F + TS = \bar{H} = k_B T^2 \frac{\partial}{\partial T} \ln Z$

(4.82)

The remaining equilibrium characteristics can be evaluated on the basis of the above by utilizing the thermodynamic methods of Section 4.1.

Numerical techniques

One practically important feature of the partition function method is associated with the *factorization* of the Gibbs canonical distribution (4.80) in applications to ideal gas systems.

Since an ideal gas is described by an additive Hamiltonian (4.74), we obtain

$$w(p, q) = \frac{1}{Z} \exp\left(-\sum_j^s \frac{h_j}{k_B T}\right) = \frac{1}{Z} \prod_j^s \exp\left(-\frac{h_j}{k_B T}\right) \quad (4.83)$$

This property can be crucial in terms of practical calculations over real-life systems. According to (4.81) and (4.83), the $2s$ -dimensional space integral for the partition function reduces to a product of two-dimensional integrals,

$$Z = \prod_j^s z_j, \quad z_j = \int \exp\left(-\frac{h_j}{k_B T}\right) dp_j dq_j \quad (4.84)$$

In the case that the system is composed of N identical monoatomic/structureless molecules moving in Cartesian coordinates, evaluation of the partition function reduces to the calculation of a single, maximum six-dimensional integral:

$$Z = z^N, \quad z = \int \exp\left(-\frac{h(\mathbf{p}, \mathbf{r})}{k_B T}\right) d\mathbf{p} d\mathbf{r} \quad (4.85)$$

Here, the partition function z is associated with the statistics of one arbitrary molecule. Thus, for a system of weakly coupled generalized coordinates, such as translational degrees of freedom of molecules in a rarefied gas, or normal modes in harmonic lattices, the method of a statistical partition function is particularly appealing. Statistics of the normal modes in a regular lattice structure is considered in Section 4.2.6.

Numerical evaluation of the thermodynamic parameters (4.82) based on the partition function requires the calculation of three values: Z , Z_T and Z_V , according to (4.81). The first value is computed for the original temperature and volume of the system. The second value is obtained by perturbing the system temperature by a small ΔT at constant volume, and the third by perturbing the volume by ΔV at constant temperature. Then the numerical values of the parameters (4.82) are found as

$$\begin{aligned} F &= -k_B T \ln Z, & S &= k_B \ln Z + \frac{k_B T}{Z} \frac{Z_T - Z}{\Delta T} \\ P &= \frac{k_B T}{Z} \frac{Z_V - Z}{\Delta V}, & U &= \frac{k_B T^2}{Z} \frac{Z_T - Z}{\Delta T} \end{aligned} \quad (4.86)$$

Analytical example: ideal gas at constant (T, V)

The partition function of the ideal gas system (Figure 4.12), maintained at constant temperature and volume can be evaluated analytically by accounting for the property (4.85). The Hamiltonian of this system is given by (4.74). Thus,

$$Z = z^N, \quad z = \int_V d\mathbf{r} \int \exp\left(-\frac{\mathbf{p}^2}{2mk_B T}\right) d\mathbf{p} \quad (4.87)$$

Recalling that $\mathbf{p}^2 = p_x^2 + p_y^2 + p_z^2$, $d\mathbf{p} = dp_x dp_y dp_z$ and

$$\int_{-\infty}^{\infty} e^{-ax^2} dx = \sqrt{\pi/a} \quad (4.88)$$

we obtain the partition function

$$Z = V^N (2\pi m k_B T)^{\frac{3}{2}N} \quad (4.89)$$

Evaluation of the thermodynamic parameters (4.82) is then straightforward:

$$\begin{aligned} F(T, V) &= -Nk_B T (\ln V + \frac{3}{2} \ln(2\pi m k_B T)), & P &= Nk_B T / V \\ S(T, V) &= Nk_B (\ln V + \frac{3}{2} \ln(2\pi m k_B T) + \frac{3}{2}), & U &= \frac{3}{2} Nk_B T \end{aligned} \quad (4.90)$$

Remarkably, the results for pressure and internal energy are equivalent to the last two equations in (4.78) corresponding to a microcanonical ensemble.

Note that in numerical molecular dynamics (MD) simulations, the temperature of an equilibrium system can be evaluated by utilizing (4.59). In the next stage, analytical tools of the canonical ensemble theory can be used to obtain an extended set of macroscopic parameters of the system.

One general conclusion regarding the material presented in Sections 4.2.3 and 4.2.4 is the following: the statistical ensemble theory utilizes statistical distributions in the phase space, the system Hamiltonian along with a limited macroscopic information (e.g. only temperature and external parameters) to produce a complete macroscopic description of the equilibrium system.

4.2.5 Maxwell–Boltzmann Distribution

The Gibbs canonical distribution allows evaluation of one-particle statistical distributions providing probabilistic information of the properties of the motion of *individual* particles in the thermodynamic system. This information is invaluable in terms of numerical analysis and simulation of atomic-scale systems; the range of usage includes generation/sampling of initial conditions, Monte Carlo methods, heat bath techniques, the study of temperature-related properties and effects, such as kinetic phenomena.

Distributions for momenta, velocities and kinetic energy

Consider a system of N identical structureless molecules characterized by the Hamiltonian (4.48). The additivity of this general Hamiltonian with respect to kinetic and potential energies assumes that the Gibbs canonical distribution can be presented as a product of two independent distributions for the momenta and coordinates,

$$w(\mathbf{p}, \mathbf{q}) = \frac{1}{Z_p} \exp\left(-\sum_i^N \frac{\mathbf{p}_i^2}{2mk_B T}\right) \times \frac{1}{Z_r} \exp\left(-\frac{U(\mathbf{r}_1, \mathbf{r}_2, \dots, \mathbf{r}_N)}{k_B T}\right) \quad (4.91)$$

Furthermore, additivity of the kinetic energy with respect to the momenta of the individual particles implies expansion of the momenta distribution in (4.91) into the independent cofactors

$$w(\mathbf{p}_i) \equiv w(\mathbf{p}) = \frac{1}{(2\pi m k_B T)^{3/2}} \exp\left(-\frac{\mathbf{p}^2}{2mk_B T}\right) \quad (4.92)$$

$w(\mathbf{p})$ is the distribution for the components of momenta of a single molecule; $\mathbf{p}^2 = p_x^2 + p_y^2 + p_z^2$. Obviously, this distribution is identical for all molecules in the system. In practice,

it is convenient to have the distribution for a given component of the momentum vector; by integrating (4.92) over p_y and p_z ,

$$w(p_x) = \frac{1}{(2\pi m k_B T)^{1/2}} \exp\left(-\frac{p_x^2}{2m k_B T}\right) \quad (4.93)$$

Here, the argument p_x varies from $-\infty$ to ∞ . Distributions for p_y and p_z have an analogous form. Finally, the distribution for the *absolute values* (magnitude) of the momentum vector is obtained by integrating over angles of the spherical coordinates in the three-dimensional momentum space spanned by components of \mathbf{p} , where $d^3 p = p^2 dp \sin \theta_p d\phi_p$. This leads to

$$w(p) = \frac{4\pi}{(2\pi m k_B T)^{3/2}} p^2 \exp\left(-\frac{p^2}{2m k_B T}\right) \quad (4.94)$$

Here, p is the magnitude of momentum of an individual particle, varying from 0 to ∞ .

The distribution for the kinetic energy E_k requires the change of variables,

$$E_k = p^2/2m, \quad \sqrt{2m E_k}, \quad p dp = 2m dE_k \quad (4.95)$$

in (4.94). Then the condition $w(p) dp = w(E_k) dE_k$ leads to

$$w(E_k) = \frac{2\pi}{(\pi k_B T)^{3/2}} \sqrt{E_k} \exp\left(-\frac{E_k}{k_B T}\right) \quad (4.96)$$

Substituting $\mathbf{p} = m\mathbf{v}$ to the equations (4.92–4.94), one obtains distributions for the velocity vector, the component v_x , and the magnitude of velocity:

$$w(\mathbf{v}) = \left(\frac{m}{2\pi k_B T}\right)^{3/2} \exp\left(-\frac{mv^2}{2k_B T}\right) \quad (4.97)$$

$$w(v_x) = \left(\frac{m}{2\pi k_B T}\right)^{1/2} \exp\left(-\frac{mv_x^2}{2k_B T}\right) \quad (4.98)$$

$$w(v) = 4\pi \left(\frac{m}{2\pi k_B T}\right)^{3/2} v^2 \exp\left(-\frac{mv^2}{2k_B T}\right) \quad (4.99)$$

The latter of these is referred to as the *Maxwell–Boltzmann distribution*.

The symmetry of distributions (4.97) and (4.92) with respect to individual components of the vectors \mathbf{p} and \mathbf{v} indicates that there is a preferred direction for the motion of particles in a state of thermodynamic equilibrium. Mathematically, this implies uniform distributions for these vectors with respect to the angles θ and ϕ in spherical coordinates.

The distributions (4.96) and (4.99) allow evaluation of the mean kinetic energy, mean velocity components, and mean magnitudes of velocity of the molecule,

$$\langle E_k \rangle = \int_0^\infty E_k w(E_k) dE_k = \frac{3}{2} k_B T \quad (4.100)$$

$$\langle v_x \rangle = \int_{-\infty}^\infty v_x w(v_x) dv_x = 0, \quad \langle v_x^2 \rangle = \int_{-\infty}^\infty v_x^2 w(v_x) dv_x = \frac{k_B T}{m} \quad (4.101)$$

$$\langle v \rangle = \int_0^\infty v w(v) dv = \sqrt{\frac{8k_B T}{\pi m}}, \quad \langle v^2 \rangle = \int_0^\infty v^2 w(v) dv = \frac{3k_B T}{m} \quad (4.102)$$

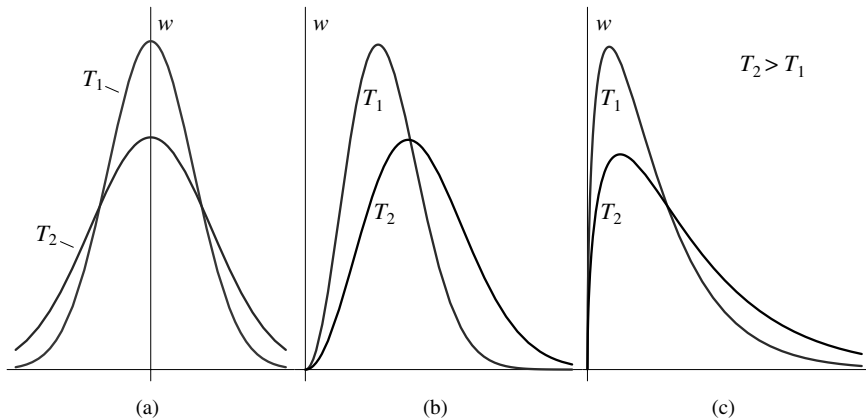


Figure 4.11 Shapes of the one-particle distributions for: (a) components of the momentum/velocity vector, (b) magnitude of the momentum/velocity and (c) kinetic energy.

Since all the Cartesian directions are statistically equivalent, the result (4.100) implies that each translational degree of freedom is associated with the energy $k_B T/2$ for a system in thermal equilibrium at temperature T . Note that substitution of $\langle v_x^2 \rangle$ from (4.101) into (4.60) yields the pressure of an ideal gas compliant with the state equation (4.6).

We point out that the distributions associated with the kinetic motion of particles, reviewed in this section, are invariant with respect to the form of potential energy function in the system; this fact serves as a consequence of the factorization (4.91). Therefore, these distributions are adequate in relation to translational degrees of freedom in most multiparticle systems, including ideal and nonideal gases, liquids, and crystal lattices. The shapes of these distributions are shown in Figure 4.11.

Boltzmann distribution for coordinates

For systems with additive potential energy, for example, noninteractive particles in an external field characterized by the one-body potential (2.47),

$$H = \sum_i^N \left(\frac{\mathbf{p}_i^2}{2m} + V_1(\mathbf{r}_i) \right) \quad (4.103)$$

the Gibbs canonical distribution can also be expanded with respect to the coordinates into the independent factors

$$w(\mathbf{r}_i) \equiv w(\mathbf{r}) = \frac{1}{z} \exp\left(-\frac{V_1(\mathbf{r})}{k_B T}\right) \quad (4.104)$$

This result is known as the *Boltzmann distribution* of the coordinates of an individual particle that comprises a large system submerged in the external field. The normalization constant z depends on the specific form of the potential V_1 ,

$$z = \int \exp\left(-\frac{V_1(\mathbf{r})}{k_B T}\right) d\mathbf{r} \quad (4.105)$$

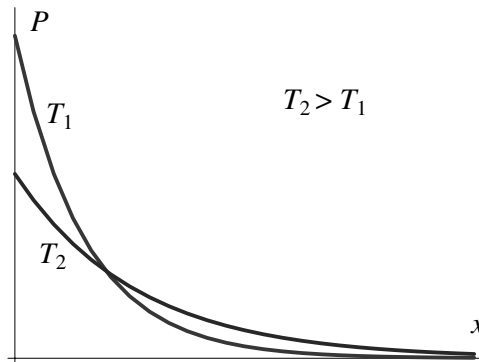


Figure 4.12 The barometric dependence (4.107) at higher and lower temperatures.

One standard application of the Boltzmann distribution is for gas particles in a gravitational field (2.50),

$$w(x) = \frac{mg}{k_B T} \exp\left(-\frac{mgx}{k_B T}\right) \quad (4.106)$$

Since the physical density of particles per unit volume, the concentration n , is proportional to the probability density (4.106), one obtains the concentration n and pressure P of the gas as functions of the height x :

$$n(x) = n_0 e^{-\frac{mgx}{k_B T}}, \quad P(x) = P_0 e^{-\frac{mgx}{k_B T}} \quad (4.107)$$

Here, n_0 and p_0 are the concentration and pressure at the Earth's surface, or another reference height level. The expression for pressure in (4.107) is often called the *barometric formula*. Barometric curves at higher and lower temperatures are shown in Figure 4.12.

Note that the Hamiltonian (4.103) is a particular case of the general structure (4.73). Hence, the Boltzmann distribution works for ideal gases only.

4.2.6 Thermal Properties of Periodic Lattices

In this section, we consider application of the canonical ensemble theory (Section 4.2.4) to the analysis of random thermal vibrations in regular polymer or crystal lattices. Various types of deterministic lattice solutions were discussed in detail in Chapter 3. Assume that the lattice of finite size is interacting weakly with an external heat bath at temperature T (Figure 4.13). After a sufficiently large period of time, the lattice achieves thermodynamic equilibrium with the heat bath. Equilibrium thermal vibrations of such a lattice can be regarded as one form of the free lattice motion. For a harmonic lattice, these vibrations can be most naturally represented by the general homogeneous solution in the form of a superposition of the lattice standing waves (3.53). This solution contains in total $2SN$ free parameters: SN normal amplitudes a and SN phases ϕ ; S is the number of degrees of freedom per lattice unit cell, and N is the number of unit cells. As shown below, these parameters can be derived in a probabilistic manner from the Gibbs canonical distribution (4.80) by utilizing the knowledge of only lattice temperature and lattice spectral properties, that is, the normal frequencies and polarization vectors in (3.53).

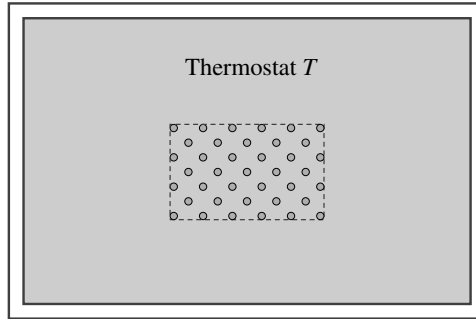


Figure 4.13 Finite lattice in thermal equilibrium with a heat bath.

Application of the Gibbs canonical distribution to lattice systems requires evaluating the lattice Hamiltonian in terms of the normal amplitudes and phases. According to (3.8) and (4.44), the Hamiltonian of a general harmonic lattice in Cartesian coordinates is given by

$$H = \frac{1}{2} \sum_{\mathbf{n}} \dot{\mathbf{u}}_{\mathbf{n}}^T \mathbf{M} \dot{\mathbf{u}}_{\mathbf{n}} - \frac{1}{2} \sum_{\mathbf{n}, \mathbf{n}'} \mathbf{u}_{\mathbf{n}}^T \mathbf{K}_{\mathbf{n}-\mathbf{n}'} \mathbf{u}_{\mathbf{n}'} \quad (4.108)$$

Substituting the displacements (3.53) into the (4.108) and further averaging in time yields

$$H = \frac{N}{4} \sum_{\mathbf{p}, s} \left(a_{\mathbf{p}, s}^2 \omega_{\mathbf{p}, s}^2 \mathbf{d}_{\mathbf{p}, s}^{\dagger} \mathbf{M} \mathbf{d}_{\mathbf{p}, s} - a_{\mathbf{p}, s}^2 \mathbf{d}_{\mathbf{p}, s}^{\dagger} \hat{\mathbf{K}}(\mathbf{p}) \mathbf{d}_{\mathbf{p}, s} \right) \quad (4.109)$$

where the dagger stands for a complex conjugate and transposed vector.

Next, introducing the characteristic mass and stiffness of the normal mode,

$$\mu_{\mathbf{p}, s} = \mathbf{d}_{\mathbf{p}, s}^{\dagger} \mathbf{M} \mathbf{d}_{\mathbf{p}, s}, \quad \varkappa_{\mathbf{p}, s} = -\mathbf{d}_{\mathbf{p}, s}^{\dagger} \hat{\mathbf{K}}(\mathbf{p}) \mathbf{d}_{\mathbf{p}, s} \quad (4.110)$$

According to (3.51), they are related to the normal frequency as

$$\omega_{\mathbf{p}, s}^2 = \varkappa_{\mathbf{p}, s} / \mu_{\mathbf{p}, s} \quad (4.111)$$

Thus, the mean values of kinetic and potential energies are equal to one half of the total energy of each normal mode. Finally, the lattice Hamiltonian gives

$$H = \frac{N}{2} \sum_{\mathbf{p}, s} a_{\mathbf{p}, s}^2 \omega_{\mathbf{p}, s}^2 \mu_{\mathbf{p}, s} = \frac{N}{2} \sum_{\mathbf{p}, s} a_{\mathbf{p}, s}^2 \varkappa_{\mathbf{p}, s} \quad (4.112)$$

Individual terms in the expression (4.112) have a remarkable resemblance with the total energy of the spring-mass oscillator ($N = 1$), Figure (4.8),

$$E = \frac{1}{2} a^2 \omega^2 m = \frac{1}{2} a^2 k \quad (4.113)$$

where a is the vibrational amplitude. Thus, complex lattice vibrations in the space of wave numbers can be regarded as a result of the oscillatory motion of SN quasi particles, characterized by the mass μ and stiffness \varkappa in accordance with (4.110). These quasi particles

are called the lattice *phonons*, and a complete set of phonons for a given lattice domain comprise the formal *phonon gas* system. Note the Hamiltonian (4.112) is additive, where the total energy is given as a sum of the energies of the individual normal nodes. Therefore, according to the general definition of the ideal gas system (4.73), the phonon gas corresponding to a harmonic lattice is ideal.

Amplitudes and phases of the normal modes

Each specific normal mode (3.53) that takes part in the thermal vibrations of the lattice is characterized by a pair of random quantities $(a_{\mathbf{p},s}, \phi_{\mathbf{p},s})$ that determine the polar coordinates of a point in the formal configuration space associated with this normal mode. In order to obtain the Gibbs canonical distributions in these coordinates, we substitute the expression (4.112) into (4.80) and multiply the result by the elementary volumes $a_{\mathbf{p},s} da_{\mathbf{p},s} d\phi_{\mathbf{p},s}$,

$$W(a, \phi) da_{\mathbf{p},s} d\phi_{\mathbf{p},s} = \frac{1}{Z} \prod_{\mathbf{p},s} a_{\mathbf{p},s} \exp \frac{-Na_{\mathbf{p},s}^2 \omega_{\mathbf{p},s}^2 \mu_{\mathbf{p},s}}{2k_B T} da_{\mathbf{p},s} d\phi_{\mathbf{p},s} \quad (4.114)$$

This equation represents an infinitesimal probability in the (a, ϕ) -space. Thus, the canonical distribution for lattice thermal vibrations takes the form, factorized with respect to the separate normal modes,

$$W(a, \phi) = \frac{1}{Z} \prod_{\mathbf{p},s} a_{\mathbf{p},s} \exp \frac{-Na_{\mathbf{p},s}^2 \omega_{\mathbf{p},s}^2 \mu_{\mathbf{p},s}}{2k_B T} \quad (4.115)$$

Equation (4.115) implies that amplitudes and phases of the individual normal modes are independent random variables distributed according to

$$w(a_{\mathbf{p},s}) = \frac{Na_{\mathbf{p},s} \omega_{\mathbf{p},s}^2 \mu_{\mathbf{p},s}}{k_B T} \exp \frac{-Na_{\mathbf{p},s}^2 \omega_{\mathbf{p},s}^2 \mu_{\mathbf{p},s}}{2k_B T}, \quad w(\phi_{\mathbf{p},s}) = \frac{1}{2\pi} \quad (4.116)$$

Note that the phases are distributed uniformly on the interval $(0, 2\pi)$.

Total energy of the normal modes

According to (4.112), the total energy of one normal mode reads

$$\varepsilon_{\mathbf{p},s} = \frac{N}{2} a_{\mathbf{p},s}^2 \omega_{\mathbf{p},s}^2 \mu_{\mathbf{p},s} \quad (4.117)$$

The statistical distribution of this quantity is found from the requirement $w(\varepsilon) d\varepsilon = w(a) da$, where $w(a)$ is the distribution for amplitudes (4.116); this yields

$$w(\varepsilon_{\mathbf{p},s}) \equiv w(\varepsilon) = \frac{1}{k_B T} \exp \frac{-\varepsilon}{k_B T} \quad (4.118)$$

This distribution is identical for all normal modes, is invariant with respect to lattice parameters, and only depends on the temperature of the system.

According to (4.118), the mean energy per vibrational degree of freedom for a lattice structure in thermal equilibrium at temperature T is

$$\bar{\varepsilon} = \int_0^\infty \varepsilon w(\varepsilon) d\varepsilon = k_B T \quad (4.119)$$

Lattice partition function

Evaluation of the thermodynamic partition function of the ideal phonon gas is straightforward. The form of equations (4.115) and (4.116) suggest that the one-mode partition function is equal to

$$z_{\mathbf{p},s} = \frac{2\pi k_B T}{N\omega_{\mathbf{p},s}^2 \mu_{\mathbf{p},s}} \quad (4.120)$$

(note the linear dependence of z on temperature). The complete partition function Z for the distribution (4.115) is then obtained as

$$Z = \prod_{\mathbf{p},s} z_{\mathbf{p},s} \quad (4.121)$$

Various thermodynamic parameters of the phonon gas, including free energy, entropy, internal energy, heat capacity, and so on, can be evaluated by utilizing Z within the partition function method presented in Section 4.2.4.

One standard approximation, known as the *Einstein model*, utilizes the assumption that $\omega_{\mathbf{p},s}$ and $\mu_{\mathbf{p},s}$ are constant for all \mathbf{p} and s . For a three-dimensional lattice, $\mathbf{p} = (p_1, p_2, p_3)$, comprising N unit cells with $s = 3$ degrees of freedom per each unit cell, this assumption leads to

$$Z = z^{3N}, \quad z = z_0 T/N \quad (4.122)$$

Here, z_0 is a constant factor, invariant with respect to T and N , the thermodynamic parameters. According to the fourth equation in (4.82), and the formula (4.36), the lattice internal energy and heat capacity read

$$U = 3Nk_B T, \quad C_V = 3Nk_B \quad (4.123)$$

Note that the same internal energy could have been obtained by multiplying (4.119) by $3N$, the total number of normal modes. Meanwhile, the partition function approach is a more general technique that allows the calculation of an extended set of parameters, including various thermodynamic potentials.

Experimental observations indicate that this approximation is only valid for moderate temperatures (see Figure 4.14). The increase of heat capacity at higher temperatures can be explained within the classical theory as a result of the growing nonlinearity of the lattice thermal vibrations. The low-temperature behavior of the heat capacity can be explained by utilizing quantum statistics of the phonon gas, Landau and Lifshitz (1980) and Pathria (1996).

Modeling the random thermal vibrations of lattices

The random thermal vibrations of periodic lattices can be modeled by sampling the amplitudes and phases of the normal modes from the distributions (4.116), and utilizing them for the real-valued solutions (3.58). Note that the mean square amplitudes of the normal modes, which determine the temperature of the lattice, are equal to

$$\overline{a_{\mathbf{p},s}^2} = \int_0^\infty a_{\mathbf{p},s}^2 w(a_{\mathbf{p},s}) da_{\mathbf{p},s} = \frac{2k_B T}{N\omega_{\mathbf{p},s}^2 \mu_{\mathbf{p},s}} \quad (4.124)$$

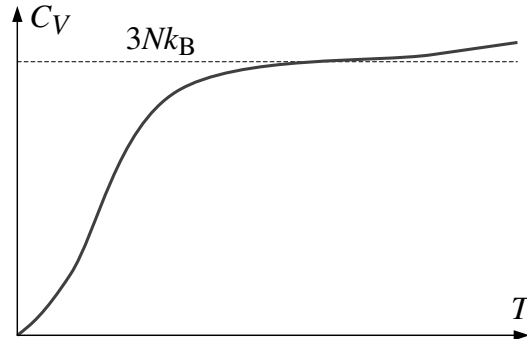


Figure 4.14 Typical experimental behavior of the heat capacity of crystalline solids as a function of temperature.

Utilizing the random normal amplitudes and phases in (3.58), we obtain a random pattern of atomic displacements and velocities, represented by

$$\mathbf{R}_n(t) = \mathbf{u}_n^+(t) + \mathbf{u}_n^-(t) \quad (4.125)$$

$$\dot{\mathbf{R}}_n(t) = \dot{\mathbf{u}}_n^+(t) + \dot{\mathbf{u}}_n^-(t) \quad (4.126)$$

Correspondingly, the initial conditions for a general MD simulation of a heated lattice structure domain are given simply by $\mathbf{R}_n(0)$ and $\dot{\mathbf{R}}_n(0)$.

In practice, the total number of modes used for the decompositions (3.58) can be less than SN . For example, the low frequency part of the spectrum may require truncation, when the period of vibration for the corresponding modes become comparable with the total time of the MD simulation. A further decrease in the number of modes can be achieved by increasing the sampling interval for the wave numbers in (3.58): $p_i = z, 2z, \dots, N_i/2$, where z is an integer. In all cases, the parameter N in (4.116) and (4.124) must be replaced with the total number of distinct triplets $\mathbf{p} = (p_1, p_2, p_3)$ employed. In order to achieve an accurate target temperature in the case of a limited number of modes (less than 10^3), one may use the mean square amplitudes provided by (4.124), rather than sampling them from the original distribution (4.116). However, the initial phases ϕ in (3.58) should be sampled randomly in all instances. Since any decrease in the number of modes will abate the initial entropy of the system, it is desirable in numerical simulations to keep a large, yet reasonable, number of normal modes.

As compared to the discussion of Section 4.2.4, the sampling from (4.116), as well as from the one-particle distributions reviewed in Section 4.2.5, implies usage of the canonical ensemble theory for an alternative purpose: evaluation of the microscopic quantities based on temperature and Hamiltonian of the system. In Section 4.2.4, on the contrary, this information was used to obtain the macroscopic thermodynamic parameters.

4.3 Numerical Heat Bath Techniques

The modeling and simulation of multiparticle systems, investigation of various temperature-dependent macroscopic properties (e.g. internal energy, pressure, viscosity) often require

the availability of numerical methods for maintaining the temperature of the system at a particular target/reference value. From the thermodynamical point of view, such a system can be regarded as interacting with an external thermostat that keeps the temperature at a constant level by providing or removing heat in the course of time. On reaching thermodynamic equilibrium, an equilibrium temperature can be evaluated according to (4.59) and further used in application of the canonical ensemble theory to the analysis of this system.

One issue associated with such an approach is the way to represent the mathematical coupling between the degrees of freedom of the simulated system and the hypothetical heat bath. Standard coupling techniques include the thermostatting approach of Berendsen et al. (1984), the stochastic collisions method of Andersen (1980), and the extended systems method originated by Nosé (1984a) and extended by Hoover (1985). The Nosé–Hoover approach incorporates the external heat bath as an integral part of the system. This is achieved by assigning the reservoir an additional degree of freedom, and including it in the system Hamiltonian. The novel phonon approach of Karpov et al. (2005a) that encapsulates the intrinsic mechanical properties of the crystalline lattice is more adequate for the modeling of nonmetallic solids, including carbon nanostructures. We review below the Berendsen, Nosé–Hoover and the phonon method in more detail.

4.3.1 Berendsen Thermostat

The Berendsen model corresponds physically to a system of particles that experience viscous friction and are subject to frequent collisions with light particles that form an ideal gas at temperature T_0 (see Figure 4.15). Mathematically, Berendsen et al. (1984) utilize the Langevin equation (2.28) with a viscous friction force (2.27) and a stochastic external

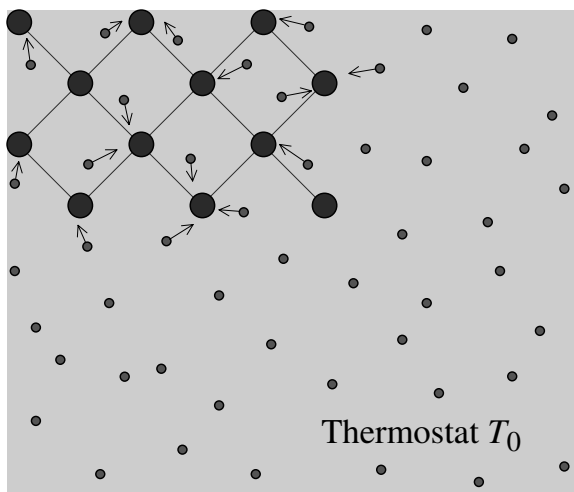


Figure 4.15 Physical model of the Berendsen thermostatting approach: molecules of the structure under analysis (large circles) experience adaptive viscous friction forces, and are subject to frequent collisions with light gas particles (small circles) at the target temperature T_0 .

force with the properties (2.29–2.30). These two forces are intended to represent coupling to an external heat bath and scale the atomic velocities during the numerical simulation to add or remove energy from the system as desired. The Langevin equations are written either for the entire set of particles (in gases and liquids), or for a local group of particles corresponding to a preboundary region of a solid structure.

For the purpose of further discussion, we rewrite the Langevin equation (2.28) in terms of the velocity components,

$$m\dot{v}_j(t) = F_j(t) - m\gamma v_j(t) + R_j(t), \quad j = 1, 2, \dots, 3N \quad (4.127)$$

where F_j is the standard interatomic force. According to the ergodic hypothesis (4.57), the time averaged quantities (2.29–2.30) for a system in thermodynamic equilibrium are equal to the corresponding ensemble average quantities; therefore,

$$\overline{R_j(t)} = \langle R(t) \rangle = 0 \quad (4.128)$$

$$\overline{R_j(t)R_j(t+t_0)} = \langle R(t)R(t+t_0) \rangle = a\delta(t_0) \quad (4.129)$$

Fluctuation-dissipation theorem

A reasonable physical assumption about the intensity of the random force R in (4.129) can be made on the basis of the *fluctuation-dissipation theorem* that gives the relationship between a fluctuating force on some degree of freedom and the damping coefficient that determines dissipation in that degree of freedom:

$$\langle R(t)R(t+t_0) \rangle = 2m\gamma k_B T_0 \delta(t_0) \quad (4.130)$$

where T_0 is the equilibrium system temperature.

This theorem can be proven by utilizing the Langevin equation (4.127), where the interatomic force is omitted as not participating in the dissipation process,

$$m\dot{v}(t) = -m\gamma v(t) + R(t) \quad (4.131)$$

The general solution of this equation reads

$$v(t) = v(0)e^{-\gamma t} + \frac{1}{m} \int_0^t R(\tau) e^{-\gamma(t-\tau)} d\tau \quad (4.132)$$

According to (4.101), the mean square value of this function for an equilibrium system is equal to

$$\overline{v^2(t)} = \langle v^2(t) \rangle = \frac{k_B T_0}{m} \quad (4.133)$$

Substituting (4.132) into (4.133), where the ensemble average is utilized, yields,

$$\begin{aligned} \langle v^2(t) \rangle &= \langle v^2(0) \rangle e^{-2\gamma t} + \frac{2}{m} \int_0^t \langle v(0)R(\tau) \rangle e^{-2\gamma(t-\tau)} d\tau \\ &\quad + \frac{2}{m^2} \int_0^t \int_0^t \langle R(\tau)R(\tau') \rangle e^{-\gamma(2t-\tau-\tau')} d\tau' d\tau \end{aligned} \quad (4.134)$$

In this expression,

$$\langle v^2(0) \rangle = k_B T_0 / m \quad (4.135)$$

$$\langle v(0)R(\tau) \rangle = \overline{v(0)R(t)} = v(0)\overline{R(t)} = 0 \quad (4.136)$$

$$\langle R(\tau)R(\tau') \rangle = a \delta(\tau - \tau') \quad (4.137)$$

Therefore, relationship (4.134) can be reduced to

$$\frac{k_B T_0}{m} (1 - e^{-2\gamma t}) = \frac{a}{m^2} \int_0^t e^{-2\gamma(t-\tau)} d\tau \quad (4.138)$$

where

$$a = 2m\gamma k_B T_0 \quad (4.139)$$

Utilizing this value for (4.129) proves the fluctuation-dissipation theorem (4.130).

Following equations (2.30) and (4.139), dynamic properties of the random force R in Langevin equation (4.127) can be summarized as

$$\overline{R_j(t)} = 0, \quad \overline{R_j(t)R_{j'}(t')} = 2m\gamma k_B T_0 \delta(t - t') \delta_{jj'} \quad (4.140)$$

where T_0 is the target system temperature. These relationships can be physically interpreted as follows: (1) the function R has no directional preference, (2) R is a Gaussian random function of time with zero mean variance $2m\gamma k_B T_0$ for all degrees of freedom interacting with the heat bath; (3) the force R_j on degree of freedom j is uncorrelated with the force $R_{j'}$ on another degree of freedom j' ; (4) the instantaneous value of R is not affected by its preceding values, that is, the function R is uncorrelated with its time history.

In practice, the random force R can be sampled at each time step of a numerical simulation as a random Gaussian variable with zero mean and variance (mean square amplitude) $2m\gamma k_B T_0$. The sampling procedure is performed independently for each degree of freedom exposed to the thermal noise. Also, samples for two successive time steps are evaluated independently of each other.

Elimination of the random force

In various applications, only the global thermodynamic behavior of the system is of importance. Then it is computationally effective to eliminate the local random noise $\mathbf{R}_i(t)$ in the Langevin equation (4.127), and to characterize the system/heat bath coupling via a *time-dependent* damping term. This damping term can be introduced on the basis of the following requirement: the new equation of motion must yield the same averaged behavior of the system's kinetic and total energy for a given target temperature T_0 , as the original equation (2.28). We detail the relevant mathematical derivations below.

First, write the time derivative of kinetic energy of the system in the form

$$\dot{E}_k = \lim_{\Delta t \rightarrow 0} \sum_{j=1}^{3N} \frac{m}{2\Delta t} (v_j^2(t + \Delta t) - v_j^2(t)) \quad (4.141)$$

and rearrange it to get

$$\dot{E}_k = \lim_{\Delta t \rightarrow 0} \sum_{j=1}^{3N} \frac{m}{2\Delta t} (2v_j \Delta v_j + \Delta v_j^2) \quad (4.142)$$

According to (4.127), the change of velocity over a short time interval is,

$$\begin{aligned}\Delta v_j &= v_j(t + \Delta t) - v_j(t) = \frac{1}{m} \int_t^{t+\Delta t} (F_j(t') - m\gamma v_j(t') + R_j(t')) dt' \\ &\simeq \frac{1}{m} (F_j(t)\Delta t - m\gamma v_j(t)\Delta t) + \frac{1}{m} \int_t^{t+\Delta t} R_j(t') dt' \quad (4.143)\end{aligned}$$

Substituting (4.143) into (4.142) and separately considering the first term,

$$\begin{aligned}\lim_{\Delta t \rightarrow 0} \sum_{j=1}^{3N} \frac{mv_j \Delta v_j}{\Delta t} &= \sum_{j=1}^{3N} (F_j v_j - m\gamma v_j^2) + \lim_{\Delta t \rightarrow 0} \sum_{j=1}^{3N} \frac{1}{\Delta t} \int_t^{t+\Delta t} v_j(t) R_j(t') dt' \\ &= -\dot{U} - 2\gamma E_k + \lim_{\Delta t \rightarrow 0} \frac{3N}{\Delta t} \int_t^{t+\Delta t} \langle v(t) R(t') \rangle dt' = -\dot{U} - 2\gamma E_k \quad (4.144)\end{aligned}$$

For this derivation, we utilized the time derivative of potential energy,

$$\dot{U} = \frac{dU(x_1, x_2, \dots, x_{3N})}{dt} = \sum_{j=1}^{3N} \frac{\partial U}{\partial x_j} \frac{dx_j}{dt} = -\sum_{j=1}^{3N} F_j v_j \quad (4.145)$$

current kinetic energy,

$$E_k = \sum_{j=1}^{3N} \frac{mv_j^2}{2} \quad (4.146)$$

and the ensemble average,

$$\frac{1}{3N} \sum_{j=1}^{3N} v_j(t) R_j(t') = \langle v(t) R(t') \rangle = 0 \quad (4.147)$$

following (4.52) and (4.136).

According to (4.143), the second term in (4.142) becomes

$$\begin{aligned}\lim_{\Delta t \rightarrow 0} \sum_{j=1}^{3N} \frac{m \Delta v_j^2}{2 \Delta t} &= \lim_{\Delta t \rightarrow 0} \frac{1}{2m \Delta t} \sum_{j=1}^{3N} \int_t^{t+\Delta t} R_j(t') dt' \int_t^{t+\Delta t} R_j(t'') dt'' \\ &= \lim_{\Delta t \rightarrow 0} \frac{3N}{2m \Delta t} \int_t^{t+\Delta t} \int_t^{t+\Delta t} \langle R(t') R(t'') \rangle dt'' dt' \\ &= \lim_{\Delta t \rightarrow 0} \frac{3N \gamma k_B T_0}{\Delta t} \int_t^{t+\Delta t} \int_t^{t+\Delta t} \delta(t' - t'') dt'' dt' \\ &= 3\gamma N k_B T_0 \lim_{\Delta t \rightarrow 0} \frac{1}{\Delta t} \int_t^{t+\Delta t} dt' = 3\gamma N k_B T_0 \quad (4.148)\end{aligned}$$

Here, we showed only one of the six terms arising from Δv_j^2 . The other five terms are trivial owing to the following arguments:

$$\begin{aligned} \lim_{\Delta t \rightarrow 0} (F_j(t)\Delta t)^2 / \Delta t &= 0 \\ \lim_{\Delta t \rightarrow 0} (v_j(t)\Delta t)^2 / \Delta t &= 0 \\ \lim_{\Delta t \rightarrow 0} (F_j(t)\Delta t)(v_j(t)\Delta t) / \Delta t &= 0 \\ \sum_j F_j(t)R_j(t') &= 3N \langle F(t)R(t') \rangle = 0 \\ \sum_j v_j(t)R_j(t') &= 3N \langle v(t)R(t') \rangle = 0 \end{aligned} \quad (4.149)$$

Next we can utilize the results of (4.144) and (4.148) for (4.142),

$$\dot{E}_k = -\dot{U} - 2\gamma E_k + 3\gamma N k_B T_0 \quad (4.150)$$

and rearrange this relationship to obtain the energy equation,

$$\dot{H} = 3\gamma N k_B (T_0 - T) \quad (4.151)$$

where H is the system Hamiltonian. This equation must be satisfied by the sought equation of motion after elimination of the random force term R . The transformation from (4.150) to (4.151) employs $E_k = 3Nk_B T/2$, where T is the current system temperature viewed as a function of time.

We can show that the equation

$$m_j \dot{v}_j = -F_j - m_j \gamma \left(1 - \frac{T_0}{T}\right) v_j, \quad j = 1, 2, \dots, 3N \quad (4.152)$$

known as *Berendsen equation of motion*, satisfies (4.151). In terms of the radius vectors, it can be written as

$$m_i \ddot{\mathbf{r}}_i = -\nabla_i U - m_i \gamma \left(1 - \frac{T_0}{T}\right) \dot{\mathbf{r}}_i, \quad i = 1, 2, \dots, N \quad (4.153)$$

Premultiplying (4.152) with v_i and summing overall the degrees of freedom gives

$$\begin{aligned} \sum_j m_j v_j \dot{v}_j &= -\sum_j v_j \nabla_j U - \gamma (1 - T_0/T) \sum_j m_j v_j^2 \Rightarrow \\ \dot{E}_k &= -\dot{U} - 2\gamma E_k (1 - T_0/T) \Rightarrow \\ \dot{H} &= -3\gamma N k_B T (1 - T_0/T) = 3\gamma N k_B (T_0 - T) \end{aligned} \quad (4.154)$$

Thus, from an energetic point of view, the Berendsen equation (4.152) is equivalent to the original Langevin equation (4.127) in application to multiparticle systems. Berendsen thermostating equations are amongst the most widely used in practical molecular dynamics simulations.

Note that the Hamiltonian H determines the internal energy of the thermodynamic system, (4.58). Assuming that the internal energy and temperature are related to each other according to (4.7), then the time rate of temperature change is represented by the first-order differential equation,

$$\dot{T} = 2\gamma(T_0 - T) \quad (4.155)$$

The value $\tau_T = (2\gamma)^{-1}$ gives the coupling constant that represents the characteristic time of equilibration of the system with the heat bath.

The time-dependent parameter

$$\xi(t) = \gamma \left(1 - \frac{T_0}{T(t)} \right) \quad (4.156)$$

in the Berendsen equation can be viewed as a dynamic damping constant. This damping constant becomes zero when the system temperature approaches the target value T_0 .

The current system temperature T for (4.152) or (4.153) can be computed on the basis of (4.59) for each successive time step of a numerical solution. The value γ should be chosen small enough so that the physical properties of the system are not violated by the artificial damping forces. On the other hand, γ has to be significantly large to ensure thermal equilibrium within a reasonable simulation time. In applications to crystal lattices, the value of γ is normally on the order of several percent of the maximum lattice frequency.

Equation (4.153) assumes the imposition of random initial conditions adequate for the target system temperature. The random velocity vectors \mathbf{v}_i can be sampled by utilizing the Maxwell–Boltzmann distribution (4.99) for the magnitudes of these vectors, while the directions of \mathbf{v}_i can be sampled as distributed uniformly on the interval $(0, 2\pi)$. Alternatively, the individual components v_x , v_y and v_z can be sampled from (4.98). Initial positions of the particles are usually uniformly distributed for gases and liquids, or associated with the equilibrium lattice positions in solid domains. Thus, the initial conditions for lattices are

$$\mathbf{u}_n(0) = 0, \quad w(\mathbf{v}) \rightarrow \mathbf{v}_n(0) = \dot{\mathbf{u}}_n(0) \quad (4.157)$$

Here, \mathbf{u} is the lattice displacement vector (3.2), w is the Maxwell–Boltzmann distribution, and the arrow sign represents random sampling. This sampling is accomplished independently for various components of the velocity vector $\dot{\mathbf{u}}$ and for various lattice sites n . Therefore, for each specific component \dot{u}_n of the initial velocity vector (4.157), the following holds:

$$\langle \dot{u}_n(0) \dot{u}_{n'}(0) \rangle = \overline{v_x^2} \delta_{n,n'} = \frac{k_B T}{m} \delta_{n,n'} \quad (4.158)$$

where the brackets stand for averaging over various realizations of \dot{u}_n and $\dot{u}_{n'}$, and $\overline{v_x^2}$ is the mean square component (4.101). In other words, the initial velocities of neighboring lattice atoms are not correlated with each other.

Consider the performance of the Berendsen thermostat in application to the monoatomic lattice chain of the type depicted in Figure 4.10. Let $N_a = 1001$ be the total number of lattice atoms; there is only one longitudinal degree of freedom per atom. The initial conditions for (4.153) are provided by (4.157); the vectors of position and displacement are related through (3.2). The interatomic potential (2.46) is the pair-wise Morse component (2.63) with the Au parameters (3.125). The cutoff radius of the potential is 1.5 interatomic distances, so that only interactions between the nearest-neighbor atoms are accounted for. The value γ for (4.153) is such that $2\gamma/\omega = 0.025$, where $\omega = 2\sqrt{k/m}$ is the maximum normal frequency; m is the atomic mass, and k is the lattice stiffness constant related to the Morse parameters as $k = 2\varepsilon\beta^2$.

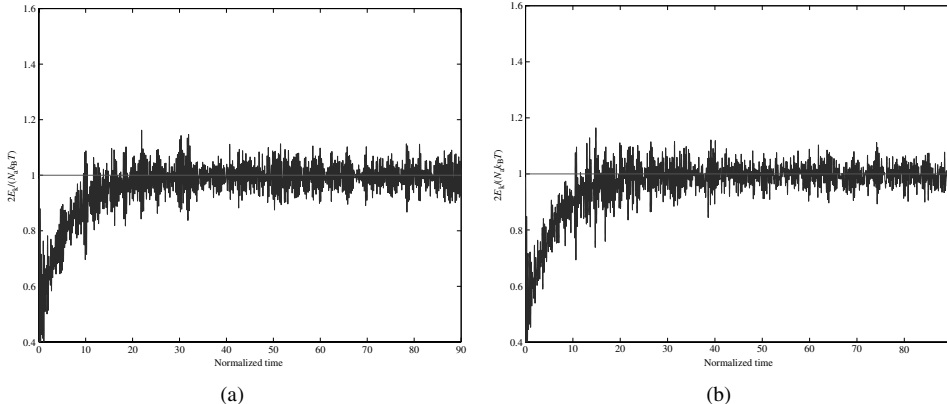


Figure 4.16 Temperature of a 1D lattice as a function of time within the Berendsen thermostat approach. Target system temperatures T_0 are (a) 300 K and (b) 600 K. The unit of time is $\sqrt{m/k}$.

The results of the simulation corresponding to two target temperatures, $T_0 = 300$ K and $T_0 = 600$ K, are shown in Figure 4.16. It is seen that the equilibration time does not depend on T_0 . Typically, the current temperature at initial times is lower than the target value; that is explained by conversion of the initial kinetic energy provided by the initial conditions into potential energy of atomic interactions. This is a standard feature associated with applications of the Berendsen thermostat to highly coupled atomic structures, such as the crystalline or polymer lattices. Thermal equilibrium with the thermostat is achieved after time $\tau_T \approx (2\gamma)^{-1}$.

4.3.2 Nosé–Hoover Heat Bath

The Nosé–Hoover heat bath utilizes a dynamic friction coefficient, which evolves according to a first-order differential equation,

$$\dot{\zeta}(t) = \frac{1}{Q} \left(\sum_j^{3N} m_j v_j^2 - (3N + 1)k_B T_0 \right) \quad (4.159)$$

where Q is a method parameter of dimension energy · (time)². Thus, the difference between the simultaneous and target kinetic energy of the system determines the *time derivative* of the friction coefficient; that contrasts with Berendsen thermostat, where the dynamic friction coefficient is simply (4.156). Hoover (1985) has shown that the Berendsen equations are overdamped and they lead to a statistical ensemble not compliant with the Gibbs canonical distribution (4.80). Provided that such a distribution is sought for the microstates associated with solution of the Langevin equation, the friction coefficient must follow the relaxation equation (4.159). Note that the term $3N + 1$ stands for the total number of degrees of freedom in the system that includes the $3N$ coordinates of the particles, plus the variable ζ .

The relaxation equation (4.159) is solved simultaneously with the Langevin equations (2.28), or (4.127), where γ is replaced by $\zeta(t)$. The Langevin equations can be presented in the alternative Hamiltonian form,

$$\dot{\mathbf{r}}_i = \frac{\mathbf{p}_i}{m_i}, \quad \dot{\mathbf{p}}_i = -\nabla_i U - \zeta(t)\mathbf{p}_i \quad (4.160)$$

The Hoover equations (4.159) and (4.160) serve as a practical update of the Nosé (1984a,b) thermostating method, which also used an additional variable for the momenta rescaling, utilized the scaled coordinates, and first reproduced canonical distribution for positions and scaled momenta. These works provided a vital background for the present method. As results, the equations (4.159) and (4.160) are usually referred to as the *Nosé–Hoover thermostat*.

Berendsen and Nosé–Hoover thermostating approaches have been used in MD simulations of a vast range of physical and engineering systems and processes, and particularly in simulations of gases and liquids. Applications to ionic and metallic crystals, where the heat is transferred by both the lattice vibrations and the “dissolved” electron gas, often yield a sufficiently accurate physical model. On the other hand, the physical concept behind these models makes them less adequate in applications to solid–solid interfaces, where the heat exchange mechanism is governed dominantly by oscillations of the lattice atoms (e.g. non-metallic crystals, carbon nanostructures), and where the heat bath cannot be viewed as a gaseous substance surrounding the simulated domain. In these instances, the below phonon, or configurational, method may provide a more accurate physical model.

4.3.3 Phonon Method for Solid–Solid Interfaces

The underlying idea of the phonon, or configurational, method for crystalline solids is related to the concept of multiscale boundary conditions, Figure 3.20, and consists in removing the unnecessary heat bath degrees by virtue of the boundary value problem solution (3.96) or (3.100). This solution represents the mechanical response and the effect of thermal motion of the heat bath atoms. Atoms associated with the interface between the simulated solid domain and the hypothetical heat bath are then oscillating, as if they were still a part of the global domain that actually includes atoms of a large crystal lattice, Figure 4.17. As a result, heat flows across such a solid–solid interface in the same natural way as across any imaginary plane within the simulated crystal structure. This feature of the phonon heat bath is particularly valuable for the purpose of multiscale and coupled atomistic/continuum simulation of materials, for example, Liu et al. (2004c), Park et al. (2005c) and Wagner and Liu (2003).

For compactness, consider a one-dimensional lattice as shown in Figure 3.2, and suppose that the simulated atoms are associated with the lattice site indices $n = 0, 1, \dots, N$, and the heat bath atoms with $n < 0, n > N$. Next, assume that the current unit cell n interacts directly with two adjacent cells, $n - 1$ and $n + 1$.

It was shown earlier (3.100) that atomic displacements in a bulk (half-space) crystal, which serves as the heat bath, can be expressed in terms of displacements in the boundary cells, $n = b$:

$$\mathbf{u}_{b+n}(t) = \int_0^t \theta_n(t - \tau)(\mathbf{u}_b(\tau) - \mathbf{R}_b(\tau)) d\tau + \mathbf{R}_{b+n}(t) \quad (4.161)$$

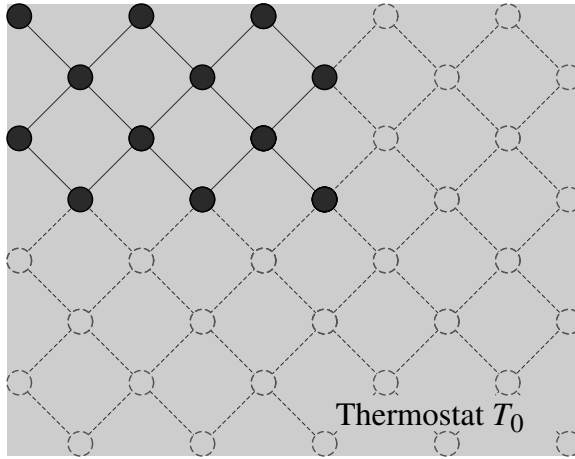


Figure 4.17 Physical model of the phonon heat bath approach: molecules of the crystalline structure under analysis (solid circles) are brought in contact with a larger crystal (dashed circles) maintained at the target temperature T_0 .

Therefore, displacement vectors associated with the heat bath cells next to the interface ($n = -1, N + 1$) are related to the interfacial vectors (at $n = 0, N$):

$$\begin{aligned}\mathbf{u}_{-1}(t) &= \int_0^t \boldsymbol{\theta}_{-1}(t-\tau)(\mathbf{u}_0(\tau) - \mathbf{R}_0(\tau)) d\tau + \mathbf{R}_{-1}(t) \\ \mathbf{u}_{N+1}(t) &= \int_0^t \boldsymbol{\theta}_1(t-\tau)(\mathbf{u}_N(\tau) - \mathbf{R}_N(\tau)) d\tau + \mathbf{R}_{N+1}(t)\end{aligned}\quad (4.162)$$

Substituting these relationships into the homogeneous equation of motion (3.46), adjusted for the current provisos,

$$\mathbf{M} \ddot{\mathbf{u}}_n(t) - \sum_{n'=n-1}^{n+1} \mathbf{K}_{n-n'} \mathbf{u}_{n'}(t) = \mathbf{0}, \quad n = 0, N \quad (4.163)$$

we obtain the sought interfacial equations in a form similar to the generalized Langevin equation (2.32):

$$\begin{aligned}\mathbf{M} \ddot{\mathbf{u}}_0(t) &= \mathbf{K}_{-1} \mathbf{u}_1(t) + \mathbf{K}_0 \mathbf{u}_0(t) \\ &\quad + \mathbf{K}_1 \int_0^t \boldsymbol{\theta}_{-1}(t-\tau)(\mathbf{u}_0(\tau) - \mathbf{R}_0(\tau)) d\tau + \mathbf{K}_1 \mathbf{R}_{-1}(t)\end{aligned}\quad (4.164)$$

$$\begin{aligned}\mathbf{M} \ddot{\mathbf{u}}_N(t) &= \mathbf{K}_1 \mathbf{u}_{N-1}(t) + \mathbf{K}_0 \mathbf{u}_N(t) \\ &\quad + \mathbf{K}_{-1} \int_0^t \boldsymbol{\theta}_1(t-\tau)(\mathbf{u}_N(\tau) - \mathbf{R}_N(\tau)) d\tau + \mathbf{K}_{-1} \mathbf{R}_{N+1}(t)\end{aligned}\quad (4.164')$$

These equations are next solved concurrently with the standard molecular dynamics equations (2.25) or (3.6) for atoms of the *internal* lattice cells, $n = 1, 2, \dots, N - 1$. Note that

the resultant model contains no explicit degrees of freedom associated with the heat bath atoms. Meanwhile, the mechanical response of the thermostat is represented by the time history kernel θ . The random thermal motion of the thermostat atoms, composed of random contributions of various lattice normal modes, is described by the function \mathbf{R} .

The random function \mathbf{R} for (4.164) is evaluated in accordance with (4.125) at each specific time step of the calculation. The amplitude and shape of this function is determined by specific realizations of the random amplitudes and phases of the normal modes distributed according to (4.116). In turn, the distribution for the amplitudes depends on the parameter $T \equiv T_0$, which is regarded as the heat bath, or target system, temperature.

Initial conditions for the molecular dynamics equations of motion are obtained from the random configuration vectors at $t = 0$:

$$\mathbf{u}_n(0) = \mathbf{R}_n(0), \quad \dot{\mathbf{u}}_n(0) = \dot{\mathbf{R}}_n(0) \quad (4.165)$$

Within the current settings, $n \equiv n = 1, 2, \dots, N$. In contrast to (4.157), these initial conditions automatically account for the statistical correlation between the positions of neighboring atoms within a strongly coupled system, such as the crystal lattice. As a result, the random phase space vector provided by (4.165) at $t = 0$ is compliant with the Gibbs canonical distribution, and it provides a physically adequate “snapshot” of the lattice in thermodynamic equilibrium with the heat bath. Each particular realization of this vector yields a phase space point that constitutes the canonical ensemble associated with the given lattice structures at temperature T .

Consider application of this method to the same lattice structure, as in the previous example for the Berendsen method: the monoatomic lattice chain (Figure 4.10), comprising $N_a = 1001$ atoms with one longitudinal degree of freedom. The lattice is governed by the Morse potential (2.63) with the Au parameters (3.125) and a cutoff radius of 1.5 equilibrium interatomic distances.

The wave numbers, $p \equiv \mathbf{p}$, for the decomposition (3.58) are chosen equidistantly from the interval $[-\pi, -\pi/2], [\pi/2, \pi]$ with a step $\pi/32$. Thus, there are in total $N = 32$ distinct

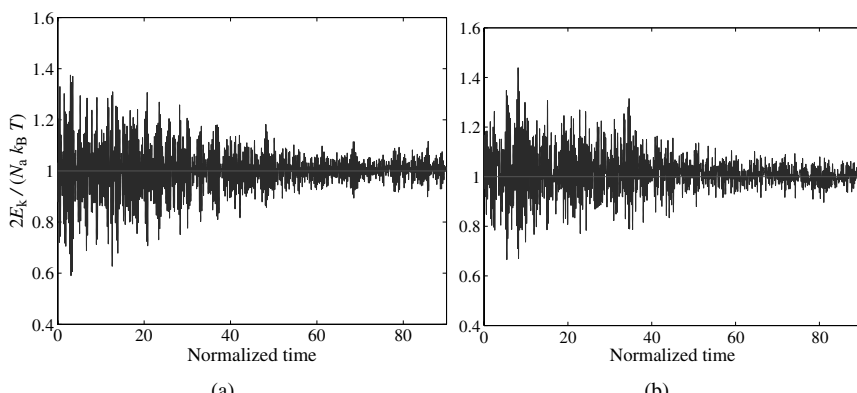


Figure 4.18 Temperature of a 1D lattice as a function of time within the phonon heat bath approach. Target system temperatures T_0 are (a) 300 K and (b) 600 K. The unit of time is $\sqrt{m/k}$.

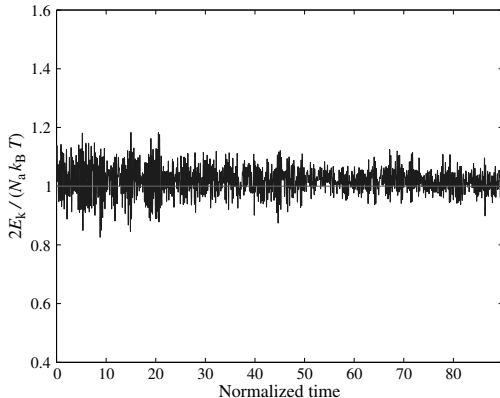


Figure 4.19 Phonon model at $T_0 = 600$ K; the number of normal modes has been increased from 32 to 128.

wave numbers, and this number is used in (4.124), which is used to evaluate the normal amplitudes a_p . The phases ϕ_p are sampled uniformly at $(0, 2\pi)$. The corresponding normal frequencies are $\omega_p = 2\sqrt{k/m} \sin p/2$. The polarization vector is unity for all the wave numbers. A time step of $\Delta t = 0.005$ was used for 20,000 steps. The atoms are given initial displacements and velocities using the relationships (4.165) for a target temperature T .

The simulation results for two target system temperatures, $T = 300$ K and $T = 600$ K are shown in Figure 4.18. The MD system temperature oscillates exactly about the target temperature for the $T = 300$ K case. For the $T = 600$ K cases, it oscillates about a value slightly higher than the target system temperature. Nonetheless, the nonlinearity results in correspondingly small errors in the target system temperature, where no diverging or non-controlled behavior is observed. Note that $T = 600$ K corresponds to 45% of the Au melting temperature; thus, the method appears accurate even for considerably large nonlinearities.

Another important feature of these results is that no equilibration period is required for the system temperature. The system temperature starts fluctuating about the correct target value immediately. Over the course of time, the decaying amplitude of fluctuations corresponds to the free energy equilibration process. For longer intervals of later times, the kinetic and potential energy are gradually redistributed between all the normal modes in the system owing to nonlinear correlation effects. The use of a larger number of normal modes in (3.58) should result in a faster minimization of fluctuations. Indeed, Figure 4.19 shows the reduction in temperature fluctuations at short times in the case of utilizing 128, instead of 32, modes. These modes are sampled for wave numbers on the interval $[-\pi, -\pi/2]$, $[\pi/2, \pi]$ with a step $\pi/128$. Thus, for a sufficiently rich normal mode sampling, the system is close to a thermodynamic equilibrium with the heat bath, even at initial times.

The phonon method is also applicable to lattices with broken translation symmetries. Spatial regularity is only required for the hypothetical heat bath in the vicinity of the simulated domain (Jacucci and Quirke (1982); Mueller (2001)).

5

Introduction to Multiple Scale Modeling

In recent years, thanks mainly to the constantly increasing surge in computational power, atomistic simulations have been utilized with great success in the modeling of nanoscale materials phenomena. However, despite these technological improvements, molecular dynamics (MD) simulations still cannot be utilized to simulate more than a few billion atoms, or a few cubic microns in volume. Thus, while the modeling and simulation of nanoscale materials is within the realm of MD simulations, many important microdevices are too large to be simulated using MD. Furthermore, in many interesting applications, nanoscale materials will be used in conjunction with other components that are larger, and have different response times, thus operating at different time and length scales. Thus, single scale methods such as ab initio quantum mechanical methods or MD, for example, Allen and Tildesley (1987) and Haile (1992), will have difficulty in analyzing such hybrid structures because of the limitations in terms of the time and length scales that each method is confined to. Therefore, the need arises to couple atomistic methods with approaches that operate at larger length scales and longer timescales.

In contrast, continuum methods have had much success in the macroscale modeling and simulation of structures. Finite element (FE) methods, for example, Belytschko et al. (2000b) and Hughes (1987), are now the standard numerical analysis tools to study such diverse problems as the modeling of crashworthiness in automobiles, the fluid–structure interaction of submarines, plasticity in manufacturing processes and blast and impact simulations. Therefore, the logical approach taken by many researchers in the desire to create truly multiple scale simulations that exist at disparate length and timescales has been to couple MD and FE in some manner. Unfortunately, the coupling of these methods is not straightforward for the reasons discussed next.

The major problem in multiscale simulations is that of pathological wave reflection, which occurs at the interface between the MD and FE regions. The issue is that wavelengths emitted by the MD region are considerably smaller than that that can be captured by the continuum FE region. Because of this and the fact that an energy-conserving formulation

is typically used, the wave must go somewhere and is thus reflected back into the MD domain. This leads to spurious heat generation in the MD region and a contamination of the simulation. The retention of heat within the MD region can have extremely deleterious effects, particularly in instances of plasticity where heat generated within the MD region is trapped; in such an extreme situation, melting of the MD region can eventually occur.

A separate, but related, issue in effective multiscale modeling is that of extending the timescale available to MD simulations. This issue still remains despite the efforts of current multiscale methods to limit the MD region to a small portion of the computational domain. Despite the reduction in the MD system size, limits still exist on the duration of time for which the MD system can be simulated. Research has been continuing in the physics community to prolong the MD simulation time, particularly for infrequent events such as surface diffusion. Two excellent examples of the types of methods currently under investigation can be found in the works of Voter (1997) and Voter et al. (2002).

Other issues that typically arise in attempting to couple simulations that operate at disparate length and timescales will be discussed within the context of the methods we will be reviewing in this chapter. While this review attempts to cover many of the existing approaches to multiple scale modeling, it is by no means complete. Two recently written review papers that comprehensively cover the field of multiple scale modeling are those of Liu et al. (2004c) and Curtin and Miller (2003).

5.1 MAAD

One pioneering multiscale approach was the work of Abraham et al. (1998). The idea was to concurrently link tight binding (TB), molecular dynamics (MD) and finite elements (FE) together in a unified approach called *MAAD* (macroscopic, atomistic, ab initio dynamics). Here, concurrent linking means that all three simulations run at the same time, and dynamically transmit necessary information to and receive information from the other simulations. In this approach, the FE mesh is graded down until the mesh size is on the order of the atomic spacing, at which point the atomic dynamics are governed by MD. Finally, at the physically most interesting point, that is, at a crack tip, TB is used to simulate the atomic bond breaking processes.

The idea of meshing the FE region down to the atomic scale was one of the first attempts to eliminate spurious wave reflections at the MD/FE interface. The logic was that a gradual increase in the FE mesh size would reduce the amount of reflection back into the MD region. However, meshing the FE region down to the atomic spacing presents two problems, one numerical and one physical. The numerical issue is that the time step in an FE simulation is governed by the smallest element in the mesh. Thus, if the finite elements are meshed down to the atomic scale, many time steps will be wasted in simulating the dynamics in these regions. Furthermore, it seems unphysical that the variables of interest in the continuum region should evolve at the same timescales as the atomistic variables.

The physical issue in meshing the FE region down to the atomic scale lies in the FE constitutive relations. The constitutive relations typically used in FE calculations, for example, for plasticity, are constructed on the basis of the bulk behavior of many dislocations. Once the FE mesh size approaches the atomic spacing, each finite element can represent only a small number of dislocations, the bulk assumption disappears, and the constitutive relation is invalidated.

The overlapping regions (FE/MD and MD/TB) are termed “*handshake*” regions, and each makes a contribution to the total energy of the system. The total energy of the handshake regions is a linear combination of the energies of the relevant computational methods, with weight factors chosen depending on which computational method contributes the most energy in the handshake region. The three equations of motion (TB/FE/MD) are all integrated forward using the same time step.

The interactions between the three distinct simulation tools are governed by conserving energy in the system as in Broughton et al. (1999):

$$H_{\text{TOT}} = H_{\text{FE}} + H_{\text{FE/MD}} + H_{\text{MD}} + H_{\text{MD/TB}} + H_{\text{TB}} \quad (5.1)$$

More specifically, the Hamiltonian or total energy of the MD system can be written as

$$H_{\text{MD}} = \sum_{i < j} V^{(2)}(r_{ij}) + \sum_{i, (j < k)} V^{(3)}(r_{ij}, r_{ik}, \Theta_{ijk}) + K \quad (5.2)$$

where the summations are over all the atoms in the system, K is the kinetic energy of the system, r_{ij} and r_{ik} indicate the distance between two atoms i and j and i and k respectively; Θ_{ijk} is the bonding angle between the three atoms. The summation convention $i < j$ is performed so that each atom ignores itself in finding its nearest neighbors. Here, the potential energy is composed of two parts. The first ($V^{(2)}$) is the two-body interaction, for example, nearest-neighbor spring interaction in 1D. The second part is the three-body interaction ($V^{(3)}$), which incorporates features such as angular bonding between atoms. The three-body interactions also make the potential energy of each atom dependent on its environment.

The FE Hamiltonian can be written as the sum of the kinetic and potential energies in the elements, that is,

$$H_{\text{FE}} = V_{\text{FE}} + K_{\text{FE}} \quad (5.3)$$

Expanding these terms, we get

$$V_{\text{FE}} = \frac{1}{2} \int_{\Omega} \boldsymbol{\epsilon}(\mathbf{r}) \cdot \mathbf{C} \cdot \boldsymbol{\epsilon}(\mathbf{r}) d\Omega \quad (5.4)$$

$$K_{\text{FE}} = \frac{1}{2} \int_{\Omega} \rho(\mathbf{r}) (\dot{\mathbf{u}})^2 d\Omega \quad (5.5)$$

where $\boldsymbol{\epsilon}$ is the strain tensor, \mathbf{C} is the stiffness tensor, ρ is the material density and $\dot{\mathbf{u}}$ are the nodal velocities. The TB total energy is written as

$$V_{\text{TB}} = \sum_{n=1}^{N_{\text{occ}}} \epsilon_n + \sum_{i < j} V^{\text{rep}}(r_{ij}) \quad (5.6)$$

This energy can be interpreted as having contributions from an attractive part ϵ_n and a repulsive part V^{rep} . N_{occ} are the number of occupied states. While a detailed overview of TB methods is beyond the scope of this work, further details can be found in Foulkes and Haydock (1989). MAAD was applied to the brittle fracture of silicon by Abraham et al. (1998).

5.2 Coarse-Grained Molecular Dynamics

An approach related to the TB/MD/FE approach of Abraham et al. was developed by Rudd and Broughton (1998) and was called *coarse-grained molecular dynamics* (CGMD). This approach removes the TB method from the MAAD method and instead couples only FE and MD. The basic idea in CGMD is that a coarse-grained energy approximation that converges to the exact atomic energy is utilized to derive the governing equations of motion. The coarse-grained energy from which the equations of motion are extracted is defined to be

$$E(\mathbf{u}_k, \dot{\mathbf{u}}_k) = U_{\text{int}} + \frac{1}{2} \sum_{j,k} (M_{jk} \dot{\mathbf{u}}_j \cdot \dot{\mathbf{u}}_k + \mathbf{u}_j \cdot K_{jk} \cdot \mathbf{u}_k) \quad (5.7)$$

where the internal energy $U_{\text{int}} = 3(N - N_{\text{node}})kT$, the kinetic energy is defined as $M_{jk} \dot{\mathbf{u}}_j \cdot \dot{\mathbf{u}}_k$, the potential energy is defined as $\mathbf{u}_j \cdot K_{jk} \cdot \mathbf{u}_k$, the displacement degrees of freedom are \mathbf{u} and the velocities are $\dot{\mathbf{u}}$. The internal energy represents the thermal energy of those degrees of freedom that have been coarse grained (eliminated) out of the system; clearly, as the number of nodes approaches the number of atoms, this term disappears, and the full atomistic energy is recovered.

The stiffness matrix K_{jk} and mass matrix M_{jk} are calculated using weight functions that are similar in form to FE shape functions. Therefore, while the explicit equation of motion that is solved in CGMD is not found in the work of Rudd and Broughton (1998), it appears as though CGMD mimics the behavior of a FE mesh that is graded down to the MD atomic spacing in regions of interest, and is coarsened away from the MD region. Therefore, it is expected that CGMD would suffer from the same issues as MAAD, that is, that the mesh grading would eventually reach a point where the high-frequency MD wavelengths would not be representable in the continuum, and hence would be reflected back into the MD domain.

This notion is supported by the paper of Rudd (2001), in which the notion of dissipative Langevin dynamics (Adelman and Doll (1976)) is introduced into the CGMD formulation. The equation of motion is then given to be

$$M_{ij} \ddot{u}_j = -G_{ik}^{-1} u_k + \int_{-\infty}^t \eta_{ik}(t - \tau) \dot{u}_k(\tau) d\tau + F_i(t) \quad (5.8)$$

where M_{ij} is a mass matrix, G_{jk} is a stiffness like quantity, η_{ik} is a time history, or memory function, and $F_i(t)$ is a random force. The addition of the dissipative terms to the equation of motion seems to clearly indicate that the original formulation of CGMD did suffer from spurious wave reflection as coarse graining of the mesh occurred.

It is interesting to note that a similar expression to (5.7) was derived by Wagner and Liu (2003) for a system involving multiple scales. In the work of Wagner and Liu, the ensemble multiple scale kinetic energy behaves similar to the energy in (5.7), in that as the number of FE nodes approaches the atomic limit, the purely atomistic kinetic energy is recovered.

5.3 Quasi-Continuum Method

A well known quasi-static multiple scale method, the quasi-continuum method, was developed by Tadmor et al. (1996). Examples of applications and further improvements on the

quasi-continuum method are the works of Miller et al. (1998) and Knap and Ortiz (2001). A recent review concentrating on the history and development of the quasi-continuum method is given by Miller and Tadmor (2003). While the quasi-continuum method is essentially an adaptive FE method, the atomistic to continuum link is achieved here by the use of the Cauchy–Born rule. The Cauchy–Born rule assumes that the continuum energy density W can be computed using an atomistic potential, with the link to the continuum being the deformation gradient \mathbf{F} . To briefly review continuum mechanics, the deformation gradient \mathbf{F} maps an undeformed line segment $d\mathbf{X}$ in the reference configuration onto a deformed line segment $d\mathbf{x}$ in the current configuration,

$$d\mathbf{x} = \mathbf{F} d\mathbf{X} \quad (5.9)$$

In general, \mathbf{F} can be written as

$$\mathbf{F} = 1 + \frac{d\mathbf{u}}{d\mathbf{X}} \quad (5.10)$$

where \mathbf{u} is the displacement. If there is no displacement in the continuum, the deformation gradient is equal to unity.

The major restriction as well as implication of the Cauchy–Born rule is that the deformation of the lattice underlying a continuum point must be homogeneous. This results from the fact that the underlying atomistic system is forced to deform according to the continuum deformation gradient \mathbf{F} , as illustrated in Figure (5.1). By using the Cauchy–Born rule, Tadmor et al. (1996) were able to derive a continuum stress tensor and tangent stiffness directly from the interatomic potential, which allowed the usage of nonlinear FE techniques. This can be done by the following relations:

$$\mathcal{P} = \frac{\partial W}{\partial \mathbf{F}^T} \quad (5.11)$$

$$\mathbf{C} = \frac{\partial^2 W}{\partial \mathbf{F}^T \partial \mathbf{F}^T} \quad (5.12)$$

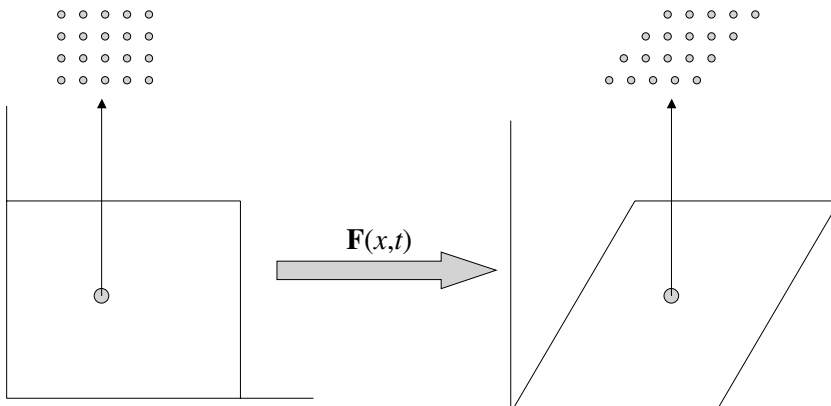


Figure 5.1 Illustration of Cauchy–Born rule. Reprinted from Computer Methods in Applied Mechanics and Engineering, 195, Park et al., Introduction and tutorial on multiple scale analysis in solids, 1733–1772, 2004, with permission from Elsevier.

where \mathbf{C} is the Lagrangian tangent stiffness and \mathcal{P} is the first Piola–Kirchoff stress tensor. An updated version of the Cauchy–Born rule was proposed by Arroyo and Belytschko (2002).

Adaptivity criteria were used in regions of large deformation so that full atomic resolution could be achieved in these instances, that is, near a dislocation. A nonlocal version of the Cauchy–Born rule was also developed so that nonhomogeneous deformations such as dislocations could be modeled. The quasi-continuum method has been applied to quasi-static problems such as nanoindentation, atomic-scale fracture and grain boundary interactions.

5.4 CADD

Recently, a new method for quasi-static coupling termed *CADD* (coupled atomistics and discrete dislocation) was presented by Curtin and Miller (2003); Shilkrot et al. (2002) and Shilkrot et al. (2004). The approach taken here is to couple molecular statics with discrete dislocation plasticity (van der Giessen and Needleman (1995)). The advantages in doing this is that defects, mainly dislocations, generated within the atomistic region are allowed to pass through the atomistic/continuum border into the continuum, where they are represented via discrete dislocation mechanics. Because discrete dislocation mechanics incorporate the elastic stress field emitted from a dislocation into the continuum stress and modulus expressions, the defects are able to be tracked once they pass into the continuum region, and also evolve in the continuum by following predefined sets of evolution laws.

As the atomistic side of the calculation relies on standard principles, we briefly discuss the discrete dislocation continuum to which the atomistic region is coupled. The continuum energy E^c is defined to be

$$E^c = \sum_{\mu} E_{\mu}(\mathbf{U}_I, \mathbf{U}_c, \mathbf{d}^i) - \int_{d\Omega_T} \mathbf{T}_0 \mathbf{u} dA \quad (5.13)$$

where \mathbf{U}_I are the MD/FE interface nodes, \mathbf{U}_c are the continuum nodes, \mathbf{d}^i are the positions of the discrete dislocations in the continuum, and \mathbf{T}_0 is the prescribed traction on the continuum boundary $d\Omega_T$.

The total stresses, strains and displacements in the continuum can all be written as functions of the contribution from the discrete dislocations and a correction term (we write for the displacement only):

$$\mathbf{u} = \tilde{\mathbf{u}} + \hat{\mathbf{u}} \quad (5.14)$$

where $\tilde{\mathbf{u}}$ is the contribution from the discrete dislocations and $\hat{\mathbf{u}}$ is a correction term that is necessary because of the fact that the discrete dislocation solution is for an infinite medium. Noting that the strains and stresses can be decomposed accordingly, the continuum energy E^c can be rewritten as

$$E^c = \frac{1}{2} \int_{\Omega_c} (\hat{\mathbf{u}} + \tilde{\mathbf{u}}) : (\hat{\boldsymbol{\epsilon}} + \tilde{\boldsymbol{\epsilon}}) dV - \int_{d\Omega_T} \mathbf{T}_0 (\tilde{\mathbf{u}} + \hat{\mathbf{u}}) dA \quad (5.15)$$

The equilibrium displacement $\tilde{\mathbf{u}}$ fields are obtained by minimizing (5.15), that is,

$$\frac{\partial E^c}{\partial \tilde{\mathbf{u}}_c} = 0 \quad (5.16)$$

After the continuum displacement fields are known, the forces \mathbf{p}^i on the discrete dislocations are calculated by minimizing E^c with respect to the discrete dislocation positions

$$\mathbf{p}^i = -\frac{\partial E^c}{\partial \mathbf{q}^i} \quad (5.17)$$

At this point, an iterative procedure involving the discrete dislocation positions, FE positions and atomic positions is solved until all degrees of freedom are at equilibrium. We note that the atomic degrees of freedom are defined separately, but the interface FE displacements \mathbf{U}_I are used to prescribe boundary conditions for the atomistic iterative procedure, and vice versa.

The approach has been validated via two-dimensional problems, including fracture, nanoindentation and atomic-scale void growth. Current issues facing the CADD developers include the extension to dynamic problems, and the passing of dislocations from the atomistic to continuum regions in three dimensions, where a dislocation is a loop that can reside in both atomistic and continuum regions at the same time.

5.5 Bridging Domain

A new dynamic multiple scale method for coupling continua with molecular dynamics termed the *bridging domain method* was presented by Xiao and Belytschko (2004). The method utilizes MD in a localized region in the problem, while coupling it with a continuum region that exists surrounding the atomistic region. The continuum and atomistic regions overlap in a small spatial region of varying size, termed the *bridging domain*. The Hamiltonian for the coupled system within the overlap region is determined to be a linear combination of the molecular and continuum Hamiltonians

$$H = (1 - \alpha)H^M + \alpha H^C \quad (5.18)$$

where α acts to scale the contribution of each domain to the total Hamiltonian. As can be seen, the energy within the overlapping region goes from entirely atomistic at one end to entirely continuum at the other end. The effect of this energy transition is that high-frequency atomic-scale energy is spatially filtered, such that it is eliminated by the time the continuum region is reached. The idea of spatial filtering is borne out in the numerical examples shown, in which a minimum overlapping distance is required for the method to begin eliminating high-frequency waves effectively.

Lagrange multipliers are introduced to enforce displacement compatibility between the molecular and continuum regions in the overlap region

$$\mathbf{g}_I = \left(\sum_J N_J(\mathbf{X}_J) u_{iJ} - d_{iI} \right) = 0 \quad (5.19)$$

where \mathbf{g}_I are the Lagrange multipliers, u_{iJ} are the FE nodal displacements, and d_{iI} are the MD displacements. The coupled equations of motion that are solved in the FE and MD regions are derived from the coupled Hamiltonian (5.18), and become

$$\bar{M}_I \ddot{\mathbf{u}}_I = \mathbf{F}_I^{\text{ext}} - \mathbf{F}_I^{\text{int}} - \mathbf{F}_I^L \quad (5.20)$$

$$\bar{m}_I \ddot{\mathbf{d}}_I = \mathbf{f}_I^{\text{ext}} - \mathbf{f}_I^{\text{int}} - \mathbf{f}_I^L \quad (5.21)$$

where the standard equations are augmented by the Lagrange multiplier-based constraint forces \mathbf{F}_I^L and \mathbf{f}_I^L . The bar symbols overlaying the FE and MD mass matrices indicate that they need to be modified within the overlapping region.

As can be seen, the equations correspond to the standard FE and MD equations of motion augmented by additional forces that result from the Lagrange multiplier in the overlapping region. An additional salient feature of the method is the ability to use different time steps for the MD and FE simulations. The bridging domain method was demonstrated on two-dimensional wave and crack propagation problems.

6

Introduction to Bridging Scale

This chapter introduces the bridging scale concurrent method, which was recently proposed to couple atomistic and continuum simulation methods. The theory will be developed in a fully generalized three-dimensional setting, including the numerical calculation of the time history kernel in multiple dimensions, such that a two-way coarse/fine coupled non-reflecting molecular dynamics (MD) boundary condition can be found.

6.1 Bridging Scale Fundamentals

The bridging scale was recently proposed by Wagner and Liu (2003) to couple atomistic and continuum simulations. The fundamental idea is to decompose the total displacement field $\mathbf{u}(\mathbf{x})$ into coarse and fine scales

$$\mathbf{u}(\mathbf{x}) = \bar{\mathbf{u}}(\mathbf{x}) + \mathbf{u}'(\mathbf{x}) \quad (6.1)$$

This decomposition has been used before in solid mechanics in the variational multiscale method of Hughes et al. (1998). The coarse scale $\bar{\mathbf{u}}$ is that part of the solution which can be represented by a set of basis functions, that is, finite element (FE) shape functions. The fine scale \mathbf{u}' is defined as the part of the solution whose projection onto the coarse scale basis functions is zero; this implies orthogonality of the coarse and fine scale solutions.

In order to describe the bridging scale, first imagine a body in any dimension which is described by N_a atoms. The notation used here will mirror that used by Wagner and Liu (2003). The total displacement of an atom α is written as \mathbf{u}_α . The coarse scale displacement is a function of the initial positions \mathbf{X}_α of the atoms. It should be noted that the coarse scale would at first glance be thought of as a continuous field, since it can be interpolated between atoms. However, because the fine scale is defined only at atomic positions, the total displacement, and thus the coarse scale, are discrete functions that are defined only at atomic positions. For consistency, Greek indices (α, β, \dots) will define atoms for the remainder of this chapter, and uppercase Roman indices (I, J, \dots) will define coarse scale nodes.

The coarse scale is defined to be

$$\bar{\mathbf{u}}(\mathbf{X}_\alpha) = \sum_I N_I^\alpha \mathbf{d}_I \quad (6.2)$$

Here, $N_I^\alpha = N_I(\mathbf{X}_\alpha)$ is the shape function of node I evaluated at the initial atomic position \mathbf{X}_α , and \mathbf{d}_I are the FE nodal displacements associated with node I .

The fine scale in the bridging scale decomposition is simply that part of the total displacement that the coarse scale cannot represent. Thus, the fine scale is defined to be the projection of the total displacement \mathbf{u} onto the FE basis functions subtracted from the total solution \mathbf{u} . We will select this projection operator to minimize the mass-weighted square of the fine scale, which we call J and can be written as

$$J = \sum_\alpha m_\alpha \left(\mathbf{u}_\alpha - \sum_I N_I^\alpha \mathbf{w}_I \right)^2 \quad (6.3)$$

m_α is the atomic mass of an atom α and \mathbf{w}_I are temporary nodal (coarse scale) degrees of freedom. It should be emphasized that (6.3) is only one of many possible ways to define an error metric. In order to solve for \mathbf{w} , the error is minimized with respect to \mathbf{w} , yielding the following result:

$$\mathbf{w} = \mathbf{M}^{-1} \mathbf{N}^T \mathbf{M}_A \mathbf{u} \quad (6.4)$$

where the coarse scale mass matrix \mathbf{M} is defined as

$$\mathbf{M} = \mathbf{N}^T \mathbf{M}_A \mathbf{N} \quad (6.5)$$

In (6.4) and (6.5), \mathbf{M}_A is a diagonal matrix with the atomic masses on the diagonal, and \mathbf{N} is a matrix containing the values of the FE shape functions evaluated at all the atomic positions. In general, the size of \mathbf{N} is $N_{a1} \times N_{n1}$, where N_{n1} is the number of FE nodes whose support contains an atomic position, and N_{a1} is the total number of atoms. The fine scale \mathbf{u}' can thus be written as

$$\mathbf{u}' = \mathbf{u} - \mathbf{N} \mathbf{w} \quad (6.6)$$

or

$$\mathbf{u}' = \mathbf{u} - \mathbf{P} \mathbf{u} \quad (6.7)$$

where the projection matrix \mathbf{P} is defined to be

$$\mathbf{P} = \mathbf{N} \mathbf{M}^{-1} \mathbf{N}^T \mathbf{M}_A \quad (6.8)$$

The total displacement \mathbf{u}_α can thus be written as the sum of the coarse and fine scales as

$$\mathbf{u} = \mathbf{N} \mathbf{d} + \mathbf{u}' \quad (6.9)$$

The final term in the above equation is called the *bridging scale*. It is the part of the solution that must be removed from the total displacement so that a complete separation of scales is achieved, that is, the coarse and fine scales are orthogonal to each other. This bridging scale approach was first used by Liu et al. (1997) to enrich the FE method with meshfree shape functions. Wagner and Liu (2001) used this approach to consistently apply essential boundary conditions in meshfree simulations. Zhang et al. (2002) applied the bridging

scale in fluid dynamics simulations. Qian et al. (2004) recently used the bridging scale in quasi-static simulations of carbon nanotube buckling. The bridging scale was also used in conjunction with a multiscale constitutive law to simulate strain localization by Kadowaki and Liu (2004).

Now that the details of the bridging scale have been laid out, some comments are in order. In (6.3), the fact that an error measure was defined implies that \mathbf{u}_α is the ‘exact’ solution to the problem. In our case, the atomistic simulation method we choose to be our ‘exact’ solution is MD. After determining that the MD displacements shall be referred to by the variable \mathbf{q} , (6.3) can be rewritten as

$$J = \sum_{\alpha} m_{\alpha} \left(\mathbf{q}_{\alpha} - \sum_I N_I^{\alpha} \mathbf{w}_I \right)^2 \quad (6.10)$$

where the MD displacements \mathbf{q} now take the place of the total displacements \mathbf{u} . The equation for the fine scale \mathbf{u}' can now be rewritten as

$$\mathbf{u}' = \mathbf{q} - \mathbf{P}\mathbf{q} \quad (6.11)$$

The fine scale is now clearly defined to be the difference between the MD solution and its projection onto a predetermined coarse scale basis space. This implies that the fine scale can thus be interpreted as a built-in error estimator to the quality of the coarse scale approximation. Finally, the equation for the total displacement \mathbf{u} can be rewritten as

$$\mathbf{u} = \mathbf{N}\mathbf{d} + \mathbf{q} - \mathbf{P}\mathbf{q} \quad (6.12)$$

6.1.1 Multiscale Equations of Motion

The next step in the multiscale process is to derive the coupled MD and FE equations of motion. This is done by first constructing a Lagrangian \mathcal{L} , which is defined to be the kinetic energy minus the potential energy

$$\mathcal{L}(\mathbf{u}, \dot{\mathbf{u}}) = \mathcal{K}(\dot{\mathbf{u}}) - V(\mathbf{u}) \quad (6.13)$$

Ignoring external forces, (6.13) can be written as

$$\mathcal{L}(\mathbf{u}, \dot{\mathbf{u}}) = \frac{1}{2} \dot{\mathbf{u}}^T \mathbf{M}_A \dot{\mathbf{u}} - U(\mathbf{u}) \quad (6.14)$$

where $U(\mathbf{u})$ is the interatomic potential energy. Differentiating the total displacement \mathbf{u} in (6.12) with respect to time gives

$$\dot{\mathbf{u}} = \mathbf{N}\dot{\mathbf{d}} + \mathbf{Q}\dot{\mathbf{q}} \quad (6.15)$$

where the complimentary projection operator $\mathbf{Q} \equiv \mathbf{I} - \mathbf{P}$. Substituting (6.15) into the Lagrangian (6.14) gives

$$\mathcal{L}(\mathbf{d}, \dot{\mathbf{d}}, \mathbf{q}, \dot{\mathbf{q}}) = \frac{1}{2} \dot{\mathbf{d}}^T \mathbf{M} \dot{\mathbf{d}} + \frac{1}{2} \dot{\mathbf{q}}^T \mathcal{M} \dot{\mathbf{q}} - U(\mathbf{d}, \mathbf{q}) \quad (6.16)$$

where the fine scale mass matrix \mathcal{M} is defined to be $\mathcal{M} = \mathbf{Q}^T \mathbf{M}_A$. One elegant feature of (6.16) is that the total kinetic energy has been decomposed into the sum of the coarse scale kinetic energy plus the fine scale kinetic energy.

The multiscale equations of motion are obtained from the Lagrangian by following the Lagrange equations

$$\frac{d}{dt} \left(\frac{\partial \mathcal{L}}{\partial \ddot{\mathbf{d}}} \right) - \frac{\partial \mathcal{L}}{\partial \dot{\mathbf{d}}} = 0 \quad (6.17)$$

$$\frac{d}{dt} \left(\frac{\partial \mathcal{L}}{\partial \ddot{\mathbf{q}}} \right) - \frac{\partial \mathcal{L}}{\partial \dot{\mathbf{q}}} = 0 \quad (6.18)$$

Substituting the Lagrangian (6.16) into (6.17) and (6.18) gives

$$\mathbf{M} \ddot{\mathbf{d}} = -\frac{\partial U(\mathbf{d}, \mathbf{q})}{\partial \mathbf{d}} \quad (6.19)$$

$$\mathcal{M} \ddot{\mathbf{q}} = -\frac{\partial U(\mathbf{d}, \mathbf{q})}{\partial \mathbf{q}} \quad (6.20)$$

The two equations (6.19) and (6.20) are coupled through the derivative of the potential energy U , which can be expressed as functions of the interatomic force \mathbf{f} as

$$\mathbf{f} = -\frac{\partial U(\mathbf{u})}{\partial \mathbf{u}} \quad (6.21)$$

Expanding the right-hand sides of (6.19) and (6.20) with a chain rule and using (6.21) together with (6.12) gives

$$\mathbf{M} \ddot{\mathbf{d}} = \frac{\partial U}{\partial \mathbf{u}} \frac{\partial \mathbf{u}}{\partial \mathbf{d}} = \mathbf{N}^T \mathbf{f} \quad (6.22)$$

$$\mathcal{M} \ddot{\mathbf{q}} = -\frac{\partial U}{\partial \mathbf{u}} \frac{\partial \mathbf{u}}{\partial \mathbf{q}} = \mathbf{Q}^T \mathbf{f} \quad (6.23)$$

Using the fact that $\mathcal{M} = \mathbf{Q}^T \mathbf{M}_A$, (6.23) can be rewritten as

$$\mathbf{Q}^T \mathbf{M}_A \ddot{\mathbf{q}} = \mathbf{Q}^T \mathbf{f} \quad (6.24)$$

Because \mathbf{Q} can be proven to be a singular matrix (Wagner and Liu 2003), there are many unique solutions to (6.24). However, one solution which does satisfy (6.24) and is beneficial to us is (including the coarse scale equation of motion):

$$\mathbf{M}_A \ddot{\mathbf{q}} = \mathbf{f}(\mathbf{q}) \quad (6.25)$$

$$\mathbf{M} \ddot{\mathbf{d}} = \mathbf{N}^T \mathbf{f}(\mathbf{u}) \quad (6.26)$$

Now that the coupled multiple scale equations of motion have been derived, we make some relevant comments

- (i) The fine scale equation of motion (6.25) is simply the MD equation of motion. Therefore, a standard MD solver can be used to obtain the MD displacements \mathbf{q} , while the MD forces \mathbf{f} can be found by using any relevant potential energy function.

- (ii) The coarse scale equation of motion (6.26) is simply the FE momentum equation. Therefore, we can use standard FE methods to find the solution to (6.26), while noting that the FE mass matrix \mathbf{M} is defined to be a consistent mass matrix.
- (iii) The coupling between the two equations is through the coarse scale internal force $\mathbf{N}^T \mathbf{f}(\mathbf{u})$, which is a direct function of the MD internal force \mathbf{f} . In the region in which MD exists, the coarse scale force is calculated by interpolating the MD force using the FE shape functions \mathbf{N} . In the region in which MD has been eliminated, the coarse scale force can be calculated in multiple ways. The elimination of unwanted MD degrees of freedom is discussed in the next section.
- (iv) We note that the total solution \mathbf{u} satisfies the same equation of motion as \mathbf{q} , that is,

$$\mathbf{M}_A \ddot{\mathbf{u}} = \mathbf{f} \quad (6.27)$$

This result is due to the fact that \mathbf{q} and \mathbf{u} satisfy the same initial conditions, and will be utilized in deriving the boundary conditions on the MD simulation in a later section.

- (v) Because of the equality of \mathbf{q} and \mathbf{u} , it would appear that solving the FE equation of motion is unnecessary, since the coarse scale can be calculated directly as the projection of \mathbf{q} , that is, $\mathbf{Nd} = \mathbf{Pq}$. However, because the goal is to eliminate the fine scale from large portions of the domain, the MD displacements \mathbf{q} are not defined over the entire domain, and thus it is not possible to calculate the coarse scale solution everywhere via direct projection of the MD displacements. Thus, the solution of the FE equation of motion everywhere ensures a continuous coarse scale displacement field.
- (vi) Owing to the Kronecker delta property of the FE shape functions, for the case in which the FE nodal positions correspond exactly to the MD atomic positions, the FE equation of motion (6.26) converges to the MD equation of motion (6.25).
- (vii) The FE equation of motion is redundant for the case in which the MD and FE regions both exist everywhere in the domain, because the FE equation of motion is simply an approximation of the MD equation of motion, with the quality of the approximation controlled by the finite element shape functions \mathbf{N} . This redundancy will be removed by eliminating the fine scale from large portions of the domain.
- (viii) We note that the right-hand side of (6.25) constitutes an approximation; the internal force \mathbf{f} should be a function of the total displacement \mathbf{u} . We utilize the MD displacements \mathbf{q} for two reasons. The first reason, as stated above, is the equality of \mathbf{q} and \mathbf{u} . The second reason relates to computational efficiency, as determining \mathbf{u} at each MD time step requires the calculation of the coarse scale solution \mathbf{Nd} , which would defeat the purpose of keeping a coarse FE mesh over the entire domain.

The last comment above motivates the developments in the next section. Because of the redundancy of the FE equation of motion, we now proceed to eliminate the MD region from a large portion of the domain, such that the redundancy of the FE equation of motion is removed.

6.2 Removing Fine Scale Degrees of Freedom in Coarse Scale Region

We imagine the bridging scale to be most applicable to problems in which the MD region is confined to a small portion of the domain, while the coarse scale representation exists everywhere. This coupled system is created by reducing the full system in which the MD region and the coarse scale exist everywhere in the domain (see Figure 6.1 for an illustrative example). This problem was solved analytically for some one-dimensional lattices by Adelman and Doll (1976), who used a harmonic approximation to eliminate the unwanted MD degrees of freedom while keeping their effects on the reduced MD system in the form of a damping kernel matrix. The equation of motion for the remaining atoms then has an additional force which takes the form of a time history integral involving the atomic velocities multiplied by a matrix $\beta(t)$, known as the *damping kernel*. The damping kernel mimics the dissipation of fine scale energy into the eliminated degrees of freedom. However, the intractability of analytically deriving the damping kernel in multiple dimensions motivated the development of methods to calculate the damping kernel numerically.

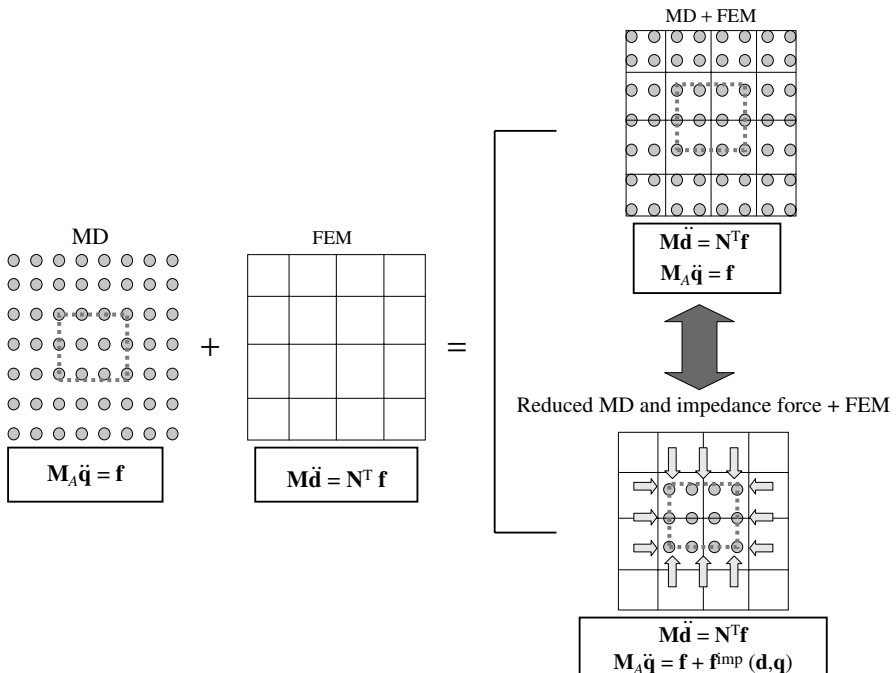


Figure 6.1 Removal of redundancy of FE equation of motion by elimination of the unnecessary MD degrees of freedom. Reprinted from Journal of Computational Physics, 207(2), Park et al., Three-dimensional bridging scale analysis of dynamic fracture, 588–609, 2005, with permission from Elsevier.

Numerical methods to calculate the damping matrix $\beta(t)$, or equivalently, its time derivative $\theta(t)$, known as the *time history kernel*, were proposed recently by Cai et al. (2000) and E and Huang (2002).

In this section, we present an approach whereby the time history kernel matrix can be calculated numerically in multiple dimensions for the bridging scale method. The key idea is to utilize the periodicity of atomic structures so that the standard technique of discrete Fourier transforms can be applied, for example, Karpov et al. (2002, 2003). Specifically, the method herein is similar to the works by Wagner et al. (2004) and Karpov et al. (2005b), which present methods to numerically calculate the damping kernel matrix in multiple dimensions for single scale, MD simulations. Here, we generalize the approach such that it can be applied to multiple scale simulations.

We close this section by noting that the assumption of a periodically repeating lattice structure implies the bridging scale method is best suited for the modeling and simulation of solids; the periodic lattice structure may lose validity if applied to fluids or amorphous solids.

6.2.1 Relationship of Lattice Mechanics to Finite Elements

Before proceeding further, we first introduce some essential lattice mechanics concepts within a simple, one-dimensional setting. Consider the one-dimensional chain of atoms shown in Figure 6.2. We presume that the lattice interacts through a harmonic potential with nearest-neighbor interactions only, with the harmonic potential being defined as

$$\Phi(r) = \frac{k}{2}(r - r_0)^2 \quad (6.28)$$

where k is the elastic spring constant, r is the separation between two atoms, and r_0 is the equilibrium interatomic distance. We note that each atom in the chain constitutes a unique unit cell, where a unit cell is the smallest subset of the lattice which is required to fully replicate the entire lattice by translation of the unit cell. For polyatomic systems, the unit cell must be enlarged to include more than just one atom.

We define the following useful relationships

$$f_n = -\frac{\partial U(u)}{\partial u_n}|_{u=0} \quad (6.29)$$

$$K_{n-n'} = \frac{\partial f_n}{\partial u_{n'}}|_{u=0} = -\frac{\partial^2 U(u)}{\partial u_n \partial u_{n'}}|_{u=0} \quad (6.30)$$

where f_n denotes the total force on atom (unit cell) n , and $K_{n-n'}$ relates the forces on atom n to the displacements of neighbor atoms n' . The range of the summation over n' is

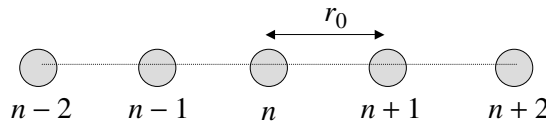


Figure 6.2 One-dimensional chain of atoms with interatomic distance r_0 .

directly related to the cutoff distance of the potential. For the one-dimensional harmonic potential with nearest-neighbor interactions, n' ranges from $n - 1$ to $n + 1$. We now write the potential energy U_n for unit cell n in Figure 6.2, which gives

$$U = \frac{1}{2}k(u_n - u_{n-1})^2 + \frac{1}{2}k(u_n - u_{n+1})^2 \quad (6.31)$$

The two terms in (6.31) result owing to each unit cell interacting with its neighboring unit cells. Using (6.30) on (6.31) give the K constants

$$K_{-1} = -\frac{\partial^2 U(u)}{\partial u_n \partial u_{n+1}}|_{u=0} = k \quad (6.32)$$

$$K_0 = -\frac{\partial^2 U(u)}{\partial u_n^2}|_{u=0} = -2k \quad (6.33)$$

$$K_1 = -\frac{\partial^2 U(u)}{\partial u_n \partial u_{n-1}}|_{u=0} = k \quad (6.34)$$

Finally, we calculate the force on unit cell n using (6.29) with (6.31) to give

$$f_n = K_{-1}u_{n-1} + K_0u_n + K_1u_{n+1} \quad (6.35)$$

$$f_n = ku_{n-1} - 2ku_n + ku_{n+1} \quad (6.36)$$

The equation of motion for the *entire* lattice can now be found using standard Lagrangian mechanics arguments. The fact that the equation of motion is the same for all atoms (unit cells) is because of the repetitive nature of the lattice structure. The Lagrangian for a linearized lattice structure can be written as

$$\mathcal{L}(u, \dot{u}) = \frac{1}{2} \sum_n \dot{u}_n^T m \dot{u}_n + \frac{1}{2} \sum_n \sum_{n'=n-v}^{n+v} u_n^T K_{n-n'} u_{n'} \quad (6.37)$$

where u_n are the atomic displacements of the unit cell n , \dot{u}_n are the atomic velocities of the unit cell n , m is the atomic mass and v indicates the range of interaction between the atoms. The equations of motion can be found by using the Lagrange equation (3.5),

$$\frac{d}{dt} \frac{\partial \mathcal{L}}{\partial \dot{u}_n} - \frac{\partial \mathcal{L}}{\partial u_n} = 0 \quad (6.38)$$

Substituting (6.37) into (6.38) gives the equation of motion for a harmonic lattice

$$m \ddot{u}_n(t) - \sum_{n'=n-v}^{n+v} K_{n-n'} u_{n'}(t) = f_n^{\text{ext}}(t) \quad (6.39)$$

where $f_n^{\text{ext}}(t)$ is the external force acting on the unit cell n . Using the K constants derived in (6.32)–(6.34), we write the equation of motion for the three atoms as

$$\begin{pmatrix} m\ddot{u}_{n-1} \\ m\ddot{u}_n \\ m\ddot{u}_{n+1} \end{pmatrix} - \begin{pmatrix} -k & k & 0 \\ k & -2k & k \\ 0 & k & -k \end{pmatrix} \begin{pmatrix} u_{n-1} \\ u_n \\ u_{n+1} \end{pmatrix} = \begin{pmatrix} f_{n-1}^{\text{ext}} \\ f_n^{\text{ext}} \\ f_{n+1}^{\text{ext}} \end{pmatrix} \quad (6.40)$$

In the FE literature, uppercase indices I are typically used to denote the FE nodal positions, for example, Belytschko et al. (2000b). For a three-node system corresponding to the three-atom system described above, the corresponding FE equation of motion becomes (assuming a lumped mass matrix, linear elastic material and a two-node linear element):

$$\begin{pmatrix} m\ddot{u}_{I-1} \\ m\ddot{u}_I \\ m\ddot{u}_{I+1} \end{pmatrix} + \begin{pmatrix} k & -k & 0 \\ -k & 2k & -k \\ 0 & -k & k \end{pmatrix} \begin{pmatrix} u_{I-1} \\ u_I \\ u_{I+1} \end{pmatrix} = \begin{pmatrix} f_{I-1}^{\text{ext}} \\ f_I^{\text{ext}} \\ f_{I+1}^{\text{ext}} \end{pmatrix} \quad (6.41)$$

The FE equation of motion (6.41) can be written in matrix/vector format and compared to the linearized MD equation of motion above (6.40):

$$\mathbf{M}_{IJ}\ddot{\mathbf{u}}_J + \mathbf{K}_{IJ}^{\text{FE}}\mathbf{u}_J = \mathbf{f}_I^{\text{ext}} \quad (6.42)$$

$$\mathbf{M}_{IJ}\ddot{\mathbf{u}}_J - \mathbf{K}_{IJ}^{\text{MD}}\mathbf{u}_J = \mathbf{f}_I^{\text{ext}} \quad (6.43)$$

As can be seen

$$\mathbf{K}_{IJ}^{\text{FE}} = -\mathbf{K}_{IJ}^{\text{MD}} \quad (6.44)$$

Thus, the K constants which relate the forces on an atom to the displacements of its neighboring atoms are simply the *negative* of the corresponding FE stiffness matrix entries, which explains the clear link between lattice mechanics and FE technology. The negative sign in front of the stiffness matrix \mathbf{K} is simply a matter of convention; as can be seen, once the negative sign is accounted for, both the FE and MD stiffness matrices and, thus, the equations of motion, are identical.

We note that for longer-ranged atomic interactions, the bandwidth of the MD stiffness matrix will increase to account for the interactions with distant neighbors. In that case, the analogous FEM stiffness matrix is that which is found using meshfree shape functions, due to the long-ranged support of the meshfree shape functions; see Belytschko et al. (2000a, 1998, 1996, 1994), Liu et al. (1995) and Li and Liu (2004).

6.2.2 Linearized MD Equation of Motion

In this section, we apply the arguments of lattice mechanics presented in the previous section to the bridging scale. In this approach, we assume that the atomistic region can be subdivided into two regions. In the first region, that is, around a crack tip, defects or other locally interesting physical phenomena, an anharmonic, or nonlinear potential is necessary to accurately represent the atomic interactions. However, at some distance away from the process of interest, an anharmonic representation of the atomistic physics no longer becomes necessary. At this point, the atomic interactions are sufficiently captured using a harmonic approximation. Therefore, the remainder of this section will summarize the methodology used to eliminate those atoms which we assume to interact harmonically; the eliminated fine scale degrees of freedom will be accounted for through the time history kernel $\theta(t)$.

The first step in this process is to linearize the MD equation of motion (6.25), while using the equality of \mathbf{q} and \mathbf{u} to obtain

$$\mathbf{M}_A\ddot{\mathbf{q}} = \mathbf{M}_A\ddot{\mathbf{u}} + \mathbf{M}_A\dot{\mathbf{u}}' = \mathbf{f}(\bar{\mathbf{u}}) + \mathbf{K}\mathbf{u}' \quad (6.45)$$

where

$$\mathbf{K} = \frac{\partial \mathbf{f}}{\partial \mathbf{u}}|_{\mathbf{u}'=0} \quad (6.46)$$

- The reason the time history kernel $\theta(t)$ must be calculated numerically in higher dimensions is due to the large size of the matrix \mathbf{K} , which is of a size of the order of the number of atoms that are to be eliminated from the domain. The number of eliminated atoms is typically of the order of millions, or even billions in multiple dimensions. The analytic solution for $\theta(t)$ as in Adelman and Doll (1976) requires a matrix inverse for \mathbf{K} , which would then be intractable. Thus, we will utilize the numerical methods presented later in this chapter.

The goal in performing the linearization is to decompose the MD equation of motion into coarse and fine scale components. In doing so, we will work exclusively with the fine scale equation so that we can achieve our stated goal of limiting the fine scale to a small region of the domain, while keeping the coarse scale everywhere in the domain. The major assumption in our derivation is that:

- We assume that we can write the fine scale equation of motion neglecting contributions from the coarse scale

This assumption is justified by the orthogonality of the coarse and fine scales, and because the timescale for the coarse scale is much larger than that of the atomic vibrations present in the fine scale. Thus, we rewrite the fine scale portion of the linearized MD equation of motion (6.45) while including the effects of external forces as

$$\mathbf{M}_A \ddot{\mathbf{u}}' - \mathbf{K} \mathbf{u}' = \mathbf{f}^{\text{ext}} \quad (6.47)$$

Note that (6.47) exactly resembles the linearized equation of motion (6.39) which was derived in the previous section for single scale MD. We also note that the complete nonlinear force $\mathbf{f}(\mathbf{u})$ has been decomposed as

$$\mathbf{f}(\mathbf{u}) = \mathbf{f}(\bar{\mathbf{u}}) + \mathbf{K} \mathbf{u}' \quad (6.48)$$

Before we can proceed to eliminate the fine scale, we first need to recall some essentials of Laplace and discrete Fourier transform techniques, Sections 3.3.2 and 3.3.3. Assuming that the function x can be defined at all atomic positions n , we denote the value of x and position n as x_n . For the convenience of the discussion below, the DFT of x is written in the following form, equivalent to (3.40),

$$\hat{x}(p) = \mathcal{F}_{n \rightarrow p}\{x_n\} \equiv \sum_{n=-N/2}^{N/2-1} x_n e^{-i2\pi pn/N} \quad (6.49)$$

Here, N denotes the number of lattice sites, and p can take any integral value between $-N/2$ and $N/2-1$. The inverse Fourier transform (IFT) is then written as

$$x_n = \mathcal{F}_{p \rightarrow n}^{-1}\{\hat{x}(p)\} \equiv \frac{1}{N} \sum_{p=-N/2}^{N/2-1} \hat{x}(p) e^{i2\pi pn/N} \quad (6.50)$$

The Laplace transform (LT) and the second time-derivative rule will be utilized in the forms (3.27) and (3.30), respectively. The inversion of LT will be done numerically by utilizing the numeral algorithm by Weeks (1966); see also (3.34).

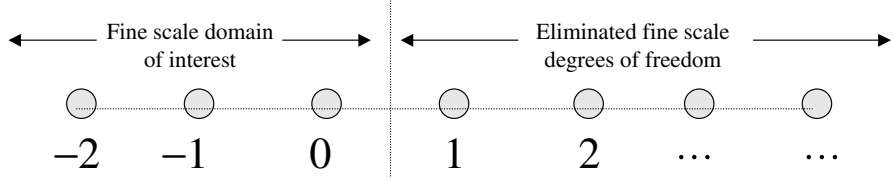


Figure 6.3 Decomposition of fine scale degrees of freedom to be kept, and those to be eliminated.

6.2.3 Elimination of Fine Scale Degrees of Freedom

Now that the necessary mathematical preliminaries have been introduced, we begin the process of eliminating the unnecessary fine scale degrees of freedom while keeping their effects on the remaining fine scale degrees of freedom. We do this first for a one-dimensional lattice for simplicity. We first rewrite (6.47) in component, or unit cell format similar to (6.39), yielding:

$$\ddot{u}'_n(t) = \sum_{n'=n-1}^{n+1} m_A^{-1} K_{n-n'} u'_{n'}(t) + m_A^{-1} f_n^{\text{ext}}(t) \quad (6.51)$$

The key to eliminating the unwanted $n > 0$ fine scale degrees of freedom, as viewed in Figure 6.3, is that the fine scale motion of boundary atom 0 can be caused either by the displacements of the atoms to be kept, or by an external force acting upon the boundary atom. Therefore, it will be assumed that the fine scale motion of the boundary atom is in fact caused by the external force which acts only on atom 0 in Figure 6.3.

$$f_n^{\text{ext}}(t) = \delta_{n,0} f_0^{\text{ext}}(t) \quad (6.52)$$

We first take a discrete Fourier transform (DFT) of (6.51) using (6.49),

$$\hat{u}'(p, t) = m_A^{-1} \hat{K}(p) \hat{u}'(p, t) + m_A^{-1} f_0^{\text{ext}}(t) \quad (6.53)$$

Taking an LT of (6.53) using (3.27) along with (3.30) and solving for the resulting displacements \hat{U} gives

$$\hat{U}'(p, s) = \hat{G}(p, s) \left(m_A^{-1} F_0^{\text{ext}}(s) + s \hat{u}'(0, p) + \hat{u}'(0, p) \right) \quad (6.54)$$

where

$$\hat{G}(p, s) = (s^2 - \hat{A}(p))^{-1} \quad (6.55)$$

where $\hat{A}(p) = m_A^{-1} \hat{K}(p)$. The goal of this process is to eliminate $F_0^{\text{ext}}(s)$. To do so, we perform an inverse discrete Fourier transform of (6.54) for p using (6.50) to give

$$U'_n(s) = G_n(s) m_A^{-1} F_0^{\text{ext}}(s) + R_n^d(s) \quad (6.56)$$

where

$$R_n^d(s) = s \sum_{n'=-N/2}^{N/2-1} G_{n-n'}(s) u'_{n'}(0) + \sum_{n'=-N/2}^{N/2-1} G_{n-n'}(s) \dot{u}'_{n'}(0) \quad (6.57)$$

and N is the total number of unit cells in the domain. The final two terms on the right-hand side of (6.56) arise from the convolution property of the Fourier transform (3.42). We next write (6.56) for $n = 0, 1$ to give

$$U'_0(s) = G_0(s)m_A^{-1}F_0^{\text{ext}}(s) + R_0^d(s) \quad (6.58)$$

$$U'_1(s) = G_1(s)m_A^{-1}F_0^{\text{ext}}(s) + R_1^d(s) \quad (6.59)$$

We use (6.58) and (6.59) to eliminate $F_0^{\text{ext}}(s)$, and obtain a relationship between $U'_0(s)$ and $U'_1(s)$:

$$U'_1(s) = G_1(s)G_0^{-1}(s)(U'_0(s) - R_0^d(s)) + R_1^d(s) \quad (6.60)$$

(6.60) can be rewritten as

$$U'_1(s) = Q(s)(U'_0(s) - R_0^d(s)) + R_1^d(s) \quad (6.61)$$

where

$$Q(s) = G_1(s)G_0^{-1}(s) \quad (6.62)$$

We can now calculate the external impedance force that is applied to boundary atom 0 via the expression

$$f_0^{\text{imp}}(s) = K_{-1}u'_1(s) \quad (6.63)$$

f_0^{imp} represents the external impedance force acting on the boundary atom 0 due to the motion of atom 1 such that atom 0 does not notice that the $n > 0$ atoms have been eliminated.

Because the expression for the displacement of atom 0 is given in terms of atom 1 via (6.61), we can simply take the inverse Laplace transform (ILT) of (6.61) and convolute the displacement with the stiffness via (6.63) to obtain the impedance force which acts upon boundary atom 0. By doing so, we obtain

$$f_0^{\text{imp}}(t) = \int_0^t \theta(t-\tau)(u'_0(\tau) - R_0^d(\tau))d\tau + R_0^f(t) \quad (6.64)$$

where the time history kernel $\theta(t)$ and random force $R_0^f(t)$ are defined to be

$$\theta(t) = \mathcal{L}^{-1}(K_{-1}Q(s)) \quad (6.65)$$

$$R_0^f(t) = K_{-1}R_1^d(t) \quad (6.66)$$

The discussion in the following section details the meaning of the random force $R_0^f(t)$ and the random displacement $R_0^d(t)$. By substituting the known relation

$$u'_0(t) = q_0(t) - \bar{u}_0(t) \quad (6.67)$$

into (6.64), the final coupled form of the equations of motion reads

$$\mathbf{M}\ddot{\mathbf{d}} = \mathbf{N}^T\mathbf{f}(\mathbf{u}) \quad (6.68)$$

$$\mathbf{M}_A\ddot{\mathbf{q}} = \mathbf{f}(\mathbf{q}) + f_0^{\text{imp}}(t) + R_0^f(t) \quad (6.69)$$

$$f_0^{\text{imp}}(t) = \int_0^t \theta(t-\tau)(q_0(\tau) - \bar{u}_0(\tau) - R_0^d(\tau))d\tau \quad (6.70)$$

where the impedance force f_0^{imp} acts *only* on the boundary atom 0.

6.2.4 Commentary on Reduced Multiscale Formulation

Now that the coupled coarse and reduced fine scale equations of motion have been determined, we make the following comments:

- (i) The meaning of the impedance force $f_0^{\text{imp}}(t)$ is that it dissipates away all fine scale information that cannot be represented in the continuum. It can be seen that $f_0^{\text{imp}}(t) = 0$ for the case when the coarse scale can exactly represent the MD displacements, that is, $q_0 = \bar{u}_0$, and the continuum is at zero temperature, that is, all the random terms $R(t)$ are zero. However, for the more general case when $q_0 \neq \bar{u}_0$, the impedance force dissipates away all information which the coarse scale cannot represent.
- (ii) The assumption of linearity was only needed to eliminate the unwanted fine scale degrees of freedom; more specifically, the assumption of linearity is contained in the behavior of the time history kernel $\theta(t)$. For the remaining atoms, the internal force $\mathbf{f}(q)$ in (6.69) can be found by using any nonlinear interatomic potential.
- (iii) The random, or stochastic force terms $R_0^d(t)$ and $R_0^f(t)$ arise from the initial conditions in the eliminated fine scale degrees of freedom. Because an arbitrarily large number of initial conditions are possible depending on the temperature of the eliminated degrees of freedom, the random terms $R_0^d(t)$ and $R_0^f(t)$ represent thermally motivated displacements and forces, respectively, exerted on the reduced MD system by the eliminated fine scale degrees of freedom.
- (iv) The FE equation of motion is no longer redundant, as the coarse scale now exists in large portions of the domain from which the fine scale MD has been eliminated. Furthermore, the coarse scale variables are allowed to influence the motion of the fine scale; this is through the $\bar{u}_0(\tau)$ in (6.69). Thus, a two-way coarse scale/fine scale coupling has been achieved at the MD boundary where information originating from the coarse scale can act as a boundary condition for the fine scale.

6.2.5 Elimination of Fine Scale Degrees of Freedom: 3D Generalization

We now generalize the ideas presented in the previous sections to three dimensions. The periodic lattice now consists of spatially repeated unit cells which are repeated in three directions. Each repeated cell has n_a atoms, each of which can move in n_{sd} spatial directions. The total number of degrees of freedom in each unit cell is then $n_{\text{dof}} = n_a \times n_{\text{sd}}$. Each unit cell can be labeled with three indices, l , m and n , indicating the position along axes in the direction of the three primitive vectors of the crystal structure. A two-dimensional example for a hexagonal lattice labelled using unit cell nomenclature is illustrated in Figure 6.4. Equation (6.51) can thus be rewritten as

$$\begin{aligned} \ddot{\mathbf{u}}'_{l,m,n}(t) = & \sum_{l'=l-1}^{l+1} \sum_{m'=m-\mu}^{m+\mu} \sum_{n'=n-v}^{n+v} \mathbf{M}_A^{-1} \mathbf{K}_{l-l', m-m', n-n'} \mathbf{u}'_{l', m', n'}(t) \\ & + \mathbf{M}_A^{-1} \mathbf{f}_{l,m,n}^{\text{ext}}(t) \end{aligned} \quad (6.71)$$

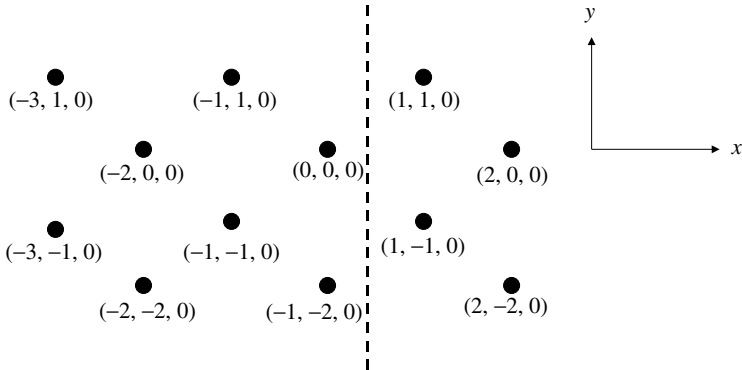


Figure 6.4 Periodic two-dimensional hexagonal lattice structure numbered using unit cell nomenclature. The solid line represents the boundary between the MD region to be simulated (bottom), and the MD region to be eliminated (top). Reprinted from Journal of Computational Physics, 207(2), Park et al., Three-dimensional bridging scale analysis of dynamic fracture, 588–609, 2005, with permission from Elsevier.

where $\mathbf{f}_{l,m,n}^{\text{ext}}(t)$ is the external force acting upon unit cell (l, m, n) , the matrices \mathbf{K} relate the displacements in cell $(-l', -m', -n')$ to the forces in cell (l, m, n) , \mathbf{M}_A is a diagonal matrix of atomic masses and μ and ν represents the range of the forces in the m and n coordinate directions. We note that while atoms in a given slab of constant l are coupled to only neighboring cells $l - 1$ and $l + 1$, the coupling in the m and n coordinate directions is not limited to nearest neighbors. This approximation can be relaxed simply by increasing the interaction range of the \mathbf{K} matrices if longer-ranged interactions are desired, and will be detailed later in this book.

The derivation begins by taking an LT and discrete Fourier transform (DFT) of (6.71)

$$\begin{aligned} s^2 \hat{\mathbf{U}}'(p, q, r, s) - s \mathbf{u}'(p, q, r, 0) - \dot{\mathbf{u}}'(p, q, r, 0) \\ = \hat{\mathbf{A}}(p, q, r) \hat{\mathbf{U}}'(p, q, r, s) + \mathbf{M}_A^{-1} \hat{\mathbf{F}}_0^{\text{ext}}(p, q, r, s) \end{aligned} \quad (6.72)$$

where p , q and r correspond to spatial indices l , m and n and the hatted notation indicates the discrete Fourier transform. $\hat{\mathbf{A}}(p, q, r)$ is the Fourier transform of $\mathbf{M}_A^{-1} \mathbf{K}_{l,m,n}$, and Laplace transformed variables are indicated by the transformed variable s . The goal of this process will be to eliminate the atoms in the $l > 0$ cells by solving for them in terms of the $l \leq 0$ degrees of freedom and resubstituting that expression into (6.71). In this manner, we will avoid the explicit solution for the $l > 0$ degrees of freedom while implicitly including their effects into the remaining system dynamics.

The key step in removing the unwanted $l > 0$ fine scale degrees of freedom is in realizing that the motion of the boundary ($l = 0$) atoms can be caused either by the displacements of the atoms to be kept, or by an external force acting upon the boundary atoms. Therefore, it will be assumed that the motion of the boundary atoms is in fact caused by the external force which acts only at $l = 0$,

$$\mathbf{f}_{l,m,n}^{\text{ext}}(t) = \delta_{l,0} \mathbf{f}_{0,m,n}^{\text{ext}}(t) \quad (6.73)$$

(6.72) can be solved to give the (LT)/(DFT) displacements in terms of the external force

$$\begin{aligned}\hat{\mathbf{U}}'(p, q, r, s) &= \hat{\mathbf{G}}(p, q, r, s) \\ &\times \left(\mathbf{M}_A^{-1} \hat{\mathbf{F}}_0^{\text{ext}}(p, q, r, s) + s\mathbf{u}'(p, q, r, 0) + \dot{\mathbf{u}}'(p, q, r, 0) \right)\end{aligned}\quad (6.74)$$

where

$$\hat{\mathbf{G}}(p, q, r, s) = (s^2 \mathbf{I} - \hat{\mathbf{A}}(p, q, r))^{-1} \quad (6.75)$$

Taking the IFT of (6.74) in the x direction gives the displacement in the x direction at atomic position l

$$\tilde{\mathbf{U}}'_l(q, r, s) = \mathbf{M}_A^{-1} \tilde{\mathbf{G}}_l(q, r, s) \hat{\mathbf{F}}_0^{\text{ext}}(q, r, s) + \tilde{\mathbf{R}}_l^d(q, r, s) \quad (6.76)$$

where

$$\tilde{\mathbf{R}}_l^d(q, r, s) = \sum_{l'=-L/2}^{L/2-1} \tilde{\mathbf{G}}_{l-l'}(q, r, s) (s\mathbf{U}'_{l'}(q, r, 0) + \dot{\mathbf{U}}'_{l'}(q, r, 0)) \quad (6.77)$$

where L is the total number of unit cells in the x -direction. By writing (6.76) for both $l = 0$ and $l = 1$, we can obtain the displacements $\tilde{\mathbf{U}}'_1$ in terms of $\tilde{\mathbf{U}}'_0$, thereby eliminating $\hat{\mathbf{F}}_0^{\text{ext}}$ and obtaining

$$\tilde{\mathbf{U}}'_1(q, r, s) = \tilde{\mathbf{Q}}(q, r, s) (\tilde{\mathbf{U}}'_0(q, r, s) - \tilde{\mathbf{R}}_0^d(q, r, s)) + \tilde{\mathbf{R}}_1^d(q, r, s) \quad (6.78)$$

where

$$\tilde{\mathbf{Q}}(q, r, s) = \tilde{\mathbf{G}}_1(q, r, s) \tilde{\mathbf{G}}_0^{-1}(q, r, s) \quad (6.79)$$

By inverting the Fourier transform of (6.78) and using the convolution property of the DFT, we obtain

$$\begin{aligned}\mathbf{U}'_{1,m,n}(s) &= \sum_{m'=-M/2}^{M/2-1} \sum_{n'=-N/2}^{N/2-1} \mathbf{Q}_{m-m', n-n'}(s) (\mathbf{U}'_{0,m',n'}(s) - \mathbf{R}_{0,m',n'}^d(s)) \\ &\quad + \mathbf{R}_{1,m,n}^d(s)\end{aligned}\quad (6.80)$$

where the random component of the displacement acting upon plane l can be written as

$$\begin{aligned}\mathbf{R}_{l,m,n}^d(s) &= \sum_{l'=-L/2}^{L/2-1} \sum_{m'=-M/2}^{M/2-1} \sum_{n'=-N/2}^{N/2-1} \mathbf{G}_{l-l', m-m', n-n'}(s) \\ &\quad \times (s\mathbf{U}'_{l',m',n'}(0) + \dot{\mathbf{U}}'_{l',m',n'}(0))\end{aligned}\quad (6.81)$$

Inversion of the LT for the above equation gives a time-dependent vector of random displacements,

$$\begin{aligned}\mathbf{R}_{l,m,n}^d(t) &= \sum_{l'=-L/2}^{L/2-1} \sum_{m'=-M/2}^{M/2-1} \sum_{n'=-N/2}^{N/2-1} (\dot{\mathbf{g}}_{l-l', m-m', n-n'}(t) \mathbf{u}'_{l',m',n'}(0) \\ &\quad + \mathbf{g}_{l-l', m-m', n-n'}(t) \dot{\mathbf{u}}'_{l',m',n'}(0))\end{aligned}\quad (6.82)$$

where $\mathbf{u}'_{l,m,n}(0)$, $\dot{\mathbf{u}}'_{l,m,n}(0)$ are the fine scale initial conditions determined by thermodynamic properties of the system, and

$$\mathbf{g}_{l,m,n}(t) = \mathcal{L}^{-1}(\mathbf{G}_{l,m,n}(s)) \quad (6.83)$$

$$\dot{\mathbf{g}}_{l,m,n}(t) = \mathcal{L}^{-1}\{s\mathbf{G}_{l,m,n}(s)\} \quad (6.84)$$

We note that the physical meaning of the vector (6.82) is analogous to the meaning of the random vector (4.125) discussed earlier in Chapter 4.

Since the fine scale portion of the coarse grain atom displacements $\mathbf{q}_{1,m,n}$ are known by (6.80), a complete coupled set of equations could be written as

$$\mathbf{M}_A \ddot{\mathbf{q}} = \mathbf{f}(\mathbf{q}) \quad (6.85)$$

$$\mathbf{M} \ddot{\mathbf{d}} = \mathbf{N}^T \mathbf{f}(\mathbf{u}) \quad (6.86)$$

$$\begin{aligned} \mathbf{q}_{1,m,n}(t) = & \int_0^t \mathbf{Q}_{m-m',n-n'}(t-\tau) \\ & \times (\mathbf{q}_{0,m',n'}(\tau) - \bar{\mathbf{u}}_{0,m',n'}(\tau) - \mathbf{R}_{0,m',n'}^d(\tau)) d\tau + \bar{\mathbf{u}}_{1,m,n}(t) + \mathbf{R}_{1,m,n}^d(t) \end{aligned} \quad (6.87)$$

In this formulation, the coarse grain atom displacements $\mathbf{q}_{1,m,n}(t)$ are semianalytically controlled as a function of the fine scale portion of the coarse grain atom displacements (the first term on the right-hand side of (6.87)) combined with a contribution of the coarse scale displacements interpolated to the coarse grain atom position. In the impedance force formulation derived later in this section, the coarse grain atom motion is completely prescribed by the FE shape functions; in this displacement formulation, the dependence on the shape functions is reduced, but not completely eliminated. We note the similarity between the coarse grain atoms and so-called *ghost* atoms, which are necessary in MD simulations such that spurious relaxation of the system due to surface effects does not occur. In the bridging scale formulation, because all atoms are initially present, the coarse grain atoms have not been artificially created; however, like ghost atoms, their motion is not explicitly solved for in the MD equation of motion.

Previous approaches to deriving nonreflecting boundary conditions, for example, Adelman and Doll (1976) and Cai et al. (2000) have utilized a force boundary condition; so we bow to convention and continue with the derivation. Equation (6.80) becomes useful if the linearized forces acting on $l = 0$ slab of atoms due to the $l = 1$ slab of atoms is written as, recalling (6.71)

$$\mathbf{F}_{m,n}^{1 \rightarrow 0}(s) = \sum_{m'=m-\mu}^{m+\mu} \sum_{n'=n-\nu}^{n+\nu} \mathbf{K}_{-1,m-m',n-n'} \mathbf{U}'_{1,m',n'}(s) \quad (6.88)$$

Substituting (6.80) into (6.88) and taking the ILT, the *impedance force boundary condition* of the layer $l = 1$ slab of atoms acting upon the $l = 0$ slab of atoms becomes

$$\begin{aligned} \mathbf{f}_{m,n}^{\text{imp}}(t) = & \mathcal{L}^{-1}\{\mathbf{F}_{m,n}^{1 \rightarrow 0}(s)\} = \sum_{m'=-M/2}^{M/2-1} \sum_{n'=-N/2}^{N/2-1} \int_0^t \boldsymbol{\theta}_{m-m',n-n'}(t-\tau) \\ & \times (\mathbf{u}'_{0,m',n'}(\tau) - \mathbf{R}_{0,m',n'}^d(\tau)) d\tau + \mathbf{R}_{0,m,n}^f(t) \end{aligned} \quad (6.89)$$

where the time history kernel $\boldsymbol{\theta}(t)$ is defined to be

$$\boldsymbol{\theta}_{m,n}(t) = \mathcal{L}^{-1}(\boldsymbol{\Theta}_{m,n}(s)) \quad (6.90)$$

$$\boldsymbol{\Theta}_{m,n}(s) = \sum_{m'=-m-\mu}^{m+\mu} \sum_{n'=n-v}^{n+v} \mathbf{K}_{-1,m-m',n-n'} \mathbf{Q}_{m',n'}(s) \quad (6.91)$$

and the random force $\mathbf{R}_{0,m,n}^f(t)$ is given by

$$\mathbf{R}_{0,m,n}^f(t) = \sum_{l'=-L/2}^{L/2-1} \sum_{m'=-M/2}^{M/2-1} \sum_{n'=-N/2}^{N/2-1} \mathbf{K}_{-1,m-m',n-n'} \mathbf{R}_{1,m,n}^d(t) \quad (6.92)$$

Here, the random displacement vector \mathbf{R}^d is given by (6.82).

As can be seen, the exact evaluation of the second term on the right-hand side of (6.89) requires a summation over all other unit cells along the boundary. Clearly, it would be computationally inefficient to actually perform the exact summation in practice, particularly if the lattice is large. Therefore, we rewrite (6.89) as

$$\begin{aligned} \mathbf{f}_{m,n}^{\text{imp}}(t) &= \sum_{m'=-n_c}^{n_c} \sum_{n'=-n_c}^{n_c} \int_0^t \boldsymbol{\theta}_{m-m',n-n'}(t-\tau) \\ &\quad \times (\mathbf{u}'_{0,m',n'}(\tau) - \mathbf{R}_{0,m',n'}^d(\tau)) d\tau + \mathbf{R}_{0,m,n}^f(t) \end{aligned} \quad (6.93)$$

where n_c refers to a maximum number of atomic neighbors which will be used to compute the impedance force. Now, the fine scale equation of motion (6.71) for the boundary $l = 0$ atoms can be rewritten as

$$\begin{aligned} \ddot{\mathbf{u}}'_{0,m,n} &= \mathbf{A}_{0,m,n} \mathbf{u}'_{0,m,n} \\ &+ \mathbf{M}_A^{-1} \sum_{m'=-n_c}^{n_c} \sum_{n'=-n_c}^{n_c} \int_0^t \boldsymbol{\theta}_{m-m',n-n'}(t-\tau) (\mathbf{u}'_{0,m',n'}(\tau) - \mathbf{R}_{0,m',n'}^d(\tau)) d\tau \\ &+ \mathbf{M}_A^{-1} \mathbf{R}_{0,m,n}^f(t) \end{aligned} \quad (6.94)$$

Note that the second term on the right-hand side of (6.94) represents the implicit effects of the $l > 0$ cells which were mathematically eliminated. Adding (6.94) and (6.85) and noting that

$$\mathbf{M}_{A0}^{-1} \mathbf{f}_{0,m,n}(\bar{\mathbf{u}}) + \mathbf{A}_{0,m,n} \mathbf{u}'_{0,m,n} = \mathbf{M}_{A0}^{-1} \mathbf{f}_{0,m,n} \quad (6.95)$$

where \mathbf{M}_{A0}^{-1} is the matrix of atomic masses for the boundary plane atoms, we obtain the modified equation of motion for the boundary atoms which does not involve any unknown degrees of freedom of the cells (l, m, n) with $l > 0$

$$\begin{aligned} \mathbf{M}_{A0} \ddot{\mathbf{q}}_{0,m,n}(t) &= \mathbf{f}_{0,m,n}(t) \\ &+ \sum_{m'=-n_c}^{n_c} \sum_{n'=-n_c}^{n_c} \int_0^t \boldsymbol{\theta}_{m-m',n-n'}(t-\tau) (\mathbf{u}'_{0,m',n'}(\tau) - \mathbf{R}_{0,m',n'}^d(\tau)) d\tau \\ &+ \mathbf{R}_{0,m,n}^f(t) \end{aligned} \quad (6.96)$$

The final step to writing the MD equations of motion for the boundary atoms is to note that the fine scale component of the MD displacements can be written as

$$\mathbf{u}'_{0,m',n'}(\tau) = \mathbf{q}_{0,m',n'}(\tau) - \bar{\mathbf{u}}_{0,m',n'}(\tau) \quad (6.97)$$

The final form for the coupled MD and FE equations of motion thus can be written as

$$\mathbf{M}_A \ddot{\mathbf{q}} = \mathbf{f}(\mathbf{q}) + \mathbf{f}_{0,m,n}^{\text{imp}}(t) + \mathbf{R}_{0,m,n}^f(t) \quad (6.98)$$

$$\mathbf{M} \ddot{\mathbf{d}} = \mathbf{N}^T \mathbf{f}(\mathbf{u}) \quad (6.99)$$

where \mathbf{R}^f is a stochastic thermal force (6.92), and \mathbf{f}^{imp} is the impedance force,

$$\begin{aligned} \mathbf{f}_{0,m,n}^{\text{imp}}(t) &= \sum_{m'=-n_c}^{n_c} \sum_{n'=-n_c}^{n_c} \int_0^t \theta_{m-m',n-n'}(t-\tau) \\ &\times (\mathbf{q}_{0,m',n'}(\tau) - \bar{\mathbf{u}}_{0,m',n'}(\tau) - \mathbf{R}_{0,m',n'}^d(\tau)) d\tau \end{aligned} \quad (6.100)$$

Equations (6.98)–(6.100) represent the major results of this section. With these key equations having been derived, several remarks are in order:

- (i) The first equation (6.98) defines the standard MD equation of motion, with interatomic forces derived from any anharmonic potential energy function. The first term on the right-hand side of (6.98), $\mathbf{f}(\mathbf{q})$, is just the standard nonlinear interatomic force that is, calculated in the MD simulation. It is important to note that this force is the standard nonlinear interatomic force; the assumption of linearity was only used in describing the motion of the $l > 0$ cells which were eliminated. Specifically, the assumption of linearity manifests itself in the time history kernel $\theta(t-\tau)$.
- (ii) The second term on the right hand side of (6.98), the impedance force $\mathbf{f}_{0,m,n}^{\text{imp}}(t)$, contains the time history kernel $\theta(t-\tau)$, and acts to dissipate fine scale energy from the MD simulation into the surrounding continuum. It is important to note that this force acts *only* on the boundary MD atoms. The numerical result is a nonreflecting boundary between the MD and FE regions, as the time history kernel allows short wavelengths that cannot be represented by the surrounding continuum to leave the MD region. Furthermore, the dependence of the impedance force on the coarse scale solution $\bar{\mathbf{u}}_{0,m',n'}(\tau)$ indicates a two-way coupled MD equation of motion, that is, that coarse scale information originating in the continuum can be passed to the MD region. This will prove essential in later numerical examples, where the boundary conditions are applied to the surrounding continuum.
- (iii) The form of the impedance force differs from that found in Wagner and Liu (2003). The major difference is that, in the work of Wagner and Liu, the damping kernel $\beta(t)$ is multiplied by the time derivative of the difference between the coarse and fine scale accelerations. While this quantity can be calculated in practice, it requires additional difficulty as the time derivative of the accelerations is not typically calculated in numerical simulations. In contrast, the displacements in (6.100) are known quantities which can easily be extracted directly from the time integration algorithm.

- (iv) The random, or stochastic force $\mathbf{R}_{0,m,n}^f(t)$ and random displacement $\mathbf{R}_{0,m',n'}^d(\tau)$ act on the reduced atomistic system due to initial conditions in the continuum region. Because the initial conditions can be known only in an averaged sense based on the temperature of the coarse scale, and because many different initial conditions are possible, the random terms represents thermally dependent forces exerted on the MD region by the surrounding coarse scale. A further explanation of the random force is given in Figure 6.5. Figure 6.5 shows that the random force comes about due to the reduction of a finite temperature MD system at temperature T to a smaller MD region having the same temperature T . Analogous to the necessity in keeping the effects of the eliminated degrees of freedom in the time history kernel $\theta(t)$, the thermal effects of the eliminated degrees of freedom must be kept in the form of the random force $\mathbf{R}(t)$. The existence of the random terms indicates that the bridging scale method can be considered a coupled finite temperature method; techniques for applying this stochastic force were proposed by Adelman and Doll (1976). In the examples presented in this book, we neglect these random terms, indicating that the temperature of the surrounding continuum is 0K.
- (v) We note that the time history kernel matrix $\theta(t)$ has the size of the minimum number of degrees of freedom in each unit cell. Thus, in 3D, $\theta(t)$ is a 3×3 matrix. The compact size of $\theta(t)$ distinguishes this approach from other methods, such as that of Cai et al. (2000) and E and Huang (2002). These differences will be elaborated upon in the next section. The small size of $\theta(t)$ enables us to achieve large computational savings by eliminating large portions of the lattice where an explicit atomistic representation is not desired. Specifically, even as the number of eliminated fine scale degrees of freedom grows, the size of $\theta(t)$ remains constant.
- (vi) Due to the elimination of the fine scale degrees of freedom for the $l > 0$ cells, the FE equation of motion (6.99) is *not* redundant. The coarse scale thus carries two major responsibilities. The first is to capture the long wavelength nonlinear response of the system, while the impedance force described in remark (ii) dissipates the high-frequency waves that cannot be captured by the coarse scale. The second major role of the coarse scale relates to the coupling of the revised MD equation of motion (6.98) such that it depends upon the coarse scale solution $\bar{\mathbf{u}}_{0,m',n'}(\tau)$ through the impedance

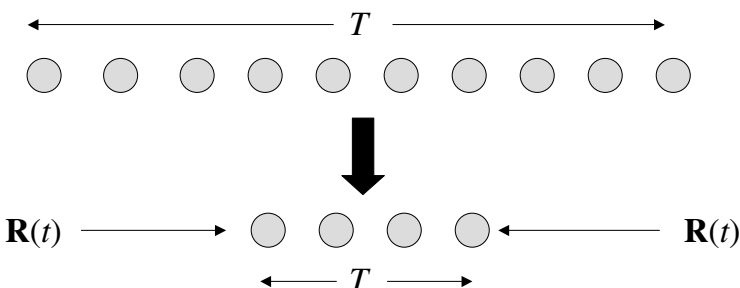


Figure 6.5 Illustration of origin of random force $\mathbf{R}(t)$.

force $\mathbf{f}_{0,m,n}^{\text{imp}}(t)$ in (6.100). The coarse scale dependence in (6.98) then serves as a boundary condition on the MD simulation, should the flow of information be from continuum to atomistic regions. In this manner, a true two-way coupling between the coarse and fine scales has been achieved.

- (vii) For the coupled system of equations describing a domain in which FEM and MD both exist everywhere, that is, (6.25) and (6.26), the global system is conservative. However, due to the elimination of the fine scale degrees of freedom in deriving the impedance force $\mathbf{f}_{0,m,n}^{\text{imp}}(t)$, the MD system described by (6.98) is dissipative.
- (viii) Due to the fact that the bridging scale involves the solution of the standard FE and MD equations of motion with few modifications, the method is extremely well suited to the reuse of existing FE and MD codes. The changes to the standard MD equation of motion, as previously mentioned in remarks (ii) and (iii), only involves the additional impedance and random forces applied to the boundary atoms. For the FE equation of motion, the FE internal forces are computed using the MD forces as a function of the total displacement \mathbf{u} ; therefore, the subroutine used to calculate the actual MD forces can be reused to calculate the FE coupling force $\mathbf{N}^T(\mathbf{u})$.
- (ix) The motion of the coarse grain atoms is controlled using the FE shape functions. This procedure is identical to that adopted to control the motion of the pad, or ghost atoms in Shilkrot et al. (2004). We adopt this procedure to follow the convention established in previous works, for example, Adelman and Doll (1976), Cai et al. (2000) and E and Huang (2002), which have utilized a force boundary condition.

6.2.6 Numerical Implementation of Impedance Force

The numerical implementation of the MD impedance force (6.100) involves two components. The first component deals with the calculation of the time history kernel $\boldsymbol{\theta}(t)$. In practice, $\boldsymbol{\theta}(t)$ is computed and stored before the actual calculation takes place. The values of $\boldsymbol{\theta}(t)$ depend on the type of lattice considered, the form of interatomic potential utilized, and the number of atomic neighbors considered in calculating the impedance force. The form of the interatomic potential and the geometry of the lattice influence the values of the stiffness matrices \mathbf{K} , for example in (6.91). In the numerical implementation, because of the decreasing nature of the time history kernel $\boldsymbol{\theta}(t)$, all components of $\boldsymbol{\theta}(t)$ are set-to zero after a certain time, which dramatically reduces the storage requirements for $\boldsymbol{\theta}(t)$.

A particular point of emphasis is that $\boldsymbol{\theta}(t)$ is *not* stored for every boundary atom. Because of the repetitive structure assumption used in deriving $\boldsymbol{\theta}(t)$, all boundary atoms in a given plane can be considered to be identical. Therefore, only one set of $\boldsymbol{\theta}(t)$ is necessary, and is reused for each boundary atom. The number of $\boldsymbol{\theta}(t)$ stored then only depends on the number of atomic neighbors (n_c in (6.100)) considered for each boundary atom.

Therefore, the only variables that are required for the impedance force which require updating during the simulation is the difference in boundary displacements, or the $\mathbf{q}_{0,m',n'}(\tau) - \bar{\mathbf{u}}_{0,m',n'}(\tau)$ term in (6.100). This difference in displacement is stored for every boundary

atom. The $\mathbf{q}_{0,m',n'}(\tau)$ term, or the displacements of each boundary atom, are clearly available at each MD time step. The $\bar{\mathbf{u}}_{0,m',n'}(\tau)$ term, or the interpolated FE displacement at each boundary atom, is calculated after each FE time step. Because that term is also necessary at each MD time step, it is integrated in time at each MD time step assuming a constant coarse scale acceleration and thus the difference $\mathbf{q}_{0,m',n'}(\tau) - \bar{\mathbf{u}}_{0,m',n'}(\tau)$ can be evaluated and stored for each MD time step. Details on the integration algorithm for both the coarse and fine scales can be found in Wagner and Liu (2003) and Park and Liu (2004), and also later in this chapter.

Because the time history kernel $\theta(t)$ is truncated after a certain period of time, the requirements for the displacement history are correspondingly truncated to hold for the same number of time steps. A further truncation on the storage of the displacement histories can be accomplished by only storing the displacement histories at certain time steps, while weighting those values accordingly to account for the fact that the displacement histories are not stored at every MD time step. While this method was shown to be very effective for one-dimensional problems (Park and Liu 2004), it has yet to be implemented in multiple dimensions.

6.2.7 Numerical Implementation of Coupling Force

We now discuss implementation-specific details of the coarse scale internal force in (6.99), that is, the $\mathbf{N}^T \mathbf{f}(\mathbf{u})$ term. This term originates naturally due to the separation of scales in constructing the multiscale Lagrangian (6.13). In general, the size of the matrix \mathbf{N}^T is $N_{n1} \times N_{a1}$, where N_{n1} is the number of FE nodes whose support contains an atomic position, and N_{a1} is the total number of atoms. The matrix \mathbf{N}^T is calculated once at the outset of the simulation as follows. First, a search is performed to determine which atoms lie within the interior of each FE. The FE shape functions are then evaluated at each initial atomic position which lies within the FE. Because each node has a compact support, the matrix \mathbf{N}^T is stored as a sparse matrix. The x , y and z components of the FE nodal forces can then be calculated as

$$f_{Ix} = \sum_{\alpha=1}^{n_{\text{atom}}^I} N_I(\mathbf{X}_\alpha) f_{\alpha x}(\mathbf{u}) \quad (6.101)$$

$$f_{Iy} = \sum_{\alpha=1}^{n_{\text{atom}}^I} N_I(\mathbf{X}_\alpha) f_{\alpha y}(\mathbf{u}) \quad (6.102)$$

$$f_{Iz} = \sum_{\alpha=1}^{n_{\text{atom}}^I} N_I(\mathbf{X}_\alpha) f_{\alpha z}(\mathbf{u}) \quad (6.103)$$

where $N_I(\mathbf{X}_\alpha)$ are the FE shape functions evaluated at the initial atomic positions \mathbf{X}_α , f_{Ix} are the x -components of finite element nodal forces, f_{Iy} are the y -components of the FE nodal forces, f_{Iz} are the z -components of the FE nodal forces, $f_{\alpha x}(\mathbf{u})$ are the x -components of the standard MD interatomic forces evaluated as a function of the total displacements \mathbf{u} , $f_{\alpha y}(\mathbf{u})$ are the y -components of the standard MD interatomic forces evaluated as a function of the total displacements \mathbf{u} , $f_{\alpha z}(\mathbf{u})$ are the z -components of the standard MD interatomic

forces evaluated as a function of the total displacements \mathbf{u} and n_{atom}^I are the number of atoms within the support of node I .

Equations (6.101)–(6.103) represent the discrete version of the coarse scale internal force derived consistently through the multiscale Lagrangian in (6.13). It is important to note that for the case in which the FE nodal positions exactly overlay the atomic lattice, the coarse scale internal forces (6.101)–(6.103) will *exactly* correspond to the actual atomistic internal forces due to the Kronecker delta property of the FE shape functions. For the more general case in which the FE nodal positions are spaced wider than the atomic lattice spacing, the coarse scale internal forces represent an average of the underlying atomic forces, with the quality of the approximation given by the finite element shape functions.

Due to the long-ranged interactions inherent in atomistic simulations, many situations will arise in which some portion of the force on a given atom will contain the effects of the motion of other atoms in different FEs. However, because the force on each atom in (6.101)–(6.103) is a *total* value, no special treatment is needed to treat atomic bonds which cross element boundaries.

The coarse scale internal force for the N_{c2} nodes in region 2 is calculated in a different manner, due to the absence of atoms in that region. This is described in a later section.

6.3 Discussion on the Damping Kernel Technique

The time history kernel matrix $\boldsymbol{\theta}(t)$ derived in the previous section bears much resemblance to other nonreflecting boundary conditions derived by Adelman and Doll (1976), Cai et al. (2000) and E and Huang (2002). All methods have been shown to eliminate high-frequency wave reflection at the MD/FE interface by the derivation and utilization of either the damping kernel $\boldsymbol{\beta}(t)$, or its time derivative $\boldsymbol{\theta}(t)$. As the methodology of Adelman and Doll was limited to one-dimensional examples, we compare our approach to the other two methods mentioned above.

The work of Cai et al. (2000) is a seminal one due to the fact that it was one of the first works to numerically calculate the damping kernel $\boldsymbol{\beta}(t)$ in multiple dimensions. However, the work contains two potential drawbacks. First, the damping kernel of Cai requires multiple MD simulations on a larger domain to be obtained; the damping kernel must be recalculated if the geometry of the problem changes. Secondly, the size of the damping kernel is proportional to the total number of degrees of freedom along the reduced MD boundary; for very large MD systems, this can lead to an extremely large damping kernel matrix.

The work of E and Huang (2002) was based on removing boundary reflections at the coarse/fine interface by optimizing the reflection coefficient at the interface. Because of this, multiple MD simulations were not required to obtain the damping kernel. The formulation of E and Huang (2002), however, introduces other difficulties. First of all, the geometry of the lattice enters their formulation explicitly, and must be accounted for in each calculation of the time history kernel. Secondly, the angles of incidence of waves approaching the interface also need to be specified; it is unclear if the formulation allows waves impinging on the boundary at arbitrary angles within a single calculation.

The work presented herein remedies the above difficulties as follows. First, and most importantly, the size of $\theta(t)$ is that of the minimum number of degrees of freedom in each unit cell. For example, in the current three-dimensional formulation, $\theta(t)$ is a 3×3 matrix. Secondly, the geometry of the lattice need not be explicitly modeled; the effects are contained in the \mathbf{K} matrices that can easily be derived for arbitrary lattice geometries and interatomic potentials. Thirdly, due to the repetitive structure of the atomic lattice, the same $\theta(t)$ is used for each boundary atom in the numerical implementation. Finally, as demonstrated in Wagner et al. (2004), the methodology for calculating $\theta(t)$ numerically can be automated, and only requires standard Laplace and Fourier transform techniques, as well as the \mathbf{K} matrices defining interactions between an atom and all of its neighbors.

To complete the discussion regarding the methodology presented herein to numerically calculate the time history kernel $\theta(t)$, we add the following comments:

- (i) Because of the fact that the force on a given boundary atom includes the displacements of all of its neighboring atoms (e.g. the sum in (6.98)), it is expected that this method will lose accuracy near lattice corners, where a full complement of atomic neighbors is generally unavailable.
- (ii) It was assumed in deriving the MD impedance force (6.98) that the boundary layer of atomic unit cells (the $l = 0$ slab in Figure 6.4) is initially planar.
- (iii) The formulation presented here is only used in this chapter for cases in which the atoms in each unit cell interact with only the atoms in the neighboring unit cells. However, this is not a general restriction on the method. For longer-ranged forces, simply increasing the interaction distance of the \mathbf{K} matrices accounts for the additional interactions, and will be detailed later in this book.
- (iv) The assumption of linearity is *only* required to hold for the atoms in the $l > 0$ unit cells which are eliminated from the formulation. Therefore, the method does not allow defects such as dislocations to propagate through the boundary. The remainder of the lattice is allowed to interact via any anharmonic potential desired.
- (v) The four components of the time history kernel $\theta(t)$ in (6.98) calculated for a nearest neighbor two-dimensional hexagonal lattice interacting via a Lennard-Jones (LJ) 6-12 potential are shown in Figures 6.6–6.9. As can be seen in the figures, the dominant order for each component is the zeroth order, which corresponds to only taking the value of the displacements at each boundary atom, and not considering the displacements of any of the neighboring atoms. Furthermore, the higher-order components are not only smaller in amplitude but are time delayed with respect to the zeroth order. This makes sense, as the response of a neighboring atomic unit cell to the perturbation of the boundary unit cell will be slower, the further away the unit cells are. It is thus expected in numerical computation that the single biggest improvement will occur by utilizing only the zeroth order component of the time history kernel; as more neighbors are used, the solution should improve, but slowly and less dramatically. The \mathbf{K} matrices utilized in calculating $\theta(t)$ for this system and potential are given in (3.19).

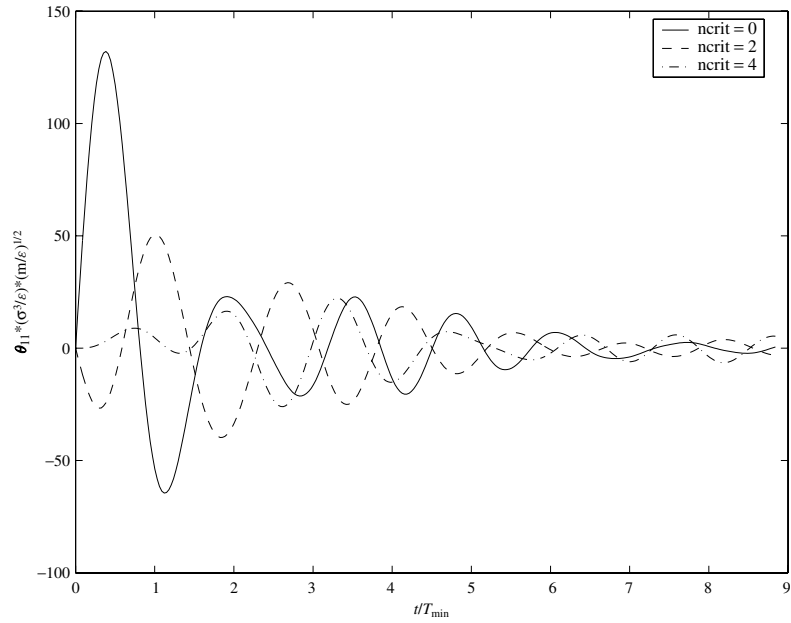


Figure 6.6 $\theta_{11}(t)$ for zero and higher orders. Reproduced with permission from Harold Park, Philosophical Magazine, published by Taylor & Francis, 2005, <http://www.tandf.co.uk>.

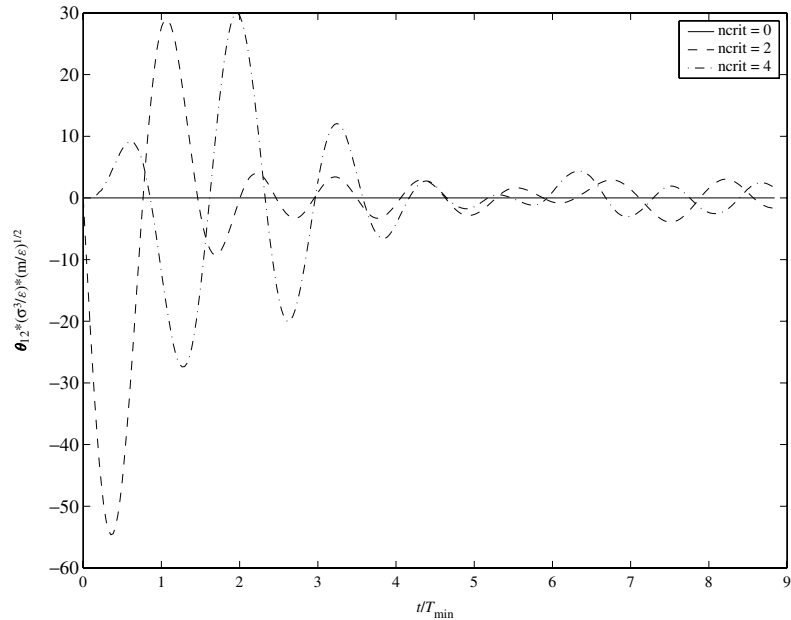


Figure 6.7 $\theta_{12}(t)$ for zero and higher orders. Reproduced with permission from Harold Park, Philosophical Magazine, published by Taylor & Francis, 2005, <http://www.tandf.co.uk>.

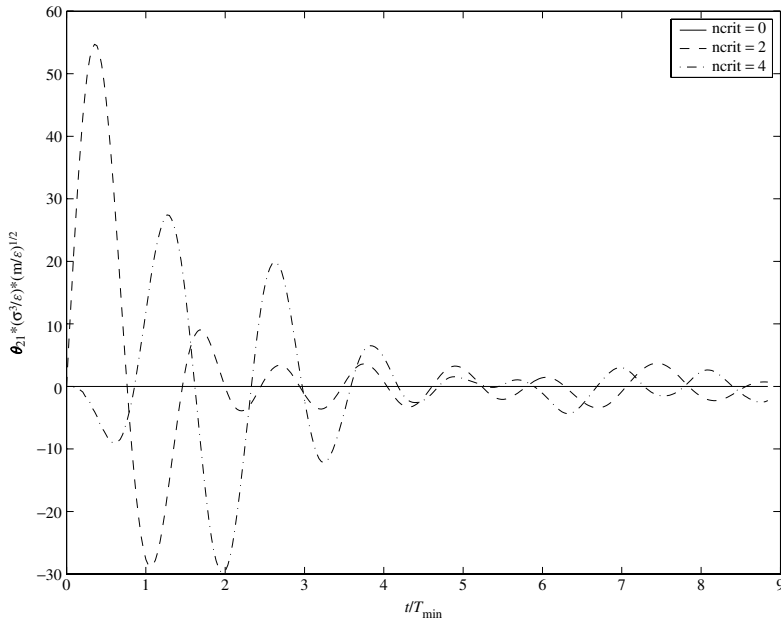


Figure 6.8 $\theta_{21}(t)$ for zero and higher orders. Note that $\theta_{21}(t) = -\theta_{12}(t)$. Reproduced with permission from Harold Park, Philosophical Magazine, published by Taylor & Francis, 2005, <http://www.tandf.co.uk>.

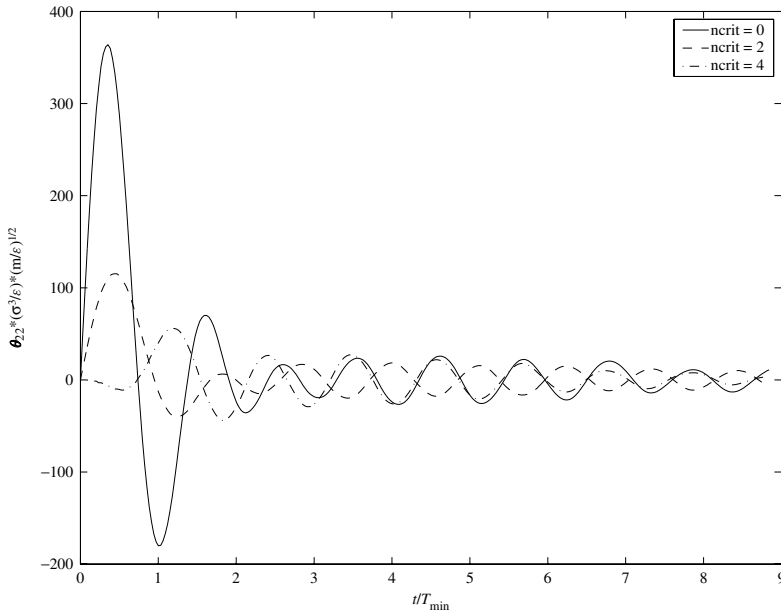


Figure 6.9 $\theta_{22}(t)$ for zero and higher orders. Reproduced with permission from Harold Park, Philosophical Magazine, published by Taylor & Francis, 2005, <http://www.tandf.co.uk>.

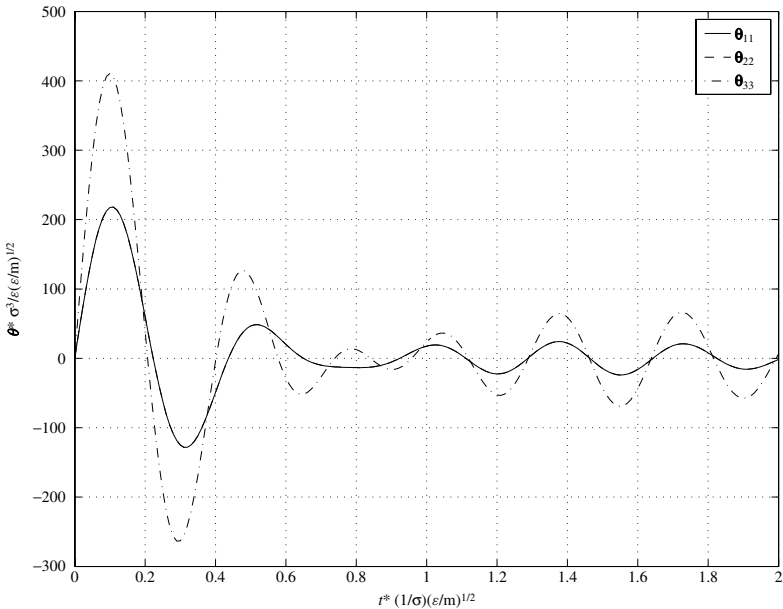


Figure 6.10 Components of $\theta(t)$ for 3D FCC lattice interacting via LJ 6-12 potential. Reprinted from Journal of Computational Physics, 207(2), Park et al., Three-dimensional bridging scale analysis of dynamic fracture, 588–609, 2005, with permission from Elsevier.

- (vi) The time history kernel $\theta(t)$ was also numerically calculated for an FCC lattice structure interacting via a nearest-neighbor LJ potential. In the numerical simulations, we use $n_c = 0$ for maximum computational efficiency. Figure 6.10 shows the three components of $\theta(t)$ in 3D with $n_c = 0$, $\theta_{11}(t)$, $\theta_{22}(t)$ and $\theta_{33}(t)$. As can be seen $\theta_{33}(t)$ is the most important component to be considered in the calculations. We neglect higher-order values of $\theta(t)$ corresponding to $n_c > 0$ as those values for $\theta(t)$ are on the order of ten percent of the values shown in (6.10). The three-dimensional time history kernel exhibits many of the salient features that were demonstrated in the two-dimensional time history kernels, specifically the quick decay in the amplitude of $\theta(t)$. The \mathbf{K} matrices for the three-dimensional case can also be found in (3.126).
- (vii) An important point that will be exploited in our numerical simulations is the decaying nature of all of the components of the time history kernels. Because the long time values of the kernels are essentially inconsequential with regards to the short time values, it is expected that the kernels can be truncated without significant loss in accuracy and with significant gains in computational efficiency.
- (viii) We note that the time axis in Figures 6.6–6.9 was normalized by the shortest period of vibration T_{\min} , corresponding to the longitudinal mode with wave vector $\mathbf{k} = \{0, \frac{2\pi}{\sqrt{3}a_0}\}$ in a two-dimensional hexagonal lattice, see Figure (6.4) with the LJ potential. In the expression for the wave vector \mathbf{k} , a_0 corresponds to the lattice parameter. It is noteworthy that the time history kernels are able to be truncated after less than

ten atomic vibrational periods, and indicate that the time history dependence of the lattice is indeed quite minimal.

6.3.1 Programming Algorithm for Time History Kernel

We now detail the programming flowchart for the numerical calculation of the time history kernel $\theta(t)$. The flowchart exactly follows that given in Wagner et al. (2004). The algorithm assumes there are L , M and N unit cells in the x , y and z directions, respectively. Our numerical experiments indicate that using values of around $L = M = N = 32$ are sufficient to mimic the response of a very large crystal. We note that due to the finiteness of the parameters and the usage of numerical Fourier transforms, the time history kernels $\theta(t)$ should be truncated at some value of time t to avoid artificial reflections of periodic boundaries.

Before initiating the procedure, it assumed that the stiffness matrices \mathbf{K} are known for a given crystal structure, for interaction ranges $|l| \leq 1$, $|m| \leq \mu$ and $|n| \leq \nu$. Once these are known, the algorithm proceeds as:

- (i) For each (p, q, r) , form $\hat{\mathbf{A}}(p, q, r)$:

$$\hat{\mathbf{A}}(p, q, r) = \sum_{l=-1}^{+1} \sum_{m=-\mu}^{+\mu} \sum_{n=-\nu}^{+\nu} \mathbf{M}_A^{-1} \mathbf{K}_{l,m,n} e^{-i2\pi(lp/L + mq/M + nr/N)} \quad (6.104)$$

- (ii) For each (p, q, r, s) , compute $\hat{\mathbf{G}}(p, q, r, s)$:

$$\hat{\mathbf{G}}(p, q, r, s) = (s^2 \mathbf{I} - \hat{\mathbf{A}}(p, q, r, s))^{-1} \quad (6.105)$$

- (iii) For each (q, r, s) , invert the DFT in the x -direction at $l = 0$ and $l = 1$:

$$\tilde{\mathbf{G}}_0(q, r, s) = \frac{1}{L} \sum_{p=-\frac{L}{2}+1}^{\frac{L}{2}} \hat{\mathbf{G}}(p, q, r, s) \quad (6.106)$$

$$\tilde{\mathbf{G}}_1(q, r, s) = \frac{1}{L} \sum_{p=-\frac{L}{2}+1}^{\frac{L}{2}} \hat{\mathbf{G}}(p, q, r, s) e^{2\pi i p/L} \quad (6.107)$$

- (iv) For each (q, r, s) , compute $\tilde{\mathbf{Q}}(q, r, s)$:

$$\tilde{\mathbf{Q}}(q, r, s) = \tilde{\mathbf{G}}_1(q, r, s) \tilde{\mathbf{G}}_0^{-1}(q, r, s) \quad (6.108)$$

- (v) For each m , n and s compute the IFT of $\tilde{\mathbf{Q}}(q, r, s)$:

$$\mathbf{Q}_{m,n}(s) = \frac{1}{MN} \sum_{q=-\frac{M}{2}+1}^{\frac{M}{2}} \sum_{r=-\frac{N}{2}+1}^{\frac{N}{2}} \tilde{\mathbf{Q}}(q, r, s) e^{2\pi i (mq/M + nr/N)} \quad (6.109)$$

(vi) For each m, n and s compute the convolution with the stiffness matrices:

$$\Theta_{m,n}(s) = \sum_{m'=m-\mu}^{m+1} \sum_{n'=n-1}^{n+1} \mathbf{K}_{-1,m-m',n-n'} \mathbf{Q}_{m',n'}(s) \quad (6.110)$$

(vii) For each m and n , compute the ILT to get the time history kernel:

$$\theta_{m,n}(t) = \mathcal{L}^{-1}\{\Theta_{m,n}(s)\} \quad (6.111)$$

Now that the algorithm has been fully laid out, we make further comments:

- The most expensive part of the algorithm are steps (i–ii), in which the inverse of $\hat{\mathbf{A}}(p, q, r, s)$ must be calculated for all (p, q, r, s) .
- The algorithm can easily be adapted to calculate the time history kernel on different faces of a crystal. For example, to calculate the kernel for the y -directions, the DFT would be inverted in the y -direction at $m = 0$ and $m = 1$ in step (iii), with the corresponding changes made in future steps.
- The IFT in step (v) need not be calculated for all m and n . Specifically, the short-ranged nature of the interatomic potential can be utilized here to truncate m and n after only a few terms.

6.4 Cauchy–Born Rule

In the coarse scale-only region, where the MD force is unavailable due to the elimination of those atomistic degrees of freedom, an approximation to the right-hand side of (6.99), the $\mathbf{N}^T \mathbf{f}(\mathbf{u})$ term, must be made. The goal is to utilize the MD potential in the expression for the coarse scale force despite the absence of the MD degrees of freedom. We shall discuss two methods for applying this force, the Cauchy–Born rule, and the virtual atom cluster (VAC) model.

The Cauchy–Born rule is a homogenization method by which continuum stress and stiffness measures can be obtained directly from an interatomic potential; the link between the atomistic and continuum is achieved by way of the deformation gradient \mathbf{F} . As the Cauchy–Born rule is a homogenization method, the major assumption invoked when using the approach is that the lattice underlying any continuum point is required to deform homogeneously according to the continuum deformation gradient \mathbf{F} . Further expositions on the Cauchy–Born rule and its application to solid mechanics can be found in Tadmor et al. (1996), Klein (1999) and Arroyo and Belytschko (2002).

To utilize the Cauchy–Born rule in the bridging scale context, we first assume that the potential energy $U(\mathbf{u})$ for the system can be decomposed as

$$U(\mathbf{u}) = \sum_{\alpha} W_{\alpha}(\mathbf{u}) \Delta V_{\alpha} \quad (6.112)$$

where W_{α} is the potential energy *density* centered at atom α . Comparing the right-hand sides of (6.19) and (6.22), we find the relation

$$(\mathbf{N}^T \mathbf{f})_I = -\frac{\partial U(\mathbf{u})}{\partial \mathbf{d}_I} \quad (6.113)$$

Substituting (6.112) into (6.113), we obtain

$$(\mathbf{N}^T \mathbf{f})_I = - \sum_{\alpha} \frac{\partial W_{\alpha}(\mathbf{u})}{\partial \mathbf{d}_I} \Delta V_{\alpha} \quad (6.114)$$

In order to use the Cauchy–Born rule, we use a chain rule on (6.114) to obtain

$$(\mathbf{N}^T \mathbf{f})_I = - \sum_{\alpha} \frac{\partial W_{\alpha}}{\partial \mathbf{F}_{\alpha}^T} \frac{\partial \mathbf{F}_{\alpha}^T}{\partial \mathbf{d}_I} \Delta V_{\alpha} \quad (6.115)$$

Simplifying further,

$$(\mathbf{N}^T \mathbf{f})_I = - \sum_{\alpha} \frac{\partial N_I}{\partial \mathbf{X}}|_{\mathbf{x}=\mathbf{x}_{\alpha}} \frac{\partial W_{\alpha}}{\partial \mathbf{F}_{\alpha}^T} \Delta V_{\alpha} \quad (6.116)$$

Noting that the derivative of the energy density W with respect to \mathbf{F}^T gives the first Piola–Kirchoff stress \mathcal{P} , the summation in (6.116) can be approximated by a discrete summation as

$$(\mathbf{N}^T \mathbf{f})_I = - \sum_q \frac{\partial N_I}{\partial \mathbf{X}}(\mathbf{X}_q) \mathcal{P}(\mathbf{X}_q) w_q \quad (6.117)$$

where w_q is the integration weight associated with point \mathbf{X}_q .

6.5 Virtual Atom Cluster Method

6.5.1 Motivations and General Formulation

An alternative approach to evaluating the coarse scale internal force (6.99) is reviewed in this section. This approach, termed the *virtual atom cluster* (VAC) method by Qian et al. (2004), was developed with the notion that although the idea of building a continuum model based on an atomistic model seems straightforward, the development of a continuum theory does not satisfy the need for revealing the full spectrum of physics involved in related nanotechnology applications. This is reflected in two major limitations of the continuum approach: first of all, by building the mechanics at fine scales into the coarse scale based on crystal elasticity, key information about the electrons is lost. This is a serious impediment to the prediction of the coupling between mechanical and other physical properties. Secondly, it has been shown that the widely used Born hypothesis needs to be modified (see Arroyo and Belytschko 2002, Smith et al. 2000 and Zhang et al. 2002) to account for nonprimitive lattices and nonlocal interactions, which are common in nanomaterials. This brings additional difficulties when it comes to interpreting the results that are obtained based on the continuum models. One example is the evaluation of the elastic modulus for nanostructures containing a single layer of atoms, which is still a disputable concept.

These difficulties, as a result of the comparison between the model and actual atomistic behaviors, recently motivated the development of a new model, which is presented in this section, to be used as a robust representation for the nanoscale system. This model is termed a *virtual atom cluster* (VAC) model for reasons that will be described in the rest of the section. The model is proposed as an effective representation of the interactions at the atomic scale and can be linked to a coarse scale simulation method such as meshfree or FE methods. The linkage ensures the scalability of the numerical implementation and

the accuracy in describing the mechanics of the nanostructure. The key feature of the VAC model is that the atomistic description is directly embedded in the FE simulation without using any stress or strain concepts. This allows for direct passage of information between the QM and FE methods, which enables a fully coupled multiphysics approach with the quantum mechanical representation at multiple scales.

To illustrate the implementation of the VAC model, the general formulation of the method is described by first writing a two-scale decomposition in which the total scale displacement variable u_α for the α th atom in a nanoscale system can be decomposed into two different components, that is,

$$\mathbf{u}_\alpha = \bar{\mathbf{u}}_\alpha + \tilde{\mathbf{u}}_\alpha \quad (6.118)$$

where $\bar{\mathbf{u}}_\alpha$ is the coarse scale component and is established by constructing FEM or meshfree shape functions over a set of nodal points, that is,

$$\bar{\mathbf{u}}_\alpha = \sum_I N_I(\mathbf{X}_\alpha) \mathbf{d}_I \quad (6.119)$$

where $N_I(\mathbf{X}_\alpha)$ is the shape function defined at computational node I and evaluated at the α th atom with material coordinate \mathbf{X}_α , and \mathbf{d}_I is the displacement vector at node I . In this section, Greek letters (such as α, β, γ) will be used as indices for atoms, and capital subscripts (such as I, J, K) will be used for computational nodes.

We use Figure 6.11 to illustrate the meaning of $\tilde{\mathbf{u}}_\alpha$. Figure 6.11 is an illustration of the multiscale decomposition for a single-walled carbon nanotube. The carbon atoms are plotted as empty circles that are connected with lines that represent the bonds. The solid circles are the computational nodes based on FEM/meshfree discretization. The shaded surface is the corresponding coarse scale approximation. The differences between the FEM/meshfree approximation and the molecular structure can be clearly seen in the zoom-in plot. For each atom α , the difference between the interpolated position on the shaded surface using (6.119) and its actual position is defined as the fine scale variable $\tilde{\mathbf{u}}_\alpha$. Note that $\mathbf{u}_\alpha, \bar{\mathbf{u}}_\alpha, \tilde{\mathbf{u}}_\alpha$ and \mathbf{d}_I are all 3×1 column vectors.

It is observed from Figure 6.11 that $\tilde{\mathbf{u}}_\alpha$ becomes insignificant in the region far away from the local buckling area, and thus we assume that FEM/meshfree approximation is sufficient to describe the deformation in these regions. Therefore, the addition of the molecular structure is needed only in the local buckling region. This assumption leads to the final multiscale discretization scheme as shown in Figure 6.12. As can be seen, there are two different computational domains: the first is the coupled domain (defined as Ω_2) in which the molecular structure coexists with the FEM/meshfree discretization. The partition based on (6.118) holds and a coupled computational scheme is expected. The second is the coarse scale domain (defined as Ω_1) where only FEM/meshfree discretization exists. The fine scale component is assumed to be zero.

Denote na as the total number of atoms in the original system, nt as the number of atoms in the coupled domain Ω_2 and nc as the number of atoms in the coarse scale domain Ω_1 , where $na = nt + nc$. Equations (6.118) and (6.119) shall hold for $\alpha = 1$ to na . Defining $\mathbf{u} = \{\mathbf{u}_1, \dots, \mathbf{u}_\alpha, \dots, \mathbf{u}_{na}\}^T$, $\bar{\mathbf{u}} = \{\bar{\mathbf{u}}_1, \dots, \bar{\mathbf{u}}_\alpha, \dots, \bar{\mathbf{u}}_{na}\}^T$ and $\tilde{\mathbf{u}} = \{\tilde{\mathbf{u}}_1, \dots, \tilde{\mathbf{u}}_\alpha, \dots, \tilde{\mathbf{u}}_{na}\}^T$, we have, corresponding to (6.118),

$$\mathbf{u} = \bar{\mathbf{u}} + \tilde{\mathbf{u}} \quad (6.120)$$

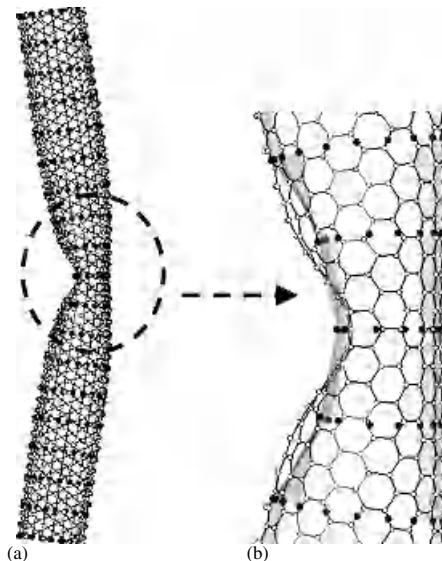


Figure 6.11 (a) Multiscale partition for a deformed single-walled carbon nanotube; see Qian et al. (2004). Empty circles connected with lines represent the molecular structures. Filled circles are computational nodes. (b) A zoom-in plot of the local region. Reprinted from Computer Methods in Applied Mechanics and Engineering, 193(17–20), Qian et al., A multiscale projection method for the analysis of carbon nanotubes, 1603–1632, 2004, with permission from Elsevier.

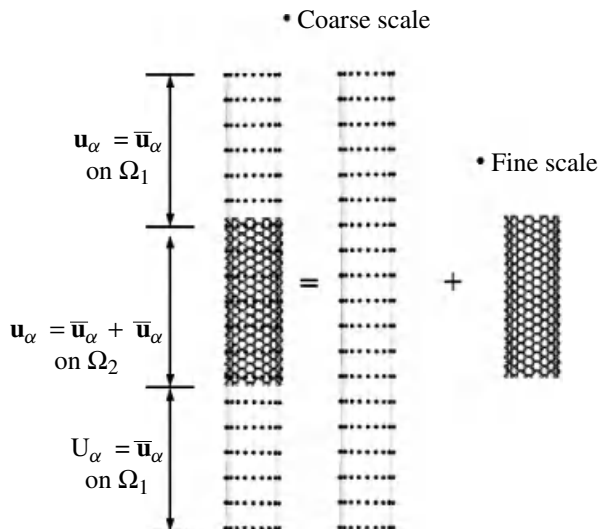


Figure 6.12 Multiscale discretization scheme for the analysis of carbon nanotubes; see Qian et al. (2004). Reprinted from Computer Methods in Applied Mechanics and Engineering, 193(17–20), Qian et al., A multiscale projection method for the analysis of carbon nanotubes, 1603–1632, 2004, with permission from Elsevier.

Defining $\mathbf{d} = \{\mathbf{d}_1, \dots, \mathbf{d}_\alpha, \dots, \mathbf{d}_{na}\}^T$ as the nodal displacement vector and NP as the total number of computational nodes, (6.119) can also be generalized as

$$\bar{\mathbf{u}} = \begin{bmatrix} \bar{\mathbf{u}}_1 \\ \vdots \\ \bar{\mathbf{u}}_\alpha \\ \vdots \\ \bar{\mathbf{u}}_{na} \end{bmatrix} = \begin{bmatrix} N_1(\mathbf{X}_1)\mathbf{I} & \dots & N_I(\mathbf{X}_1)\mathbf{I} & \dots & N_{NP}(\mathbf{X}_1)\mathbf{I} \\ \vdots & \ddots & \vdots & \ddots & \vdots \\ N_1(\mathbf{X}_\alpha)\mathbf{I} & \dots & N_I(\mathbf{X}_\alpha)\mathbf{I} & \dots & N_{NP}(\mathbf{X}_\alpha)\mathbf{I} \\ \vdots & \ddots & \vdots & \ddots & \vdots \\ N_1(\mathbf{X}_{na})\mathbf{I} & \dots & N_I(\mathbf{X}_{na})\mathbf{I} & \dots & N_{NP}(\mathbf{X}_{na})\mathbf{I} \end{bmatrix} \begin{bmatrix} \bar{\mathbf{d}}_1 \\ \vdots \\ \bar{\mathbf{d}}_I \\ \vdots \\ \bar{\mathbf{d}}_{NP} \end{bmatrix} = \mathbf{N}\mathbf{d} \quad (6.121)$$

where \mathbf{I} is a 3×3 identity matrix and N represents the corresponding $(3 \times na)$ by $(3 \times np)$ shape function matrix.

On the basis of (6.120) and (6.121), the multiscale decomposition finally reads

$$\mathbf{u} = \bar{\mathbf{u}} + \tilde{\mathbf{u}} = \mathbf{N}\mathbf{d} + \tilde{\mathbf{u}} \quad (6.122)$$

The coarse and fine scale components can also be obtained by applying projection operators \mathbf{P} and \mathbf{Q} on the total scale, that is,

$$\begin{aligned} \bar{\mathbf{u}} &= \mathbf{P}\mathbf{u} \\ \tilde{\mathbf{u}} &= \mathbf{Q}\mathbf{u} \end{aligned} \quad (6.123)$$

where \mathbf{P} and \mathbf{Q} are square matrices with dimension of $3 \times na$. The details on how to obtain \mathbf{P} and \mathbf{Q} will be discussed later.

With the two-scale decomposition scheme given by (6.122), the variation of the test function is given as

$$\delta\mathbf{u} = \mathbf{N}\delta\mathbf{d} + \delta\tilde{\mathbf{u}} \quad (6.124)$$

For a nanoscale system, the total energy is now

$$W = W^{\text{int}} - W^{\text{ext}} + W^{\text{kin}} \quad (6.125)$$

where W^{int} , W^{ext} and W^{kin} are the internal energy, external work and kinetic energy, respectively. The principle of virtual work requires that

$$\delta W(\mathbf{u}) = 0 \quad (6.126)$$

Given the multiscale decomposition in (6.122), the variational equation can be further expressed as

$$\delta W(\mathbf{u}) = \frac{\partial W}{\partial \mathbf{u}} \delta \mathbf{u} = \frac{\partial W}{\partial \mathbf{u}} \delta (\bar{\mathbf{u}} + \tilde{\mathbf{u}}) = 0 \quad (6.127)$$

Note that $\partial W / \partial \mathbf{u} = \partial(W^{\text{int}} - W^{\text{ext}} + W^{\text{kin}}) / \partial \mathbf{u} = (\mathbf{f}^{\text{int}} - \mathbf{f}^{\text{ext}} + \mathbf{f}^{\text{kin}})^T$ is a row vector in (6.127) in which \mathbf{f}^{int} , \mathbf{f}^{ext} and \mathbf{f}^{kin} are the column vectors that represent the internal, external and inertial forces at the atomistic scale.

Substituting the test function given in (6.124) into (6.127), we have

$$\delta W(\mathbf{u}) = [\mathbf{f}^{\text{int}} - \mathbf{f}^{\text{ext}} + \mathbf{f}^{\text{kin}}]^T [\mathbf{N}\delta\mathbf{d} + \delta\tilde{\mathbf{u}}] \quad (6.128)$$

Since $\delta W(\mathbf{u})$ is a scalar, $\delta W = [\delta W]^T$ and (6.128) gives

$$\begin{aligned}\delta W(\mathbf{u}) &= [\delta W(\mathbf{u})] T = [\mathbf{N} \delta \mathbf{d} + \delta \tilde{\mathbf{u}}]^T [\mathbf{f}^{\text{int}} - \mathbf{f}^{\text{ext}} + \mathbf{f}^{\text{kin}}] \\ &= \delta \mathbf{d}^T \mathbf{N}^T [\mathbf{f}^{\text{int}} - \mathbf{f}^{\text{ext}} + \mathbf{f}^{\text{kin}}] + \delta \tilde{\mathbf{u}}^T [\mathbf{f}^{\text{int}} - \mathbf{f}^{\text{ext}} + \mathbf{f}^{\text{kin}}] \\ &= 0\end{aligned}\quad (6.129)$$

On the basis of the basic principles of variational calculus, (6.129) is equivalent to solving the following:

$$\mathbf{N}^T [\mathbf{f}^{\text{int}}(\bar{\mathbf{u}}, \tilde{\mathbf{u}}) + \mathbf{f}^{\text{kin}}(\bar{\mathbf{u}}, \tilde{\mathbf{u}})] = \mathbf{N}^T \mathbf{f}^{\text{ext}}(\bar{\mathbf{u}}, \tilde{\mathbf{u}}) \quad (6.130)$$

and

$$\mathbf{f}^{\text{int}}(\bar{\mathbf{u}}, \tilde{\mathbf{u}}) + \mathbf{f}^{\text{kin}}(\bar{\mathbf{u}}, \tilde{\mathbf{u}}) = \mathbf{f}^{\text{ext}}(\bar{\mathbf{u}}, \tilde{\mathbf{u}}) \quad (6.131)$$

Remarks: Although the expression of (6.131) is the same as the one commonly used in atomistic simulation, it serves a different purpose, that is, to recover the fine scale component $\tilde{\mathbf{u}}$ in the enriched region that cannot be solved from (6.130).

Because (6.130) provides the discretized equation that is, solved for each computational node, we term it the *coarse scale equation* in the sense that the density of computational nodes is typically coarser than the atomic density. For instance, at node I , the corresponding discretized equation reads

$$\sum_{\alpha=1}^{na} N_I(\mathbf{X}_\alpha) [\mathbf{f}_\alpha^{\text{int}}(\bar{\mathbf{u}}, \tilde{\mathbf{u}}) + \mathbf{f}_\alpha^{\text{kin}}(\bar{\mathbf{u}}, \tilde{\mathbf{u}}) - \mathbf{f}_\alpha^{\text{ext}}(\bar{\mathbf{u}}, \tilde{\mathbf{u}})] = 0 \quad (6.132)$$

As mentioned previously, the fine scale variable $\tilde{\mathbf{u}}$ is assumed to be zero in the coarse scale domain Ω_1 . Therefore, (6.132) can be further written as

$$\begin{aligned}&\sum_{\alpha \in \Omega_1} N_I(\mathbf{X}_\alpha) [\mathbf{f}_\alpha^{\text{int}}(\bar{\mathbf{u}}) + \mathbf{f}_\alpha^{\text{kin}}(\bar{\mathbf{u}}) - \mathbf{f}_\alpha^{\text{ext}}(\bar{\mathbf{u}})] \\ &+ \sum_{\alpha \in \Omega_2} N_I(\mathbf{X}_\alpha) [\mathbf{f}_\alpha^{\text{int}}(\bar{\mathbf{u}}, \tilde{\mathbf{u}}) + \mathbf{f}_\alpha^{\text{kin}}(\bar{\mathbf{u}}, \tilde{\mathbf{u}}) - \mathbf{f}_\alpha^{\text{ext}}(\bar{\mathbf{u}}, \tilde{\mathbf{u}})] = 0\end{aligned}\quad (6.133)$$

It can be seen that two summations are involved in this coarse scale equation and they are defined in different domains. The first summation in (6.133) requires additional treatment, as the direct implementation will only increase the computational cost as compared with a full-scale atomistic simulation. This is simply due to the fact that the exact number of atoms nc in Ω_1 is very large. To reduce the computational cost, a representative VAC model is established to replace this summation with a reduced quadrature. Details on how to build a VAC model will be given in the following section. The second summation in (6.133) is implemented as the exact sum of the atoms that are located in domain Ω_2 . Since Ω_2 is a local region, the number of atoms nt is far less than nc and can be treated directly.

6.5.2 General Idea of the VAC Model

The VAC model is developed by directly considering the dependence of the energy on the displacement or, equivalently, the deformation mapping instead of strain. Since such dependence is considered, there is no need for concepts such as stress and strain.

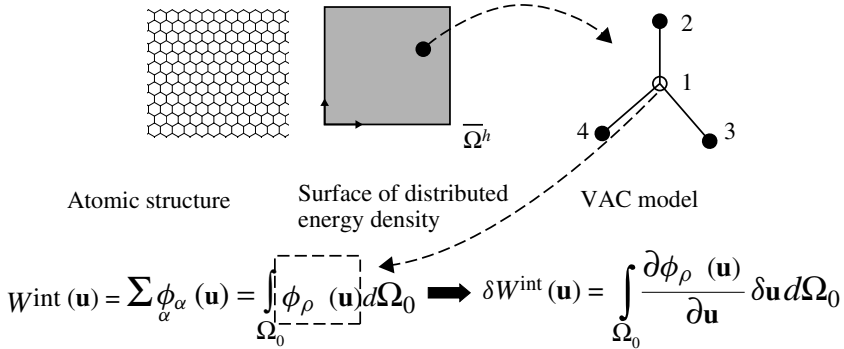


Figure 6.13 VAC model for the graphene sheet. The molecular model is converted to a structure of the same geometry with the energy density represented by the VAC; see Qian et al. (2004). Reprinted from Computer Methods in Applied Mechanics and Engineering, 193(17–20), Qian et al., A multiscale projection method for the analysis of carbon nanotubes, 1603–1632, 2004, with permission from Elsevier.

A VAC model is the minimum set of atoms that forms a cluster for representing the energy density. It can be extracted from the lattice structure on the basis of its translational symmetry properties. Figure 6.13 illustrates the steps to obtain the VAC for a graphene sheet, which can be represented using linear combinations of Bravais Lattices (Kittel 1976). The next step is to convert the original molecular structure to a structure of the same geometry with a continuous energy density distribution. The energy density corresponding to any point within the geometry is represented by the VAC. The word “virtual” comes from the fact that the VAC does not have to correspond to the physical atoms as in the quasi-continuum method of Knap and Ortiz (2001) and Tadmor et al. (1996).

Since the VAC represents the continuously distributed energy density, the potential energy of the nanoscale system can be evaluated using a continuous integral rather than the exact summation of the atoms (the first equation in Figure 6.13). This allows the use of numerical quadrature (such as Gauss) in the implementation of the first equation in (6.132) and (6.133), which results in a great reduction in the computational cost as compared with MD. On the basis of the VAC formulation, (6.133) can be rewritten as

$$\begin{aligned}
 & \int_{\Omega_1} N_I(\mathbf{X}) \frac{\partial \phi_{\rho}(\mathbf{u})}{\partial \mathbf{u}} d\Omega_1 + \sum_{\alpha \in \Omega_1} N_I(\mathbf{X}_{\alpha}) [\mathbf{f}_{\alpha}^{\text{kin}}(\bar{\mathbf{u}}) - \mathbf{f}_{\alpha}^{\text{ext}}(\bar{\mathbf{u}})] \\
 & + \sum_{\alpha \in \Omega_2} N_I(\mathbf{X}_{\alpha}) [\mathbf{f}_{\alpha}^{\text{int}}(\bar{\mathbf{u}}, \tilde{\mathbf{u}}) + \mathbf{f}_{\alpha}^{\text{kin}}(\bar{\mathbf{u}}, \tilde{\mathbf{u}}) - \mathbf{f}_{\alpha}^{\text{ext}}(\bar{\mathbf{u}}, \tilde{\mathbf{u}})] = 0
 \end{aligned} \quad (6.134)$$

In numerical implementations, the first term in (6.134) will be evaluated by prescribing quadrature points and imposing the VAC model on these quadrature points.

6.5.3 Three-Way Concurrent Coupling with QM Method

As can be seen from (6.130) and (6.131), the implementation requires the coupling between three different scales: the coarse scale represented by the FE, the fine scale represented by

the atoms and the quantum scale represented by the QM equations. The general solution methodology shall provide procedures on how to realize the concurrent coupling among these three different scales. Note that the energy density function ϕ_ρ in the VAC model (Figure 6.13) can be calculated from the QM method. In the region where the FE approximation represents the coarse scale deformation, it is assumed that the translational symmetry properties of the lattice still hold locally since the deformation is moderate. Therefore, the QM method can be directly applied to the VAC model by taking advantage of the symmetry to give ϕ_ρ and its derivatives based on the Hellmann–Feynman (1939) theorem. These quantities will then be fed back to the FE through (6.132) and (6.133); the FE, in turn, provides the updated configuration of the VAC through the FE shape functions. This interaction realizes the coupling between FE and QM.

Secondly, the interaction between QM and MD can be implemented directly by coupling MD with the same quantum mechanical model as used in FE. This ensures consistency between the FE and MD. Although a different QM method will be used here, the resulting QM/MD formulation follows the idea similar to that in *ab initio* MD (Car and Parrinello 1985), in which electronic wave functions and the motion of the system are solved simultaneously. The remaining questions are when and how to initiate the concurrent scheme. In general, MD is not needed until fine scale deformation such as buckling starts. Therefore, the question is how to identify such a region. Here, we utilize the maximum bond length and angle that can be directly taken from the VAC model. The reason is that the convexity of molecular potential is directly related to the bond length and angle. Once the threshold value is attained in a certain region, the deformed atomistic structure will be reproduced in that region using the shape functions, and the concurrent coupling scheme is initialized. The three-way coupling scheme is shown in Figure 6.14.

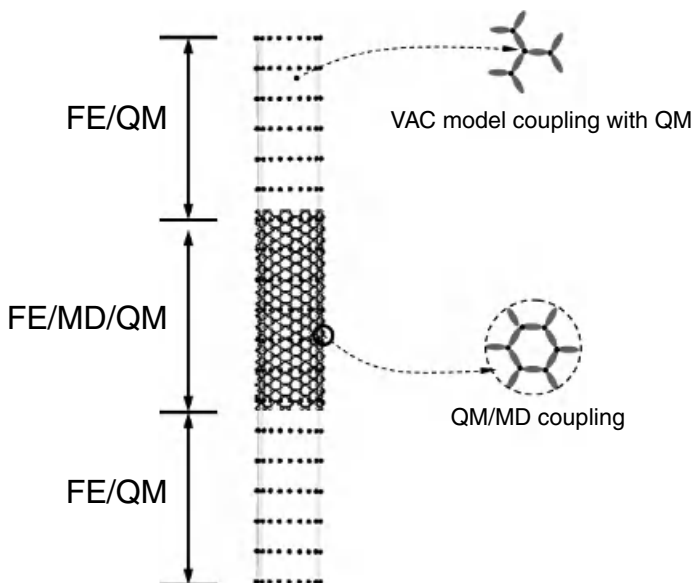


Figure 6.14 An illustration of the concurrent scheme that couples among FE, MD and QM methods.

Before any specific QM method is introduced, we first write the Schrödinger equation, which is

$$H|\psi\rangle = E|\psi\rangle \quad (6.135)$$

The goal of the QM method is to solve (6.135) as a typical eigenvalue problem to obtain the energy eigenvalues E_k in which k ranges from 1 to nq and nq is the total number of atomic orbitals. Correspondingly, $|\psi\rangle_k$ is the eigenstate. If both of the quantities are known, the total internal energy is

$$W^{\text{int}} = \sum_{k=1}^{\text{HOMO}} \langle \psi_k | H | \psi_k \rangle + E^{\text{ion}}(u) \quad (6.136)$$

where HOMO stands for the highest occupied molecular orbitals. Correspondingly, the summation is performed only from the ground state ($k = 1$) to the highest that can be occupied by the electrons. Any $k > \text{HOMO}$ will lead to the antibonding state and will not be considered here. The second term E^{ion} represents the energy due to the presence of ions and can be typically expressed in an empirical formula. To combine this with the VAC model, we note that

$$\phi_\rho = \frac{W^{\text{int}}}{V_0} = \left[\sum_{k=1}^{\text{HOMO}} \langle \psi_k | H_{\text{vac}} | \psi_k \rangle + E_{\text{vac}}^{\text{ion}}(u) \right] / V_0 \quad (6.137)$$

where V_0 is the original volume that the VAC model occupies in the original configuration. Subscript vac indicates that the QM method is only applied to the VAC model instead of the entire system, which brings in additional computational efficiency. The details of the implementation will be provided later. One can further write

$$\frac{\partial \phi_\rho}{\partial u} = - \left[\sum_{k=1}^{\text{HOMO}} \left\langle \psi_k \left| \frac{\partial H_{\text{vac}}}{\partial u} \right| \psi_k \right\rangle + \frac{\partial E_{\text{vac}}^{\text{ion}}(u)}{\partial u} \right] / V_0 \quad (6.138)$$

on the basis of the Hellmann–Feynman (1939) theorem. Note that the differentiation operator in (6.136) can be performed analytically. To combine (6.136) with MD, we can write

$$f_\alpha^{\text{int}} = - \left[\sum_{k=1}^{\text{HOMO}} \left\langle \psi_k \left| \frac{\partial H_{\text{MD}}}{\partial u} \right| \psi_k \right\rangle + \frac{\partial E_{\text{MD}}^{\text{ion}}(u)}{\partial u} \right] \quad (6.139)$$

Finally, the three-way coupling scheme described above can be expressed as the following equations.

QM/FE coupling:

$$\begin{aligned} \int_{\Omega_1} N_I(\mathbf{X}) \frac{\partial \phi_\rho(u)}{\partial u} d\Omega_1 + \sum_{\alpha \in \Omega_1} N_I(\mathbf{X}_\alpha) [\mathbf{f}_\alpha^{\text{kin}}(\bar{\mathbf{u}}) - \mathbf{f}_\alpha^{\text{ext}}(\bar{\mathbf{u}})] \\ + \sum_{\alpha \in \Omega_2} N_I(\mathbf{X}_\alpha) [\mathbf{f}_\alpha^{\text{int}}(\bar{\mathbf{u}}, \tilde{\mathbf{u}}) + \mathbf{f}_\alpha^{\text{kin}}(\bar{\mathbf{u}}, \tilde{\mathbf{u}}) - \mathbf{f}_\alpha^{\text{ext}}(\bar{\mathbf{u}}, \tilde{\mathbf{u}})] = 0 \end{aligned} \quad (6.140)$$

$$\frac{\partial \phi_\rho}{\partial u} = -\frac{1}{V_0} \left[\sum_{k=1}^{\text{HOMO}} \left\langle \psi_k \left| \frac{\partial H_{\text{vac}}}{\partial u} \right| \psi_k \right\rangle + \frac{\partial E_{\text{vac}}^{\text{ion}}(u)}{\partial u} \right] \quad (6.141)$$

$$H_{\text{vac}}|\psi\rangle = E_{\text{vac}}|\psi\rangle \quad (6.142)$$

$$f_\alpha^{\text{int}} = - \left[\sum_{k=1}^{\text{HOMO}} \left\langle \psi_k \left| \frac{\partial H_{\text{MD}}}{\partial u} \right| \psi_k \right\rangle + \frac{\partial E_{\text{MD}}^{\text{ion}}(u)}{\partial u} \right] \quad (6.143)$$

QM/MD coupling:

$$\mathbf{f}^{\text{int}}(\bar{\mathbf{u}}, \tilde{\mathbf{u}}) + \mathbf{f}^{\text{kin}}(\bar{\mathbf{u}}, \tilde{\mathbf{u}}) = \mathbf{f}^{\text{ext}}(\bar{\mathbf{u}}, \tilde{\mathbf{u}}) \quad (6.144)$$

$$f_\alpha^{\text{int}} = - \left[\sum_{k=1}^{\text{HOMO}} \left\langle \psi_k \left| \frac{\partial H_{\text{MD}}}{\partial u} \right| \psi_k \right\rangle + \frac{\partial E_{\text{MD}}^{\text{ion}}(u)}{\partial u} \right] \quad (6.145)$$

6.5.4 Tight-Binding Method for Carbon Systems

The Tight-Binding (TB) method has been applied to a large variety of covalent-bonded materials such as C, Si, Ga and Ge and various metals. Here, the TB model that was developed for carbon system by Xu et al. (1992) will be reviewed. For a system of carbon atoms, the total energy of the system shall consist of two parts: the energy due to the electrons and the energy due to the short-range ion–ion repulsion,

$$E = E^{\text{TB}} + E^{\text{Rep}} \quad (6.146)$$

In Xu's model, the molecular orbital bases that are used include $2s$, $2p_x$, $2p_y$, and $2p_z$ basis states of the carbon atom. Considering that carbon atom i interacts with j , the possible interactions among the atomic orbitals are $ss\sigma$, $sp\sigma$, $pp\sigma$ and $pp\pi$ bonds. Correspondingly, these interactions are represented by the elements in $H_{ij} = \langle \phi_i | H | \phi_j \rangle$, which are shown in Figure 6.15.

The interactions on the same atom correspond to the diagonal terms in the matrix, in which ε_s and ε_p are values determined from first-principle calculations. In Xu's model, $\varepsilon_s = -2.99$ (eV) and $\varepsilon_p = -3.71$ (eV). The interactions between different atoms are represented by the off-diagonal elements, which are also usually referred to as *hopping integrals*. Owing to both the orientation of the atomic orbitals and the relative positions between the atoms, the hopping integrals are parametrized as functions of these geometric factors, which are given according to the two-center formulation proposed by Slater and Koster (1954). The detailed forms are given as follows:

$$E_{ss}(r_{ij}) = V_{ss\sigma}s(r_{ij}), \quad E_{sx}(r_{ij}) = lV_{sp\sigma}s(r_{ij}) \quad (6.147)$$

$$E_{sy}(r_{ij}) = mV_{sp\sigma}s(r_{ij}), \quad E_{sz}(r_{ij}) = nV_{sp\sigma}s(r_{ij}) \quad (6.148)$$

$$E_{xx}(r_{ij}) = [l^2 V_{pp\sigma} + (1 - l^2) V_{pp\pi}] s(r_{ij}) \quad (6.149)$$

$$E_{yy}(r_{ij}) = [m^2 V_{pp\sigma} + (1 - m^2) V_{pp\pi}] s(r_{ij}) \quad (6.150)$$

$$E_{zz}(r_{ij}) = [n^2 V_{pp\sigma} + (1 - n^2) V_{pp\pi}] s(r_{ij}) \quad (6.151)$$

$$\begin{array}{c}
 \begin{array}{c} i \\ j \end{array} \left\{ \begin{array}{c} \overbrace{i} \\ \overbrace{j} \end{array} \right\} = \left[\begin{array}{cc} \hat{H}_{ii} & \hat{H}_{ij} \\ \hat{H}_{ji} & \hat{H}_{jj} \end{array} \right] \\
 \begin{array}{|c|c|c|c|c|c|c|c|c|} \hline
 & s & p_x & p_y & p_z & s & p_x & p_y & p_z \\ \hline
 s & \varepsilon_s & 0 & 0 & 0 & E_{ss}(r_{ji}) & E_{sx}(r_{ji}) & E_{sy}(r_{ji}) & E_{sz}(r_{ji}) \\ \hline
 p_x & 0 & \varepsilon_p & 0 & 0 & E_{xs}(r_{ji}) & E_{xx}(r_{ji}) & E_{xy}(r_{ji}) & E_{xz}(r_{ji}) \\ \hline
 p_y & 0 & 0 & \varepsilon_p & 0 & E_{ys}(r_{ji}) & E_{yx}(r_{ji}) & E_{yy}(r_{ji}) & E_{yz}(r_{ji}) \\ \hline
 p_z & 0 & 0 & 0 & \varepsilon_p & E_{zs}(r_{ji}) & E_{zx}(r_{ji}) & E_{zy}(r_{ji}) & E_{zz}(r_{ji}) \\ \hline
 s & E_{ss}(r_{ji}) & E_{sx}(r_{ji}) & E_{sy}(r_{ji}) & E_{sz}(r_{ji}) & \varepsilon_s & 0 & 0 & 0 \\ \hline
 p_x & E_{xs}(r_{ji}) & E_{xx}(r_{ji}) & E_{xy}(r_{ji}) & E_{xz}(r_{ji}) & 0 & \varepsilon_p & 0 & 0 \\ \hline
 p_y & E_{ys}(r_{ji}) & E_{yx}(r_{ji}) & E_{yy}(r_{ji}) & E_{yz}(r_{ji}) & 0 & 0 & \varepsilon_p & 0 \\ \hline
 p_z & E_{zs}(r_{ji}) & E_{zx}(r_{ji}) & E_{zy}(r_{ji}) & E_{zz}(r_{ji}) & 0 & 0 & 0 & \varepsilon_p \\ \hline
 \end{array} \right]
 \end{array}$$

Figure 6.15 Matrix that represents the interaction between atomic orbitals in tight-binding method.

$$E_{xy}(r_{ij}) = lm(V_{pp\sigma} - V_{pp\pi})s(r_{ij}) \quad (6.152)$$

$$E_{xz}(r_{ij}) = ln(V_{pp\sigma} - V_{pp\pi})s(r_{ij}) \quad (6.153)$$

In (6.147–6.153), l , m and n are directional cosines of the vector that point from atom i to j with its length defined as r_{ij} . The function $s(r_{ij})$ has been proposed by Goodwin et al. (1989) and takes the following form:

$$s(r) = \left(\frac{r_0}{r}\right)^n \exp\left\{n\left[-\left(\frac{r}{r_c}\right)^{n_c} + \left(\frac{r_0}{r_c}\right)^{n_c}\right]\right\} \quad (6.154)$$

with $n = 2.0$, $n_c = 6.5$, $r_c = 2.18 \text{ \AA}$ and $r_0 = 1.536329 \text{ \AA}$, according to Xu's model. Finally, the remaining parameters in (6.147–6.153) are

$$\begin{array}{ll}
 V_{ss\sigma} = -5.0 \text{ eV}, & V_{ss\sigma} = 4.7 \text{ eV} \\
 V_{ss\sigma} = 5.5 \text{ eV}, & V_{ss\sigma} = -1.55 \text{ eV}
 \end{array} \quad (6.155)$$

The ion–ion repulsive energy E^{Rep} in (6.146) is modeled by a fourth-order polynomial functional,

$$E^{\text{Rep}} = \sum_i f \left(\sum_j \phi(r_{ij}) \right) \quad (6.156)$$

where

$$\phi(r) = \phi_0 \left(\frac{d_0}{r}\right)^m \exp\left(m\left[-\left(\frac{r}{d_c}\right)^{m_c} + \left(\frac{d_0}{d_c}\right)^{m_c}\right]\right) \quad (6.157)$$

and $\phi_0 = 8.18555$ (eV), $m = 3.30304$, $m_c = 8.6655$, $d_c = 2.1052$ (\text{\AA}), $d_0 = 1.64$ (\text{\AA}), and $d_1 = 2.57$ (\text{\AA}). The functions s and ϕ are truncated at $r_1 = 2.45$ (\text{\AA}) and $d_1 = 2.57$ (\text{\AA}), respectively. Polynomial functions are further added to the tails of s and ϕ to enforce

that the two functions go smoothly to zero at a certain cutoff length. Coefficients for the polynomials of functions are given in the TB model of Xu et al. (1992).

Once the total energy due to both TB and ion–ion repulsion is determined from a given configuration, the internal force is evaluated by taking the derivative of the total energy with respect to the spatial coordinates of the atom,

$$\mathbf{f}_\alpha^{\text{int}} = -\frac{\partial W^{\text{int}}}{\partial \mathbf{x}} \quad (6.158)$$

The contribution from the ion–ion repulsion can be directly obtained by differentiating (6.154) using the chain rule. Calculation of the contribution from the TB model involves two steps. First of all, the secular equation must be solved to give n sets of energy eigenvalues and eigenstates in which n is the total number of atomic orbitals used. Once the k th eigenvalue and eigenstate are given, the electronic energy corresponding to the TB calculation is given as

$$E_k = \langle \psi_k | H | \psi_k \rangle \quad (6.159)$$

The total energy from the TB calculation is a summation over k for all the occupied electronic state, that is,

$$E^{\text{TB}} = \sum_{k=1}^{\text{HOMO}} E_k \quad (6.160)$$

The second step is to evaluate the derivatives of E^{TB} , which requires the differentiation of E_k . According to the Hellmann–Feynman (1939) theorem,

$$\frac{dE_k}{d\mathbf{x}} = \left\langle \psi_k \left| \frac{\partial H}{\partial \mathbf{x}} \right| \psi_k \right\rangle \quad (6.161)$$

Combining (6.160), (6.161) and (6.158), we obtain the procedure for evaluating the forces among the atoms.

6.5.5 Coupling with the VAC Model

The computational cost associated with force evaluations for a specific system depends on the number of basis functions n used in the TB formulation. Because the solution to the eigenvalue problem is involved, this cost is proportional to n^3 . For a system containing N carbon atoms, $n = 4N$. This is extremely expensive even for a system of a few thousand atoms. Alternatively, the computational cost can be greatly reduced by coupling the TB formulation with the VAC model.

As discussed earlier, we shall begin with the assumption given in the general description of the method, that is, translational symmetry shall hold under moderate deformation. With this assumption, the TB formulation can be applied to the unit cell of the crystal structure. An example of a two-dimensional graphene sheet is shown in Figure 6.16, where the diamond box defined by the dash-dotted lines gives the unit cell for the graphite system containing two inequivalent carbon atoms. Different shades of gray are used to define the atoms belonging to the two different groups along with a different set of indices i and j . The atoms that are used in the VAC model are defined in the circle marked by dashed

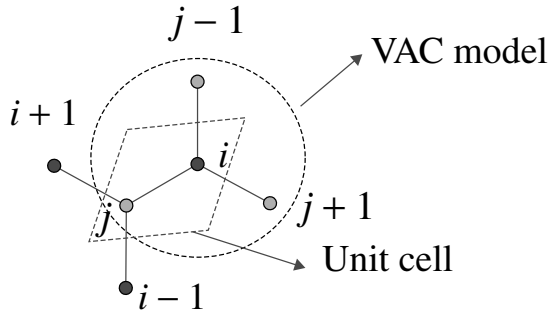


Figure 6.16 Unit cell and VAC model for two-dimensional graphite.

lines. Because of the translational symmetry, the TB Hamiltonian is an 8×8 matrix, which corresponds to the unit cell, that is,

$$\hat{H} = \begin{bmatrix} \hat{H}_{ii} & \sum_{j=1}^{j+1} \hat{H}_{ij} \\ \sum_{i=1}^{i+1} \hat{H}_{ji} & \hat{H}_{jj} \end{bmatrix} \quad (6.162)$$

All terms in (6.162) are defined on the basis of Xu's TB model in Figure 6.15. Therefore, at each quadrature point, once the configuration of the VAC model is provided, the eigenvalue problem corresponding to the TB Hamiltonian defined in (6.162) will be solved. The interatomic forces will then be evaluated on the basis of (6.161) and (6.158), which will be used to solve both the fine and coarse scale equations. As a brief summary, a flow chart of the implementation TB on the VAC model is given in Figure 6.17. Note that meshfree discretization is an approximation scheme similar to FE but requires no efforts on meshing. More details on meshfree methods and coupling TB with the VAC model can be found in Li and Liu (2002, 2004) and Qian and Gondhalekar (2004), respectively.

6.6 Staggered Time Integration Algorithm

As was previously mentioned, one strength of the bridging scale lies in the ability to update the MD and FE equations of motion using appropriate time increments for each equation. In fact, both simulations are integrated through time using widely utilized integration algorithms: velocity Verlet for MD and explicit central difference for FE. We note that the velocity Verlet and explicit central difference algorithms are equivalent; the only difference is that half-step velocities are computed for the velocity Verlet algorithm.

6.6.1 MD Update

The basic idea is that, for each computational period, both simulations are advanced by a time step Δt . The MD simulation is advanced first by m steps of size $\Delta t/m$ while the FE simulation is advanced through a single time step of size Δt . A small modification in the standard MD velocity Verlet update is required because the MD simulation requires information from the FE simulation near the boundary (see (6.100)). The modification is

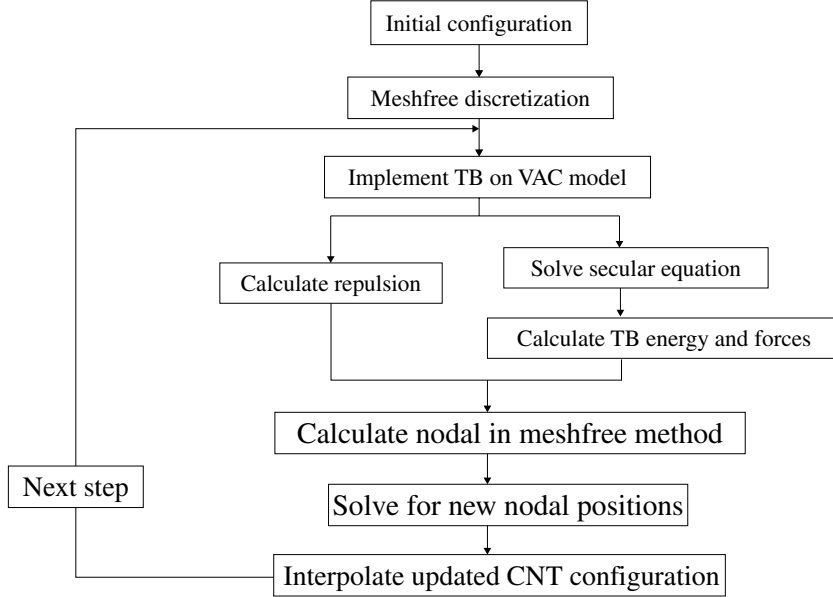


Figure 6.17 A flow chart of implementing TB scheme on the VAC model.

that the FE boundary displacement and velocity will be interpolated at fractional time steps, while the FE boundary acceleration will be assumed to be constant during the MD time subcycle. The FE boundary acceleration is assumed to be constant such that the actual FE equations of motion are not solved at each MD time step. The stability of similar staggered time integration methods with subcycling was explored in Liu (1983), Liu and Belytschko (1982) and Farhat and Lesoinne (2000).

Superscripts will be used to denote the time step, bracket notation $[j]$ will be shorthand for the fractional time step $n + \frac{j}{m}$, and the subcycle time step will be denoted $\Delta t_m = \Delta t/m$. The subscript Γ will denote FE quantities that are only needed close to the boundary. Finally, $\mathbf{f}(\mathbf{q}, \bar{\mathbf{u}}, \mathbf{h})$ will represent the entire right-hand side of (6.98) where \mathbf{h} is used to represent the time history quantities that are needed in the integration. Assuming that $\ddot{\mathbf{u}}_\Gamma^n, \dot{\mathbf{u}}_\Gamma^n, \ddot{\mathbf{u}}_\Gamma^n, \mathbf{q}^n, \mathbf{p}^n$ and \mathbf{s}^n are known, these quantities are updated by the velocity verlet algorithm as follows:

$$\ddot{\mathbf{u}}_\Gamma^{[j+1]} = \ddot{\mathbf{u}}_\Gamma^{[j]} + \dot{\mathbf{u}}_\Gamma^{[j]} \Delta t_m + \frac{1}{2} \ddot{\mathbf{u}}_\Gamma^n \Delta t_m^2 \quad (6.163)$$

$$\dot{\mathbf{u}}_\Gamma^{[j+1]} = \dot{\mathbf{u}}_\Gamma^{[j]} + \ddot{\mathbf{u}}_\Gamma^n \Delta t_m \quad (6.164)$$

$$\mathbf{q}^{[j+1]} = \mathbf{q}^{[j]} + \mathbf{p}^{[j]} \Delta t_m + \frac{1}{2} \mathbf{s}^{[j]} \Delta t_m^2 \quad (6.165)$$

$$\mathbf{p}^{[j+\frac{1}{2}]} = \mathbf{p}^{[j]} + \frac{1}{2} \mathbf{s}^{[j]} \Delta t_m \quad (6.166)$$

$$\mathbf{s}^{[j+1]} = \mathbf{M}_A^{-1} \mathbf{f}(\mathbf{q}^{[j+1]}, \ddot{\mathbf{u}}_\Gamma^{[j+1]}, \mathbf{h}^{[j+1]}) \quad (6.167)$$

$$\mathbf{p}^{[j+1]} = \mathbf{p}^{[j+\frac{1}{2}]} + \frac{1}{2} \mathbf{s}^{[j+1]} \Delta t_m \quad (6.168)$$

\mathbf{p} is the MD velocity, $\bar{\mathbf{u}}_\Gamma$ is the FE boundary displacement, $\dot{\bar{\mathbf{u}}}_\Gamma$ is the FE boundary velocity, \mathbf{q} is the MD displacement, \mathbf{s} is the MD acceleration and \mathbf{M}_A is the MD mass matrix.

6.6.2 FE Update

Once the MD quantities are obtained using the above algorithm at time $n + 1$, the FE displacements \mathbf{d} , velocities \mathbf{v} and accelerations \mathbf{a} are updated from time n to $n + 1$. This is done using a central difference scheme:

$$\mathbf{d}^{n+1} = \mathbf{d}^n + \mathbf{v}^n \Delta t + \frac{1}{2} \mathbf{a}^n \Delta t^2 \quad (6.169)$$

$$\mathbf{a}^{n+1} = \mathbf{M}^{-1} \mathbf{N}^T \mathbf{f}(\mathbf{Nd}^{n+1} + \mathbf{Q}\mathbf{q}^{n+1}) \quad (6.170)$$

$$\mathbf{v}^{n+1} = \mathbf{v}^n + \frac{1}{2} (\mathbf{a}^n + \mathbf{a}^{n+1}) \Delta t \quad (6.171)$$

where \mathbf{M} is the consistent FE mass matrix. The internal force \mathbf{f} is computed by combining the coarse scale part of the displacement \mathbf{Nd} with the fine scale part of the MD simulation $\mathbf{Q}\mathbf{q}$.

6.7 Summary of Bridging Scale Equations

In this section, we recap the important equations of this chapter, and highlight the crucial steps that are needed to obtain the desired sets of equations (6.98)–(6.100).

- (i) The first step is to obtain coupled MD and FEM equations of motion for the case in which both the coarse and fine scales coexist *everywhere* in the domain. These equations are the standard FEM momentum equation, and MD equation of motion obeying Newton's law:

$$\mathbf{M}_A \ddot{\mathbf{q}}(t) = \mathbf{f}(\mathbf{q}) \quad (6.172)$$

$$\mathbf{M} \ddot{\mathbf{d}}(t) = \mathbf{N}^T \mathbf{f}(\mathbf{u}) \quad (6.173)$$

- (ii) Owing to the desire to keep a tractable number of fine scale degrees of freedom, the fine scale was eliminated from a large portion of the domain by utilizing the inherent periodicity and repetitive structure of crystalline lattices. The key assumption was in taking the behavior of the eliminated fine scale degrees of freedom to be linear. In doing so, the coupled coarse scale and reduced fine scale equations of motion were found to be:

$$\mathbf{M}_A \ddot{\mathbf{q}}(t) = \mathbf{f}(\mathbf{q}) + \mathbf{f}_{0,m,n}^{\text{imp}}(t) + \mathbf{R}_{0,m,n}^f(t) \quad (6.174)$$

$$\mathbf{M} \ddot{\mathbf{d}}(t) = \mathbf{N}^T \mathbf{f}(\mathbf{u}) \quad (6.175)$$

where

$$\begin{aligned} \mathbf{f}_{0,m,n}^{\text{imp}}(t) &= \sum_{m'=-n_c}^{n_c} \sum_{n'=-n_c}^{n_c} \int_0^t \boldsymbol{\theta}_{m-m', n-n'}(t-\tau) \\ &\times (\mathbf{q}_{0,m',n'}(\tau) - \bar{\mathbf{u}}_{0,m',n'}(\tau) - \mathbf{R}_{0,m',n'}^d(\tau)) d\tau \end{aligned} \quad (6.176)$$

and \mathbf{R}^f is the stochastic thermal force (6.92). The random displacement vector \mathbf{R}^d for (6.92) can be derived according to (6.82), where $\mathbf{u}'(0)$ is replaced by $\mathbf{q}(0) - \bar{\mathbf{u}}(0)$; alternatively, it can be derived on the basis of a normal mode decomposition by utilizing (3.58) and (4.125).

- (iii) Removing the fine scale degrees of freedom from large parts of the domain causes the coarse scale internal force, the $\mathbf{N}^T \mathbf{f}(\mathbf{u})$ term, to be calculated differently when the MD force \mathbf{f} is not available owing to elimination. In those regions where the MD force is unavailable, the coarse scale internal force can be written as the general nonlinear finite element internal force using a hyperelastic stress such as:

$$(\mathbf{N}^T \mathbf{f})_I = - \sum_q \frac{\partial N_I}{\partial \mathbf{X}} (\mathbf{X}_q) \mathcal{P}(\mathbf{X}_q) w_q \quad (6.177)$$

where w_q is the integration weight associated with point \mathbf{X}_q . The Cauchy–Born rule (Tadmor et al. 1996) can be utilized to calculate the first Piola–Kirchoff stress \mathcal{P} using the desired interatomic potential. Likewise, the VAC method of (Qian et al. 2004) can be utilized to directly calculate the MD interatomic force \mathbf{f} at coarse scale quadrature points.

6.8 Discussion on the Bridging Scale Method

Now that the development of the bridging scale theory has been completed, a comparison between the bridging scale and the other multiscale methods is in order. The first point of comparison stems from the fact that the bridging scale is an approach inherently geared for finite temperature, dynamic problems. An approach in this direction has been undertaken by Park et al. (2004), in which the projection property of the bridging scale was utilized to derive a continuum temperature equation directly from the underlying atomistic motion. While it can be easily applied to static problems as in Qian et al. (2004), the current formulation and applications have been for dynamic simulations. This contrasts with the quasi-continuum or CADD methods, which to date have been used only for quasi-static problems.

In comparing the bridging scale with the other dynamic multiscale methods (CGMD, MAAD), one clear advantage for the bridging scale is that the coarse scale is represented everywhere, and is *not* meshed down to the atomic scale. Furthermore, the coupled MD and FE equations of motion arise naturally from a Lagrangian formulation, which combines the kinetic and potential energies of the coupled system. The effect of this is that the coarse scale time step is not restricted by the smallest, atomic-sized elements in the mesh. More importantly, this allows the use of a staggered time integration scheme, as was detailed by Wagner and Liu (2003). Thus, the coarse scale variables can evolve on an appropriate timescale, while the fine scale variables can evolve (appropriately) on a much smaller timescale.

A major advantage of the bridging scale is that the high-frequency MD waves that typically cannot be represented by the continuum are eliminated in a physically and mathematically sound manner by way of lattice mechanics arguments. The reduced MD lattice behaves as if it is part of a larger lattice owing to the impedance force (6.100), which allows

the high-frequency information typically found in the MD region to naturally dissipate into the continuum. Furthermore, the time history kernel $\theta(t)$ can be found by an automated numerical procedure that requires only standard Laplace and Fourier transform techniques. Moreover, the resulting size of $\theta(t)$ is that of the minimum number of spatial degrees of freedom; this stands in contrast to previously derived damping kernels, for example, Cai et al. (2000) and E and Huang (2002), whose size depended on the remaining number of degrees of freedom in the reduced MD region, or required that the geometry of the lattice be explicitly included in the formulation. The resulting formulation can be applied to both static and dynamics problems; examples include nonreflecting MD boundary conditions, as in Wagner et al. (2004) and Karpov et al. (2005b), quasi-static nanoindentation, as in Karpov et al. (2005), multiple scale analysis of dynamic fracture in multiple dimensions, as in Park et al. (2005b,c), and analysis of dynamic strain localization in granular materials, as in Kadouaki and Liu (2004).

Finally, as we will show in the ensuing section, the numerical examples utilizing the bridging scale have all been compared to full MD benchmark simulations. In all cases, the bridging scale simulations agree extremely well with the full MD benchmarks, even for highly nonlinear problems such as lattice fracture. These comparisons are extremely important in multiple scale simulations, as confidence in the ability of a method to faithfully reproduce the correct physics normally seen within a full MD simulation must be established.

Copyright

Material of Section 6.2.5 is reproduced from Park et al. (2005b), Copyright 2005, with permission from Elsevier. Material of Section 6.3 is reprinted from Park et al. (2005c), Copyright 2005, with permission from Taylor & Francis. The algorithm presented in Section 6.3.1 is reproduced from Park et al. (2005a) with permission from Wiley.

Bridging Scale Numerical Examples

In this chapter, we present numerical examples in one, two and three dimensions to validate the bridging scale methodology presented in the previous chapter. The one-dimensional examples concentrate on demonstrating the ability of the bridging scale to eliminate high-frequency wave reflection at the MD/FE interface. One additional simplicity that results from the one-dimensional nature of the problems is that the time history kernel $\theta(t)$ can be found analytically, unlike in higher dimensions.

Therefore, the two- and three-dimensional numerical examples are meant to validate the numerical representation for the time history kernel $\theta(t)$, which was presented in Chapter 2. The bridging scale method is furthermore tested on highly nonlinear dynamic fracture and wave propagation examples, and the ability of the numerically calculated time history kernel in eliminating high-frequency wave reflection at the MD/FE interface is shown. All results are further compared to benchmark full MD simulations for verification and validation. The results in this chapter are a summary of the one-dimensional work of Park and Liu (2004), and the two- and three-dimensional work of Park et al. (2005b,c).

7.1 Comments on Time History Kernel

As discussed in the introduction, one crucial element to the treatment of fine scale waves at the MD/FE boundary is the time history kernel $\theta(t)$. In the work of Wagner and Liu (2003), $\theta(t)$ was derived in 1D assuming a harmonic lattice, and was shown to be

$$\theta(t) = \frac{2k}{t} J_2(2\omega t) \quad (7.1)$$

where J_2 indicates a second-order Bessel function, k is the spring stiffness, and the frequency $\omega = \sqrt{k/m}$, where m is the atomic mass. The spring stiffness can be determined by

taking the second derivative of the potential V_{LJ} with respect to the atomic positions r as:

$$k = \frac{\partial^2 V_{\text{LJ}}(r)}{\partial r^2} \quad (7.2)$$

For a harmonic solid, k is simply the spring stiffness, which is constant in time. For a general nonlinear potential, k varies as a function of deformation. The numerical examples presented here utilize the Lennard-Jones (LJ) 6–12 potential. The LJ potential takes the familiar form (2.60), page 22, where σ has units of length, r is the distance between two atoms and ϵ has units of energy. In the numerical examples utilizing the LJ 6–12 potential below, the following definition will be used for k :

$$k = \frac{624\epsilon\sigma^{12}}{r^{14}} - \frac{168\epsilon\sigma^6}{r^8} \quad (7.3)$$

Since the LJ spring stiffness k is a function of position r , it is not independent of deformation. In order to obtain a constant k for the LJ potential, we evaluate k about the equilibrium lattice separation distance r_{eq} . The equilibrium lattice separation distance r_{eq} is that which minimizes the potential energy in (2.60); for the LJ 6–12 potential in one dimension, $r_{\text{eq}} = 2^{1/6}\sigma$. Setting $r = r_{\text{eq}}$ in (7.3) and then substituting that value for k into (7.1), gives the time history kernel $\theta(t)$ that is used in this chapter.

7.2 1D Bridging Scale Numerical Examples

7.2.1 Lennard-Jones Numerical Examples

We now show numerical examples utilizing a standard nonlinear interatomic potential, the LJ 6–12 potential. For simplicity, σ and ϵ were assumed to be unity, and the atoms were given a prescribed displacement containing both high- and low-frequency wavelengths similar to the Gaussian wave boundary condition used by Wagner and Liu (2003). We define low-frequency wavelengths as those wavelengths that can be represented by the finite elements, while high frequency implies wavelengths that are too short to be represented using finite elements. The purpose of using such a wave is that we will be able to conclusively show the deleterious effects of not accounting for the eliminated fine scale degrees of freedom via the time history kernel $\theta(t)$ in the MD impedance force (6.100). The initial MD displacements are shown in Figure 7.1.

Forty linear finite elements spanned the entire domain between $x = -200r_{\text{eq}}$ and $x = 200r_{\text{eq}}$, and 111 atoms were used between $x = -55r_{\text{eq}}$ and $x = 55r_{\text{eq}}$. The initial amplitude of the wave was 13% of the equilibrium spacing r_{eq} , and the FE nodal spacing was 10 times the MD atomic spacing. Fifty-five FE time steps were used, with 50 MD time steps per FE time step. The FE nodal forces in the coarse scale outside the coupled MD/FE region were calculated using the Cauchy–Born rule using the LJ 6–12 potential. Finally, the random force $\mathbf{R}(t)$ in (6.98) was taken to be zero, implying that the MD calculation was done at 0 K.

Figures 7.2 and 7.3 show the final MD and FE displacements for two distinct cases. In Figure 7.2, the MD impedance force (6.100) has been applied correctly; this is evident as the initial MD wave has propagated into the continuum, with no remaining displacements in the

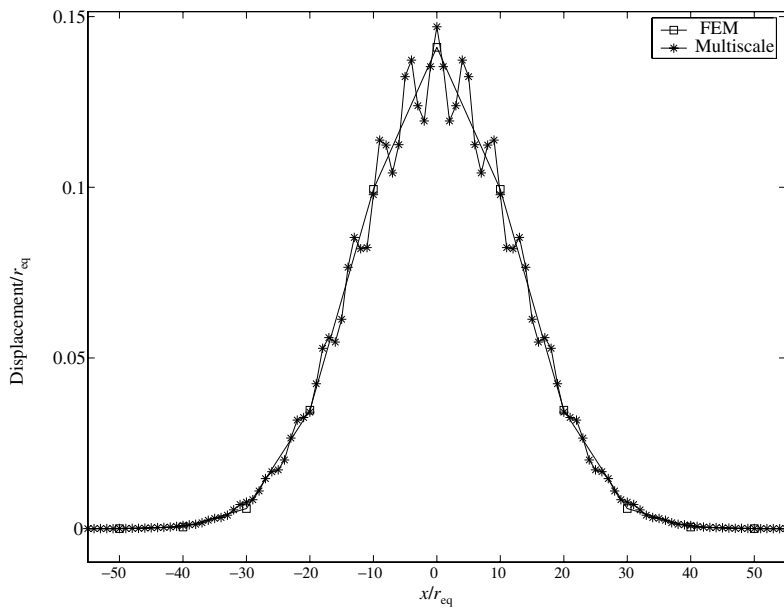


Figure 7.1 Initial MD displacements showing a combination of high- and low-frequency wavelengths.

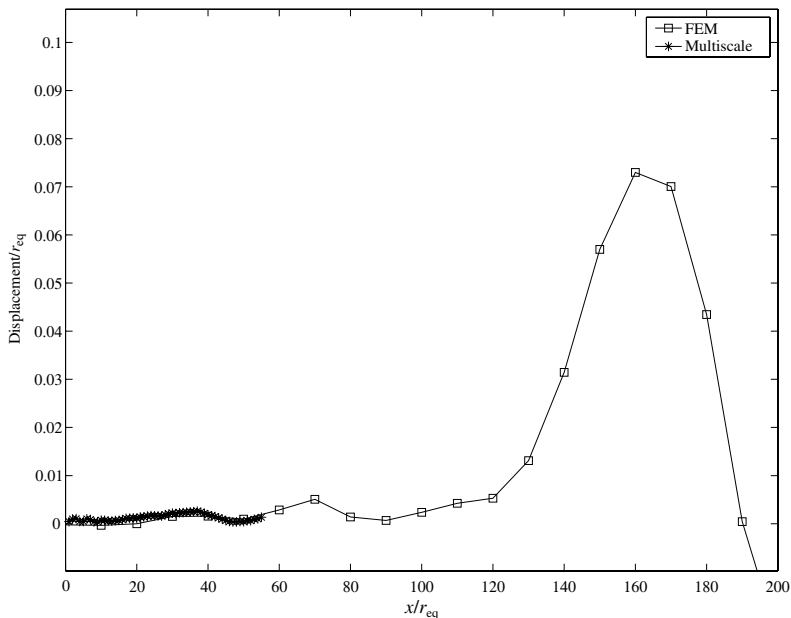


Figure 7.2 Snapshot of MD/FE displacements if MD impedance force (6.100) is applied correctly.

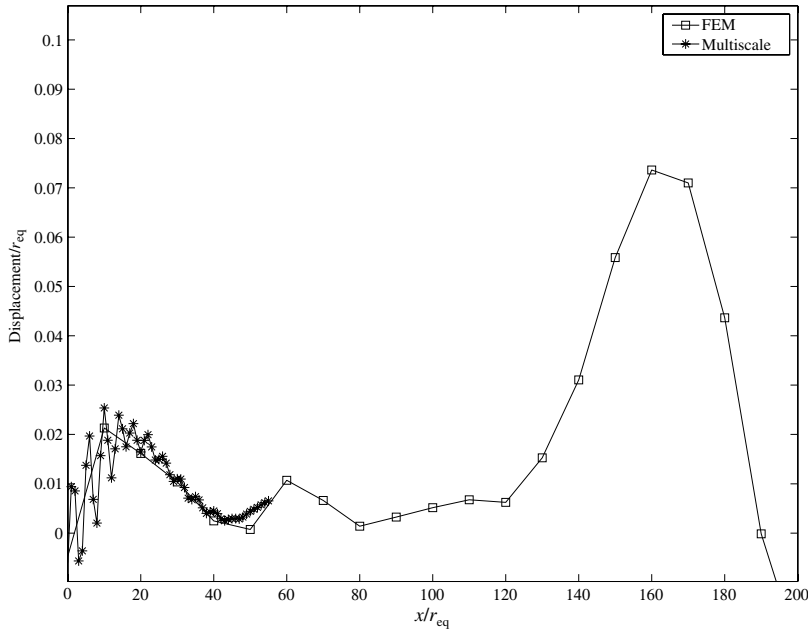


Figure 7.3 Snapshot of MD/FE displacements if MD impedance force (6.100) is not applied correctly.

MD region. In contrast, Figure 7.3 shows the case where the MD impedance force (6.100) was not applied. In this case, all the high-frequency wavelengths have been reflected back into the MD region. This fact is further visualized by monitoring the total energy (kinetic plus potential) in the MD region during the course of the simulation. As can be seen in Figure 7.4, if the MD impedance force (6.100) is not applied, the majority of the initial MD energy is trapped within the MD region. However, if the impedance force is applied correctly, the reduced MD region dissipates away the energy correctly, as is seen in the comparison with a full MD.

Figures 7.2 and 7.3 further illustrate the physical meaning of the impedance force (6.100). In both the figures, the final FE displacements are quite similar. This is because, in both the cases, regardless of whether the MD impedance force was applied, the finite elements capture that part of the initial MD wave that are representable by the FE basis functions. The MD impedance force (6.100) then acts to dissipate that part of the MD displacements that are not representable by the finite element shape functions.

7.2.2 Comparison of VAC Method and Cauchy–Born Rule

In an earlier section, two different methods of approximating the coarse scale force $\mathbf{N}^T \mathbf{f}(\mathbf{u})$ outside of the MD region were described. In this section, we briefly compare the Cauchy–Born rule as in Tadmor et al. (1996) and the VAC method of Qian and Gondhalekar (2004) and Qian et al. (2004) within the context of the bridging scale via one-dimensional wave propagation examples.

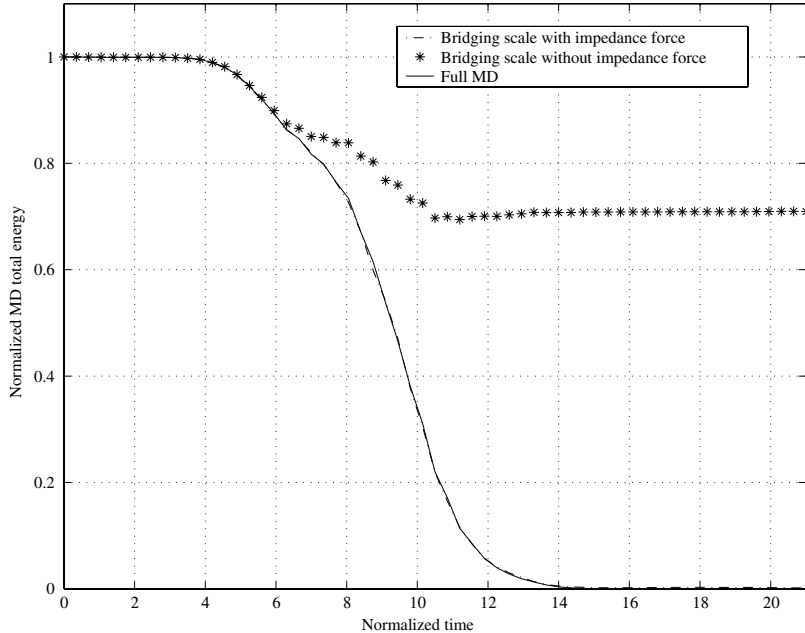


Figure 7.4 Bridging scale versus full MD energy comparison.

Figure 7.5 shows the energy transfer comparison between the Cauchy–Born rule and the VAC method for the 1D nonlinear wave propagation example of the previous section. As can be seen, the two methods yield essentially identical results in the one-dimensional case. The VAC method, however, has the added advantage that it is valid for nonplanar crystalline structures, such as carbon nanotubes, without special modifications.

7.2.3 Truncation of Time History Kernel

An issue that will be crucial in multiple dimensions will be that of truncating the time history kernel to a computationally manageable size. Recall from (6.100) that the impedance force is written as

$$\mathbf{f}^{\text{imp}} = \int_0^t \boldsymbol{\theta}(t - \tau)(\mathbf{q} - \bar{\mathbf{u}})(\tau) d\tau \quad (7.4)$$

In order to evaluate this integral exactly, it is necessary to store the displacements of the boundary atoms (and the coarse scale at the MD boundary) for the entire duration of the simulation. In one dimension, this is feasible owing to the fact that the time history kernel $\boldsymbol{\theta}(t)$ is known analytically, and furthermore because displacement histories are only necessary for two boundary atoms. In two and three dimensions, because there will be many boundary atoms, any successful approach demands that only a few displacement histories be stored for each boundary atom, lest the memory requirements overwhelm the simulation.

Motivated by this fact, we now present a study of time history truncation in one dimension. The basis for the truncation was presented by Karpov et al. (2005b). The truncation itself occurs in two forms. The first form is motivated by the physical behavior of the

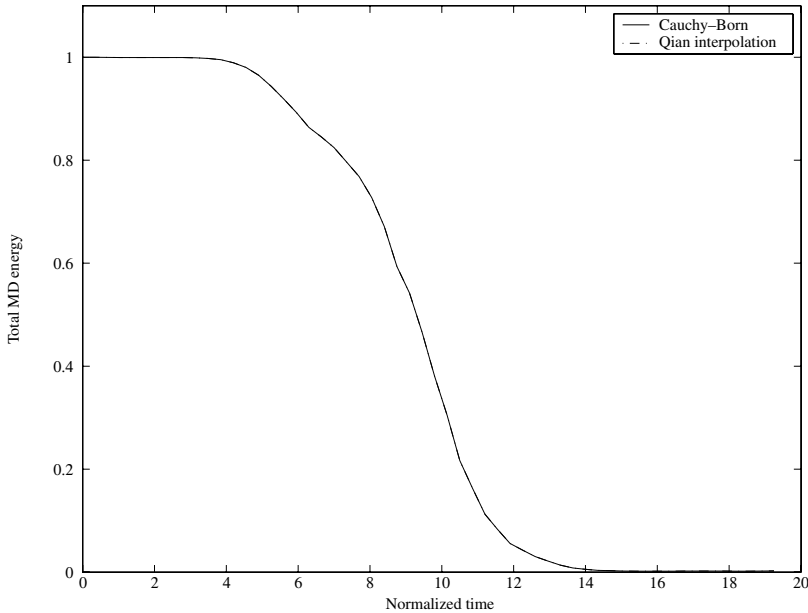


Figure 7.5 Comparison of energy transferred from MD region using Cauchy–Born rule and VAC method.

time history kernel $\theta(t)$. In Figure 7.6, $\theta(t)$ is shown. A salient feature of $\theta(t)$ is that its amplitude decreases quickly (to less than 10% of its maximum amplitude) after only a few oscillations. On the basis of this fact, an approximation is made in which the later components of $\theta(t)$ are deemed to be insignificant, and are simply set to zero. This truncation is shown in Figure 7.7, where $\theta(t)$ is truncated after three full oscillations.

The second major truncation occurs in the evaluation of the convolution integral (7.4). By increasing the time step of the convolution integral with respect to the MD simulation time step, a further significant computational reduction will occur owing to the fact that fewer boundary atom displacements will need to be stored. In simple parlance, the idea is to integrate a smooth curve using a Gaussian-type integration rule. If a larger convolution integral time step is used, the integral in (7.4) can be rewritten in summation form as

$$\mathbf{f}(t_n) = h \Delta t \sum_{k=0}^{n,h} \theta_{t_n - \tau_k} (\mathbf{q} - \bar{\mathbf{u}})_{\tau_k} \quad (7.5)$$

where t_n is the current time, h is an integer that describes the frequency of the sampling and Δt is the MD time step. The summation is therefore a discrete summation, with k incremented in factors of h . Therefore, \mathbf{u} does not change between discrete sampling points, and is only augmented at each discrete sampling point. The factor $h = \frac{\Delta t_{conv}}{\Delta t_{md}}$ acts as a quadrature weight that accounts for the remainder of the time history points and displacements that are not stored and hence are not calculated. It is because of this integration weight h that the boundary atom displacement history can be truncated after a small number of points.

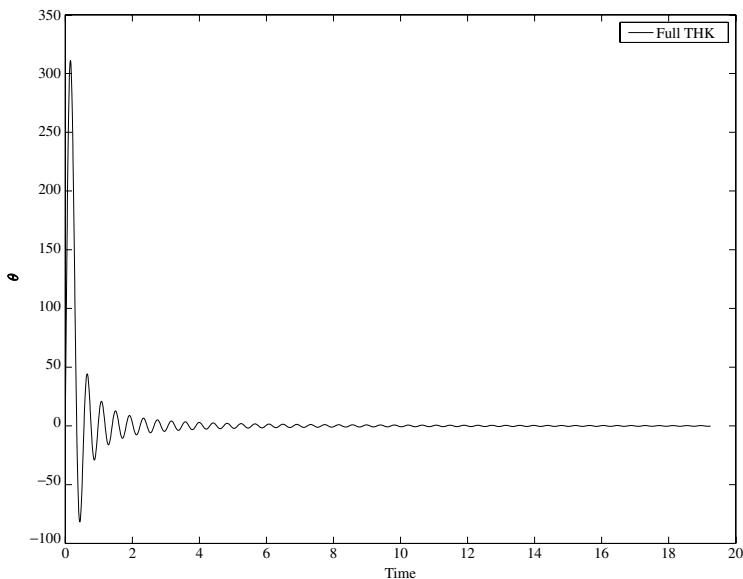


Figure 7.6 Plot of the time history kernel $\theta(t)$. Reprinted from Computer Methods in Applied Mechanics and Engineering, 195, Park et al., Introduction and tutorial on multiple scale analysis in solids, 1733–1772, 2004, with permission from Elsevier.

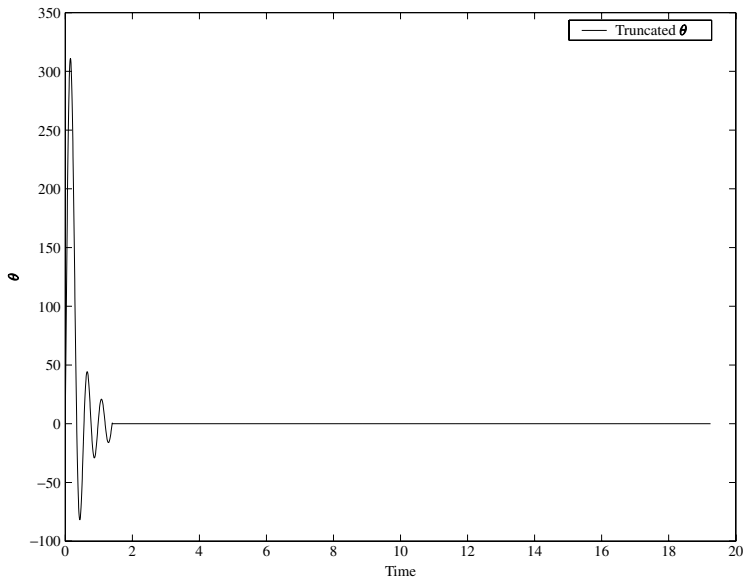


Figure 7.7 Plot of the time history kernel $\theta(t)$ truncated after three complete oscillations. Reprinted from Computer Methods in Applied Mechanics and Engineering, 195, Park et al., Introduction and tutorial on multiple scale analysis in solids, 1733–1772, 2004, with permission from Elsevier.

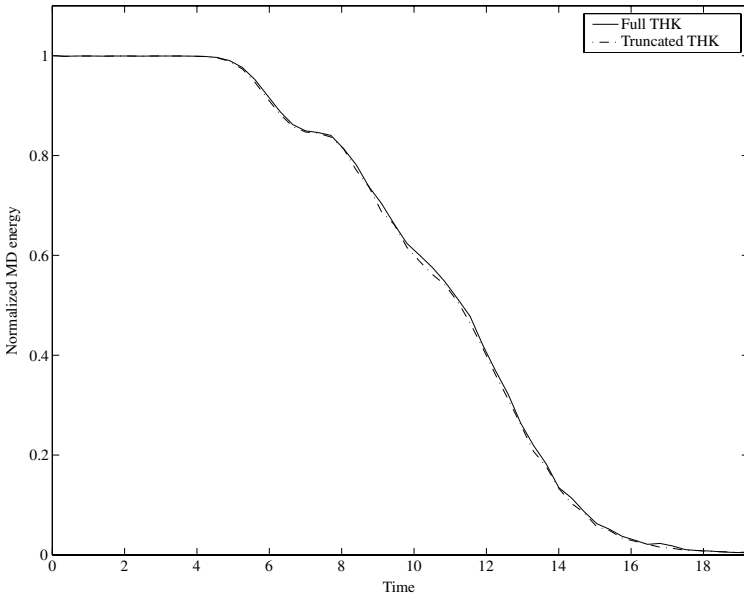


Figure 7.8 Comparison between a fully integrated time history integral and a truncated time history integral. Reprinted from Computer Methods in Applied Mechanics and Engineering, 195, Park et al., Introduction and tutorial on multiple scale analysis in solids, 1733–1772, 2004, with permission from Elsevier.

The example in Figure 7.8 shows a comparison between using the fully integrated time history integral and the truncated time history integral using the process just described. The example problem was the same as the high-frequency initial displacement example shown earlier in this chapter using the LJ 6–12 potential. For the truncated time history integral, the truncated $\theta(t)$ shown in Figure 7.7 was used. In our simulation, that $\theta(t)$ corresponds to 200 MD time steps. The boundary atom displacement history was updated every 25 MD time steps, which means that only 8 displacement histories need to be stored for each boundary atom. This implies that k in (7.5) has a maximum value of $8h$, and also that $h = 25$.

As can be seen in Figure 7.8, the results using the truncated time history kernel are nearly identical to that using the full-time history kernel, validating the truncation method proposed. Furthermore, the computational saving is immense; in the full-time history integral, the storage of approximately 2700 displacements (i.e. the total number of MD time steps) is necessary per boundary atom. Moreover, 2700 is an arbitrary number; the number of displacements stored is simply equal to the total number of time steps of the MD simulation, which can be much larger. Most importantly, we have established a framework by which the truncation of the time history kernel in multiple dimensions can be easily performed.

7.3 2D/3D Bridging Scale Numerical Examples

All two- and three-dimensional MD/bridging scale calculations presented in this section utilize the LJ potential (2.60) where r is the distance between two atoms. The examples

were run with parameter values $\sigma = \epsilon = 1$ considering nearest-neighbor interactions only, while all atomic masses were chosen as $m = 1$. The examples utilize the equilibrium interatomic distance, $r_{\text{eq}} = 2^{1/6}\sigma$, corresponding to the minimum of the potential (2.60).

A hexagonal lattice structure corresponding to the (111) plane of an fcc crystal was considered for the two-dimensional MD simulations, while the actual fcc lattice was considered for the three-dimensional simulations. In both the cases, the atoms were initially in an equilibrium configuration. Because of the symmetry between the top and bottom layers of a hexagonal lattice, the time history kernels for the top and bottom layers can be related by

$$\theta_n^{\text{top}}(t) = \theta_{-n}^{\text{bottom}}(t) \quad (7.6)$$

and the storage requirements for the time history kernels can be reduced by one-half. A schematic demonstrating the atomic directions along which the impedance force (6.100) was applied for all two-dimensional numerical bridging scale examples is shown in Figure 7.9. In (7.6), $\theta^{\text{top}}(t)$ corresponds to the $[\bar{1}2\bar{1}0]$ direction of a hexagonal lattice while $\theta^{\text{bottom}}(t)$ can then be found using the symmetry arguments in (7.6). Figures (6.6)–(6.9) show the time history kernel for an LJ 6–12 potential computed for $\theta^{\text{bottom}}(t)$. All simulations were performed with the random force $\mathbf{R}(t)$ in (6.98) set to zero, indicating an MD region at zero temperature.

For the regions that satisfy a coarse scale–only description, the Cauchy–Born rule was used to calculate the coarse scale internal force. The LJ 6–12 potential was used to describe the continuum strain energy density, such that the coarse scale internal force could be derived from the same potential that was used for the MD force calculations. Four-node bilinear quadrilateral finite elements were utilized for all two-dimensional numerical examples.

We comment here on the usage of a general interatomic potential with parameters that do not match those of any real material. These choices were made in the interest of generality, such that large classes of realistic physical systems could be simulated without concentrating on a specific material. Future work could, of course, use specific values for σ and ϵ to match the behavior of a given material, should a detailed study of a specific physical process be desired. Finally, the LJ potential was chosen to represent a model brittle material.

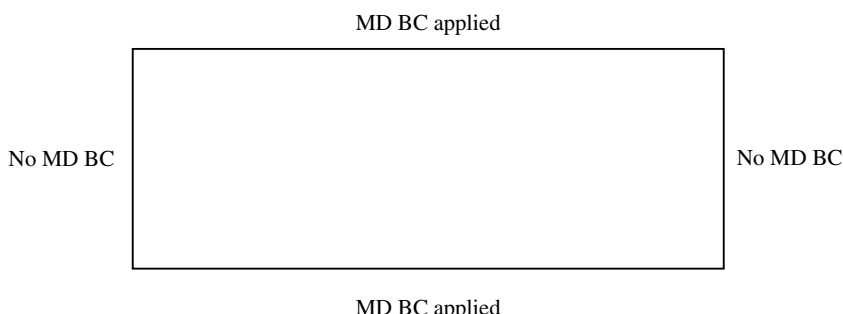


Figure 7.9 Schematic illustrating the boundaries on which the MD impedance force (6.100) was applied for two-dimensional numerical examples. Reproduced with permission from Harold Park, Philosophical Magazine; published by Taylor & Francis, 2005, <http://www.tandf.co.uk>.

In this section, all units that are related to atomistic simulations, such as velocity, position and time, are given in reduced units. It should be noted that because of the choice of mass σ and ϵ as unity, all normalization factors end up as unity. Finally, all numerical examples shown in this work were performed using the general-purpose simulation code Tahoe, which was developed at Sandia National Laboratories (Tahoe 2004).

7.4 Two-Dimensional Wave Propagation

In this example, we demonstrate the effectiveness of the bridging scale in eliminating high-frequency wave reflections between the FE and MD regions. To do so, a two-dimensional wave propagation example was run. A part of the MD region was given initial displacements corresponding to a two-dimensional circular-type wave. The components of the initial displacements given in polar coordinates were

$$\mathbf{u}_r(r) = \frac{A}{A - u_c} \left(1 + b \cos\left(\frac{2\pi r}{H}\right) \right) \left(A e^{(-\frac{r}{r_c})^2} - u_c \right) \hat{\mathbf{e}}_r \quad (7.7)$$

The corresponding parameters had values of $\sigma = 15$, $H = \sigma/4$, $A = .015$, $b = 0.1$, $r_c = 5\sigma$ and $u_c = A e^{(-\frac{r_c}{b})^2}$, where A controls the wave amplitude, b controls the degree of high-frequency content in the wave ($b = 0$ implies zero high-frequency content) and r_c controls the cutoff distance of the initial displacements. The initial configuration for the problem is shown in Plate 3(a).

In order to have a comparison for the bridging scale simulations, a larger MD simulation was performed, and taken to be the benchmark solution. In this simulation, the same initial displacements prescribed by (7.7) for the bridging scale simulation were prescribed for the MD lattice. For the full MD region to match the entire bridging scale region, 91,657 atoms, or 301 atoms in the x -direction along with 301 atoms in the y -direction, were used. The wave was allowed to propagate away from the center of the lattice until just before the domain boundaries were reached.

The corresponding bridging scale simulation contained 31,157 atoms (301 atoms in the x -direction by 101 atoms in the y -direction) and 1920 finite elements, of which 600 were in the coupled MD/FE region. Twenty MD time steps were used for each FE time step. The bridging scale MD domain contained as many atoms in the x -direction as the full MD simulation, but only one-third the number of atoms in the y -direction. Because the MD boundary conditions were only enforced on the top and bottom of the bridging scale MD lattice, this would ensure that the waves reached and passed through the top and bottom boundaries before the left and right boundaries were reached by the waves.

In order to test the accuracy of the MD impedance force, five cases were run. The first case involved not applying the impedance force (6.100), which would expectedly lead to large amounts of high-frequency wave reflection at the MD/FE boundary. Then, four cases were run in which the number of neighbors used in calculating the impedance force (n_c in (6.100)) was increased. A snapshot showing the natural propagation of the wave that originated in the MD region into the surrounding continuum is shown in Plate 3(b). It is important to note that while the continuum representation exists everywhere, that part of the FE mesh overlaying the MD region is not shown so as to better illustrate how the coarse scale captures the information originating in the MD region.

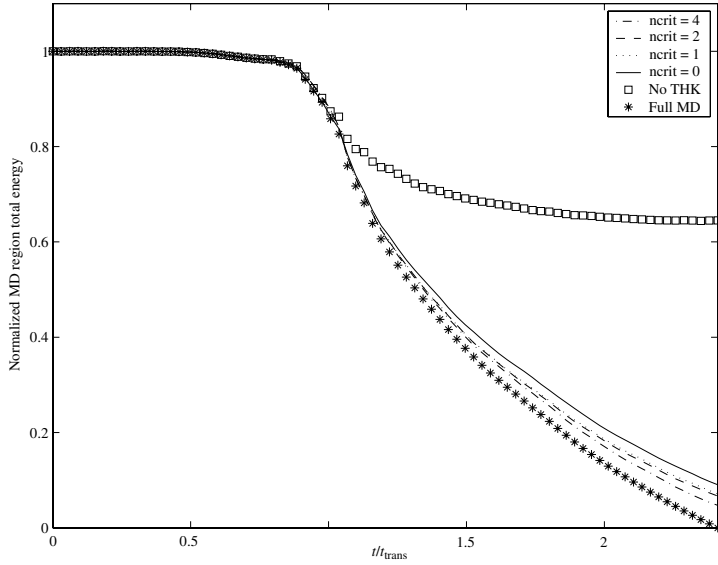


Figure 7.10 Comparison of energy transfer for the two-dimensional wave propagation example. Reproduced with permission from Harold Park, Philosophical Magazine, published by Taylor & Francis, 2005, <http://www.tandf.co.uk>.

The resulting total energy (kinetic energy + potential energy) transferred from the MD region using the bridging scale is shown in Figure 7.10. The full MD energy was measured only in the same region in which the bridging scale MD existed, so that a valid comparison could be made. The full MD energy was then normalized to be the reference solution, such that it tends to zero (Figure 7.10). Of course, because the wave has not fully exited the system, the actual energy in all systems does not go to zero, but this normalization is performed so that a percentage measurement and comparison between the full MD and bridging scale MD systems can be obtained.

As Figure 7.10 shows, if the MD impedance force (6.100) is not applied, only about 35% of the MD energy is transferred in comparison to the full MD. However, if the impedance force that is presented in this work is utilized, even if only one neighbor is used in calculating the boundary force (i.e. $n_c = 0$), about 91% of the MD energy is transferred in comparison with the full MD simulation. The percentage steadily increases until more than 95% of the energy is transferred if nine neighbors ($n_c = 4$) are used to calculate the impedance force. These results show the necessity to correctly account for the eliminated fine scale degrees of freedom in the form of the impedance force (6.100). The time axis of Figure 7.10 has been normalized by t_{trans} , which represents the transit time that the shortest wavelength the FE mesh can support takes to reach the MD boundary from the center of the MD region. As might be expected, energy begins to dissipate from the MD region around the normalized time of one.

A final note of importance is made in further analyzing the bridging scale result shown in Figures 7.11 and 7.12. One element of the bridging scale simulation results is a long wave-

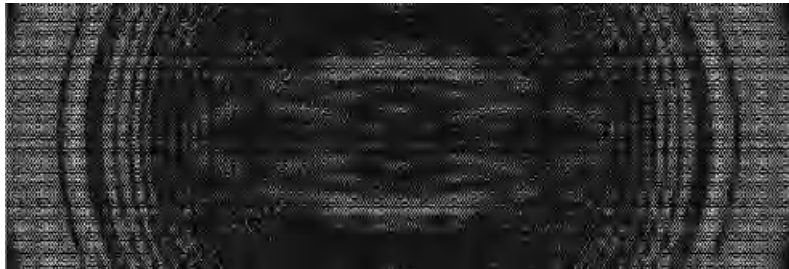


Figure 7.11 Final displacements in MD region if MD impedance force is applied. Reproduced with permission from Harold Park, Philosophical Magazine, published by Taylor & Francis, 2005, <http://www.tandf.co.uk>.



Figure 7.12 Final displacements in MD region if MD impedance force is not applied. Reproduced with permission from Harold Park, Philosophical Magazine, published by Taylor & Francis, 2005, <http://www.tandf.co.uk>.

length reflection back into the MD region. The reason for this long wavelength reflection is due to the fact that the FE internal force is calculated by two different means for the boundary nodes. The result of this is a system with slightly different stiffnesses. For the problem shown in this section, because most of the initial MD energy is concentrated in the high-frequency waves, the majority of the energy is transferred into the continuum. In general, this may not be the case, and more of the system energy may be concentrated in the longer wavelengths.

There are multiple ways of reducing this effect. One approach is to split the boundary element such that it receives a contribution from both the MD forces and the Cauchy–Born forces. By doing so, a transition element is created whose properties are an average of the two systems. By creating this transition element, the long wavelength reflection is eliminated, as has been done in one-dimensional problems by Park and Liu (2004) and Wagner and Liu (2003).

Another option is to use meshfree shape functions everywhere in the domain. Because of the nonlocal nature of the meshfree shape functions, the transition element described above will be naturally created without the need for special integration techniques for the boundary element. This issue will be addressed more carefully in a later work.

7.5 Dynamic Crack Propagation in Two Dimensions

The previous example dealt with a specific case in which all the initial energy of the problem was in the MD domain, and then was dissipated into the surrounding continuum. This type of example, while useful for verifying the effectiveness of the derived MD impedance force (6.100), does not demonstrate all relevant facets of a generalized multiple scale simulation. In fact, it could be reasonably argued that for problems such as the wave propagation example in which the only goal is to allow passage of the fine scale waves out of the MD region without causing internal reflection, using techniques such as those introduced in Karpov et al. (2005b) or Wagner et al. (2004) would be sufficient, thereby rendering the coarse scale redundant.

However, many problems of interest involve those in which the MD region is not initially in a state of motion, and instead moves as a result of some initial continuum deformation that is passed to the MD region via the coarse scale/fine scale coupling established in (6.100). Because of this, it is important that the MD boundary condition act as a two-way filter: first, that it allow large scale continuum information into the MD region and second, that it still dissipate away the high-frequency MD waves that cannot be represented by the surrounding continuum. To demonstrate the truly two-way coarse/fine coupled nature of the bridging scale, we solve a two-dimensional dynamic crack propagation in which the boundary conditions are applied to the coarse scale. The problem schematic is shown in Figure 7.13.

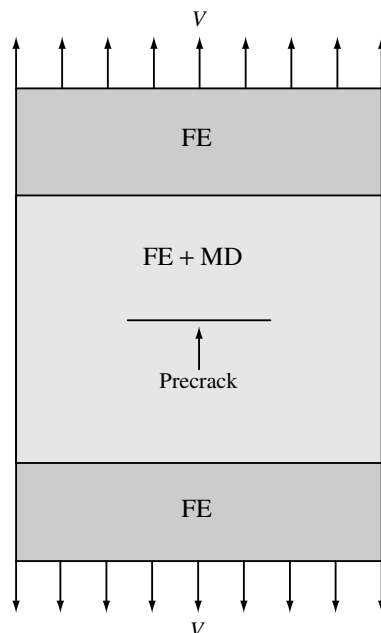


Figure 7.13 Configuration for two-dimensional dynamic crack propagation examples. Reproduced with permission from Harold Park, *Philosophical Magazine*, published by Taylor & Francis, 2005, <http://www.tandf.co.uk>.

The precrack is generated by preventing the interaction of two rows of atoms. In this way, the atoms on the faces of the precrack effectively behave as if on a free surface, and the crack opens naturally in tension. A ramp velocity is applied to the top and bottom nodes of the continuum region so that the atomistic fracture occurs in a mode-I fashion. The application of the ramp velocity is shown in Figure 7.14.

A full MD simulation was also run in which the entire domain was composed of atoms. The bridging scale simulation consisted of 91,051 atoms and 1800 finite elements, of which 900 were in the coupled MD/FE region. Forty MD time steps were run for each FEM time step. Correspondingly, the full MD simulation consisted of 181,201 atoms. The identical velocity boundary condition as shown in Figure 7.14 was applied on the full MD simulation as with the bridging scale simulation, with the peak velocity $V_{\max} = .04$. For all bridging scale simulations shown in this section, only one neighbor was utilized in evaluating the impedance force, that is, $n_c = 0$.

A comparison between the full MD simulation and bridging scale simulations is shown in Figures 7.15(a) and 7.15(b). In these figures, the potential energy of the MD domain is shown. As can be seen, both the simulations show the same dominant characteristics, notably the size and intensity of the process zone immediately ahead of the crack tip, and also in the high-frequency radiation emitted from the crack tip. This high-frequency radiation, which appears as concentric circles radiating away from the crack tip, is emitted each time a single atomic bond is broken by the propagating crack. The opening of the crack is shown clearly by magnifying the y -component of the displacement by a factor of three. It should be noted that while the interatomic interactions have been restricted to nearest neighbors, the potential is not truncated at any point such that the potential energy and force are fully continuous functions of interatomic distance.

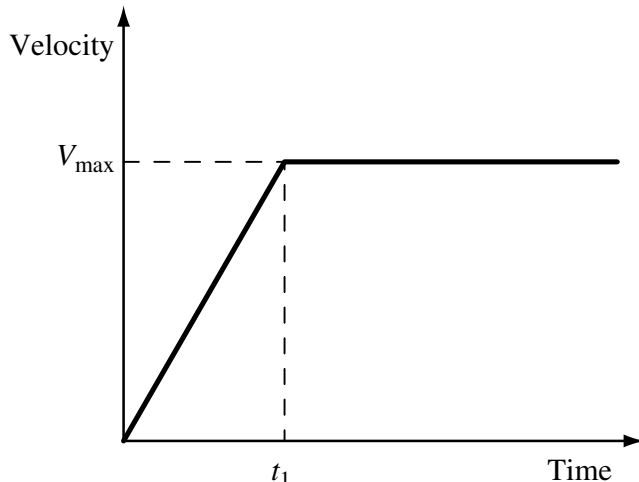


Figure 7.14 Ramp velocity boundary condition that is applied on the FE region in dynamic fracture examples. Reproduced with permission from Harold Park, *Philosophical Magazine*, published by Taylor & Francis, 2005, <http://www.tandf.co.uk>.

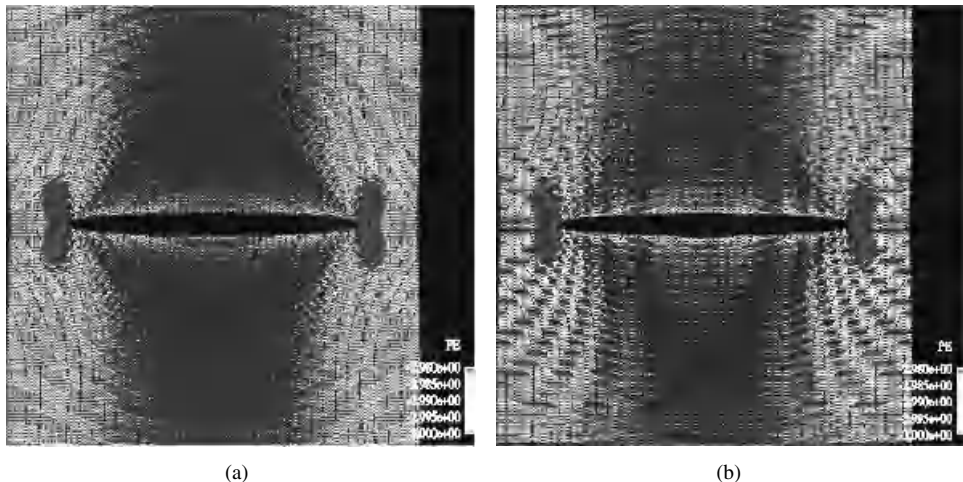


Figure 7.15 Comparison of potential energy contours for (a) full MD and (b) bridging scale fracture simulations. Reproduced with permission from Harold Park, Philosophical Magazine, published by Taylor & Francis, 2005, <http://www.tandf.co.uk>.

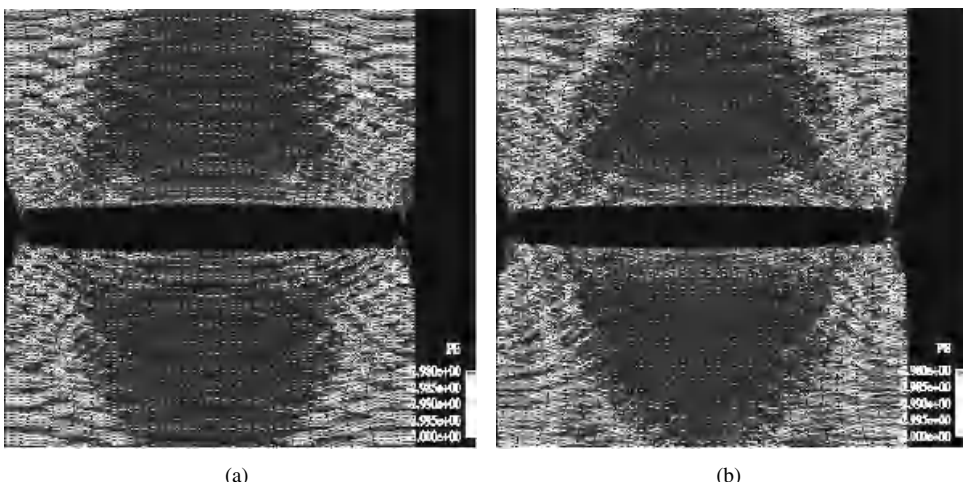


Figure 7.16 Comparison of potential energy contours for (a) full MD and (b) bridging scale simulations after complete fracture of lattice has occurred. Reproduced with permission from Harold Park, Philosophical Magazine, published by Taylor & Francis, 2005, <http://www.tandf.co.uk>.

If a larger peak velocity V_{\max} is chosen for the velocity boundary condition or the simulation is run for a sufficiently lengthy period of time, complete fracture of the atomic lattice into two sections will occur. This is demonstrated in Figures 7.16(a) and 7.16(b), where the peak velocity was chosen as $V_{\max} = 0.06$. As can be seen in Figures 7.16(a) and 7.16(b), the bridging scale simulation agrees very well with the full MD simulation.

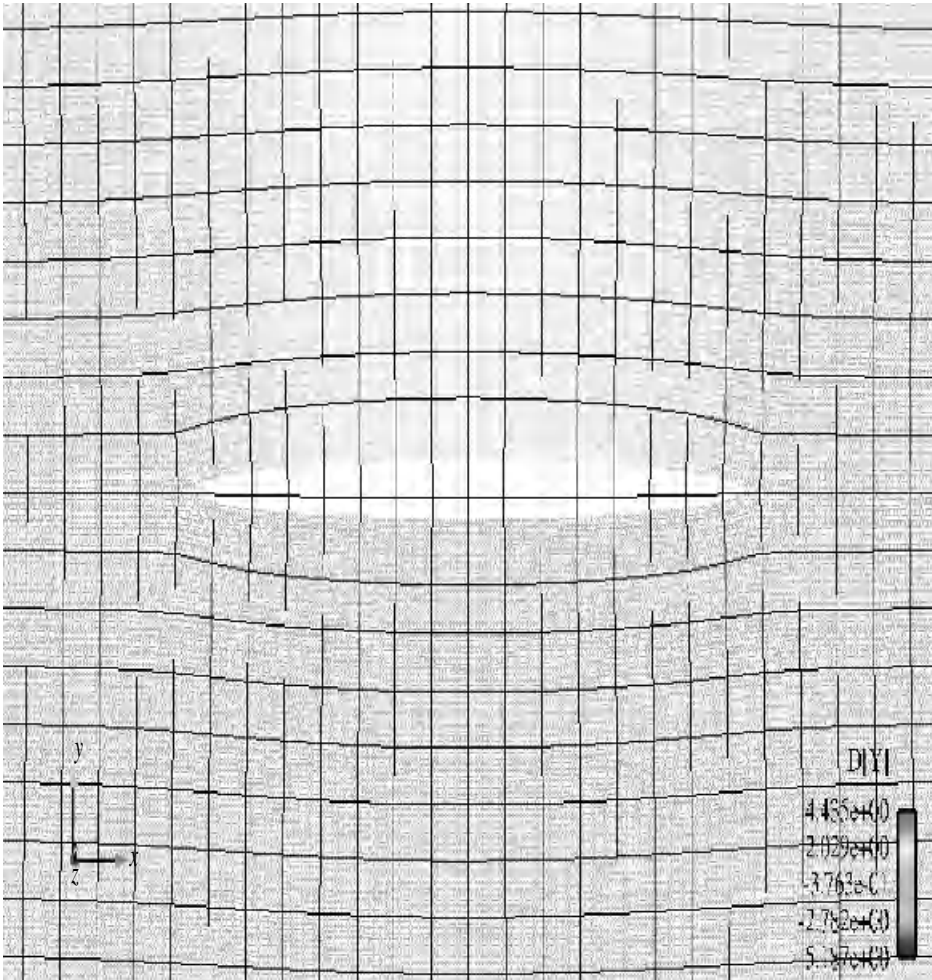


Figure 7.17 Snapshots of FEM deformation as a response to MD crack propagation.

It is also noteworthy that complete fracture of the underlying MD lattice is allowed in the coupled simulation; this is because the finite element nodal forces in that region are obtained directly from the underlying atomistic forces via the projection illustrated in (6.101) and (6.102). Because of this fact, no calculation of deformation gradients in the coupled MD/FE region is necessary. Therefore, the finite elements that overlay the MD region can deform in a manner that finite elements governed by traditional constitutive laws cannot.

The utility of the force projection is shown in Figures 7.17 and Figure 7.18. In Figure 7.17, the top image shows a snapshot of the MD/FEM region as the crack initiates and begins to propagate. Note that the crack is discrete, and completely contained within the MD region. However, the finite elements surrounding the crack deform similarly, that is, the elements



Figure 7.18 Snapshots of FEM deformation as a response to MD crack propagation.

that contain the crack show crack opening-like displacements, while the elements far from the crack show very small deformations.

A zoom-in of the crack is shown in Figure 7.18. In this image, the left-hand crack tip has propagated and is approaching the domain boundary. Again, the top image of Figure 7.18 shows the finite elements that contain the crack, presenting a mode-I type opening displacement, while those elements away from the crack near the domain boundary are deforming inward, showing the Poisson effect. In the bottom snapshot of Figure 7.18, the crack has propagated through the domain wall and fractured the MD region into two distinct specimens. This can also be seen in Figure 7.19 snapshots. Of note here is the pinching effect that is seen in the boundary finite element; this type of pinching effect is

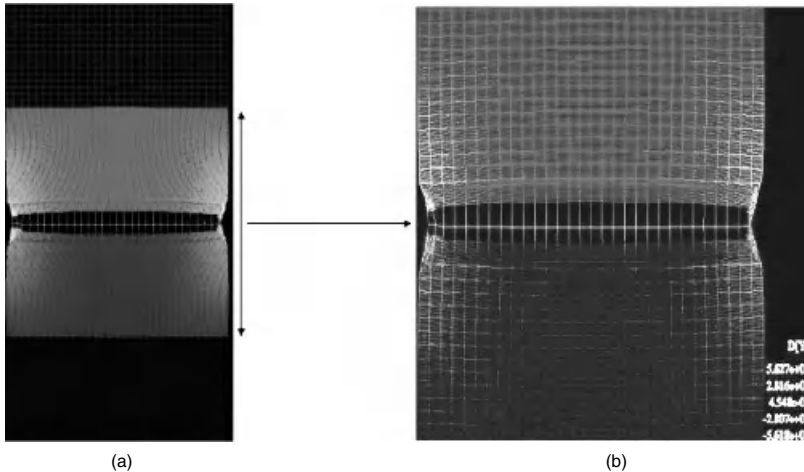


Figure 7.19 (a): y -displacements of the entire structure. Note that MD exists only in a small part of the domain, while FE exists everywhere. (b): Zoom-in of y -displacements in coupled MD/FE region. Reproduced with permission from Harold Park, Philosophical Magazine, published by Taylor & Francis, 2005, <http://www.tandf.co.uk>.

clearly unphysical, and would not be allowed by standard finite element formulations. In contrast, within the bridging scale, because the finite elements deform according to the underlying MD forces, such deformations are allowed to occur.

Another useful measure of comparison between the bridging scale and a full MD simulation is in tracking the initiation times and subsequent position of the crack tips. In our simulations, because the location of the precrack is known, the location of the crack tip could be easily ascertained by comparing the y -displacements of the atoms ahead of the precrack, and checking if they had exceeded a critical value. The comparison between the full MD and two different bridging scale simulations using different MD domain sizes is shown in Figure 7.20 for the case $V_{\max} = .04$. As can be seen, the bridging scale simulations predict the identical crack initiation time as observed in the full MD simulation. The bridging scale model also yields the accurate position of the crack tip as it evolves through time.

A slightly different system was run for further comparison. In this case, the full MD system contained 362,101 atoms (601 atoms in the x -direction by 601 atoms in the y -direction). Three different bridging scale simulations with varying MD system sizes (601×301 , 601×201 , 601×101) along with 3600 finite elements were run. The crack tip history is shown in Figure 7.21. As can be seen, the first two bridging scale simulations match the crack initiation time and time history exactly. However, for the smallest MD region within a bridging scale simulation (the 601×101 atom case), the crack initiates at a slightly earlier time than in the full MD case. After initiation, the velocity of the crack appears to match the velocity of the crack in the full MD case. We note that other simulations were run in which the number of atoms in the y -direction were reduced to less than 101. For these simulations, the crack either initiated much earlier or later than expected, or did not initiate at all. It appears as though the incorrect physics demonstrated in these cases reflects the assumption of linearity at the MD boundary being violated if the MD region is too small.

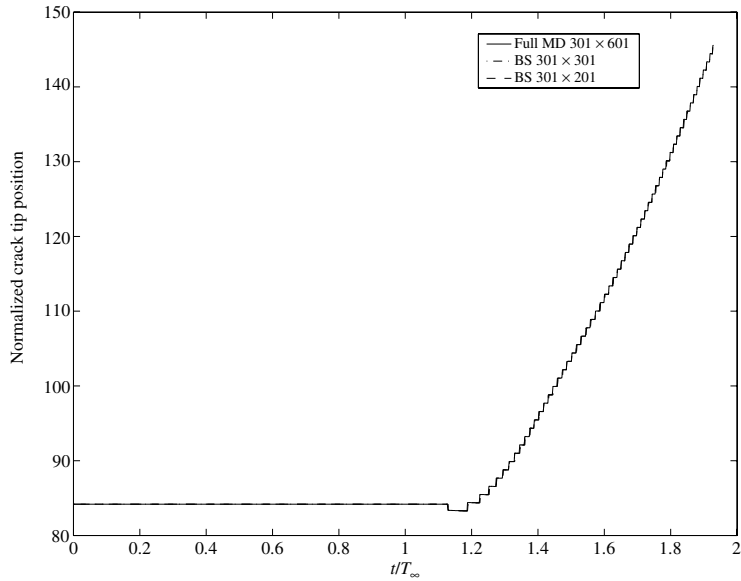


Figure 7.20 Comparison of crack position with respect to time for full MD and two different bridging scale simulations. Reproduced with permission from Harold Park, Philosophical Magazine, published by Taylor & Francis, 2005, <http://www.tandf.co.uk>.

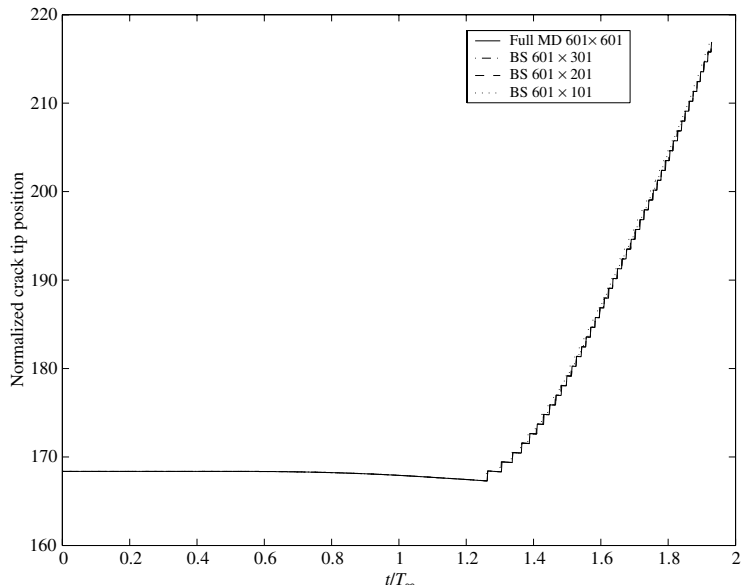


Figure 7.21 Comparison of crack position with respect to time for full MD and three different bridging scale simulations. Reproduced with permission from Harold Park, Philosophical Magazine, published by Taylor & Francis, 2005, <http://www.tandf.co.uk>.

Taken together, Figures 7.20 and 7.21 demonstrate the truly two-way coupled nature of the derived MD boundary condition (6.100). First, the large scale information that is passed to the MD region as a boundary condition is being passed correctly; this is borne out by the fact that the crack initiation times in the bridging scale simulations match the initiation times in the full MD simulations. Secondly, the derived MD boundary condition is effectively dissipating high-frequency waves emitted from the crack tip; this is revealed by the fact that the position of the crack tip over the entire duration of propagation matches that of the full MD simulation. More simply, the high-frequency waves emitted by the crack tip are not reflecting from the boundary and interfering with the crack propagation dynamics.

The time axis in Figures 7.20 and 7.21 was normalized by a critical time T_∞ corresponding to the time that a crack in an infinite strip would begin initiation under mode-I type loading, where the crack driving force under plane stress is given to be

$$G = \frac{E\delta^2}{2h(1 - \nu^2)} \quad (7.8)$$

In (7.8), G is the crack driving force, E is the Young's modulus, ν is the Poisson's ratio, δ is the applied displacement to the strip edge and h is the total height of the strip. In the cleavage plane created by the simulation, extension of the crack by a distance of the lattice parameter a_0 requires the breaking of two bonds. Therefore, the fracture energy is $\frac{2\epsilon}{a_0}$. For both the full MD system as well as the bridging scale calculations, crack initiation occurred later than predicted by the analytical relations, indicating that the specimen considered is not sufficiently long in the x -direction for (7.8) to hold.

Finally, a comparison of the computational expense incurred utilizing the bridging scale and a pure atomistic simulation is shown in Figure 7.22. The full MD simulation of 362,101 atoms was set as the benchmark simulation in terms of computational time. This benchmark full MD simulation was then compared with two bridging scale simulations. The first used approximately one-third the number of atoms, 121,901, along with 3721 FE nodes. The second used approximately one-sixth the number of atoms, 61,851, along with 3721 FE

Simulation	Normalized time
Full MD: 362,101 atoms = 724,202 DOF s	1.0
Bridging scale: 121,901 atoms + 3721 nodes = 251,244 DOF s	0.51
Bridging scale: 61,851 atoms + 3721 nodes = 131,144 DOF s	0.33

Figure 7.22 Comparison of simulation times using bridging scale and full MD. n_c in (6.100) is taken to be zero for bridging scale simulations. Reproduced with permission from Harold Park, Philosophical Magazine, published by Taylor & Francis, 2005, <http://www.tandf.co.uk>.

nodes. As can be seen, computational speedups of two and three times were observed, respectively, using the bridging scale for the case in which all computations were performed in serial. The bridging scale simulation times do not scale exactly as the fraction of MD degrees of freedom owing to the additional expense of the terms introduced by the bridging scale coupling, and also because certain optimization tools, such as the truncation of the number of displacement histories stored per boundary atom as done in Park and Liu (2004), or Section (7.2.3), have not yet been implemented.

7.6 Dynamic Crack Propagation in Three Dimensions

In this section, we show numerical examples for the bridging scale in three dimensions. Specifically, we validate the method on dynamic crack propagation examples within an fcc crystal. For the MD simulation, we utilize the LJ 6–12 potential, though with a slightly altered form. The LJ potential we utilize contains a smooth cutoff, such that the revised potential takes the form

$$\Phi(r_{ij}) = \Phi_{\text{LJ}}(r_{ij}) - \Phi_{\text{LJ}}(r_c) - (r_{ij} - r_c)\Phi'_{\text{LJ}}(r_c) \quad (7.9)$$

where $\Phi_{\text{LJ}}(r_{ij})$ is the standard, unshifted LJ 6–12 potential (2.60), which is a function of the distance r_{ij} between two atoms i and j , and the shifted distance r_c is defined as

$$r_c = \alpha\sigma \quad (7.10)$$

The shifted LJ potential described in (7.9) has a smooth cutoff in both the force and energy at the value $r_{ij} = \alpha$. For the new shifted potential, we utilize parameter values $\sigma = \epsilon = 1$, $\alpha = 1.50$; all atomic masses are taken to be unity.

The dynamic fracture problem schematic is shown in Figure 7.23. As is shown, the specimen under consideration is covered by finite elements everywhere, while the atomistic region is confined to the central region of the domain. A precrack is specified in the atomistic region by prescribing that two adjacent planes of atoms do not interact, and the crack opens naturally in a mode-I type failure under the ramp velocity loading shown in Figure 7.14. The normalized velocity applied to the top and bottom (001) surfaces was taken to be $V_{\max} = 0.035$.

We note that the precrack is initially fully contained within the interior of the MD domain; the interactions between the crack and the surfaces shown later are a result of the propagation of the crack. A visual image of the precrack is given in Figure 7.24. For visualization purposes, the images in this section display only those atoms whose potential energy is greater than 90% of the equilibrium value; this technique is useful for highlighting the defective parts of the lattice, which may be of interest in fracture and failure simulations.

The simulations were run using nearest-neighbor interactions only. The bridging scale simulation employed 1024 eight-node hexahedral finite elements and 117,121 atoms, while the full atomistic simulation was composed of 225,121 atoms. Different time steps were used for both the simulations; the MD time step was taken to be $\Delta t_{\text{md}} = .014$, and 20 MD time steps were run for each FEM time step. The MD impedance force (6.100) was applied to the top and bottom planes of the reduced MD region as shown in Figure 7.23. All other boundary faces of the reduced MD region were taken to be free surfaces.

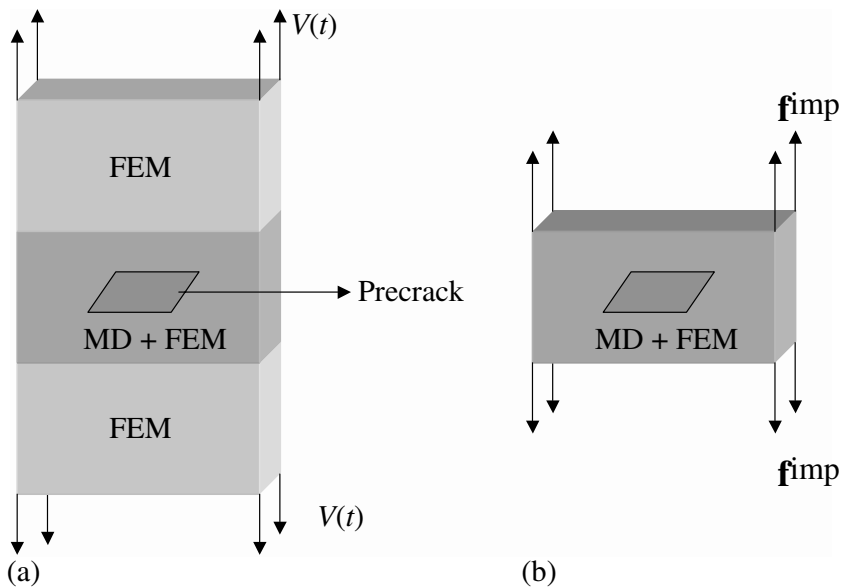


Figure 7.23 (a): Schematic of 3D bridging scale crack propagation example. (b): Application of MD impedances forces (6.100) to top and bottom (001) planes of the reduced MD domain. Reprinted from Journal of Computational Physics, 207(2), Park et al., Three-dimensional bridging scale analysis of dynamic fracture, 588–609, 2005, with permission from Elsevier.

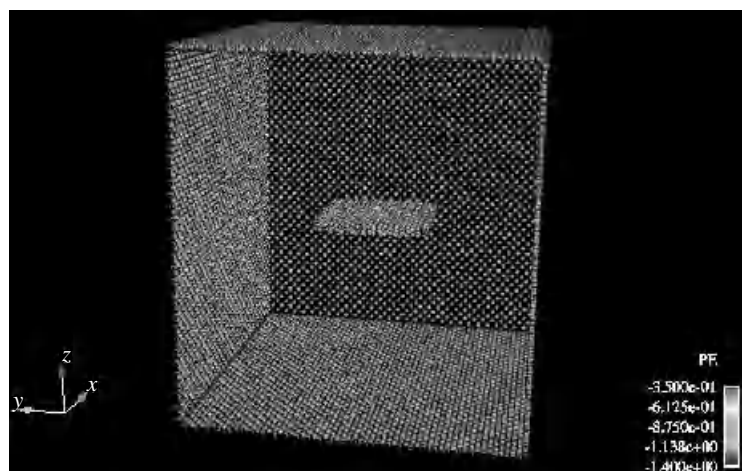


Figure 7.24 Initial precrack for the dynamic crack propagation example. Contours of potential energy are shown. Only those atoms with potential energy greater than 90 percent of the equilibrium value are shown. Reprinted from Journal of Computational Physics, 207(2), Park et al., Three-dimensional bridging scale analysis of dynamic fracture, 588–609, 2005, with permission from Elsevier.

The time history kernel $\theta(t)$ was numerically calculated for an fcc lattice structure and the shifted LJ potential for the (001) plane of atoms. The $3 \times 3 \theta(t)$ matrices in (6.100) for the top and bottom surfaces of the reduced MD region in Figure 7.23 can be found to be related as

$$\begin{pmatrix} \theta_{11}^{\text{top}}(t) & \theta_{12}^{\text{top}}(t) & \theta_{13}^{\text{top}}(t) \\ \theta_{21}^{\text{top}}(t) & \theta_{22}^{\text{top}}(t) & \theta_{23}^{\text{top}}(t) \\ \theta_{31}^{\text{top}}(t) & \theta_{32}^{\text{top}}(t) & \theta_{33}^{\text{top}}(t) \end{pmatrix} = \begin{pmatrix} \theta_{11}^{\text{bot}}(t) & \theta_{12}^{\text{bot}}(t) & -\theta_{13}^{\text{bot}}(t) \\ \theta_{21}^{\text{bot}}(t) & \theta_{22}^{\text{bot}}(t) & -\theta_{23}^{\text{bot}}(t) \\ -\theta_{31}^{\text{bot}}(t) & -\theta_{32}^{\text{bot}}(t) & \theta_{33}^{\text{bot}}(t) \end{pmatrix} \quad (7.11)$$

Similar relationships relating the $\theta(t)$ matrices for opposite faces of the fcc cube can also be determined.

Figure 6.10 shows the three components of $\theta(t)$ in 3D with $n_c = 0$, $\theta_{11}(t)$, $\theta_{22}(t)$ and $\theta_{33}(t)$. As can be seen, $\theta_{33}(t)$ is the most important component to consider in the calculations. We neglect higher-order values of $\theta(t)$ corresponding to $n_c > 0$ as those values for $\theta(t)$ are on the order of 10% of the values shown in Figure 6.10. In the numerical simulations, we set $n_c = 0$ in (6.100) for maximum computational efficiency. The three-dimensional time history kernel exhibits many of the salient features that were demonstrated in the two-dimensional time history kernels for the LJ potential by Park et al. (2005c), specifically the quick decay in the amplitude of $\theta(t)$, which allows the truncation of the kernels after short durations.

A comparison between the bridging scale simulation and the full atomistic simulation is given in four distinct snapshots, which chronicle the time history of the crack propagation. In the first snapshot seen in Figure 7.25, the initially square precrack has evolved under loading

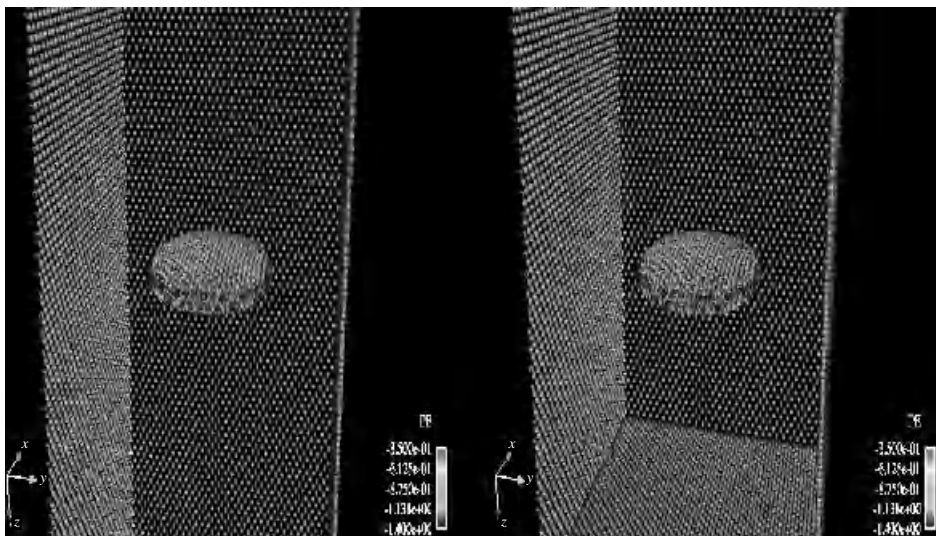


Figure 7.25 Onset of crack growth for left full MD simulation and right bridging scale simulation. Reprinted from Journal of Computational Physics, 207(2), Park et al., Three-dimensional bridging scale analysis of dynamic fracture, 588–609, 2005, with permission from Elsevier.

to resemble a penny-shaped crack. Figure 7.25 shows the crack just before propagation initiates; this figure and all subsequent figures show contours of potential energy, while the crack opening displacement has been magnified by a factor of five for easy viewing. After the crack propagation has initiated and the crack nears the surfaces of the cube, the onset and subsequent branching of the crack is seen in Figures 7.26 and 7.27. In this simulation, it is important to note that the branching is a surface effect, that is, the branching is caused when the crack front approaches the free surface. The branching is caused by a lack of constraint as the crack approaches the surface; in essence, a truly mode-I type loading does not exist near the surface. Hence, the crack is not constrained to propagate directly through the surface, and instead branches to cause material failure.

The final configurations of the bridging scale simulation and the full MD simulation are shown in Figure 7.28. Again, the bridging scale simulation matches the full MD simulation well, including the final configuration of the crack branches and potential energy. Another interesting fact is that the crack branches have reached the MD boundary in the bridging scale simulations; this fact violates the postulates made in deriving the MD boundary condition, and is an example of a case in which some sort of adaptive insertion of new atoms or “remeshing” in the MD region would be necessary to continue such a large deformation failure simulation.

Extreme element distortion is also seen in the three-dimensional examples of dynamic fracture. This is illustrated in Plate 4. In this example, note the distinct bowing out of the elements through which the MD crack branches pass. Also note the extreme distortion of the elements in the center of the face; this distortion is caused by the MD crack penetrating the free surface, causing opening and separation between atomistic material points.

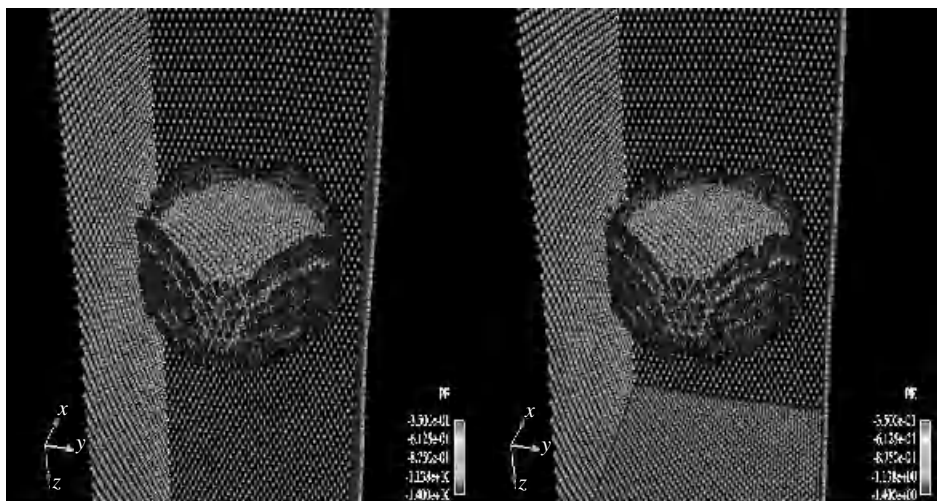


Figure 7.26 Onset of crack branching in left full MD simulation and right bridging scale simulation. Reprinted from Journal of Computational Physics, 207(2), Park et al., Three-dimensional bridging scale analysis of dynamic fracture, 588–609, 2005, with permission from Elsevier.

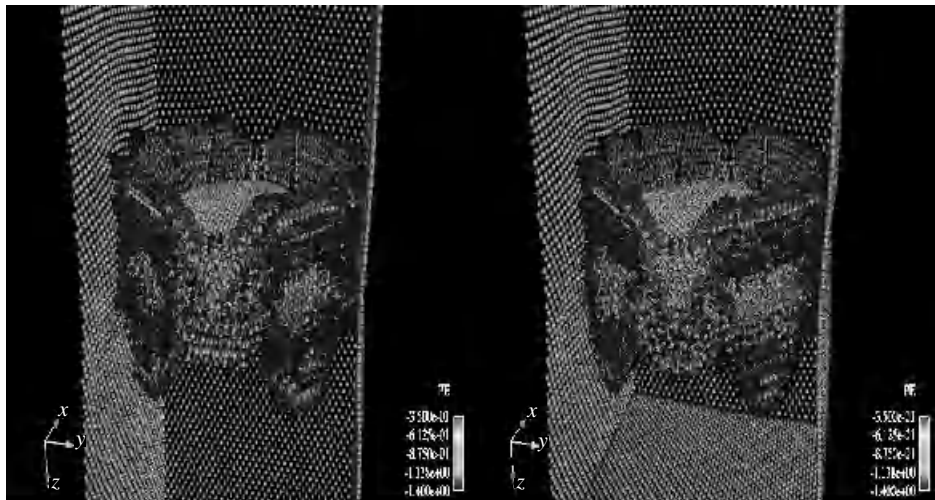


Figure 7.27 Out of plane crack branching for left full MD simulation and right bridging scale simulation. Reprinted from Journal of Computational Physics, 207(2), Park et al., Three-dimensional bridging scale analysis of dynamic fracture, 588–609, 2005, with permission from Elsevier.

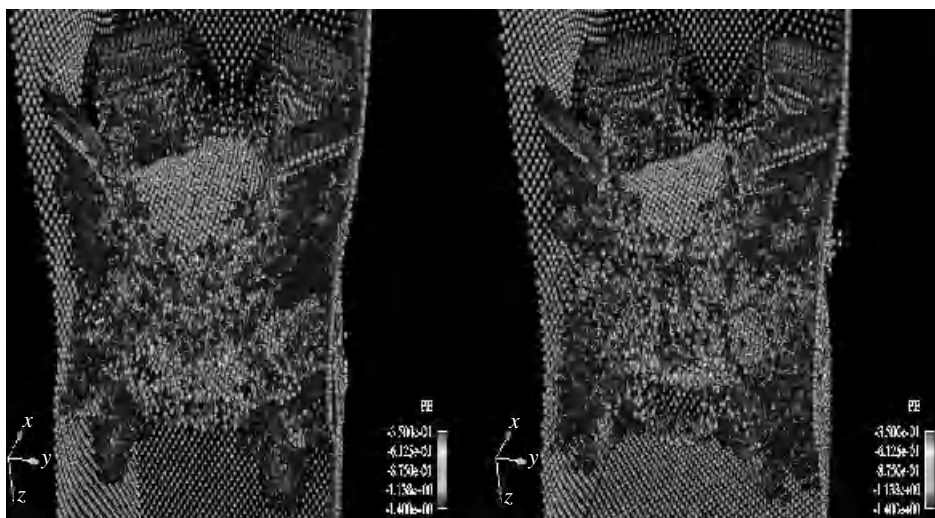


Figure 7.28 Final configuration in left full MD simulation and right bridging scale simulation. Reprinted from Journal of Computational Physics, 207(2), Park et al., Three-dimensional bridging scale analysis of dynamic fracture, 588–609, 2005, with permission from Elsevier.

We note that the crack initiation time and progress during propagation appear to match correctly between both the full MD simulation and bridging scale simulations, as measured visually. Unlike the two-dimensional multiple scale fracture simulations considered by Park et al. (2005c), the crack tip position has not been detailed as a function of time, owing to the inherent difficulty in tracking a planar crack front in three dimensions.

Finally, Figures 7.25 and 7.28 powerfully demonstrate the utility of multiple scale methods. In these images, it is clearly seen that only a small percentage of the atoms are largely perturbed from their equilibrium positions, even during catastrophic material failure processes such as a fracture. Owing to the fact that only a small percentage of the atoms play a critical role in describing the onset and subsequent propagation of cracks and defects, it seems clear that multiple scale methods are well suited for eliminating the unnecessary atomistic degrees of freedom in favor of a continuum representation, as is done here.

7.7 Virtual Atom Cluster Numerical Examples

7.7.1 Bending of Carbon Nanotubes

In this section, we review the application of the virtual atom cluster (VAC) method, Section 6.5, to the analysis of bending and buckling of carbon nanotubes; see Liu et al. (2004b), Qian et al. (2004) and Liu et al. (2005d). The approach is utilized for a 15-walled carbon nanotube (CNT) model with the outermost shell being a (150, 150) nanotube, and all inner shells of the (n, n) type; from the outer most shell, n reduces by 5 every layer. The length of the tube is 110 nm and the original MD system contains more than 3 million atoms. This is replaced with a system of 27,450 particles. In addition to the particles, two sections along the tube are enriched with the molecular structure of multiwalled nanotubes. The position of the enrichment region is determined by a multiresolution analysis of the coarse scale simulation. Therefore, the scheme is adaptive. The length of each enrichment region is 3.7 nm. Each section contains 42,000 atoms, which add 246,000 more atomistic degrees of freedom.

A bending angle with an increment of 0.25 degree/step is imposed on both ends of the tube for a total of 100 steps. The multiscale configuration is illustrated in Figure 7.29(a). Figure 7.29(b) shows the buckling pattern approximated by the meshfree approximation at the final stage of loading, followed by the energy density contour plot for each layer of the CNT. Two distinctive buckling patterns can be seen from the meshfree approximation, while the contour plot clearly shows the strain energy concentration at the buckling point. A unique advantage of using the multiscale method is that the details of the molecular structure at the kinks are able to be resolved; these cannot be resolved by the coarse scale representation alone. The atomic structure of the buckling region for each layer of multiwalled CNT is plotted on the right-hand side of Figure 7.29(b).

7.7.2 VAC Coupling with Tight Binding

Since the VAC model allows for the direct passage of information between the first-principles quantum-mechanical model and the FEM model a fully coupled multiphysics approach can be developed to further extend the capabilities of the present FEM/meshfree-based simulation tools. Owing to the fact that the VAC model is a local representation,

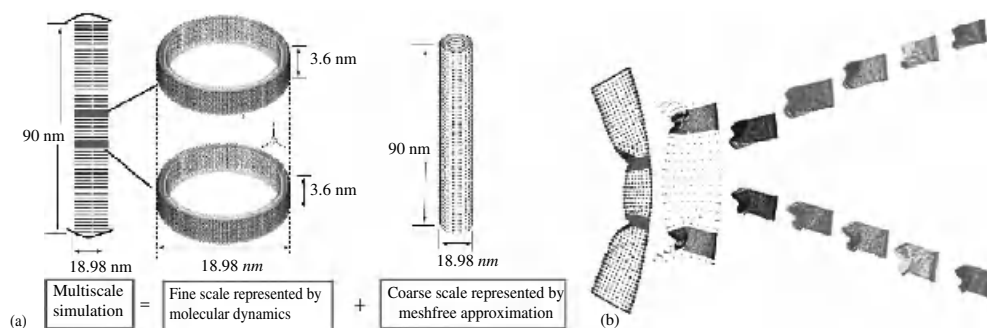


Figure 7.29 Multiscale analysis of a 15-walled CNT by the VAC method of Liu et al. (2004b) and Qian et al. (2004). (a) Multiscale simulation consists of 10 rings of carbon atoms (with 42,000 atoms each) and a meshfree continuum approximation of the 15-walled CNT by 27,450 finite element nodes. (b) Global buckling pattern is captured by the meshfree method whereas the detailed local buckling of the ten rings of atoms is captured by the molecular dynamics simulation. Reprinted from Computer Methods in Applied Mechanics and Engineering, 193(17–20), Liu et al., An introduction to computational nano mechanics and materials, 1529–1578, 2004, with permission from Elsevier.

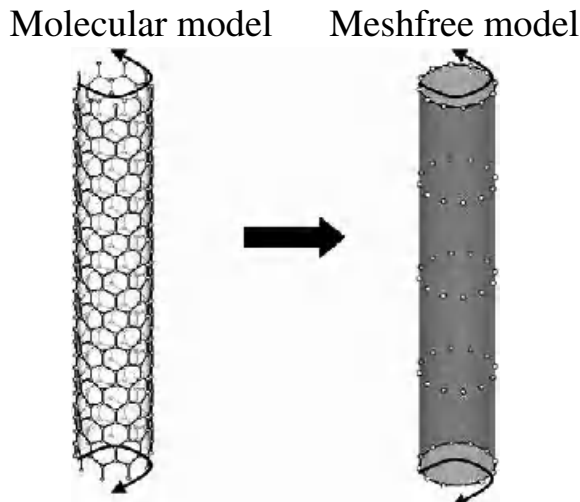


Figure 7.30 Meshfree discretization of a (9, 0) single-walled carbon nanotube. Reprinted from Computer Methods in Applied Mechanics and Engineering, Liu WK, Park HS, Qian D and Karpov EG et al., Bridging scale methods for nanomechanics and materials, 2005, with permission from Elsevier.

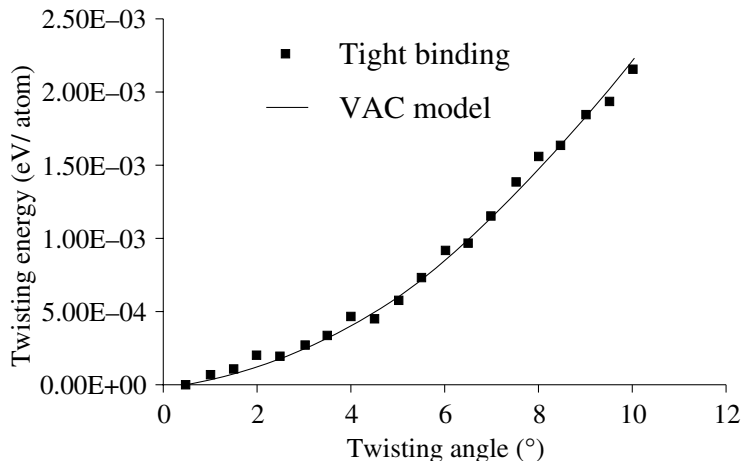


Figure 7.31 Comparison of the average twisting energy between VAC model and tight-binding model. Reprinted from Computer Methods in Applied Mechanics and Engineering, Liu WK, Park HS, Qian D and Karpov EG et al., Bridging scale methods for nanomechanics and materials, 2005, with permission from Elsevier.

the resulting formulation is computationally more efficient than the full-scale first principle method, and therefore the length scale limit can be further extended. The details of this extension can be found in Qian and Liu (2004).

In the following text, we will show a preliminary example in which the VAC model is fully coupled with a semiempirical tight-binding method. The system being considered is a (9, 0) single-walled carbon nanotube with 360 atoms (for an overview of the mechanics of carbon nanotubes, see Qian et al. (2002)). As shown in Figure 7.30, the system is discretized with 60 particles using a meshfree interpolation (Li and Liu 2002). An incremental twisting angle of $0.25^\circ/\text{step}$ is imposed on both ends for 20 steps. For the purpose of verifying the proposed VAC model, a benchmark simulation using a full-scale tight-binding method is also performed. A comparison of the average energy of the system is shown in Figure 7.31. As can be seen, the results from the VAC model closely match those from the tight-binding method. However, the VAC model is computationally much more efficient compared to a full-scale tight-binding simulation.

Non-Nearest Neighbor MD Boundary Condition

8.1 Introduction

The motivation for this chapter stems from the fact that the MD impedance force boundary condition (6.100) used in the previous chapters was limited to a nearest neighbor formulation only. Because of the fact that many important physical phenomena cannot be modeled using a nearest neighbor approximation, and also because atomic interactions are, in general, nonlocal, in this section we endeavor to extend the impedance force boundary condition to account for non-nearest neighbor interactions. We present the methodology in three dimensions, and demonstrate the effectiveness of the approach via simple one-dimensional wave propagation examples. This chapter constitutes a summary of the work presented in Park et al. (2005a).

8.2 Theoretical Formulation in 3D

In this section, we present the theoretical formulation of the non-nearest neighbor boundary conditions in three dimensions, which represents a generalization of the work by Wagner et al. (2004) and Karpov et al. (2005b). The three-dimensional analog of the fine scale equation of motion (6.71) for an arbitrary atom n can be written as

$$\ddot{\mathbf{u}}'_{l,m,n}(t) = \sum_{l'=l-2}^{l+2} \sum_{m'=m-2}^{m+2} \sum_{n'=n-2}^{n+2} \mathbf{M}_A^{-1} \mathbf{K}_{l-l', m-m', n-n'} \mathbf{u}'_{l', m', n'}(t) + \mathbf{f}_{l,m,n}^{\text{ext}}(t) \quad (8.1)$$

where \mathbf{M}_A is a diagonal matrix of atomic masses, \mathbf{K} are the stiffness coefficients relating the force on atom (l, m, n) to displacements of neighboring atoms (l', m', n') , and $\mathbf{f}_{l,m,n}^{\text{ext}}(t)$ is the external force acting on atom (l, m, n) . It is a noteworthy fact that the summation over the stiffness coefficients extends from $n - 2$ to $n + 2$, indicating the longer-ranged interactions.

The key point in extending the impedance force formulation to non-nearest neighbors is in recognizing that owing to the non-nearest atomic interactions, the virtual external load

$$\mathbf{f}_{l,m,n}^{\text{ext}}(t) = \delta_{n,0}\mathbf{f}_{l,m,0}^{\text{ext}}(t) + \delta_{n,1}\mathbf{f}_{l,m,1}^{\text{ext}}(t) \quad (8.2)$$

acts upon multiple planes of atoms near the boundary. We note that while the material to be presented can be generalized for any number of atomic interactions, this generalization is simply that the virtual external force must act upon all planes of boundary atoms whose neighbor lists include those atoms to be eliminated. For example, for a third shell potential, the virtual external load would be written as:

$$\mathbf{f}_{l,m,n}^{\text{ext}}(t) = \delta_{n,0}\mathbf{f}_{l,m,0}^{\text{ext}}(t) + \delta_{n,1}\mathbf{f}_{l,m,1}^{\text{ext}}(t) + \delta_{n,2}\mathbf{f}_{l,m,2}^{\text{ext}}(t) \quad (8.3)$$

For clarity, we show the details for the second-nearest neighbor case. For the case where second-nearest neighbor interactions are required, the virtual external force acts upon two planes of boundary atoms. Taking a Laplace and discrete Fourier transform of (8.1) and solving for the resulting fine scale displacements $\hat{\mathbf{U}'}$ gives

$$\begin{aligned} \hat{\mathbf{U}'}(p, q, r, s) &= \hat{\mathbf{G}}(p, q, r, s) \\ &\times (\hat{\mathbf{F}}_0^{\text{ext}}(p, q, r, s) + e^{-ip}\hat{\mathbf{F}}_1^{\text{ext}}(p, q, r, s) + s\mathbf{u}'(p, q, r, 0) + \dot{\mathbf{u}'}(p, q, r, 0)) \end{aligned} \quad (8.4)$$

where

$$\hat{\mathbf{G}}(p, q, r, s) = (s^2\mathbf{M}_A - \hat{\mathbf{K}}(p, q, r))^{-1} \quad (8.5)$$

The goal of this process is to eliminate $\hat{\mathbf{F}}_0^{\text{ext}}(p, q, r, s)$ and $\hat{\mathbf{F}}_1^{\text{ext}}(p, q, r, s)$. To do so, we perform an inverse discrete Fourier transform of (8.4) for r to give

$$\tilde{\mathbf{U}}'_n(p, q, s) = \tilde{\mathbf{G}}_n(p, q, s)\hat{\mathbf{F}}_0^{\text{ext}}(p, q, s) + \tilde{\mathbf{G}}_{n-1}(p, q, s)\hat{\mathbf{F}}_1^{\text{ext}}(p, q, s) + \tilde{\mathbf{R}}_n(p, q, s) \quad (8.6)$$

where

$$\tilde{\mathbf{R}}_n(p, q, s) = \sum_{n'=-N/2}^{N/2-1} \tilde{\mathbf{G}}_{n-n'}(p, q, s) (s\mathbf{U}'_{n'}(p, q, 0) + \dot{\mathbf{U}}'_{n'}(p, q, 0)) \quad (8.7)$$

We note that in deriving (8.6), the expression

$$\mathcal{F}(g_{n+h}) = \hat{g}(p) e^{ihp} \quad (8.8)$$

known as the *shift theorem* was utilized. Here, as in the previous chapters, p , q and r correspond to spatial indices l , m and n . Next, we write (8.6) for $n = 0, 1, 2, 3$ (atoms 2 and 3 constitute coarse grain atoms) to obtain

$$\tilde{\mathbf{U}}'_0(p, q, s) = \tilde{\mathbf{G}}_0(p, q, s)\hat{\mathbf{F}}_0^{\text{ext}}(p, q, s) + \tilde{\mathbf{G}}_{-1}(p, q, s)\hat{\mathbf{F}}_1^{\text{ext}}(p, q, s) + \tilde{\mathbf{R}}_0(p, q, s) \quad (8.9)$$

$$\tilde{\mathbf{U}}'_1(p, q, s) = \tilde{\mathbf{G}}_1(p, q, s)\hat{\mathbf{F}}_0^{\text{ext}}(p, q, s) + \tilde{\mathbf{G}}_0(p, q, s)\hat{\mathbf{F}}_1^{\text{ext}}(p, q, s) + \tilde{\mathbf{R}}_1(p, q, s) \quad (8.10)$$

$$\tilde{\mathbf{U}}'_2(p, q, s) = \tilde{\mathbf{G}}_2(p, q, s)\hat{\mathbf{F}}_0^{\text{ext}}(p, q, s) + \tilde{\mathbf{G}}_1(p, q, s)\hat{\mathbf{F}}_1^{\text{ext}}(p, q, s) + \tilde{\mathbf{R}}_2(p, q, s) \quad (8.11)$$

$$\tilde{\mathbf{U}}'_3(p, q, s) = \tilde{\mathbf{G}}_3(p, q, s)\hat{\mathbf{F}}_0^{\text{ext}}(p, q, s) + \tilde{\mathbf{G}}_2(p, q, s)\hat{\mathbf{F}}_1^{\text{ext}}(p, q, s) + \tilde{\mathbf{R}}_3(p, q, s) \quad (8.12)$$

We can now use the above equations to make two relations. First, we will relate the virtual forces to the displacements of atoms 0 and 1. We use (8.9) and (8.10) to obtain

$$\begin{pmatrix} \hat{\mathbf{F}}_0^{\text{ext}}(p, q, s) \\ \hat{\mathbf{F}}_1^{\text{ext}}(p, q, s) \end{pmatrix} = \begin{pmatrix} \tilde{\mathbf{G}}_0(p, q, s) & \tilde{\mathbf{G}}_{-1}(p, q, s) \\ \tilde{\mathbf{G}}_1(p, q, s) & \tilde{\mathbf{G}}_0(p, q, s) \end{pmatrix}^{-1} \begin{pmatrix} \tilde{\mathbf{U}}'_0(p, q, s) - \tilde{\mathbf{R}}_0(p, q, s) \\ \tilde{\mathbf{U}}'_1(p, q, s) - \tilde{\mathbf{R}}_1(p, q, s) \end{pmatrix} \quad (8.13)$$

We next utilize (8.11) and (8.12) to express the displacements of atoms 2 and 3 in terms of the virtual external forces as

$$\begin{pmatrix} \tilde{\mathbf{U}}'_2(p, q, s) \\ \tilde{\mathbf{U}}'_3(p, q, s) \end{pmatrix} = \begin{pmatrix} \tilde{\mathbf{G}}_2(p, q, s) & \tilde{\mathbf{G}}_1(p, q, s) \\ \tilde{\mathbf{G}}_3(p, q, s) & \tilde{\mathbf{G}}_2(p, q, s) \end{pmatrix} \begin{pmatrix} \hat{\mathbf{F}}_0^{\text{ext}}(p, q, s) \\ \hat{\mathbf{F}}_1^{\text{ext}}(p, q, s) \end{pmatrix} + \begin{pmatrix} \tilde{\mathbf{R}}_2(p, q, s) \\ \tilde{\mathbf{R}}_3(p, q, s) \end{pmatrix} \quad (8.14)$$

Finally, substitute (8.13) into (8.14) to obtain

$$\begin{pmatrix} \tilde{\mathbf{U}}'_2(p, q, s) \\ \tilde{\mathbf{U}}'_3(p, q, s) \end{pmatrix} = \tilde{\mathbf{Q}}(p, q, s) \begin{pmatrix} \tilde{\mathbf{U}}'_0(p, q, s) - \tilde{\mathbf{R}}_0(p, q, s) \\ \tilde{\mathbf{U}}'_1(p, q, s) - \tilde{\mathbf{R}}_1(p, q, s) \end{pmatrix} + \begin{pmatrix} \tilde{\mathbf{R}}_2(p, q, s) \\ \tilde{\mathbf{R}}_3(p, q, s) \end{pmatrix} \quad (8.15)$$

where

$$\tilde{\mathbf{Q}}(p, q, s) = \begin{pmatrix} \tilde{\mathbf{G}}_2(p, q, s) & \tilde{\mathbf{G}}_1(p, q, s) \\ \tilde{\mathbf{G}}_3(p, q, s) & \tilde{\mathbf{G}}_2(p, q, s) \end{pmatrix} \begin{pmatrix} \tilde{\mathbf{G}}_0(p, q, s) & \tilde{\mathbf{G}}_{-1}(p, q, s) \\ \tilde{\mathbf{G}}_1(p, q, s) & \tilde{\mathbf{G}}_0(p, q, s) \end{pmatrix}^{-1} \quad (8.16)$$

$$\tilde{\mathbf{Q}}(p, q, s) \equiv \begin{pmatrix} \tilde{\mathbf{Q}}^{(11)}(p, q, s) & \tilde{\mathbf{Q}}^{(12)}(p, q, s) \\ \tilde{\mathbf{Q}}^{(21)}(p, q, s) & \tilde{\mathbf{Q}}^{(22)}(p, q, s) \end{pmatrix} \quad (8.17)$$

By inverting the Fourier and Laplace transforms in (8.17), we can analytically obtain the displacements of the coarse grain atomic planes ($n = 2, 3$) in terms of the boundary plane displacements ($n = 0, 1$) as

$$\begin{aligned} & \begin{pmatrix} \mathbf{u}'_{l,m,2}(t) \\ \mathbf{u}'_{l,m,3}(t) \end{pmatrix} - \begin{pmatrix} \mathbf{R}_{l,m,2}(t) \\ \mathbf{R}_{l,m,3}(t) \end{pmatrix} \\ &= \sum_{l'=-L/2}^{L/2-1} \sum_{m'=-M/2}^{M/2-1} \int_0^t \boldsymbol{\theta}_{l-l', m-m'}(t-\tau) \begin{pmatrix} \mathbf{u}'_{l',m',0}(\tau) - \mathbf{R}_{l',m',0}(\tau) \\ \mathbf{u}'_{l',m',1}(\tau) - \mathbf{R}_{l',m',1}(\tau) \end{pmatrix} d\tau \quad (8.18) \end{aligned}$$

where

$$\boldsymbol{\theta}_{l,m}(t) \equiv \begin{pmatrix} \boldsymbol{\theta}_{l,m}^{(11)}(t) & \boldsymbol{\theta}_{l,m}^{(12)}(t) \\ \boldsymbol{\theta}_{l,m}^{(21)}(t) & \boldsymbol{\theta}_{l,m}^{(22)}(t) \end{pmatrix} \quad (8.19)$$

and

$$\boldsymbol{\theta}_{l,m} = \mathcal{L}_{s \rightarrow t}^{-1} \mathcal{F}_{p \rightarrow l}^{-1} \mathcal{F}_{q \rightarrow m}^{-1} \{ \tilde{\mathbf{Q}}(p, q, s) \} \quad (8.20)$$

Equation (8.18) is important because it shows that the fine scale portion \mathbf{u}' of the coarse grain atom displacements can be calculated exactly using analytically derived relationships according to the time-history kernel $\boldsymbol{\theta}(t)$. Because the total displacement \mathbf{u} is a sum of the coarse and fine portions of the displacement field as in (6.1), we can add the interpolated coarse scale displacements $\bar{\mathbf{u}}$ at the coarse grain atoms to the fine scale portion calculated from (8.18) to obtain the total displacements of the coarse grain atoms. By doing so, no additional terms are necessary to augment the MD equation of motion; instead, the

coarse grain atomic positions are simply computed and used exactly in the MD internal force subroutine as before. The fact that the fine scale portion of the coarse grain atomic displacements contains the contribution from the time-history kernel ensures that spurious high-frequency wave reflections at the MD/FE interface will be properly eliminated.

In contrast, previous incarnations of the bridging scale have utilized an impedance force formulation to remove spurious wave reflection at the MD/FE interface. To derive the impedance force formulation, we simply note that

$$\mathbf{F}_{l,m,1}^{\text{imp}}(s) = \sum_{l'=l-2}^{l+2} \sum_{m'=m-2}^{m+2} \mathbf{K}_{l-l',m-m',-2} \mathbf{U}_{l',m',2}(s) \quad (8.21)$$

$$\begin{aligned} \mathbf{F}_{l,m,0}^{\text{imp}}(s) &= \sum_{l'=l-2}^{l+2} \sum_{m'=m-2}^{m+2} \mathbf{K}_{l-l',m-m',-1} \mathbf{U}_{l',m',2}(s) \\ &\quad + \sum_{l'=l-2}^{l+2} \sum_{m'=m-2}^{m+2} \mathbf{K}_{l-l',m-m',-2} \mathbf{U}_{l',m',3}(s) \end{aligned} \quad (8.22)$$

where we have assumed that the fine scale displacements in (8.21) and (8.22) have already been inverted using Fourier transforms. We note that the impedance force that acts upon boundary plane $n = 1$ has contributions from two planes of atoms $n = 2$ and $n = 3$ owing to the fact that the impedance force accounts for the missing interactions on plane $n = 0$. In contrast, the impedance force on boundary plane $n = 0$ contains only one term, as it is missing only one plane of atomic neighbors, $n = 2$.

By taking the inverse Fourier transform of (8.21) and (8.22), we obtain the impedance forces that act upon the boundary planes to be

$$\begin{aligned} &\left(\begin{array}{c} \mathbf{f}_{l,m,0}^{\text{imp}}(t) \\ \mathbf{f}_{l,m,1}^{\text{imp}}(t) \end{array} \right) - \left(\begin{array}{c} \mathbf{R}_{l,m,0}^f(t) \\ \mathbf{R}_{l,m,1}^f(t) \end{array} \right) \\ &= \sum_{l'=-L/2}^{L/2-1} \sum_{m'=-M/2}^{M/2-1} \int_0^t \bar{\boldsymbol{\theta}}_{l-l',m-m'}(t-\tau) \left(\begin{array}{c} \mathbf{u}'_{l',m',0}(\tau) - \mathbf{R}_{l',m',0}(\tau) \\ \mathbf{u}'_{l',m',1}(\tau) - \mathbf{R}_{l',m',1}(\tau) \end{array} \right) \end{aligned} \quad (8.23)$$

where

$$\bar{\boldsymbol{\theta}}_{l,m}(t) = \left(\begin{array}{cc} \bar{\theta}_{l,m}^{(11)}(t) & \bar{\theta}_{l,m}^{(12)}(t) \\ \bar{\theta}_{l,m}^{(21)}(t) & \bar{\theta}_{l,m}^{(22)}(t) \end{array} \right) \quad (8.24)$$

If an impedance force formulation is desired, then an additional step is required to convolute the stiffnesses with the displacements. The bar notation using $\bar{\boldsymbol{\theta}}$ simply indicates the distinction due to the additional convolution with the stiffnesses as opposed to the $\boldsymbol{\theta}(t)$ shown in (8.18). If the impedance force formulation is used, then an additional external force is added to the boundary planes of atoms as dictated by (8.23). The additional impedance force acts to eliminate high-frequency waves that cannot be represented in the continuum region.

8.2.1 Force Boundary Condition: 1D Illustration

In this section, we illustrate the theoretical formulation of the non-nearest neighbor impedance force in one dimension. We consider a chain of atoms interacting via linear springs, as shown in Figure 8.1. The one-dimensional analog of the fine scale equation of motion (6.71) of an arbitrary atom n reads

$$\ddot{u}'_n(t) = \sum_{n'=n-2}^{n+2} m_A^{-1} k_{n-n'} u'_{n'}(t) + m_A^{-1} f_n^{\text{ext}}(t) \quad (8.25)$$

where m_A is the atomic mass of atom n , k are the stiffness coefficients relating the force on atom n to displacements of neighboring atoms n' , and $f_n^{\text{ext}}(t)$ is the external force acting on atom n .

For the case where second-nearest neighbor interactions are required, the virtual external force

$$f_n^{\text{ext}}(t) = \delta_{n,0} f_0^{\text{ext}} + \delta_{n,1} f_1^{\text{ext}} \quad (8.26)$$

acts upon the two boundary atoms at the end of the 1D chain, atoms 0 and 1 in Figure 8.1. Taking a Laplace and discrete Fourier transform of (8.25) and solving for the resulting displacements \hat{U}' gives

$$\hat{U}'(p, s) = \hat{G}(p, s) (F_0^{\text{ext}}(s) + e^{-ip} F_1^{\text{ext}}(s) + s u'(p, 0) + \dot{u}'(p, 0)) \quad (8.27)$$

where

$$\hat{G}(p, s) = (s^2 m_A - \hat{k}(p))^{-1} \quad (8.28)$$

The goal of this process is to eliminate the vectors $F_0^{\text{ext}}(s)$ and $F_1^{\text{ext}}(s)$. To do so, we perform an inverse discrete Fourier transform of (8.27) for p to obtain

$$U'_n(s) = G_n(s) F_0^{\text{ext}}(s) + G_{n-1}(s) F_1^{\text{ext}}(s) + R_n(s) \quad (8.29)$$

where

$$R_n(s) = s \sum_{n'=-N/2}^{N/2-1} G_{n-n'}(s) u'_{n'}(0) + \sum_{n'=-N/2}^{N/2-1} G_{n-n'}(s) \dot{u}'_{n'}(0) \quad (8.30)$$

We note that in deriving (8.29) the expression

$$\mathcal{F}(g_{n+h}) = \hat{g}(p) e^{ihp} \quad (8.31)$$

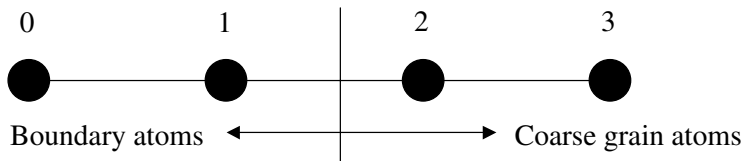


Figure 8.1 1D chain of atoms. Atoms 0 and 1 constitute the boundary atoms upon which the impedance boundary condition will be applied. Atoms 2 and 3 are the coarse grain atoms.

known as the *shift theorem* was utilized. We next write (8.31) for $n = 0, 1, 2, 3$ (atoms 2 and 3 constitute coarse grain atoms) to obtain

$$U'_0(s) = G_0(s)F_0^{\text{ext}}(s) + G_{-1}(s)F_1^{\text{ext}}(s) + R_0(s) \quad (8.32)$$

$$U'_1(s) = G_1(s)F_0^{\text{ext}}(s) + G_0(s)F_1^{\text{ext}}(s) + R_1(s) \quad (8.33)$$

$$U'_2(s) = G_2(s)F_0^{\text{ext}}(s) + G_1(s)F_1^{\text{ext}}(s) + R_2(s) \quad (8.34)$$

$$U'_3(s) = G_3(s)F_0^{\text{ext}}(s) + G_2(s)F_1^{\text{ext}}(s) + R_3(s) \quad (8.35)$$

We can now use the above equations to formulate two relations. First, we will relate the virtual forces to the displacements of atoms 0 and 1. We use (8.32) and (8.33) to give

$$\begin{pmatrix} F_0^{\text{ext}}(s) \\ F_1^{\text{ext}}(s) \end{pmatrix} = \begin{pmatrix} G_0(s) & G_{-1}(s) \\ G_1(s) & G_0(s) \end{pmatrix}^{-1} \begin{pmatrix} U'_0(s) - R_0(s) \\ U'_1(s) - R_1(s) \end{pmatrix} \quad (8.36)$$

We use (8.34) and (8.35) to express the displacements of coarse grain atoms 2 and 3 in terms of the virtual external forces as

$$\begin{pmatrix} U'_2(s) \\ U'_3(s) \end{pmatrix} = \begin{pmatrix} G_2(s) & G_1(s) \\ G_3(s) & G_2(s) \end{pmatrix} \begin{pmatrix} F_0^{\text{ext}}(s) \\ F_1^{\text{ext}}(s) \end{pmatrix} + \begin{pmatrix} R_2(s) \\ R_3(s) \end{pmatrix} \quad (8.37)$$

We substitute (8.36) into (8.37) to obtain

$$\begin{pmatrix} U'_2(s) \\ U'_3(s) \end{pmatrix} = \mathbf{Q}(s) \begin{pmatrix} U'_0(s) - R_0(s) \\ U'_1(s) - R_1(s) \end{pmatrix} + \begin{pmatrix} R_2(s) \\ R_3(s) \end{pmatrix} \quad (8.38)$$

where

$$\mathbf{Q}(s) = \begin{pmatrix} G_2(s) & G_1(s) \\ G_3(s) & G_2(s) \end{pmatrix} \begin{pmatrix} G_0(s) & G_{-1}(s) \\ G_1(s) & G_0(s) \end{pmatrix}^{-1} \quad (8.39)$$

$$\mathbf{Q}(s) \equiv \begin{pmatrix} Q^{(11)}(s) & Q^{(12)}(s) \\ Q^{(21)}(s) & Q^{(22)}(s) \end{pmatrix} \quad (8.40)$$

We can now calculate the impedance forces that are applied to boundary atoms 0 and 1 via the expressions

$$f_1^{\text{imp}}(s) = k_{-1}u'_2(s) + k_{-2}u'_3(s) \quad (8.41)$$

$$f_0^{\text{imp}}(s) = k_{-2}u'_2(s) \quad (8.42)$$

f_1^{imp} and f_0^{imp} represent the external impedance forces acting on the boundary atoms 0 and 1 such that those atoms do not notice that the $n > 1$ atoms have been eliminated.

Because the expressions for the displacements of coarse grain atoms 2 and 3 are given in terms of atoms 1 and 0 via (8.38), we can simply take the inverse Laplace transform of (8.38) and convolute the displacements with the stiffnesses via (8.41) and (8.42) to obtain

the impedance forces that act upon the boundary atoms 0 and 1. By doing so, we obtain

$$\begin{aligned} f_0^{\text{imp}}(t) &= \int_0^t \theta_1(t-\tau) (u'_0(\tau) - R_0(\tau)) d\tau \\ &\quad + \int_0^t \theta_2(t-\tau) (u'_1(\tau) - R_1(\tau)) d\tau \end{aligned} \quad (8.43)$$

$$\begin{aligned} f_1^{\text{imp}}(t) &= \int_0^t \theta_3(t-\tau) (u'_0(\tau) - R_0(\tau)) d\tau \\ &\quad + \int_0^t \theta_4(t-\tau) (u'_1(\tau) - R_1(\tau)) d\tau \end{aligned} \quad (8.44)$$

where

$$\theta_1(t) = \mathcal{L}^{-1}(k_{-2}Q^{(11)}(s)) \quad (8.45)$$

$$\theta_2(t) = \mathcal{L}^{-1}(k_{-2}Q^{(12)}(s)) \quad (8.46)$$

$$\theta_3(t) = \mathcal{L}^{-1}(k_{-1}Q^{(11)}(s) + k_{-2}Q^{(21)}(s)) \quad (8.47)$$

$$\theta_4(t) = \mathcal{L}^{-1}(k_{-1}Q^{(12)}(s) + k_{-2}Q^{(22)}(s)) \quad (8.48)$$

The coupled equations of motion for boundary atoms 0 and 1 can now be written by adding the coarse and fine scale solutions and using the equality of q and u to give

$$m_A \ddot{q}_0(t) = f_0(t) + f_0^{\text{imp}}(t) + R_0^f(t) \quad (8.49)$$

$$m_A \ddot{q}_1(t) = f_1(t) + f_1^{\text{imp}}(t) + R_1^f(t) \quad (8.50)$$

where

$$R_0^f(t) = \mathcal{L}^{-1}(k_{-2}R_2(s)) \quad (8.51)$$

$$R_1^f(t) = \mathcal{L}^{-1}(k_{-1}R_2(s) + k_{-2}R_3(s)) \quad (8.52)$$

By substituting the known relations

$$u'_0(t) = q_0(t) - \bar{u}_0(t) \quad (8.53)$$

$$u'_1(t) = q_1(t) - \bar{u}_1(t) \quad (8.54)$$

into (8.43) and (8.44), the final coupled form of the equations of motion can be derived as

$$\mathbf{M} \ddot{\mathbf{d}}(t) = \mathbf{N}^T \mathbf{f}(\mathbf{u}) \quad (8.55)$$

$$\mathbf{M}_A \ddot{\mathbf{q}}(t) = \mathbf{f}(t) + f_0^{\text{imp}}(t) + f_1^{\text{imp}}(t) + R_0^f(t) + R_1^f(t) \quad (8.56)$$

where the external impedance forces $f_0^{\text{imp}}(t)$ and $f_1^{\text{imp}}(t)$ and random forces $R_0^f(t)$ and $R_1^f(t)$ act *only* on the boundary atoms 0 and 1.

8.2.2 Displacement Boundary Condition: 1D Illustration

In some instances, it may be preferable to use a displacement formulation for the impedance boundary condition instead of the force formulation presented earlier. The main reason for this is that, in most multiple scale methods, the motion of the ghost, or pad atoms, is strictly a function of the finite element interpolation functions. By ghost atoms, we mean those atoms that exist on the boundary of the atomistic domain but whose motion is not solved for in the MD equations of motion. These ghost atoms exist such that the boundary atoms do not sense that they are at a surface; because their motion is not solved for explicitly, it is typically prescribed in multiple scale simulations using the motion of the coarse scale. The coarse grain atoms in the bridging scale act equivalently as ghost atoms, that is, they ensure that the atoms whose motion is solved for using the MD equation of motion see a full complement of atomic neighbors. However, because all atoms in the bridging scale system originally existed before the elimination of unwanted MD degrees of freedom, we maintain the distinction between ghost atoms and coarse grain atoms.

Thus, it would be preferable to control the motion of the coarse grain atoms $n = 2, 3$ using semianalytic means, or as a function of both coarse scales and fine scales. In that case, the formulation is identical to that presented earlier, and we begin using (8.38) and (8.40):

$$\begin{pmatrix} U'_2(s) \\ U'_3(s) \end{pmatrix} = \mathbf{Q}(s) \begin{pmatrix} U'_0(s) - R_0(s) \\ U'_1(s) - R_1(s) \end{pmatrix} + \begin{pmatrix} R_2(s) \\ R_3(s) \end{pmatrix} \quad (8.57)$$

where

$$\mathbf{Q}(s) = \begin{pmatrix} G_2(s) & G_1(s) \\ G_3(s) & G_2(s) \end{pmatrix} \begin{pmatrix} G_0(s) & G_{-1}(s) \\ G_1(s) & G_0(s) \end{pmatrix}^{-1} \quad (8.58)$$

$$\mathbf{Q}(s) \equiv \begin{pmatrix} Q^{(11)}(s) & Q^{(12)}(s) \\ Q^{(21)}(s) & Q^{(22)}(s) \end{pmatrix} \quad (8.59)$$

Because (8.57) gives the analytic solution for the fine scale portion of the displacements, calculation of the total displacements requires a contribution from the coarse scale portion of the total displacements. Computing the coarse scale portion of the total displacement and adding that to the fine scale portion calculated above gives

$$u_2(t) = \bar{u}_2(t) + u'_2(t) \quad (8.60)$$

$$u_3(t) = \bar{u}_3(t) + u'_3(t) \quad (8.61)$$

The fine scale portion of the coarse grain atomic displacements is found taking the inverse Laplace transform of (8.57):

$$\begin{aligned} u'_2(t) &= \int_0^t \theta_1^d(t-\tau) (u'_0(\tau) - R_0(\tau)) d\tau \\ &\quad + \int_0^t \theta_2^d(t-\tau) (u'_1(\tau) - R_1(\tau)) d\tau + R_2(t) \end{aligned} \quad (8.62)$$

$$\begin{aligned} u'_3(t) &= \int_0^t \theta_3^d(t-\tau) (u'_0(\tau) - R_0(\tau)) d\tau \\ &\quad + \int_0^t \theta_4^d(t-\tau) (u'_1(\tau) - R_1(\tau)) d\tau + R_3(t) \end{aligned} \quad (8.63)$$

where

$$\theta_1^d(t) = \mathcal{L}^{-1}(Q^{(11)}(s)) \quad (8.64)$$

$$\theta_2^d(t) = \mathcal{L}^{-1}(Q^{(12)}(s)) \quad (8.65)$$

$$\theta_3^d(t) = \mathcal{L}^{-1}(Q^{(11)}(s) + Q^{(21)}(s)) \quad (8.66)$$

$$\theta_4^d(t) = \mathcal{L}^{-1}(Q^{(12)}(s) + Q^{(22)}(s)) \quad (8.67)$$

This development is significant, as it allows the standard interatomic forces for boundary atoms 0 and 1 to be computed using the total displacements for coarse grain atoms 2 and 3. If this is possible, then no additional external impedance forces will be necessary. In other words, the coarse grain atom displacements 2 and 3 can now be calculated analytically using (8.60) and (8.61) such that the standard MD interatomic force subroutine can be used throughout with no other modification to the equation of motion. Finally, the motion of the ghost atoms is thus calculated semianalytically; the fine scale portion is calculated analytically, while the coarse scale portion is prescribed numerically using the coarse scale interpolation functions.

8.2.3 Comparison to Nearest Neighbors Formulation

While comparing the non-nearest neighbor impedance force formulation found in (8.49) and (8.50) to the nearest neighbor case, for example, Park and Liu (2004) and Wagner and Liu (2003), the following conclusions can be drawn:

- Instead of one time-history kernel $\theta(t)$ in the nearest neighbors case, there are four instances of $\theta(t)$ in the non-nearest neighbors case. This is due to the fact that not only the boundary atom but also nonboundary atoms depending on the cutoff radius of the potential require additional forces to replace the effects of missing atomic neighbors.
- The impedance forces on the boundary atoms 0 and 1 still depend only on the displacement histories of those atoms.
- The underlying formulation has not changed; the major difference is that the summation over the stiffness matrices in (8.25) has been increased to account for non-nearest neighbor interactions.
- The size of the $\theta(t)$ matrices in (8.45)–(8.48) and the $\theta^d(t)$ matrices in (8.64)–(8.67) has not changed; each θ matrix still has the size of the minimum number of degrees of freedom in each unit cell. In one dimension, $\theta(t)$ is a scalar; in two dimensions, $\theta(t)$ is 2×2 , and in three dimensions, $\theta(t)$ is 3×3 .
- We note that the work of Wagner et al. (2004) considered situations in which the atomic interactions extended beyond the nearest neighbor. However, in that work, the size of the unit cell was extended to account for the nonlocal interactions. The effect of extending the size of the unit cell is that the size of the time-history kernel matrix $\theta(t)$ grows correspondingly. In this work, because the size of the unit cell is always the number of degrees of freedom for a single atom, the size of $\theta(t)$ stays constant regardless of the number of atomic interactions.

8.2.4 Advantages of Displacement Formulation

It may be advantageous to use the displacement formulation rather than the force formulation for the following reasons:

- The formulation assures that the coarse grain atomic displacements u_2 and u_3 are calculated accurately, as a combination of coarse and fine scales as in (8.60) and (8.61). In the force formulation, only the coarse scale component is used to calculate the ghost atom displacements.
- The displacement $\theta^d(t)$ requires less computational effort than the force $\theta(t)$, because the additional convolution with the stiffnesses is not necessary to compute it.
- The displacement $\theta^d(t)$ is of the same size as the force $\theta(t)$ matrices. Therefore, the comment regarding the relation of the size of $\theta(t)$ to the number of degrees of freedom holds in this case too.

8.3 Numerical Examples: 1D Wave Propagation

In this section, we present the one-dimensional verification of the time-history kernel derived for non-nearest neighbor interactions. The examples take the form of simple one-dimensional wave propagation examples, similar to those presented earlier in this thesis, and also similar to those originally shown by Wagner and Liu (2003), with the major difference being that both the MD forces and the Cauchy–Born rule for the coarse scale are calculated using second-nearest neighbor effects.

A harmonic potential that takes the form

$$\Phi(r) = \frac{1}{2}k(r - r_0)^2 \quad (8.68)$$

was used to describe the atomic interactions, while the Cauchy–Born rule was used based on the same harmonic potential to derive the coarse scale nodal forces where the MD region does not exist. Two hundred and forty one atoms were used in the bridging scale simulation between $x = -0.4$ and $x = 0.4$, while 40 finite elements spanned the entire domain between $x = -1.0$ and $x = 1.0$. The spring constant k and the atomic mass m were set to be unity, with $r_0 = 0.005$ and the initial atomic spacing was $r = 2r_0/3$. Sixty FE time steps were used, with 20 MD time steps for each FE time step. The initial configuration for the coupled problem is shown in Figure 8.2.

The time-history kernels $\theta^d(t)$ are shown in Figure 8.3. As can be seen, the time-history kernels that result from the second-nearest neighbor interactions behave similar to the nearest neighbor kernels, specifically in the quick decay in the amplitude of the kernels. Therefore, the kernel functions can again be truncated after a short period of time without much loss in accuracy.

The energy transfer from the MD region was calculated for the coupled problem, and compared with the full MD simulation. Figure 8.4 shows the results from simulations in which the impedance forces were applied to the boundary atoms. As can be seen, the bridging scale simulation agrees almost perfectly with the full MD simulation. In contrast, if the impedances forces are not applied correctly to the MD boundary atoms, nearly 90% of the MD energy is reflected at the boundary.

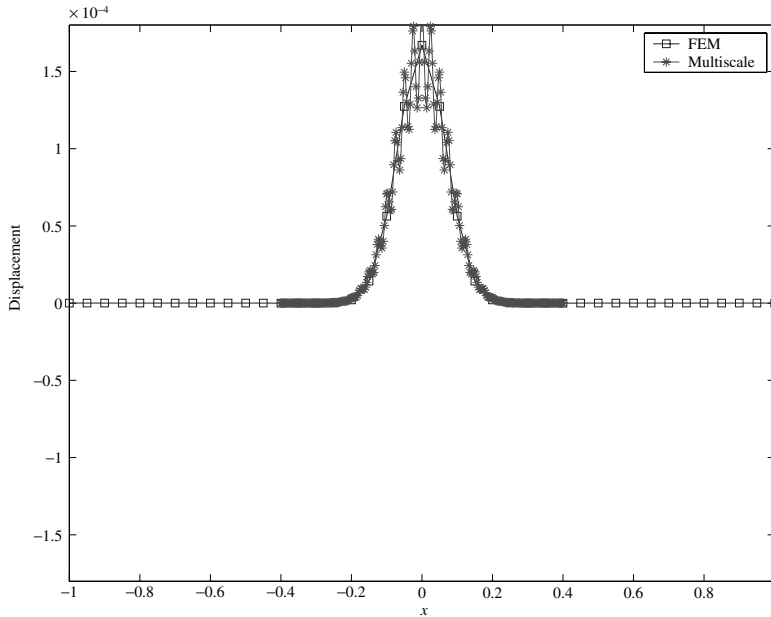


Figure 8.2 Initial MD and FEM displacements for non-nearest neighbor wave propagation example.

8.4 Time-History Kernels for FCC Gold

In this section, we present calculations for the time-history kernel $\theta(t)$ for face-centered cubic (FCC) gold using the embedded atom method (EAM) of Daw and Baskes (1984). The parameters used for FCC gold are identical to those found in Foiles et al. (1986), which have been implemented in the Sandia simulation code Tahoe (2004). The parameters for FCC gold result in a third shell potential, which means that 43 \mathbf{K} matrices need to be found in order to calculate $\theta(t)$ correctly. Those \mathbf{K} matrices were found by systematically perturbing all neighbors of a unit cell, and are given in the Appendix.

Recalling that each submatrix of $\theta(t)$ is itself a 3×3 matrix, as in (8.19), we show only selected components of $\theta^{(22)}$. In particular, note that $\theta^{(22)}$ can be represented as

$$\theta^{(22)}(t) = \begin{pmatrix} \theta_{11}^{(22)}(t) & \theta_{12}^{(22)}(t) & \theta_{13}^{(22)}(t) \\ \theta_{21}^{(22)}(t) & \theta_{22}^{(22)}(t) & \theta_{23}^{(22)}(t) \\ \theta_{31}^{(22)}(t) & \theta_{32}^{(22)}(t) & \theta_{33}^{(22)}(t) \end{pmatrix} \quad (8.69)$$

We show only the specific components $\theta_{32}^{(22)}(t)$ and $\theta_{33}^{(22)}(t)$. These are shown in Figures 8.5–8.10. To aid in the visualization, we introduce Figure 8.11, which depicts all neighbors for atom $(0, 0, 0)$ within the xy -plane.

One interesting feature present in all the figures is that the time history kernels all have a value of zero for those lattice sites at which a neighboring atom is not present. These

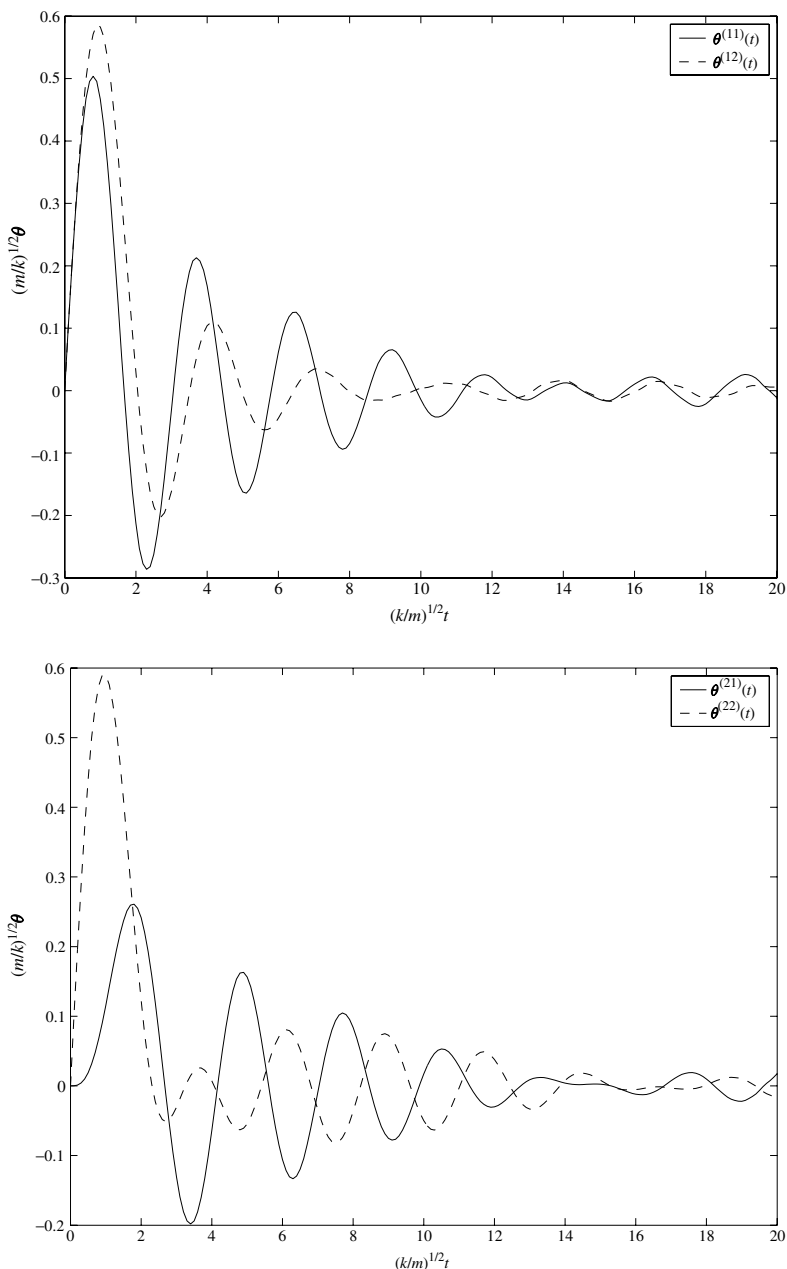


Figure 8.3 Components of the time-history kernel matrix for second-nearest neighbor interactions. Reproduced with permission from H. S. Park et al., International Journal for Numerical Methods in Engineering, published by John Wiley and Sons Ltd., 2005.

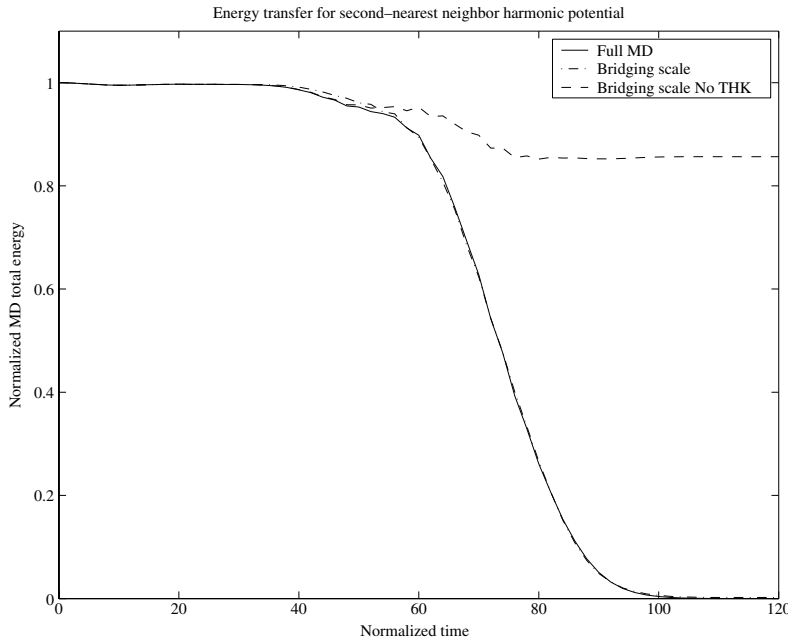


Figure 8.4 Energy transferred from MD region in coupled simulation.

zero atom positions correspond to lattice sites $l = -1, m = 0, l = 0, m = -1, l = 0, m = 1$ and $l = 1, m = 0$, and can be seen to be true by direct comparison with Figure 8.11. In Figures 8.5–8.10, all the values of $\theta(t)$ are zero for those positions at which a neighboring atom is not present, and represent a check on the accuracy of the method.

Another interesting feature is in the symmetries exhibited by the time-history kernels. Owing to the symmetry of an FCC crystal, one would expect to correspondingly see some sort of symmetry in the crystal response, and that is indeed observed. Specifically, those pairs of atoms with one spatial coordinate as the negative of the other, such as $l = -1, m = 1$ and $l = -1, m = 1$, either have the same time-history values, as in Figures 8.8–8.10, or are related by a negative, as in Figures 8.5–8.7.

Finally, most values of the kernels tend to decay quickly over relatively short periods of time. This again leads to gains in computational efficiency by reducing the storage requirements necessary for the boundary atom displacement histories.

8.5 Conclusion for the Bridging Scale Method

In Chapters 7 and 8 of this book, we presented a detailed overview of the bridging scale method, which is a recently developed multiple scale method to concurrently couple atomistic and continuum simulation techniques. The bridging scale offers two clear *advantages* to previously developed multiple scale methods. One advantage is in the distinct separation between coarse and fine scales made possible by the projection operator technique, and more specifically, the fact that a truly coarse finite element mesh can be used throughout

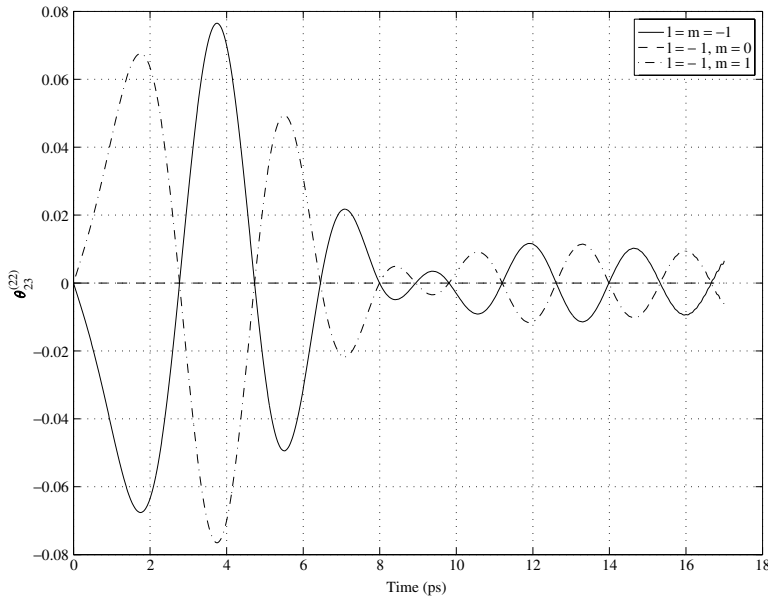


Figure 8.5 $\theta_{23}^{(22)}(t)$ for $l = -1, m = -1, 0, 1$. Reproduced with permission from H. S. Park et al., International Journal for Numerical Methods in Engineering, published by John Wiley and Sons Ltd., 2005.

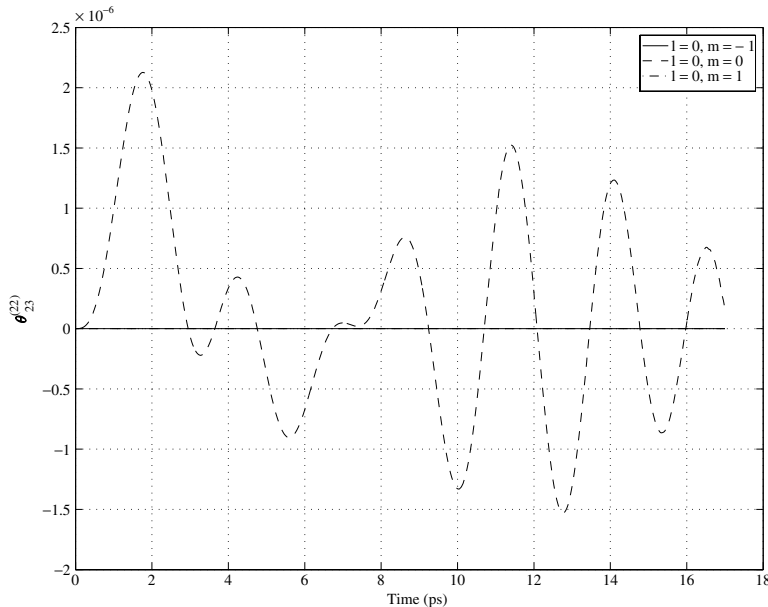


Figure 8.6 $\theta_{23}^{(22)}(t)$ for $l = 0, m = -1, 0, 1$. Reproduced with permission from H. S. Park et al., International Journal for Numerical Methods in Engineering, published by John Wiley and Sons Ltd, 2005.

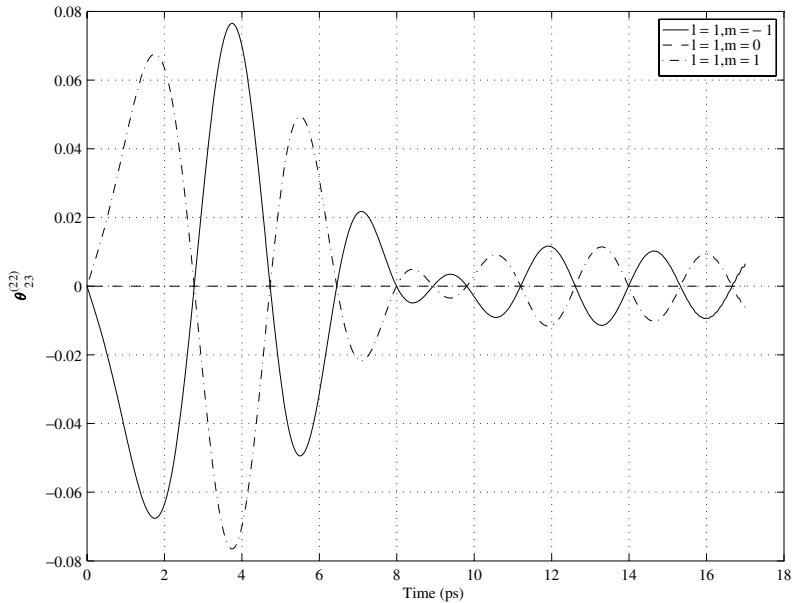


Figure 8.7 $\theta_{23}^{(22)}(t)$ for $l = 1, m = -1, 0, 1$. Reproduced with permission from H. S. Park et al., International Journal for Numerical Methods in Engineering, published by John Wiley and Sons Ltd, 2005.

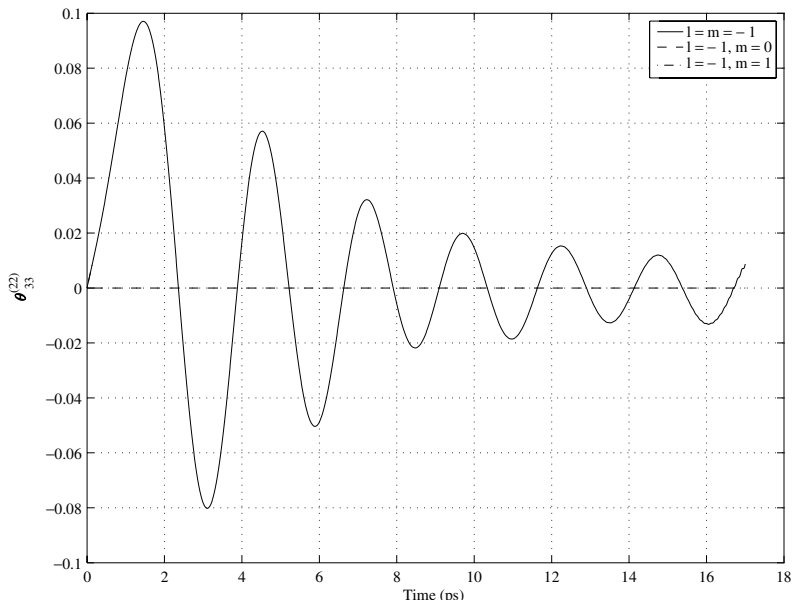


Figure 8.8 $\theta_{33}^{(22)}(t)$ for $l = -1, m = -1, 0, 1$. Reproduced with permission from H. S. Park et al., International Journal for Numerical Methods in Engineering, published by John Wiley and Sons Ltd, 2005.

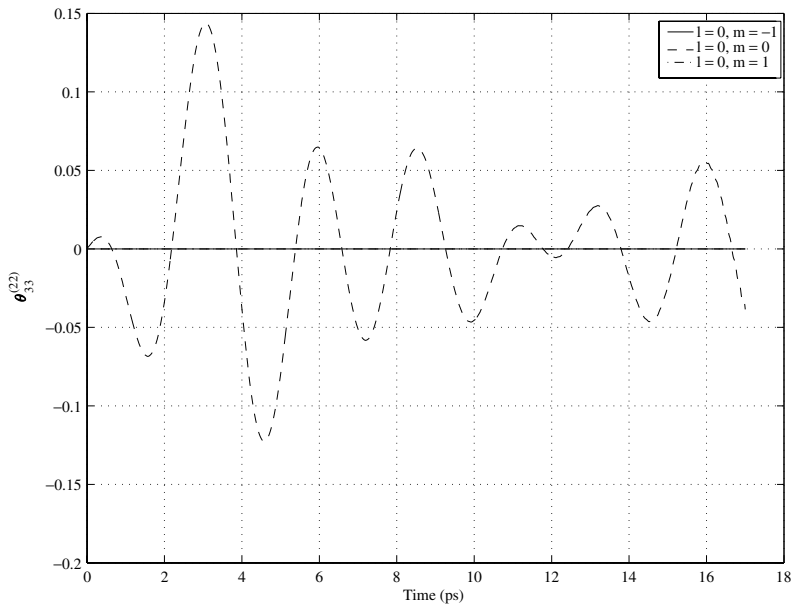


Figure 8.9 $\theta_{33}^{(22)}(t)$ for $l = 0, m = -1, 0, 1$. Reproduced with permission from H. S. Park et al., International Journal for Numerical Methods in Engineering, published by John Wiley and Sons Ltd, 2005.

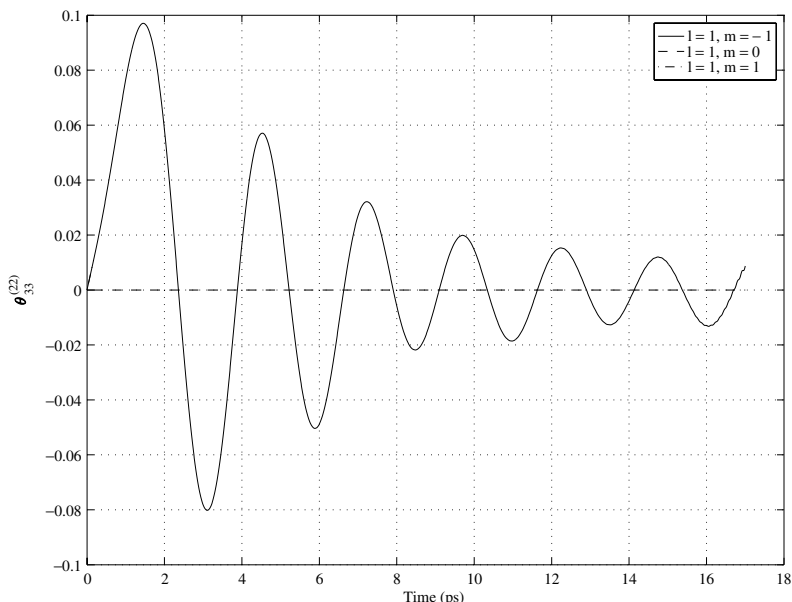


Figure 8.10 $\theta_{33}^{(22)}(t)$ for $l = 1, m = -1, 0, 1$. Reproduced with permission from H. S. Park et al., International Journal for Numerical Methods in Engineering, published by John Wiley and Sons Ltd, 2005.

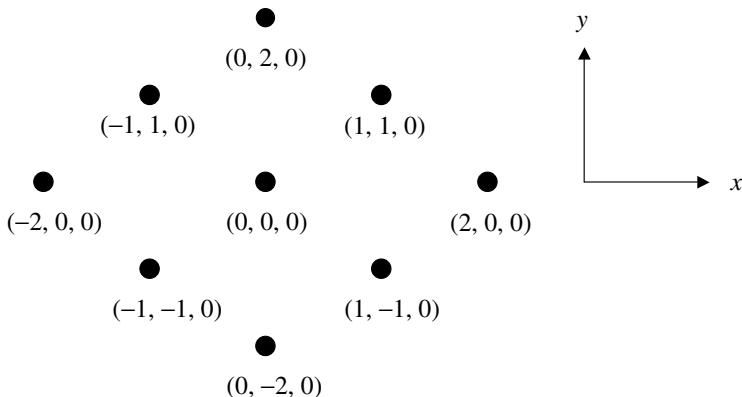


Figure 8.11 All neighbors of atom $(0, 0, 0)$ within the xy - plane. Reproduced with permission from H. S. Park et al., International Journal for Numerical Methods in Engineering, published by John Wiley and Sons Ltd, 2005.

the domain. This leads to a combined spatial and temporal savings, both in the time step needed to integrate the FE equations of motion, and also in the number of integration points needed owing to the coarse mesh. The second major advantage lies in the fact that the time-history kernel matrix $\theta(t)$, which acts to dissipate fine scale waves that cannot be represented by the continuum, can be calculated numerically for arbitrary interatomic potentials applied to arbitrary crystal structures. The numerical algorithm involves only standard Laplace and Fourier transform techniques and can be easily automated. Finally, the bridging scale is valid for finite temperature, dynamic problems.

Numerical validation of the method has been presented for one-, two- and three-dimensional problems. Wave propagation examples in one and two dimensions illustrated the effectiveness of the derived impedance force in eliminating potentially spurious high-frequency fine scale waves at the MD/FE interface. More interestingly, crack propagation problems in two and three dimensions were solved. In this case, the truly two-way coupled nature of the MD boundary condition was illustrated. The coupling to the coarse scale allowed large-scale information originating in the continuum to be transferred naturally to the MD region, causing the crack to initiate at the correct time. Correspondingly, the MD impedance force once again dissipated the high-frequency fine scale waves generated by the moving crack as it broke fine scale atomic bonds. The three-dimensional examples illustrated some of the interesting physics that can be captured using the bridging scale, as crack branching was seen to occur. In all the cases, comparisons to full MD simulations were made such that the validity of the bridging scale simulations could be assessed.

An interesting point of discussion concerns the fact that the numerical examples presented in this book concentrated on the modeling and simulation of fracture and material failure. There are three major reasons for this emphasis. The first is due to practical considerations; because the backbone of the bridging scale method, and more generally multiple scale methods, is MD, all inherent limitations in MD will correspondingly manifest themselves in the bridging scale. As was discussed, one major shortcoming of MD is in the timescales available for simulation; because of this, MD and, thus, the bridging scales are

currently not well suited for infrequent event-type simulations such as diffusion. In contrast, the bond breaking that occurs during fracture and failure simulations are not infrequent events, and thus lend themselves elegantly to multiple scale modeling.

The second major reason for the emphasis on fracture and failure simulations is that the global aim of multiple scale simulations is to accurately model and predict failure in micro- and nanoscale devices and structures. The envisaged goal for multiple scale analysis is in the prediction of material constants, particularly near or at material failure for these novel small-scale materials. Thus, the numerical examples shown mark a first attempt at analyzing the effectiveness of multiple scale methods at predicting the onset and subsequent propagation of defects and cracks in nanoscale materials.

Finally, in many MD simulations of interest, most of the atoms in the simulation remain unperturbed from their equilibrium minimum potential energy state. This was demonstrated in the visualization of the three-dimensional fracture examples. As was shown, only those atoms at a surface, or equivalently surrounding the crack and crack tip, were shown to have an energy state far from equilibrium. Multiple scale methods, which advocate the elimination of unnecessary atomistic degrees of freedom, or in this case those that behave linear elastically, are perfectly suited for this degree of freedom reduction.

8.5.1 Bridging Scale Perspectives

There are many possible avenues for future research, and we shall discuss some of the most important ones. One major achievement would be to correctly derive and implement the stochastic force $\mathbf{R}(t)$ such that a truly coupled finite temperature multiple scale simulation could be run. Work in this direction is under way and is based on the method outlined in Section 4.3.3. At present, there is no limitation on the temperature that can be supported within the MD region. However, because the random force was not implemented in any of the multiple scale simulations described in this book, the continuum is required to be at 0 K. Implementing the random force would fulfill the requirement that the eliminated fine scale degrees of freedom exert forces on the reduced MD region corresponding to their level of thermal excitation.

A second major improvement would be in showing fully the three-dimensional simulations in which the atomic interactions extend beyond nearest neighbor. This is crucial for increased simulation realism, as longer-ranged potentials such as EAM are the norm in the materials science and physics communities. This is particularly important for the high strain-rate and failure type applications for which multiple scale methods seem best suited, as those simulations have been shown to yield vastly disparate results when using nearest neighbor compared to longer-ranged atomic interactions; see Holian et al. (1991).

Relaxation of the small displacement assumption in deriving the MD boundary condition would also constitute a major improvement on the method. We note that the boundary atom displacements in the two- and three-dimensional fracture examples were quite large. However, the relative displacements of the atoms due to the stretching being applied to the system was quite small. Therefore, the issue of large rotations of the atoms at the boundary is of greater interest. Currently, the impedance force represents the zeroth order term in the linearization of the interatomic force at the MD boundary. It is expected then that keeping higher-order terms in the linearization would increase the validity of the method when the boundary incurs moderate nonlinearities or rotations.

The corner effect, which arises in numerical simulations owing to the asymmetry in evaluating the summation in the MD impedance force over n_c in (6.100), is another subject that demands closer study. It was found in the numerical examples that, while taking a small value for n_c was sufficient for accuracy and computational efficiency, a systematic means for eliminating the corner effect has not been developed.

Further development of the bridging scale method is necessary so that problems involving fluids can be solved. More specifically, two issues need to be resolved before the application of the bridging scale to fluids can be performed. First, the elimination of the unnecessary MD degrees of freedom is based on the assumption that the atomic lattice is periodic and repetitive; clearly, this requirement is not met in an amorphous fluid, or polymeric-type material. Secondly, the issue of obtaining a constitutive relationship similar to the Cauchy–Born rule when the MD region is not present is also an open question; both these issues require a great deal of thought and research to be resolved adequately.

Finally, incorporating some sort of adaptive procedure or ‘remeshing’ of the atomistic region would be a great benefit to the method. The motivation for this lies in the fact that, during large deformation simulations, defects or instabilities such as cracks can possibly propagate toward the MD boundary. In these cases, it is necessary to adaptively increase the size of the atomistic region such that the defect in question can continue to propagate unimpeded. An alternative approach would be to modify the continuum region such that it can accommodate the passing of defects from the atomistic region. In either case, such an improvement would constitute a large improvement in increasing the realism of the bridging scale simulations.

Copyright

Material of Sections 8.2, 8.2.4 and 8.4, is reproduced from Park et al. (2005a), Copyright 2005, with permission from John Wiley and Sons Ltd.

9

Multiscale Methods for Material Design

New technological advances have led to a range of advanced materials, including nanofiber-matrix composites, microstructured and multilayer materials. The potential range of applications for this sort of material optimization is extremely broad, and promises new materials for use in lightweight vehicles, military armor, fusion, hydrogen storage and virtually any application that requires materials to operate under extreme environments. By designing the internal structure of materials intelligently, we may hope to create new materials with desirable combinations of properties like strength, toughness and density. The ability to do this will require new computational methods that can be used to predict macroscale properties accurately on the basis of the internal structure of material micro and nanostructure.

Thus, the focus of this chapter is on presenting applications of *hierarchical* multiple scale constitutive models and computational methods to problems of interest in materials design and modeling. Hierarchical models are those in which the constitutive response at very small length scales is used as input to boundary value problems at larger length scales. The input typically takes the form of an initial condition, constitutive parameter or boundary condition. Hierarchical models have been successful for certain reasons. One is their ability to embed material length scales into the homogenized model; this can, for instance, provide regularization in the numerical implementation. More generally, hierarchical models offer a natural way of incorporating small-scale material physics into macroscale constitutive behavior such that constitutive coupling occurs between the length scales. This coupling allows the ability to determine, in an average sense, the effect of parameters and material properties across many length scales, and fills a critical need in materials design and analysis.

The relationship between material microstructure and properties is the key to *optimization and design* of lightweight, strong and tough materials. Material properties are inherently a function of the microscale interactions at each distinct scale of deformation in a material. Currently, researchers rely on empirical data to define the structure–property link in the material design chain. A model is proposed here in which a material is physically and

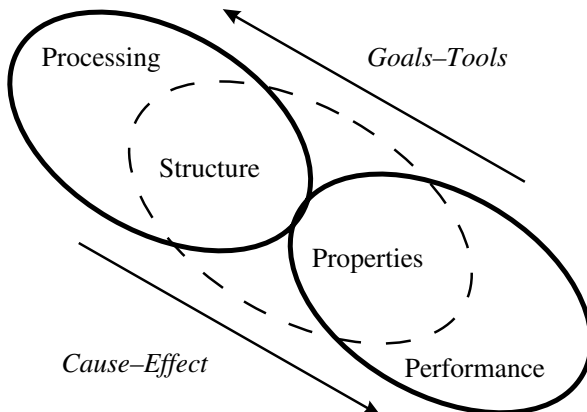


Figure 9.1 From processing to performance. A general technique to determine a complex material's structure–property relationship is difficult. Reprinted from Computer Methods in Applied Mechanics and Engineering, McVeigh et al., Multiresolution analysis for material design, 2005, with permission from Elsevier.

mathematically decomposed to each individual scale of interest. Material deformation can subsequently be resolved to each of these scales. The constitutive behavior at each scale can also be determined analytically or computationally by examining the micromechanics at each scale.

Figure 9.1 represents the life of a component from the initial processing of the raw material, to resulting material microstructure, the subsequent properties and the final product's performance. Material scientists focus on the relationship between processing and the resulting microstructure. Specialized imaging techniques, including electron microscopy, are utilized to characterize the microstructure. Over the years, designers have gathered extensive amounts of experimental data relating the processing parameters, such as processing temperature and deformation rate, to the final microstructure. The relationship between processing parameters and microstructure is well understood for traditional processing techniques such as extrusion (Borrego et al. 2002 and Wang et al. 2003), rolling (Brand et al. 1996, Karhausen and Roters 2002 and Sellars and Zhu 2000), as well as in new areas such as friction stir welding (Sutton et al. 2002). Processing charts and empirically based mathematical models are widely available. It is thus possible to *design* a microstructure by controlling the processing parameters.

The relationship between the properties and performance is also well understood. Design engineers select materials on the basis of performance requirements. Materials are chosen depending on their mechanical properties, density, chemical resistance and other pertinent physical characteristics. The suitability of a material for a particular application can be determined directly through the use of design charts or computationally through numerical techniques such as the finite element method, for example, Hughes (1987) and Belytschko et al. (2000b), or meshfree methods (for example, Belytschko et al. 2000a, 1998, 1996, 1994 and Li and Liu 2004).

At an elementary level, material design is a method of linking the material processing (input) to the material performance (output). There is a cause–effect relationship associated

with moving from processing to performance; changing a processing parameter will have an effect on the microstructure, properties and performance. Moving in the opposite direction, the goal is to achieve the desired performance capability by defining the needed properties, relating those to the required microstructure and ultimately choosing the correct processing technique/parameters.

The discussion in this chapter starts with multiresolution continuum analysis of materials with a complex internal structure that have important constituent elements at various spatial scales (Section 9.1). As an outcome of this analysis, the complex relationships between the internal microstructure and material performance can be established. For structural components, inclusions and irregularities on the scales close to the atomic resolution, as well as for detailed analyses that require the development of small-scale constitutive laws, researchers must consider hierarchical models incorporating continuum, molecular dynamics and *ab initio* methods within a single analytical and computational framework. These approaches are discussed in Section 9.2 in application to multiple scale analysis of ductile failure in high-strength steels. Other applications discussed in this chapter include multiple scale cell models of solids for manufacturing processes, and an overview of potential areas of research in biologically inspired self-healing materials (Section 9.3).

We would like to stress that the modeling of materials across many length- and timescales is one of the current grand challenges in computational nanomechanics. Thus, it should be emphasized that the results presented in this chapter are preliminary in nature, and represent the tip of the iceberg, not only in terms of both current applications and methods, but also in terms of what breakthroughs future developments will allow researchers to make in understanding material behavior from atoms to continua.

9.1 Multiresolution Continuum Analysis

Modern materials science and nanoengineering applications require approaches that allow adaptive multiresolution decomposition of the *continuum* solution field (Figure 9.2), where each computational grid corresponds to a specific spatial scale of the system under analysis.

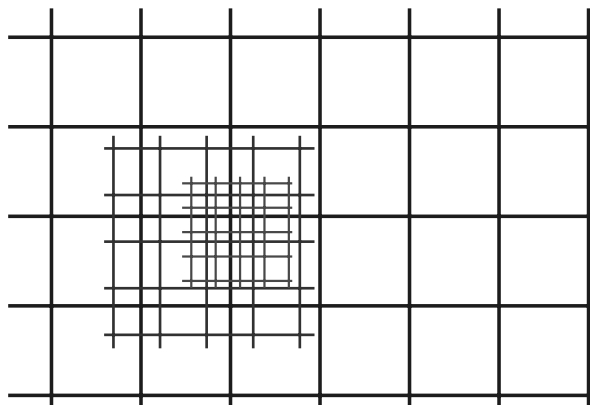


Figure 9.2 Schematic illustration of a multigrid approach.

When designing a material for a particular application, an iterative optimization process is employed to achieve the desired properties: a material with a specific microstructure is produced and its properties, such as strength and fracture behavior, are found experimentally. A new microstructure is then devised that results in improved properties. The question remains: *what microstructure will produce the desired material properties?* For many materials, including the next generation of lightweight alloys, granular materials and bio-inspired composites, the relationship between microstructure and properties is complicated. The general problem of calculating the inherent properties of a complex multicomponent material from the knowledge of its constituent components' properties has been challenging. Inherent length scales in a material typically include submicron-scale inclusions, microstructures, and so on. A multiresolution continuum formulation would enable one to resolve the physics on these scales.

Kadowaki and Liu (2004, 2005) first accomplished a *concurrent* multiresolution continuum analysis by utilizing a two-scale grid (Figure 9.3), to predict the complex failure behavior of a granular material. The fine-/coarse-scale decomposition procedure for this work was similar to the bridging scale projection method for concurrent atomistic/continuum coupling discussed in Chapters 5–8 of this book.

The *hierarchical* methodologies, also known as *serial coupling* or parameter passing (see Section 9.2), represent a more straightforward way of injecting limited multiple scale physics into a macroscale constitutive law. Here, interscale information flow is accomplished typically by means of a computational/representative cell modeling technique. The average constitutive behavior at the smallest scale is used to determine the behavior at the next largest scale, and so on until the macroscale behavior is determined. The resultant material laws are an improvement on conventional homogenized constitutive relationships as they contain some microscale parameters. However, they are still used within a conventional continuum framework to determine a sample's behavior.

Conventional continuum approximations cannot capture highly localized deformation fields on the order of the microstructure's characteristic length. Also, constitutive behavior at these smaller scales is generally different from the macroscale average behavior. Important material behavior may not be captured, such as the inherent inhomogeneity of

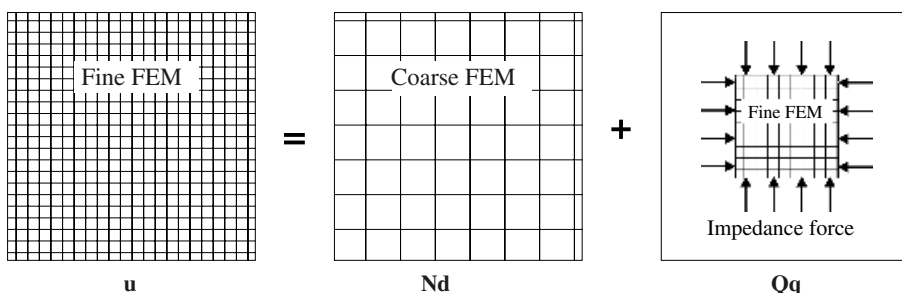


Figure 9.3 The two-grid bridging scale decomposition: continuum fine-scale global solution is approximated by a coarse-scale solution overlaid by a fine-scale solution. By incorporating an impedance force, the fine-scale calculation can be limited to the region of interest. See (Kadowaki and Liu 2004).

plastic deformation, plastic flow localization in shear bands and the effect of crack size and geometry on fracture behavior. These phenomena control the important mechanical behavior such as fracture toughness and strength. They must be captured to provide a link between structure and properties.

Vernerey et al. (2005) and McVeigh et al. (2005) proposed an N -scale continuum approach that would maintain a material's identity at each scale of interest, that is, it would allow an inherent multiresolution analysis. By the very nature of multiresolution decomposition, the fine-scale fluctuations of strain and stress measures were decomposed into a sequence of fluctuations at different length scales. The deformation and constitutive behavior of each scale is examined separately while determining the overall material properties. In this way, the properties are elucidated in terms of the key microstructural parameters that control the micromechanics at each scale; this is achieved analytically or through simulation techniques.

This approach is discussed in greater detail in Section 9.1.1, where the mathematical formulation is illustrated by a two-scale porous material. Further applications are discussed in Sections 9.1.2 and 9.1.3, as well as in later Section 9.3.3, where the method is applied to modeling and simulation of self-healing composite materials.

9.1.1 Generalized Stress and Deformation Measures

A multiscale, also *micromorphic*, material is one that contains discrete microstructural constituents at N scales of interest. For example, a material may contain weakly bonded microscale particles and nanoscale dislocations. In this example, three scales are of interest: the macroscale, the microscale and the nanoscale. The material behavior of each scale will differ considerably. A model that hopes to simulate the structure–property relationship of a material must capture the micromechanics at each distinct scale. A *general multiresolution framework* is thus defined as one in which: (1) the material structure and the deformation field are resolved at each scale of interest; (2) the resulting internal power is a multifield expression with contributions from the average deformation at each scale (that is, the overall properties depend on the average deformation at each scale); (3) the deformation behavior at each scale is found by examining the micromechanics at each scale; (4) the constitutive relations can be developed at each scale.

Two-scale material

We begin by deriving the internal power of a simple two-scale material containing a metal matrix with microscale inclusions or voids. One example is the porous material shown in Figure 9.4. In such a material, microscale deformation is controlled by the growth of voids. Void growth is a volumetric process and a function of the hydrostatic stress only. It is reasonable to assume that the volumetric part of the microdeformation plays a prominent role in the microscale deformation of such materials. Here, the macroscale and microscale behavior are of interest. Therefore, the goal is to resolve the material structure and deformation to the macro- and microscales. The general equations for N scales will be discussed next.

In a conventional continuum simulation, homogenized constitutive behavior at a point is predetermined by finding the average behavior of a material sample. This can be achieved through experimental mechanical testing. Alternatively, for a multicomponent material with

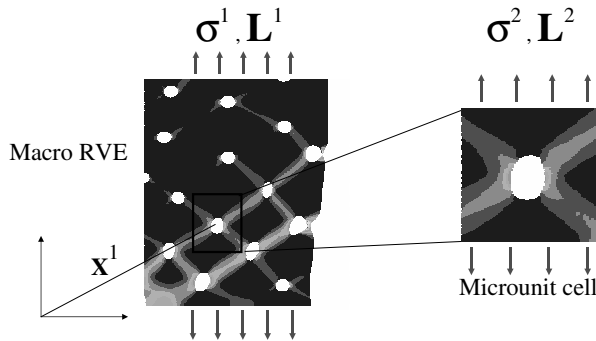


Figure 9.4 A macro RVE and a unit cell and their respective stress and rate of deformation measures.

known individual component properties, computational simulations can be performed on a sample called a *representative volume element (RVE)*. This is directly analogous to an experimental test.

To determine the influence of the subscales, additional deformation fields corresponding to each scale are introduced. This is achieved by mathematically decomposing the position and velocity within a RVE into components associated with each scale of interest. Figure 9.4 shows the mathematical decomposition for a simple two-scale micromorphic material along with a physical interpretation. For such a case, the position and velocity of a material point become:

$$\mathbf{x} = \mathbf{x}^1 + \mathbf{x}^2, \quad \mathbf{v} = \mathbf{v}^1 + \mathbf{v}^2 \quad (9.1)$$

where \mathbf{v}^1 is the macrovelocity and \mathbf{v}^2 is the relative microvelocity. The macro RVE incorporates a microstructural feature as an *inclusion*. Thus, the unit cell is defined at each scale so that the gradient of the relative microvelocity can be considered constant within the cell, that is, the relative microvelocity varies linearly,

$$\mathbf{v}^2(\mathbf{x}^2) = \mathbf{L}^2 \cdot \mathbf{x}^2 \quad (9.2)$$

Figure 9.4 represents a macro RVE with an average macrostress, σ^1 and macrorate of deformation, \mathbf{L}^1 . These are the average macrostress and rate of deformation over a macroscopic RVE of the material, which are constant within the micro unit cell. By zooming into a micro unit cell in the RVE, we can examine the total microstress, σ^2 and rate of deformation, \mathbf{L}^2 associated with a micro unit cell. These will differ from the corresponding macromeasures as long as the RVE is not homogeneous. The relative rate of microdeformation associated with a micro unit cell is defined as $(\mathbf{L}^2 - \mathbf{L}^1)$. The microstress associated with a micro unit cell is denoted β^2 .

The *internal power* of a unit cell can be provided as a resultant of the contributions from the macroscopic rate of deformation, \mathbf{L}^1 , and the rate of relative microdeformation, $(\mathbf{L}^2 - \mathbf{L}^1)$,

$$p_{\text{int}} = \sigma^1 : \mathbf{L}^1 + \beta^2 : (\mathbf{L}^2 - \mathbf{L}^1) \quad (9.3)$$

The microstress associated with a unit cell, β^2 , is defined as the power conjugate of the relative rate of microdeformation. The microstress is therefore constant within the micro unit

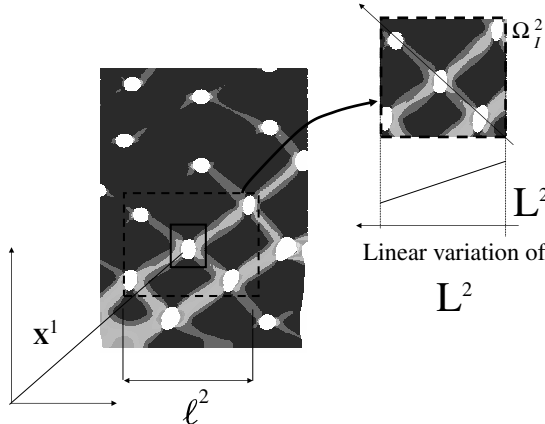


Figure 9.5 Domain of influence chosen at the microscale, where the rate of microdeformation varies linearly in space.

cell. The value β^2 is the measure of a stress field's tendency to produce a strain gradient in the averaging domain. An average value of the internal power (at a discrete position \mathbf{x}) is required for use within the mathematical multiscale framework. This is determined numerically by averaging the internal power over a microdomain of influence. This domain is chosen to be representative of the range of interactions between the microstructural features at the microscale. In Figure 9.5, the micro domain of influence (DOI) is chosen to include nearest-neighbor interactions between the voids.

The average internal power is given by averaging over the micro DOI:

$$\bar{p}_{\text{int}}(\mathbf{x}) = \frac{1}{V_I^2} \int_{\Omega_I^2} p_{\text{int}}(\mathbf{x} + \mathbf{y}) d\Omega_I^2 \quad (9.4)$$

where an overbar represents an average value and \mathbf{y} is simply an integration position variable within the DOI. p_{int} is given by (9.3). An expression for the variation of the rate of microdeformation within the DOI can be obtained through a Taylor expansion. Truncating at first-order terms, we get:

$$\mathbf{L}^2(\mathbf{x} + \mathbf{y}) = \bar{\mathbf{L}}^2(\mathbf{x}) + \mathbf{y} \cdot \nabla \bar{\mathbf{L}}^2(\mathbf{x}) \quad (9.5)$$

where $\bar{\mathbf{L}}^2(\mathbf{x})$ is the average microdeformation rate for the micro DOI and $\nabla \bar{\mathbf{L}}^2(\mathbf{x})$ is the average gradient of the rate of microdeformation over the micro DOI. The linear approximation in (9.5) is justified in Figure 9.5 showing the variation in total microdeformation along a micro DOI.

The average internal power for a two-scale micromorphic material gives

$$\bar{p}_{\text{int}} = \sigma^1 : \mathbf{L}^1 + \bar{\beta}^2 : (\bar{\mathbf{L}}^2 - \bar{\mathbf{L}}^1) + \bar{\beta}^2 : \nabla \bar{\mathbf{L}}^2 \quad (9.6)$$

where $\bar{\beta}$ is the average of the relative microstress over the domain of influence and $\bar{\beta}$ is the average of the first moment of the microstress, that is, $\mathbf{y} \cdot \bar{\beta}$, over the domain of

influence. Equation (9.6) includes the contributions to the power density from the macro- and microdeformation rates. It also includes the gradient of these rates. This gradient term arises from the variation in the microdeformation within the domain of influence. Indeed, the DOI should be chosen such that this variation can be considered linear and the first-order approximation (9.5) holds within the micro DOI. Physically, the gradient arises owing to the interaction between microstructural features as shown in Figure 9.5. Use of a DOI implicitly imbeds a length scale into the mathematical framework at the microscale that is closely related to the size of the smallest microstructural feature at that scale. Not only does this make the model more physically realistic, it also eliminates the pathological mesh dependency associated with conventional continuum approaches.

Note that in a conventional continuum approach, where only the homogenized macroscale behavior is considered, the macrodomain of influence coincides with the macro RVE shown in Figure 9.4. The total microrate of deformation \mathbf{L}^2 is equal to the total macrorate of deformation \mathbf{L}^1 and expression (9.6) reduces to give the average internal power of a conventional homogenized continuum,

$$\bar{p}_{\text{int}} = \sigma^1 : \mathbf{L}^1 \quad (9.7)$$

The *external power* can similarly be derived in terms of average measures. By applying the principle of virtual power and using the divergence theorem, the resulting strong form gives rise to a coupled multifield system of governing differential equations. This forms the basis of the mathematical model used in multiscale micromorphic finite element simulations.

The *generalized stress and deformation tensors* can be defined as

$$\Sigma = [\sigma^1 \quad \bar{\beta}^2 \quad \bar{\beta}^2], \quad \Upsilon = [\mathbf{L}^1 \quad [\bar{\mathbf{L}}^2 - \bar{\mathbf{L}}^1] \quad \overline{\nabla \mathbf{L}^2}] \quad (9.8)$$

These are related through an elasto-plastic micromorphic multiscale constitutive law.

N-scale material

The multiresolution internal power, stress and strain tensors have been developed and generalized to N scales of interest by Vernerey et al. (2005). The N -scale internal power density is given by

$$\bar{p}_{\text{int}} = \sigma^1 : \mathbf{L}^1 + \sum_{\alpha=2}^N \left(\bar{\beta}^\alpha : (\bar{\mathbf{L}}^\alpha - \bar{\mathbf{L}}^1) + \bar{\beta}^\alpha : \overline{\nabla \mathbf{L}^\alpha} \right) \quad (9.9)$$

where we denoted the coarsest and finest length scales as the first and N th, respectively.

The generalized stress and deformation measures can be defined as

$$\Sigma = [\sigma^1 \quad \bar{\beta}^2 \quad \bar{\beta}^2 \quad \bar{\beta}^3 \quad \bar{\beta}^3 \quad \dots \quad \bar{\beta}^N \quad \bar{\beta}^N] \quad (9.10)$$

$$\Upsilon = [\mathbf{L}^1 \quad [\bar{\mathbf{L}}^2 - \bar{\mathbf{L}}^1] \quad \overline{\nabla \mathbf{L}^2} \quad [\bar{\mathbf{L}}^3 - \bar{\mathbf{L}}^1] \quad \overline{\nabla \mathbf{L}^3} \quad \dots \quad [\bar{\mathbf{L}}^N - \bar{\mathbf{L}}^1] \quad \overline{\nabla \mathbf{L}^N}] \quad (9.11)$$

In concise notations, the internal power density (9.9) can be written as

$$\bar{p}_{\text{int}} = \Sigma \cdot \Upsilon \quad (9.12)$$

For finite element implementation, the principle of virtual power can be applied and discretized as usual. The generalized stress Σ and generalized deformation rate Υ tensors replace the standard stress and strain tensors. Hence the multiresolution approach can be implemented in a standard finite element code with increased degrees of freedom.

Multiresolution constitutive laws

In a multiresolution finite element analysis, a generalized constitutive relation is required to relate the generalized stress to the generalized deformation. The first step is to derive individual constitutive relationships at each scale by examining the micromechanics at each scale. The individual constitutive relationships at each scale can then be combined to create a generalized constitutive relation,

$$\Sigma = \mathbf{C}^{ep} : \Upsilon \quad (9.13)$$

where \mathbf{C}^{ep} is a generalized elastic–plastic tangent modulus.

Analytical derivation of a generalized constitutive relation, and hence determination of \mathbf{C}^{ep} may be possible if the mechanics are simple and well understood. This approach was demonstrated for a polycrystalline material and a granular material by McVeigh et al. (2005). For more complex problems involving more than two scales, a multiresolution cell modeling approach can be used. In a manner similar to the hierarchical approach, a constitutive relationship can be determined at the lowest scale of interest first. This relationship is used as an input when finding the constitutive behavior at the next largest scale and so on. The average behavior at each scale is determined by examining the average response over the averaging domain Ω^α , a domain of influence at the scale α . At the macroscale, the averaging domain is simply the RVE. A generalized constitutive law is then formed on the basis of the scale-specific behavior. In Section 9.3.3, this technique is applied to the design of a bio-inspired self-healing material containing shape-memory alloy (SMA) inclusions.

Potentially, the cell modeling approach can be enriched through incorporation of data from atomistic modeling of interfacial bonding strengths between particles of various sizes and matrix materials. We point out that one can utilize these techniques to also resolve the inverse problem – finding the way to *design the microstructure of materials, on the basis of desired macroscopic properties*. Some successful applications of multiscale continuum analysis are reviewed in the following section.

9.1.2 Interaction between Scales

The use of a multiscale micromorphic approach allows one to consider the interactions between scales. Consider a sample of material containing two microsized particles in a matrix. Under a pure shear stress state, conventional hierarchical void-damage models cannot predict the correct localized strains and hence the proper softening behavior. In reality, the material often fails in this manner owing to the nucleation of submicro voids within the zone of tensile stress that arises between the large voids, even under pure shear conditions.

A multiscale micromorphic material model can capture the interactions between the particles at different scales that cause this void sheet mechanism. The tensile submicrostress region between the two microparticles will trigger a response in the submicro part of the potential, leading to severe softening. This mechanism is illustrated in Plate 5 for a microscale domain subjected to a pure shear deformation. Each scale will undergo varying levels of softening depending on the average amount of damage at that particular scale. However, there is also a degree of interaction between the scales. For example, even if the macro deformation $\bar{\mathbf{L}}^1$ is zero and the average microdeformation rate $\bar{\mathbf{L}}^2$

is a pure shear quantity, the overall constitutive response will still show a softening effect. Softening generally occurs only under hydrostatic loading. This can be explained by examining the submicroscale. An average hydrostatic stress field occurs at the submicroscale because of localization between the microscale particles. This leads to void nucleation and growth at the submicroscale (Plate 5). The stress field between the two microscale inclusions has a hydrostatic component. The material within the localized stress field contains submicroscale strengthening particles. This material is represented by a Gurson (1977)-type material law derived by studying the average response of a submicroscale averaging domain. Plate 5 shows that the average shear response over the microscale domain displays a softening regime. This directly corresponds to the void sheet mechanism.

From a computational viewpoint, detail continuum simulations are restricted to small domains as the mesh resolution should be refined to encompass the intrinsic length scale, when averaging over the domain of influence. In case large-scale simulations are needed together with a fine-scale resolution, multiresolution continuum approaches can provide an accurate description of the subscale response while solving large-scale continuum problems.

9.1.3 Multiscale Materials Modeling

During the past decade, multiscale continuum approaches have also been used to successfully predict the behavior of various micromorphic materials. Besides, researchers have also engaged in efforts at multiscale continuum modeling and simulation of manufacturing processes. In the following text, we overview several interesting applications.

A micromechanical cell modeling approach, similar to the one outlined in Section 9.1.1, has been used by McVeigh and Liu (2005) to predict the constitutive behavior of Al–Cu alloy with two scales of weakly bonded small precipitates. A debonding criterion for void nucleation was used along with cell modeling to define a macro constitutive law. The model incorporated micro damage measures and was used within a conventional continuum framework to simulate fracture during manufacturing processes (Figure 9.6).

McVeigh et al. (2005) applied a multiresolution cell modeling technique to the study of granular materials. A granular material is a large assembly of discrete solid grains such as sand, soil, gravel, coal, coffee beans, and so on. Although the behavior of individual grains is quite simple, the overall system behavior is complex. The importance of understanding granular materials lies in their usage in industrial processes and their disastrous effects in natural phenomena such as landslides. Energy dissipation and momentum transfer are complicated as they occur because of direct interaction between neighboring grains. Hence, the flow characteristics of such materials are directly related to the granular architecture. Industrially, increased understanding of granular materials has the potential to save millions of dollars (Knowlton et al. 1994).

Kadowaki and Liu (2004, 2005) used a multiscale continuum approach for the study of shear band plasticity, as well as the complex failure behavior of a granular material. The elasto-plastic material constitutive law was characterized by deriving the relationship between the microstress and the friction between grains. Hao et al. (2003, 2004a) used atomistic simulations within a multiscale approach to model a two-scale micromorphic material known as cybersteel (see also Section 9.2). This next-generation steel contains particles at the micro and submicro scales. The model accounted for interfacial strengths

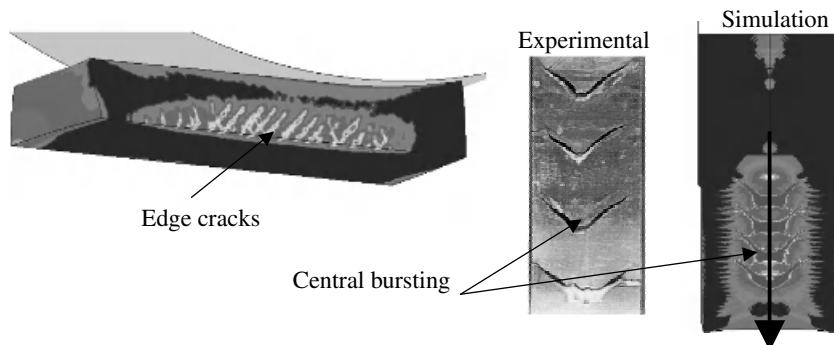


Figure 9.6 Rolling and extrusion using a micromechanical cell model-based constitutive law. Defects are due to microscale void nucleation and growth, captured by the constitutive law. Simulation images (right and left) are reproduced from McVeigh and Liu (2005), and experimental – from Ko and Kim (2000), with permission from Elsevier.

and void damage at each scale. This work is being extended by Vernerey et al. (2005) to *three scales* of deformation and to account for the interactions between the scales, as was explained in Section 9.1.2 and Plate 5. Vernerey et al. (2005) have shown that the multiscale approach is consistent with, and can be applied to, the gradient plasticity theory of Fleck et al. (1994) and Fleck and Hutchinson (1997). Gradient plasticity theory proposes that the creation of geometrically necessary dislocations is controlled by the strain gradient. The internal work has a contribution from this strain gradient. This is consistent with a two-scale micromorphic material when the microstress is zero and the microdomain of influence is chosen to be the same as the macrorepresentative volume element. One current research topic is the extension of the above to the general case of N -scale, such that a fully resolved framework could be developed.

In summary, the multiresolution continuum modeling is capable of linking overall material properties to the underlying microstructure via the micromechanics at each scale of interest, provided that the detailed chemistry, kinetics and phase transitions in complex material systems can be considered in an averaged continuum manner. The small-scale deformation phenomena that have a profound impact on macroscale properties can be captured. The technique can be used for materials that exhibit different constitutive behavior at each scale, and it can be implemented in a general finite element framework. Multiresolution continuum modeling has the potential to elucidate the resultant macroscopic properties of hierarchical materials through computational cell modeling.

In terms of material design, the multiresolution approach is a method capable of describing the crucial link between material microstructure and properties. It offers the prospect of eliminating the need for expensive and time-consuming mechanical testing and prototyping. As industry is pushing for lighter and stronger materials, the multiresolution theory offers an opportunity for optimization of properties in terms of microstructural architecture. The predictive capabilities of the theory can also aid the rapid advancement of bio-inspired self-healing composites, which are currently in their infancy. Advance knowledge of the optimum microstructure of these next-generation composites can assist in the search for a capable fabrication process.

9.2 Multiscale Constitutive Modeling of Steels

One of the principal objectives of studying the micro/nanomechanics of materials is to account for the observed phenomena and properties of macroscopic solid bodies, such as the strength and fracture toughness of steels, on the basis of the quantum mechanical theory of the behavior of atomic particles. Success will have been achieved when it becomes possible to calculate the quantities that describe the constitution of materials and their response to macroscopic mechanical boundary conditions from the knowledge of the component elements and their hierarchical structures from atomistic scales to micro- and macroscales. This is particularly important for the design of structural steels.

Both strength and fracture toughness are key property-indices for steels. Although advanced technology currently provides many ways to achieve either high strength or high toughness in steel through manufacturing processes, it remains a challenge to achieve both of them simultaneously. This is because toughness characterizes the resistance of a material against fracture at a crack tip. The difference between the local and the global properties reflects the natural heterogeneity of the microstructure of steels. The design of steels seeks to achieve desirable micro/nanostructures with optimized properties through alloy component/phase selection and metallurgical processes based on the quantitative understanding of fundamental deformation mechanisms and the relationships among these at different scales.

In this section, we review a bottoms-up computational methodology proposed to establish a hierarchical multiscale constitutive model that builds up the relationships among the macroscale properties, micro- and submicro structures, and atomistic failure modes for steels as in Hao et al. (2003, 2004a). The innovations presented here can be summarized as follows:

- An atomistic adhesion model that accounts for both the separation normal to newly created interfaces and gliding-induced dislocations. The normal separation is described as the creation of empty sites, which may trigger gliding-induced dislocations that translate the short-ranged covalent bonding force into a long-ranged decohesion law. The criterion of Rice (1992) is used to determine these two competing mechanisms. The computed results provide a quantitative explanation as to why the practical strength of steel is much lower than the value predicted on the basis of atomic separation and how plasticity occurs in steel.
- A first-principles *ab initio* technique to calculate the generalized fault energy against dislocation-induced sliding in a BCC-Fe crystal.
- A “quasi-particle dynamics approach”, which transforms an atomistic system into a “particle system” while maintaining intrinsic structural properties such as crystal elastic constants and molecular kinetics. Each particle can be a “superatom” containing several atoms, or represent an inclusion particle, depending upon the scales of interest. As the particle system can have fewer degrees of freedom than the atomistic system, the method can be used for bridging atomistic and continuum scales.
- A hierarchical multiphysics computational constitutive model that is based on a unified thermodynamic framework. This model is applied in a computational procedure that is called the “*ductile fracture simulator*”, to support the quantitative trade-off analysis in microstructural optimization for fracture toughness.

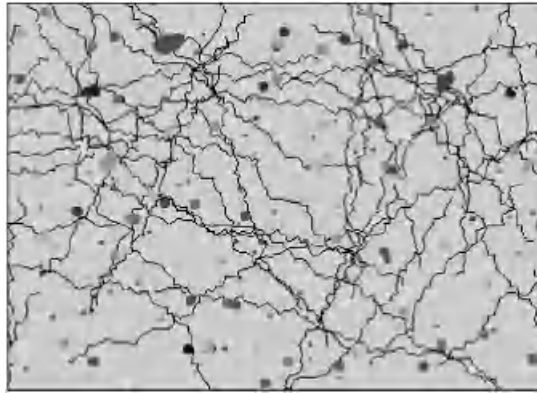


Figure 9.7 Schematic internal structure of steel.

- A toughness–strength–adhesion diagram is obtained for steel design. This diagram establishes the relationship among alloy matrix strength, inclusion adhesion interfacial energy and fracture toughness.

9.2.1 Methodology and Approach

Similar to all conventional materials, steels are heterogeneous in nature. A modern ultra-high-strength steel generally consists of an alloy matrix with several levels of hard, dispersed inclusion particles (see Figure 9.7). Interfacial strength between the different phases plays an important role in the strength and toughness of steels.

For the ultra-high-strength steels considered here, dispersions of hard particles occur at two distinct scales: primary particles (such as TiN, MgS, Fe₃C) that are typically on the order of microns in size, and secondary particles (such as TiC, TiC₂S and M₂C compounds) that are on the order of tens of nanometers in size.

In Figure 9.8(b) and in the following analysis, σ_{ij} and ε_{ij} denote the stresses and strains at the submicroscale. The submicroscale cell model homogenizes σ_{ij} and ε_{ij} into the microscale stress and strain, which are denoted by $\Sigma_{ij}^{\text{micro}}$ and E_{ij}^{micro} , respectively; a microscale plastic potential Φ_{micro} is then developed. By repeating this procedure for the macroscale stress–strain: $\Sigma_{ij}^{\text{macro}}$, E_{ij}^{macro} , and the corresponding macroscale plastic potential Φ_{macro} , are obtained for fracture simulation of laboratory specimens.

In the following section, we begin with a description of the crystal separation behavior and the underlying quantum mechanical consideration, leading to a continuum-mechanics force-separation law.

9.2.2 First-Principles Calculation

For a metallic or intermetallic system in which each atom has a sufficient number of electrons, the Thomas (1927)–Fermi (1928) model is applicable. This model approximates the system as a combination of static atomic cores that form the crystal and an electronic gas that fills the space among the atoms. The theorems of Hohenberg and Kohn

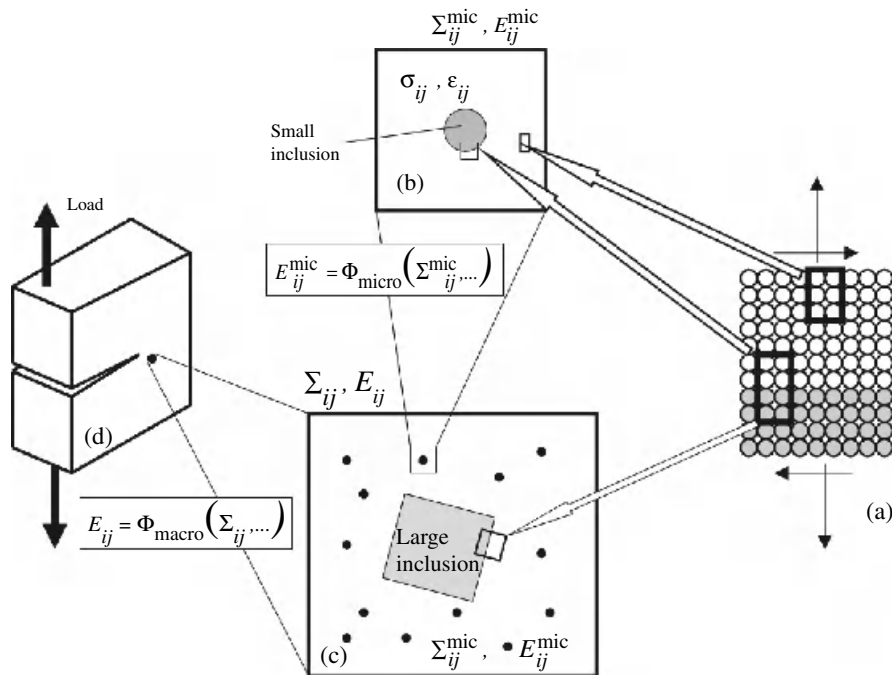


Figure 9.8 An illustration of the hierarchical model that links a) the quantum scale, b) sub-microscale, c) microscale, d) macroscale. Reprinted from Computer Methods in Applied Mechanics and Engineering, 193, Hao et al., Multi-scale constitutive model and computational framework for the design of ultra-high strength, high toughness steels, 1865–1908, 2004, with permission from Elsevier.

(1964) and Kohn and Sham (1965) indicate that the ground state energy of such a many-body system, which is an eigenvalue of the corresponding wave solution of Schrödinger's equation, is determined by the electron density distribution. On the basis of the augmented plane wave method introduced by Slater (1937), various numerical methods have been developed to determine the electron density distribution, for example, Krakauer and Freeman (1979), NRL (2002), Mehl and Papaconstantopoulos (1996) and Papaconstantopoulos and Mehl (1997). Among them, the full-potential spin-polarized linear augmented plane wave (FLAPW) (Wimmer et al. 1981) is presently considered to be the most accurate scheme as it holds the fewest approximations.

For the steel application, first-principles calculations are used to compute the binding energy relations for the following systems:

- iron matrix: normal adhesion and sliding
- interfacial decohesion between alloy matrix and $\text{TiC}_x\text{N}_{1-x}$ particles ($x = 0$: primary particle; $x = 1$: secondary particle)

9.2.3 Hierarchical Unit Cell and Constitutive Model

In this section, we discuss the response of the submicro unit cell and microcell models with secondary and primary inclusions by employing the first principle-based potential obtained in the previous section. The procedure summarized in Figures 9.7 and 9.8 is utilized in this analysis. The resulting macroscale constitutive law will then be applied in a macroscale simulation of ductile fracture. The experimental results of modified 4340 steel by Briant (2002) and Olson and Hsieh (2002) are used as an example in the simulation. For the constitutive modeling of heterogeneous systems, refer to Eshelby (1961) and Sanders et al. (1997).

Two-Level Cell Modeling

The cell models for determining the constitutive response are based on periodic distributions of inclusion particles. Hence, according to the arrangements of the inclusions, three representative cells are illustrated in Figure 9.9. Using periodic and symmetric properties, the three-dimensional cubic primitive distribution can be simplified to a two-dimensional rectangular cell with a single inclusion; the 3D body-centered cubic or hexagonal distribution can be simplified to a 2D rectangular cell with double inclusions, as shown in Figure 9.9. By varying the shape, size and distributions of the primary/secondary inclusion particles and the decohesion energies, the methodology of computational cell modeling introduced, for example, in Rice and Tracey (1969), Tvergaard and Hutchinson (1982), Duva and Hutchinson (1984) and Hao et al. (2000), is applied to the present system.

The relationships drawn by Bishop and Hill (1951),

$$\Sigma_{ij} = \frac{1}{V_{\text{cell}}} \int_{V_{\text{cell}}} \sigma_{ij}^{\text{cell}} dV; \quad \dot{E}_{ij} = \frac{1}{V_{\text{cell}}} \int_{V_{\text{cell}}} \dot{\varepsilon}_{ij}^{\text{cell}} dV \quad (9.14)$$

are employed in the analysis that establishes the relationship between the homogenized average stress/strain (Σ_{ij}, E_{ij}) response and cell stress/strain ($\sigma_{ij}^{\text{cell}}, \dot{\varepsilon}_{ij}^{\text{cell}}$). The amplitudes and

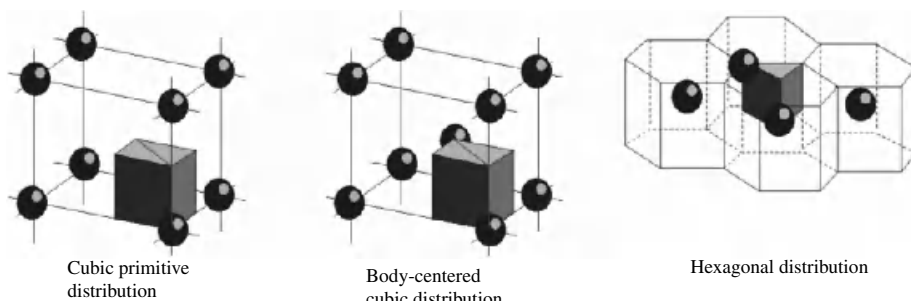


Figure 9.9 The cell model: three classes of periodic distributions of inclusions. Reprinted from Computer Methods in Applied Mechanics and Engineering, 193, Hao et al., Multi-scale constitutive model and computational framework for the design of ultra-high strength, high toughness steels, 1865–1908, 2004, with permission from Elsevier.

distributions of $\sigma_{ij}^{\text{cell}}$, $\varepsilon_{ij}^{\text{cell}}$ are determined by parameters such as the material properties of the cell matrix and inclusion, the interfacial cohesion, the size and geometries of inclusions, and the load imposed on the cell. Both two-dimensional and three-dimensional cells are analyzed.

Plotted in Plate 6 are a set of snapshots of the submicro equivalent plastic strain contours during debonding and the corresponding micro shear stress-strain response. The cell is under shear-dominant boundary conditions. However, a localized normal separation may also occur. These results demonstrate that the incipience of localization is characterized by the onset of the shear bands connecting two inclusions, which triggers a rapid debonding along the interface and results in a sudden drop of the microscale stress. For an intrinsically ductile material like BCC Fe, gliding-induced dislocation motion dominates. The results of numerical modeling agree, in principle, with experimental observations indicating that shear bands induce the coalescence of microvoid ductile materials.

It is well known that parameters such as volume fraction, orientation and distribution of the secondary particles, as well as the stress state and decohesion energy, determine the submicrocell's deformation and failure behavior. According to the computational results plotted in Plate 6, we conclude that among these parameters, the decohesion energy is particularly important. Plotted in Figure 9.10 is a set of computations in which the decohesion energy varies from zero to the upper bound value corresponding to the Fe–C site configuration. In these computations, the spacing and volume fraction of the secondary particles are fixed. If we use the microscale strain E_{12}^{micro} at debonding as a threshold value for the micro stress-strain relation, then from Figure 9.10, we find that this debonding strain increases substantially when the decohesion energy increases. When the decohesion energy reaches its upper bound (3.8 J m^{-2}), no debonding occurs.

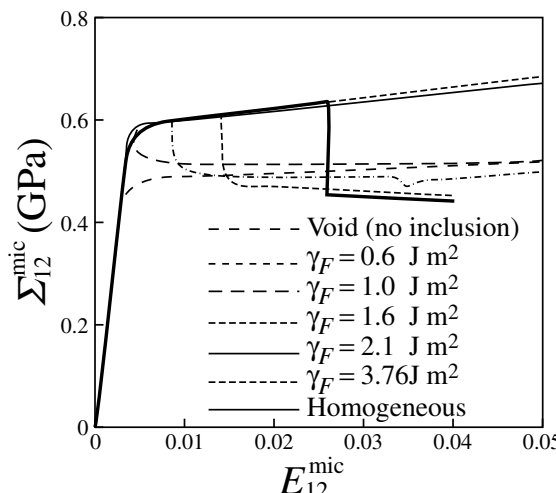


Figure 9.10 The effect of decohesion energy on the global stress–strain curve. Reprinted from Computer Methods in Applied Mechanics and Engineering, 193, Hao et al., Multiscale constitutive model and computational framework for the design of ultra-high strength, high toughness steels, 1865–1908, 2004, with permission from Elsevier.

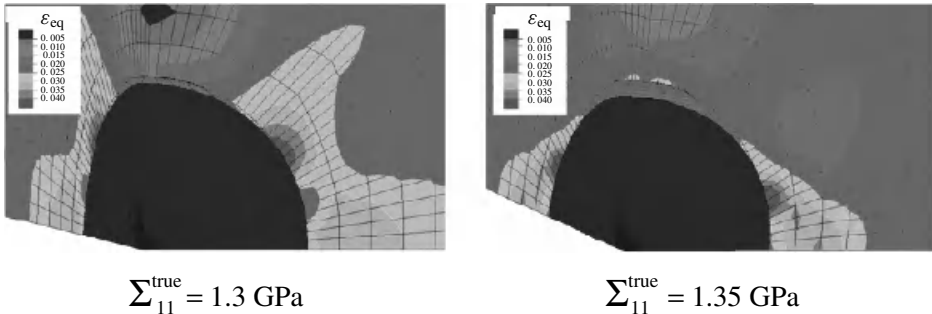


Figure 9.11 Three-dimensional cell modeling. Reprinted from Computer Methods in Applied Mechanics and Engineering, 193, Hao et al., Multi-scale constitutive model and computational framework for the design of ultra-high strength, high toughness steels, 1865–1908, 2004, with permission from Elsevier.

Figure 9.11 shows a 3D simulation performed by the finite element method. The cell is under uniaxial tension with the interfacial decohesion energy 0.6 J m^{-2} . This simulation is used to test the model and the parameter setup.

On the basis of a large amount of numerical simulation and the methodology of cell modeling introduced by Hao et al. (2000), a general multiscale constitutive model has been developed, which couples interfacial debonding, void nucleation and growth, localization with strain-gradient effects and phase transformation. For an isotropic material, the corresponding plastic potential is expressed as:

$$\begin{aligned} \Phi_{\text{plasticity}}(f_0, f, \sigma_{ij}) = & \left(\frac{\bar{\sigma}}{\sigma_{\text{intr}}} \right)^2 + A_0 \frac{\sigma_m}{\sigma_{\text{intr}}} + A_1 (f + g_1) \exp \left(-\frac{\sigma_m}{\sigma_{\text{intr}}} \right) \\ & + A_2 (f + g_2) \exp \left(\frac{\sigma_m}{\sigma_{\text{intr}}} \right) - (q_0 + q_1 (f))^2 = 0 \quad (9.15) \end{aligned}$$

where σ_{ij} , $\bar{\sigma}$, σ_m , f_0 and f denote in turn the stress tensor, equivalent stress, mean stress, inclusion and void volume fraction at a given scale; σ_{intr} denotes the “material intrinsic strength” that contains the effects of internal variables associated with strain softening in the postbifurcation stage; the constants A_i and q_i are calibrated through the cell models.

When the constants A_i and q_1 in (9.15) vanish, this potential degenerates to conventional J_2 plasticity except that the yield strength is replaced by $\sqrt{q_0} \sigma_{\text{intr}}$. (9.15) becomes a “Drucker–Prager–like” plastic potential when A_0 is nonzero, whereas it converts to a “Gurson–like” model when $A_0 = 0$ but $A_1 = A_2$ and $g_1 = g_2 = 0$.

9.2.4 Laboratory Specimen Scale: Simulation and Results

Fracture toughness simulation

In this section, we describe ductile fracture simulations carried out on a center-cracked panel according to the ASTM Standard E399-E1737, which has been applied in the simulations by Hao et al. (2000) and Hao and Brocks (1997) using the hierarchical constitutive model

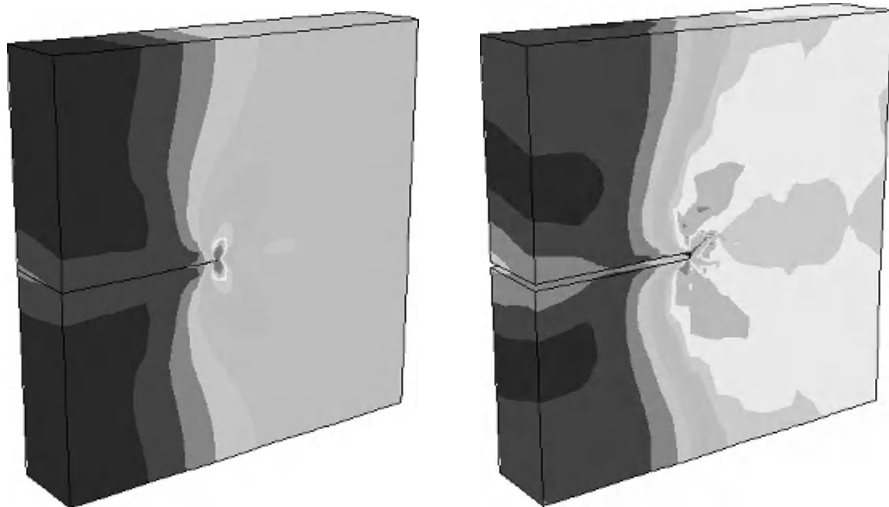


Figure 9.12 Crack growth: contours of equivalent stress at subsequent stages of a three-dimensional simulation. Reprinted from Computer Methods in Applied Mechanics and Engineering, 193, Hao et al., Multi-scale constitutive model and computational framework for the design of ultra-high strength, high toughness steels, 1865–1908, 2004, with permission from Elsevier.

developed in the previous sections and a meshfree method (see Li and Liu 2004, Liu et al. 1995, Belytschko et al. 1994, Liu et al. 2004d, Hao et al. 2002 and Hao et al. 2004c). As discussed in Moran et al. (1991) and Hao and Brocks (1997), the loading speed and material strain rate sensitivity may have a strong effect on damage evolution and thus, fracture toughness. However, in this section, only the results under quasi-static loading are presented.

Figure 9.12 presents two snapshots of 3D crack propagation using the macroscale plastic potential described in (9.15). Figure 9.13 shows the contours of equivalent plastic strain around a blunted crack tip at small-scale yielding, where a Rice–Johnson–type crack tip strain field is present. Figure 9.14 shows the contours after considerable crack growth with large deformation. In this computation, the primary particles (TiN) are explicitly embedded into the matrix that includes the secondary particles so that the microscale plastic potential (9.15), in conjunction with the quasi-particle dynamics approach, is applied. Plotted in Figure 9.15 is the corresponding load–CTOD (crack tip opening displacement) curve, where a black square indicates the CTOD at crack initiation, which defines the fracture toughness of the material. Figures 9.12–9.15 demonstrate that the computational approach is capable of capturing this class of phenomenon. On the other hand, it also reveals that the computational results depend upon many factors such as the geometry and distribution of inclusions, which are not readily captured by the periodic cell models in Figure 9.9.

Ductile fracture simulator and toughness–strength–adhesion diagram

The hierarchical constitutive and computational methodology introduced in this section results in a “ductile fracture simulator”, illustrated in Figure 9.16. Starting from the lower

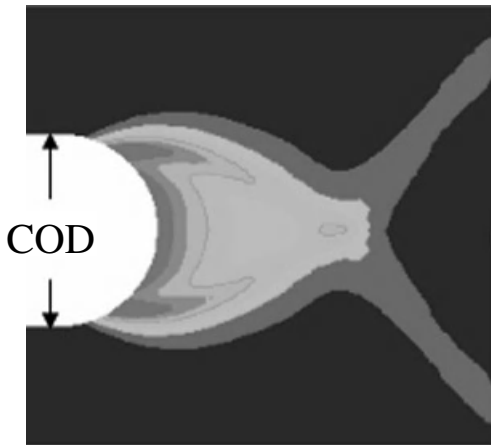


Figure 9.13 Simulation of crack growth: contour plot of stress. Reprinted from Computer Methods in Applied Mechanics and Engineering, 193, Hao et al., Multi-scale constitutive model and computational framework for the design of ultra-high strength, high toughness steels, 1865–1908, 2004, with permission from Elsevier.

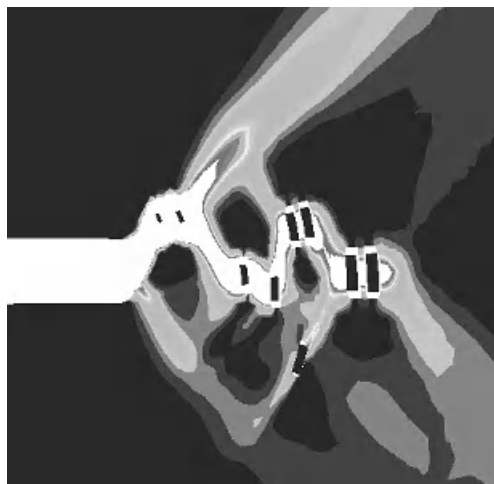


Figure 9.14 Simulation of crack growth: contour plot of stress. Reprinted from Computer Methods in Applied Mechanics and Engineering, 193, Hao et al., Multi-scale constitutive model and computational framework for the design of ultra-high strength, high toughness steels, 1865–1908, 2004, with permission from Elsevier.

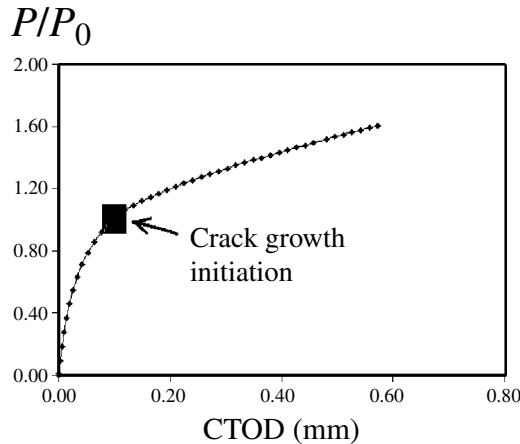


Figure 9.15 A simulation of crack growth: load–CTOD curve. Reprinted from Computer Methods in Applied Mechanics and Engineering, 193, Hao et al., Multi-scale constitutive model and computational framework for the design of ultra-high strength, high toughness steels, 1865–1908, 2004, with permission from Elsevier.

left corner, the quantum mechanics analysis explores the fundamental atomistic-electronic structure of the alloy matrix and the matrix/inclusion interface. This provides the corresponding energy-adhesion relations that are applied in the submicro- and microcell modeling to obtain the corresponding constitutive relations for the matrix material in each scale. For the modified 4340 steel, the computational results have been calibrated by experiments. The constitutive law of an inclusion induced voiding/microvoiding steel is implemented into the computer code for calculating crack parameters such as the crack tip opening displacement (COD); see Figure 9.13 and the J-integral using the method introduced by Moran and Shih (1987a,b). The COD (or J-integral) at crack growth initiation represents the fracture toughness of the material according to the ASTM standard. The simulated results are summarized by the Toughness–Strength–Adhesion (TSA) diagram that is at the upper right corner of Plate 7, which provides insight into the correlations between the steel strength, interfacial decohesion and fracture toughness.

The TSA diagram of Plate 7 is detailed in Figure 9.16(b). In Figure 9.16(a), the first principle-based traction–separation relations are plotted at various adhesion energy levels. Obviously, higher adhesion energy results in higher peak decohesion stress. Figure 9.16(b) is the TSA diagram corresponding to the traction–separation–adhesion curves presented in Figure 9.16(a).

In the TSA diagram (Figure 9.16(b)), the dashed lines represent the computed load–crack tip opening displacement curves for the center-cracked panel under tension. Simulations with values of matrix yield strengths of 500, 700, 900 and 1030 MPa are performed using the proposed hierarchical multiphysics constitutive models by Hao et al. (2004a). Along each dashed line, the circle, delta, solid circle and triangle denote in turn the COD_i (the COD at crack growth initiation) corresponding to the different levels of decohesion energy of the interface between the iron matrix and the inclusion particles, illustrated in Figure 9.16(a).

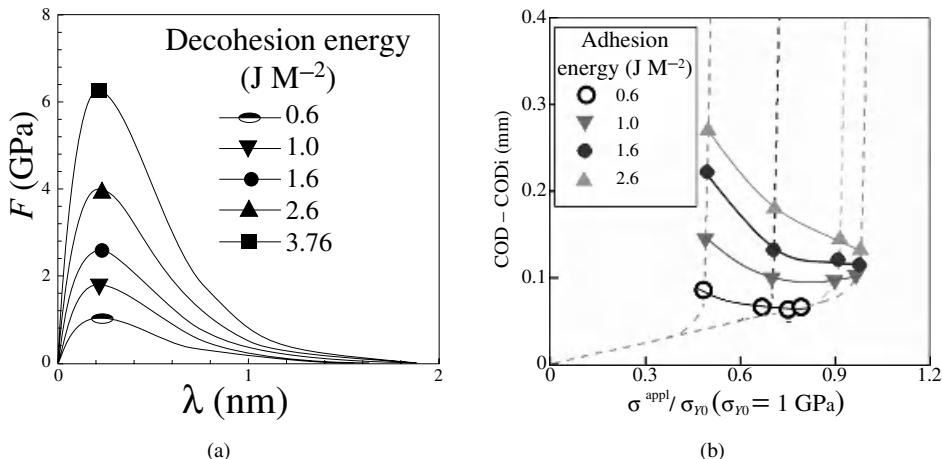


Figure 9.16 Toughness–Strength–Adhesion (TSA) diagram for steel design: (a) interfacial traction–separation relations with various decohesion energy; (b) TSA diagram where COD_i refers the COD at crack initiation. Reprinted from Computer Methods in Applied Mechanics and Engineering, 193, Hao et al., Multi-scale constitutive model and computational framework for the design of ultra-high strength, high toughness steels, 1865–1908, 2004, with permission from Elsevier.

The solid lines indicate the variation of fracture toughness when the decohesion energy is fixed but the strength of the iron matrix is varied. For example, at the decohesion energy of 0.6 J m^{-2} , the circle at extreme right denotes the COD at crack initiation for the matrix with the yield strength of 1.1 GPa . Similarly, the circle at extreme left on the line with 0.6 J m^{-2} denotes the COD at crack initiation for the steel with the matrix yield strength 0.5 GPa .

In the simulations presented in the TSA diagram, the diameters of the primary TiN particles ranged from 1 to $2 \mu\text{m}$ with a volume fraction from 0.02 to 0.2% ; the diameters of the secondary particles ranged from 20 to 200 nm with a volume fraction from 0.02 to 0.4% . The computation shows that crack propagation is mainly governed by the decohesion-debonding process of the primary TiN particles (inclusions), whereas the uniformly distributed small inclusion particles have a relatively stronger effect on strengthening, rather than on fracture. More detailed investigations, especially for the system with nonuniformly distributed inclusions, are required for clarifying the dual effects of secondary particles on strengthening and toughness.

Figure 9.16(b) reveals that increasing adhesion energy is a way of improving fracture toughness while maintaining strength. However, the TSA diagram also indicates that the toughening effect of adhesion energy is relatively reduced at high strength. Apparently, fixing interfacial strength but varying alloy matrix strength or vice versa may have a similar effect on fracture toughness. The trend obtained from the TSA diagram coincides with several experimental reports, for example, Argon et al. (1975), Landes and Brown (1998), McDougall et al. (1983), Saxena (1991) and Schwalbe (1977).

The TSA diagram in Figure 9.16(b), in conjunction with the analyses presented in the previous sections, provides several guidelines for steel design:

- Both interfacial adhesion energy and strength ratio are crucial for obtaining high toughness with high strength. A quantitative description of these relationships is given in Figure 9.16(a).
- Large inclusions ($>1\text{ }\mu\text{m}$) cannot maintain high interfacial strength, which is the major cause of lower toughness.
- For smaller dispersed particles, spatial uniformity of the dispersions may be particularly important for enhanced toughness.
- The densities of point defects in an alloy matrix, such as vacancies and dislocations, have strong effects on the strength and fracture mode of the alloy. The ratio between the normal separation energy and the energy barrier against dislocation motion determines the macroscale strength of alloys.

9.3 Bio-Inspired Materials

The notion of “self-healing” materials originates in biomimicry, the study and design of high-tech products that mimic biological systems. This technology is expected to have a huge range of applications from microelectronics to aerospace, where unchecked damage could lead to massive failure. “The day may come when cracks in buildings or in aircraft structures close up on their own, and dents in car bodies spring back into their original shape”—SRIC-BI (2004).

In general, self-healing is the ability of a material to restore mechanical properties, which were earlier perturbed by a plastic deformation or failure involving cracks and voids. Investigation of possible self-healing mechanisms is an important emerging field of nanotechnology.

9.3.1 Mechanisms of Self-Healing in Materials

One recent experimental effort in autonomous healing of composite materials is described in the works of White et al. (2001), Kessler and White (2001), Kessler et al. (2003) and Brown et al. (2003, 2002). Composite materials and polymers are vulnerable to damage in the form of cracks that lead to degradation of mechanical and electric properties of the material. Meanwhile, identification and repair of these cracks is virtually impossible.

The authors developed a composite material with a microencapsulated healing agent and a catalytic chemical trigger embedded within an epoxy matrix (Figure 9.17). An approaching crack disrupts the nearest microcapsules and releases the healing agent into the crack plane through capillary action. Consequently, polymerization of the healing agent is initiated by contact with the embedded catalyst, so that the crack faces appear bonded to each other. There is a direct analogy between self-healing structures and biological systems in that, having sustained damage, both automatically and autonomically initiate self-repair. Fracture experiments by the authors reveal 75% recovery in toughness, as well as possibilities for similar technologies in other brittle material systems, including ceramics and glasses. Issues associated with the effect of strain and dynamic load on the capillarity of a self-healing agent, optimal design of the microcapsules and matrix, and the crack/capsule effects require relevant multiscale, multiphysics simulation methods.

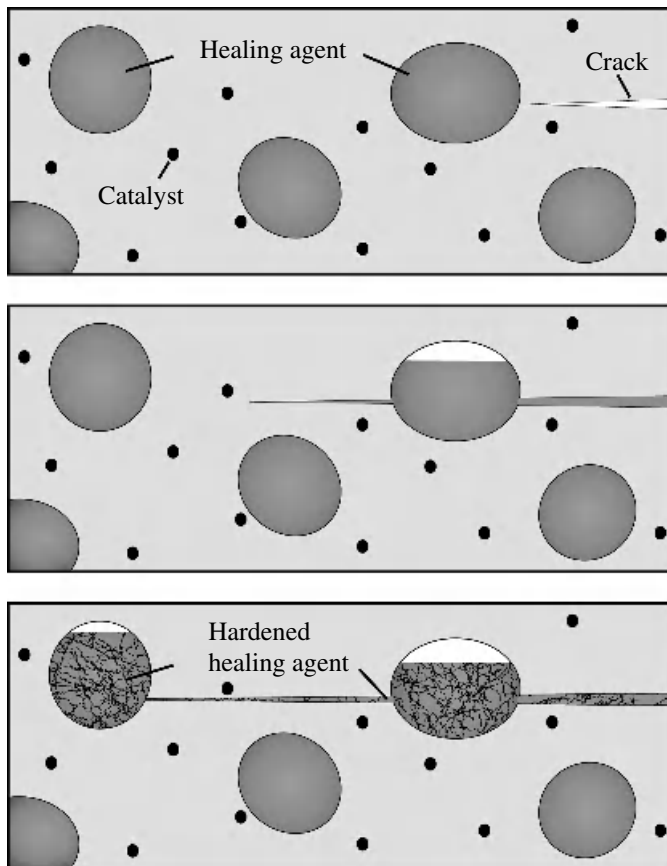


Figure 9.17 Self-healing of a structural composite matrix with an encapsulated healing agent; concept by White et al. (2001).

An alternative self-healing mechanism was recently reported in the theoretical work by Lee et al. (2004b). It was shown that adding nanoparticles to the polymers yields materials in which the particles become localized at nanoscale cracks and effectively form "patches" to repair the damaged regions.

Other materials, such as SiC/C/SiC model composites (Filipuzzi et al. 1994, and Filipuzzi and Naslain 1994), Si-Ti-C-O fiber-bonded ceramics (Tohyama et al. 1998), fine-grained composites (Fan et al. 2003) and even cement pastes (Farage et al. 2003) may initiate self-healing mechanisms on being heated to high temperatures. Liu (1994) reports the occurrence and recombination of surface cracks in a glass ceramic immersed in a simulated bodily fluid for sufficient periods, which can also be explained in terms of a self-healing mechanism.

One interesting mechanism of self-repair in steels was verified experimentally by Shinya et al. (2003). The authors have shown that the precipitation of a stable compound in a newly formed creep cavity improves creep rupture properties of the material.

Damage self-healing characteristics are observed in mullite/SiC samples (Chu et al. 1995) with different microstructures, and in some polymer coatings (Bertrand et al. 2000). Bachorczyk et al. (2000) advocate that self-healing protective scales can be achieved by diffusional transport of the coating and substrate elements.

Semiorganic (Kleiman et al. 1995) and ceramic (Westwood et al. 1996) protective coatings for aerospace applications, silicate nanocomposites (Fong et al. 2001), and SiC/SiC fibrous composites (Naslain et al. 2004), may reveal chemical mechanisms of self-healing on exposure to oxygen. Chromate coatings were confirmed to have a self-healing function preventing corrosion of metal under coating and coating defects (Suda and Shinohara 2002). Self-healing properties of beta-lactoglobulin (protein) films at large strains due to protein transport are also reported by Jones and Middelberg (2002).

Polypropylene metallized capacitors, used in power electronics, reveal self-healing capabilities in AC applications (Kumar 1996 and Rabuffi and Picci 2002). Evidently, exposure to an electromagnetic field initiates self-restoring phenomena in polypropylene thin films.

Interestingly, some of the available materials are believed to have natural self-healing mechanisms as opposed to those that are designed intentionally. One example is the plastic material “Surlyn”, which is found in a variety of ordinary commercial products, from bowling pins to dog-chew toys, because of its ability to withstand mechanical impact. Some researchers advocate that surlyn heals itself at the nano-level when damaged (Becker 2003). For reasons still being studied, Surlyn’s molecules reunite once external forces disintegrate them.

Self-restoring mechanical phenomena are also observed in some intrinsic atomic-scale systems; examples include self-repairing Lennard-Jones monolayers (Joos and Duesbery 1993 and Joos et al. 1994), and vacancy rearrangement in amorphous silicon (Miranda et al. 2004). In these systems, vacancies/voids in lattice structure are transformed to a set of lattice dislocations, corresponding to a lower potential energy or higher entropy of the system; meanwhile, the resultant configuration demonstrates improved mechanical properties. Here, the engineer’s objective consists of a comprehensive analysis of physical mechanisms governing these processes and their proper utilization in the nanostructured materials systems.

Another interesting possibility exists in the development of the so-called *shape-memory* alloys, and successive prototyping of micro- and nanocomposite materials with a shape-restoring function. Advances in this research are outlined in the following section. A summary of known phenomena that can potentially determine a self-healing function in a man-made material is provided in Table 9.1.

9.3.2 Shape-Memory Composites

Development of polymer and metal matrix composites (MMCs) with shape-memory alloy (SMA) inclusions (Files 1997, Forbell et al. 1997, Shimamoto et al. 2001, Gao et al. 2005, Hamada et al. 2003 and McVeigh et al. 2005) represents one interesting concept of a biomimetic material. Potentially, SMAs can be used for shape, fracture and damping control of composite materials.

The unique behavior of SMAs is due to a reversible thermoelastic phase transformation between *martensite* and *austenite*. The SMA parent phase, austenite, displays a cubic crystal lattice structure (Figure 9.18a). In the absence of an applied load, and upon cooling, the austenite transforms into another stable phase, “self-accommodated” martensite

Table 9.1 Basic mechanisms of self-healing

Mechanism	Examples in literature
1. Capillary transport and polymerization	White et al. (2001)
2. Diffusional bonding of crack edges	Files (1997) and Forbell et al. (1997)
3. Diffusional transport of inclusions/nanoparticles and cross diffusion of heterogeneous interfaces	Bachorczyk et al. (2000) and Lee et al. (2004a)
4. Precipitation of stable compounds in cracks	Shinya et al. (2003)
5. Recombination of vacancies and defects	Joos et al. (1994) and Miranda et al. (2004)
6. Shape-memory effects in alloys and composite materials	Files (1997), Forbell et al. (1997) and Shimamoto et al. (2001)

(Figure 9.18b). Different variants of martensite form, which are all crystallographically equivalent, but with differing spatial orientation. In self-accommodated martensite, no observable macroscopic deformation occurs because all variants (usually 24 habit plane variants for a particular twinning system) appear equally when martensite is formed by cooling. Upon heating, the transformation is fully reversible. Four temperatures are associated with this transformation:

- (i) Martensitic start temperature (M_s) – the temperature at which the material starts transforming from austenite to martensite.
- (ii) Martensitic finish temperature (M_f) – signifies that the transformation is complete, that is, the material is fully martensitic.
- (iii) Austenite start temperature (A_s) – the reverse transformation begins.
- (iv) Austenite finish temperature (A_f) – the reverse phase transformation is completed and the material is in the austenitic phase.

If a load is applied to the martensite at constant temperature, the crystallographic twinned structure will reorient to variants preferred by the load direction. This reorientation leads to a “detwinned” martensitic structure and an associated macroscopic strain (Figure 9.18c). Assuming there is no change in temperature, the macroscopic strain remains constant during unloading—a process analogous to a plastic deformation. However, this strain can be reversed through a temperature-induced phase transformation back to the austenite phase shown in Figure 9.18(a). Steps b–c–d (load–unload–heat) form the basis of the shape-memory effect (SME).

If the austenite phase material is loaded, the material will deform through a stress-induced phase transformation to martensite. As the stress required for this phase transformation is higher than that required for reorientation, an appropriate precipitate structure is necessary to impede dislocation motion. As in reorientation, an oriented martensitic structure is formed with an associated macroscopic strain. Upon unloading, the reverse

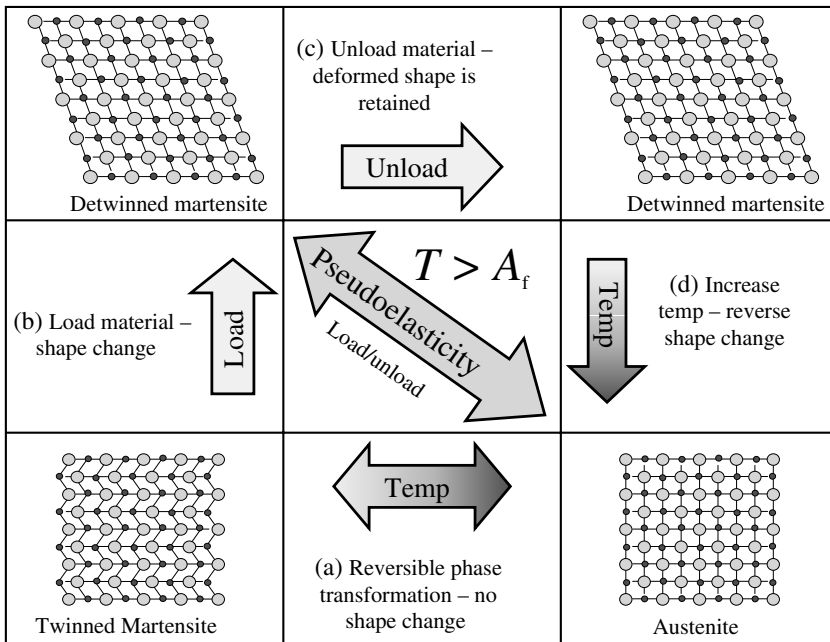


Figure 9.18 Schematic of pseudoelasticity and shape memory effects for NiTi. Austenite shown in (a), twinned martensite in (b), oriented martensite by loading in (c) and (d). Shape-memory effect and pseudoelasticity indicated by arrows. Reprinted from Computer Methods in Applied Mechanics and Engineering, McVeigh et al., Multiresolution analysis for material design, 2005, with permission from Elsevier.

transformation occurs as the martensite is no longer stable at the elevated temperature; indeed, the transformation temperatures are often modeled as being linearly related to the applied load. This elevated temperature load–unload cycle is often called “pseudoelasticity” or “superelasticity”.

Prototyping and design

A *prototype* MMC with shape-memory properties was produced at Northwestern University by Gao et al. (2005). The prototype composite consists of SMA wires oriented unidirectionally in a brittle metal matrix. It is loaded in the axial direction of the wires and allowed to crack in a line perpendicular to the wires (Figure 9.19). During fracture, the SMA wires undergo a thermoelastic phase transformation from austenite to martensite and/or a reorientation of Martensitic variants such that large strains (up to 10%) can be reversibly accommodated. Healing is initiated by heating the material, that induces the reverse phase transformation to austenite to take place in the SMA wires, whereby they recover their strain, close the crack, and apply positive closure forces on the matrix material.

Though the current self-healing MMC prototype is crude, with 100 micron diameter unidirectional wires in the matrix, the concept is quite general and ideal systems can have

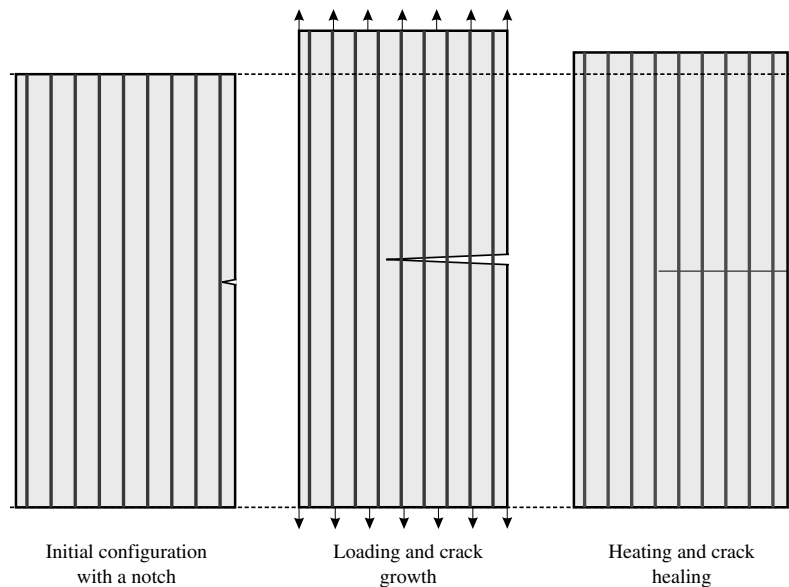


Figure 9.19 Schematic of self-healing composite showing SMA reinforcing wires, propagating crack and healed composite after heating; concept by Gao et al. (2005).

smaller scale inclusions of differing morphology throughout the matrix to provide a reliable self-healing function.

An alternative design concept of shape-memory composites is shown in Figure 9.20. This composite consists of a brittle metal matrix with short randomly oriented *bone-shaped* inclusions (Zhou 1998, Zhu et al. 2001, Zhu and Beyerlein 2002 and Zhu and Beyerlein 2003). The bone-shaped SMA inclusions provide a similar mechanism of self-healing as illustrated in Figure 9.19.

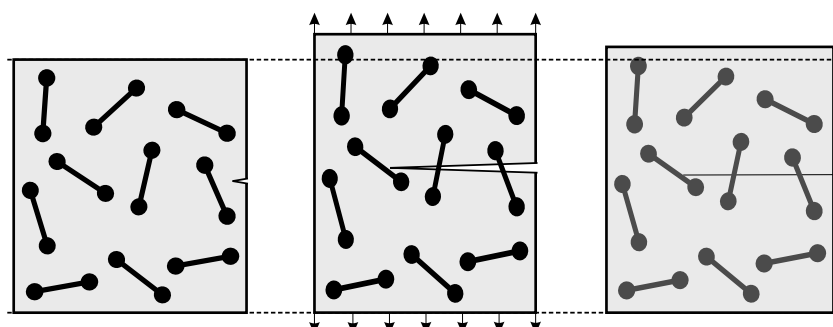


Figure 9.20 Left: composite with SMA dumbbell-shaped inclusions. Middle: loading, crack propagation and fibers transformation. Right: crack closure due to heat-induced shape restoration of the SMA inclusions.

The matrix material is chosen to be elastic–plastic for this application, with hardening and temperature-dependent softening: brittle at room temperature, but ductile at the (higher) healing temperature. The matrix softening at high temperature enables the crack to fully close when the wires pull the crack back together and also enables rewelding of the crack faces in contact by liquification of the eutectic phase. Currently, similar mechanisms are also investigated at the nanoscale, Gao et al. (2005), with potential applications in self-healing nanocomposite structures. These studies are also devoted to resolving the interaction between the SMA fibers and fiber balls with the matrix material on the basis of quantum mechanical calculations.

9.3.3 Multiscale Continuum Modeling of SMA Composites

In this section, we consider the application of the multiresolution continuum approach of Section 9.1 to the modeling of shape-memory alloy composites with bone-shaped inclusions illustrated by Figure 9.20.

SMA constitutive law

An integral component of continuum modeling is a constitutive law that may have a peculiar form for the pseudoelastic shape-memory inclusions. A one-dimensional SMA constitutive model, required to characterize the fiber inclusions, was proposed by Tanaka et al. (1986), modified by Liang and Rogers (1990) and subsequently by Brinson (1993), Brinson and Huang (1996) and Bekker and Brinson (1998). The volume fraction of the martensite phase is related to material stress and temperature history. Figure 9.21 shows a stress–temperature phase diagram of the austenite and martensite transformation zones for a typical SMA. The material is considered to be composed of a fraction of austenite and a fraction of

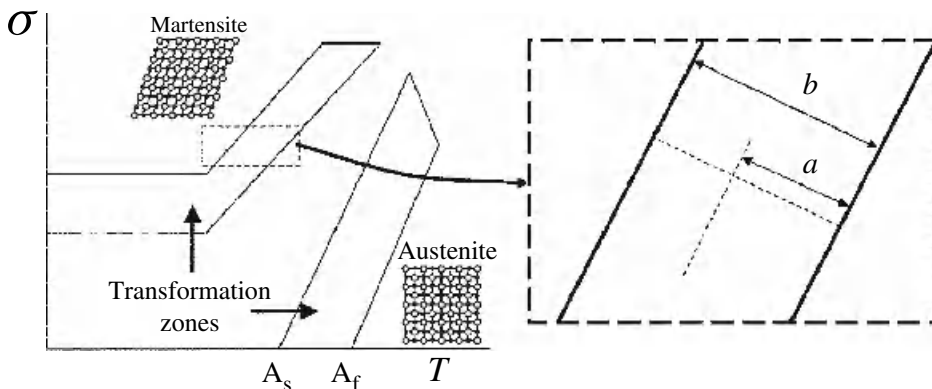


Figure 9.21 Stress–temperature map of austenite and martensite transformation zones. The martensite and austenite start and finish times are modeled as linearly related to the applied load. At lower temperatures, the transformation behavior is controlled by the applied load only. Reprinted from Computer Methods in Applied Mechanics and Engineering, McVeigh et al., Multiresolution analysis for material design, 2005, with permission from Elsevier.

martensite. Within the martensite transformation zone, the fraction of martensite is related to the stress–temperature path history and the ratio a/b , the relative distance across the transformation zone. The martensite volume fraction increases when moving across the martensite transformation zone in the direction from the martensitic start temperature (M_s) side to the martensitic finish temperature (M_f) side. In the reverse manner, the martensite fraction decreases in the austenite transformation zone.

The flow stress of the SMA is then related to the fraction of martensite by

$$\sigma = E(\varepsilon - \varepsilon_L \xi_s) + \Theta \Delta T \quad (9.16)$$

where E is the elastic modulus, ε is the strain, ε_L is the maximum transformation strain, ξ is the stress-induced martensite fraction, Θ is related to the thermal-expansion coefficient and T is the temperature. A kinetic law, Bekker and Brinson (1998), is coupled with equation (9.16) to determine the value of ξ via a phase diagram kinetics approach using Figure 9.21 as briefly described above.

Bone-shaped short fibers

The use of relatively ductile bone-shaped short (BSS) fibers (see Figure 9.20), to geometrically reinforce brittle materials has proved capable of improving both strength and toughness significantly; see Jiang and Valdez (2000), Zhu et al. (2001) and Zhu and Beyerlein (2002, 2003). These authors have shown that the use of BSS fibers maximized energy dissipation through fiber debonding and matrix deformation, yet avoided complete fracture by prohibiting fiber pullout. The BSS fibers bridged the crack and resisted crack opening and further propagation. A weak interface that debonds is essential in order to take advantage of the crack bridging capabilities. Thus, the presence of BSS fibers will provide superior energy dissipation by crack bridging, debonding and crack deflection. If the BSS fiber is composed of an SMA, the enforced phase transformation that occurs during crack bridging will also cause some energy dissipation. In addition, by using an SMA for the bone-shaped inclusion material, it is possible to produce a self-healing composite by taking advantage of the shape-memory properties of the inclusions. Subsequent to loading, the composite can be heated. This causes the matrix material to become softer and a reverse phase transformation within the inclusions leads the BSS fibers' attempt to return to their original shape, closing up any small microcrack in the softened material in the process.

The behavior at the microscale differs from that at the macroscale during both the deformation and healing stages as shown schematically in Figure 9.22. In this figure, a crack develops at the microscale. The material is subsequently heated, causing the BSS fibers to shrink and close the crack. The material can again sustain a load. The average fracture behavior and healing effect over the microscale region is invariably more extreme than that over the macroscale region. The profound effects of localized deformation and material healing are thus lost through macroscale averaging.

Two-scale modeling

The SMA composite with BSS inclusions can be resolved to two scales: the macroscale and the microscale, using the theoretical approach of Section 9.1.1. The healing effect

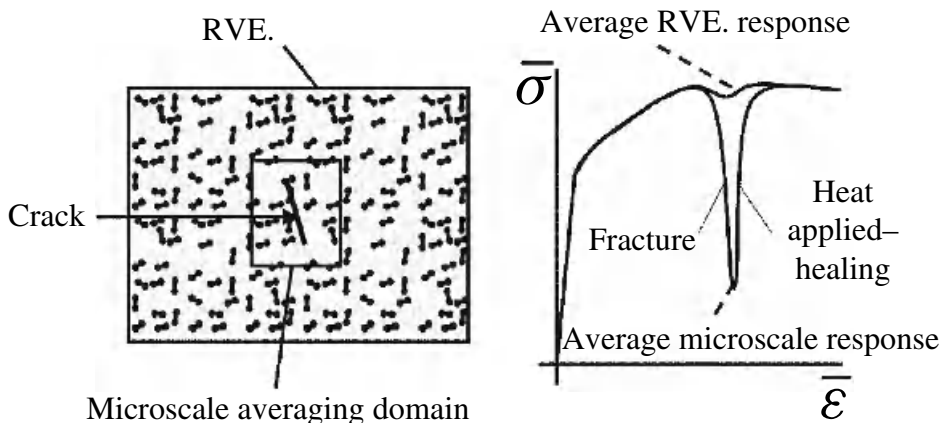


Figure 9.22 The *average* microbehavior is more extreme than the *average* macrobehavior. The graph shows the stress and strain averaged over each domain. The crack causes severe average fracture behavior over the microscale domain shown. However when the average behavior of the RVE is considered, the resulting average fracture is much less severe. The healing effect is also more pronounced at the microscale. Reprinted from Computer Methods in Applied Mechanics and Engineering, McVeigh et al., Multiresolution analysis for material design, 2005, with permission from Elsevier.

is a microscale event. The microaveraging domain contains a population of SMA BSS fibers. For simplicity, the BSS fibers are modeled as having elastic ends joined together by an SMA rod. In this way, the 1D SMA constitutive law can be applied to the rod, without losing the important mechanics. Contact between the BBS fiber and the matrix is modeled as hard contact with a nonlinear elastic law representing the interfacial debonding. Interfacial debonding occurs at the elastic limit of the matrix material, that is, the interface is modeled as being weakly bonded. An averaging domain is simulated that captures the interactions between BSS fibers and the geometrical crack bridging mechanism. The average microscale constitutive behavior can be examined over this domain. The matrix material is considered to be elastic–plastic with some strain softening because of accumulated plastic strain and also temperature softening. A typical microaveraging domain is illustrated in Figure 9.23.

With reference to Figure 9.24(a), during loading, the BSS fibers succeed in geometrically strengthening the material and the martensite fraction increases in the loaded BSS fibers. Energy is dissipated through the mechanisms described above. The bridging effect of the SMA BSS fibers is evident by comparing the average constitutive behavior of the microaveraging domain with fibers and a microaveraging domain without fibers (dotted line in Figure 9.24a). Upon unloading, the elastic strain is released and a residual average plastic strain remains. During the subsequent heating phase, the fraction of martensite decreases and the BSS fibers attempt to return to their original size. From Figure 9.24(b), the reduction in strain caused by fiber 'shrinkage' is most pronounced in the temperature range 130° to 150° , which coincides with austenite transformation zone. During cooling, the average strain in the microdomein decreases to below 0.001 and finally levels off at

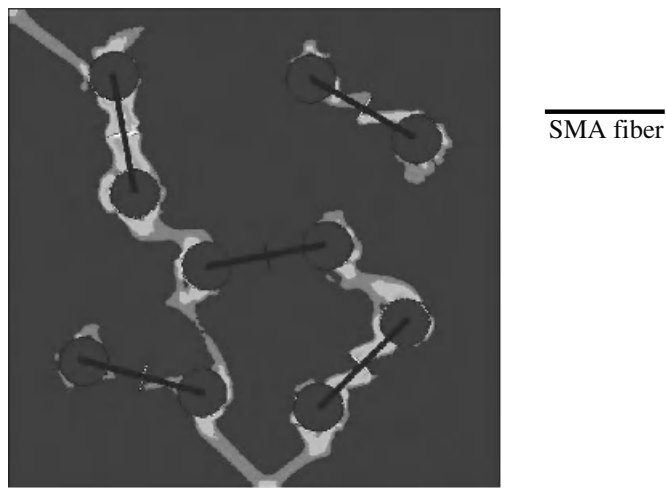


Figure 9.23 Microaveraging domain of a composite containing SMA composite with bone-shaped short fibers modeled as two elastic spheres joined by a SMA fiber. The fiber volume fraction is 0.08. Reprinted from Computer Methods in Applied Mechanics and Engineering, McVeigh et al., Multiresolution analysis for material design, 2005, with permission from Elsevier.

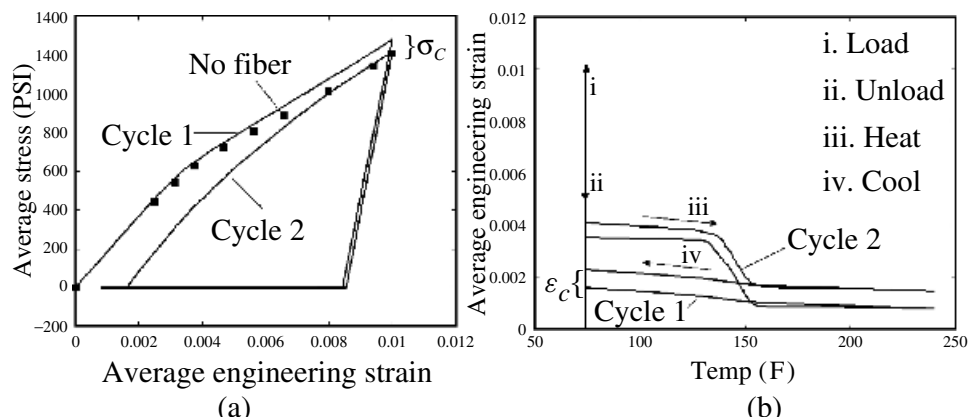


Figure 9.24 Stress versus strain (a), and strain versus temperature (b) for the microaveraging domain. A hysteresis-type behavior is evident. Reprinted from Computer Methods in Applied Mechanics and Engineering, McVeigh et al., Multiresolution analysis for material design, 2005, with permission from Elsevier.

a value below 0.002. A second load, unload, heat and cool cycle results in a hysteresis-type average behavior at the microscale. However, each successive cycle results in a greater value of the residual plastic strain ε_C and a reduction in material strength σ_C due to damage accumulation in the matrix material (Figure 9.24b).

The crack bridging and healing effect of the BSS fibers can be considered as a process that is predominant at the microscale. The multiresolution approach can therefore capture the localized deformation and healing effect through an average microscale constitutive relation that describes the behavior shown in Figure 9.24. The macroscale average behavior can be determined by examining the average behavior of a representative volume element. The material within the RVE is characterized by the predetermined microscale constitutive relationship. A generalized constitutive law can be formed by combining the constitutive laws at each scale,

$$\Phi(\sigma, \bar{\varepsilon}, f) = \left(\frac{\sqrt{3J_2}}{\sigma_y(\bar{\varepsilon})} \right)^2 + q_1 \frac{\varepsilon_m}{\sigma_y(\bar{\varepsilon})} - 1 - q_2 f \cosh \left(q_3 \frac{3\varepsilon_m}{2\sigma_y(\bar{\varepsilon})} \right) - q_3 f^2 = 0 \quad (9.17)$$

When localization occurs, it becomes much more severe because of the microdeformation contribution. On the other hand, the healing effect within the localized region will be more pronounced because of the contribution from the microscale healing. Both of these microscale phenomena are captured in the microscale part of the generalized constitutive relation. Importantly, the healing properties can then be determined in terms of the material constants that comprise the constitutive law (9.17), which in turn depends on the key microstructural parameters such as fiber size and spacing. Thus, the inverse *design problem* can also be considered: to determine the microstructure of the composite on the basis of desired self-healing properties via representative cell modeling.

Detailed simulation snapshots for a local (microaveraging) domain that contains a single SMA inclusion fiber are given in Figure 9.25. The domain is subjected to one load–unload–heat–cool cycle. During loading, the matrix material becomes damaged (fracture occurs) and the inclusion undergoes a deformation-driven crystallographic transformation. The subsequent heating drives a reverse crystallographic transformation within the SMA inclusion. As the SMA inclusion attempts to reassume its original shape, it produces a mechanical closure force on the crack. The damage (crack) in the matrix material is healed, and the specimen can sustain a greater load. If the cycle is repeated several times, the closure force becomes unable to completely heal the matrix material and some residual damage may remain present after each cycle. The simulated average constitutive behavior of a domain subjected to several damage–heal cycles is shown in Figure 9.26. When healing is performed at the end of each cycle, the composite exhibits increased strength and ductility.

Homogenized continuum modeling

The homogenized material law (9.17) can also be utilized for traditional continuum modeling. An example is shown in Plate 8, where a two-dimensional homogenized continuum model represents crack propagation in the SMA composite material. The specimen undergoes the load–unload–heating cycle, where cooling effects are considered to be negligible; the crack can be seen to heal itself.

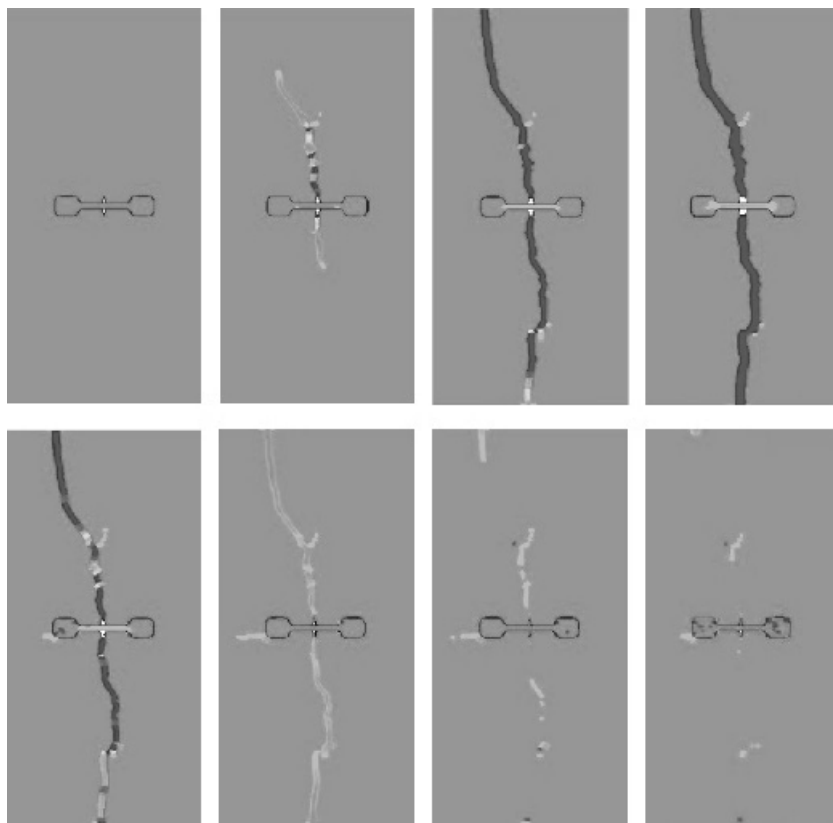


Figure 9.25 Simulation snapshots for a local averaging domain with a single bone-shaped SMA fiber.

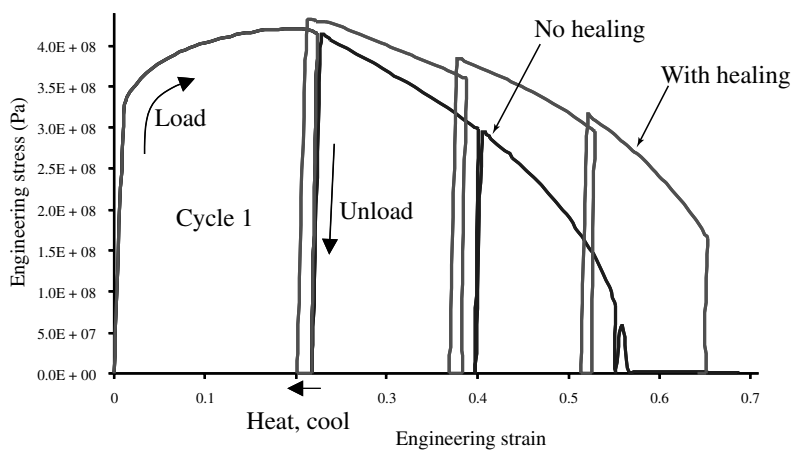


Figure 9.26 Strength of a macroscopic specimen of the SMA composite at four successive load/unload cycles.

9.3.4 Issues of Modeling and Simulation

Macroscopic constitutive behavior of composite materials has been extensively performed through continuum homogenization methods. This approach involves predicting the material response by implicitly averaging atomic-, nano- and microscale dynamics and defect evolution over time and space. However, some material behavior, typical of self-healing structures, cannot be explained in a conventional continuum-mechanics framework such as the inherent inhomogeneity of plastic deformation, plastic flow localization in shear bands, the effects of crack geometry on fracture toughness, capillary flow, polymerization, phase transformation-induced healing properties of SMA inclusions, and others.

In relation to the shape-memory composites, as an example, the available modeling schemes only account for the continuum level description of the SMA wires and the elastic–plastic matrix behavior (Gao et al. 2005 and Shimamoto et al. 2001). Issues of the detailed phase transformation ongoing in the SMA wires, the interaction with the matrix at the interface, the matrix liquification and resolidification, and diffusional bonding across the healing crack face cannot be considered without the development of novel multiscale models. The issue of fiber–matrix interaction is explained in Plate 9. This continuum simulation indicates that debonding on the interface between the bone-shaped SMA fibers and the matrix can occur in the course of the loading cycle. The relevant cohesive law needs to be determined in advance on the basis of quantum mechanics calculations. As in the area of nanocomposites (e.g. Odegard et al. (2003, 2002)), tractable multiscale methods are required to begin capturing the fundamental physics underlying self-healing of SMA composites. Taking into account microscale inhomogeneities of the self-memory composites, one possibility exists in the conjoint use of the bridging scale method for concurrent atomistic/continuum coupling (Chapters 6–8), with a multiresolution continuum approach, such as discussed in Section 9.1.

From the engineering perspective, studying the basic self-healing mechanisms, and their effect on material performance is crucial in developing advanced bio-mimetic materials. Meanwhile, computer modeling, simulation and characterization of engineering structures and materials with an intrinsic self-healing function cannot be versatile within the available approaches, and requires the development of novel numerical methods that allow multiple scales resolution in both space and time. Provided that the relevant methods for modeling, simulation and characterization are developed, self-healing and self-repairing structures could become commonplace within the next few decades.

Currently, we realize that the basic mechanisms of self-healing (see Table 9.1) are mostly nonequilibrium, *slow-rate*, atomistic processes determined by diffusion, capillary, polymerization and recombination effects at the atomistic level, as well as phase transition phenomena. Concurrent numerical modeling of these processes and their concurrent coupling with continuum formulation, that is, dynamic effect on the constitutive laws and stress fields, is a long-term goal.

Multiple timescales

The basic mechanisms of self-healing listed in Table 9.1 are often associated with the passage of particles through local potential barriers, where the driving force arises because of concentration/pressure differences, potential and free energy minimization, and external incentives: stress, pressure, vibrations, heat, electric field, and so on. In closed (fully

autonomous) systems with an absence of external effects, the diffusion, capillary and recombination phenomena are initiated by atomic thermal vibrations, and accompanied by maximization of the system's entropy. Each individual passage from one local minimum of potential energy to another requires a fluctuation of the kinetic energy of thermal vibrations, sufficient to overcome the potential barrier. An average time $\Delta\tau$ between two sufficiently large fluctuations determines the rate of the process, $r = 1/\Delta\tau$. This time depends on the system's properties, number and types of the constituent atoms/molecules, and thermodynamic state parameters: temperature, pressure and concentration. Quite commonly, this time is multiple orders of magnitude larger than the characteristic period of thermal vibrations t_v , $\Delta\tau \gg t_v$. Therefore, an acceptable numerical model should provide sufficient resolution at both of these disparate timescales.

Meanwhile, the time step of a typical molecular dynamics simulation is limited to characteristic times of atomic thermal vibrations, which is on the order of a femtosecond, and the slow-rate self-healing phenomena may not be accessible by the direct MD modeling. These phenomena determine macroscopic material properties, so that a typical multiple space-scale situation arises. However, modeling these slow-rate processes and their concurrent effect on the macroscopic material performance, and vice versa, is difficult. Such a multiscale method would span incommensurable, in the traditional sense, timescales—from femtoseconds to minutes and hours. Even though, the concurrent multiscale methods (e.g. Liu et al. (2004b) and Curtin and Miller (2003)) are versatile and applicable to a variety of nanoengineering problems, their bottleneck is still time. The strongly coupled atomistic and continuum domains evolve in a common timeline. Therefore, the total physical time accessible by the multiscale model is limited, in principle, by the total time allowed for the atomistic (MD) simulation. Selected concurrent methods, including the bridging scale approach presented in this book, allow some staggering of time integration procedures over the coarse scale. While this technique leads to noticeable savings in computer efforts, physical time in the simulated system is still determined by evolution of the MD model, and remains, in principle, single-scale.

The timescales issue also has a negative effect on the spatial coarsening, where a drastic increase of the total problem size becomes impossible. Indeed, the most advanced MD computations comprise several million time steps, so that the maximum time achieved in MD simulations is on the order of a nanosecond. Meanwhile, the continuum domain size is limited by the distance passed by acoustic waves between two opposite ends of the domain, for a total time of the MD simulation. Recalling that the typical group velocity of acoustic waves in solids is $3000\text{--}5000\text{ m s}^{-1}$, we find that the maximum allowed domain size is limited to several microns.

The issue of overcoming the timescale limitations of the molecular dynamics simulations was discussed by some authors, including Voter (1997), Voter et al. (2002), Jacobsen et al. (1998), Passerone and Parrinello (2001, 2003) and Lee et al. (2004a); however, an efficient concurrent method allowing multiple scales for both space and time is still being sought after.

Discussion on probabilistic approaches

In Figure 9.27, we show an example of a scheme of multiscale, multiphysics modeling of a material with the capillary/polymerization self-healing mechanism by White et al. (2001), which was shown in Figure 9.17. There are two competing mechanisms in this model,

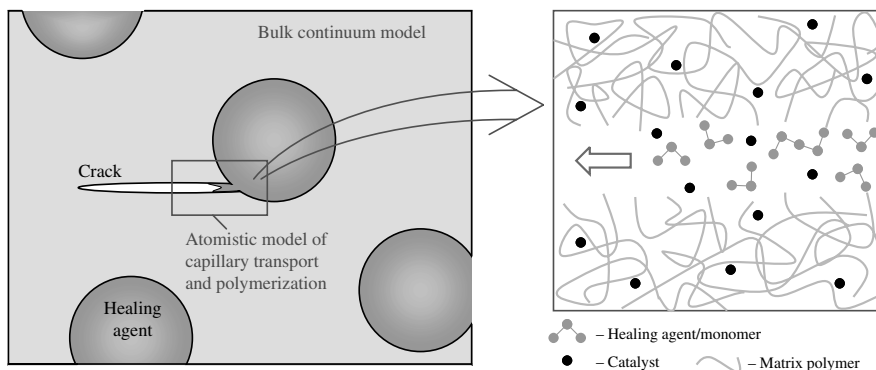


Figure 9.27 Approach to modeling the capillary/polymerization self-healing mechanism in polymer materials. Slow-rate atomistic models are concurrently coupled to the bulk continuum model.

which are the crack propagation and self-healing processes. Efficiency of the atomistic self-healing process depends concurrently on numerous provisos determined by the macroscopic material behavior, such as crack size and crack propagation speed, external forces and resultant vibration of the crack cavity walls, dynamic response of the healing capsule, and so on. In turn, the self-healing process affects material properties that determine the macroscopic performance, so that a strongly coupled concurrent atomistic/continuum approach is required for modeling this material. Another example proving these arguments is depicted in Figure 9.28, where the crack growth competes with the process of self-healing by precipitation of healing inclusions inside the crack cavity.

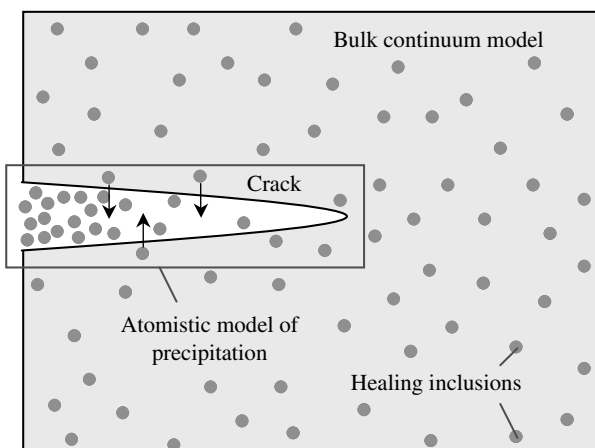


Figure 9.28 Modeling of the competing mechanisms of crack growth and self-healing by precipitation of the molecular scale inclusion inside the crack cavity.

Because of timescale limitations, the standard MD and concurrent simulation methods may fail to serve as a tool for modeling and simulation of slow-rate relaxation and transport phenomena responsible for the self-healing properties. Note that the time evolution of a Lagrangian system is fully determined by initial/boundary conditions, interatomic potentials and materials laws utilized. For these reasons, explicit time integration methods are referred to as *deterministic methods*. Since recently, the authors of this book are also making efforts in the development of *nondeterministic* multiscale methods that would involve a probabilistic description of the atomistic domain coupled with a continuum domain.

The probabilistic multiscale approach can become a reality, provided that three constitutive elements are available beforehand: (1) a probabilistic atomic-scale simulation method, (2) a probabilistic continuum (macro) scale method, (3) an atomistic/continuum coupling approach. In fact, the first two of these components are readily available. There exists a promising approach to treating slow-rate atomistics in a probabilistic manner, the *kinetic Monte Carlo* (KMC) method by Fichthorn and Weinberg (1991). Furthermore, a probabilistic finite element method for continuum modeling, including stochastic crack growth, is also available because of the efforts by Liu et al. (1986, 1988, 1996b), Besterfield et al. (1990, 1991) and Moon et al. (2004), and other researchers. Thus, the challenge is to bring together the probabilistic atomic-scale and continuum methods into a coupled multiscale approach. Within this approach, the atomistic model would utilize a statistical description of the physical quantities, and the time evolution of the system will be viewed as a stochastic state transition process characterized by specific expectation times for the intermediate states of the system.

The KMC method for modeling slow-rate atomistic phenomena is an essentially probabilistic method that still provides time-dependent information about a system's evolution. This method gives a coarse-grained picture of time evolution, built on a detailed microscopic understanding of the system's dynamics. In contrast to traditional Monte Carlo techniques, associated with obtaining static or equilibrium properties of the system, the KMC technique can be utilized to study nonequilibrium phenomena determined by kinetic motion of atoms and molecules. The KMC method simulates nonequilibrium and equilibrium dynamics of the system with a straightforward correspondence to the real physical time. The basic idea of KMC is that of considering the simulated process as a cumulative result of a large number of independent elementary processes (events), whose statistics can be prescribed with a sufficient accuracy. For example, the complicated process of interdiffusion in materials can be viewed as a result of multiple individual events, such as hopping and permutation of atoms in a potential field inside the material.

The mathematical interpretation of basic assumptions made within the KMC method consists in characterization of a stationary series of random independent events occurring with an average rate r in terms of a Poisson process, for example, Cinlar (2004). The probability P of n events occurring within time t at the known average rate r is given by $P(n) = (rt)^n e^{-rt} / n!$. One feature attributed to the Poisson process, which is crucial for multiple time scale modeling, is an expression for the probability density of time intervals t between successive events:

$$p(t) = r e^{-rt} \quad (9.18)$$

Thus, the mean time period between successive events is given by $\Delta\tau = 1/r$. Furthermore, a resultant of N independent Poisson processes is also a Poisson process, where the

probability of n events within time t is given by

$$P(n) = \frac{(\lambda t)^n}{n!} e^{-\lambda t}, \quad \lambda = \sum_{i=1}^N r_i \quad (9.19)$$

where r_i are the rates of individual events, and the mean time between two events is $\Delta\tau = 1/\lambda$. For nonequilibrium systems, the overall rate λ varies in the course of time. The quantity Δt can be viewed as an essential time step of the atomistic process, that is, the time of passage between two essentially different configurations of the atomic system. Since this time has a straightforward physical interpretation, it can be utilized within the multiscale framework. The basic input information required for KMC is a table of time rates for all the elementary events that need to be accounted for. This information will be gathered from localized MD simulations, analytical arguments and empirical data. Within the KMC method, the physical time step Δt has no direct impact on the cost of the simulation, and normally serves as a simple postprocessing result. Subsequently, the KMC run can provide dynamics of large atomistic domains up to macroscopic time intervals that can span characteristic times of the self-healing processes.

A probabilistic multiscale approach may involve the KMC model of the atomic-scale capillary transport and polymerization of the healing monomer (Figure 9.27 (right)), and a probabilistic FEM model of the fatigue-crack propagation process. As an example, Liu's probabilistic FEM formulation involves a characteristic vector \mathbf{b} of random system parameters, including the applied stress and fatigue parameters, and a random state vector \mathbf{x} that determine the current configuration of a growing crack, as well as the rate of crack growth. Successively, a finite element Lagrangian can be written in terms of the components of random vectors \mathbf{b} and \mathbf{x} , and the crack growth viewed as a stochastic process whose rates and direction are determined by the finite element model. Finally, continuum constitutive laws for the FE model can be updated at specific steps on the basis of current atomistic configurations provided by KMC model. Thus, the stochastic processes of fatigue crack growth on the continuum scale and the competing self-healing process on the atomic scale can be coupled within a unified numerical method.

9.4 Summary and Future Research Directions

The potential versatility of the multiscale methodologies imply application to any material that has features on various length scales that are important to the macroscopic deformation. Current efforts include the design of high-strength steels, micro- and nanocomposites, as well as bio-inspired self-healing materials. It is expected that this new generation of composites and alloys will be used for aerospace and other lightweight applications. The drive for endlessly lighter materials has highlighted the applicability of multiscale methods in automobiles. Another potential application is the design of high-strength and high toughness-to-weight ratio braided composite tubes for use as energy absorbents during vehicular impact.

Bio-inspired materials could have a massive impact on various industries by reducing maintenance requirements, increasing safety and product lifetime. Researchers envision autonomous devices, medical implants, sensors and even space vehicles that, similar to biological organisms, would have the ability to identify and subsequently heal the damage while

serving their design purpose. These structures could particularly find use in applications in which repair is impossible or impractical, for example, in implanted medical devices, electronic circuit boards and space systems. Numerous research organizations, agencies and universities have shown a significant interest in self-healing technologies. As an example, NASA is planning to significantly improve the reliability of future aerospace vehicles by developing a new class of sensors integrated within aerospace structures; the sensors would continuously monitor an aircraft structure's condition and take corrective actions, if damaged (Strothman 2002). Meanwhile, constitutive parts of such a structure, the self-healing polymers, alloys and high-performance nanocomposites are still in an initial phase of their development. Evidently, one of the reasons is that research in this direction requires novel methodologies for multiscale modeling, simulation and characterization.

Novel numerical approaches are sought to predict the important role of the inclusions in preventing crack propagation and healing the cracks through a crystallographic transformation in the shape-memory alloy inclusions, as well as to resolve the multiple timescales issue by incorporating the important atomic-scale kinetics, transfer phenomena and chemistry into the continuum formulation. Consequently, there is great interest in accurate multiple scale computational methods and material models for linking atomistic and macroscale constitutive behavior.

An area of future emphasis should be on the issue of disparate timescales present during the deformation of a typical engineering material. To date, a much greater emphasis has been placed in the literature on the spatial coupling of length scales. However, the issue of timescales is a problem that runs concurrently with the length scale issue. Without similar breakthroughs in modeling disparate timescales as has been achieved in the length scale area, multiple scale modeling will stagnate and opportunities for significant achievements will diminish greatly. We believe that future research will concentrate on this area, which is crucial to developing truly multiple scale models that bridge relevant space and timescales.

Copyright

Material of Section 9.2 first appeared in Hao et al. (2004b), Copyright 2004, and was reproduced here with permission from Elsevier.

10

Bio–Nano Interface

This chapter summarizes the newly developed immersed finite element method (IFEM) and its application to the modeling of biological systems. In IFEM, a Lagrangian solid mesh moves on top of a background Eulerian fluid mesh, which spans the entire computational domain. Hence, mesh generation is greatly simplified, while both fluid and solid domains can be modeled with the finite element method. The distribution of forces and continuity of velocities on the interface between the fluid and solid domains are enforced by implementing the reproducing kernel particle method (RKPM) delta function. The method is applied to fluid–structure interaction problems encountered in human cardiovascular systems. Currently, a heart model is being constructed and the deployment process of an angioplasty stent is investigated in numerical simulations. Some preliminary results on monocyte and platelet deposition are discussed in this chapter. Recent approaches to modeling blood rheology, in particular, the shear-rate–dependent deaggregation of red blood cell (RBC) clusters and the transport of deformable cells, are illustrated. Furthermore, IFEM is combined with electrokinetics to study the mechanisms of electro-manipulation, including dielectrophoresis and electroosmotic flow, as well as nano/bio-filament assembly for the understanding of cell motility.

10.1 Introduction

For the past few decades, significant research efforts have been directed to the development of modeling and simulation approaches for fluid–structure interaction problems. Methods developed by Tezduyar (1992, 2001) and his coworkers are widely used in the simulation of fluid–particle (rigid) and fluid–structure interactions. To accommodate the complicated motion of fluid–structure boundaries, adaptive meshing or the arbitrary Lagrangian Eulerian (ALE) techniques are typically used; see Huerta and Liu (1988), Hughes et al. (1981), Liu (1981), Liu and Gvildys (1986), Liu and Ma (1982) and Wagner et al. (2003, 2001). Recently, such approaches have also been adopted by Hu et al. (2001) in the modeling of fluid–particle (rigid) systems. Nevertheless, mesh update or remeshing algorithms can be

time consuming and expensive. A detailed discussion on this issue is presented in Johnson and Tezduyar (1999).

In the 1970s, Peskin (1977) developed the immersed boundary (IB) method, which was applied later to the study of flow patterns around heart valves; see McQueen and Peskin (1997) and Peskin and McQueen (1989, 1993). The mathematical formulation of the IB method employs a mixture of Eulerian and Lagrangian descriptions for fluid and solid domains. In particular, the entire fluid domain is represented by a uniform background grid, which can be solved by finite difference methods with periodic boundary conditions, whereas the submerged structure is represented by a fiber network. The interaction between fluid and structures is accomplished by distributing the nodal forces and interpolating the velocities between the Eulerian and Lagrangian domains through a smoothed approximation of the Dirac delta function. The advantage of the IB method is that the fluid–structure interface is tracked automatically, which circumvents costly mesh update algorithms.

Nevertheless, one major disadvantage of the IB method is the assumption of a fiberlike one-dimensional immersed structure, which may carry mass, but occupies no volume in the fluid domain. This assumption also limits the accurate representation of immersed flexible solids, which may occupy a finite volume within the fluid domain. Furthermore, uniform fluid grids also set limitations in resolving fluid domains with complex shapes and boundary conditions.

Recently, following the pioneering work of Peskin and coworkers on the IB method, an alternative approach, the immersed finite element method (IFEM), was developed by Zhang et al. (2004). This method is able to eliminate the aforementioned drawbacks of the IB method by adopting parts of the extended immersed boundary method (EIBM) developed by Wang and Liu (2004). With finite element formulations for both fluid and solid domains, the submerged structure is solved more realistically and accurately in comparison to the corresponding fiber network representation. The fluid solver is based on a stabilized equal-order finite element formulation applicable to problems involving moving boundaries; see Hughes et al. (1986) and Tezduyar (1992, 2001). This stabilized formulation prevents numerical oscillations without introducing excessive numerical dissipation. Moreover, in the proposed IFEM, the background fluid mesh does not have to follow the motion of the flexible fluid–structure interfaces and thus it is possible to assign a sufficiently refined fluid mesh within the region around the immersed, moving, deformable structure.

Unlike the Dirac delta functions in the IB method, which yield C^1 continuity, Peskin (2002) and Wang (2003), the discretized delta function in IFEM is the C^n shape function often employed in the meshfree reproducing kernel particle method (RKPM); see Li and Liu (2004), Li and Liu (2002b) and Liu et al. (1996a, 1995). Because of the higher-order smoothness of the RKPM delta function, the accuracy is increased in the coupling procedures between fluid and solid domains (Wang and Liu 2004). Furthermore, the RKPM shape function is also capable of handling nonuniform fluid grids.

The outline of this chapter is as follows. We first give a review of the IFEM formulations and algorithm in Section 10.2. Application of IFEM to the modeling of human blood circulation systems is given in Section 10.3, where a heart model, angioplasty stent deployment, monocyte and platelet deposition, and RBC aggregation problems are studied. Furthermore, the IFEM is combined with electrokinetics to study the mechanisms of nano/bio-filament assembly for the understanding of cell motility (Sections 10.4–10.6). In Section 10.7, we summarize the IFEM concept, its attributes and future applications.

10.2 Immersed Finite Element Method

The IFEM was recently developed by Zhang et al. (2004) to solve complex fluid and deformable structure interaction problems. In this section, we overview the basic formulation and algorithmic aspects of this method. For further details, the interested readers are referred to the original work.

10.2.1 Formulation

Consider an incompressible three-dimensional deformable structure in Ω^s completely immersed in an incompressible fluid domain Ω^f . Together, the fluid and the solid occupy a domain Ω , but they do not intersect:

$$\Omega^f \cup \Omega^s = \Omega \quad (10.1a)$$

$$\Omega^f \cap \Omega^s = \emptyset \quad (10.1b)$$

In contrast to the IB formulation, the solid domain can occupy a finite volume in the fluid domain. Since we assume both fluid and solid to be incompressible, the union of two domains can be treated as one incompressible continuum with a continuous velocity field. In the computation, the fluid spans the entire domain Ω , and thus an Eulerian fluid mesh is adopted; a Lagrangian solid mesh is constructed on top of the Eulerian fluid mesh. The coexistence of fluid and solid in Ω^s requires some consideration when developing the momentum and continuity equations.

In the computational fluid domain Ω , the fluid grid is represented by the time-invariant position vector \mathbf{x} , while the material points of the structure in the initial solid domain Ω_0^s and the current solid domain Ω^s are represented by \mathbf{X}^s and $\mathbf{x}^s(\mathbf{X}^s, t)$, respectively. The superscript s is used in the solid variables to distinguish the fluid and solid domains.

In the fluid calculations, the velocity \mathbf{v} and the pressure p are the unknown fluid field variables; the solid domain involves the calculation of the nodal displacement \mathbf{u}^s , which is defined as the difference between the current and initial coordinates: $\mathbf{u}^s = \mathbf{x}^s - \mathbf{X}^s$. The velocity \mathbf{v}^s is the material derivative of the displacement $d\mathbf{u}^s/dt$.

As in Zhang et al. (2004) and Wang and Liu (2004), we define the fluid–structure interaction force within the domain Ω^s as $f_i^{\text{FSI}, s}$, where FSI stands for fluid–structure interaction:

$$f_i^{\text{FSI}, s} = -(\rho^s - \rho^f) \frac{d\mathbf{v}_i}{dt} + \sigma_{ij, j}^s - \sigma_{ij, j}^f + (\rho^s - \rho^f) g_i, \quad \mathbf{x} \in \Omega^s \quad (10.2)$$

Naturally, the interaction force $f_i^{\text{FSI}, s}$ in (10.2) is calculated with the Lagrangian description. Moreover, a Dirac delta function δ is used to distribute the interaction force from the solid domain onto the computational fluid domain:

$$f_i^{\text{FSI}}(\mathbf{x}, t) = \int_{\Omega^s} f_i^{\text{FSI}, s}(\mathbf{X}^s, t) \delta(\mathbf{x} - \mathbf{x}^s(\mathbf{X}^s, t)) d\Omega \quad (10.3)$$

Hence, the governing equation for the fluid can be derived by combining the fluid terms and the interaction force as:

$$\rho^f \frac{d\mathbf{v}_i}{dt} = \sigma_{ij, j}^f + \rho^f g_i + f_i^{\text{FSI}}, \quad \mathbf{x} \in \Omega \quad (10.4)$$

In vector form, this equation gives

$$\rho^f \dot{\mathbf{v}} = \nabla \cdot \boldsymbol{\sigma}^f + \rho^f \mathbf{g} + \mathbf{f}^{\text{FSI}}, \quad \mathbf{x} \in \Omega \quad (10.5)$$

Since we consider the entire domain Ω to be incompressible, we only need to apply the incompressibility constraint once in the entire domain Ω :

$$v_{i,i} = 0 \quad (10.6)$$

In some applications, the interaction between different solid structures immersed in the fluid needs to be taken into account. One example is the interaction between the red blood cells (RBC) that determine important properties of the vascular flow, such as blood clotting and RBC aggregation (Section 10.3). The solid–solid interaction force can be obtained by introducing a sphere with the diameter of a cutoff length, which is used to identify the surface \mathbf{Y}^c of one structure within an influence domain \mathbf{X}^c on the surface of another (neighboring) structure. Then, a typical cell–cell interaction force can be written as

$$\mathbf{F}^c(\mathbf{X}^c) = - \int_{\Gamma(\mathbf{Y}^c)} \frac{\partial \phi(r)}{\partial r} \frac{\mathbf{r}}{r} d\Gamma \quad (10.7)$$

where $\mathbf{r} = \mathbf{X}^c - \mathbf{Y}^c$, $r = \|\mathbf{X}^c - \mathbf{Y}^c\|$, and $\Gamma(\mathbf{Y}^c)$ represents the cell surface area within the domain of influence surrounding surface \mathbf{X}^c . The function ϕ is similar to the molecular dynamics pair-wise potentials (Section 2.2.2) and it is usually chosen in the form of a Lennard-Jones (2.60) or Morse (2.63) potential. This force is treated as an additional term to the right-hand side of (10.5).

The interaction force (10.7) is applied on the surface of the structure, so that

$$\sigma_{ij}^s n_j = F_i^c, \quad (10.8)$$

To delineate the Lagrangian description for the solid and the Eulerian description for the fluid, we introduce different velocity field variables v_i^s and v_i to represent the motion of the solid in the domain Ω^s and the fluid within the entire domain Ω . The coupling of both the velocity fields is accomplished with the Dirac delta function:

$$v_i^s(\mathbf{X}^s, t) = \int_{\Omega} v_i(\mathbf{x}, t) \delta(\mathbf{x} - \mathbf{x}^s(\mathbf{X}^s, t)) d\Omega \quad (10.9)$$

Assume that no traction is applied on the fluid boundary, that is,

$$\int_{\Gamma_{h_i}} \delta v_i h_i d\Gamma = 0 \quad (10.10)$$

By applying integration by parts and the divergence theorem, we can get the final weak form (with stabilization terms):

$$\begin{aligned} & \int_{\Omega} (\delta v_i + \tau^m v_k \delta v_{i,k} + \tau^c \delta p_{,i}) [\rho^f (v_{i,t} + v_j v_{i,j}) - f_i^{\text{FSI}}] d\Omega + \int_{\Omega} \delta v_{i,j} \sigma_{ij}^f d\Omega \\ & - \sum_e \int_{\Omega_e} (\tau^m v_k \delta v_{i,k} + \tau^c \delta p_{,i}) \sigma_{ij,j}^f d\Omega + \int_{\Omega} (\delta p + \tau^c \delta v_{i,i}) v_{j,j} d\Omega = 0 \end{aligned} \quad (10.11)$$

The nonlinear systems are solved with the Newton–Raphson method. Moreover, to improve computational efficiency, we also employ the GMRES iterative algorithm and compute the residuals based on matrix-free techniques; see Saad and Schultz (1986) and Zhang et al. (2002).

The transformation of the weak form from the updated Lagrangian to the total Lagrangian description is to change the integration domain from Ω^s to Ω_0^s . Since we are considering an incompressible fluid and a solid, and the Jacobian determinant is 1 in the solid domain, the transformation of the weak form to total Lagrangian description yields

$$\int_{\Omega_0^s} \delta u_i \left[(\rho^s - \rho^f) \ddot{u}_i^s - \frac{\partial P_{ji}}{\partial X_j^s} - (\rho^s - \rho^f) g_i + f_i^{\text{FSI},s} \right] d\Omega_0^s = 0 \quad (10.12)$$

where the first Piola–Kirchhoff stress P_{ij} is defined as $P_{ij} = J F_{ik}^{-1} \sigma_{kj}^s$ and the deformation gradient F_{ij} as $F_{ij} = \partial x_i^s / \partial X_j^s$.

Using integration by parts and the divergence theorem, we can rewrite (10.12) as

$$\begin{aligned} \int_{\Omega_0^s} \delta u_i (\rho^s - \rho^f) \ddot{u}_i^s d\Omega_0^s &+ \int_{\Omega_0^s} \delta u_{i,j} P_{ji} d\Omega_0^s - \int_{\Omega_0^s} \delta u_i (\rho^s - \rho^f) g_i d\Omega_0^s \\ &+ \int_{\Omega_0^s} \delta u_i f_i^{\text{FSI},s} d\Omega_0^s = 0 \end{aligned} \quad (10.13)$$

Note again that the boundary integral terms on the fluid–structure interface for both fluid and solid domains will cancel each other and, for brevity, are not included in the corresponding weak forms.

For structures with large displacements and deformations, the second Piola–Kirchhoff stress S_{ij} and the Green–Lagrangian strain E_{ij} are used in the total Lagrangian formulation:

$$S_{ij} = \frac{\partial W}{\partial E_{ij}} \quad \text{and} \quad E_{ij} = \frac{1}{2}(C_{ij} - \delta_{ij}) \quad (10.14)$$

where the first Piola–Kirchhoff stress P_{ij} can be obtained from the second Piola–Kirchhoff stress as $P_{ij} = S_{ik} F_{jk}$.

Finally, in the interpolation process from the fluid onto the solid grid, the discretized form of (10.9) can be written as

$$v_{iI}^s = \sum_J v_{iJ}(t) \phi_J(\mathbf{x}_J - \mathbf{x}_I^s), \quad \mathbf{x}_J \in \Omega_{\phi I} \quad (10.15)$$

Here, the solid velocity \mathbf{v}_I^s at node I can be calculated by gathering the velocities at fluid nodes within the influence domain $\Omega_{\phi I}$. A dual procedure takes place in the distribution process from the solid onto the fluid grid. The discretized form of (10.3) is expressed as

$$f_{iI}^{\text{FSI}} = \sum_I f_{iI}^{\text{FSI},s}(\mathbf{X}^s, t) \phi_I(\mathbf{x}_J - \mathbf{x}_I^s), \quad \mathbf{x}_I^s \in \Omega_{\phi J} \quad (10.16)$$

By interpolating the fluid velocities onto the solid particles in (10.15), the fluid within the solid domain is bounded to solid material points. This ensures not only that the no-slip boundary condition on the surface of the solid is satisfied but also automatically stops the fluid from penetrating the solid, provided the solid mesh is at least twice as dense as the surrounding fluid mesh. This heuristic criterion is based on numerical evidence and needs further investigation.

Nondeformable solid

For a nondeformable solid structure immersed in the liquid domain, the system of equations (10.2) and (10.4) becomes incomplete, since $\sigma_{ij}^s = 0$. The additional *kinematic constraints* are then applied to the velocity vector:

$$\mathbf{v}^s = \mathbf{V}^s + \boldsymbol{\omega}^s \times \mathbf{r}^s \quad (10.17)$$

where \mathbf{V} is the velocity of the structure's center of mass,

$$\mathbf{V}^s = \frac{1}{m^s} \int_{\Omega^s} \rho^s \mathbf{v}^s d\Omega \quad (10.18)$$

and $\boldsymbol{\omega}$ is the angular velocity vector,

$$\boldsymbol{\omega}^s = \frac{1}{I^s} \int_{\Omega^s} \rho^s \mathbf{r}^s \times (\mathbf{v}^s - \mathbf{V}^s) d\Omega \quad (10.19)$$

Here, \mathbf{r}^s is the coordinate of a material point with respect to the center of mass; m_s and I^s are the mass and moment of inertia of the structure.

10.2.2 Computational Algorithm of IFEM

The governing equations of IFEM in discretized form (except the Navier–Stokes equations, for convenience) are summarized to give

$$f_{iI}^{\text{FSI},s} = -f_{iI}^{\text{inert}} - f_{iI}^{\text{int}} + f_{iI}^{\text{ext}}, \quad \text{in } \Omega^s \quad (10.20a)$$

$$f_{iJ}^{\text{FSI}} = \sum_I f_{iI}^{\text{FSI},s}(\mathbf{X}^s, t) \phi_I(\mathbf{x}_J - \mathbf{x}_I^s), \quad \mathbf{x}_I^s \in \Omega_{\phi J} \quad (10.20b)$$

$$\rho^f(v_{i,t} + v_j v_{i,j}) = \sigma_{ij,j} + \rho g_i + f_i^{\text{FSI}}, \quad \text{in } \Omega \quad (10.20c)$$

$$v_{j,j} = 0, \quad \text{in } \Omega \quad (10.20d)$$

$$v_{iI}^s = \sum_J v_{iJ}(t) \phi_J(\mathbf{x}_J - \mathbf{x}_I^s), \quad \mathbf{x}_J \in \Omega_{\phi I} \quad (10.20e)$$

An outline of IFEM algorithm with a semiexplicit time integration is illustrated below:

- (i) Given the structure configuration $\mathbf{x}^{s,n}$ and the fluid velocity \mathbf{v}^n at time step n ,
- (ii) evaluate the nodal interaction forces $\mathbf{f}^{\text{FSI},s,n}$ for solid material points, using (10.20a),
- (iii) distribute the material nodal force onto the fluid mesh, from $\mathbf{f}^{\text{FSI},s,n}$ to $\mathbf{f}^{\text{FSI},n}$, using the delta function as in (10.20b),
- (iv) solve for the fluid velocities \mathbf{v}^{n+1} and the pressure p^{n+1} implicitly using (10.20c) and (10.20d),
- (v) interpolate the velocities in the fluid domain onto the material points, that is, from \mathbf{v}^{n+1} to $\mathbf{v}^{s,n+1}$ as in (10.20e) and
- (vi) update the positions of the structure using $\mathbf{u}^{s,n+1} = \mathbf{v}^{s,n+1} \Delta t$ and go back to step 1.

Note that even though the fluid is solved fully implicitly, the coupling between fluid and solid is explicit. If we rewrite the fluid momentum equation (for clarity, only discretized in time), we have

$$\rho^f \left[\frac{v_i^{m+1} - v_i^m}{\Delta t} + v_j^{m+1} v_{i,j}^{m+1} \right] = \sigma_{ij,j}^{f,m+1} + \rho^f g_i + f_i^{\text{FSI},m} \quad (10.21)$$

It is clear that the interaction force is not updated during the iteration, that is, the solid equations are calculated with values from the previous time step. For a fully implicit coupling, this force must be a function of the current fluid velocity and the term $f_i^{\text{FSI},m+1}$ should be included in the linearization of the fluid equations.

10.3 Vascular Flow and Blood Rheology

There are various scales involved in a biological system (Fung 1996). Plate 1 depicts the multiple scale phenomena in the cardiovascular system to which researchers are applying multiscale and multiphysics analysis. Here, the objective is to predict blood flow, its effect on blood vessels and in turn the effect on the blood cells, which are interrelated. The far left subfigure shows a model of the heart, which includes interaction with blood flow. The next bar to the right shows models of the blood vessels, where the properties of the vessel wall and thrombus deposition on the wall are the interactions of interest. The third scale is the cellular scale, where blood components such as RBCs, white blood cells (WBCs), and platelets, as well as their interactions, are considered. The next two scales are the subcellular and molecular scales. Efforts at modeling these scales are focused on understanding how a cell migrates. Modeling the mechanics of the cell is one of the major challenges of the next few decades. A model of cell motility (migration) can provide the information for possible treatments such as the obstruction of cancer metastasis and an understanding of critical cell functions such as neuronal development and embryonic morphogenesis.

The ultimate goal of the three-dimensional (3D) multiple scale modeling is to better understand biological phenomena that span the five scales depicted in Plate 1 on page 6. The multiscale/multiphysics modeling will help understand diseases, such as vascular atherosclerosis, a disease that affects a large portion of the elderly population. They can also potentially be used to design surgical corrective procedures, such as angioplasty. The measurements of traction forces and the simultaneous imaging of the fibrous structure of the cell provide critical input to the simulation of cell motility; recent successes in cell migration modeling and experimentation will be outlined in Section 10.6.

Sections 10.3.1–10.3.6 summarize the application of the IFEM to the various scales of the human blood circulation system, from the macroscopic organ level to the molecular level.

10.3.1 Heart Model

Within the multiscale modeling, the heart and its associated arteries, veins, valves and blood represent the largest scale at which continuum solid and fluid mechanics can be considered. At the macroscopic scale, the heart is modeled as an elastic body. A tetrahedral heart mesh was constructed from volumetric data using an extended dual contouring method (Liu et al.

2004b), where the inlet/outlet meshes of the heart were extended to the surface of the surrounding fluid domain in order to apply pressure boundary conditions periodic in time. The heart model includes essential features such as the aorta, pulmonary artery, inferior vena cava, superior vena cava, pulmonary vein, four chambers (left/right atriums and ventricles), heart valves (tricuspid valve, pulmonary valve, aortic valve, and left ventricle valve) and muscles. Plate 10(a) shows the heart mesh with extended vessels immersed in the fluid mesh. Plate 10(b) shows an aortic valve. The dynamic process of heartbeats and the blood flow pattern inside the heart can be modeled through IFEM.

10.3.2 Flexible Valve–Viscous Fluid Interaction

In order to validate the IFEM, results from a simple flexible valve–viscous fluid interaction analysis are compared with experiments performed recently at ABIOMED, a leading manufacturer of artificial hearts. In these experiments, water was pulsed through a column with a square cross section (5×5 cm) at a frequency of 1 Hz. A rubber sheet was located inside this column. Results of the simulation depicted in Figure 10.1 reveal excellent correlation between experimental observations of structural displacement and the numerical modeling.

10.3.3 Angioplasty Stent

Coronary stents physically open the channel of arterial segments that are constricted by fatty deposits or calcium accumulations. During stenting, the internal balloon deploys the stent; the balloon is kept inflated for 30 s and then deflated. At the end of the process, the expanded stent is embedded into the wall of the diseased artery and holds it open. The objective of our research is to study the mechanical behavior of angioplasty stents during implantation using the fluid–structure interaction computational technique. The deployment of a balloon-expandable stent has been simulated using the IFEM; see Gay et al. (2004).

Using this method, we model a stainless steel stent in a blood vessel. A balloon is deployed to assist the expansion of the stent that is to be plastically deformed. A balloon

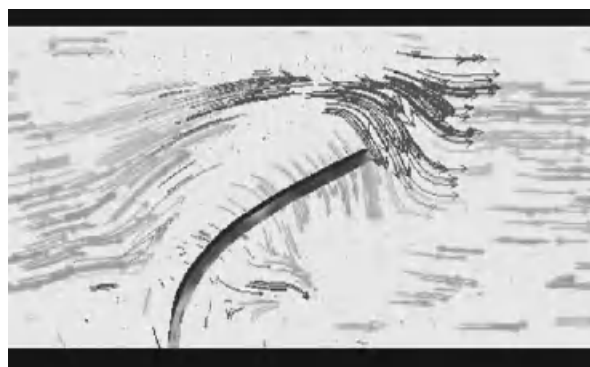


Figure 10.1 Simulation result of a rubber sheet deflecting in a column of water. Pulsatile flow through the column (square cross section) is from left to right at a frequency of 1 Hz. Velocity vectors and beam stress concentration can be seen in the simulation.

is designed in its initial undeformed configuration with deflated tips at the two ends. The balloons used for stenting are made of a very stiff polyamide (nylon) material, which is modeled as a hyperelastic material in the simulation. A stent is a cylindrical, symmetrical assembly of interconnected diamond-shaped members. Our studies focus on the Medtronic AVE Modular stents S7. Each of the 16 structural members has a length of 8 mm. The cross section of the wire has a width of 0.08 mm before expansion. Stents are made from materials like stainless steel 316L, which can be plastically deformed through the inflation of a balloon. Finally, the stent is mounted around the balloon as shown in Figure 10.2.

The expansion mechanism is modeled as uniform radial internal pressure. This pressure difference is applied from the centerline toward the outer diameter of the balloon and the artery wall and is an intrinsic property of the balloon and stent. Figure 10.3 shows the deployment of the stent through the expansion of the balloon at different time steps.



Figure 10.2 Design of the catheter, balloon and stent before inflation. Reprinted from Computer Methods in Applied Mechanics and Engineering, Gay M , Zhang LT and Liu WK, Angioplasty stent modeling using immersed finite element method, 2005, with permission from Elsevier.



Figure 10.3 Deployment of the stent through the inflation of the balloon at different time steps. Reprinted from Computer Methods in Applied Mechanics and Engineering, Gay M , Zhang LT and Liu WK, Angioplasty stent modeling using immersed finite element method, 2005, with permission from Elsevier.

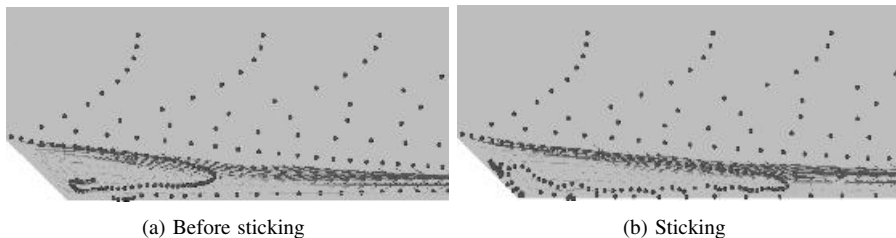


Figure 10.4 Simulation of monocyte deposition in idealized blood vessel.

During the deployment, the diameter of the stent increases from 1.64 to 2.82 mm. As expected, the stent deforms uniformly in its radial direction and expands to 1.7 times its initial diameter for our given material.

By using the IFEM method, we were able to study the flow pattern during the deployment of a stent, its deformation and stress distribution. The results show that this computational method provides a useful tool for future stent designs.

10.3.4 Monocyte Deposition

Figure 10.4 illustrates some preliminary results of a study of the deposition of monocytes (WBCs) near the expansion of a large blood vessel, a condition that may be the result of a poorly matched vascular graft. The vessel sections upstream of the graft may differ in size, creating a geometry similar to a diverging duct. This geometry results in a classical flow recirculation region into which particles suspended in the bulk fluid may become entrained. This recirculation region allows the cells to approach and deposit on the vessel wall owing to the interaction of the proteins present on the monocyte surface and endothelium. We use tools previously developed in Liu et al. (2004e) to model the interactions of monocytes suspended in a fluid, extended to include cell-vessel wall attraction/repulsion via a similar potential approach. The eventual goal of the study is the development of a predictive tool that would be of use during the design and evaluation of engineered grafts, stents, and so on, and to provide a model beyond the typical continuum formulation with a growth prediction model.

10.3.5 Platelet Adhesion and Blood Clotting

The repair of capillary blood vessels and the mediation of hemostasis involves the adhesion and aggregation of platelets to certain portions of the vessel wall. Platelets are initially nonadhesive; however, if in contact with the adhesive wounded region of the vessel wall or activated by the above threshold concentration of ADP (adenosine diphosphate), platelets will become adhesive, glue together, and eventually form aggregates to block the blood flow. Such aggregation processes were first studied mathematically by Fogelson (1985) and Wang and Fogelson (1999). Here, we use a simplified model to demonstrate the capabilities of our proposed IFEM method.

Using the IFEM formulation, we study a simple case of blood flow through a capillary vessel, where the middle quarter of the vessel is designated as injured and capable of activating platelets. The capillary vessel has a diameter of 50 μm and a length of 100 μm .

The adhesion between the platelet and the injured vessel wall is described by an attractive force combined with an elastic link, which provides the resistance of the platelet to shear after bonding to the blood vessel. The activation of the platelet is described by dynamically updating the array that stores information for the activated platelet. Owing to the small scale of the platelet (the diameter is around 2 μm), it is treated as a rigid particle immersed in plasma. The density of the platelet is very close to that of the plasma; thus, $\rho_s = \rho_f$.

Using the method described above, we modeled the platelet aggregation process. The potential energy of interaction between activated platelets, ϕ_{pp} , is chosen to be a Lennard-Jones type potential, (2.60), where r is the distance between two platelets. Also, a spring potential is used to model interactions between platelets and the injured wall with a spring constant k and equilibrium length λ , so that $\phi_{pw}(r) = k(r - \lambda)^2/2$. The total potential energy function is $\phi = \phi_{pp} + \phi_{pw}$, which is utilized for the computation of solid-solid interaction forces \mathbf{F}^c , using the relationship (10.7). These are integrated into the IFEM formulation as extra terms to the vector \mathbf{f}^{FSI} in (10.5).

The simulation results are shown in Figure 10.5 (simulation time is normalized to the time when steady state flow is reached). At $t = 0.0$, the initial stage, the platelets are positioned uniformly. A pseudoperiodic boundary condition is used where the platelets that leave the right boundary will reenter the left boundary in a random position. At $t = 0.33$, the first layer of platelets form bonds with the injured vessel wall and become activated as well. More platelets stick to either activated platelets or the injured vessel wall. At $t = 0.66$, an aggregate of platelets is formed and accumulates, and at $t = 1.0$, a steady form of platelet clot is formed.

It should be noticed that RBCs are not included in this model. Actually, RBCs also play an important role in blood clotting: RBCs' dense packing and tumbling will push

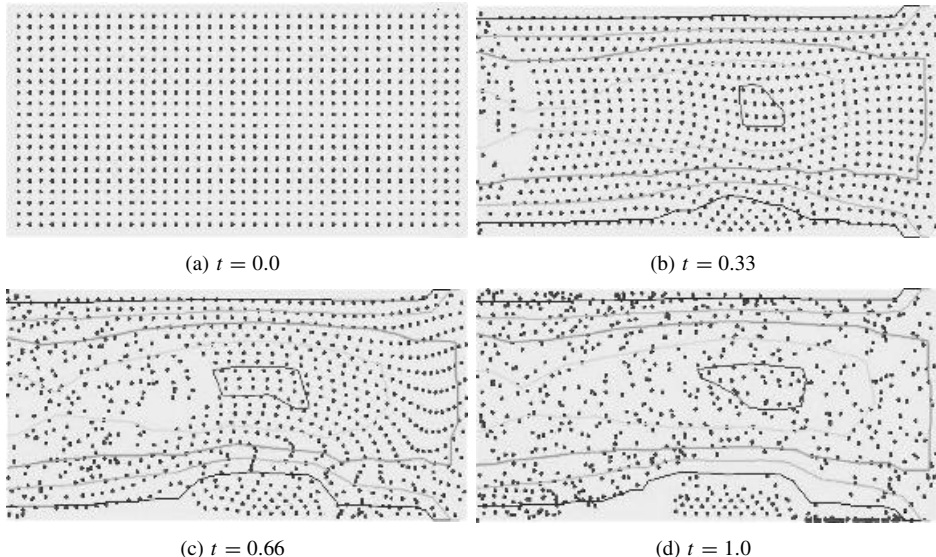


Figure 10.5 Preliminary result of platelets' adhesion and aggregation simulation. The streamline of the flow is plotted.

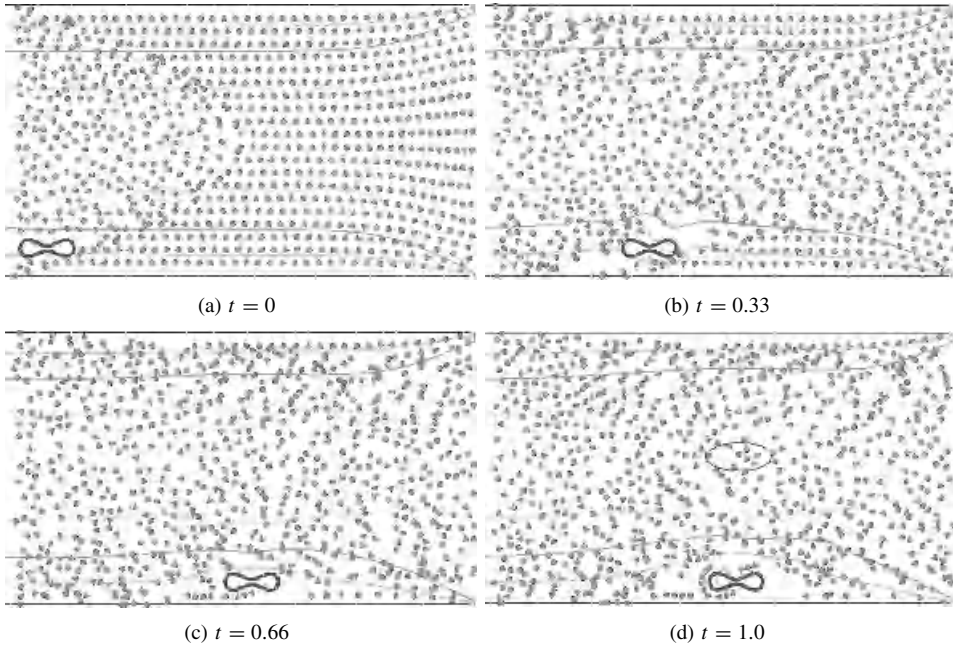


Figure 10.6 Preliminary result of platelet adhesion in blood flow.

platelets to be in contact with the injured vessel wall, thus accelerating the aggregation process. Secondly, with its large size compared to a platelet, RBC can block the blood flow more efficiently. The coexistence of the RBCs and platelets can be easily achieved in our model. The interaction between activated platelets and RBCs is simplified into a spring model and the RBCs are assumed to be rigid. Our preliminary results are shown in Figure 10.6. It can be observed that platelets adhere and cover the RBCs' surface. The collisions between the RBCs and platelets push platelets toward the wound site, and thus help platelets to adhere. In the future, the RBC–RBC interaction, RBC–platelet interaction, and platelet–platelet interaction can be combined in a uniform way for the description of the blood-clotting and wound-healing process.

10.3.6 RBC Aggregation and Interaction

The human blood circulatory system has evolved to supply nutrients and oxygen to, and carry the waste away from, the cells of multicellular organisms through the transport of blood, a complex fluid composed of deformable cells, proteins, platelets and plasma. Overviews of recent numerical procedures for the modeling of macroscale cardiovascular flows are available in Taylor et al. (1998). While theories of suspension rheology generally focus on homogeneous flows in infinite domains, the important phenomena of blood flows in microcirculation depend on the combined effects of vessel geometry, cell deformability, wall compliance, flow shear rates, and many microscale chemical, physiological and biological factors; see Diamond (2001). There have been studies in the past on shear flow effects on one or two cells, leukocyte adhesion to vascular endothelium, and particulate flow based

on continuum enrichment methods; Wagner et al. (2001). However, no mature theory is yet available for the prediction of blood rheology and blood perfusion through microvessels and capillary networks. The different time and length scales as well as large displacements and deformation of immersed solids pose tremendous challenges to the mathematical modeling of blood flow at that level.

In this section, we present simulations of biological fluid flow problems with deformable cells using a newly developed modeling technique by Liu et al. (2004e) with a combination of the IFEM of Zhang et al. (2004) and protein molecular dynamics. The effects of cell-cell interaction (adhesive/repulsive) and hydrodynamic forces on RBC aggregates are studied by introducing equivalent protein molecular potentials into the IFEM. For a detailed description of the IFEM coupled with cell interactions, and its applications to hemodynamics, we refer the reader to Liu et al. (2004e). Here, we concentrate on the rheological aspects of flow systems of arterioles, capillaries and venules, which involve deformable cells, cell-cell interactions and various vessels. The demonstrated problems are shear of a cluster of deformable RBCs, normal and sickle RBCs passing through capillary vessels, and finally a single cell squeezing through a microvessel constriction.

Discrete RBC model

The RBC is modeled as a flexible membrane enclosing an incompressible fluid. As shown in Plate 11, to account for both bending and membrane rigidities, the RBC membrane is modeled with a three-dimensional finite element formulation using a Lagrangian description. In this work, a typical membrane is discretized with 1043 nodes and 4567 elements. The static shape of a normal RBC is a biconcave discoid. The material behavior of the RBC membrane is depicted by a Neo-Hookean strain energy function.

RBC aggregation

Cell-cell adhesion plays an important role in various physiological phenomena including the recognition of foreign cells. Although the exact physiological mechanisms of RBC coagulation and aggregation are still ambiguous, it has been found that both the RBC surface structure and membrane proteins are key factors in producing adhesive/repulsive forces. The proposed explanations in general fall into two categories: the bridging and adsorption models with adsorption and exclusion of the plasmatic macromolecules at surfaces of the RBCs, respectively. The primary macromolecules that cause RBC aggregation are fibrinogens. The depletion layer results in a reduction of osmotic pressure in the gap between nearby RBCs, which consequently produces an attractive force. The repulsive forces include steric forces due to the glycocalyx and the electrostatic repulsive force induced from the same negative fixed charges at RBC surfaces.

Recently, Neu and Meiselman (2002) proposed a theoretical model for depletion-mediated aggregation of RBCs in polymer solutions. The basic behavior of the interaction forces between two RBCs is simply illustrated as the weak attractive and strong repulsive forces at far and near distances. Owing to the complexity of the aggregation process, we accumulate the intermolecular force, electrostatic force, and protein dynamics into a potential function, similar to an interatomic potential. Here, we adopt the Morse potential (2.63), found to be capable of generating a similar interaction energy versus RBC-RBC separation distance dependence as the one given in Neu and Meiselman (2002). The Morse potential is

plotted in Figure 2.6(b), page 23. As will be seen later, the aggregation behavior simulated by this potential qualitatively agrees with experimental observations.

The interaction force between neighboring RBCs is evaluated in accordance with (10.7), where the function ϕ is replaced by the Morse potential.

Blood viscoelasticity

Blood plasma can be accurately modeled with a Newtonian fluid model, yet blood flows do exhibit non-Newtonian or viscoelastic behavior, in particular, at low Reynolds numbers. In a typical blood viscoelasticity test, as the shear rate increases, the blood viscosity decreases initially and eventually reaches a plateau marking the plasma viscosity, and the blood elasticity continues to decrease.

On the microscopic level, RBCs play an important role in the viscoelastic behavior of blood; see Fung (1996). In the quiescent state, normal RBCs tend to aggregate. Under low shear rates, aggregates are mainly influenced by cell-cell interaction forces; in the mid-shear-rate region, RBC aggregates start to disintegrate and the influence of the deformability gradually increases, and under high shear rates, RBCs tend to stretch, align with the flow and form layers. The illustration of these three different stages is provided in Figure 10.7.

Cell interaction and shear-rate effects

Aggregation of RBCs is one of the main causes of the non-Newtonian behavior of blood flows. Owing to the presence of the cross-linking proteins fibrinogen on cell membranes and

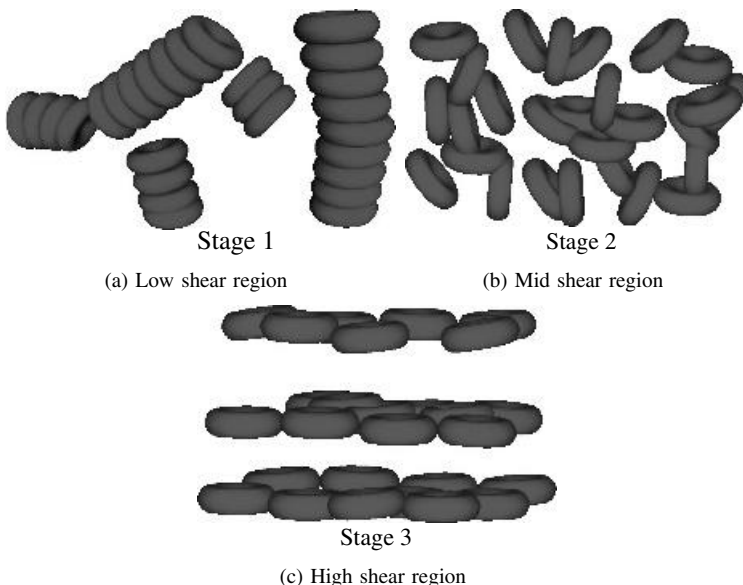


Figure 10.7 Blood microscopic changes under different shear rates. Reproduced with permission from Liu Y et al., International Journal for Numerical Methods in Fluids, published by John Wiley and Sons Ltd, 2004.

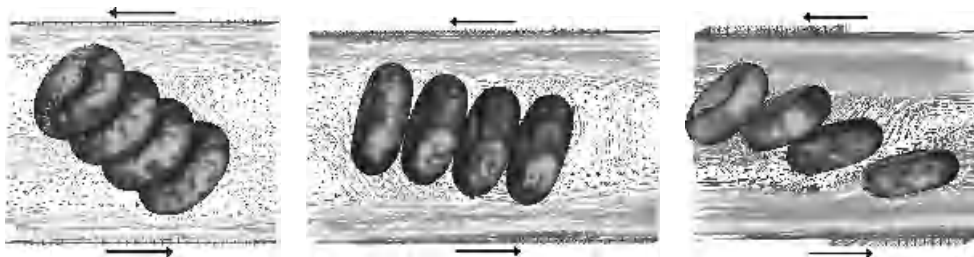


Figure 10.8 The shear of a four-RBC cluster at shear rates of 0.25 , 0.5 and 3.0 s^{-1} respectively. The vectors represent the fluid velocity field.

globulin in the plasma, RBCs tend to form aggregates called *rouleaus*, in which the cells adhere loosely like a stack of coins. The presence of massive rouleaus can impair blood flow through micro- and capillary vessels and cause fatigue and shortness of breath. The variation in the level of RBC aggregation may be an indication of thrombotic disease. In general, cell-cell interaction forces are not sufficient to deform cell membranes. However, the ensuing aggregate could alter the surrounding fluid significantly.

In a set of numerical experiments, we subject the RBC aggregate to low shear rates and observe that the aggregate of RBCs rotates as a bulk, as shown in Figure 10.8. With an intermediate shear rate, our numerical simulation demonstrates that after the initial rotations the RBC aggregate aligns with the shear direction and then disaggregates. At higher shear rates, the RBC aggregate completely disintegrates and the cells begin to orient themselves into parallel layers. The disintegration of RBC aggregates with the increase in the shear rate is an indication of the decrease of the macroscopic viscosity, which is consistent with experimental observations.

Shear-rate-dependent viscosity

The effective viscosity of the blood is calculated from our simulation by measuring the shear force exerted by the plasma onto the shear velocity boundary. A shear velocity of $-U_0$ and $+U_0$ is applied on the top and bottom boundaries respectively. The fluid domain has a height of $2H$ and a length of L . Periodic boundary conditions are used for the left and right boundaries (i.e. the RBCs nodes that move out of the left boundary reenter through the right boundary).

Without suspended RBCs, the flow velocity in the x -direction is given by $u = U_0y/H$ and the shear force on the top and bottom walls are given by $F = \mu LU_0/H$. With suspended RBCs, the effective viscosity of the blood is defined as:

$$\mu_{\text{eff}} = \frac{HF}{LU_0} \quad (10.22)$$

The effective viscosities of the blood at shear rates between 0.125 s^{-1} and 24 s^{-1} are plotted in Figure 10.9. There is a large drop in the viscosity between the shear rates of 0.5 s^{-1} and 3.0 s^{-1} , indicating the dispersion of RBC rouleaus. The effective viscosity changes very slowly for shear rates below 0.125 or above 24 s^{-1} , indicating the massive aggregation of RBCs and partial parallel dispersion of RBCs, respectively. For a precise

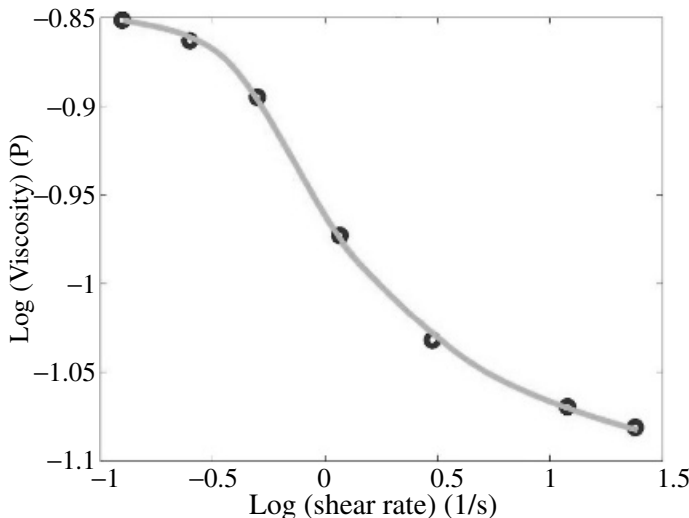


Figure 10.9 The calculated effective viscosities of the blood at different shear rates.

comparison to the experimental results, more RBCs have to be used in the simulation, which is too computationally expensive at the current stage. However, to our knowledge, this is the first attempt that links the microscopic mechanism of RBC aggregation to the macroscopic blood viscosity.

Micro- and capillary vessels

RBCs are important for blood flows in microcirculation. The typical diameter of a microvesSEL is $1.5 \sim 3$ times larger than that of a cell. On the other hand, a capillary vessel's diameter is about $2 \sim 4 \mu\text{m}$, which is significantly smaller. The pressure gradient that drives the flow is usually around $3.2 \sim 3.5 \text{ KPa}$. For the chosen diameter and pressure, the Reynolds number in a typical capillary is around 0.01. In fact, in the process of squeezing through capillaries, large deformations of RBCs not only slow down the blood flow but also enable the exchange of oxygen through capillary vessel walls.

Sickle-cell anemia occurs because of genetic abnormalities in hemoglobin. When sickle hemoglobin loses oxygen, the deoxygenated molecules form rigid rods, which distort the cell membrane into a sickle or crescent shape. The sickle-shaped cells are both rigid and sticky and tend to block capillary vessels and cause blood flow blockage to the surrounding tissues and organs. To relate blood rheology to sickle-cell anemia, we consider the normal and sickle RBCs passing through a microvessel contraction. The strong viscous shear introduced by such a flow contraction leads to some interesting phenomena of the RBC aggregation with respect to cell–cell interaction forces and cell deformability. Furthermore, the modeling of this complex fluid–solid system also demonstrates the capability of coupling the Navier–Stokes equations with protein molecular dynamics.

As shown in Figure 10.10, as RBCs pass the diffuser stage of the contraction, the deceleration of the RBCs forms a blockage for the incoming cells. Therefore, dilation of

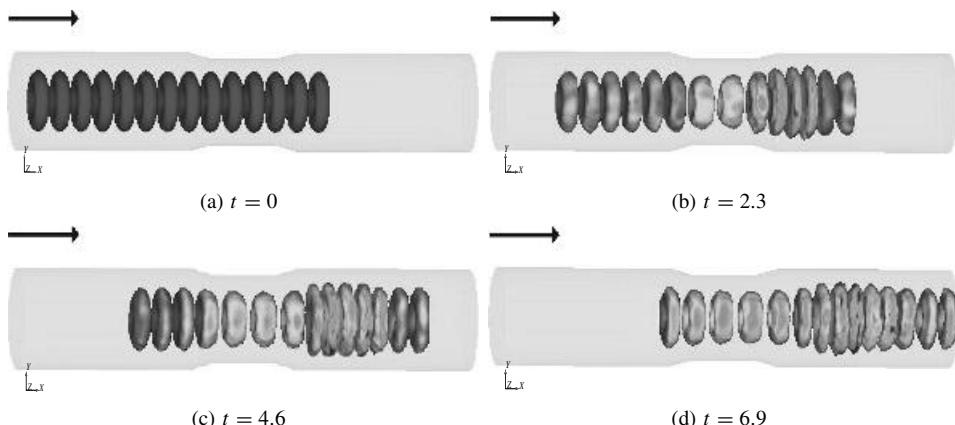


Figure 10.10 Normal red blood cell flow for an inlet velocity of $10 \mu\text{m s}^{-1}$ at different time steps. Reproduced with permission from Liu Y et al., International Journal for Numerical Methods in Fluids, published by John Wiley and Sons Ltd, 2004.

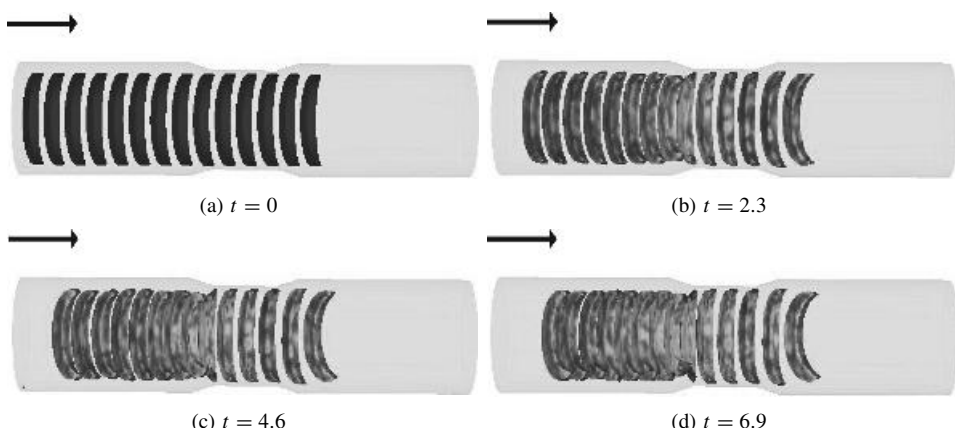


Figure 10.11 Sickle-cell flow for an inlet velocity $10 \mu\text{m s}^{-1}$ at different time steps. Reproduced with permission from Liu Y et al., International Journal for Numerical Methods in Fluids, published by John Wiley and Sons Ltd, 2004.

RBCs is coupled with the pileup of RBCs at the outlet of the vessel constriction. As seen in Figure 10.11, under similar flow conditions, rigid and sticky sickle cells eventually block the microvessel entrance, which will certainly result in deoxygenation of surrounding tissues.

To demonstrate the effect of vessel constriction more clearly, we accomplish a three-dimensional simulation of a single RBC squeezing through a capillary vessel. The RBC's diameter is 1.2 times larger than that of the capillary vessel, which leads to the divergence of the cytoplasm (internal liquid) to the two ends of the capsule by deforming into a slug during the squeezing process. During the exiting process, there is a radial expansion of the slug owing to the convergence of the cytoplasm, which deforms the capsule into an

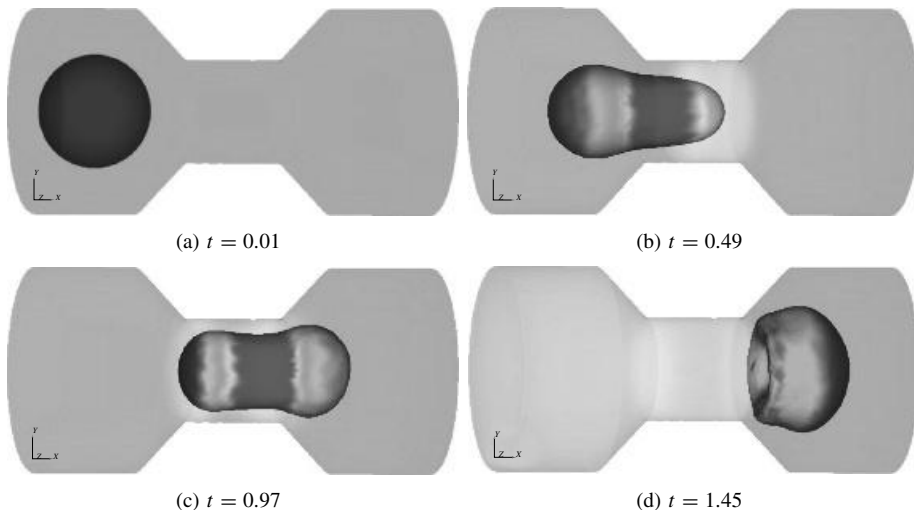


Figure 10.12 Three-dimensional simulation of a single red blood cell (essentially a hollow sphere for simplicity) squeezing through a capillary vessel. Reprinted from Computer Methods in Applied Mechanics and Engineering, 193(17–20), Liu et al., An introduction to computational nano mechanics and materials, 1529–1578, 2004, with permission from Elsevier.

acaleph (or jellyfish) shape. In Figure 10.12, four snapshots illustrate various stages of the RBC with respect to the capillary vessel. The pressure drop within the capillary vessel is also presented in Figure 10.13. The driving pressure here is defined as the average pressure difference between the inlet and outlet of the flow. The driving pressure reaches maximum level, once the flow is plugged by the deformable cell. This corresponds to the period of time when the cell is moving inside the narrow part of the capillary vessel. The increase in pressure for the cell to squeeze through a capillary with a diameter smaller than its size directly leads to an increase in blood's apparent viscosity, a phenomenon called the *reverse Fahraeus–Lindqvist effect*.

10.4 Electrohydrodynamic Coupling

Electric fields are widely used to manipulate biological objects such as cells or biofibers. It is important to incorporate the electric field into the fluid–structure interaction problem, thus solving an electrohydrodynamic problem. A typical electrohydrodynamic problem involves three components: the liquid domain, the solid structure immersed in the liquid and an external electrostatic field. The structure is responsive to the electric field due to induction of an electric dipole moment. The liquid remains electrically neutral and does not respond to the electric field. In this section, we discuss electrohydrodynamic coupling that utilizes the IFEM formulation of Section 10.2.

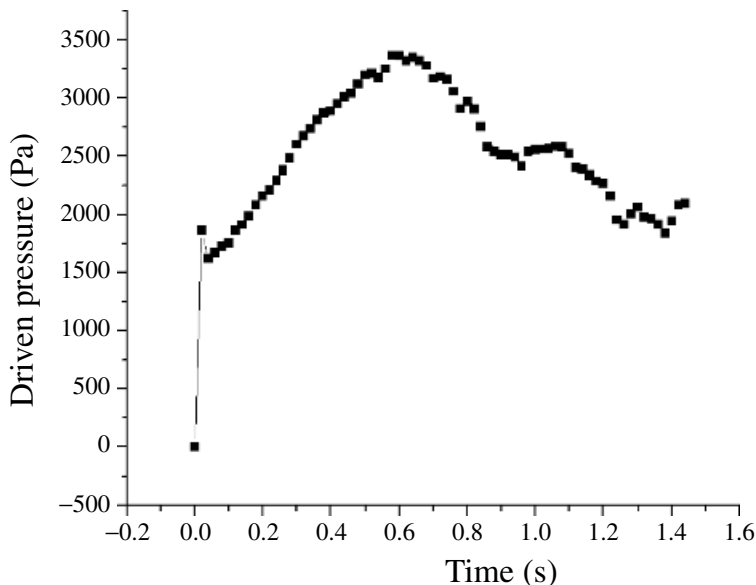


Figure 10.13 The history of the driven pressure during the squeezing process. Reprinted from Computer Methods in Applied Mechanics and Engineering, 193(17–20), Liu et al., An introduction to computational nano mechanics and materials, 1529–1578, 2004, with permission from Elsevier.

10.4.1 Maxwell Equations

The electrostatic field in a continuous media or structure is governed by a system of time-independent *Maxwell equations* that can be written in the differential form,

$$\begin{aligned} \nabla \times \mathbf{E} &= 0 \\ \nabla \cdot \mathbf{D} &= 4\pi\rho \\ \mathbf{D} &= \mathbf{E} + 4\pi\mathbf{P} \end{aligned} \tag{10.23}$$

or, equivalently, in the integral form,

$$\begin{aligned} \oint \mathbf{E} \cdot d\mathbf{l} &= 0 \\ \oint \mathbf{D} \cdot d\mathbf{S} &= 4\pi Q \\ Q &= \int_V \rho dV \end{aligned} \tag{10.24}$$

Here, the continuum structure occupies physical volume V , and carries distributed charge of density $\rho(r)$; Q is the total volume charge of the structure. The other quantities in the above equations characterize the electric field and charge distributions: vector \mathbf{E} is a

measure of the intensity of the field, \mathbf{D} is the vector of electric displacement, and \mathbf{P} is the polarization vector defined as a dipole moment, $d\mathbf{p}$, of a unit volume,

$$\mathbf{P} = \frac{d\mathbf{p}}{dV} \quad (10.25)$$

In case of a homogeneous isotropic media, one obtains

$$\mathbf{D} = \epsilon \mathbf{E} \quad (10.26)$$

where ϵ is the electric permittivity of the media.

Vector \mathbf{E} is called the *intensity of the electric field*, or *field strength*, and it serves as the force characteristic of the electric field. In particular, for a point charge q , the electrostatic force is given by

$$\mathbf{F} = \mathbf{E}q \quad (10.27)$$

The field strength is determined by the electric potential φ that determines the voltage V_{AB} between two points A and B :

$$\mathbf{E} = -\nabla \varphi, \quad \varphi_A - \varphi_B \equiv V_{AB} = \int_A^B \mathbf{E} \cdot d\mathbf{l} \quad (10.28)$$

The electric potential satisfies the Poisson equation,

$$\nabla^2 \varphi(\mathbf{r}) = -\frac{4\pi}{\epsilon} \rho(\mathbf{r}) \quad (10.29)$$

whose solution is written in the form

$$\varphi(\mathbf{r}) = \frac{1}{\epsilon} \int_V \frac{\rho(\mathbf{r}')}{|\mathbf{r} - \mathbf{r}'|} dV' \quad (10.30)$$

The electric potential $\varphi(\mathbf{r})$ is a special case of the general one-body potential $V_1(\mathbf{r})$ discussed in Section 2.2.1 of this book; see (2.47) on page 18. For simple systems, such as point charge, spherical charge, charged straight line, half-space, and so on, the function $\varphi(\mathbf{r})$ is known in closed form, for example, Benenson et al. (2002).

The vector of electric displacements \mathbf{D} represents the quantity of charge ΔQ per element ΔA displaced by electrostatic induction. The magnitude of this vector is equal to the surface charge density,

$$|\mathbf{D}| = \lim_{\Delta A \rightarrow 0} \frac{\Delta Q}{\Delta A} = \frac{dQ}{dA} \quad (10.31)$$

The second equation in (10.24) is also called as *Gauss theorem*. This equation is particularly convenient in cases where the symmetry of the system allows evaluation of the surface integral for this equation in closed form. Note that if there is a finite surface S_0 at which the normal vector $d\mathbf{S}$ and vector \mathbf{D} are coplanar, and $|\mathbf{D}| = \text{const}$, then the flux of vector \mathbf{D} through this surface,

$$\oint_{S_0} \mathbf{D} \cdot d\mathbf{S} = D_n S_0 \quad (10.32)$$

In this case, the second equation of the system (10.24) reduces to an algebraic form, allowing a straightforward evaluation of the vector \mathbf{D} .

Table 10.1 Mechanisms of electro-manipulation

Mechanism	Applicable condition
Electrophoresis (EP)	DC or low frequency AC
Dielectrophoresis (DEP)	AC or DC
Electroosmosis flow	DC or low frequency AC
Drag force	Viscous fluid
Brownian motion	Nano/microscale particles

10.4.2 Electro-manipulation

Experimental techniques used for the manipulation of particles and small-scale structures are generally referred to as electro-manipulation, as well as *nanomanipulation*, when associated with directed motion of nanoscale objects.

A general list of factors that can be involved in electro-manipulation and their applicable conditions are summarized in Table 10.1.

Electrophoresis (EP)

The first mechanism of electro-manipulation, *electrophoresis*, is based on directed motion of suspended charged particles in a nonconductive liquid under the action of external electric fields. The driving force of electrophoresis is, in principle, the electrostatic force given by the expression (10.27).

Dielectrophoresis (DEP)

In contrast to electrophoresis, *dielectrophoresis* (DEP) utilizes the movement of *uncharged*, that is, electrically neutral, structures caused by a spatially nonuniform electrical field. The structure becomes polarized when immersed into the electric field. DEP arises only when the structure and the surrounding media, typically, a nonconductive gas or liquid, have different polarizabilities. If the structure is more polarizable compared to the surrounding media, it will be pulled toward regions of stronger field; this effect is called *positive DEP*. Otherwise, the structure is repelled toward regions of weaker field; this is known as *negative DEP*. One commonly known demonstration of positive DEP is the attraction of small pieces of paper to a charged plastic comb or stick. The general concept of positive DEP is illustrated in Figure 10.14.

The driving force of DEP results from a dipole moment induced in the structure, when it is immersed into an electric field. If the electric field is inhomogeneous, the field strength, and thus distribution of the electrostatic force acting on each part of the structure, is not uniform; this leads to a relative motion of the structure in the medium. The force exerted by an electric field \mathbf{E} on a dipole with dipole moment \mathbf{p} is generally given by

$$\mathbf{F}^{\text{dep}} = (\mathbf{p} \cdot \nabla) \mathbf{E} \quad (10.33)$$

A widely used expression for the time-averaged DEP force on a particle is given as (Jones 1995):

$$\langle \mathbf{F}^{\text{dep}} \rangle = \Gamma \cdot \varepsilon_1 \text{Re}\{K_f\} \nabla |\mathbf{E}|^2, \quad (10.34)$$

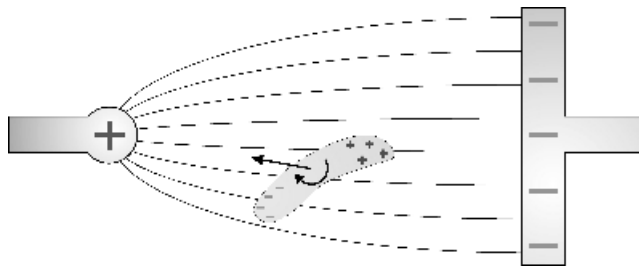


Figure 10.14 Positive dielectrophoresis. Positive and negative charges polarized in the structure are equal. The structure will rotate clockwise and move left, to the area of stronger field.

where Γ is a parameter that depends on the particle shape and size, ε_1 is the real part of the permittivity of the medium and K_f is a factor that depends on the complex permittivities of both the particle and the medium and $\nabla |\mathbf{E}|^2$ is the gradient of the energy density of the electric field. For a sphere with a radius a , $\Gamma = 2\pi a^3$, $K_f = (\varepsilon_2^* - \varepsilon_1^*)/(\varepsilon_2^* + 2\varepsilon_1^*)$ (called the *Clausius-Mossotti factor*). For a cylinder with a diameter r and a length l , $\Gamma = \pi r^2 l / 6$ and $K_f = (\varepsilon_2^* - \varepsilon_1^*)/\varepsilon_1^*$. The frequency dependent complex permittivities shown with the asterisk are expressed by the complex combination of conductivity σ , permittivity ε , and electric field frequency ω as: $\varepsilon_1^* = \varepsilon_1 - j\sigma_1/\omega$, and $\varepsilon_2^* = \varepsilon_2 - j\sigma_2/\omega$, where $j = \sqrt{-1}$, and the indices 1 and 2 refer to the medium and the particle, respectively.

For an arbitrarily shaped solid structure, the DEP force can be computed as a surface or volume integral,

$$\mathbf{F}^{\text{dep}} = \int_{\Gamma} (\sigma^M \cdot \mathbf{n}) dA = \int_{\Omega^S} \nabla \cdot \sigma^M d\Omega \quad (10.35)$$

where σ^M is the Maxwell stress tensor

$$\sigma^M = \varepsilon_1 \mathbf{E} \mathbf{E} - \frac{1}{2} \varepsilon_1 \mathbf{E} \cdot \mathbf{E} \mathbf{I} \quad (10.36)$$

Electroosmotic flow (DEP)

The electroosmotic flow, or electroosmosis, is driven by the electric static force applied onto the charged double layer (Figure 10.15). Electroosmosis flow can be induced by DC electric field or by low frequency AC electric field.

Within the IFEM, electroosmosis is treated as a slip boundary condition for the fluid. Also, since the Debye layer, the layer close to the wall where the velocity is varying, is only of a few nanometers, only the steady velocity is taken into account, (Solomentsev et al. 1997),

$$\mathbf{v} = -\frac{\varepsilon \psi_0 \mathbf{E}}{\mu} \quad (10.37)$$

where ψ_0 is the zeta potential (the electric potential at the slipping plane close to the solid surface), and μ and ε are the viscosity and permittivity of the medium, respectively.

The Brownian force induced by thermal fluctuations will influence the motion of nanoscale particles. The approach described in the work by Sharma and Patankar (2004) on

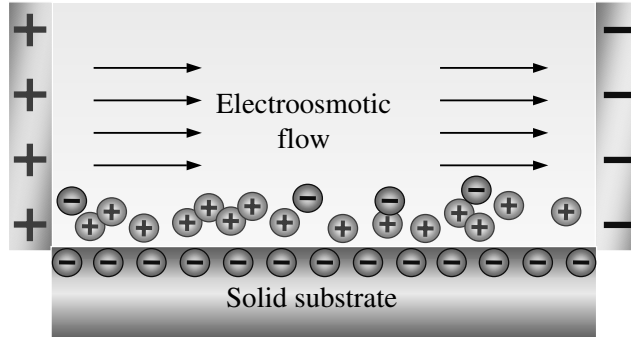


Figure 10.15 Illustration of electroosmosis developed within a channel.

Brownian motion of rigid particles can be used to capture the thermal motion of complex-shaped objects without using approximations for the viscous drag on these objects.

Governing equations

The coupled electrohydrodynamic equation of motion (Liu et al. 2005a) is written in the context of the IFEM formulation by revising (10.2) and (10.4) to give two coupled governing equations: (1) a fluid equation with fluid–structure interaction force and (2) a solid equation.

The fluid equation with fluid–structure interaction takes the form

$$\rho^f \dot{\mathbf{v}} = \nabla \cdot \boldsymbol{\sigma}^f + \mathbf{f}^{\text{FSI}} \quad (10.38)$$

The interaction force, representing the solid equation, reads

$$\mathbf{f}^{\text{FSI}} = -(\rho^s - \rho^f) \dot{\mathbf{v}}^s + \nabla \cdot (\boldsymbol{\sigma}^s - \boldsymbol{\sigma}^f) + \mathbf{F}^{\text{ext}} + \mathbf{F}^e + \mathbf{F}^{\text{dep}} + \mathbf{F}^c \quad (10.39)$$

where \mathbf{F}^{ext} , \mathbf{F}^e , \mathbf{F}^{dep} and \mathbf{F}^c are the external, electrostatic, DEP and solid–solid interaction forces, respectively. The external force is usually the gravity force. Expressions for the electrostatic force and DEP force are given in (10.27) and (10.35). The force of interaction between two charged solid surfaces is evaluated in accordance with (10.7). In this equation, function ϕ is the Coulomb potential (2.57), modified by replacing the point charges with surface charge densities. The other variables have been defined in Section 10.2.1. In this formulation, as well as in applications considered later in this chapter, thermal and Brownian motion effects are ignored.

In this way, the solid, fluid and electrokinetic equations are coupled together. In the current simulations, the electrokinetic equation and solid/fluid motion equation are solved iteratively, that is, a semistatic approach is used. Since the transition time of the electric field is much shorter than the characteristic time of the solid/fluid motion, this iterative approach is reasonable.

10.4.3 Rotation of CNTs Induced by Electroosmotic Flow

In this section, we demonstrate the application of the coupled IFEM electrohydrodynamics formulation to the study of effects of electroosmotic flow on carbon nanotube (CNT) assembly

immersed in ethanol suspension. The velocity boundary condition for this equation is given by (10.37) for the diffusive layer, that is, surface of electrodes, and $\mathbf{v}=0$ at uncharged walls.

The electrostatic force applied to the charged double layer drives the electroosmotic flow. The charge relaxation time of a liquid is defined as $\tau = \epsilon/\sigma$; for ethanol, $\tau \approx 0.01$ s. For the AC potential frequency, such that $f < 1/(2\pi\tau)$, the charge of the electrodes and the double layer alternates according to the change in sign of the potential. The charge experiences an electrostatic force tangential to the surface, which acts on the electric double layer and induces the AC electroosmotic flow. The forces are maximal at the electrode edge and decrease rapidly with the increase in distance from the edge; such nonuniform forces may form a vortex. For the simulation (see Figure 10.16), an AC field of $0.5 \text{ V}/\mu\text{m}$, 100 Hz, was applied on parallel-shaped electrodes with a 5- μm gap. Local electroosmotic flow near the edges of electrodes is found to induce vortexes and lead to the rotation of the nanotubes. The similar rotation of nanotubes has been observed in experiments, Figure 10.17. Note that Figure 10.16 reproduces vortex flow in the bottom view cross section of the experimental snapshots shown in Figure 10.17.

The phenomenon of vortex flow of CNT suspensions induces local circulative flows that transport nanotubes toward gaps; this can improve the orientation of the nanotubes along the e-field direction.

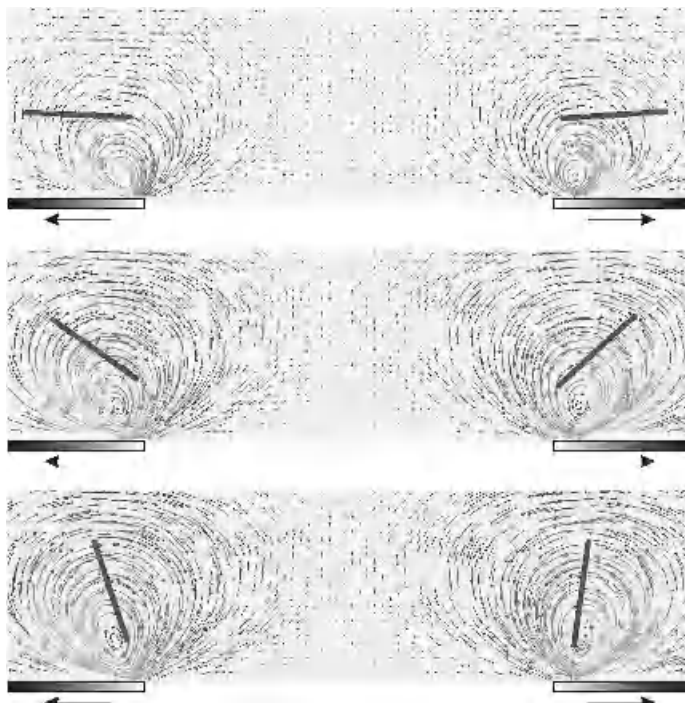


Figure 10.16 Rotation of carbon nanotubes induced by electroosmotic flow; a coupled electrohydrodynamics IFEM simulation. Black arrows show direction of the electroosmotic flow at the surface of the electrodes.

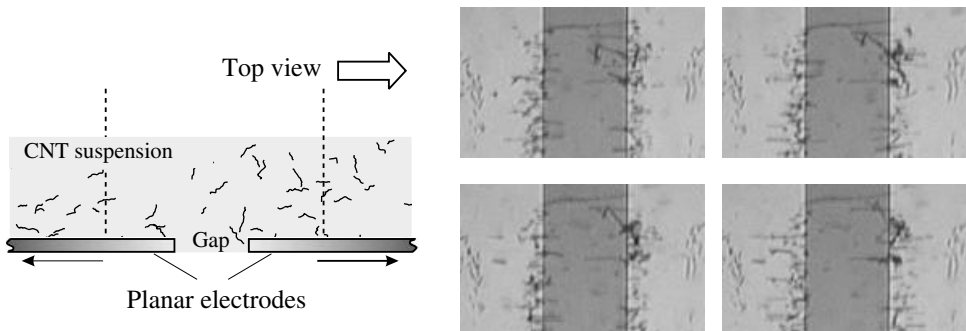


Figure 10.17 Rotation of carbon nanotubes induced by electroosmotic flow. Experimental images on the right are the courtesy of Dr. Jae Chaung, University of Washington.

10.5 CNT/DNA Assembly Simulation

The remaining part of this chapter demonstrates further applications of multiphysics methods for biological and biomedical systems, in particular, the CNT/DNA assembly modeling Liu et al. (2005b), and cell migration problems.

The assembly of nano/bio materials is of great interest and demand since the development of scanning probe microscopes, specifically the atomic force microscope (AFM). Many unique methods have been proposed to immobilize those materials and accomplish an array format. Recently, a more precise assembly method was proposed by Chung et al. (2004, 2002a,b) to assemble multiwalled CNTs and DNAs by combining an AC with a DC electric field. However, its fundamental mechanism was not fully understood because of the complexity of the deposition processes at the nanoscale. The coupled electrohydrodynamic modeling approach described in Section 10.4 is applied below in this citation to the study of the deposition process of nano/bio materials using electric fields.

To model the sorting and assembly of CNTs, the electric fields induced by semicircular electrodes are computed, the DEP force is evaluated and electroosmotic flow governed by the Navier–Stokes equation is calculated with a slip boundary condition, as described in Section 10.4. The dynamic process of the attraction, alignment and deposition of CNTs between microelectrodes is modeled by fully resolving the electrokinetics and fluid dynamics. Our simulations show that a pure AC field can lead to bundles owing to the high electric field gradient near the deposited CNTs. For short CNTs, each CNT cannot bridge across a large gap by itself. Instead, they tend to form bridges by end-to-end linking or form bundles by side-to-side linking (Plate 12). It can be also shown that different electrode geometries can lead to different bundle patterns, Plate 12 that is, parallel bundles for parallel-rectangular-shaped electrodes and cross-linked bundles for semicircular electrodes. For sharp tip-shaped electrodes, a straight bundle (also called *CNT fibril*) can be achieved; see Figure 10.18. The high electric gradient region close to the tip electrode will attract CNT nearby toward the tip. Meanwhile, all CNTs can be attracted toward the central high electric field region between the tip electrodes.

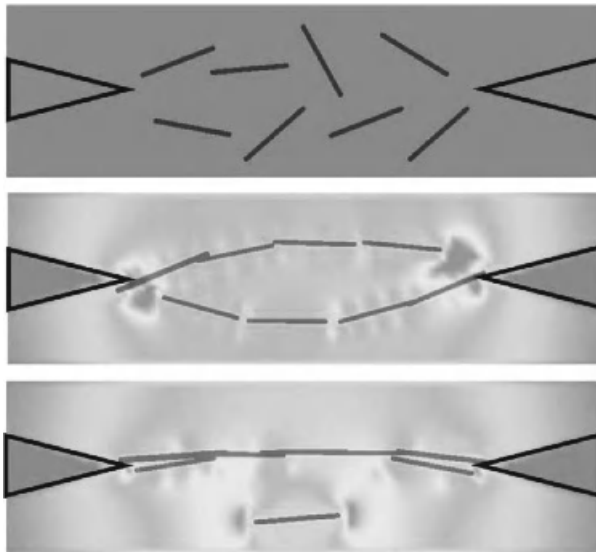
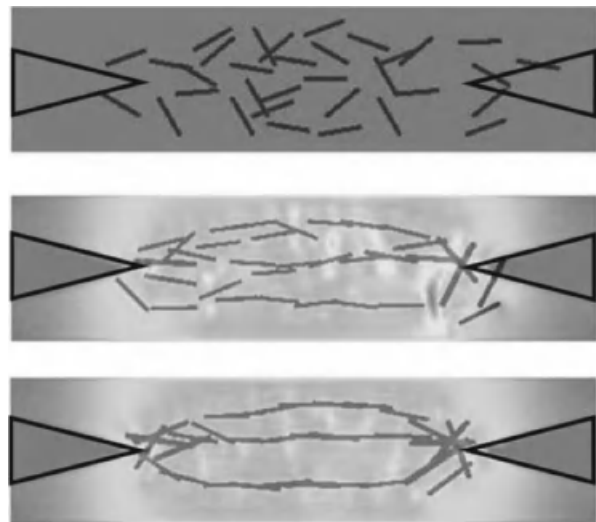
(a) Alignment of $6 \mu\text{m}$ CNTs between tip-shaped electrodes(b) Alignment of $3 \mu\text{m}$ CNTs between tip-shaped electrodes

Figure 10.18 Sequential images of short CNTs line up between sharp-tip electrodes.

In the simulation, a pair of sharp tip-shaped electrodes with a tip angle of 26.6° is located at the two sides of the simulation domain, with a gap size of 10 μm. Owing to the high electric field gradient near the sharp tip and the deposited CNTs, assembly of short CNTs into a fibril between the sharp tips is observed. The fibril assembly is achieved by four sequential processes: alignment of CNTs along the electric field direction by rotation, local bridge formation of CNTs, transport of the CNT bridges toward the center, and full



(a) Assembly pattern of CNTs with a length longer the gap size



(b) Assembly pattern of CNTs with a length close to the gap size



(c) Assembly pattern of CNTs with a length shorter than the gap size

Figure 10.19 Simulation of the assembly of CNTs by the application of an AC field. The three sets of figures correspond to short CNTs, medium CNTs, and long CNTs assembling in AC field between semicircular electrodes.

fibril formation of CNTs. This assembly process and the final form of the fibrils are shown in Figure 10.18.

The immersed electrohydrodynamic formulation of Section 10.4 can also be used to study the CNT deposition pattern for CNTs of various lengths. An electrode array with four pairs of semicircular electrodes ($R = 2.5 \mu\text{m}$, minimum gap length $5 \mu\text{m}$) was used in the simulation (Figure 10.19). The influence of CNT length was considered by separately running simulations for $3 \mu\text{m}$ CNTs, $5.2 \mu\text{m}$ CNTs, and $7 \mu\text{m}$ CNTs. It was found that CNTs much longer than the gap size, that is, the $7 \mu\text{m}$ long CNTs, are difficult to deposit between circular electrodes. The repulsive dielectrophoretic (DEP) forces close to the edge of the electrodes will lead to a rotational torque if the CNT is not coincidentally aligned perpendicular to the electrode edge, thus tilting the long CNTs away from the center of the gap. In an AC field, only CNTs with lengths close to the gap size (here, the CNTs are $5.2 \mu\text{m}$ long) can be deposited such that they are essentially aligned with the electrodes, and for multiple deposition, aligned parallel with each other. The longer CNTs can be tilted, while the shorter ($3 \mu\text{m}$ long) CNTs are found to form bundles and the bundles bridge the gap. Through the simulation, the mechanisms of length-selective deposition of CNTs on circular electrodes are rationalized. Various patterns of deposited CNTs can be obtained for CNTs of different lengths.

This approach can be extended to model the electrohydrodynamic assembly of flexible, arbitrary-shaped particles. The uniqueness of our proposed method is that one can use direct numerical simulation techniques (no assumptions of the drag force and fluid flow are used) to study the electrohydrodynamic motion of multiple, flexible, arbitrary-shaped nano/bio filaments in complex environments such as complex electrode geometries, composite DC/AC fields, and so on. The present simulations are in 3D and are dynamic, thus enabling one to reproduce the assembly in a physical and precise way.

10.6 Cell Migration and Cell–Substrate Adhesion

According to their motility, cells can be roughly divided into two categories: passive cells such as RBCs, and active cells such as cancer cells, activated WBCs and fibroblasts. The deformation of simple passive cells such as RBCs can be studied by continuum models. However, motility models of most living cells require the detailed accounts of internal structure, spatial granularity, heterogeneity and the active features unique to active cells. We consider a general momentum equation for the effective behavior of the cell material:

$$\rho \frac{D\mathbf{v}}{Dt} = \nabla \cdot \sigma_{\text{pass}} + \nabla \cdot \sigma_{\text{act}}, \quad (10.40)$$

where ρ is the material density, \mathbf{v} is the velocity field, σ_{pass} is the passive stress in the material and σ_{act} is the active stress generated by cytoskeleton filament polymerization or molecular motor induced contraction. A simplistic view is that the passive stress is the response of the material to the imposed flow, for example, shearing. The passive stress directly depends on the material properties of the fluid and the filaments inside the cell and the structure of the filaments. It is expected to be a viscoelastic response. The filament structure in turn depends on various factors, most importantly on the active processes (e.g. polymerization and motors) among others. Thus, the active processes affect the passive stress primarily through the filament structure, that is, indirectly. The active stress directly depends on the active processes.

The movement of ameboid cells involves at least four stages: protrusion, attachment to the substrate, translocation of the cell body, and detachment of the rear part; see, for example, Mogilner and Oster (1996), Mitchison and Cramer (1996), Sheetz et al. (1999), Gracheva and Othmer (2004) and Stossel (1993). Protrusion of the cell front involves the dynamic assembly and disassembly of actin filaments. Protrusions are stabilized by adhesive complexes. Actomyosin filaments contract at the rear and the cytoplasm is squeezed forward. Finally, cells detach the adhesive sites at the rear, allowing the tail of the cell to follow the main cell body. The actin filaments are usually accumulated at the cell–substrate anchoring sites. Cell–substrate adhesion dynamics can usually be tracked through the dynamic changes of the actin filament concentration. We will modulate the continuum simulations to match detailed experiments to be conducted by our collaborators. The experiments are based on nano-electromechanical system (NEMS) devices that can measure the cell–substrate traction force with high precision and spatial resolution. The substrate is patterned differently with ligands so that the corresponding changes in the cell–substrate traction and the cell motion can be quantified. Simultaneous imaging of the cytoskeletal structure can be conducted and compared with the structures from biofiber suspension simulations to obtain clues regarding the underlying active processes. Continuum simulations

of cell migration with appropriate boundary conditions can then be conducted by solving equations of motion together with the conservation equations, for example, filament and motor concentrations. The cell membrane can be modeled as an elastic material enclosing the cell interior. It is particularly interesting to perform simulations that reproduce the cellular motion observed in experiments. To this end, one uses cell–substrate traction forces measured from the experiments as boundary conditions in the continuum simulations discussed in the following text. One can assume a rheological model for the passive stress. The active force distribution is regarded as the unknown. Then, various active force distributions that most closely reproduce the cell motion observed in experiments are considered.

As a test case for 3D cell migration simulation, we have used a simple model in which $\mathbf{f}_{\text{pass}}(\mathbf{x})$ is an elastic stress while $\mathbf{f}_{\text{act}}(\mathbf{x})$ was prescribed such that realistic cell motion was reproduced. The cell is simply modeled as an elastic material. A nonslip boundary condition is applied at the substrate surface. A dynamically prescribed nonuniform active force is exerted onto the cell body at different migration stages: at the protrusion stage, a pulling force is applied onto the leading edge, representing the force induced by the actin polymerization. At the contraction stage, a contractile force is applied onto the rear part, representing the contractile force induced by the actomyosin filaments. At the translocation stage, no active force is applied. Some results obtained through the simple approach described above are shown in Figure 10.20.

Cell adhesion is an important issue of numerical modeling. When the cell adheres to the substrate, receptors on the cell membrane bond with ligands on the substrate, forming the

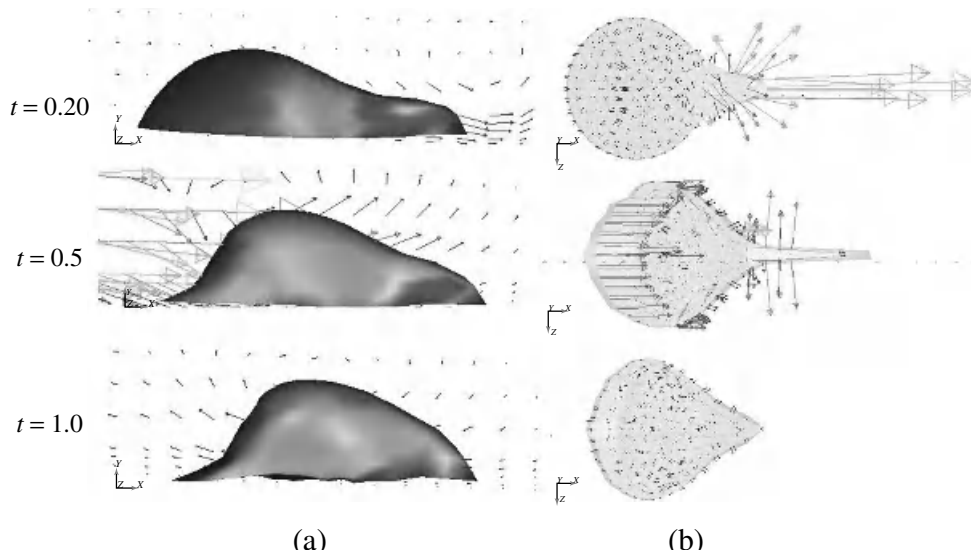


Figure 10.20 Continuum scale 3D simulation of cell migration. Stages of cell migration – protrusion, contraction, translocation – are shown. Grey shades indicate the stress inside the cell; the velocity vectors in the surrounding gel are also shown. The traction force vectors at the bottom of the cell are shown on the right. This force field can be measured by novel NEMS devices.

so-called focal adhesion (FA) complexes. Dembo et al. (1988) proposed a reaction model (also called an adhesion kinetic equation), where the bond density N_b is calculated as:

$$\frac{\partial N_b}{\partial t} = k_f(N_l - N_b)(N_r - N_b) - k_r N_b, \quad (10.41)$$

where N_l and N_r are the ligand and receptor densities, respectively, and k_r and k_f are the reverse and forward reaction rates, respectively. This reaction model represents a conservation equation of the different species (ligands, receptors and bonds). The receptor–ligand bonds are modeled as springs with spring constant σ and equilibrium length λ ; thus, the bond forces are described as a function of bond length L as:

$$f_L = \sigma(L - \lambda). \quad (10.42)$$

In this model, bonds form and break according to some empirical statistical law: $P_f = 1 - \exp(-k_{\text{on}}/\Delta t)$, $P_r = 1 - \exp(-k_{\text{off}}\Delta t)$, where P_f is the forward (bond formation) probability and P_r is the bond breaking probability, k_{on} and k_{off} are functions of bond length and temperature. Then, the ligand–receptor bond forces can be accumulated on the FEM element surface through an integration over the cell surface: $\sigma^s \cdot \mathbf{n} = \int_{\Gamma} \mathbf{f}_L(X^c) d\Gamma$. This adhesion force will be equivalent to a surface traction on the cell membrane. Such an approach has been used by Chang et al. (2000) and Dong et al. (1999) in the study of WBC rolling. As a test of this adhesion model, we simulate the steady state rolling speed of a WBC on a capillary wall (inflow velocity = $40 \mu\text{m s}^{-1}$). The rolling speed of the WBC without ligand–receptor binding was found to be $7.46 \mu\text{m s}^{-1}$, while that with a ligand–receptor binding density of $10^{10} \text{ sites/cm}^2$ was $6.55 \mu\text{m s}^{-1}$. This approach can be applied to model the rolling of multiple deformable WBCs and cell-ExtraCellular-Matrix (cell-ECM) adhesion in the future.

The contractile force generation inside actomyosin filaments is important in understanding contraction during cell migration. The proteins that are capable of transducing the chemical energy of ATP to mechanical energy are called *molecular motors*. The principal molecular motors associated with actin are myosin-I and myosin-II. Myosin-I has a single globular head containing the actin-binding site, while myosin-II is a dimer with two actin-binding heads attached to a flexible tail. Each actin filament has a specific polarity, pointing from its fast-growing, barbed end to slow-growing, pointed end. Two aligned actin filaments with the same polarity are referred to as parallel actin filaments, while the ones with opposite polarities are referred to as antiparallel actin filaments. The contractile forces are generated by myosin-II motor mediated sliding of antiparallel actin filaments. Despite the extensive study on how double-headed myosin-II motors can induce sliding movements along actin filaments, it is yet to be investigated as to how tension is generated between FAs that are interconnected by actin filament bundles.

The force generated by a single myosin motor has been measured by Ishijima et al. (1991) to be around 1 pN by the hydrolysis of an ATP. The myosin-II motor can bind or unbind onto an actin filament at a rate of about 10 times every second. A bound myosin can travel toward the plus end of the actin filament it binds to at about $1 \mu\text{m s}^{-1}$. However, when a double-headed myosin-II motor binds simultaneously onto two antiparallel actin filaments, it generates two forces of 1 pN per step at its binding sites in two opposite directions, leading to the contractile sliding of the two actin filaments. The unbound motors can diffuse freely in the cytoplasm, described as: $\langle (\Delta x)^2 \rangle = 6Dt$, where t is the current

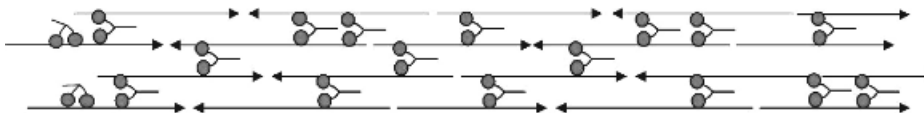


Figure 10.21 A schematic figure of the actomyosin contraction model. Each actin filament is illustrated as an arrow and its polarity is indicated. The double-headed myosin-II motors are assumed to be distributed randomly inside the domain.

time, D is the diffusion coefficient, given as $D = k_B T/f$, and $f = 6\pi\eta a$ for a sphere with diameter a in a fluid with the viscosity η , T is the temperature and k_B is the Boltzmann constant. Since only translocation is involved in actin filament sliding, the motion of an actin filament can be described by the standard Langevin equation as:

$$m_i \frac{d\boldsymbol{v}_i}{dt} = \sum_m f_{i,m} - \gamma \boldsymbol{v}_i + \boldsymbol{R}_i(t) \quad (10.43)$$

where m_i is the mass of the i th actin filament, \boldsymbol{v}_i is the velocity, $f_{i,m}$ is the force applied by the myosin motors, γ is the drag coefficient and $\boldsymbol{R}_i(t)$ is a random term.

It can be expected that the contraction rate of an actomyosin bundle will depend on the concentration of myosin motors. For modeling, we assume that an actin filament bundle is made of 60 filaments with an average length and spacing of 1 μm and 15 nm respectively; they are composed into a simulation box of 60 μm by 2 μm . The initial configuration is shown in Figure 10.21. It is expected that with random polarity and a myosin concentration of 5 μM ($1 \mu\text{M} = 10^{-21} \text{ mol } \mu\text{m}^{-3}$), the average contraction of the actin bundles will be around two-thirds of their original length. Using this model, we consider the contraction or elongation of actomyosin bundles under various myosin concentrations and actin filament polarity distributions. Such a microscopic simulation can help reveal the contractile force generation mechanism of actin-based cytoskeleton such as stress fibers, which are believed to play a significant role in cell migration.

FAs form during spreading or migration of a cell on a substrate coated with ECM components. The assembly of FAs starts from the FA complex that forms at the periphery of a spreading cell or at the leading edge of a migrating cell. The FA complex is not strong enough to form a firm adhesion and has to be stabilized by assembling it together with cytoskeleton structures, such as in the formation of stress fibers. The FA complex matures into FAs when tension induced by the stress fibers or external forces are applied onto the FA sites. The assembly of FAs involves cross talk between integrin and other associated proteins. The clustering of integrin is associated with cytoskeletal and signaling networks that promote actomyosin bundle formation. The formation of actomyosin bundles into stress fibers and the application of tension will, in turn, enhance integrin clustering and FAs' development. The FAs' development and contractile force generation is thus a positive feedback loop; see Sastry and Burridge (2000).

Combining adhesion and contraction together, we propose a multiscale model that includes a single stress fiber (an actomyosin bundle consisting of actin filaments and myosin motors) interconnecting two FA sites, as shown in Figure 10.22. The positive feedback loop between the FAs and tension can be studied via novel quantum and molecular dynamic simulations of integrin–fibronectin binding, and the conformational transition of integrin

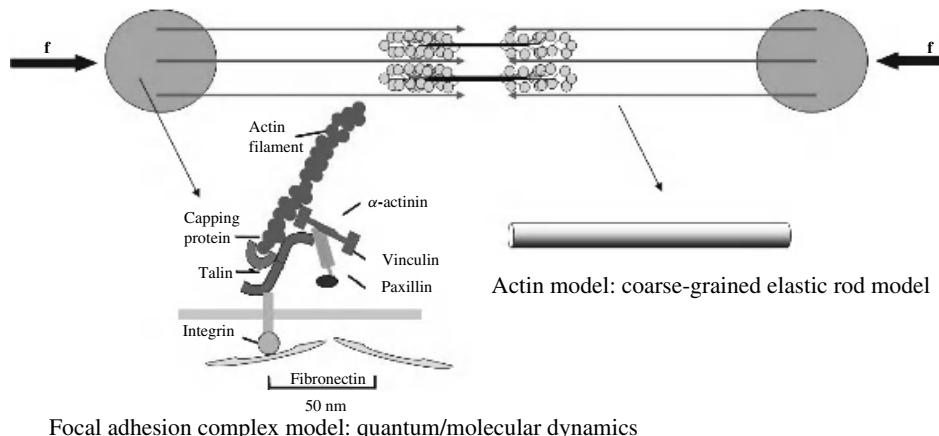


Figure 10.22 A schematic figure of the actomyosin-focal adhesion model. Each actin filament is illustrated as an arrow and its polarity is indicated. The two circular areas represent the FA sites. The double-headed myosin-II motors are assembled into bipolar ‘minifilaments’ that connect actin filaments of opposite polarities. The FA complex can be modeled by quantum or molecular dynamic simulations. The actin filaments can be modeled as coarse-grained elastic rods. The contractile force is applied onto the FA complex via atomistic-continuum coupling methods.

associated proteins under mechanical force. The contractile force (tension) generated by the stress fiber can be applied onto the FA sites via other linking proteins. An actin filament can be modeled as a continuum elastic rod while the associated linking proteins can be modeled as atomistic structures. To achieve this, coupled continuum mechanics and quantum or molecular dynamic simulation such as the approach described in Liu et al. (2004c) need to be used.

The predictions of this model can be verified by experimental measurements of the cellular forces applied by a stress fiber onto the FA sites. Such cellular forces can be measured through an elastic membrane supported by a bed of microneedles, as shown in Figure 10.23. The elastic membrane can be coated with ligands (an ECM component), so that a cell will contact the membrane by the specific receptor-ligand binding mode. The traction forces can be calibrated by performing the topographic surface mapping of the membrane. Although innovative, this technique does not isolate traction forces from contractile forces and adhesive forces. To overcome this problem, the NEMS device shown in Figure 10.24 was proposed. This device is equipped with a channel filled with a gel to mimic natural ECM. Along the bottom of the device, nanowires, for example, the CNTs, are assembled into a parallel array. The nanowire sensor is coated with ligands. In this device, the deflections of the nanowires can be measured by diffraction-limited microscopy and force patterns and magnitudes are reconstructed via the IFEM simulations. The calibrated traction force distribution pattern, when combined with the actomyosin contraction and FA models, can provide valuable information on determining the mechanisms of cell migration.

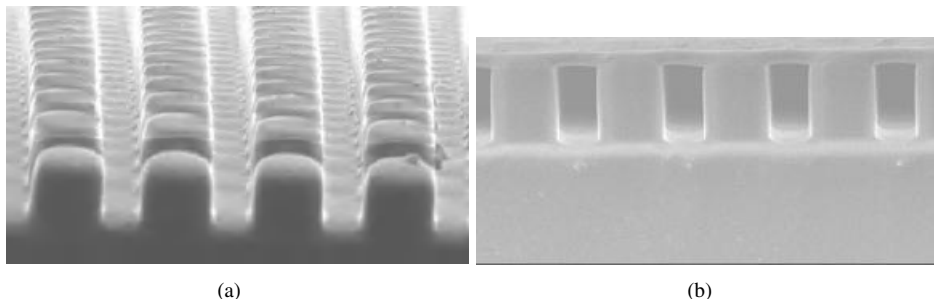


Figure 10.23 An elastic silicone membrane supported by a bed of silicone microneedles. (a) Bed of microneedles. (b) The membrane supported by the microneedle bed. The membrane is coated with ECM ligands such that cells are attached and migrate in a similar manner as they do in vivo. The cellular traction forces posed on every FA is quantitated by defining the topographic map of the membrane. Images are the courtesy of Juhee Hong and Junghoon Lee, School of Mechanical and Aerospace Engineering, Seoul National University. Reproduced with permission from Junghoon Lee.

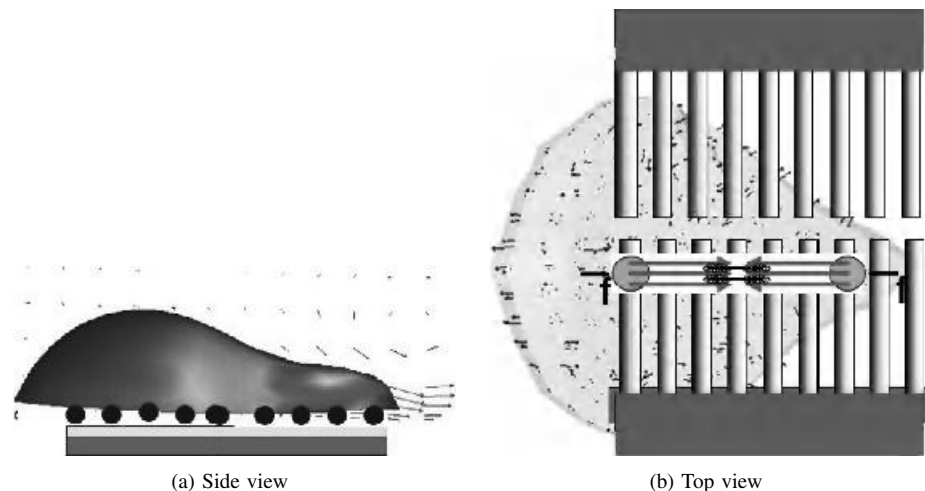


Figure 10.24 A schematic drawing of the proposed NEMS device to be used to measure the cellular traction forces. The device is fabricated using nanowires.

10.7 Conclusions

In this chapter, we overviewed the IFEM and related coupling techniques for solving complex multiphysics problems.

Within the IFEM, the structural models are not restricted to one-dimensional volumeless structures such as fibers; instead, they may occupy finite volumes in the fluid. Finite elements are used to discretize the submerged solid, and as a consequence, the calculated stresses are more realistic and accurate. Furthermore, within the IFEM, different material

laws can be assigned to the submerged solid. The higher-ordered RKPM delta function has the ability to handle nonuniform grids and is particularly useful for fluid domains with arbitrary geometries and boundaries. Finally, unlike the periodic boundary conditions implemented in most IB applications, essential and natural boundary conditions in the context of finite element methods are relatively easy to implement in IFEM.

For the applications of IFEM to biological systems, we considered fluid–structure interaction problems encountered in the human blood circulation system, including deployment processes and rheological properties of the blood incorporating the deformable RBCs. In the context of blood rheology, the shear-rate–dependent deaggregation of RBC clusters and the transportation of deformable cells was demonstrated. Furthermore, we discussed coupling of the IFEM and electrostatic equations in application to nanomanipulation and bio-NEMS devices. In these 3D dynamic simulations, the fluid flow and solid deformation/motion are reasonably captured.

In the near future, it will be possible to simultaneously visualize the cellular scale structures and measure the cellular traction forces and cell-ECM adhesion forces using the recently developed NEMS devices. The research in this direction should provide a powerful means to understand the structural and functional aspects of molecules, cells and tissues. Ultimately, the outcome may have a great impact on a broad range of medical sciences.

Copyright

Material of Sections 10.1–10.3 and 10.6 is reproduced from Liu et al. (2005c) with permission from Elsevier.

Appendix A

Kernel Matrices for EAM Potential

Here, we provide numerically derived \mathbf{K} -matrices for the third shell EAM interaction in FCC gold. These matrices are utilized for the lattice governing equations, both dynamic (3.9) and quasi-static (3.106), in the harmonic approximation. They also serve as input information in derivation of the lattice Green's function (3.75) and the time history kernel (3.97).

The EAM interaction model is regarded as an extension of the nearest-neighbor model represented by the matrices (3.126) on page 73. The unit cell numbering for the fcc lattice structure is shown in Figure 3.22 on page 72.

The parameters used for FCC gold are identical to those found in the work of Foiles et al. (1986), which has been implemented in the Sandia simulation code Tahoe (2004). For a third shell fcc potential, each atom has 43 neighboring atoms; each of the 43 atoms in this test lattice was perturbed in such a manner that the resulting force on cell $(0, 0, 0)$ resulting from the perturbation could be determined. The \mathbf{K} -matrices, which are given in units of $\text{eV} \cdot \text{\AA}^{-2}$, are as follows:

$$\mathbf{K}_{0,0,0} = \begin{pmatrix} -4.415218 & 0 & 0 \\ 0 & -4.415218 & 0 \\ 0 & 0 & -4.415218 \end{pmatrix}$$

$$\mathbf{K}_{0,0,2} = \mathbf{K}_{0,0,-2} = \begin{pmatrix} -0.06714876 & 0 & 0 \\ 0 & -0.06714876 & 0 \\ 0 & 0 & 0.0371758 \end{pmatrix}$$

$$\mathbf{K}_{2,0,0} = \mathbf{K}_{-2,0,0} = \begin{pmatrix} 0.03717614 & 0 & 0 \\ 0 & -0.06714876 & 0 \\ 0 & 0 & -0.06714876 \end{pmatrix}$$

$$\mathbf{K}_{0,2,0} = \mathbf{K}_{0,-2,0} = \begin{pmatrix} -0.06714876 & 0 & 0 \\ 0 & -0.03717614 & 0 \\ 0 & 0 & -0.067114876 \end{pmatrix}$$

$$\mathbf{K}_{-1,0,1} = \mathbf{K}_{1,0,-1} = \begin{pmatrix} 0.5980579 & 0 & -0.710314 \\ 0 & -0.1736703 & 0 \\ -0.710314 & 0 & 0.5980579 \end{pmatrix}$$

$$\mathbf{K}_{-1,0,-1} = \mathbf{K}_{1,0,1} = \begin{pmatrix} 0.5980579 & 0 & 0.710314 \\ 0 & -0.1736703 & 0 \\ 0.710314 & 0 & 0.5980579 \end{pmatrix}$$

$$\mathbf{K}_{0,-1,1} = \mathbf{K}_{0,1,-1} = \begin{pmatrix} -0.1736703 & 0 & 0 \\ 0 & 0.5980579 & -0.710314 \\ 0 & -0.710314 & 0.5980418 \end{pmatrix}$$

$$\mathbf{K}_{0,-1,-1} = \mathbf{K}_{0,1,1} = \begin{pmatrix} -0.1736703 & 0 & 0 \\ 0 & 0.5980579 & 0.710314 \\ 0 & 0.710314 & 0.5980579 \end{pmatrix}$$

$$\mathbf{K}_{1,1,0} = \mathbf{K}_{-1,-1,0} = \begin{pmatrix} 0.5980418 & 0.710314 & 0 \\ 0.710314 & 0.5980418 & 0 \\ 0 & 0 & -0.1736703 \end{pmatrix}$$

$$\mathbf{K}_{1,-1,0} = \mathbf{K}_{-1,1,0} = \begin{pmatrix} 0.5980418 & -0.710314 & 0 \\ -0.710314 & 0.5980418 & 0 \\ 0 & 0 & -0.1736703 \end{pmatrix}$$

$$\mathbf{K}_{1,1,2} = \mathbf{K}_{-1,-1,-2} = \begin{pmatrix} -0.003171257 & 0.03711209 & 0.04007788 \\ 0.03711209 & -0.003171257 & 0.04007788 \\ 0.04029503 & 0.04029503 & 0.07131029 \end{pmatrix}$$

$$\mathbf{K}_{1,1,-2} = \mathbf{K}_{-1,-1,2} = \begin{pmatrix} -0.003171257 & 0.03711209 & -0.04007788 \\ 0.03711209 & -0.003171257 & -0.04007788 \\ -0.04029503 & -0.04029503 & 0.07131029 \end{pmatrix}$$

$$\mathbf{K}_{1,-1,2} = \mathbf{K}_{-1,1,-2} = \begin{pmatrix} -0.003171257 & -0.03711247 & 0.04007788 \\ -0.03711209 & -0.003171455 & -0.04007788 \\ 0.04029503 & -0.04029528 & 0.07131029 \end{pmatrix}$$

$$\mathbf{K}_{1,-1,-2} = \mathbf{K}_{-1,1,2} = \begin{pmatrix} -0.003171257 & -0.03711247 & -0.04007829 \\ -0.03711209 & -0.003171455 & 0.04007829 \\ -0.04029503 & 0.04029528 & 0.0713109 \end{pmatrix}$$

$$\mathbf{K}_{-1,-2,1} = \mathbf{K}_{1,2,-1} = \begin{pmatrix} -0.003171455 & 0.04007829 & -0.03711209 \\ 0.04029528 & 0.0713109 & -0.04029503 \\ -0.03711247 & -0.04007829 & -0.003171257 \end{pmatrix}$$

$$\mathbf{K}_{-1,-2,-1} = \mathbf{K}_{1,2,1} = \begin{pmatrix} -0.003171455 & 0.04007829 & 0.03711247 \\ 0.04029528 & 0.0713109 & 0.04029528 \\ 0.03711247 & 0.04007829 & -0.003171455 \end{pmatrix}$$

$$\mathbf{K}_{1,-2,-1} = \mathbf{K}_{-1,2,1} = \begin{pmatrix} -0.003171257 & -0.04007829 & -0.03711247 \\ -0.04029503 & 0.0713109 & 0.04029528 \\ -0.03711209 & 0.04007829 & -0.003171455 \end{pmatrix}$$

$$\mathbf{K}_{1,-2,1} = \mathbf{K}_{-1,2,-1} = \begin{pmatrix} -0.003171257 & -0.04007829 & 0.03711209 \\ -0.04029503 & 0.0713109 & -0.04029503 \\ 0.03711209 & -0.04007829 & -0.003171257 \end{pmatrix}$$

$$\mathbf{K}_{-2,-1,1} = \mathbf{K}_{2,1,-1} = \begin{pmatrix} 0.0713109 & 0.04029528 & -0.04029503 \\ 0.04007829 & -0.003171455 & -0.03711209 \\ -0.04007829 & -0.03711247 & -0.003171257 \end{pmatrix}$$

$$\mathbf{K}_{-2,-1,-1} = \mathbf{K}_{2,1,1} = \begin{pmatrix} 0.0713109 & 0.04029528 & 0.04029528 \\ 0.04007829 & -0.003171455 & 0.03711247 \\ 0.04007829 & 0.03711247 & -0.003171455 \end{pmatrix}$$

$$\mathbf{K}_{2,-1,-1} = \mathbf{K}_{-2,1,1} = \begin{pmatrix} 0.07131029 & -0.04029528 & -0.04029528 \\ -0.04007788 & -0.003171455 & 0.03711247 \\ -0.04007788 & 0.03711247 & -0.003171455 \end{pmatrix}$$

$$\mathbf{K}_{2,-1,1} = \mathbf{K}_{-2,1,-1} = \begin{pmatrix} 0.07131029 & -0.04029528 & 0.04029503 \\ -0.04007788 & -0.003171455 & -0.03711209 \\ 0.04007788 & -0.03711247 & -0.003171257 \end{pmatrix}$$

Bibliography

- Abraham F and Gao H 2000 How fast can cracks propagate? *Physical Review Letters* **84**(14), 3113–3116.
- Abraham F, Brodbeck D, Rudge W and Xu X 1997 A molecular dynamics investigation of rapid fracture mechanics. *Journal of the Mechanics and Physics of Solids* **45**(9), 1595–1619.
- Abraham F, Walkup R, Gao H, Duchaineau M, la Rubia TD and Seager M 2002 Simulating materials failure by using up to one billion atoms and the world's fastest computer: Brittle fracture. *Proceedings of the National Academy of Sciences of the United States of America* **99**(9), 5777–5782.
- Abraham FF, Broughton J, Bernstein N and Kaxiras E 1998 Spanning the continuum to quantum length scales in a dynamic simulation of brittle fracture. *Europhysics Letters* **44**, 783–787.
- Adelman SA and Doll JD 1976 Generalized langevin equation approach for atom/solid-surface scattering: General formulation for classical scattering off harmonic solids. *Journal of Chemical Physics* **64**, 2375–2388.
- Adelman SA and Garrison BJ 1976 Generalized langevin theory for gas/solid processes: Dynamic solid models. *Journal of Chemical Physics* **65**, 3751–3761.
- Allen MP and Tildesley D 1987 *Computer Simulation of Liquids*. Oxford University Press.
- Andersen HC 1980 Molecular dynamics simulations at constant pressure and/or temperature. *Journal of Chemical Physics* **72**(4), 2384–2393.
- Arfken GB and Weber HJ 2001 *Mathematical Methods for Physicists*. Harcourt Academic Press, San Diego, CA.
- Argon AS, Im J and Safoglu R 1975 Cavity formation from inclusions in ductile fracture. *Metallurgical Transactions* **6**(4), 825–837.
- Arroyo M and Belytschko T 2002 An atomistic-based finite deformation membrane for single layer crystalline films. *Journal of the Mechanics and Physics of Solids* **50**, 1941–1977.
- Arroyo M and Belytschko T 2004 Finite crystal elasticity of carbon nanotubes based on the exponential Cauchy-Born rule. *Physical Review B* **69**(11), 115415.
- Bachorczyk R, Danielewski M, Datta PK and Filipek R 2000 Model of heterogenous reactions controlled by diffusion. *Journal of Molecular Liquids* **86**(1–3), 61–67.
- Becker T 2003 Self-healing material seen in movies is real possibility. *Dow Jones Newswires*. <http://www.matr.net/article-7424.html>.
- Bekker A and Brinson LC 1998 Phase diagram based description of the hysteresis behavior of shape memory alloys. *Acta Materialia* **46**(10), 3649–3665.
- Belytschko T, Guo Y, Liu W and Xiao S 2000a A unified stability analysis of meshless particle methods. *International Journal for Numerical Methods in Engineering* **48**(9), 1359–1400.
- Belytschko T, Liu WK and Moran B 2000b *Nonlinear Finite Elements for Continua and Structures*. Wiley, Chichester, UK.

- Belytschko T, Krongauz Y, Dolbow J and Gerlach C 1998 On the completeness of meshfree particle methods. *International Journal for Numerical Methods in Engineering* **43**(5), 785.
- Belytschko T, Krongauz Y, Organ D, Fleming M and Krysl P 1996 Meshless methods: An overview and recent developments. *International Journal for Numerical Methods in Engineering* **139**(1–4), 3–47.
- Belytschko T, Lu YY and Gu L 1994 Element-free galerkin methods. *International Journal for Numerical Methods in Engineering* **37**, 229–256.
- Benenson W, Harris J, Stocker H and Lutz H 2002 *Handbook of Physics*. Springer, New York.
- Berendsen HJC, Postma JPM, van Gunsteren WF, DiNola A and Haak JR 1984 Molecular dynamics with coupling to an external bath. *Journal of Chemical Physics* **81**(8), 3684–3690.
- Bertrand P, Jonas A, Laschewsky A and Legras R 2000 Ultrathin polymer coatings by complexation of polyelectrolytes at interfaces: Suitable materials, structure and properties. *Macromolecular Rapid Communications* **21**(7), 319–348.
- Besterfield GH, Liu WK, Lawrence MA and Belytschko T 1990 Brittle-fracture reliability by probabilistic finite elements. *Journal of Engineering Mechanics—ASCE* **116**(3), 642–659.
- Besterfield GH, Liu WK, Lawrence MA and Belytschko T 1991 Fatigue crack-growth reliability by probabilistic finite elements. *Computer Methods in Applied Mechanics and Engineering* **86**(3), 297–320.
- Bishop JF and Hill R 1951 A theory of the plastic distortion of polycrystalline aggregate under combined stresses. *Philosophical Magazine* **42**, 414–427.
- Biswas R and Hamann DR 1985 Interatomic potential for silicon structural energies. *Physical Review Letters* **55**(19), 2001–2004.
- Biswas R and Hamann DR 1987 New classical models for silicon structural energies. *Physical Review B* **36**(12), 6434–6445.
- Bolton K and Gustavsson S 2003 Energy transfer mechanisms in gas-carbon nanotube collisions. *Chemical Physics* **291**(2), 161–170.
- Bolton K and Rosen A 2002 Computational studies of gas-carbon nanotube collision dynamics. *Physical Chemistry Chemical Physics* **4**(18), 4481–4488.
- Borrego A, Fernandez R, del Carmen Cristina M, Ibanez J and Gonzalez-Doncel G 2002 Influence of extrusion temperature on the microstructure and the texture of 6061al-15 vol. % sicwpm composites. *Composites Science and Technology* **62**(6), 731–742.
- Brand AJ, Kalz S and Kopp R 1996 Microstructural simulation in hot rolling of aluminium alloys. *Computational Materials Science* **7**(1–2), 242–246.
- Brenner DW 1990 Empirical potential for hydrocarbons for use in simulating the chemical vapor deposition of diamond films. *Physical Review B* **42**(15), 9458–9471.
- Brenner DW, Shenderova OA, Harrison JA, Stuart SJ, Ni B and Sinnott SB 2002 A second-generation reactive empirical bond order (rebo) potential energy expression for hydrocarbons. *Journal of Physics: Condensed Matter* **14**, 783–802.
- Briant CL 2002 Void nucleation in a low alloy steel. Proceedings of the 131st Annual Meeting & Exhibition of The Minerals, Metals & Materials Society, Seattle, WA.
- Brinson LC 1993 One dimensional constitutive behavior of shape memory alloys: Thermomechanical derivation with non-constant material functions. *Journal of Intelligent Material Systems and Structures* **4**(2), 229–242.
- Brinson LC and Huang MS 1996 Simplifications and comparisons of shape memory alloy constitutive models. *Journal of Intelligent Material Systems and Structures* **7**(1), 108–114.
- Broughton JQ, Abraham FF, Bernstein N and Kaxiras E 1999 Concurrent coupling of length scales: Methodology and applications. *Physical Review B* **60**, 2391–2403.

- Brown EN, Sottos NR and White SR 2002 Fracture testing of a self-healing polymer composite. *Experimental Mechanics* **42**(4), 372–379.
- Brown EN, Kessler MR, Sottos NR and White SR 2003 In situ poly(urea-formaldehyde) microencapsulation of dicyclopentadiene. *Journal of Microencapsulation* **20**(6), 719–730.
- Cai W, DeKoning M, Bulatov VV and Yip S 2000 Minimizing boundary reflections in coupled-domain simulations. *Physical Review Letters* **85**, 3213–3216.
- Car R and Parrinello M 1985 Unified approach for molecular-dynamics and density-functional theory. *Physical Review Letters* **55**, 2471.
- Chang K, Tees D and Hammer D 2000 The state diagram for cell adhesion under flow: Leukocyte rolling and firm adhesion. *Proceedings of the National Academy of Sciences of the United States of America* **97**(21), 11262–11267.
- Chu MC, Sato S, Kobayashi Y and Ando K 1995 Damage healing and strengthening behavior in intelligent mullite/sic ceramics. *Fatigue and Fracture of Engineering Materials and Structures* **18**(9), 1019–1029.
- Chung J, Lee K, Lee J and Ruoff R 2004 Toward large-scale integration of carbon nanotubes. *Langmuir* **20**(8), 3011–3017.
- Chung J, Lee J, Ruoff RS and Liu WK 2002a Integration of single multi-walled carbon nanotube on micro systems *International Mechanical Engineering Congress and Expositions*, New Orleans, LA 2002-33325.
- Chung J, Lee J, Ruoff RS and Liu WK 2002b Nanoscale gap fabrication and integration of carbon nanotubes by micromachining. *Solid-State Sensor, Actuator, and Microsystems Workshop*, Hilton Head Island, SA.
- Cinlar E 2004 *An Introduction to Stochastic Processes*. Prentice Hall, Englewood Cliffs, NJ.
- Clementi E and Roetti C 1974 Roothaan-hartree-fock atomic wavefunctions. *Atomic Data and Nuclear Data Tables* **14**(3–4), 177–478.
- Curtin WA and Miller RE 2003 Atomistic/continuum coupling in computational materials science. *Modelling and Simulation in Materials Science and Engineering* **11**, R33–R68.
- Davies B and Martin B 1979 Numerical inversion of the laplace transforms: A survey and comparison of methods. *Journal of Computational Physics* **33**, 1–32.
- Daw MS 1989 Model of metallic cohesion: The embedded-atom method. *Physical Review B* **39**(11), 7441–7452.
- Daw MS and Baskes ML 1984 Embedded-atom method: Derivation and application to impurities, surfaces, and other defects in metals. *Physical Review B* **29**(12), 6443–6453.
- Daw MS, Foiles SM and Baskes MI 1993 The embedded-atom method: A review of theory and applications. *Materials Science Reports* **9**, 251–310.
- Dembo M, Torney D, Saxman K and Hammer D 1988 The reaction limited kinetics of membrane to surface adhesion and detachment. *Proceedings of the Royal Society of London* **234**, 55–83.
- Diamond SL 2001 Reaction complexity of flowing human blood. *Biophysical Journal* **80**, 1031–1032.
- Dong C, Cao J, Struble EJ and Lipowsky HW 1999 Mechanics of leukocyte deformation and adhesion to endothelium in shear flow. *Annals of Biomedical Engineering* **27**(3), 298–312.
- Duffy DG 1993 On the numerical inversion of laplace transforms: Comparison of three new methods on characteristic problems from applications. *ACM Transactions on Mathematical Software* **19**(3), 333–359.
- Duva JM and Hutchinson JW 1984 Constitutive potentials for dilutely voided non-linear materials. *Mechanics of Materials* **3**, 41–54.
- Eshelby JD 1961 *Elastic Inclusions and Inhomogeneities*. North-Holland Publishing, Amsterdam, NY.
- E W and Huang ZY 2002 A dynamic atomistic-continuum method for the simulation of crystalline materials. *Journal of Computational Physics* **182**(1), 234–261.

- Fan ZJ, Song YZ, Li JG, Liu L, Song JR, Chen JL, Zhai GT and Shi JL 2003 Oxidation behavior of fine-grained sic-b4c/c composites up to 1400 degrees c. *Carbon* **41**(3), 429–436.
- Farage MCR, Sercombe J and Galle C 2003 Rehydration and microstructure of cement paste after heating at temperatures up to 300 degrees c. *Cement and Concrete Research* **33**(7), 1047–1056.
- Farhat C and Lesoinne M 2000 Two efficient staggered algorithms for the serial and parallel solution of three-dimensional nonlinear transient aeroelastic problems. *Computer Methods in Applied Mechanics and Engineering* **182**, 499–515.
- Fermi E 1928 A statistical method for the determination of some atomic properties and the application of this method to the theory of the periodic system of elements. *Zeitschrift fur Physik* **48**, 73–79.
- Feynman RP 1939 Forces in molecules. *Physical Review* **56**, 340.
- Fichthorn KA and Weinberg WH 1991 Theoretical foundations of dynamical Monte-Carlo simulations. *Journal of Chemical Physics* **95**(2), 1090–1096.
- Files BS 1997 *Design of a Biomimetic Self-Healing Superalloy Composite*. Ph.D. Thesis, Northwestern University, Evanston, IL.
- Filipuzzi L and Naslain R 1994 Oxidation mechanisms and kinetics of 1d-sic/c/sic composite-materials: 2) modeling. *Journal of The American Ceramic Society* **77**(2), 467–480.
- Filipuzzi L, Camus G, Naslain R and Thebault J 1994 Oxidation mechanisms and kinetics of 1d-sic/c/sic composite-materials: 1) an experimental approach. *Journal of The American Ceramic Society* **77**(2), 459–466.
- Finnis MW and Sinclair JE 1984 A simple empirical n-body potential for transition metals. *Philosophical Magazine A* **50**(1), 45–55.
- Fleck NA and Hutchinson JW 1997 Strain gradient plasticity. *Advances in Applied Mechanics* **33**, 295–361.
- Fleck NA, Muller GM, Ashby MF and Hutchinson JW 1994 Strain gradient plasticity: Theory and experiment. *Acta Metallurgica et Materialia* **42**(2), 475–487.
- Fogelson A 1985 A mathematical model and numerical method for studying platelet adhesion and aggregation during blood clotting. *Journal of Computational Physics* **56**, 111–134.
- Foiles SM, Baskes ML and Daw MS 1986 Embedded-atom-method functions for the fcc metals cu, ag, au, ni, pd, pt, and their alloys. *Physical Review B* **33**(12), 7893–7991.
- Fong H, Vaia RA, Sanders JH, Lincoln D, Vreugdenhil AJ, Liu WD and Bultman J 2001 Self-passivation of polymer-layered silicate nanocomposites. *Chemistry of Materials* **13**(11), 4123–4129.
- Forbell C, Barney M, Scharff C and Lai W 1997 *Tin Based Self-Healing Alloy. MSC Design Team Report*. Northwestern University, Evanston, IL.
- Foulkes WMC and Haydock R 1989 Tight-binding models and density-functional theory. *Physical Review B* **39**, 12520.
- Frenkel D 1986 Free energy computation and first-order phase transitions In *Molecular Dynamics Simulation of Statistical-Mechanical Systems* (ed. Ciccotti G and Hoover WG). North-Holland Publishing, Amsterdam, NY.
- Fung YC 1996 *Biomechanics: Circulation*. Springer-Verlag.
- Gao H, Huang Y and Abraham F 2001 Continuum and atomistic studies of intersonic crack propagation. *Journal of Mechanics and Physics of Solids* **49**(9), 2113–2132.
- Gao X, Burton D and Brinson LC 2005 Finite element simulation of a self-healing shape memory alloy composite. *Mechanics of Materials* In press.
- Gay M, Zhang LT and Liu WK 2004 Stent modeling using immersed finite element method. *Computer Methods in Applied Mechanics and Engineering* Accepted.
- Goldstein H 1980 *Classical Mechanics*. Addison-Wesley, Reading, MA.

- Goodwin L, Skinner AJ and Pettifor DG 1989 Generating transferable tight-binding parameters – Application to silicon. *Europhysics Letters* **9**, 701.
- Gracheva ME and Othmer HG 2004 A continuum model of motility in ameiboid cells. *Bulletin of Mathematical Biology* **66**(1), 167–193.
- Gurson AL 1977 Continuum theory of ductile rupture by void nucleation and growth: Part I –yield criteria and flow rules for porous ductile media. *Journal of Engineering Materials Technology* **99**(1), 2–15.
- Haile J 1992 *Molecular Dynamics Simulations*. John Wiley & Sons.
- Hamada K, Kawano F and Asaoka K 2003 Shape recovery of shape memory alloy fiber embedded resin matrix smart composite after crack repair. *Dental Materials Journal* **22**(2), 160–167.
- Hao S and Brocks W 1997 The gurson-tvergaard-needleman-model for rate and temperature-dependent materials with isotropic and kinematic hardening. *Computational Mechanics* **20**(1–2), 34–40.
- Hao S, Liu WK and Klein P 2000 Inhomogeneous electron gas. *Multi-Scale Damage Model*. IUTAM2000, Chicago, IL.
- Hao S, Park HS and Liu WK 2002 Moving particle finite element method. *International Journal for Numerical Methods in Engineering* **53**(8), 1937–1958.
- Hao S, Moran B, Liu WK and Olson GB 2003 A hierarchical multi-physics model for design of high toughness steels. *Journal of Computer-Aided Materials Design* **10**, 99–142.
- Hao S, Liu WK, Moran B, Vernerey F and Olson GB 2004a Multi-scale constitutive model and computational framework for the design of ultra-high strength, high toughness steels. *Computer Methods in Applied Mechanics and Engineering* **193**, 1865–1908.
- Hao S, Liu WK, Moran B, Vernerey F and Olson GB 2004b Multi-scale constitutive model and computational framework for the design of ultra-high strength, high toughness steels. *Computer Methods in Applied Mechanics and Engineering* **195**, 1865–1908.
- Hao S, Liu WK and Belytschko T 2004c Moving particle finite element method with global smoothness. *International Journal for Numerical Methods in Engineering* **59**(7), 1007–1020.
- Harrison DE 1988 Application of molecular dynamics simulations to the study of ion-bombarded metal surfaces. *Critical Reviews in Solid State and Materials Science* **14**(Suppl. 1), S1–S78.
- Hohenberg P and Kohn W 1964 Inhomogeneous electron gas. *Physical Review* **136**(3B), 864–871.
- Holian BL, Voter AF, Wagner NJ, Ravelo RJ, Chen SP, Hoover WG, Hoover CG, Hammerberg JE and Dontje TD 1991 Effects of pairwise versus many-body forces on high-stress plastic deformation. *Physical Review A* **43**(6), 2655–2661.
- Hoover WG 1985 Canonical dynamics: Equilibrium phase-space distributions. *Physical Review A* **31**(3), 1695–1697.
- Hu HH, Patankar NA and Zhu MY 2001 Direct numerical simulations of fluid-solid systems using the arbitrary Lagrangian-Eulerian technique. *Journal of Computational Physics* **169**, 427–462.
- Huerta A and Liu WK 1988 Viscous flow with large free surface motion. *Computer Methods in Applied Mechanics and Engineering* **69**, 277–324.
- Hughes TJR 1987 *The Finite Element Method: Linear Static and Dynamic Finite Element Analysis*. Prentice Hall.
- Hughes TJR, Franca LP and Balestra M 1986 A new finite element formulation for computational fluid dynamics: V. Circumventing the Babuška-Brezzi condition: A stable Petrov-Galerkin formulation of the Stokes problem accommodating equal-order interpolations. *Computer Methods in Applied Mechanics and Engineering* **59**, 85–99.
- Hughes TJR, Liu WK and Zimmerman TK 1981 Lagrangian-Eulerian finite element formulations for incompressible viscous flows. *Computer Methods in Applied Mechanics and Engineering* **29**, 329–349.

- Hughes TJR, Feijoo GR, Mazzei L and Quincy JB 1998 The variational multiscale method – a paradigm for computational mechanics. *Computer Methods in Applied Mechanics and Engineering* **166**, 3–24.
- Ishijima A, Doi T, Sakurada K and Yanagida T 1991 Sub-piconewton force fluctuations of actomyosin in vitro. *Nature* **352**, 301–306.
- Jacobsen J, Cooper BH and Sethna JP 1998 Simulations of energetic beam deposition: From picoseconds to seconds. *Physical Review B* **58**(23), 15847–15865.
- Jacucci G and Quirke N 1982 Free energy calculations for crystals In *Computer Simulations of Solids* (eds. Catlow CRA and Mackrodt WC). Springer-Verlag, Berlin, Germany.
- Jiang H and Valdez J 2000 Strength and toughness of cement reinforced with bone-shaped steel wires. *Composites Science and Technology* **60**(9), 1753–1761.
- Johnson RA 1988 Analytic nearest-neighbor model for fcc metals. *Physical Review B* **37**(8), 3924–3931.
- Johnson A and Tezduyar TE 1999 Advanced mesh generation and update methods for 3d flow simulations. *Computational Mechanics* **23**, 130–143.
- Jones JE 1924a On the determination of molecular fields. I. From the variation of the viscosity of a gas with temperature. *Proceedings of the Royal Society of London A* **106**, 441–462.
- Jones JE 1924b On the determination of molecular fields. II. From the equation of state of a gas. *Proceedings of the Royal Society of London A* **106**, 463–477.
- Jones TB 1995 *Electromechanics of Particles*. Cambridge University Press, New York.
- Jones DB and Middelberg APJ 2002 Direct determination of the mechanical properties of an interfacially adsorbed protein film. *Chemical Engineering Science* **57**(10), 1711–1722.
- Joos B and Duesbery MS 1993 Self-repair of monolayers with vacancy damage. *Physical Review Letters* **70**(18), 2754–2757.
- Joos B, Zhou Z and Duesbery MS 1994 Dislocation-mediated healing of ideal and adsorbed monolayers with vacancy damage. *Physical Review B* **50**(12), 8763–8772.
- Kadowaki H and Liu WK 2004 Bridging multi-scale method for localization problems. *Computer Methods in Applied Mechanics and Engineering* **193**, 3267–3302.
- Kadowaki H and Liu WK 2005 A multiscale approach for the micropolar continuum model. *Computer Modeling in Engineering and Sciences* **7**(3), 269–282.
- Karhausen KF and Roters F 2002 Development and application of constitutive equations for the multiple-stand hot rolling of al-alloys. *Journal of Materials Processing Technology* **123**(1), 155–166.
- Karpov EG, Park HS and Liu WK 2005a A Phonon heat bath approach for the atomistic and multiscale simulation of solids. Preprint.
- Karpov EG, Wagner GJ and Liu WK 2005b A Green's function approach to deriving non-reflecting boundary conditions in molecular dynamics simulations. *International Journal for Numerical Methods in Engineering* **62**(9), 1250–1262.
- Karpov EG, Stephen NG and Liu WK 2002 On static analysis of finite repetitive structures by discrete Fourier transform. *International Journal of Solids and Structures* **39**(16), 4291–4310.
- Karpov EG, Stephen NG and Liu WK 2003 Initial tension in randomly disordered periodic lattices. *International Journal of Solids and Structures* **40**(20), 5371–5388.
- Karpov EG, Yu H, Park HS, Liu WK, Wang QJ and Qian D 2005 Multiscale boundary conditions in crystalline solids: Theory and application to nanoindentation. *International Journal of Solids and Structures*. Accepted.
- Kessler MR and White SR 2001 Self-activated healing of delamination damage in woven composites. *Composites Part A: Applied Science And Manufacturing* **32**(5), 683–699.

- Kessler MR, Sottos NR and White SR 2003 Self-healing structural composite materials. *Composites Part A: Applied Science And Manufacturing* **34**(8), 743–753.
- Kittel C 1976 *Introduction to Solid State Physics*. Wiley, New York.
- Kleiman JI, Iskanderova ZA, Perez FJ and Tennyson RC 1995 Protective coatings for leo environments in spacecraft applications. *Surface and Coatings Technology* **77**(1-3), 827–834.
- Klein PA 1999 *A Virtual Internal Bond Approach to Modeling Crack Nucleation and Growth. Ph.D. Thesis, Stanford University*.
- Knap J and Ortiz M 2001 An analysis of the quasicontinuum method. *Journal of the Mechanics and Physics of Solids* **49**(9), 1899–1923.
- Knowlton TM, Carson JW, Klinzing GE and Yang WC 1994 The importance of storage, transfer, and collection. *Chemical Engineering Progress* **90**(4), 44–54.
- Kohn W and Sham LJ 1965 Self-consistent equations including exchange and correlation effects. *Physical Review* **140**(4A), 1133–1138.
- Konishi T, Ohsawa K, Abe H and Kuramoto E 1999 Determination of n-body potential for fe-cr alloy system and its application to defect study. *Computational Materials Science* **14**(1-4), 108–113.
- Krakauer H and Freeman AJ 1979 Linearized augmented plane-wave method for the electronic band-structure of thin-films. *Physical Review* **19**(4), 1706–1719.
- Kumar K 1996 Plastic film capacitors (pfcs) a status report. *Electronics Information and Planning* **23**(10), 545–570.
- Landau LD and Lifshitz EM 1976 *Mechanics*. Pergamon Press, Oxford, England.
- Landau LD and Lifshitz EM 1980 *Statistical Physics*. Pergamon Press, Oxford, England.
- Landes J and Brown K 1998 Results from a round robin on a standard method for measurement of fracture toughness. *Journal of Testing and Evaluation* **26**(4), 396–403.
- La Paglia SR 1971 *Introductory Quantum Chemistry*. Harper and Row Publishers, New York.
- Lee IH, Kim SY and Jun S 2004a An introductory overview of action-derived molecular dynamics for multiple time-scale simulations. *Computer Methods in Applied Mechanics and Engineering* **193**(17-20), 1633–1644.
- Lee JY, Buxton GA and Balazs AC 2004b Using nanoparticles to create self-healing composites. *Journal of Chemical Physics* **121**(11), 5531–5540.
- Li S and Liu WK 2002 Meshfree and particle methods and their applications. *Applied Mechanics Review* **55**, 1.
- Li S and Liu WK 2002a. *Applied Mechanics Reviews* **55**, 1.
- Li S and Liu WK 2002b Meshfree and particle methods and their applications. *Applied Mechanics Review* **55**, 1–34.
- Li S and Liu WK 2004 *Meshfree Particle Methods*. Springer, Berlin, Germany.
- Li J, Lu Y, Ye Q, Cinke M, Han J and Meyyappan M 2003 Carbon nanotube sensors for gas and organic vapor detection. *Nano Letters* **3**(7), 929–933.
- Liang C and Rogers CA 1990 One-dimensional thermomechanical constitutive relations for shape memory materials. *Journal of Intelligent Material Systems and Structures* **1**(2), 207–234.
- Lide DR 2004 *CRC Handbook of Chemistry and Physics*. CRC Press, New York.
- Lieber CM 2003 Nanoscale science and technology: Building a big future from small things. *MRS Bulletin* **28**(7), 486–491.
- Lifshitz EM and Pitaevskii LP 1981 *Physical Kinetics*. Pergamon Press, Oxford, England.
- Liu WK 1981 Finite element procedures for fluid-structure interactions and application to liquid storage tanks. *Nuclear Engineering and Design* **65**, 221–238.
- Liu WK 1983 Development of mixed time partition procedures for thermal analysis of structures. *International Journal for Numerical Methods in Engineering* **19**, 125–140.

- Liu DM 1994 Bioactive glass-ceramic–formation, characterization and bioactivity. *Materials Chemistry and Physics* **36**(3-4), 294–303.
- Liu S Q (1998) Prevention of focal intimal hyperplasia in rat vein grafts by using a tissue engineering approach. *Atherosclerosis* **140**(2)365–377.
- Liu WK, Karpov E, Zhang S and Park H 2004a An introduction to computational nano mechanics and materials. *Computer Method in Applied Mechanics and Engineering* **193**(17-20), 1529–1578.
- Liu WK, Chen X, Wang X, Zhang Y, Bajaj C and Hughes TJR 2004b A study of a three-dimensional heart model using immersed continuum method. ICES Technical Report, ICES.
- Liu WK, Karpov EG, Zhang S and Park HS 2004c An introduction to computational nano mechanics and materials. *Computer Methods in Applied Mechanics and Engineering* **193**, 1529–1578.
- Liu WK, Han W, Lu H and Li S 2004d Reproducing Kernel Element Method, Part I Theoretical Formulation. *Computer Methods in Applied Mechanics and Engineering* **193**, 933–951.
- Liu Y, Zhang LT, Wang X and Liu WK 2004e Coupling of Navier-Stokes equations with protein molecular dynamics and its application to hemodynamics. *International Journal for Numerical Methods in Fluids* **46**, 1237–1252.
- Liu Y, Liu WK, Patankar and Belytschko T 2005a Immersed Electrohydrodynamics Finite Element Method. Preprint.
- Liu Y, Chung J, Liu WK and Ruoff R 2005b Dielectrophoretic assembly of nanowires. Preprint.
- Liu WK, Liu Y, Farrell D, Zhang L, Wang XS, Fukui Y, Patankar N, Zhang Y, Bajaj C, Lee J, Hong J, Chen X and Hsu H 2005c Immersed finite element method and its applications to biological systems. *Computer Methods in Applied Mechanics and Engineering*. Accepted.
- Liu WK, Sukky J and Qian D 2005d Computational nanomechanics of materials, in *Handbook of Theoretical and Computational Nanotechnology*, M. Reith and W. Schommers, Editors. American Scientific Publishers.
- Liu WK and Belytschko T 1982 Mixed-time implicit-explicit finite elements for transient analysis. *Computers and Structures* **15**, 445–450.
- Liu WK and Gvildys J 1986 Fluid-structure interaction of tanks with an eccentric core barrel. *Computer Methods in Applied Mechanics and Engineering* **58**, 51–77.
- Liu WK and Ma D 1982 Computer implementation aspects for fluid-structure interaction problems. *Computer Methods in Applied Mechanics and Engineering* **31**, 129–148.
- Liu WK, Belytschko T and Mani A 1986 Probabilistic finite-element method for nonlinear structural dynamics. *Computer Methods in Applied Mechanics and Engineering* **56**(1), 61–81.
- Liu WK, Besterfield GH and Belytschko T 1988 Variational approach to probabilistic finite-elements. *Journal of Engineering Mechanics-ASCE* **114**(12), 2115–2133.
- Liu WK, Chen Y, Uras RA and Chang CT 1996a Generalized multiple scale reproducing kernel particle methods. *Computer Methods in Applied Mechanics and Engineering* **139**, 91–158.
- Liu WK, Chen YJ, Belytschko T and Lua YJ 1996b Three reliability methods for fatigue crack growth. *Engineering Fracture Mechanics* **53**(5), 733–752.
- Liu WK, Jun S and Zhang YF 1995 Reproducing kernel particle methods. *International Journal for Numerical Methods in Fluids* **20**, 1081–1106.
- Liu WK, Uras R and Chen Y 1997 Enrichment of the finite element method with the reproducing kernel particle method. *Journal of Applied Mechanics* **64**, 861–870.
- Liu WK, Park HS, Qian D, Karpov EG, Kadowaki H, Wagner GJ (2005) Bridging scale methods for nanomechanics and materials. *Computer Methods in Applied Mechanics and Engineering*. In Print.
- Los JH and Fasolino A 2002 Monte Carlo simulations of carbon-based structures based on an extended brenner potential. *Computer Physics Communications* **147**(1-2), 178–181.
- Mayer JE and Mayer MG 1977 *Statistical Mechanics*. Wiley, New York.

- Mcdougall PG, Olson GB and Cohen M 1983 Interphase crystallography and interfacial structure. *Journal of Metals* **35**(12), 17–17.
- McQueen DM and Peskin CS 1997 Shared-memory parallel vector implementation of the immersed boundary method for the computation of blood flow in the beating mammalian heart. *The Journal of Supercomputing* **11**, 213–236.
- McVeigh C and Liu W 2005 Prediction of central bursting during axisymmetric cold extrusion of a metal alloy containing particles. *International Journal of Solids and Structures*. In print.
- McVeigh C, Vernerey F, Liu W and Brinson L 2005 Multiresolution analysis for material design. *Computer Methods in Applied Mechanics and Engineering*. Accepted.
- Medyanik S, Karpov E and Liu W 2005 Domain reduction method for atomistic simulations. Preprint.
- Mehl MJ and Papaconstantopoulos DA 1996 Applications of a tight-binding total-energy method for transition and noble metals: Elastic constants, vacancies, and surfaces of monatomic metals. *Physical Review* **54**(7), 4519–4530.
- Mezei M and Beveridge DL 1986 Free energy simulations. *Annals of the New York Academy of Sciences* **482**(1), 1–23.
- Miller RE and Tadmor EB 2003 The quasicontinuum method: Overview, applications and current directions. *Journal of Computer-Aided Materials Design* **9**, 203–239.
- Miller RE, Tadmor EB, Phillips R and Ortiz M 1998 Quasicontinuum simulation of fracture at the atomic scale. *Modelling and Simulation in Materials Science and Engineering* **6**(5), 607–638.
- Miranda CR, Antonelli A, da Silva AJR and Fazzio A 2004 Vacancy-like defects in a-si: A first principles study. *Journal of Non-Crystalline Solids* **338**(40), 400–402.
- Mitchison TJ and Cramer LP 1996 Actin-based cell motility and cell locomotion. *Cell* **84**(3), 371–379.
- Mogilner A and Oster G 1996 Cell motility driven by actin polymerization. *Biophysical Journal* **71**(6), 3030–3045.
- Moon BY, Kang GJ, Kang BS and Cho DS 2004 Dynamic and reliability analysis of stochastic structure system using probabilistic finite element method. *Structural Engineering and Mechanics* **18**(1), 125–135.
- Moran B and Shih F 1987a Crack tip and associated domain integrals from momentum and energy-balance. *Engineering Fracture Mechanics* **27**(6), 615–642.
- Moran B and Shih F 1987b A general treatment of crack tip contour integrals. *International Journal of Fracture* **35**(4), 295–310.
- Moran B, Asaro RJ and Shih CF 1991 Effects of material rate sensitivity and void nucleation on fracture initiation in a circumferentially cracked bar. *Metallurgical Transactions A* **22**(1), 161–170.
- Mueller M 2001 *Fundamentals of Quantum Chemistry*. Kluwer Academic/Plenum Publisher, New York.
- Naslain R, Guette A, Rebillat F, Pailler R, Langlais F and Bourrat X 2004 Boron-bearing species in ceramic matrix composites for long-term aerospace applications. *Journal of Solid State Chemistry* **177**(2), 449–456.
- Neu B and Meiselman HJ 2002 Depletion-mediated red blood cell aggregation in polymer solutions. *Biophysical Journal* **83**, 2482–2490.
- Nosé S 1984a A molecular dynamics method for simulations in the canonical ensemble. *Molecular Physics* **53**, 255–268.
- Nosé S 1984b A unified formulation of the constant temperature molecular dynamics methods. *Journal of Chemical Physics* **81**(1), 511–519.
- NRL 2002 DoD planewave: a general scalable density functional code.
- Oberhettinger F and Badii L 1973 *Tables of Laplace Transforms*. Springer-Verlag, Berlin, Germany.
- Odegard GM, Gates TS, Wise KE, Park C and Siochi EJ 2003 Constitutive modeling of nanotube-reinforced polymer composites. *Composites Science and Technology* **63**(11), 1671–1687.

- Odegard G, Gates T, Nicholson LM and Wise KE 2002 Equivalent-continuum modeling of nanostructured materials. *Composites Science and Technology* **62**(14), 1869–1880.
- Olson GB and Hsieh KC 2002 Hsieh, Technical Report, Department of Materials Science and Engineering, Northwestern University.
- Papaconstantopoulos DA and Mehl MJ 1997 The tight-binding method for interpolating first-principles total energy results. *Journal of Phase Equilibria* **18**(6), 593–597.
- Park HS and Liu WK 2004 Introduction and tutorial on multiple scale analysis in solids. *Computer Methods in Applied Mechanics and Engineering* **193**, 1733–1772.
- Park HS and Zimmerman JA 2005 Modeling inelasticity and failure in gold nanowires. *Physical Review B* **72**, 054106.
- Park HS, Karpov EG and Liu WK 2004 A temperature equation for coupled atomistic/continuum simulations. *Computer Methods in Applied Mechanics and Engineering* **193**, 1713–1732.
- Park HS, Karpov EG and Liu WK 2005a Non-reflecting boundary conditions for atomistic, continuum and coupled atomistic/continuum simulations. *International Journal for Numerical Methods in Engineering* **64**(2), 237–259.
- Park HS, Karpov EG, Klein PA and Liu WK 2005b Three-dimensional bridging scale analysis of dynamic fracture. *Journal of Computational Physics* **207**, 588–609.
- Park HS, Karpov EG, Liu WK and Klein PA 2005c The bridging scale for two-dimensional atomistic/continuum coupling. *Philosophical Magazine* **85**(1), 79–113.
- Passerone D and Parrinello M 2001 Action-derived molecular dynamics in the study of rare events. *Physical Review Letters* **87**(10), 108302.
- Passerone D and Parrinello M 2003 A concerted variational strategy for investigating rare events. *Journal of Chemical Physics* **118**(5), 2025–2032.
- Pathria RK 1996 *Statistical Mechanics*. Butterworth-Heinemann, Oxford, England.
- Peskin C 2002 The immersed boundary method. *Acta Numerica* **11**, 479–517.
- Peskin CS 1977 Numerical analysis of blood flow in the heart. *Journal of Computational Physics* **25**, 220–252.
- Peskin CS and McQueen DM 1989 A three-dimensional computational method for blood flow in the heart. I. Immersed elastic fibers in a viscous incompressible fluid. *Journal of Computational Physics* **81**(2), 372–405.
- Peskin CS and McQueen DM 1993 Computational biofluid dynamics. *Contemporary Mathematics* **141**, 161–186.
- Qian D and Gondhalekar RH 2004 A Virtual Atom Cluster approach to the mechanics of nanostructures. *International Journal for Multiscale Computational Engineering* **2**(2), 277–289.
- Qian D and Liu WK 2004 A cluster model for integrating quantum-mechanical descriptions at multiple length scales. In Preparation.
- Qian D, Wagner GJ and Liu WK 2004 A multiscale projection method for the analysis of carbon nanotubes. *Computer Methods in Applied Mechanics and Engineering* **193**, 1603–1632.
- Qian D, Wagner GJ, Liu WK, Yu MF and Ruoff RS 2002 Mechanics of carbon nanotubes. *Applied Mechanics Reviews* **55**(6), 495–533.
- Rabuffi M and Picci G 2002 Status quo and future prospects for metallized polypropylene energy storage capacitors. *IEEE Transactions on Plasma Science* **30**(5), 1939–1942.
- Ratner MA and Schatz GC 2001 *Introduction to Quantum Mechanics in Chemistry*. Prentice Hall, Upper Saddle River, NJ.
- Rice JR 1992 Dislocation nucleation from a crack tip –an analysis based on the peierls concept. *Journal of the Mechanics and Physics of Solids* **40**(2), 239–271.
- Rice JR and Tracey DM 1969 On the ductile enlargement of voids in triaxial stress field. *Journal of the Mechanics and Physics of Solids* **17**, 2–15.

- Rosenblum I, Adler J and Brandon S 1999 Multi-processor molecular dynamics using the brenner potential: Parallelization of an implicit multi-body potential. *International Journal of Modern Physics C* **10**(1), 189–203.
- Rudd RE 2001 Coarse-grained molecular dynamics: Dissipation due to internal modes. *Materials Research Society Symposium Proceedings*, **695** Boston, MA **695**.
- Rudd RE and Broughton JQ 1998 Coarse-grained molecular dynamics and the atomic limit of finite elements. *Physical Review B* **58**, 5893–5896.
- Saad Y and Schultz MH 1986 GMRES: A generalized minimal residual algorithm for solving non-symmetric linear systems. *SIAM Journal on Scientific and Statistical Computing* **7**(3), 856–869.
- Saether E, Frankland S and Pipes R 2003 Transverse mechanical properties of single-walled carbon nanotube crystals. Part I: Determination of elastic moduli. *Composites Science and Technology* **63**(11), 1543–1550.
- Sanders PG, Youngdahl CJ and Weertman JR 1997 The strength of nanocrystalline metals with and without flaws. *Materials Science and Engineering a-Structural Materials Properties Microstructure and Processing* **234**, 77–82.
- Sastry S and Burridge K 2000 Focal adhesions: A nexus for intracellular signaling and cytoskeletal dynamics. *Experimental Cell Research* **261**, 25–36.
- Saxena A 1991 Creep crack-growth in high-temperature ductile materials. *Engineering Fracture Mechanics* **40**(4–5), 721–736.
- Schwalbe KH 1977 Influence of microstructure on crack-propagation mechanisms and fracture toughness of metallic materials. *Engineering Fracture Mechanics* **9**(4), 795–832.
- Sellars CM and Zhu Q 2000 Microstructural modeling of aluminium alloys during thermomechanical processing. *Materials Science and Engineering A* **280**, 1–7.
- Sharma N and Patankar NA 2004 Direct numerical simulation of the Brownian motion of particles by using fluctuating hydrodynamic equations. *Journal of Computational Physics* **201**(2), 466–486.
- Sheetz MP, Felsenfeld D, Galbraith CG and Choquet D 1999 Cell migration as a five-step cycle. *Cell Behaviour: Control and Mechanism of Motility* **65**, 233–243.
- Shilkrot LE, Curtin WA and Miller RE 2002 A coupled atomistic/continuum model of defects in solids. *Journal of the Mechanics and Physics of Solids* **50**, 2085–2106.
- Shilkrot LE, Miller RE and Curtin WA 2004 Multiscale plasticity modeling: coupled atomistics and discrete dislocation mechanics. *Journal of the Mechanics and Physics of Solids* **52**, 755–787.
- Shimamoto A, Nam J, Oguchi T and Azakami T 2001 Effect of crack closure by shrinkage of embedded shape-memory tini fiber epoxy composite under mixed-mode loading. *International Journal of Materials and Product Technology* (Suppl. 1), 263–268. .
- Shinya N, Kyono J and Laha K 2003 Improvement of creep rupture properties of heat resisting steels by the self-heating of creep cavities. *Materials Science Forum* **426**(4), 1107–1112.
- Slater JC 1937 Wave functions in a periodic potential. *Physical Review* **51**, 846–851.
- Slater JC and Koster GF 1954 Simplified LCAO method for the periodic potential problem. *Physical Review* **94**, 1498.
- Smith GS, Tadmor EB and Kaxiras E 2000 Multiscale simulation of loading and electrical resistance in silicon nanoindentation. *Physical Review Letters* **84**, 1260.
- Solomentsev Y, Bohmer M and Anderson J 1997 Particle clustering and pattern formation during electrophoretic deposition: A hydrodynamic model. *Langmuir* **13**, 6058–6068.
- SRIC-BI 2004 *Next-Generation Technologies: Self-Repairing Structural Materials*. www.sric-bi.com.
- Stillinger FH and Weber TA 1985 Computer simulation of local order in condensed phases of silicon. *Physical Review B* **31**(8), 5262–5271.
- Stossel T 1993 On the crawling of animal cells. *Science* **260**(5111), 1086–94.
- Strothman J 2002 Self-healing materials for aircraft. *Instrumentation Technology* **49**(9), 16.

- Suda A and Shinohara T 2002 Effects of colloidal silica addition on the self-healing function of chromate coatings. *ISIJ International* **42**(5), 540–544.
- Sutton MA, Yang B, Reynolds AP and Taylor R 2002 Microstructural studies of friction welds in 2024-t3 aluminum. *Materials Science and Engineering* **A323**, 160–166.
- Tadmor E, Ortiz M and Phillips R 1996 Quasicontinuum analysis of defects in solids. *Philosophical Magazine A* **73**, 1529–1563.
- Tahoe 2004 <http://tahoe.ca.sandia.gov>.
- Takai T, Halicioglu T and Tiller WA 1985 Prediction for the pressure and temperature phase transitions of silicon using a semiempirical potential. *Scripta Metallurgica* **19**(6), 709–713.
- Tanaka KS, Kobayashi S and Sato Y 1986 Thermomechanics of transformation pseudoelasticity and shape memory effect in alloys. *International Journal of Plasticity* **2**(1), 59–72.
- Taylor CA, Hughes TJR and Zarins C 1998 Finite element modeling of blood flow in arteries. *Computer Methods in Applied Mechanics and Engineering* **158**, 155–196.
- Terletskii YP 1971 *Statistical Physics*. North-Holland Publishing, Elsevier, Amsterdam, NY.
- Tersoff J 1986 New empirical model for the structural properties of silicon. *Physical Review Letters* **56**(6), 632–635.
- Tersoff J 1988a Empirical interatomic potential for carbon, with applications to amorphous carbon. *Physical Review Letters* **61**(25), 2879–2882.
- Tersoff J 1988b New empirical approach for the structure and energy of covalent systems. *Physical Review B* **37**(12), 6991–7000.
- Tezduyar T 1992 Stabilized finite element formulations for incompressible-flow computations. *Advances in Applied Mechanics* **28**, 1–44.
- Tezduyar T 2001 Finite element methods for flow problems with moving boundaries and interfaces. *Archives of Computational Methods in Engineering* **8**(2), 83–130.
- Thomas LH 1927 The calculation of atomic fields. *Proceedings of the Cambridge Philological Society* **23**, 542–548.
- Tohyama N, Kim BN, Enoki M and Kishi T 1998 Oxidation behavior of si-ti-c-o fiber-bonded-ceramics. *Fracture and Strength of Solids, Pts 1 and 2: Key Engineering Materials* **145**(9), 919–924.
- Tvgaard V and Hutchinson JW 1982 On localization in ductile materials containing spherical voids. *International Journal of Fracture* **18**, 237–252.
- van der Giessen E and Needleman A 1995 Discrete dislocation plasticity: A simple shear model. *Modelling and Simulation in Materials Science and Engineering* **3**, 689–735.
- Vernerey F, Liu W and Moran B 2005 Continuum theory for multi-scale micromorphic materials. Preprint.
- Voter AF 1997 Hyperdynamics: Accelerated molecular dynamics of infrequent events. *Physical Review Letters* **78**(20), 3908–3911.
- Voter AF, Montalenti F and Germann TC 2002 Extending the time scale in atomistic simulation of materials. *Annual Review of Materials Research* **32**, 321–346.
- Wagner GJ and Liu WK 2001 Hierarchical enrichment for bridging scales and meshfree boundary conditions. *International Journal for Numerical Methods in Engineering* **50**, 507–524.
- Wagner GJ and Liu WK 2003 Coupling of atomistic and continuum simulations using a bridging scale decomposition. *Journal of Computational Physics* **190**, 249–274.
- Wagner GJ, Ghosal S and Liu WK 2003 Particulate flow simulations using lubrication theory solution enrichment. *International Journal for Numerical Methods in Engineering* **56**(9), 1261–1289.
- Wagner GJ, Karpov EG and Liu WK 2004 Molecular dynamics boundary conditions for regular crystal lattices. *Computer Methods in Applied Mechanics and Engineering* **193**, 1579–1601.

- Wagner GJ, Moës N, Liu WK and Belytschko TB 2001 The extended finite element method for rigid particles in stokes flow. *International Journal for Numerical Methods in Engineering* **51**(3), 293–313.
- Walther J, Jaffe R, Halicioglu T and Koumoutsakos P 2001 Carbon nanotubes in water: Structural characteristics and energetics. *Journal Of Physical Chemistry* **105**(41), 9980–9987.
- Walther J, Jaffe R, Kotsalis E, Werder T, Halicioglu T and Koumoutsakos P 2004 Hydrophobic hydration of c-60 and carbon nanotubes in water. *Carbon* **42**(5-6), 1185–1194.
- Wang X 2003 On the discretized delta function and force calculation in the immersed boundary method In *Computational Fluid and Solid Mechanics* (ed. Bathe KJ), Elsevier, pp. 2164–2169.
- Wang NT and Fogelson A 1999 Computational methods for continuum models of platelet aggregation. *Journal of Computational Physics* **151**, 649–675.
- Wang X and Liu WK 2004 Extended immersed boundary method using FEM and RKPM. *Computer Methods in Applied Mechanics and Engineering* **193**(12–14), 1305–1321.
- Wang PT, Van Geertruyden WH and Misiolek WZ 2003 *Proceedings from ASM Materials Solutions 2003 Conference & Exposition*, Pittsburgh, PA pp. 199–208.
- Weeks WT 1966 Numerical inversion of laplace transforms using Laguerre functions. *Journal of the Association for Computing Machinery* **13**(3), 419–429.
- Westwood ME, Webster JD, Day RJ, Hayes FH and Taylor R 1996 Oxidation protection for carbon fiber composites. *Journal of Materials Science* **31**(6), 1389–1397.
- White SR, Sottos NR, Geubelle PH, Moore JS, Kessler MR, Sriram S, Brown EN and Viswanathan S 2001 Autonomic healing of polymer composites. *Nature* **409**, 794–797.
- Wimmer E, Weinert HKM and Freeman AJ 1981 Full-potential self-consistent linearized-augmented-plane-wave method for calculating the electronic-structure of molecules and surfaces –o2 molecule. *Physical Review B* **24**(2), 864–875.
- Xiao SP and Belytschko T 2004 A bridging domain method for coupling continua with molecular dynamics. *Computer Methods in Applied Mechanics and Engineering* **193**, 1645–1669.
- Xu CH, Wang CZ, Chan CT and Ho KM 1992 A transferable tight-binding potential for carbon. *Journal of Physics –Condensed Matter* **4**, 6047.
- Yang P 2005 The chemistry and physics of semiconductor nanowires. *MRS Bulletin* **30**(2), 85–91.
- Zhang LT, Wagner GJ and Liu WK 2002 A parallelized meshfree method with boundary enrichment for large-scale CFD. *Journal of Computational Physics* **176**, 483–506.
- Zhang LT, Gerstenberger A, Wang X and Liu W 2004 Immersed finite element method. *Computer Methods in Applied Mechanics and Engineering* **193**(21–22), 2051–2067.
- Zhou BL 1998 Improvement of mechanical properties of materials by biomimetic treatment. *Fracture and Strength of Solids, Pts 1 and 2: Key Engineering Materials* **145**(9), 765–773.
- Zhu YTT and Beyerlein IJ 2002 Bone-shaped short fiber composites –an overview. *Materials Science and Engineering a-Structural Materials Properties Microstructure and Processing* **326**(2), 208–227.
- Zhu YTT and Beyerlein IJ 2003 Issues on the design of bone-shaped short fiber composites. *Advanced Materials* **35**(2), 51–60.
- Zhu YTT, Beyerlein IJ, Valdez JA and Lowe TC 2001 Fracture toughness of a composite reinforced with bone-shaped short fibers. *Materials Science and Engineering A* **317**(1-2), 93–100.
- Zimmerman JA, Gao H and Abraham FF 2000 Generalized stacking fault energies for embedded atom fcc metals. *Modelling and Simulation in Materials Science and Engineering* **8**, 103–115.

Index

- K*-matrix, 46
diatomic chain, 48
EAM potential, 297
fcc lattice, 73
hexagonal lattice, 49
monoatomic chain, 47
N-scale material, 230
- acoustic frequency, 55
adiabatic approximation, 43
adiabatic system, 81
advanced materials, 225
amount of substance, 83
angular momentum, 12
associate cell, 44
associate substructure, *see* associate cell
atomic force constant, 16, 46
austenite phase, 246
autocorrelation function, 14
Avogadro number, 83
- barometric formula, 107
Berendsen equation, 116
binomial coefficient, 87
biomimicry, 244
blood plasma, 276
Boltzmann constant, 83
Boltzmann distribution, 106
Boltzmann equation, 87
bond length, 21
bond stiffness, 16
bond-order functions, 25
boundary condition operator, 69
boundary value problem, 62, 63
Brenner potential, *see* potential
- bridging scale, 131
coarse scale, 132
comparison to other multiple scale methods, 173
fine scale, 132
future research directions, 220
governing equations, 172
impedance force (1D), 142
impedance force (3D), 148, 172
Lagrangian, 133
numerical examples, 176
1D wave propagation, 176
1D wave propagation
(non-nearest neighbor potential), 212
2D dynamic fracture, 187
2D wave propagation, 184
3D dynamic fracture, 195
numerical implementation
coupling force, 151
impedance force, 150
random force (1D), 142
staggered time integration, 170
- Brownian motion, 13
- canonical distribution, 97, 101
ideal gas, 103
periodic lattice, 109
canonical ensemble, 101
carbon nanotube (CNT), 29, 202, 287
bending and buckling, 200
- Cauchy–Born rule, 127
bridging scale, 158
quasi-continuum (QC) method, 127

- Cauchy–Born rule (*continued*)
 comparison to virtual atom cluster
 method, 178
- central field, 13
- characteristic stiffness, 108
- CNT, *see* carbon nanotube
- collision diameter, 22
- composite material, 246
- compressibility, 82, 84, 90
- concentration, 107
- constraints, 8
 holonomic, 8
 nonholonomic, 8
- coordinate, 8
 generalized, 8
- Coulomb potential, *see* potential
- crystal lattice, 23, 37
- crystal plane, 42
- crystallographic axis, 42
- cubic lattice, 39
- cutoff function, 24
- cutoff radius, 23
- damping kernel, *see* time history
 kernel
- Debye layer, 284
- decohesion energy, 238
- deterministic method, 259
- dielectrophoresis (DEP), 283
 driving force, 283, 284
 positive and negative DEP, 283
- diffusion constant, 96
- Dirac delta function, 51
- discrete Fourier transform, 53
 convolution theorem, 54
 numerical inversion, 54
- dislocation energy, 22
- dispersion branch, 55
- dispersion law, 55
- drift of particle, 96
- ductile fracture simulator, 240
- Einstein model, 110
- electric charge, 20
- electric displacement, 282
- electric permittivity, 282
- electric potential, 282
- electro-manipulation, 283
- dielectrophoresis, 283
- electroosmosis, 284
- electrophoresis, 283
 driving force, 284
- electron cloud, 21
- electron-volt, 22
- electroosmotic flow, *see* electroosmosis
- elementary cell, 38
- elementary charge, e_0 , 20
- elimination of degrees of freedom, 69
- embedded atom potential, *see* potential
- embedding energy function, 26
- energy
 potential energy, 9
 energy fluctuation, 101
 ensemble average, 94
 enthalpy, 85, 89
 entropy, 86, 96
 ideal gas, 100
 microcanonical ensemble, 98
 probabilistic interpretation, 87
- equation of motion
 diatomic chain, 48
 free 1D lattice, 120
 free lattice, 54
 general lattice, 46
 Hamilton, 92
 hexagonal lattice, 49
 Lagrange, 10
 Newtonian, 13
- equation of state
 ideal gas, 83, 101
 in thermodynamics, 82
- equilibrium bond length, *see* bond length
- ergodic hypothesis, 95
- ergodic system, 95
- Fahraeus–Lindqvist effect, 280
- fcc lattice, 39
- field strength, 282
- finite difference equation, 46
- finite elements, 123
- first-principles calculation, 236
- fluctuation, 80
- fluctuation-dissipation theorem, 113
- fluid–structure interaction, 29 265

- force, 7
 conservative, 8
 external, 7
 generalized, 10
 internal, 7
 nonconservative, 8, 11
 dissipative, 9
 gyroscopic, 9
- Fourier transform, 50
- fracture toughness simulation, 239
- frame invariance principle, 10, 12
- free energy, 89, 91, 96
 mechanical interpretation, 91
- free lattice, 54
- functional transform, 49
- gas-structure interaction, 29
- Gauss theorem, 282
- generalized coordinate, *see* coordinate
- generalized Langevin equation, 14
- generalized momentum, 92
- generalized strain, 230
- generalized stress, 230
- generalized velocity, *see* velocity
- Gibbs canonical distribution, *see*
 canonical distribution
- Gibbs potential, 89, 91
- granular material, 232
- Green's function, 59
 dynamic, 60
 monoatomic chain lattice, 65
 quasi-static, 67
- Green's function method, 59
- Hamilton function, *see* Hamiltonian
- Hamiltonian, 91, 92
 ideal gas, 99
 periodic lattice, 108
- handshake region, 68
- harmonic approximation, 46
- heat bath, 101, 102
 Berendsen thermostat, 112
 Hoover-Nosé method, 118
 numerical techniques, 111
 phonon method, 119
- heat capacity, 84, 90
 numerical calculation, 90
- periodic lattice, 110
- heat conductivity, 96
- Heaviside step function, 99
- hierarchical modeling, 234, 237, 240
- IB method, *see* immersed boundary
 method
- ideal gas, 99, 103
- IFEM, *see* immersed finite element
 method
- immersed boundary method, 264
- immersed finite element method (IFEM),
 263, 265
- impedance boundary conditions, 146
- impedance force, 146
- indentation, 31
- initial-value problem, 62
- integral of motion, 12
- integral transform, 50
- interaction between scales, 231
- interatomic potential, *see* potential
- internal energy, 89, 96, 98
 periodic lattice, 110
- inverse transform, 50
- isothermal system, 80, 91, 101
- kinematic constraints, 268
- kinetic energy, 10
 distribution, 105
- kinetic Monte Carlo method, 259
- Kronecker delta, 53
- Lagrange equation, 10
 conservative systems, 10
 nonconservative systems, 10
- Lagrange function, *see* Lagrangian
- Lagrangian, 10
 in Cartesian coordinates, 11
 in generalized coordinates, 11
 periodic lattice, 45
- Langevin equation, 13, 14
 stochastic force, 14
- Langevin particle, 14
- Laplace transform, 51
 convolution theorem, 51
 numerical inversion, 52
 time-derivative rule, 51

- lattice mechanics, 37, 137
 relationship to finite elements, 139
 lattice origin vector, 38
 lattice potential energy, 43
 lattice site index, 43
 lattice site vector, 38
 lattice standing waves, 56
 lattice stiffness matrix, 175
 1D Lennard-Jones, 176
 3D fcc lattice/EAM gold, 297
 lattice symmetry, 37
 lattice thermal vibration, 110
 Lennard–Jones potential, 22
 linear transform, 50
 Liouville theorem, 94
 local environment potential, *see*
 potential
 long-range interaction, 21
 martensite phase, 246
 material design, 223, 233, 234
 properties vs. microstructure, 223
 self-healing composites, 254
 Maxwell equations, 281
 Maxwell stress tensor, 284
 Maxwell–Boltzmann distribution, 105
 mean free path, 96
 mean square force, 96
 mechanical system, *see* system
 mechanisms of self-healing, 247
 microcanonical distribution, 97
 microcanonical ensemble, 97
 micromorphic material, *see* multiscale
 material
 molar heat capacity, 84
 molecular dynamics, 7, 28, 123
 evaluation of thermodynamic
 parameters, 96
 simulation, 7
 visualization, 28
 momentum, 12
 distribution, 104
 monocrystal, 37
 Morse potential, 22
 multiple scale methods, xi, 124
 bridging domain, 129
 bridging scale, 131
 coarse-grained molecular dynamics
 (CGMD), 126
 coupled atomistic discrete
 dislocation (CADD), 128
 macroscopic atomistic ab initio
 dynamics (MAAD), 124
 quasi-continuum (QC) method, 126
 multiresolution constitutive law, 231
 multiresolution framework, 227
 multiscale boundary conditions, 69
 multiscale equations of motion, 143
 multiscale internal power, 230
 multiscale material, 227
 multiscale simulation, 68
 nano-electromechanical system, 290
 nanodeposition, 33
 nanoindentation, 31, 71
 nanomanipulation, 283
 nanomechanics, xi
 Nernst's postulate, *see* third law of
 thermodynamics
 Newton equation, 13
 dissipative system, 13
 nondeterministic method, 259
 normal amplitude, 17, 56
 normal coordinate, 16, 17
 normal frequencies, 56
 normal frequency, 17, 55, 108
 normal mode, 17, 56, 108
 mean energy, 109
 one-particle distribution, 104
 optical frequency, 55
 pair-wise potential, *see* potential
 partition function, 92, 102
 ideal gas, 103
 periodic lattice, 110
 periodic cell model, 240
 permittivity constant, ϵ_0 , 21
 phase point, 93
 phase space, 93
 phase space integral, 98
 phase trajectory, 93
 phase vector, 93
 phonon, 109

- phonon gas, 109
point symmetry, 37
Poisson equation, 282
polarization vector, 56, 282
polycrystal, 37
polymer chain, *see* polymers
polymers, 37
polytropic process, 85
porous materials, 227
postprocessing, 92
potential, 7, 9
 Brenner, 26
 Coulomb, 21
 cutoff radius, 23
 embedded atom, 26
 interatomic, 18
 Lennard-Jones, 22
 local environment, 25
 Morse, 22
 multibody, 18
 skin, 25
potential barrier, 19
potential well, 19
pressure, 96, 98
pressure coefficient, 83, 89, 90
probabilistic FEM, 260
pseudoelasticity, 248
quantity of heat, 84
quasi-static approximation, 66
 in thermodynamics, 81
quasi-static process, 81
RBC, *see* red blood cell
red blood cell (RBC), 5, 266,
 275–279
regular lattice, 37
relaxation, 81
representative volume element,
 228
second law of thermodynamics,
 86
self-healing material, 244
serial coupling, 226
shape-memory alloy, 246
 constitutive law, 250
shape-memory composite, 248
spring-mass oscillator, 98, 108
state equation, *see* equation of state
state function, 80, 89
state vector
 in Hamiltonian mechanics, 93
 in Lagrangian mechanics, 11
 in thermodynamics, 82
statistical ensemble, 93, 97, 101
statistical mechanics, 79
 systems in thermodynamic
 equilibrium, 92
statistical weight of a microstate,
 87
Stirling's formula, 88
Stokes' friction, *see* viscous friction
superelasticity, 248
symmetric field, 12
system
 closed, *see* isolated
 conservative, 12
 constrained, 8
 isolated, 8
 nonconstrained, 8, 10
 nonisolated, 8
system nonconstrained, 10
temperature, 81, 96
 ideal gas, 100
 microcanonical ensemble, 98
thermal expansion coefficient, 84, 89
thermal vibration, 54
thermodynamic equilibrium, 80
thermodynamic parameter, 79, 96, 97,
 101
 internal or external, 82
 state parameter, 80, 90
 system parameter, 80, 90
thermodynamic potential, *see* state
 function
thermodynamic system, 81
 isolated, 81, 97
 nonisolated, 81
thermodynamics, 79
 fundamental equation, 86
thermostat, *see* heat bath
third law of thermodynamics, 89

- time average, 95
time history, 9
time history kernel, 14, 64, 142
 1D chain/Lennard-Jones, 175
 2D hexagonal
 lattice/Lennard-Jones, 154
 3D FCC/Lennard-Jones, 156
 comparison to previous methods,
 152
 extension to non-nearest neighbors,
 203
 monoatomic chain lattice, 66
 programming flowchart, 157
 truncation for numerical simulation,
 179
time history damping kernel, *see* time
 history kernel
toughening effect, 243
trajectory, 7, 11
transformation equation, 8
translation vector, 38
translational symmetry, 37
uniform distribution, 109
unit cell, 43
van der Waals equation, 83
velocity
 distribution, 105
 generalized, 8
 mean values, 105
virtual atom cluster (VAC) method, 159
 comparison to Cauchy–Born rule,
 178
viscosity, 96
viscous friction, 13
volume expansion coefficient, 82
wall function, 19
zeta potential, 284